Advanced
Nondestructive Evaluation II

Proceedings of the International Conference on ANDE 2007
Volume 1

The 2nd International Conference on
Advanced Nondestructive Evaluation

ANDE
Since2005

ANDE 2007

Editors

Seung-Seok Lee
Joon Hyun Lee · Ik-Keun Park
Sung-Jin Song · Man-Yong Choi

Advanced
Nondestructive Evaluation II

Proceedings of the International Conference on ANDE 2007

Editors

Seung-Seok Lee

Korea Research Institute of Standards & Science, Korea

Joon Hyun Lee • Ik-Keun Park

Pusan National University, Korea
Seoul National University of Technology, Korea

Sung-Jin Song • Man-Yong Choi

Sungkyunkwan University, Korea
Korea Research Institute of Standards & Science, Korea

World Scientific

ADVANCED NONDESTRUCTIVE EVALUATION II
(In Two Volumes, with CD-ROM)
Proceedings of the International Conference on ANDE 2007

COMMITTEES

PREFACE

This volume includes the papers presented for the 2nd International Conference on Advanced Nondestructive Evaluation (The 2nd ANDE) held in Busan, Korea, 17-19 October, 2007. The aim of the conference is to discuss the current state of nondestructive technologies, which are rapidly progressing by integrating emerging technologies in the various fields.

Of the 583 papers presented at the conference, 240 manuscripts were included in this Volume. We believe that this proceedings volume includes many of the excellent papers presented at the 2nd International Conference on Advanced Nondestructive Evaluation.

Various technical sessions were scheduled that should be noted for both the advances made and the high technical interest shown. There are twenty six organized sessions in Aging and Degradation, Bio and Medical NDE, Composite Materials and Structures, Fatigue and Fracture, Guided Wave, Health Monitoring of Structure, Image Processing, IR Thermography, Materials Properties, Micro Sensor and MEMS, Modeling and Simulation, NDE for Biosytem and Agriculture, NDE in Electronic Industry, NDE in Materials Processing, NDT for Infrastructure, NDT in Nuclear Industry, NDT in Power Plant, Neutron Radiography, New Methods and Devices, Nonlinear Phenomenon, Optical Methods, Railways, Reliability, Signal Processing, Smart Structure and System, and Vibration.

We are grateful to all the members of the committee who have contributed with their invaluable experience and suggestions. We would like to thank all of the sponsoring institutions, organizations and companies which have supported the 2nd ANDE 2007 both financially and otherwise.

Finally, the organizers appreciate the support and contributions of the individuals whose efforts and participation were essential to the successful conference.

CONTENTS

Part 1

SECTION 1 : AGING & DEGRADATION

SECTION 2 : BIO & MEDICAL NDE

CONTENTS

SECTION 3 : COMPOSITE MATERIALS & STRUCTURES

SECTION 4 : FATIGUE & FRACTURE

SECTION 5 : GUIDED WAVE

SECTION 6 : HEALTH MONITORING OF STRUCTURE

SECTION 7 : IMAGE PROCESSING

SECTION 8 : IR THERMOGRAPHY

SECTION 9 : MATERIALS PROPERTIES

SECTION 10 : MICRO SENSOR AND MEMS

SECTION 11 : MODELING AND SIMULATION

SECTION 12 : NDE FOR BIOSYSTEM AND AGRICULTURE

SECTION 13 : NDE IN ELECTRONIC INDUSTRY

SECTION 14 : NDT FOR INFRASTRUCTURE

SECTION 15 : NDT IN NUCLEAR INDUSTRY

SECTION 16 : NDT IN POWER PLANT

SECTION 17 : NEUTRON RADIOGRAPHY

SECTION 18 : NEW METHODS AND DEVICES

SECTION 19 : NONLINEAR PHENOMENON

SECTION 20 : OPTICAL METHOD

SECTION 23 : SIGNAL PROCESSING

SECTION 24 : SMART STRUCTURE & SYSTEM

SECTION 25 : VIBRATION

STATOR INSULATION QUALITY ASSESSMENT FOR HIGH VOLTAGE MOTORS BASED ON PROBABILITY DISTRIBUTIONS

HEE-DONG KIM, CHUNG-HYO KIM

KEPCO Korea Electric Power Research Institute, 103-16 Munji-dong, Yuseong-gu, Daejeon 305-380, Korea

Stator insulation quality assessment for high voltage motors is a major issue for reliable maintenance of industrial and power plants. To assess the condition of stator insulation, nondestructive tests are performed on the sixty coil groups of twelve motors. The stator winding of each motor is classified into five coil groups; one group with healthy insulation and four groups with four different types of artificial defects. To analyze the breakdown voltage statistically, Weibull distribution is employed for the tests on the fifty coil groups of ten motors. The 50th percentile values of the measured breakdown voltages based on the statistical data of the five coil groups of ten motors were 26.1kV, 25.0kV, 24.4kV, 26.7kV and 30.5kV, respectively. Almost all of the failures were located in the line-end coil at the exit of the core slot. The breakdown voltages and the types of defects are strongly related to the stator insulation tests such as the dissipation factor and ac current. It is shown that the condition of the motor insulation can be determined from the relationship between the probability of failure and the type of defect.

1. Introduction

Industrial surveys and other studies on machine reliability show that the winding insulation is the most vulnerable component in high voltage (HV) rotating and stationary electric machines [1,2]. Since the insulation of the electric machine windings is continuously exposed to a combination of thermal, electrical, mechanical, and environmental stresses during operation, the insulation material deteriorates gradually over time. Thermal stress causes formation of voids in the mica barrier, weak bonding between layers, and delamination. Electrical and mechanical stresses also contribute to formation of voids in the insulation, and environmental stress causes rupture of the chemical bonds. The synergistic effect of the stresses causes gradual deterioration of stator winding insulation, which leads to eventual electrical failure.

There are many different types of nondestructive and destructive tests used for evaluating the degree of insulation degradation in HV motors. Nondestructive tests include measurements of insulation resistance, ac current, capacitance, dissipation factor (tanδ), and partial discharge (PD). To assess the

insulation condition in power plants, periodic nondestructive tests must be performed in HV motors [3,4]. Destructive testing of the stator winding can be conducted by gradually increasing ac voltage until the insulation fails. Analysis of breakdown voltage is considered a more sensitive indicator and a more reliable way of estimating insulation deterioration than nondestructive tests.

This paper describes several test results from both nondestructive and destructive tests in sixty coil groups of twelve HV motors. Weibull probability distribution is employed to analyze the ac breakdown voltage from a selected group of coils.

2. Test Specimen and Experimental Procedure

To assess the deterioration of stator winding insulation in HV motors, a total of 576 coils were manufactured for twelve motors (48 slots), where the motor is a 6.6kV motor. All 48 coils for each motor (12 turn coil) are inserted in the stator slot when performing the tests. The 48 coils are classified into five groups where one group of coils (E) is healthy, artificial defects are introduced into four coil groups (A~D). The four different types of coils inserted in the four coils groups are shorted turn (strand), internal separation between conductor and groundwall (GW) insulation, large void within the GW insulation, and removal of semi-conductive tape. All the coil groups other than coil group D, have the semi-conductive tape on the outer surface of the slot section. Table 1 summarizes the description of each coil group (A~E), and the number of windings with each defect. A photograph of the test motor with the five coil groups of the HV motor is shown in Figure 1. Twelve motors were manufactured with identical coil groups with the artificial defects. Nondestructive tests were performed on the individual coil groups of twelve motors to obtain the statistical data.

The ac current and dissipation factor (tanδ) were measured using a commercial Schering bridge in all five coil groups of motor stator windings. The Schering bridge consists of a HV power supply (Tettex, Type 5283), and bridge (Tettex, Type 2818). The ac current and tanδ measurements were obtained between 0.95kV and 6.6kV for all five coil groups. ΔI is the difference between the actual measurement of the current at 6.6kV and ideal expected current at 6.6kV estimated based on the increase in current. Δtanδ is the difference between the tanδ measurements at 2kV and at 6.6kV. PD measurements were also obtained in accordance with IEC 270 using a wide band (40~400 kHz) partial discharge detection system (TE-571) in a calibrated measuring circuit. The AC breakdown test was performed using a variable ac power supply.

Table 1. Defect classifications in five coil groups of motor

Coil Group	Defect Classifications	Winding Numbers
A	Shorted turn of strand	10
B	Internal separation between conductor and insulation	10
C	Large void within insulation	8
D	Removal of semi-conductive tape	10
E	Healthy	10
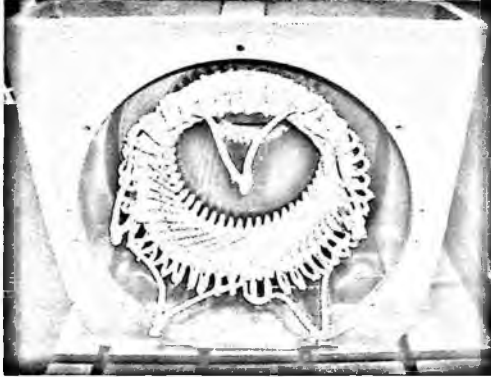
Figure 1. Five coil groups of motor with healthy and artificial defects

3. Results and discussion

Before the ac breakdown test was performed, nondestructive tests that include the ac current, dissipation factor (tanδ), and partial discharge tests were performed on the sixty coil groups of twelve motors. The measurements of the ac current and tanδ were obtained with the voltage between 0.95kV and 6.6kV for each individual coil group for the twelve motors. For each coil group (A~E) of the twelve motors, the minimum and maximum values of ΔI and Δtanδ were removed in the statistical analysis (ten of sixty coil groups for the twelve motors have been removed). The average of the ΔI and Δtanδ measurements with the minimum and maximum values removed are summarized in Table 2.

According to [5], coils with the values of ΔI and Δtanδ lower than 8.5% and 6.5%, respectively, are acceptable at 6.6kV. It can be seen in Table 2 that the measurements of ΔI and Δtanδ for coil groups A and E have the lowest values. The values of ΔI and Δtanδ being below 8.5% and 6.5% indicate that the stator winding insulation in coil groups A and E is in serviceable condition. The values of the ΔI and Δtanδ measurements in coil groups B, C, and D are above the 8.5%

and 6.5% threshold, which indicate that they must be replaced since they have deteriorated significantly. Coil group B appears to be prone to delamination and debonding between the conductor and insulation. The tanδ values of coil group C at 0.95kV and at 6.6kV were measured to be 6.2~8.0% and 11.0~16.0%, respectively. The tanδ values of coil group D (no semiconductive tape) at 0.95kV and 6.6kV were between 0.5~2.0% and 11.0~22.4%, respectively, which was roughly eight times higher than those for coil group E (healthy).

Table 2. The measured results of ΔI and $\Delta \tan\delta$

Coil Group	$\Box\tan\delta$ [%]	$\triangle I$ [%]
A	4.31	5.35
B	6.62	10.90
C	7.74	9.87
D	11.03	15.21
E	1.37	1.89

Table 3. The results of PD measurement

Coil Group	PD magnitude [pC]					
	Noise [pC]	DIV [kV]	3.81 [kV]	4.76 [kV]	6 [kV]	6.6 [kV]
A	410	4.3	1100	2200	3800	5600
B	470	3.4	1700	3700	6000	6900
C	430	3.7	1300	2500	6300	8800
D	450	3.3	2900	8700	14000	17000
E	420	3.5	1300	2000	4000	5700

As in the case of the ΔI and $\Delta \tan\delta$ measurements, the data with the minimum and maximum values of PD magnitudes were removed in the statistical analysis for each coil group (A~E). For each coil group, the external noise, discharge inception voltage (DIV) and the average PD magnitude with the minimum and maximum values removed are summarized in Table 3. The PD magnitudes were measured for each individual coil group at 3.81kV, 4.76kV, 6kV, and 6.6kV, respectively. As the voltage was increased from 3.81kV to 6.6kV, the PD magnitudes increased, as expected. It can be seen that the PD magnitudes at line-to-ground voltage (3.81kV) and at 4.76kV are in good condition for the five coil groups. The PD magnitudes at 6.6kV were 5,600pC, 6,900pC, 8,800pC, and 5,700pC for coil groups A, B, C, and E, and unacceptably high for coil D at the same voltage. The PD magnitudes in coil group D are high enough to cause significant damage to the insulation. The PD pattern in the coil group A, C, and

E measurements indicated internal discharges, and the PD patterns of coil groups B and D indicated discharge at conductor surface and slot discharges, respectively, as expected from the artificial defects. Although the PD magnitude of coil group D are much higher than that of coil group C, internal discharge causes more serious insulation problems than slot discharge.

The AC breakdown test, which is a test applied to HV motor insulation to test suitability of service, was performed on the sixty coil groups of twelve motors to confirm the results of the nondestructive test. As in the nondestructive tests, the minimum and maximum breakdown voltages were removed from the measurements of each coil group (A~E). The results of the average of the breakdown voltage measurements from the ten coils groups are summarized in Table 4. Breakdown of coil groups A, B, C, D and E occurred at an average of 25.9kV, 24.8kV, 24.1kV, 26.5kV and 30.4kV, respectively, which indicates that the stator insulation is in serviceable condition. The breakdown voltage of the healthy coil group (E) is higher than that of the coil groups with artificial defects (A~D). The lowest breakdown voltage was observed in the coil group C with a large void in the bulk of the GW insulation. Most of the failures occurred in the line-end coil at the exit of the core slot section; only the failures in two coils occurred in slot section.

Table 4. The results of the average breakdown voltage

Coil Group	Breakdown Voltage [kV]	Failure Location
A	25.9	Line-end coil
B	24.8	Line-end coil
C	24.1	Line-end coil
D	26.5	Line-end coil
E	30.4	Line-end coil

Figure 2 shows the Weibull plot of the ac breakdown voltage for the five coil groups A~E described in Table 1. It is possible to estimate the failure rate of fifty coil groups of ten motors from the Weibull distribution analysis for breakdown voltage. The 50th percentile (median) values of the measured breakdown voltages based on statistical data in coil groups A, B, C, D and E were 26.1kV, 25.0kV, 24.4kV, 26.7kV and 30.5kV, respectively. It can be seen in Table 4 that data is similar to the average values of the measured breakdown voltage. This results shows that destructive testing is more reliable although nondestructive testing is performed to estimate insulation deterioration rate for breakdown voltage.

Figure 2. Weibull plot of breakdown voltage for five coil groups

4. Conclusion

The measurements of ΔI and $\Delta\tan\delta$ indicated that the insulation of coil groups A and E are n serviceable condition, but the insulation of coil groups B, C, and D are in poor condition. The PD magnitudes at 4.76 kV were around 2200pC, 3700pC, 2500pC, 8700pC, and 2000pC for coil groups A, B, C, D and E, respectively. These results indicated that that the stator insulation of the five coil groups is in good serviceable condition. It has been observed in the tests that internal discharge (coil group C) causes more serious insulation problems than slot discharge (coil group D). The 50th percentile (median) values of measured breakdown voltages based on statistical data in coil groups A, B, C, D and E were 26.1kV, 25.0kV, 24.4kV, 26.7kV, and 30.5kV, respectively. This data is in close proximity to the average of the breakdown voltage measurements. It has also been observed that almost all of the failures were located in the line-end coil at the exit from the core slot section. The test results show that destructive testing is more reliable although nondestructive testing is performed to estimate insulation deterioration rate for breakdown voltage.

References

1. H.A. Toliyat and G.B. Kliman, *Handbook of Electric Motors,* (Marcel Dekker, 2004).
2. H.G. Sedding, R. Schwabe, D. Levin, J. Stein and B.K. Gupta, *IEEE EIC/EMCW Conf,* 455 (2003).
3. B.K. Gupta and I.M. Culbert, *IEEE Trans. on EC,* **Vol. 7,** 500 (1992).
4. G.C. Stone, H.G. Sedding, B.A. Lloyd and B.K. Gupta, *IEEE Trans. on EC,* **Vol. 3,** 833 (1988).
5. H. Yoshida and U. Umemoto, *IEEE Trans. on EI,* **Vol. 6,** 1021 (1986).

EFFECT OF LEAKAGE ON DETERIORATION OF CONCRETE LINING IN CONVENTIONAL TUNNEL

HO-SEOP JUNG

*Underground Structure Research Division, KICT, 2311 Daehwa-dong Ilsanseo-gu,
Goyang, Kyeonggi-do, 411-712, KOREA*

DONG-GYOU KIM

*Underground Structure Research Division, KICT, 2311 Daehwa-dong Ilsanseo-gu,
Goyang, Kyeonggi-do, 411-712, KOREA*

SEUNG-TAE LEE

*Department of Civil Engineering, Kunsan National University, San 65 Miryong-dong
Kunsan, Jeollabuk-do, 573-701, KOREA*

SEONG-SOO KIM

*Department of Civil Engineering, Daejin University, San 11-1 Seondan-dong
Pocheon, Kyeonggi-do, 487-711, KOREA*

The deterioration of concrete lining in conventional tunnel may occur by various internal and external causes. In general, tunnel is constructed in the ground. Concrete ling as support of tunnel may contact with groundwater with hazardous ions. The hazardous water may deteriorate the concrete lining in tunnel. The leakage in tunnel may affect the durability of concrete lining. This study is to evaluate the effect of water leakage on durability and deterioration of concrete lining in tunnel. Therefore, surface examination, nondestructive inspection, compressive strength test, carbonation depth test, XRD analysis, and EDS analysis were performed to analyze the deterioration of concrete lining in several tunnels constructed over 50 years ago in Korea. From surface examination, tunnels had been repaired and reinforced in several times. Also, tunnels had many cracks, leakage, efflorescence, and exploitation. Compressive strengths obtained from nondestructive inspection and compressive strength test varies according to the concrete lining condition. Carbonation depth was between 3mm and 27mm. From XRD analysis, ettringite, gypsum and thaumasite were detected in the concrete lining having water leakage. It seems that the deterioration of concrete lining was caused by thaumasite and gypsum formation.

1. Introduction

Although the main supporting materials of tunnel structure reveal the time-dependent hardening characteristic right after the construction, they necessarily

deteriorate over time as they are commonly used for a long period. Their durability happens to decline gradually. However all current guides and manuals for safety management of tunnel structures are established and applied by individual agencies separately. Also, the radical causes of deteriorations on the tunnel structures cannot be reflected appropriately. Those guides or manuals do not consider the long-term durability deterioration of main supporting materials for tunnel structure, because of the limitation on the radical investigation due to the fact that it is impossible to access the back of tunnel structure. Nevertheless, existing criteria and systems for tunnel safety management are only focused on evaluation, repair and reinforcement of tunnels in which deteriorations have already occurred, without reflecting the radical variation in internal and external environments well, regarding the deteriorations on tunnel structures. In addition, current standards for tunnel safety management do not establish the sufficient criteria for either the grading evaluation based on usage, importance and main elements of tunnels, or the performance improvement after repair/reinforcement. Most of deterioration on tunnel structures have been caused by crack and leakage from the investigation and analysis of deteriorations on tunnel concrete lining structures,

Therefore this study will identify the causes of deterioration on tunnel concrete lining due to crack and leakage, by utilizing the field investigation results such as exterior examination, compressive strengths, and permeability evaluation, as well as the instrumental analyses such as XRD, SEM and EDS. In addition, this study will provide the fundamental data for designing the durability of tunnel concrete lining.

2. Review of Test Results

2.1. *Visual Appearance*

Deteriorations on tunnel structures can be largely categorized into crack, leakage, corrosion, falling off, etc., and as shown in Figure 1, more than 50 percent of deteriorations on domestic/foreign tunnels have been caused by crack and leakage. Tunnels are constructed under the base rock, and such underground structures tend to contact with groundwater.
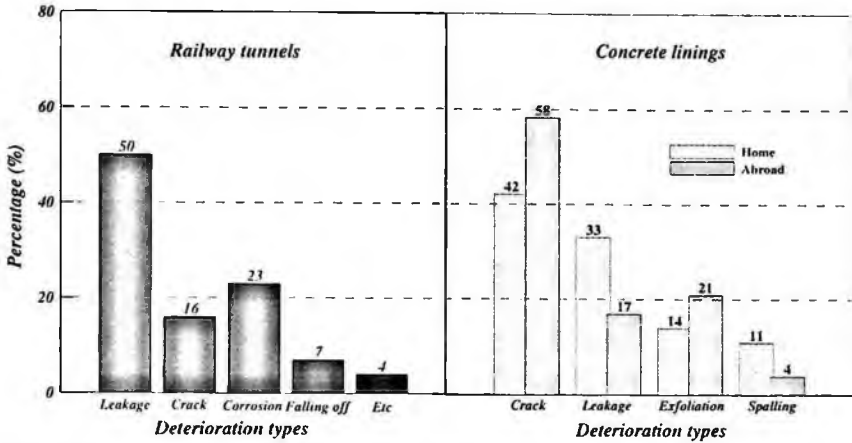
Figure 1. Case studies of deteriorations on tunnel structures

In most of tunnel structures to be examined, there existed vertical and horizontal cracks in the entire sections. The width of cracks ranged from 0.1mm to 1mm or more, and various types including vertical and horizontal cracks, slanted cracks and net-shaped cracks were distributed. The causes of cracks on tunnel structures are mostly either the offsets in materials and construction such as heat of hydration, drying shrinkage, plastic shrinkage and construction joint, or the bending crack within the crack width allowance. Cracks by heat of hydration and drying shrinkage were mainly generated from the horizontal crack on the lower part of lining and then developed toward the upper part. Cracks by plastic shrinkage appeared irregularly in any directions on the ceiling areas of tunnels with relatively large sections. Regions where leakage frequently occurred by cracks were also investigated in the upper part including the ceiling area.

Since cracks and subsequent leakages occurred in most tunnels, tunnel concrete linings were considered in danger of being chemically eroded when the harmful ions are contained in groundwater or leachate. Therefore samples were collected from leachate generated in the leakage areas, to perform the water quality analysis. Especially in the tunnel B, lateral ice and icicles due to the leakage in winter were observed, and in case of the tunnel F, leachate erupted from certain locations (refer to Figure 2 and Figure 3).

Table 1 shows the analysis result of groundwater collected from the tunnels examined in this study in comparison with tap water. In most tunnels, leachate's pH ranged from 5.90 to 7.58, meaning weak acidity or neutrality. The highest concentration of sulfate ion was measured as 291.2ppm, which is not enough to

affect the concrete directly, but the durability degradation by chemical erosion shall be still considered in case of long-term exposure to this amount.

Figure 2. Lateral ice   Figure 3. Eruption of leachate   Figure 4. Efflorescence
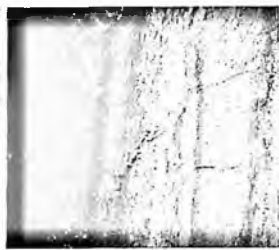
Table 1. Results of water quality analysis, ppm

Tunnel	pH	Cl⁻	SO_4^{2-}	Ca^{2+}	Mg^{2+}
Tap water	7.21	16.1	13.29	19.4	5.1
A	6.43	28.5	51.312	37.20	14.8
B	5.90	5.1	4.548	20.80	9.2
C	6.84	ND*	2.880	22.02	2.9
D	7.25	8.025	20.907	22.42	1.69
E	7.58	ND*	291.2	124.12	52.03
F	6.6~7.5	-	3.6~201.3	5.4~116.1	1.7~49.5

* ND : Not Detected,

As shown in Figure 4, the efflorescence of concrete lining means that either calcium hydroxide or alkali in the cement of concrete or mortar is dissolved in the water, flows out through the openings in the structure, and is extracted to the form of soluble alkali sulfate or insoluble calcium carbonate after all the water has been vaporized, or is solidified to the form of carbon oxide such as calcium carbonate or sodium carbonate by reacting with carbon dioxide in the air.

As the results of field examination performed in this study, it turned out severe performance degradation, including leakage, desquamation and exfoliation due to cracks in the tunnel, occurred in most cases regardless of the years of use. The efflorescence accompanied with the leakage could be observed many times in the areas of cracks and construction joints. The efflorescence basically consists of calcium hydroxide, alkali compound, and carbon oxide compound, although it depends on the elapsed time from the generation, environmental conditions, additives, and raw materials. Special attention needs to be made to the region

where the efflorescence occurred, since it indicates the deterioration of concrete lining and thus the degraded durability of the structure.

2.2. *Compressive Strength and Permeability*

Table 2 summarizes the compressive strength of concrete lining by evaluating the rebound hardness method with the Schmidt hammer as well as the compressive strengths measured on core specimens. The compressive strengths estimated from the rebound hardness method do not indicate the strength of concrete itself. The compressive strength measurement was to identify the degree of erosion on the concrete lining, caused by the performance degradation factors. That is, the compressive strength by rebound hardness method was low because the surface of concrete lining was affected by the leakage and the reaction product, whereas the rebound hardness was relatively high when the surface was sound.

Table 2. Compressive strength, MPa

Tunnel	Core specimen	Schmidt hammer
A	12.8 ~ 41.7	17.3 ~ 34.7
C	5.1 ~ 13.3	-
D	8.3 ~ 13.6	10.5 ~ 24.0
E	11.5 ~ 26.6	8.8 ~ 16.0
F	6.0 ~ 16.0	6.4 ~ 23.2

The compressive strength by rebound hardness method and that of core specimens largely differ depending on the measured locations. This is presumably because the cores were collected from locations where the degree of crack and leakage are considerably different one another. In permeability test, the total passed charge varied depending on the collected locations in the same tunnel, ranging from 1,272 coulombs up to 3,352coulomb. This tendency is different from the compressive strength of core specimen, presumably because 1) the compressive strength has no direct relation to the durability, and 2) the use of big aggregates in the concrete lining reduces the reliability of criteria for evaluating the permeability. However, it is expected that permeability test will be effectively applied in evaluating the durability of concrete lining in the future.

2.3. *Results from Instrumental Analyses*

Figure 5 shows the microstructures of core specimens, which were collected from locations with severe leakage on the side of concrete lining in the tunnel structures, evaluated through XRD, SEM and EDS analyses. As shown in Figure 5(a), peaks of ettringite and thaumasite were detected through the XRD analysis of concrete surface, and accordingly it can be assumed that the sulfate ions in groundwater reacted with cement components dominantly. In addition, SEM analysis demonstrates that the concrete lining generated the reaction product and accordingly increased the porosity prominently. The reaction product was needle shape. Fibrous materials were found in the stable structure, and a large amount of needle shaped materials, such as ettringite and thaumasite were observed.

(a) XRD analysis

(b) SEM image and EDS analysis
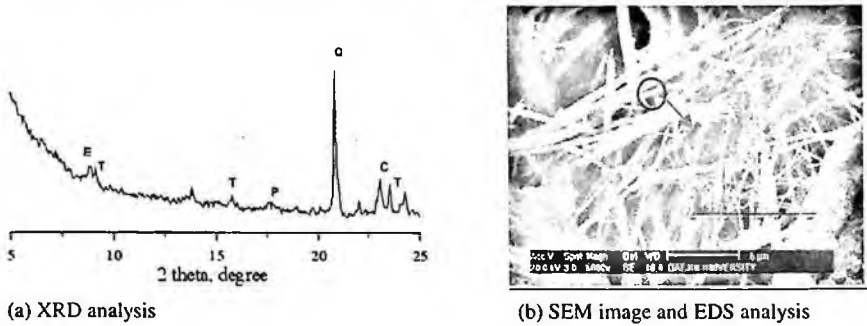
Figure 5. Micro-structural analysis

3. Conclusion

The concrete structures in the underground are always exposed to the groundwater, and the harmful ions in the groundwater may cause all the deterioration of concrete structures. Although the groundwater can flow through openings in the concrete, it can be accelerated when there are internally any cracks, which may become the main course of deterioration eventually.

It is difficult to prevent completely the tensile crack from occurring. By investigating causes and types of cracks, the concrete structure ensuring both safety and durability can be produced by reducing the cracks on the concrete structure. The results of investigation can give their effects on safety and usability and appropriate prevention measures.

SULFATE ATTACK OF SHOTCRETE MADE WITH ALKALI-FREE ACCELERATOR

SEUNNG-TAE LEE

*Department of Civil Engineering, Kunsan National University
Kunsan, Jeonbuk 573-701, South Korea*

DONG-KYOU KIM, HO-SEOP JUNG, GYU-PHIL LEE

*KICT, 2311 Daewha-dong
Ilsan,Kyeonggi 411-712, South Korea*

SEONG-SOO KIM, KWANG-PIL PARK

*Department of Civil Engineering, Daejin University
Pocheon, Kyeonggi 487-711, South Korea*

This paper presents the findings on the resistance of shotcrete specimens with or without alkali-free accelerator exposed to sodium sulfate solution for 270 days. The resistance of shotcrete specimens was evaluated using visual examination and expansion measurements. Main variables for the resistance evaluation consist of the concentrations (2.5%, 5% and 10% sodium sulfate solution) and temperatures (4 and 20°C) of sulfate solutions. Test results confirmed a negative effect of alkali-free accelerator on sulfate resistance of shotcrete specimens. Furthermore, regarding concentrations of sulfate solution, the higher expansion of shotcrete specimens with alkali-free accelerator was clearly observed with the increasing concentration of solution. In addition, the low temperature of solution provided an opportunity to lead to the severe deterioration on the shotcrete specimens with alkali-free accelerator compared to those without alkali-free accelerator. Thus, it is concluded that it is necessary to pay special attention when using alkali-free accelerator in shotcrete exposed to highly concentrated sulfate and cold climate environments.

1. Introduction

Durability of concrete structures exposed to sulfate-bearing environments has been of concern for concrete engineers and scientists. Until now, however, it has been difficult to define the precise nature of the mechanism of sulfate attack, because of its complex process. In order to solve this problem, a number of hypotheses have been proposed to describe the mechanisms responsible for the degree and modes of deterioration of concrete by sulfate attack.[1-3]

A variety of additives and admixtures have been used for concrete structures. Especially for tunnel structures, accelerator is very important chemical admixture in producing shotcret. The choice of a particular accelerator and its dosage is commonly determined by the setting time required for the shotcrete application. Most of the accelerators used today are based on alkali aluminates due to the rapid setting behavior. However, the use of alkali-free accelerator has been increased with respect to the performance of shotcrete containing it and safety for worker.[4] This work describes the effect of alkali-free accelerator on the sulfate resistance of mortar specimen exposed to sodium sulfate solution. Additionally, the influence of exposure concentration and temperature of sulfate solution was experimentally investigated. The finding of this experiment may provide some information in the design of shotcrete in tunnel structures.

2. Experimental

The cement used in this study was Type-10 cement (OPC) satisfying ASTM C 150 standard specification. The chemical composition, as provided by the cement manufacturer, are presented in Table 1. The C_3A content in the cement was 9.3%. Ottawa standard grade sand, which was produced from Illinois, USA, was selected for making mortar specimens. During testing, it is assumed that no chemical influences by fine aggregate are excluded. Accelerator based on alkali-free system was used in mortar mixture. For comparison, control mortar specimens without alkali-free accelerator were also used.

The exposure solution used to provide sulfate attack to the specimens was made by dissolving reagent grade chemical in tap water. The chemical used was Na_2SO_4. Three levels of concentrations of sulfate solution (2.5%, 5% and 10% sodium sulfate solution) were prepared. In order to investigate the effect of solution temperature, mortar specimens with or without alkali-free accelerator were exposed to 4 and 20°C, respectively.

The prism bars with a size of 25 × 25 × 285 mm were used for expansion measurement. The mixture proportion of the mortars is cement : sand = 1 : 2.75. Mortar specimens were made at a water-cement ratio of 48.5%. Based on ASTM C1012, expansion was measured at each exposure period. All expansion values were compared with the initial length of prism mortar.

Table 1. Chemistry composition of the cement (by mass, %)

SiO_2	Al_2O_3	Fe_2O_3	CaO	MgO	SO_3	LOI	Insoluble residue	Free CaO
19.9	5.0	2.4	63.8	2.5	3.0	2.3	0.8	0

3. Results and discussion

3.1. *Effect of exposure temperature*

Metha[5] reported the effect of solution temperature on the sulfate attack in the literature. At a low temperature, the deterioration mode by sulfate attack is significantly related to the thaumasite formation ($CaCO_3 \cdot CaSO_4 \cdot CaSiO_3 \cdot 15H_2O$). Figure 1 presents the effect of solution temperature on the expansion of mortar specimens with alkali-free accelerator. The specimens stored in sulfate solution at a low temperature (4□) were completely disintegrated after 120 days of exposure. After the exposure time, the expansion value of mortar specimens was about 0.261%, while there was about 0.088% in expansion for mortar specimens exposed to room temperature. However, in case of mortar specimens without accelerator (Figure 2), the difference of expansion values with the increase of solution temperature was not significant. This implies that the effect of solution temperature on the sulfate degradation was much more dominant in mortar specimens with alkali-free accelerator.

3.2. *Effect of exposure concentration*

Figure 3 presents the expansion results of mortar specimens with alkali-accelerator exposed to sodium sulfate solutions for 270 days. From the test results, it was observed that the expansion was greatly associated with the concentration of attacking solution. At a higher concentration of sulfate ions (10% sodium sulfate solution), the ultimate expansion value was as high as about 0.943% after 270 days of exposure, while there is only about 0.081% for a low concentration of sulfate solution (2.5% Na_2SO_4 solution) at the same exposure period. Expansion data on mortar specimens without accelerator were plotted in Figure 4. As expected, the mortar specimens exposed to 10% sodium sulfate solution had a relative big expansion value compared to those exposed to 2.5% sulfate solution. The sharp increase in expansion for mortar specimens in 10% sulfate solution was observed after 150 days of sulfate exposure, while the expansion of mortar specimens in 2.5% sulfate solution was almost stable during exposure period.

Figure 5 shows the photos of mortar specimens with alkali-free accelerator exposed to different concentrations of sulfate solutions. This photo clearly explains the relationship between the degree of deterioration due to sulfate attack with exposure concentration. For the mortar specimen in 10% sulfate solution, a lot of cracks formed by excessive expansion were observed in all faces of the specimen.
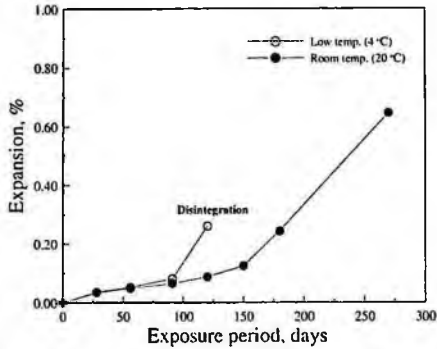
Figure 1. Expansion of mortar specimens with alkali-free accelerator under different exposure temperature
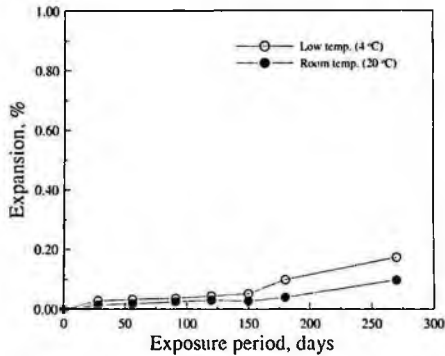
Figure 2. Expansion of mortar specimens without alkali-free accelerator under different exposure temperature
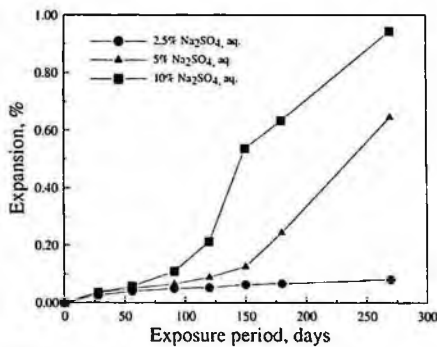
Figure 3. Expansion of mortar specimens with alkali-free accelerator under different exposure concentration
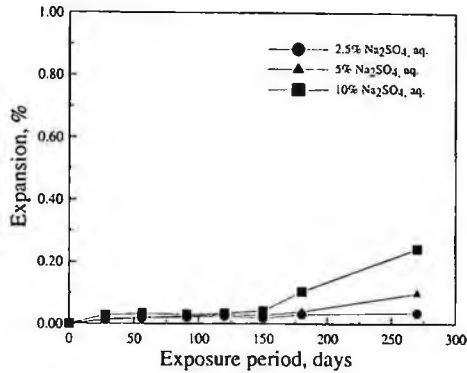
Figure 4. Expansion of mortar specimens without alkali-free accelerator under different exposure concentration
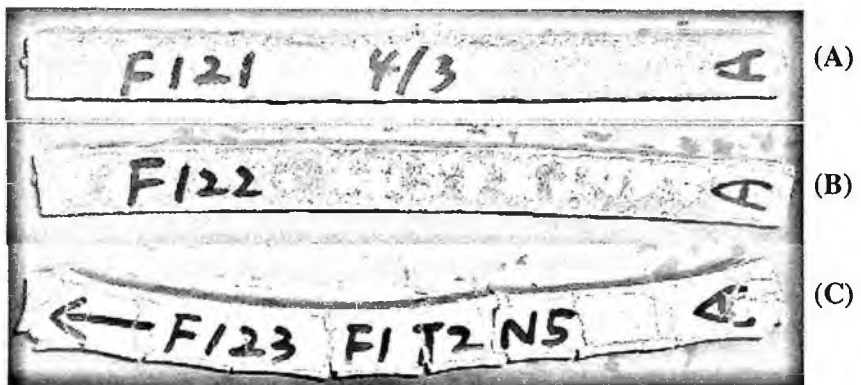
Figure 5. Mortar specimens with alkali-free accelerator. (A) 2.5% Na_2SO_4, aq., (B) 5% Na_2SO_4, aq., (C) 10% Na_2SO_4, aq.

4. Conclusions

1. The expansion of mortar specimens, especially with alkali-free accelerator, was greatly associated with the exposure concentration of sulfate solution. With an increase of the concentration, there was a remarkable increase in expansion of the mortar specimens.

2. While the effect of exposure temperature on the sulfate deterioration of mortar specimens was less in the cement system without accelerator, the mortar specimens with alkali-free accelerator were deteriorated at a low temperature.

18

References

1. T. H. Wee, A. K. Suryavanshi, S. F. Wong and A. F. A. Rahman, *ACI Mat. J.* **97**, 536 (2000).
2. P. K. Mehta, *Cem. Conc. Res.* **13**, 401 (1983).
3. M. D. Cohen and B. Mather, *Mat. J.* **88**, 62 (1991).
4. C. Paglia, F. W. Wombacher and H. Bohni, *Cem. Conc. Res.* **33**, 387 (2003).
5. P. K. Metha, *Materials Science of Concrete III*, American Ceramic Society, Westerville, OH, (1992).

NON-DESTRUCTIVE ASSESSMENT FOR DEGRADATION OF 9 CR STEEL

JONG-SEO PARK, UN BONG BAEK, WAN KYU LEE AND SEUNG HOON NAHM[†]

Division of Metrology for Quality Life, Korea Research Institute of Standards and Science, Daejeon, 305-340, Korea

A electrical resistivity method was attempted for the estimation of the creep damage of degraded 9Cr steel. The specimens with six different kinds of aging periods were prepared by an isothermal heat treatment at 690 ℃. The electrical resistivity was determined by a standard DC four-point probe method at 24±0.5 ℃. The self-made probe station and Burster 2304 were utilized for the resistance measurement. The correlation between the measured electrical resistivity and the tensile properties was studied. The electrical resistivity has a declining tendency with the increase of aging time. Because electrical resistivity is strongly dependent on the microstructural changes. A correlation between the electrical resistivity and aging parameter was established, which allows one to estimate the material degradation of 9Cr steel.

1. Introduction

The temperature and pressure of steam must be raised to improve thermal efficiency of power plant. Materials that have superior strength at high temperature to existent materials should be used to endure such severe operating conditions. Many studies on the development of new high temperature materials that can be served in the middle strength class of low alloy steel and stainless steel have been carried out. By the result, high Cr (8 ~ 14%) ferritic steels that high temperature strength and fracture toughness was improved than those of existent ferritic steel were developed[1-3].

Although 2.25Cr-1Mo steel is used ordinarily as a tube wall material if the operating temperature is below 590℃, austenitic stainless steel that has high strength and oxidation-proof at high temperature region is used if the service temperature exceeds 590℃. But, austenitic stainless steel is expensive and stress corrosion cracking or intergranular corrosion can be happened under particular environment conditions. Also, great stresses are happened at piping restraint point or nozzle because of large heat expansion coefficient and low thermal

conduction comparing with ferritic steel. New ferritic steel is required, which can be used as the substitue material of austenitic stainless steel at high temperature that exceed the operating temperature limit of existing ferritic steel.

Modified 9Cr-1Mo steel has been studied and developed as the material of steam generator of fast breeder reactor since 1974[4]. The strengths of modified 9Cr-1Mo steel at between 550 and 600℃ are double of those of usual 9Cr-1Mo steel or 2.25Cr-1 Mo steel, and is similar with those of 304 stainless steel. Also, it is known that weldability and machining of the steel are very superior. Recently, this steel is used in fossil power plant and petrochemical plant etc. because of superior weldability and high temperature strength.

In this study, modified 9Cr-1Mo steel was degraded artificially, and then correlationship between the deterioration of strength and the change of electrical resistivity by degradation degree was examined.

2. Experimental

Test material is modified 9Cr-1Mo steel which is widely used as a steam tube material. Virgin(as received) material was artificially aged by the isothermal heat treatment at 690℃ for 0, 235, 444, 644, 838, 1215, 1582 hours, which is an accelerating aging process for simulating the microstructures of materials in service at the turbine steam temperature of 610 ℃ for about 0, 25000, 50000, 75000, 100000, 150000, 200000 hours respectively. Periods of heat treatment for the simulation were selected based on Larson-Miller parameter.

$$LMP = T(C+\log t) \qquad (1)$$

Where T is heat treatment temperature (K), t is heat treatment time (h). They are summarized in Table 1.

Table 1. Determination of the heat treatment time at 690 ℃ corresponding to the equivalent microstructure served at 610 ℃.

Heat treatment time at 690 ℃ (h)	198	458	644	820	1215	1582
Time served at 610 ℃ (h)	25000	50000	75000	100000	150000	200000
Larson-Miller parameter	21,472	21,822	21,965	22,066	22,229	22,341

The electrical resistivity of specimens with the seven different heat treatment periods was measured by a direct current four-point potential method at 24±0.5℃. Plane specimens of 55 × 5 × 1 mm (length × width × thickness)

were prepared. Four point probes of the measuring system (two probes for the current supply and the others for the voltage measurements) were equally spaced by 1.0 mm and aligned along a line and pressed on a surface of specimen for the measurement.

The distance between two output probes was carefully measured using a traveling microscope since the measurement error of only 0.05 mm would cause an error of 0.13 $\mu\Omega$cm. The polarity of input current supplied to the system was altered during the measurement, i.e. forward and backward, in order to reduce the measurement error due to the thermoelectromotive force. An average of output voltages obtained from the forward and backward currents was adopted as a datum of resistivity. A common electrical ground was shared to avoid a common mode noise signal.

3. Results and Discussions

3.1. *Microstructures of modified 9Cr-1Mo steel with isothermal aging*

The microstructure of the modified 9Cr-1Mo steel after austenitization and quenching is composed of lath martensite and ferrite (α-Fe) at the prior austenite grain boundaries, as shown in Fig. 1(a). Average grain size of the prior austenite characterized by a mean linear intercept method was about 53 μm. High carbon concentration and dislocation density in the ferrite and lath phases enhanced yield and ultimate tensile strengths but reduced work-hardening capacity (see Fig. 2). 198 h-aged specimen in Fig. 1(b), the microstructural change due to the isothermal ageing was negligible but the yield and ultimate tensile strengths are rapidly down to 95.9 % and 97.5 % of those of virgin material, respectively. This softening is attributed to the annealing of the highly tangled dislocations of quenched structure. Cementite segregated at the prior austenite, lath martensite and ferrite boundaries is thermally destabilized at 963 K and partially dissolved into matrix. Since the lath annihilation displays same effects of grain growth, the mechanical strength of the aged alloy decreased continuously until 820 h ageing. Furthermore, high carbon concentration at the various phase boundaries promotes nucleation of a thermally stable carbide $\{Cr,Fe\}_{23}C_6$ at long-time ageing. Thus, an overall strength of the long-time-aged specimen is governed by the competition of the lath dissolution coarsening, matrix softening and precipitation hardening.

22

(a) Virgin   (b) 198 h   (c) 458 h

(d) 644 h   (e) 820 h   (f) 1210 h
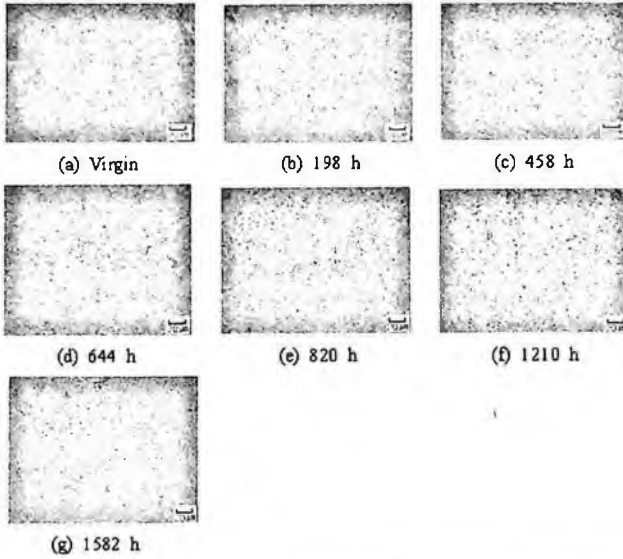
(g) 1582 h

Figure 1. (a) Lath martensite and ferrite microstructure after austenitization and quenching of modified 9Cr-1Mo steel, and six microstructures after subsequent isothermal ageing at 963 K for (b) 198 h, (c) 458 h, (d) 644 h, (e) 820 h, (f) 1210 h, and (g) 1582 h.

3.2. Mechanical and electrical degradation parameters and their correlation

Although the yield and tensile strengths in Fig. 2 can provide softening or hardening information of each aged material, it is impossible to assess deformability and brittleness from these data. Thus, we tried to look for a new parameter that can provides deformability information of aged specimen. We checked changes in the yield ratio (the ratio of yield strength to tensile strength ratio) with the thermal ageing and investigated its applicability as a parameter for degradation evaluation in this study. Fig. 3 represents the variation of yield ratio with the increase of aging time. As the period of aging increases, the value of yield ratio decreases rapidly down to approximately 96.8 % of that of virgin material and then becomes constant after 644 hours. Fig. 3 shows that as aging time increases, there is no noticeable dufference between the yield ratio variation tendency and tensile properties variation tendency.

Fig. 4 shows the variation of electrical resistivity with the increase of aging time. As the period of aging increases, the value of electrical resistivity decreases rapidly down to approximately 98.8 % of that of virgin material and then decreases slowly with further aging. Fig. 5 represents the variation of the ratio of
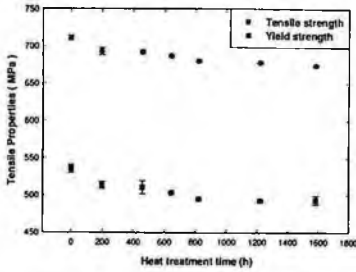
Figure 2. Dependency of yield strength and tensile strength on aging time.
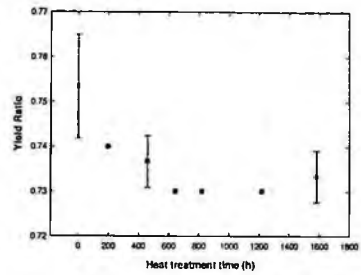
Figure 3. Dependency of yield ratio on aging time

electrical resistivity normalized by the electrical resistivity (ρ_o) of virgin material with the increase of Larson-Miller parameter. Since the electrical resistivity decreases continuously with the increase of aging time, the extent of degradation can be evaluated by the measuring electrical resistivity. Thus the electrical resistivity method would be effective for the evaluation of the extent of 9Cr steel material degradation
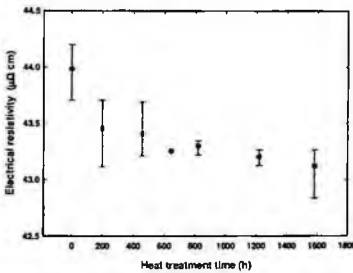
Figure 4. Dependency of electrical resistivity on aging time.
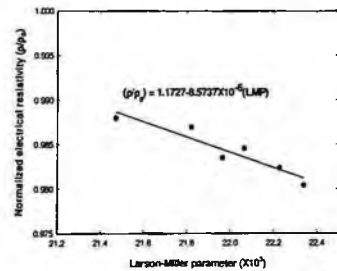
Figure 5. Dependency of normalized electrical resistivity on Larson-Miller parameter.

Fig. 6 represents the correlation between normalized electrical resistivity and yield strength of degraded 9Cr steel. Fig. 7 shows the correlation between normalized electrical resistivity and yield ratio of degraded 9Cr steel. The electrical resistivity is proportional to the yield strength and the yield ratio as shown in Figs. 6 and 7, respectively. The relationship between normalized electrical resistivity and yield strength or yield ratio is in a good lineality. The relationship allows one to estimate the deformability of aged 9Cr steel indirectly through the electrical resistivity. Moreover the remained life can be deduced from the measured electrical resistivity value, if the correlation between life assessment parameter and yield ratio is available.
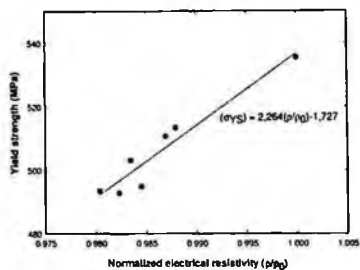
Figure 6. Correlation between normalized
electrical resistivity and yield strength
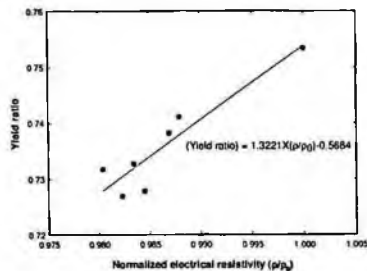
Figure 7. Correlation between normalized
electrical resistivity and yield ratio

4. Conclusions

A nondestructive method for evaluating the creep damage of 9Cr steel was developed using electrical resistivity. The obtained results are summarized as follows:

1) The electrical resistivity decreases rapidly with the increment of the aging at the early stage, which becomes to be decreased slowly after 198 hours aging time. The variation of tensile properties is similar to that of electrical resistivity.

2) A linear correlation between the normalized electrical resistivity and the yield strength or yield ratio was established, which allows one to estimate the creep damage of aged 9Cr steel.

3) At the aging proceeded, more amount of $\{Cr,Fe\}_{23}C_6$ was observed at the grain boundary of 9Cr steel.

References

1. V. K. Shamardin, V. N. Golovanov. T. M. BNulanova, A. V. Povstyanko, A. E. Fedoseev, Z. E. Ostrovsky and Yu. D. Goncharenko, Journal of Nuclears Materilas, 307-311 (2002) 229.
2. Y. Kohno, A. Kohyama, T. Hirose, M. L. Hamilton and M. Narui, Journal of Nuclears Materilas, 271&272 (2002) 145.
3. S. Sathyanarayanan, G. Sasikala and S. K. Ray, International Journal of Pressure Vessels and Piping 81 (2004) 419.
4. Y. Dai, X. J. Jia and K. Farrell, Journal of Nuclears Materilas, 318 (2003) 192.

FRETTING WEAR OF INCONEL 690 TUBES TESTED BY PIEZO-ACTUATED RIG

ILSUP CHUNG, MYUNGHO LEE and YOUNG S. CHAI

Mechanical Engineering, Yeungnam University, Daedong 214-1
Kyungsan, Kyungbuk 712-749, Korea

A fretting wear test rig employing a high voltage PZT actuator is introduced. Using the novel test rig, the characterization of Inconel 690 tube for the fretting wear is attempted in ambient room temperature condition. The reciprocating amplitude ranges from a few microns up to 100 microns. The maximum normal load on the contacting tubes is up to 35N. The typical wear scars are observed microscopically, and the wear damage is investigated.

1. Introduction

Inconel 690 tubes have been widely used in the steam generators (SG) of nuclear power plants. The dense packing of the tubes within a limited space of SG and the fluid induced vibration bring up concerns about the localized wear damage on the tubes. Cases of prematurely worn SG tubes have been reported in practice.

Attia and Magel [1] tested a full-scale multi-span SG tube including U-bend section for about two month period and suggested design guidelines. For the material characterization purpose, Lee et al.[2] and Kim and Lee[3] tested the tubes against stainless steels. Wear behavior under water was tested by Lee and his colleagues[4,5].

As a part of wear characterization program of nuclear power plant materials, this work aims the experimental study of fretting wear behavior of Inconel 690 tubes with sliding amplitude up to 100μm and normal load up to 35N in ambient condition. In order to enable the infinitesimal sliding distance tests, a test rig employing an axial type of piezoelectric actuator has been developed. The inherent driving mechanism of the actuator makes the structure of the tester very simple. Wear testing by piezo-actuator has not been reported often, but Endo and Marui[6,7] developed a machine and studied fretting wear of metals and ceramics.

The profiles of the worn tube surfaces were measured by a 3D optical profiler, from which the wear volume was computed using an in-house program. The wear damage has been studied in terms of wear volume and scar size, and it is shown that the mode of wear varies depending on test conditions.

2. Experiments

2.1. *Fretting Wear Test Rig*

Piezoelectric actuators with sub nano-meter resolution are widely applied in various precision devices, and are also suitable for the generation of sliding motion in fretting wear test. Its advantage over conventional electric motor and cam type of wear tester is that inaccuracy due to the backlash, friction or sticking can be avoided. Since only electric signal from a function generator is imposed on the actuator through an amplifier, the operation is very simple. In addition, it is possible to test in high frequency depending on the actuators. The fretting wear test rig for cross-contacting tube specimens driven by such an actuator is illustrated in Figure 1.
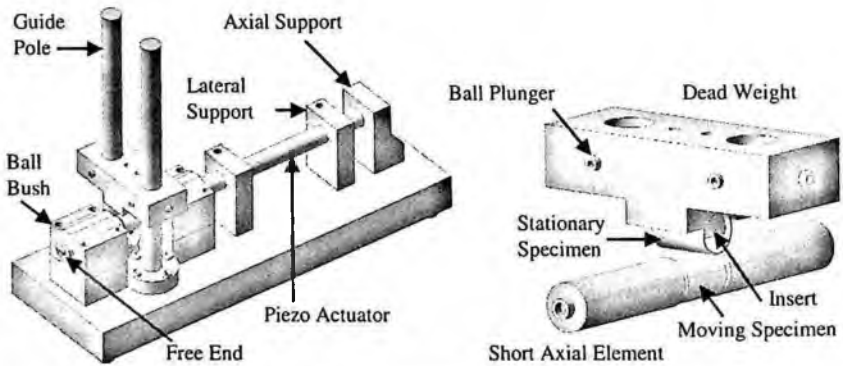
Figure 1. Schematics for fretting wear test rig and specimen installation

The actuator and a moving specimen installed between two short axial elements form a combined shaft. The short axial elements are supported by the ball bushes against transverse direction motion. A side plane of the elements facing the moving specimen is chamfered so that the sliding tube specimen can be self-aligned. The sliding displacement of the specimen is measured by a laser displacement sensor at the outer-most free end of the combined shaft. A stationary specimen is bolt-fastened between the dead weight and an insert through the inside of the tube. The weight is slid down through the guide poles until the fixed specimen contacts with the moving specimen. The influence of the gap between the poles and the holes in the dead weight, which is inevitable due to the fabrication tolerance, is minimized by ball plungers.

A PiezoMechanik PSt VS18 HVPZT actuator was used, whose maximum stroke, stiffness, and force capacity are 200μm, 10N/μm and 5kN, respectively. The base plate of the rig is clamped on a rigid flat surface. The sliding amplitude

is not feed-back controlled so far, but the fluctuation of the amplitude was found not to exceed several microns over the test period.

2.2. *Specimen and Test Condition*

All specimens tested in this study are Inconel 690 tubes of 19.05mm outer diameter, 1mm thickness, and 25mm length. The average roughness, R_a, of the tube surface measured from six virgin tubes was 0.51μm. The tube surface was not treated in order to remain closer to real application.

Fretting wear tests were carried out for 10^6 cycles with 10Hz frequency under normal loads of 10, 15, 25, and 35N in ambient room temperature. After debris removed by compressed air and ultrasonic cleansing, the wear scar was observed by optical microscopy and SEM.

3. Results and Discussion

3.1. *Worn Surface Observation*

Optical micrographs for stationary specimens under 35N are shown in Table 1, where the relative sliding is in horizontal direction. When the sliding amplitude, Δ, is small, the shape of the scar is irregular. But they become larger and closer to circular pattern as the sliding motion grows. In cases of (b) and (c), wear seems to occur in a non-uniform manner, which is the typical phenomenon of fretting wear due to mixed slip.

Table 1. Wear scar of stationary specimens for 35N. (D_H : horizontal dia., D_V: vertical dia.)

	(a) Δ=9.23μm	(b) Δ=21.35μm	(c) Δ=30.53μm	(d) Δ=60.98μm
D_V(μm)	353.6	777.1	763.7	1945.7
D_H(μm)	395.5	789.4	760.3	1897.5

Inconel 690 is a ductile material with the failure strain over 45% in room temperature. Substantial plastic deformation due to normal and friction force is expected although its extent is limited to the tiny contact area. The worn area under the smaller sliding amplitude in Figure 2 looks rather complicated. In addition to the thin layer islands similarly to the report by Lee and Kim [4], thick multi-stacked rugged protrusion is observed in the enlarged view A. It does not

appear to have been formed solely by the loss of surrounding material, but adhesion of debris or transferred material from the mating specimen may have been the cause. In the view B, bulk of material seems to have been forced to slip into the sliding direction. It seems that substantial plastic deformation has occurred. The development of crack at its lower part is obvious as well.

Figure 2. SEM micrograph for wear scar of 15N moving specimen (Δ=10.87μm)

Figure 3. SEM micrograph for wear scar of 15N moving specimen (Δ=53.07μm)

The scar surface in Figure 3, tested with larger sliding amplitude, looks much smoother. Although relatively thick protrusion is also observed in view A, its size is smaller than in Figure 2. The islands of low profile are still observed over the scar in view B. The surfaces of the layers are quite flat and smooth. However, relatively rough regions where tiny debris particles are spotted locate beside the cliffs of the layers. It appears that the separation of some parts of the layers is imminent.

3.2. Wear Profile

The topography of wear scar was measured by using a 3D optical profiler, as shown in Figure 4(a) for 35N(Δ=21.38μm) specimen. A peak at the center of the scar has been formed by the loss of surrounding material. The hairlines transverse to the tube axis direction are pre-existing scratches.

The 3D profile data have been flattened by subtracting the cylindrical surface geometry components using the in-house program which yields the

resolved profile data and wear volume after a surface integration. In the mean time, pre-existing scratches with significant size or depth can be eliminated according to the user's discretion, if any.

The profiles of 10N sliding specimens at the center of wear scar are illustrated in Figure 4(b), where the horizontal axis is in sliding direction. When $\Delta=3.19\mu m$, almost no sink is noted. The 38.95μm case shows only shallow scar, and a rise area exists just like the Figure 4(a). The other two cases have deeply worn-out profile, and they are believed in gross slip.
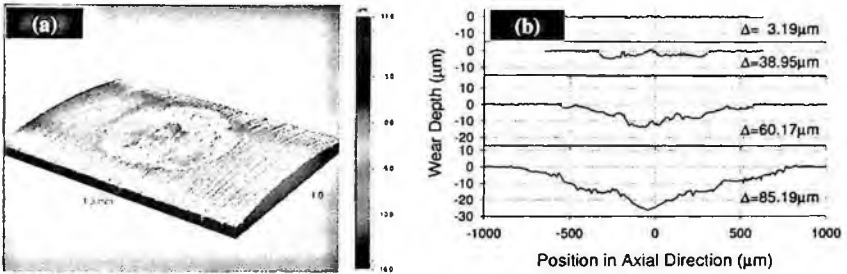
Figure 4. Profile of wear scar; (a) 3D topography for 35N($\Delta=21.38\mu m$) specimen, (b) profile for 10N specimens at the center of scar in sliding direction.
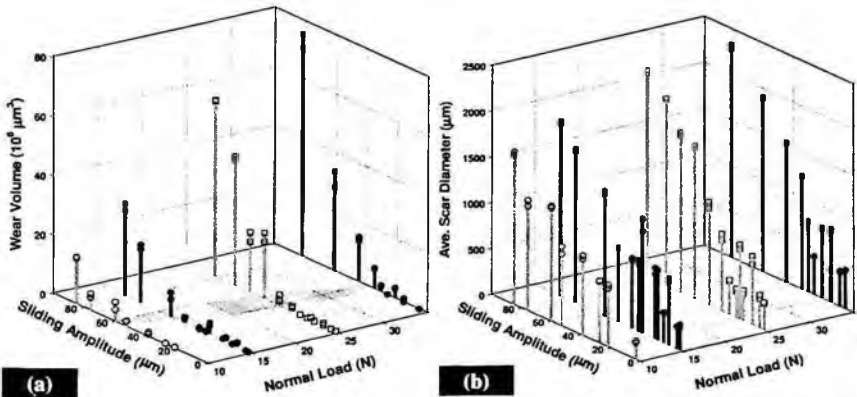
Figure 5. Profile of wear scar; (a) 3D topography for 35N($\Delta=21.38\mu m$) specimen, (b) profile for 10N specimens at the center of scar in sliding direction

3.3. Wear Volume

Wear volumes and the scar sizes for all the specimens have been collected in Figure 5. When the load and sliding amplitude is small, the diameter of wear scar is less than 500μm, which is in the range of the elastic contact area prediction. In fact, the shape of scar is not circular as shown in Table 1(a), probably because

the surface roughness or small primitive debris affects the contact between specimens. Wear volume is very little, and some specimens have even negative number as the first case in Figure 4(b).

For the conditions around the hatched area in Figure 5(b), wear volume is still very small, but the scar diameter has grown to 600~800 μm range. The growth of scar is hesitant despite of increase in sliding amplitude. Figure 4(a) and Δ=38.95μm case in Figure 4(b) belong to this category. Only part of the whole contact area is in relative slip, and material loss is localized accordingly.

As normal load and sliding amplitude increase beyond the shaded area in Figure 5(a), scar and wear volume grows rapidly. The profiles of Δ=60.17μm and 85.19 μm cases in Figure 4(b) show deep sink without remarkable local rises.

Because of severe plastic deformation and separated particles from the layers, the typical ring shape of fretting wear mark is not easy to be formed in many specimens. Nevertheless, the relations between the scar size and wear volume in the above-mentioned three different categories of wear evolution is similar to those in each fretting wear regime.

4. Summary

A novel test rig for fretting wear of cross-contacting tubes was introduced. The inherent characteristics of piezoelectric actuator were found suitable, and several additional measures worked well for test accuracy and simplicity of its operation.

Fretting wear of Inconel 690 tubes was studied experimentally. Micrographs showed the development of the wear scars and severe plastic deformation within the contact area. The relationship between wear volume and scar size was able to be categorized into three groups, which are believed to correspond to the fretting wear regimes. These results would be useful for generating fretting wear map.

References

1. M.H. Attia and E. Magel, *Wear* **225-229**, 563 (1999).
2. Y.H. Lee, I.S. Kim, S.S. Kang and H.D. Chung, *Wear* **250**, 718 (2001).
3. D.G. Kim and Y.Z. Lee, *Wear* **250**, 673 (2001).
4. Y.H. Lee and I.S. Kim, *Wear* **253**, 438 (2002).
5. Y.H. Lee, H.K. Kim, H.D. Kim, C.Y. Park and I.S. Kim, *Wear* **255**, 1198 (2003).
6. H. Endo and E. Marui, *Wear* **253**, 795 (2002).
7. H. Endo and E. Marui, *Wear* **257**, 80 (2004).

ASSESSMENT OF CREEP DAMAGE ON A PIPE BEND OF 1/2CR1/2MO1/4V STEEL

JUNG-SEOB HYUN

*Plant Integrity Group, Korea Electric Power Research Institute, 103-16 Munji-dong,
Yuseong-gu, Daejeon city, 305-380, Korea*

HYUN-SUN CHOI, WOO-SUNG CHOI, GEE-WOOK SONG

*Plant Integrity Group, Korea Electric Power Research Institute, 103-16 Munji-dong,
Yuseong-gu, Daejeon city, 305-380, Korea*

Components in power plants and chemical plants are subjected to service conditions under which creep processes take place causing material exhaustion. Comprehensive creep damage investigations have been performed on a 1/2Cr1/2Mo1/4V pipe bend which had been taken out of service after 117,603h and 501 start-ups because of severe cracks. The propagation of creep damage in a service-exposed component has been analysed by the metallography. Indentation and hardness tests have been performed on damaged material. Also, Calculation of creep lifetime has been investigated. By measuring diametrical expansion, Accumulated creep strain and actual creep strain rate were calculated. By using the Larson-Miller Parameter, total creep lifetime was calculated. This lifetime is good agreement with actual service-exposed hour.

Keywords : Creep damage, metallography, indentation, hardness

1. Introduction

High temperature components operating in power plants under predominant static load at high temperature, are subjected to time-dependent deformation, i.e., creep in the region of notches or welded joints of structures, even a small amount of stress yields generally a limited local damage zone as a results of increase in local stress due to the stress concentration. The damage starts with an increase in irreversible strain under constant stress, cavity formations, a growth of micro cracks up to macro cracks, which will end up with the component failure.

A variety of methods evaluating creep damage has been examined. They are techniques using matallography, indentation, hardness, creep strain rate, and etc.

So far, the metallographic methods, i.e., the replica technique, has been successfully used for the inspection of components.

In this work, a creep damaged pipe bend of 1/2Cr1/2Mo1/4V steel has been investigated to point out the importance of damage analysis for the assessment of

service-exposed components. The bend has been taken out of the main steam pipe(OD 446.9mm x t 52mm) of a fossil-fired power plant after severe cracks in outer tension zone had occurred. Service parameters and pipe dimensions are given in Figure 1.

(a) Main steam pipe

(b) Cross-section

(c) Surface crack

(d) Area 1, 2, 3
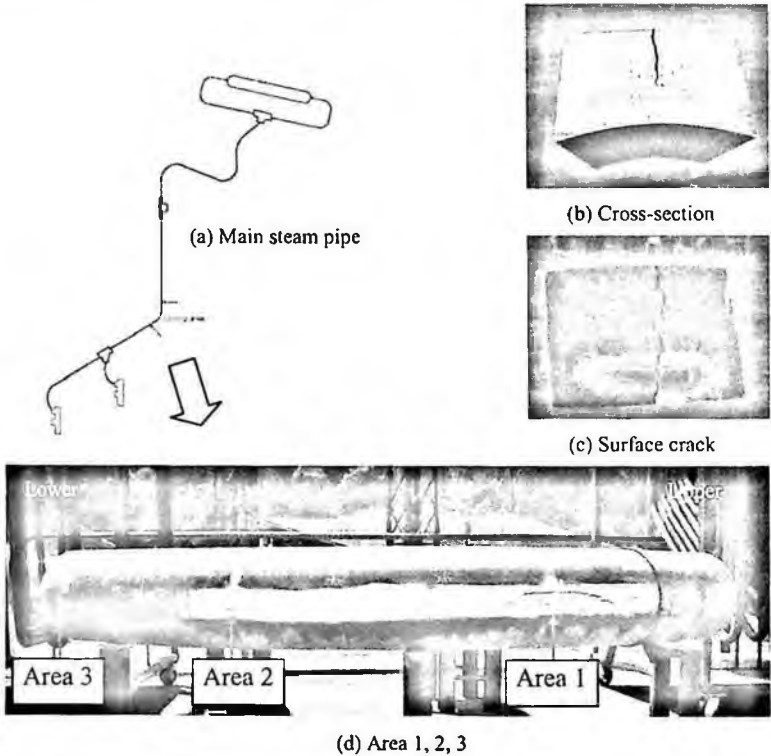
Figure 1. Creep damaged pipe bend of 14MoV63 steel (operating Time : 117,603hr, start-ups : 501, design temperature : 541℃, design pressure : 170 bar)

2. Results

2.1. *Metallographic Results*

The typical damage pattern in the surroundings of the main crack area in shown in Figure 2. The specimen has been taken from an damaged section of the bend. Several replica tests have been made to see how damage has spread through the wall thickness. As a result, high damage grades at the outer surface rapidly decrease towards the inner surface. The damage grade has been classified from A to E according to visible impression by ERA Code. According to this

classification, the damage profile of the crack is represented in Figure 2 (b)-(e). Starting from the undamaged state (damage grade A), several isolated cavities appear at damage grade B. After formation of cavity chains (damage grade C), micro crack formation over several grain boundaries appear (damage grade D). Finally, damage grade E shows macro crack formation over several grain boundaries.
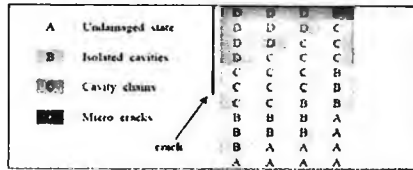
(a) Damage profile of the crack area

(b) Class "B"(×400)   (c) Class "C"(×400)   (d) Class "D"(×400)

Figure 2. Damage profile of the crack area.

Also, Figure 3 (a) shows the number of creep cavity in the circumferential direction at area 1, 2 and 3. We found numerous cavities in the cracked area (outer tension zone - $0°$) and compression zone ($180°$) of the bend. On the other hand, small cavities were observed in the $90°$. Figure 3 (b) shows the number of creep cavity in the cross sectional direction at small distance(5-35mm) from cracked area. It was found that cavity distribution linearly decreased from outer surface to inner surface area.
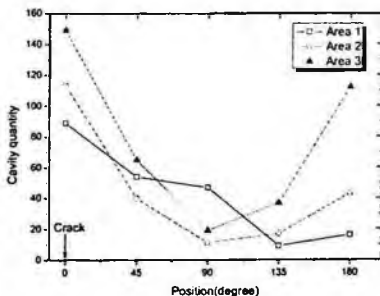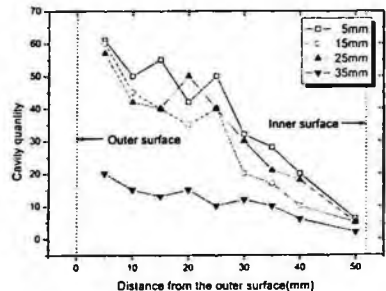
(a) circumferential direction   (b) cross sectional direction

Figure 3. Cavity distribution of the crack area.

2.2. Investigation of Mechanical Properties

2.2.1. Indentation tests

To characterize the mechanical properties indentation tests were performed on damaged material. During the tests, load and penetration depth are continuously recorded as the indentation progressed into the specimen. Figure 4 shows variation of yield strength and tensile strength. Long-term exposure to elevated temperature under operating stresses affects the tensile properties of 1/2Cr1/2Mo1/4V steel, this is expressed more in the yield strength than in tensile strength [2]. The difference between yield strength and ultimate tensile strength is more expressed. The yield strength at the inner surface was remarkably decreased towards the outer surface. On the other hand, tensile strength and strain hardening coefficient were slightly increased.

2.2.2. Hardness tests

Hardness is most likely means resistance to indentation. A hardness test is one of the most frequently used methods of estimating the mechanical properties of a metal. Vickers, Brinell and Rockwell hardness are generally used as hardness number. In this paper, Vickers hardness was used in estimating strength of test material. Figure 5 shows variation of hardness in the cross sectional at crack area and circumferential direction at area 1, 2 and 3. Number of Vickers hardness was remarkably decreased from upper crack (150Hv) to lower crack (120Hv). Also, we found the lowest hardness number in the cracked area (outer tension zone - $0°$) and compression zone ($180°$) of the bend in the cross sectional direction at area 1, 2 and 3.
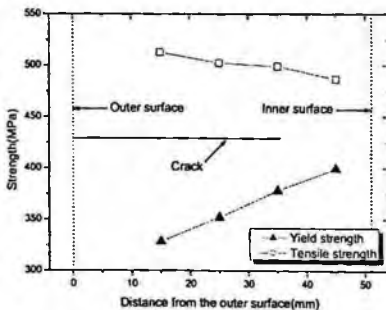
Figure 4. Mechanical properties(cross section).   Figure 5. Hardness number in cracked area.
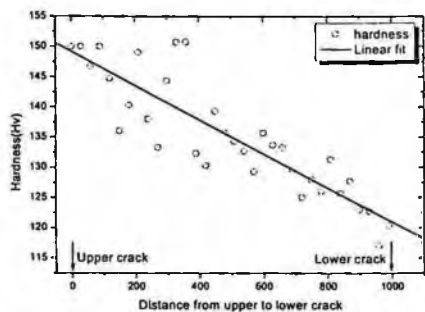
2.3. Determination of the creep lifetime

2.3.1. Calculation of creep strain rate

We measured expansion diameter and thickness of a cracked area in order to calculate creep strain rate[4]. Eq. (1) and (2) are show calculated creep strain and actual creep strain rate. It is significant that hardly 2% creep in terms of diametrical expansion occurred after service hour 117,603hr. Calculated hoop stress is 63.3MPa

position	Thickness(mm)				Average Diameter(mm)
	0°	90°	180°	270°	
Upper	52.8	56.6	58.9	55.4	455.35
Lower	53.5	54.4	56.9	57.5	456.97
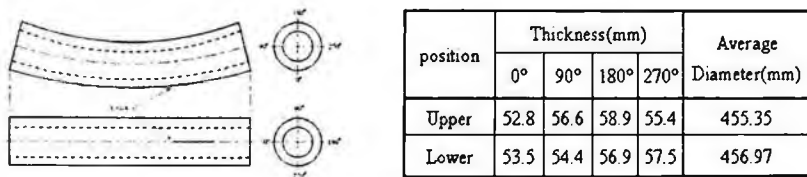
Figure 6. Measuring point and results.

$$\text{Accumulated creep strain (\%)} = (456.2\text{-}446.9) / 446.9 = 2.07\% \qquad (1)$$

$$\text{Actual creep strain rate}(\varepsilon) = 0.0207 / 117630h = 1.76 \times 10^{-7}/h \qquad (2)$$

2.3.2. Calculation of creep lifetime

By using the reference[4] equation $\varepsilon^{0.25} = 3 \times 10^{-4}$ σ, calculated creep rate at 550℃ is 1.30×10^{-7}/h. This is equivalent to 144,894hr at 541℃ using Larson-Miller Parameter where the value constant assumed to 20. Because calculated creep rate(1.30×10^{-7}/h) is 26% lower than the actual creep rate(1.76×10^{-7}/h), Calculated creep lifetime at 541℃ is 107,000 hr. This value is good agreement with actual service-exposed hour 117,603 hr. Also, we calculated creep life time in the Larson-Miller Parameter by using the NRIM creep data. Calculated creep lifetime at 541℃ is 110,782 hr.
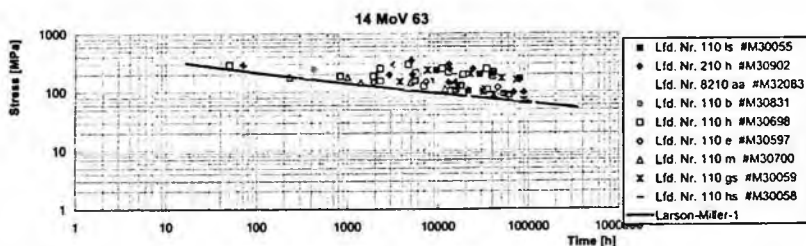
Figure 7. Calculated creep damage for 1/2Cr1/2Mo1/4V steel.

3. Summary

Comprehensive creep damage investigations have been performed on a 1/2Cr1/2Mo1/4V pipe bend which had been taken out of service after 117,603hr because of a severe crack. The propagation of creep damage in a service-exposed component has been analysed by metallography, and the influence of damage on the mechanical properties has been investigated. By measuring

The propagation of creep damage through the wall has been investigated. Low damage grades were spread homogeneously through the whole wall thickness, whereas high damage grades at the outer surface rapidly decreased towards the inner surface.

To characterize the mechanical properties, indentation and hardness tests were performed on damaged material. yield strength at the inner surface remarkably decreased towards the outer surface. Number of Vickers hardness was remarkably decreased from upper crack to lower crack.

Calculation of creep lifetime has been investigated. By measuring diametrical expansion, Accumulated creep strain and actual creep strain rate were calculated. By using the Larson-Miller Parameter, total creep lifetime was calculated. This lifetime is good agreement with actual service-exposed hour.

References

1. F. M. Haggag, Proc. of the small specimen test Techniques Applied to Nuclear Reactor Vessel Thermal Annealing and Plant Life Extension, ASTM STP 1204 (1993)
2. Milorad ZRILIC & Radoslav ALEKSIC, The effect of long term exposure to elevated temperature on steam line steel properties, Thermal Science, Vol. 7, No. 1, 33-46(2003)
3. J. Dobrzanski & A. Zielinski & H. Krzton, Mechanical properties and structure of the Cr-Mo-V low-alloyed steel after long-term service in creep condition, Journal of Achievements in Materials and Manufacturing Engineering, Vol. 23, Issue 1(2007)
4. R. Singh & S. R. Singh, Remaining creep life study of Cr-Mo-V main steam pipe lines, Int. J. Pres. Ves. & Piping 73, 89-95(1997)
5. W. Bendick & H. Webber, Analysis of creep damage and material exhaustion on a pipe bend 1/2Cr1/2Mo1/4V steel, VGB KRAFTWERKSTECHNIK 69, No. 9, 817-825(1989)

DETECTION OF OIL-PAPER INSULATION AGING WITH DIELECTRIC SPECTROSCOPY IN TIME AND FREQUENCY DOMAIN MEASUREMENTS

SEI-HYUN LEE[1]

[1]*Department of Electrical Measurement and Control, Daejeon Polytechnic College, 99-1 Gayang 2(i)-dong, Dong-gu, Daejeon 300-702, Korea*

JU-HAN KIM[2], SANG-OK HAN[2]

[2]*Department of Electrical Engineering, Chungnam National University, 220 Gung-dong, Yuseong-gu, Daejeon 305-764, Korea*

In transformer, temperature and moisture of oil-paper are the most influential parameter affecting the aging behavior of insulation systems. Especially, dielectric properties of oil-paper insulation systems in transformer are remarkably influenced by moisture and aging time. Therefore, aged condition of transformer can be diagnosed using dielectric response measurements. Thus, we investigated Recovery or Return Voltage Measurements (RVM) in time domain (0.02 ~ 2000 s) and dielectric spectroscopy, i.e., measurement of relative permittivity and loss factor (tanδ) in frequency domain (1^{-3} ~ 10^6 Hz) for evaluating the effects of moisture and aging time.

In this paper, the accelerated aging processes of oil-paper samples were investigated at a temperature of 150 °C. Because of simulating the possible oxidation process, typical transformer proportions of copper, silicon steel and iron have been added to oil-paper insulation during the accelerated aging process. For the evaluation of aging behavior, the oil-paper insulation sample were thermally aged at different aging durations at 150, 300, 450 hours which simulate long time service condition due to the used server aging conditions.

1. Introduction

According to how industrial structure has been developed higher voltage and bigger capacity stability of electrical plant supplied with electrical power and reliable maintenance of electric power distribution and transmission system are most important. If faults occur in power system, a spreading effect is expanded more widely and economical loss is extremely serious. Especially, transformers are one of the most important components in power system, have a great ripple effect in failure. Therefore, efficient and accurate diagnosis technique is required for reliable and stable operation for many years. A lot of power companies mainly use a type of liquid immersed transformers using

mineral oil and cellulose paper that is good for overall electrical characteristic. The transformer has been degraded by influences of operating condition under higher temperature, higher moisture and oxidation; in that case, it mostly shows changes of the electrical, chemical and mechanical characteristics. Thermal aging of oil-paper has function of the temperature and time, according to ANSI/IEEE C57.91, it is generally informed that the life in case of operating temperature has rapidly decreased [1]. Furthermore, moisture content of oil-paper has considerably decreased electrical, mechanical properties. Thus, we have investigated Return Voltage Measurement (RVM) in time domain and dielectric spectroscopy in frequency domain for evaluating the effects of temperature and moisture.

2. Experimental

2.1. *Pretreatment of test samples*

In order to remove the moisture contents of the samples, oil and paper were dried under vacuum drying oven for 24 hours at 105 °C. By using vacuum pump, the impregnation of papers was performed with degassed and dried oil with moisture content of 11.2 ppm. When the bubble was removed until, the impregnation process maintained. The moisture content of oil-paper samples were measured by Karl Fischer titration method. Oil-paper test samples were used mineral oil and Kraft cellulose paper.

2.2. *Thermal aging condition of test samples*

The accelerated aging processes of test samples were investigated at a temperature of 150 °C. In order to confirm the effect of aged time, oil-paper samples had different aging duration at New, 150, 300, 450 hours. Oil-paper samples put in glass vessel and the method which applied a heat from outside it. Also it rolled up the paper sample in the electrode and after in order measurement to be possible, impregnated in the oil.

3. Result and Discussions

3.1. *Return Voltage Measurements (RVM) in time domain*

The return voltage measurements were performed on uniform test sample by placing 3mm tick impregnated paper samples in a parallel plate cell with copper electrodes. The parallel electrodes were arranged in oil-filled glass vessel and the parallel electrode was connected to the RVM meter (Tettex RVM 5462).
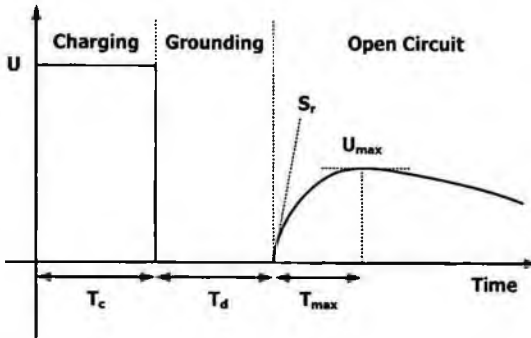
Figure 1. Principle of a Return Voltage Measurement. Charging with U during $0 \le t \le Tc$, grounding period from $Tc < t \le Td$, for $t > Td$, the return voltage is measured at open circuit conditions.

Figure 1 is shown principle of a Return Voltage Measurement (RVM). A dc 2000 V source U_c is applied to the test object (which was previously completely discharged) during an interval $t_1 = T_c$ which should be "so long that at its end the after-effects produced by the application of the potential U_c have dispersed completely" [1]. After a short, but often not well defined short-circuiting period, a "return" or "recovery" voltage can then be measured across the test object, if the input impedance of the voltmeter used is very high [2]. The sequence of return voltage measurement is repeated sequentially for charging time T_c from 0.02 to 2000 s. The charging time to discharging time ratio is 2. The polarization spectrum is measured by recording the maximum value of return voltage U_{max}. Sr or dU/dt is initial slope when return voltage record maximum value. Charging time, taken off form global maximum of voltage spectrum curve, is called T_{max} or dominant time constant T_{cdom} [3].

Figure 2 is shown the influence of aging time on the polarization spectrum curves of oil-paper insulation. These measurements show the dominant time constant T_{max} decrease with increasing aging time and moisture content increase with aging time. In Figure 2, initial slope of maximum return voltage S_r (dU/dt) regarding aging time and moisture content confirmed that it is a clear reaction from the segment where the charging time is short. Table 1 is shown the aging time on moisture content, maximum return voltage U_{max} and dominant time constant T_{max}. It follows in moisture content and aging time and it is clear it will be able to confirm the tendency which the dominant time constant T_{max} decreases.

But, magnitudes of maximum return voltage Umax, any trend with the aging time and moisture content.
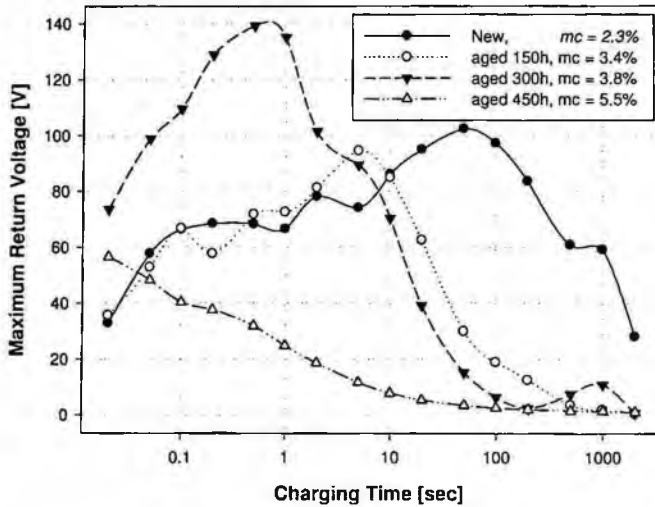
Figure 2. Maximum return voltage at different aging time.
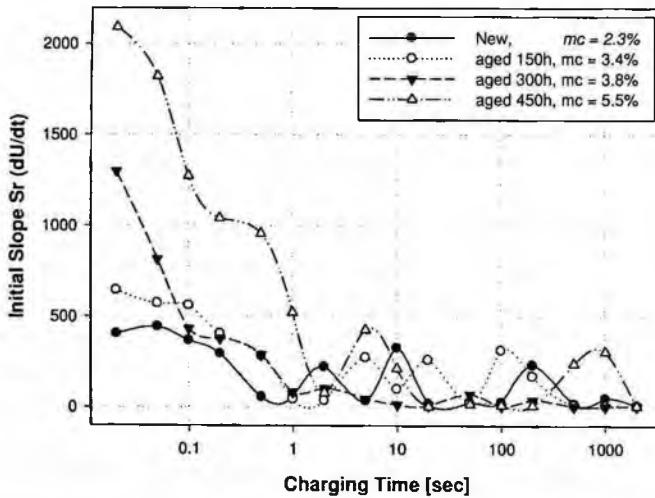
Figure 3. Initial slope of maximum return voltage at different aging time.

Table 1. Aging time on moisture content, maximum return voltage U_{max} and dominant time constant T_{max}.

Aging time	Moisture content	U_{max}	T_{max}
New	2.3 %	102.3 V	50 s
150 h	3.4 %	94.3 V	5 s
300 h	3.8 %	139.3 V	0.5 s
450 h	5.5 %	56.6 V	0.02 s

3.2. Dielectric spectroscopy measurement in Frequency Domain

A WinDETA system (Novocontrol) was used to evaluate the dielectric spectroscopy of the test samples. Frequency was selected as a parameter, and permittivity, dissipation factor (tan δ) were measured by scanning the frequency over the range 0.001 Hz to 1000 kHz. Temperature of test cell was kept at 23 ˚C.
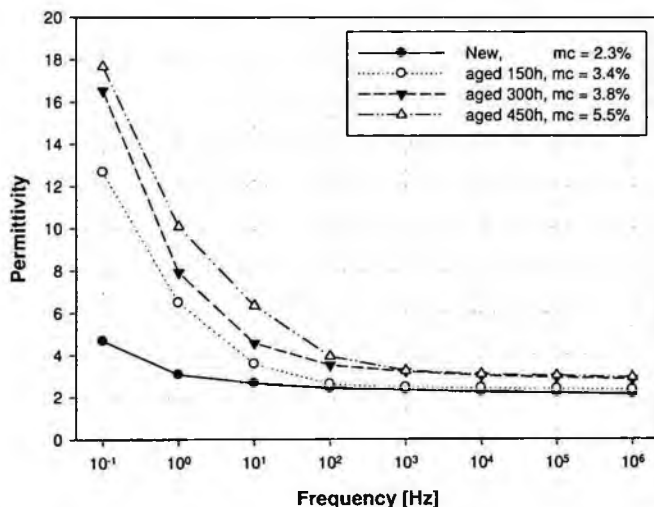
Figure 4. Relative permittivity as a function of frequency at different aging time.

The permittivity and dissipation factor (tanδ) of insulating papers were measured, and Figure 4, Figure 5 Show the results. As shown the result, the permittivity and dissipation factor (tanδ) of paper decreased with frequency especially that of the paper exponentially dropped below 100 Hz. And aged paper remarkably compared with new paper under low frequency. Therefore, at the lower frequencies, aging time can be detected.
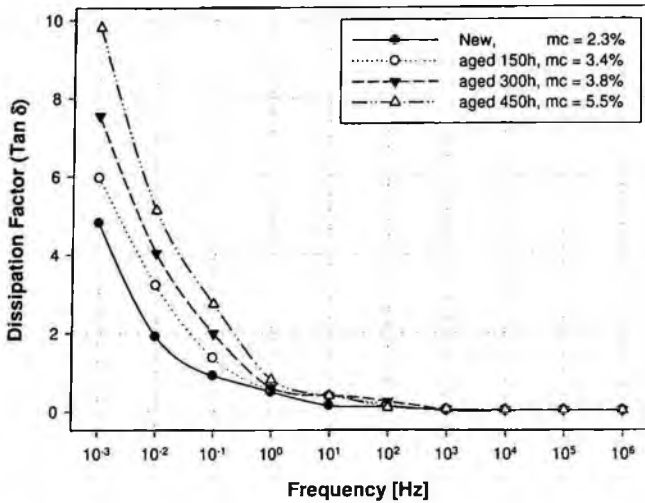
Figure 4. Dissipation factor (tan δ) as a function of frequency at different aging time.

4. Conclusions

To evaluate influence by moisture content and aging time, return voltage measurement and dielectric spectroscopy of oil-paper samples were measured in this paper. The RVM parameter show the dominant time constant T_{max} against aging time and moisture content sensitively, it reacted. Especially, initial slope of maximum return voltage S_r (dU/dt) regarding aging time and moisture content confirmed that it is a clear reaction from the range where the charging time is short. In dielectric spectroscopy, the permittivity and dissipation factor (tanδ) of paper exponentially dropped below 100 Hz. And aged paper remarkably compared with new paper under low frequency. Therefore, as the lower test frequency range, aged samples can be detected.

References

1. ANSI/IEEE C57.91-1981, *"Guide for loading mineral-oil-immersed overhead and pad-mounted distribution transformers"*. July 31, 1981.
2. B. Gross, *"On after-effects in solid dielectrics"*, Physical Review, vol. 57, pp 57-59, 1940.
3. Walter S. Zaengl, *"Dielectric Spectroscopy in Time and Frequency Domain for HV Power Equipment, Part 1: Theoretical Considerations"*. IEEE Electrical Insulation Magazine, vol 19, No. 5, 2003.
4. V. Aschenbrenner, T. Ucik, *"The Contribution to interpretation of Recovery Voltage Method Influence of Oil Resistivity"*, 12th ISH. Paper6.17, 2001.

TEMPERATURE DEPENDENCE OF RETURN VOLTAGE CHARACTERISTICS

SEI-HYUN LEE

Electrical engineering, Korea Polytechnic collages, 91-2 Gayang-2dong Dong-gu Daejeon, 300-700, Korea

YOON-HYOUNG KIM, JIN-HYE JOENG, SANG-GIL HAN, DOO-GIE PARK, SANG-OK HAN

Material and High voltage laboratory, Chungnam National University, 220 Gung-dong Yuseong-gu, Daejeon, 305-764, Korea

Recently the return voltage measurements have been proposed for the diagnostics on the high voltage equipment characterising the dielectric properties of insulation systems. The application of return voltage method at the diagnostics of the accelerating aging equipment such as power transformer are presented in this paper. The return voltage, the intial slope of return voltage and the time to peak value dependencies on charging time are discussed. These characteristics vary depending on the ageing changes of the insulation. That indicate for a possible applicability of the technique for assessing the state of transformer insulation.

The investigations of temperature influence on the return voltage characteristics were aimed to determine the state of the insulation under operating conditions. The theoretical analysis of the results allows to calculate the temperature of insulation that corresponds to the thermal breakdown of insulation.

1. Introduction

Recently, interest about decision of that is state diagnosis and replace of transformer over the world is growing, and much experiment is carried out actually and much diagnosis techniques are developed. The most country is keeping time-based maintenance present, but there is no different view though condition-based maintenance is useful method by economically than time-based maintenance. Therefore, development of transformer state diagnosis techniques may act important role to change from time-based maintenance to condition-based maintenance. Transformer ageing diagnosis techniques until present is PD, DP, HPLC, PDC, RVM, etc., and RVM is important diagnosis techniques that can distinguish ageing degree of transformer and degree of water content in the transformer by nondestructive diagnosis method. RVM's results receive big

effect quantity and state of water in the transformer, therefore, mechanism experiment of water in the transformer is important.

Oil and paper are important material of transformer insulation system, and water affects bad insulation system of transformer that is consisted of oil and paper. State of water in the transformer receives much effect by temperature and this phenomenon affects big RVM's result. Therefore, can speak that thing which study relation with water and temperature in the transformer and consider effect of water in RVM's result is important[5].

2. Theory

2.1. *Return Voltage Measurement*
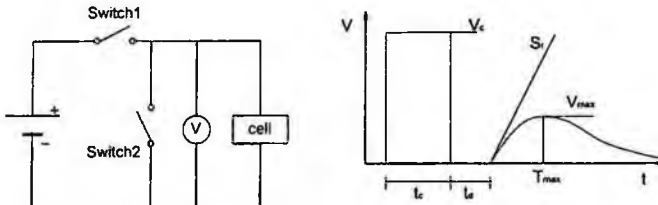
Figure 1. Return Voltage Circuit and time diagram of return voltage

In Figure 1., if Switch1 closed, the cell is charged for charging time. Next, if Switch1 opened and Switch2 closed, the cell is discharged for discharging time. Ratio of charging time and discharging time is two. That late polarization such as orientation polarization don't depolarize for discharge time. Therefore, voltage are detected to voltmeter if open Switch2.

In Figure 2., t_c is charging time, V_c is charging voltage, t_d is discharging time, $V_{r\,max}$ is maximum return voltage, S_r is initial slope of return voltage, T_{max} is time that take when return voltage arrive in maximum value. Among this parameters, $V_{r\,max}$ and S_r are important parameters that decide water contents and degree of ageing of insulating material.

2.2. *Moisture content on inhomogeneous temperature*

Water and heating are important factor which deteriorate insulation performance of electric power transformer insulation system that using oil-paper. Moisture content of oil-paper and pressboard in that use electric power transformer increases by breathing by load change of transformer and water creation of cellulose material by heat and aging phenomenon. If such water is existed to power transformer breakdown voltage of insulation system is reduced, and

becomes factor which shorten life of transformer. Therefore, need to measure water content of transformer and diagnose periodically.

Dynamic behavior of water in transformer can be analyzed by mass transfer between paper and oil [1]. Analysis about heat and mass transfer can express by following way when particular condition

$$\tau_{paper} \frac{\partial C}{\partial t} + C = C_{ss} \tag{1}$$

Where C is moisture content of the paper in percent, C_{ss} is steady state moisture content of paper in percent. τ_{paper} is diffusion time constant for moisture diffusing from both sides in to and out of the paper as following calculate

$$\tau_{paper} = \frac{d^2}{\pi^2 D_{AB}} \tag{2}$$

Where d is the thickness of paper [2], D_{AB} is the diffusion coefficient of material A in B as following being function of density and temperature.

$$D_{AB}(C,T) = D_0 e^{0.5C + E_a\left(\frac{1}{T_0} - \frac{1}{T}\right)} \tag{3}$$

Where E_a, D_0 and T_0 are constant as following for oil-impregnated paper[3].

$$E_a = 8074°K, \quad D_0 = 1.34 \times 10^{-13} m^2 / s, \quad T_0 = 298°K,$$

Diffusion coefficient changes according to moisture density C of insulating paper and temperature T. Eq.(1) shows that water density on insulating paper changes according to thickness d of insulating paper, temperature T, initial water content C_0, steady state water content C_{ss}. If here changelessly in thickness, initial water content, steady state water content, we can know water content of insulating paper by time at each temperature T. As can know in Eq.(2), diffusion time constant is inverse proportion to diffusion coefficient D. Also, can know in Eq.(3), when density C is fixed diffusion coefficient D is proportional to temperature T. Also it can be analogized water equilibrium curved line of oil- paper by temperature by Oommen.[4] This shows that water absorbed in paper can exist in form of free water according to temperature increases. Number of free water increasing RVM's maximum recovery voltage value may move to short charge time.

3. Experimental
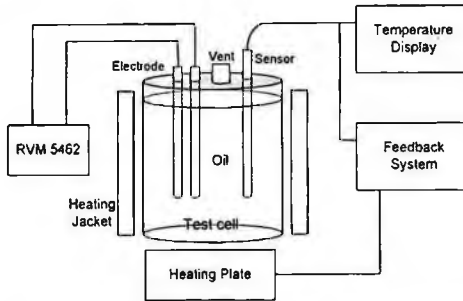
Figure 2. Schematic diagram of Return Voltage Measurement System

Electrodes were made from copper(45mm×20mm×1.5mm) and closed by cellulose paper(50×290×0.18). Such made electrode and insulation oil dried during 10 hours at 105 ℃ in vacuum oven. Test cell that put electrode in insulation oil is impregnated for 5 hours by vacuum pump. Test cell made from glass, so the lower part of test cell was heated by heating-plate, and the side part of test cell was heated by heating-jacket. Temperature in the test cell is measured by thermocouple in the test cell. Also temperature in the test cell is fixed by feedback system. If cell is heated by heating equipment, pressure in the test cell rise and transformation of cell itself can occur. Besides, water in the test cell can escape. Therefore vent was installed to cover of cell to protect this, and if water escapes in cell, device that can measure the quantity was installed.

RVM meter is 5462 that come out in Tettex. Charging voltage is 1000 V and charging time is from 0.02 s to 100 s. Measurement was carried out at 25 ℃, 45 ℃, 65 ℃, 85 ℃ to see dependence of temperature. Measurement was carried out after waiting for 5 hours at each temperature. And acceleration thermal ageing method was used to see effects of ageing. Measurement was carried out at new, 200 hours, 400hours. A screened shield was made to reduce error, because RVM meter receives much noise's effect.

4. Results Analysis and Discussion

Ageing time is prolonged, maximum value of maximum return voltage curve move to left direction at each temperature, see in Figure 3. Cause of this phenomenon is conjectured that is because water increased by ageing in transformer. In addition, maximum value of maximum return voltage curve is situated between about 50 s and 100 s at 25 ℃, and 5 s and 50 s at 45 ℃, 0.5 s and 10 s at 65 ℃, 0.02 s and 1 s at 85 ℃. That is, maximum value of maximum return voltage curve move to left direction at each ageing time. This can predict that free water in transformer is increased according to temperature increasing.

On this occasion, if effect of temperature is very small than effect by ageing, Effect of temperature can be ignored. However preferably, when compared, degree that moved by temperature is big than degree that moved by ageing, see Table 1. Therefore, when measure RVM, if don't consider temperature dependence on RVM's result, RVM's result may not be trusted.
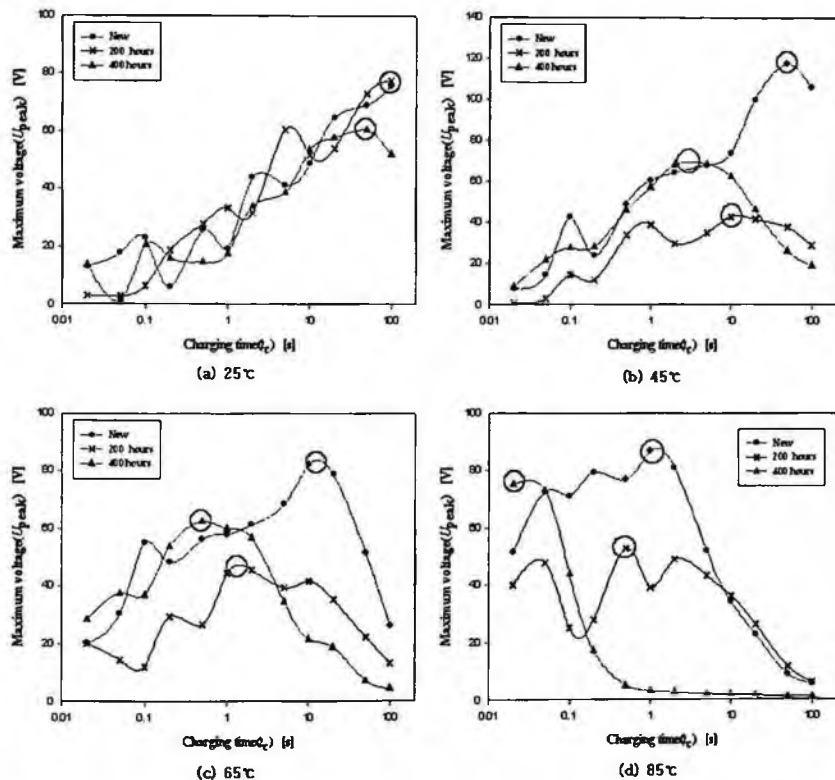
Figure 3. Maximum voltage curves at each temperature

Table 1. Charging time of maximum voltage curve arrive maximum value

	new	200 hours	400 hours
25 °C	$100\,s < t_c$	$100\,s < t_c$	50 s
45 °C	50 s	10 s	5 s
65 °C	10 s	2 s	0.5 s
85 °C	1 s	0.5 s	$t_c < 0.02\,s$

5. Conclusions

This experiment is thing about RVM's temperature dependence that is nondestructive diagnosis techniques of transformer. RVM is diagnosis techniques relatively depend on the effect of water between electrodes. If water between electrodes is much, maximum recovery voltage value moved to short charge time. As a result of experiment, RVM's maximum recovery voltage moved to short charge time by temperature higher. It can expect that as a temperature increases, moisture absorbed in insulation paper becomes free moisture between electrodes. And result is assumed to assessing the Oommens's curved line that water of insulating paper decreases relatively and that water equilibrium between paper and oil.

Maximum recovery voltage value moved by short charge time as aging reaches much. This can assume that cellulose insulating paper that is used for transformer insulator creates water through break of molecular structure by aging.

Through this experiment, could confirm that must consider temperature characteristic as well as aging at using RVM diagnostic. If more experiments are gone, RVM initial characteristic and aging property reference of transformer will be obtained. And using data based on reference, it will be helped to transformer diagnosis. Also, more economical and safety advantages can be obtained for power transformer maintenance by using with other diagnosis method.

References

1. Y. Du, A. V. Mamishev, B.C. Lesieurtc, M. Zahn 'measurement of moisture diffusion as a function of temperature and moisture concentration in transformers pressboard' Cambridge, MA 02139. U.S.A.
2. B. Garcia, J.C. Burgos, A. Alonso, J. Sanz, and , 'A moisture in oil model for power transformer monitoring-PartI: theoretical foundation,' IEEE Trans. Power Delivery, vol. 19, Oct. 2004.
3. S. Foss, "Power transformer drying model," Tech. Rep. DS-002-87, Dynamic Systems, Pittsfield, MA, Oct, 1987. Prepared for General Electric Company, Large Transformer Operation, Pittsfield, MA, and Consolidated Edison Corporation, New York, NY.
4. T. V. Oommen, "Moisture Equilibrium in Paper-Oil Systems," Proceedings of the Electrical / Electronics Insulation Conference, Chicago, IL, pp. 162-166, October 3-6, 1983.
5. T. K. Saha and P. Purkait, "Impact of the condition of oil on the polarisation based diagnostics for assessing the condition of transformers insulation," proceedings of the Power Engineering Society General Meeting, 2005. IEE

FINITE ELEMENT ANALYSIS TO EVALUATE WALL THINNED PIPE USING PVDF COMB TRANSDUCER[*]

BONG-MIN SONG [†]

Graduate School of Mechanical Engineering, Pusan National University,
Research Institute of Mechanical Technology 311
30, Jangeon-dong, Geumjeong-gu, Busan, 609-735, Korea [‡]

JOON-HYUN LEE

School of Mechanical Engineering, Pusan National University,
Research Institute of Mechanical Technology 318
30, Jangeon-dong, Geumjeong-gu, Busan, 609-735, Korea

DAE-HOON LEE

Graduate School of Mechanical Engineering, Pusan National University,
Research Institute of Mechanical Technology 311
30, Jangeon-dong, Geumjeong-gu, Busan, 609-735, Korea

Conventional PVDF transducer has several advantages such as low production cost, easy to produce, fully contact on curved surface due to flexibility and generation of wideband signal. This also can be used for selective mode generation of guided wave when PVDF transducer is produced with the shape of comb type and tone burst instrument is utilized. Therefore, PVDF transducer has better eligibility for precise generation of guided wave mode than using PZT transducer with variable angle wedge. This study evaluated the signal characteristic of guided wave for wall thinned carbon steel pipe. Commercial FEM software was used to analyze mode characteristic of guided wave and the simulation result was compared with experimental result.

1. Introduction

The inspection of pipe lines for nuclear power plants, chemical plants, and the oil and gas industry is very important in order to prevent the possibility of disastrous accidents. As a means of overcoming the threat of such accidents, the guided wave method is utilized in these industries. The selection of the appropriate mode of guided wave is essential to achieve a reliable inspection

result. A comb type transducer is used to adjust wavelength, while a tone burst instrument is used to adjust frequency [1]. However, a piezoelectric comb transducer needs to be fabricated according to the radius of the pipe, which is a costly and time- consuming procedure. Laser based ultrasound with slit array makes it possible to launch selective modes of guided waves by adjusting the interval of the slit array. However, laser based ultrasound generates signals with broadband frequency and this launches multi modes of guided waves [2]. In comparison to the techniques mentioned above, a PVDF comb transducer has several advantages in that it is easily fabricated and inexpensive, is a single mode generation of guided wave and is flexible so that it can be attached to a curved surface [3]. Because of these characteristics, a PVDF comb transducer can be utilized for the condition monitoring method [4]. In the study for this paper, a finite element analysis is carried out for wave propagation in a wall-thinned model of pipe. In addition, an experiment is conducted in order to compare a simulated result with an experimental result.

2. Mode selection of guided wave

The design of a transducer starts with the analysis of a phase velocity dispersion curve. Fig. 1 shows a specimen that is a 6mm thick carbon steel pipe. The longitudinal velocity of this specimen is 5.77km/s and the transverse velocity is 3.138 km/s..
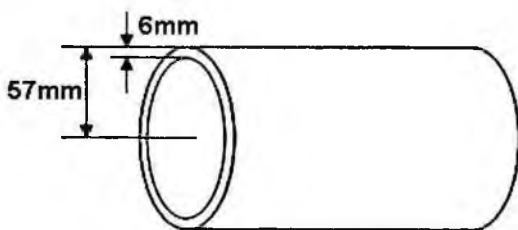
Figure 1.   Geometry of pipe used to model dispersion curve

Figures 2(a) and 2(b) show phase velocity and group velocity dispersion curves. In Figure 2(a), the points where the diagonal line crosses over other curves are available modes to be generated with 6mm wavelength. Although the model used in this study is of a hollow cylinder type, the wave is not launched axisymmetrically and the length of pipe is not long enough to shape a

longitudinal mode of guided wave. Therefore, this model can be assumed to be a plate with a thickness of 6mm.The S2 mode is selected and the phase and group velocity of this mode are 6 km/s and 3.9 km/s, respectively.

$$Cp = f \bullet \lambda \qquad (1)$$

Eq.(1) represents the relationships between phase velocity and frequency and wavelength. Phase velocity and wavelength are already determined and therefore, frequency is 1MHz.
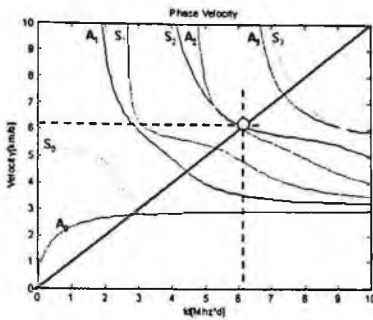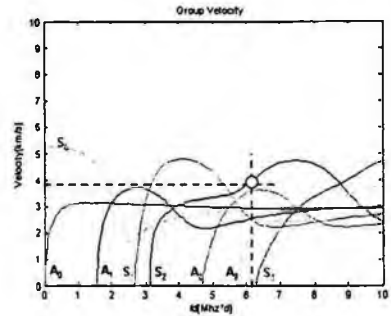
(a) Phase velocity dispersion curve   (b) Group velocity dispersion curve

Figure 2. Dispersion curve for 6mm carbon steel pipe

3. Finite element analysis and experiment of wave propagation for a short pipe

3.1. Finite element model of pipe

An FEA package is utilized in order to analyze the propagation pattern of a guided wave in a pipe. In terms of modeling ultrasound, temporal and spatial resolution is the most critical problem. Generally, the shorter the integration time step (Δ t), the more accurate is the result. [5]. Therefore, a compromise must be found. In Ref. [6], it is recommended that 20 points per cycle of the highest frequency is used.

$$\Delta t = \frac{1}{20f_{max}} \qquad (2)$$

Spatial resolution depends on the number of nodes in wavelength. Alleyne suggested 10 nodes per wavelength [7]. However, discretization of full model of pipe with 10 nodes per wavelength takes a lot of time and usual personal computer can not come up to its performance needed. In this paper, only launching and reception area of guided wave have fine mesh and other area have relatively coarse mesh.
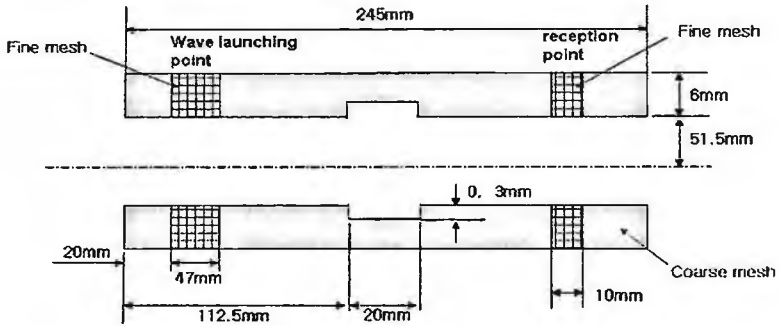
Figure 3. Geometry of pipe model : 2 models with 3mm depth defect and without defect

Fig 3 shows the schematic of the pipe model. Two types of pipe models are analyzed with and without defect. Wall-thinned pipe usually shows a large distribution of corrosion, with a gradual decrease in the thickness of the pipe. However, this model is simplified so as to evaluate the effect that wave propagation has on the wall-thinned part of the pipe.

3.2. Experimental setup and results

Experiments were performed using a PVDF comb transducer. Fig 4 shows the experimental setup. A unit of arbitrary function generator and a gated amplifier make it possible for the generation of a signal with a specific frequency and then to amplify the signal. The wave of 1MHz is launched through the PVDF comb transducer with a 6 mm wavelength. A PZT transducer is used to receive the signal.
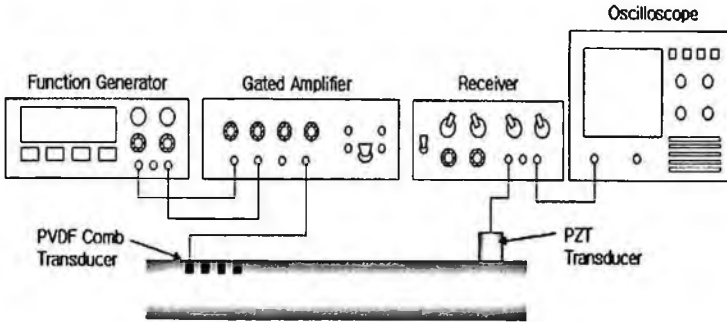
Figure 4. Experimental setup of PVDF transducer

Figs 5(a) and 5(b) show the simulation and experiment results for pipes with and without defect. Many wave packets following the A2 mode are reflected waves due to the short length of pipe.
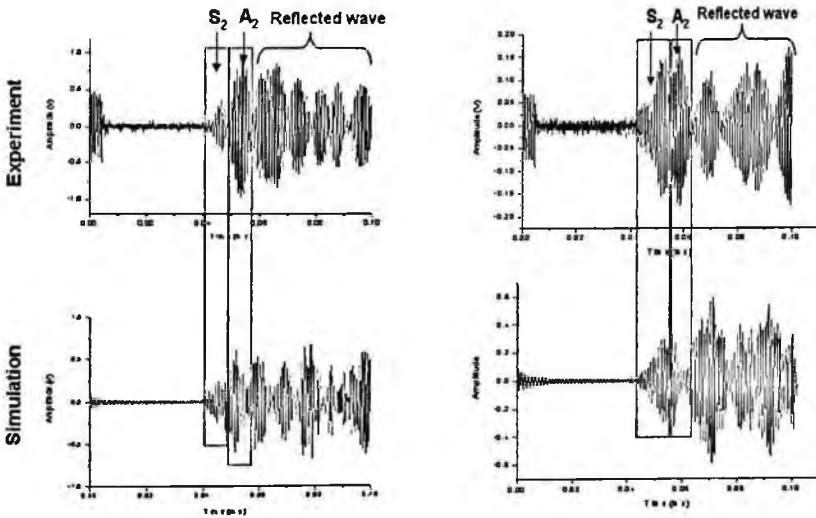
(a) defect free   (b) 3mm depth defect

Figure 5. Simulation and experimental result

A high pass filter filters the signals from simulation and the cut off frequency is 700 kHz. The distance between the launching point and the

reception point of the guided wave is 18.3 cm and the time of flight (TOF) of the S2 mode is 0.046ms. The first wave packet in Fig 5(a) concurs with the arrival time of the S2 mode. The second wave packet coincides well with the arrival time of the A2 mode. In the pipe with a defect, the TOF of the A2 mode increases. Mode conversion is in process due to the variance of wall thickness.

4. Conclusion

A finite element analysis and an experiment of the propagation of the guided wave in the wall-thinned pipe were carried out. In this study, since the geometry of the pipe model is not long enough and the technique of the launching wave is not an axisymmetrical generation of the guided wave, the pipe model is regarded as a plate and the dispersion curve for the plate is applied.. The S2 mode was selected in order to evaluate the pattern of wave propagation. In terms of the finite element analysis of the ultrasound with high frequency, the most critical points are the mesh size and the integration time interval. Fine mesh discretization was conducted only for the area around the launching and reception points of the guided wave. The result from the finite element analysis concurs with the experimental result. The A2 mode is more sensitive to the variance of the thickness of the pipe.

Acknowledgments

References

1. H.Gao, M.J.Guers and ,J.L.Rose, *QNDE.*Vol. 25
2. Jong-Ho Park, Joon-Hyun Lee, *Key Engineering Materials.* Vols 321-323(2006) 743-746
3. Thomas R.Hay and Joseph L. Rose, *Sensors and Actuators* , A 100(2002) 18-23
4. D. H. Wang and S. L. Huang, *Journal of Intelligent Material Systems and Structures* , 11, 482 (2000)
5. Friedrich Moser, Laurence J. Jacobs, and Jianmin Qu, *NDT&E International.* 32, 225-234 (1999)
6. ANSYS 9.0 user's manual
7. Alleyne D, Cawley P.A , *J Acoust Soc.* Am 89(3) 1159-68 (1991)

PROPERTIES OF SHOTCRETE IMMERSED IN VARIOUS HARMFUL SOLUTIONS

DONG-GYOU KIM

Underground Structure Research Division, KICT, 2311 Daehwa-dong Ilsanseo-gu, Goyang, Kyeonggi-do, 411-712, KOREA

HO-SEOP JUNG

Underground Structure Research Division, KICT, 2311 Daehwa-dong Ilsanseo-gu, Goyang, Kyeonggi-do, 411-712, KOREA

SEUNG-TAE LEE

Department of Civil Engineering, Kunsan National University, San 65 Miryong-dong Kunsan, Jeollabuk-do, 573-701, KOREA

HYU-SEONG SHIN

Underground Structure Research Division, KICT, 2311 Daehwa-dong Ilsanseo-gu, Goyang, Kyeonggi-do, 411-712, KOREA

Shotcrete lining as support of tunnel may contact with groundwater in the ground. As the shotcrete is exposed to groundwater with harmful ion on long-term, cement hydration leaching may occur. In this study, in order to evaluate the deterioration of shotcrete in variously environmental condition, compressive strength, adhesive strength and micro-structural analysis were performed on cast-in-place shotcrete immersed in three harmful solutions. From the laboratory test results, the compressive strength of the shotcrete immersed in acid solution (HCl) decreased with the pH value. It was caused by disintegration of the cement hydration products from the shotcrete due to penetration of acid solution in the shotcrete. The compressive strength of shotcrete immersed in sulfate solution increased at 56 days of immersion period. This is attributable to the filling up of the pores by cement hydrate reaction products, and the cement matrix is densified in early period of immersion. After 56 days of immersion period, the compressive strength decreased with immersion period, irrespective of sulfate ion concentration. The micro-structural analysis was conducted to evaluate the shotcrete deteriorated by acid and sulfate solutions. The main factor causing deterioration of shotcrete was the thaumasite and gypsum formation.

1. Introduction

The performance of a cement concrete structure, such as the material quality and function, may degrade over time due to external and internal effects as well as

physical and chemical factors. The chemical erosion of cement concrete structure has been considered as a problem only in special circumstances such as manufacturing facilities including chemical plants or food factories, marine environments and hot-spring regions, but not in the normal surroundings. However, the degradation of concrete structures caused by acid rain, decomposition of hydrate by carbonic acid gas, and sulfate generated by microorganism in sewage disposal plants or sewers recently increase the importance of this problem.

Meanwhile, it has been reported that the amount of sulfate ions contained in soils in Korea is about 0.01 ~ 0.1%, even though it depends on the regional or environmental conditions. The tunnel structure, which is normally constructed under the ground or in the base rock, may be eroded by harmful ions contained in the groundwater, depending on the circumstance to which the support material of tunnel is exposed. Such harmful components can deteriorate the engineering characteristics of shotcrete related to the supporting capability, when the tunnel structure has been commonly used for a long term. It is necessary to prepare measures against the chemical erosion of tunnel shotcrete lining because this problem can reduce the stability of the tunnel structure. Also, it may cause a loss of lives and properties. However, there has been no investigation performed in Korea regarding the performance degradation such as the deterioration of shotcrete.

Therefore, in order to the degree of erosion in shotcrete caused by various harmful ions in contact with the tunnel supporting materials, it was conducted the compressive strength of shotcrete and the adhesive force between shotcrete and rock by immersing shotcrete specimens in sodium sulfate solution, acid solution and artificial seawater with different concentrations. Instrumental analysis was performed to compare the microstructure of shotcrete immersed in three solutions with that of shotcrete immersed in the water.

2. Experimental Details

(1) Materials: The shotcrete for this study consisted of the ordinary Portland cement (OPC) which is appropriate for ASTM C 150, 13mm coarse aggregate (specific gravity 2.60) and fine aggregate (specific gravity 2.59), which are produced from Gyungsan region in Korea, and aluminate setting accelerator which amounts up to 5% of cement. The intended design compressive strength of shotcrete is 21MPa at 28days.

(2) Specimens prepare: In order to evaluate the compressive strength of shotcrete as well as the adhesive strength between shotcrete and rock deteriorated in the

harmful environment, the rock sample (granite) was installed in the rectangular mold (250×500×200mm) made of steel. The shotcrete was sprayed on the rock sample in the mold inside the tunnel construction site and cured in the air for 28 days. The specimen for this study was cored with the diameter of 55mm.

(3) Test methods: In order to identify the characteristics in strength variation of shotcrete, the compressive strength test was conducted on the specimens of shotcrete at each immersion time according to KS F 2405, KS F 2422. The direct tensile test based on ASTM D 2936 and C 1404 was conducted to measure the adhesive strength between shotcrete and rock sample. The compressive strength and adhesive strength tests were conducted on three of them at each immersion time to find the average value. In order to determine the product generated from the reaction of shotcrete, X-ray diffraction analysis was performed in the measurement condition of CuK (Ni, filter) 35kV, 20mA, scanning speed 80/min, full scale 14cps, and $2\Theta = 5 \sim 60°$. The scanning electron microscope (SEM) used in this study is Philips XL 30 ESEM, and EDS (Energy Dispersive X-ray Spectroscopy) type electron microscope analyzer was used together with SEM analysis to observe the microstructure of shotcrete.

(4) Test solutions: As shown in Table 1, acid solution, artificial seawater, and sodium sulfate solution were made to evaluate the characteristics of chemically-immersed shotcrete, and replaced in every two weeks to reduce the dilution of concentration.

Table 1. Types of test solutions

	Concentration condition	Notation
Standard condition	Immersion in water	TW
Acid-erosion environment	pH 1, pH 2, pH3	CA
Seawater environment	Single concentration, Double concentration	SW
Sulfate environment	1%, 2%, 5%	SS

3. Test Results and Analysis

3.1. *Variation in Strength of Shotcrete at Each Immersion Time*

Figure 1 shows the compressive strengths of shotcrete specimens, which were immersed in various solutions and water, at the day of immersion, 14th, 28th, 56th, 112th and 245th days after the immersion. The compressive strength was increased in the early stage. That is because the moisture was not provided to the shotcrete cured in the air for 28 days after being casted, and then specimens have cement hydrate reaction after being immersed in the water or test solutions. As shown in Figure 1, the compressive strength has increased over time until the

56th day after the immersion, in all solutions except pH-1 acid solution. Also, until the 56th day, the compressive strengths of all shotcrete specimens, except the one immersed in the acid solution, have exceeded those of shotcrete cured in the water, regardless of their concentrations. On the other hand, the compressive strength began to decline on the 112th day after the immersion. In the case of the shotcrete immersed in the sodium sulfate solution, the specimen collapsed in all conditions on the 245th day, so that the compressive strength test was not available anymore. These results are caused presumably because the expansion substances, which were produced by the reaction of cement hydrate with SO_4^{2-} ion (sodium sulfate) in the early immersion, fill up the hydration tissues closely. However, as shown in Figure 1, such expansion substances produced expansion cracks and gypsum on the surface, softened the specimens, and thus gradually reduced the compressive strength as the immersion period continued. The compressive strength was not able to be measured anymore since the 245th day after the immersion.
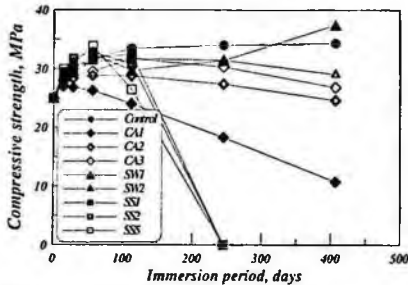
Figure 1. Compressive strengths of shotcretes immersed in various solutions
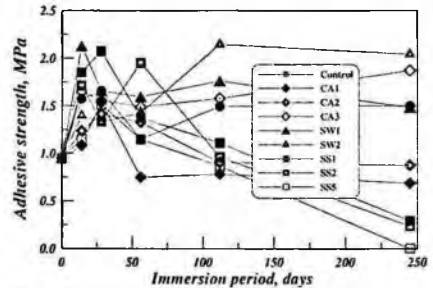
Figure 2. Adhesive Strengths of shotcretes immersed in various solutions

Figure 2 shows the adhesive strengths of shotcrete-rock specimens. In the same situation mentioned above, the adhesive strengths were increased in the early stage because of cement hydrate reaction in specimens. At the same time, the production of expansion substances presumably made the inner structure more dense and the adhesive strength were increased. On the 112th day after the immersion, specimens immersed in sodium sulfate solution had very low adhesive strengths relative to specimens cured in the water. It turned out the adhesive strength of a specimen rather declines when the concentration of sodium sulfate solution is on the increase. Until the 245th day, the deterioration was developed far enough to make the adhesive strength impossible to be measured, in the case of specimens immersed in 5% sodium sulfate solution.

Specimens immersed in 1% and 2% sodium sulfate solutions also showed similar tendencies.

3.2. XRD Analysis

The chemical erosion by acid gradually progresses from the surface to the inside. That is, acid produces Ca^{2+}, silicate, alumina hydrate and calcium sulfate dihydrate by reacting with cement hydrate, and Ca^{2+} is either deposited or dissolved in acid again. According to previous studies, calcium hydroxide has the highest decomposition rate of cement hydrate by acid, although it normally depends on the type of hydrate produced. Such a reaction softens the cement paste on the surface, eliminates its adhesive ability, and eventually washes it out from the surface. The aggregate is exposed and is further fallen off as the erosion is continuously developed, resulting in reducing the section. The graph in Figure 3(a) depicts the result of XRD analysis conducted on shotcrete specimens immersed in pH-1 solution for 1 year. The cement hydrate was not detected as far as the crystal peaks such as quarts or feldspar, originated from the aggregate in the non-cement area, are found.

In addition, the result from the XRD analysis of shotcrete specimens immersed in the artificial seawater for 1 year is depicted in Figure 3(b). The peak of portlandite was not found regardless of concentration, whereas peaks of ettringite, thaumasite and brucite, which cause the deterioration of shotcrete, were detected.
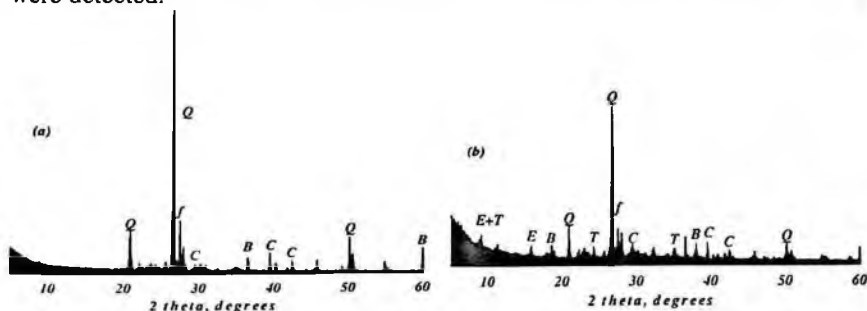
Figure 3. The results of XRD analysis of shotcrete immersed in (a) the acid and (b) artificial seawater.

3.3. SEM and EDS Analyses

2000 times-magnified images of SEM and EDS analyses results from shotcrete specimens, which had been immersed in the water, acid solution, artificial seawater and sodium sulfate solution for 1 year, are shown in Figure 4. It is noticeable, in Figure 4(a), that the tissues of specimen cured in the water are

close and in good condition without any micro-cracks, while showing C-S-H hydrates. As shown in Figure 4(b) ~ (d), The deterioration substances of shotcrete specimen, such as ettringite, thaumasite, brucite and gypsum, were produced during the reaction, and they are in accordance with the XRD results. In case of shotcrete specimens immersed in 5% sodium sulfate solution, it turned out ettringite as the erosive substance was identified, portlandite disappeared, and the hydration structure was not as close as when being cured in the water.

(a)Being cured in tap water   (b)pH-1

(c)Artificial seawater(double concentration)   (d)5% sodium sulfate
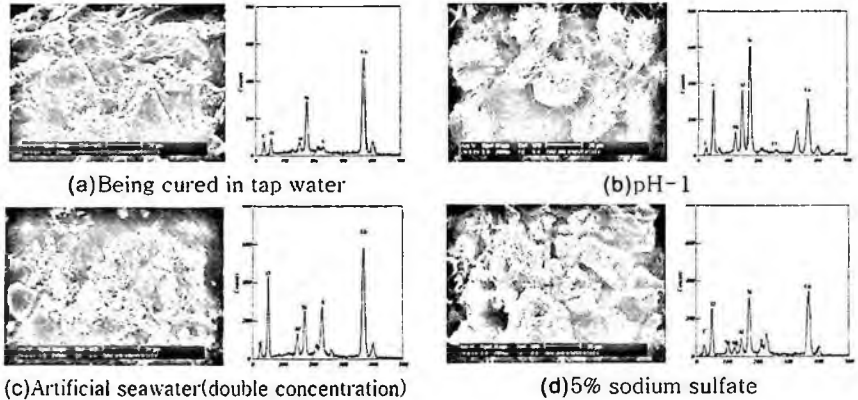
Figure 4. Results of SEM and EDS analyses of shotcretes immersed in various solutions

4. Conclusion

This study is to investigate the chemical erosion of shotcrete specimen with the aluminate setting accelerator. The summaries of results are as followed.

(1) The compressive strength and the adhesive strength of shotcrete specimens, immersed in harmful solutions with different concentrations, were high until the 8th week since the immersion began. However, they rapidly declined in case of sodium sulfate, regardless of concentration.

(2) As the immersion continued longer, various harmful ions penetrated into the shotcrete specimen. Expansion substances were generated by reacting with the cement hydrate, and eventually the performance of shotcrete was degraded by producing the expansion cracks and softening the surface of specimens.

(3) The results from XRD, SEM and EDS analyses showed that the expansion substances, such as ettringite, thaumasite, brucite and gypsum, degraded the performance of shotcrete, and softened shotcrete.

A MORPHOLOGICAL STUDY IN THE MANDIBULAR SECOND PREMOLAR USING A MICRO-CT

KEYOUNG JIN CHUN

*Fusion Tech Center, KITECH, 35-3 Hongcheon Ypjang
Cheonan, Chungnam 330-825, Korea*

OUI SIK YOO

*Fusion Tech Center, KITECH, 35-3 Hongcheon Ypjang
Cheonan, Chungnam 330-825, Korea*

YE YEON WON

*Department of Orthopaedic Surgery, Ajou University, San 5 Wonchun Yeongtong
Suwon, Gyeonggi, 443-749, Korea*

Tooth morphology has an important role in esthetical characteristics, functional performance, and physiological action. Mandibular second premolars among teeth were taken for a close investigation with a micro-CT, which is representative equipment for a non-destructive measurement. Thus, the shape of the tooth was classified into a few partitions and measured by setting the reference axis for expressing internal and external morphology numerically. About a thousand tomographic medical images were obtained for each of eleven specimens from Korean males and females, which were reconstructed to three-dimensional form. The length and width of each dental tissue was measured to determine the average value. In this tooth type, the width of dentine is comparatively larger than that of enamel, and buccal tissue of the crown is thicker than lingual tissue. Hence, buccal tissue can afford to withstand against exterior impact or stimulus. We have noticed a point of difference and similarity from Caucasian's data and by gender and get some results in tooth standardization technique. These results are able to be used for development of dental equipment, clinical trial, dental jurisprudential reference, and anthropological data.

1. Introduction

Tooth morphology is used in the field of clinic, dental equipments, dental materials, and implant machining. It is clinically or technologically essential for surgical, conservative, root canal, coronal polishing, endodontic, and orthodontic treatment.

Normal shapes of teeth, suitable arrangement on dental arch and natural occlusion are closely related to a functional performance and a physiological

action. The shape of the tooth has an important role in masticating and protecting periodontal tissue as the tooth has the function of mastication, protection of inner tissue, facial forming, pronunciation, and etc. [1].

A mandibular second premolar has a similar shape to that of a mandibular first premolar [2, 3]. Thus, measurement criterions for the mandibular first premolar had also been applied to the second one. Using a computerized tomography, an internal morphological study has progressed through a precise and non-destructive method. Europe, on the other hand, paid attention to an investigation by histomorphological measurement and America, Germany, etc. did the same to an external morphological study [4, 5] by connection with the tooth brush manufacturers and dental resources firms, etc.

2. Materials and Methods

2.1. *Specimen*

Five male mandibular second premolars and 6 female ones from persons mainly in their 20s or 30s were used as the test specimens. In order to be tomographed in accordance with the compatible coordinate, they should be set up by the tooth datum axial line as shown in Figure 1. This line was based on the view of the dental arch, which is the axis of the tooth planted in the mandible.

Figure 1. Datum Line of Specimen.

2.2. *Criterion for Measurement*

The measurement criterion for the external morphological data is identical to those applied by G. V. Black [6] for Caucasians and to the advice of the clinician as shown in Figure 2 in order to compare two sets of data morphology.
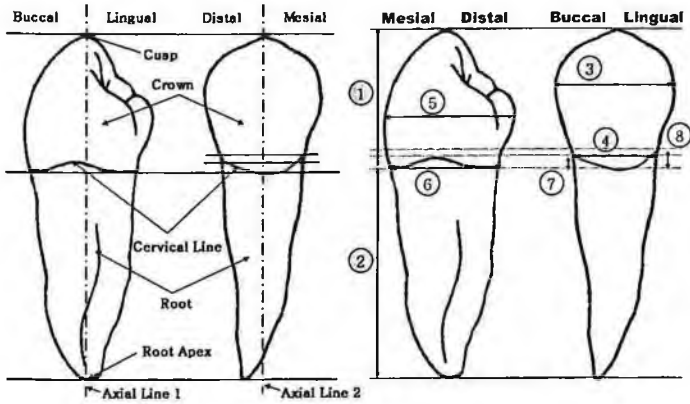
Figure 2. External Criterion

External measurement part numbers signify the following terms:

1. Length of crown
2. Length of root
3. Mesio-distal diameter of crown
4. Mesio-distal diameter of crown at cervix
5. Labio-lingual diameter of crown
6. Labio-lingual diameter of crown at cervix
7. Mesial curvature of cemento-enamel junction
8. Distal curvature of cemento-enamel junction
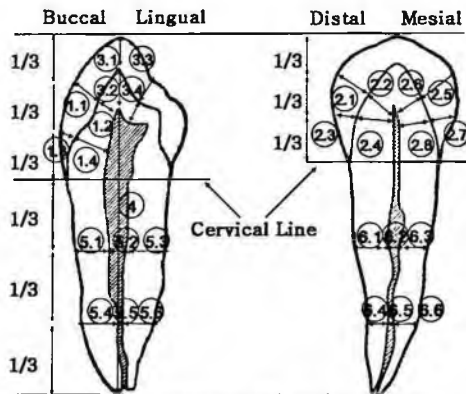
Figure 3. Internal Criterion.

The measurement criterion for the internal morphological data has not been presented in the dental research. Thus, according to the clinician, it was

originated to apply the trisection method [7] of the tooth morphology as shown in Figure 3.

2.3. *Measurement*

As illustrated in Figure 4, the datum axes should be lined up on a jig and the axes of the jug and specimen should be lined up to obtain the specimen's slice in a consistent view. Figure 5 demonstrates the micro-CT (SkyScan 1072) with 8 μm resolution. Precise two dimensional cross sectional morphological data was converted to the model of STL format using Vworks (CyberMed, Ver 4.0), the 3D manipulation images software used in the medical field. Values measured were leveled and applied to t-test (two-tailed, α=0.05) for comparison by gender.
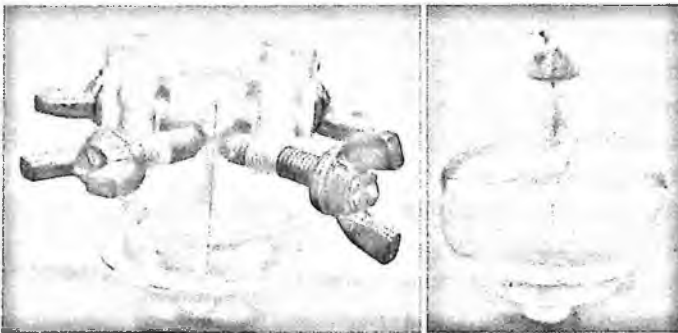
Figure 4. Jig.
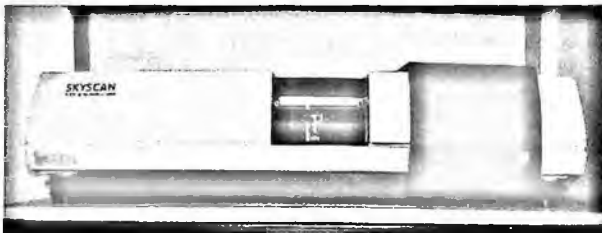
Figure 5. Micro-CT.

3. Results

Table 1 reveals the statistical external morphological data (average and standard deviation) of the mandibular second premolar of Korean adult males and females compared with G. V. Black's.

Table 1. External Morphological Value (unit: mm)

EMPN[*]	Male's Ave. (Standard Deviation)	Female's Ave. (Standard Deviation)	G. V. Black's Data
①	7.48(1.07)	6.98(1.08)	8
②	14.60(3.10)	12.32(1.37)	14.5
③	7.50(0.59)	7.36(0.53)	7
④	5.40(0.35)	5.04(0.43)	5
⑤	8.64(0.55)	8.37(0.63)	8
⑥	7.43(0.47)	6.92(0.30)	7
⑦	0.57(0.44)	0.44(0.27)	1
⑧	0.84(0.40)	0.63(0.37)	0

* EMPN (External Morphological Part Number)

Table 2 reveals the statistical internal morphological data (average and standard deviation) by gender.

Table 2. Internal Morphological Value (unit: mm)

IMPN[*]	Male's Ave. (Std. Dev.)	Female's Ave. (Std. Dev.)	IMPN[*]	Male's Ave. (Std. Dev.)	Female's Ave. (Std. Dev.)
1-1	1.30(0.20)	1.33(0.36)	3-4	3.23(0.44)	2.45(0.94)
1-2	2.31(0.35)	2.00(0.19)	4	17.58(3.36)	15.44(1.80)
1-3	0.62(0.12)	0.68(0.13)	5-1	2.27(0.24)	2.19(0.22)
1-4	2.42(0.18)	2.42(0.12)	5-2	1.48(0.41)	1.10(0.21)
2-1	1.26(0.04)	1.29(0.18)	5-3	2.38(0.29)	2.48(0.37)
2-2	3.22(1.06)	2.94(0.29)	5-4	1.78(0.15)	1.80(0.18)
2-3	0.89(0.13)	0.92(0.21)	5-5	0.78(0.42)	0.62(0.28)
2-4	2.23(0.43)	1.98(0.06)	5-6	1.93(0.26)	1.70(0.81)
2-5	1.16(0.20)	1.19(0.23)	6-1	1.70(0.08)	1.61(0.13)
2-6	2.98(1.16)	2.92(0.12)	6-2	0.85(0.09)	0.73(0.19)
2-7	0.73(0.02)	0.89(0.20)	6-3	1.59(0.12)	1.68(0.27)
2-8	2.20(0.41)	1.93(0.24)	6-4	1.37(0.19)	1.31(0.20)
3-1[**]	1.42(0.22)	0.96(0.24)	6-5	0.43(0.17)	0.48(0.11)
3-2	3.35(0.46)	3.48(0.14)	6-6	1.22(0.25)	1.38(0.17)
3-3	1.56(0.49)	1.54(0.72)			

* IMPN (Internal Morphological Part Number)
** There are significant differences in the mean value of Korean male and female internal morphology (t-test, $\alpha=0.05$).

4. Discussion

The morphological value measured indicates some differences according to race and gender. The difficulty lied in the comparison between Korean and Caucasian teeth because G. V. Black's data has few significant figures. However, from the external morphological data, it was found that Korean crowns are shorter and thicker than Caucasian's on the average, even considering the standard deviation. Furthermore, the distal curvature of cemento-enamel junction didn't appear in Caucasian teeth while it did at a comparatively high ratio to the length of crown in Korean teeth. The statistically significant difference in the mean value of Korean male and female internal morphology was found in the enamel thickness of the cusp (IMPN 3-1).

The width of dentine was comparatively larger than that of enamel, and buccal tissue of the crown was thicker than lingual tissue. Hence, it was noticed that buccal tissue can afford to withstand against exterior impact or stimulus.

5. Conclusion

Distinctive feature of teeth according to race and gender, as well as internal and external morphological value as suggested above could be helpful for the development of dental equipment, clinical trials, dental jurisprudential reference, and anthropological data. Through this criterion and method, maxilla teeth as well mandible ones can be expressed in internal and external morphological data. It is expected that the technology of artificial teeth and clinic treatments would be advanced for Koreans and, by extension, for Asians as well.

Acknowledgments

References

1. H. Horiuchi, et al., *Oral physiology,* Gomoonsa (2003).
2. R. E. Jordan, *Kraus' dental anatomy and occlusion,* Mosby-Year Book (1992).
3. K. J. Chun, et al., *Conf. IEEE Ind. Elec. Soc.* SA7-3 (2004).
4. L. Bodner, et al., *J. Orthod. Dentof. Orthop.* **120**, 623 (2001).
5. A. Pegoretti, et al., *Biomat.* **23**, 2667 (2002).
6. G. V. Black, *A work on operative dentistry,* Medico dental publisher (1924).
7. B. J. Bae, et al., *Carving of Tooth,* Chunggusa (2001).

BIOMECHANICAL NONDESTRUCTIVE EVALUATION OF JOINT MOVEMENTS AND MUSCLE LENGTH OF LOWER LIMBS DURING HEMIPLEGIC WALKING[*]

SUNGJAE HWANG, JONGSANG SON, YOUNGHO KIM[†]

Department of Biomedical Engineering, Institute of Medical Engineering
Yonsei University, 234 Maeji-ri, Heungup-myun
Wonju-si, Gangwon-do 220-710, South Korea

JUNGMI PARK

Department of Rehab. Med. Wonju College of Med., Yonsei University, 612 Ilsan-dong
Wonju-si, ChungNam 220-701, South Korea

Many studies have been unsuccessful to classify biomechanical characteristics in pathological gaits of hemiplegic patients using joint motions of the lower extremity. In this paper, we analyzed nondestructively changes in joint movements and the muscle length of lower limbs during hemiplegic walking by 3D motion analysis and musculoskeletal modeling. Twenty young healthy volunteers and three hemiplegic patients participated in this study. 3D motion analyses were performed by using six infra-red cameras and four force plates. The musculoskeletal model was made based on subjects' anthropometric data and 3D motion capture data. The musculoskeletal model included twelve major lower extremity muscles based on the modified Hill-type muscles in each lower limb. Results showed that significant differences in ankle joint motions during pre-swing and initial swing. Insufficient push-off was found during pre-swing in hemiplegic walking, without enough contraction of gastrocnemius and soleus. Semimembranosus was shown to be tighter and thus knee flexion was larger during loading response than those in the normal subjects. Length changes of extensor muscles were also very comparable to joint motions in the sagittal plane. The present study would be very useful to classify and characterize various abnormal gait patterns.

1. Introduction

Hemiplegic patients have paralyzed motor/sensory nerves due to stroke, traumatic brain injury and so on. These patients, in general, involve impaired inter-segmental coordination, abnormal movement and pathological gait patterns

[†] Corresponding author: younghokim@yonsei.ac.kr

because of the muscle spasticity, muscle weakness and disorder of controlling motor nerve [1].

Various studies have been performed to solve problems of hemiplegic walking, because the gait ability is very important for better quality of life and abnormal gait can induce other musculoskeletal disorders. Sutherland *et al.* [2] analyzed common gait abnormalities of the knee in cerebral palsy, and Christopher *et al.* [3] reported quantitative kinematics of gait patterns during the recovery period after stroke. In addition, Hullin *et al.* [4] studied kinetic gait patterns in cerebral palsy. Most of researches about analyzing hemiplegic gait pattern were performed by observational analysis or motion analysis system, and these methods could determine simultaneous motions from various view points. However, abnormal joint motions in hemiplegic walking occur as a result of abnormal muscular activities due to the spasticity and impaired inter-segmental coordination. There're no proper measurement methods to analyze various muscle activities during dynamic conditions like walking or running. The surface electromyogram (EMG) measurement, the most common method to analyze muscle activities, is not also enough to analyze activities of deep muscles during walking. In addition, limitations of surface EMG and the complexity of movements such as bi-articular muscle activities make it very difficult to analyze interactions among muscles during movements [5]. Nevertheless, recent developments in techniques regarding musculoskeletal modeling of the human body has enabled anatomically accurate placement of muscle models. It has become possible to calculate muscle length and its accompanying muscle force by inputting relative muscle parameters [6]. Thelen *et al.* [7] performed dynamic simulations using a computed muscle control. Lloyd *et al.* [8] also developed a musculoskeletal model to estimate muscle forces and joint moments in the knee in vivo. However, unfortunately, these studies were based on normal walking.

In this paper, we analyzed changes in joint movements and the muscle length of lower limbs in hemiplegic walking by using the 3D motion analysis and the musculoskeletal modeling.

2. Method

In the present study, twenty young healthy adult volunteers who had no previous history of musculoskeletal or neurological disorders and three hemiplegic patients were chosen for the subjects (Table 1). Gait analyses were performed using the 3D motion analysis system (VICON 612 system, VICON, U.K.) with six infrared cameras, coupled with four force plates (AMTI, U.S.A.; Kistler, Switzerland). All gait analysis data were transferred to a musculoskeletal

modeling software, SIMM (Musculographics Inc., U.S.A.), and inverse dynamic analyses were performed with a lower extremity musculoskeletal model of twelve major muscles in each limb: gluteus maximus, gluteus medius, gluteus minimus, adductor magnus, psoas, semimembranosus, biceps femoris short head, rectus femoris, vastus intermedius, medial gastrocnemius, soleus, and tibialis anterior. Muscle parameters, such as muscle action line, origin and insertion were referenced with the Delp's work [6]. In addition, a modified Hill-based muscle model [9] was used to calculate individual muscle length. Joint angles, joint moments and muscle forces in the lower extremity were also calculated. Differences between changes in muscle length were plotted as positive value (+) when the muscle lengthened, and as negative value (-) when the muscle shortened, based on the muscle length in the static condition as zero (0).

Table 1. Characteristics of subjects.

	Normal (n=20)	Patient A	Patient B	Patient C
Age(years)	23.2 ± 1.1	43	43	68
Height(cm)	167.6 ± 8.7	165	166.5	167
Weight(kg)	64.9 ± 9.5	70	76.2	75
Diagnosis	-	Lt Hemi d/t CVA	Lt Hemi d/t CVA	Rt Hemi d/t CVA
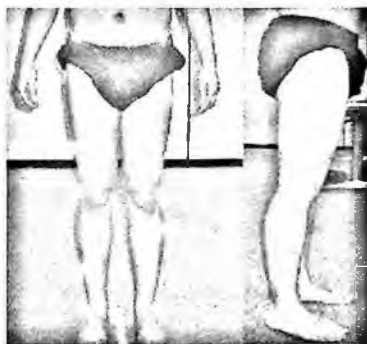
Figure 1. The Helen-Hayes marker set[10] for 3D motion analysis
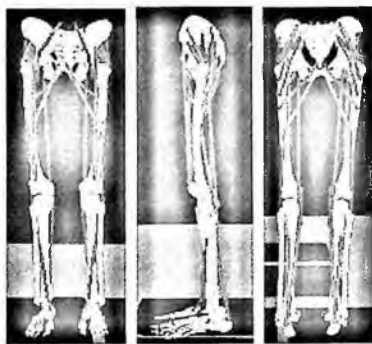
Figure 2. The musculoskeletal model with major 24 muscles

3. Results and Discussions

Figure 1 shows joint angles, joint moments and changes in muscle length for both normal and hemiplegic walking. Hemiplegic walking showed excessive ankle dorsiflexion during stance phase and rapid plantarflexion for push-off during late stance and pre-swing did not occur, comparing to the normal. These are typical characteristics in hemiplegic walking, as reported by Rodda *et al.* [1]

and Sutherland *et al.* [2]. The joint ROM (range of motion) in hemiplegic patients was smaller than those in the normal and toe drag was also found during swing phase. These characteristics in hemiplegic patients could be explained by changes of muscle length, as shown in Figure 1. Gastrocnemius and soleus, ankle plantarflexors, were not shortened enough for push-off during pre-swing, thus considerably weak push-off was found. On the other hand, tibialis anterior, ankle dorsiflexor, was less lengthened during pre-swing due to the contracture of plantarflexors. In hemiplegic walking, comparing to the normal, large knee flexion was found during loading response, but small knee flexion during mid-swing. These were because semimembranosus, a knee flexor, contracted excessively and biceps femoris short head less shortened in hemiplegic walking. Additionally, considerable lengthening of vastus intermedius, a knee extensor, was also found in hemiplegic walking. Hip joint motions in hemiplegic walking were very similar to those in normal walking. Hemiplegic patients walked with more flexed hip joint compared with the normal. As hip extensors, gluteus maximus, gluteus medius and gluteus minimus shortened rapidly during pre-swing in normal walking, but relatively small shortening was observed in hemiplegic walking. Changes in muscle length of extensor muscles, e.g. gastrocnemius and soleus of ankle joint, vastus intermedius of knee joint and gluteus maximus of hip joint, were also very comparable to joint motions in the sagittal plane. These results show changes in muscle using musculoskeletal model has strong correlations with both kinematic and kinetic results based on the classical gait analysis. In addition, changes in muscle lengths, as the source of joint movements could provide very useful information to examine and solve causes of abnormal walking.

71
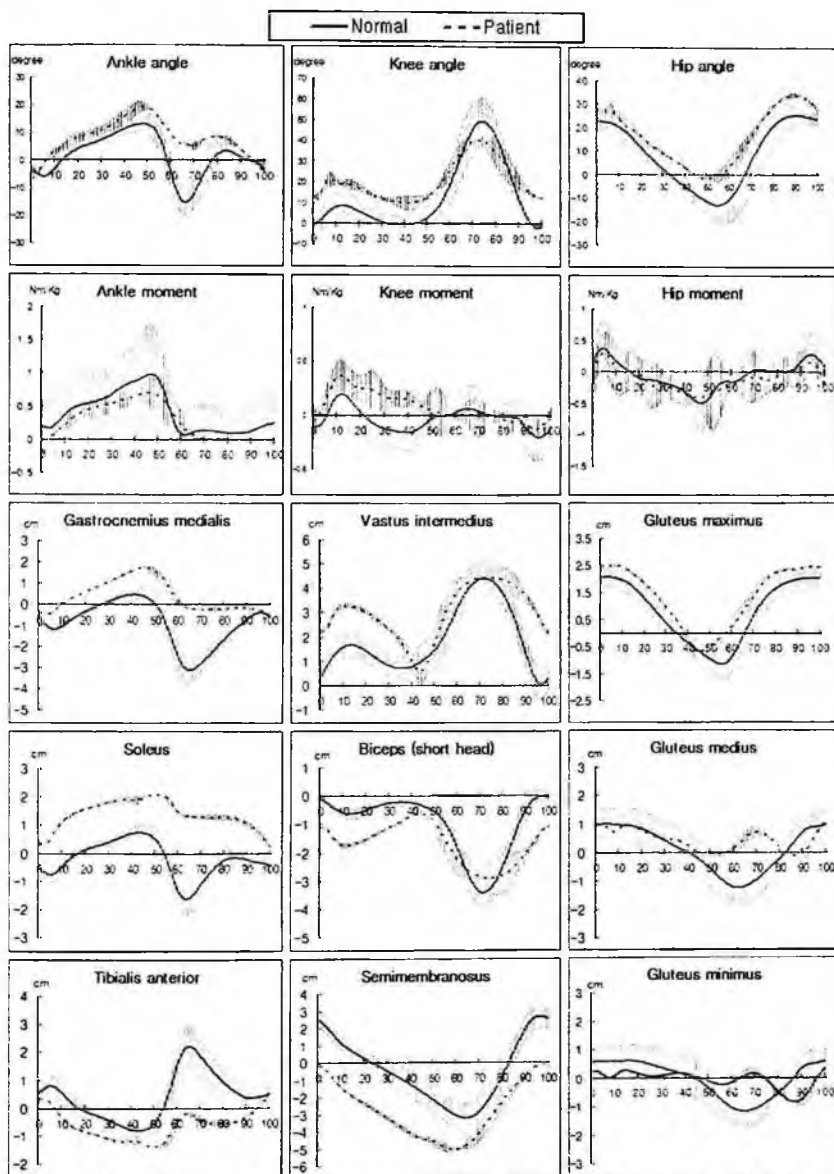
Figure 3. Joint angles, joint moments and changes in muscle length during hemiplegic walking

4. Conclusion

In this paper, we analyzed changes in lower limb muscle length and joint movements for hemiplegic walking by the 3D motion analysis and the musculoskeletal modeling. In hemiplegic walking, ankle plantarflexion was not sufficient because of some contracture of gastrocnemius and soleus during pre-swing. Knee flexion during loading response was large as the result of semimembranosus tightness. Since changes in muscle length result from joint motions, the present study would be very helpful to examine causes of abnormal walking and to provide better interpretation of the clinical gait analysis.

References

1. J. Rodda and H. K. Graham, *Eur. J. Neurol.* **8**, 98(2001).
2. D. H. Sutherland and J. R. Davids, *Clin. Orthop.* **288**, 139(1993).
3. D. M. Christopher, H. Manuel, S. O. Irene and G. L. Robert, *Journal of Stoke and Cerebrovascular diseases* **8**, 312(1999).
4. M. G. Hullin, J. E. Robb and I. R. Loudon, *Gait and Posture* **2**, 37(1994).
5. I. Jonkers, C. Stewart and A. Spaepen, *Gait and Posture* **17**, 97(2003).
6. S. L. Delp, P. L. Loan, M. G. Hoy, F. E. Zajac, E. L. Topp and J. M. Rosen, *IEEE Trans Biomed Eng.* **37**, 757(1990).
7. D. G. Thelen, F. C. Anderson and S. L. Delp, *Journal of Biomechanics* **36**, 765(2003).
8. D. G. Lloyd and T. F. Besier, *Journal of Biomechanics* **37**, 665(2003).
9. F. E. Zajac, *Revs. Biomed. Eng.* **17**, 359(1989).
10. R. B. Davis, S. Ounpuu, D. Tyburski and J. G. Gageet, *Human Movement Science* **10**, 575(1991).

FAULT DIAGNOSIS BASED ON VOXEL DATA OBTAINED FROM CT[*]

JONG CHUL HAN, HAN BEAN YOUN, HO KYUNG KIM[†]

School of Mechanical Engineering, Pusan National University, Jangjeon, Geumjeong Busan 609-735, Republic of Korea

We present computer-assisted fault diagnosis procedures based on volumetric voxel data obtained from x-ray computed tomography (CT). Procedures, such as, image reconstruction with the obtained CT data, volume rendering, segmentation, and mesh data generation, *etc.*, are coded in graphical user interface form. The developed graphical toolkit can extract computer-aided design (CAD) model for a CT-scanned object, and provide a quantitative evaluation by comparing with the object's original CAD data if available. The developed toolkit is useful for the non-destructive evaluation as well as to generate a rapid prototyping (RP) model.

1. Introduction

X-ray computed tomography (CT) is a well recognized imaging modality both in medicine and industry. Although the detailed technologies in CT, such as imaging detectors, scanning geometry, and image reconstruction algorithms, are still on progress, the overall frameworks have been matured enough to be referred to diverse applications.

Three-dimensional (3D) volume CT can allow the output voxel data to rapid prototyping (RP) and reverse engineering applications. Thus, the extraction of computer-aided design (CAD) models of an object is essential. In this study, we have developed a toolkit for extracting standard triangulation language (STL) files from voxel data provided by 3D CT scans. Adapted algorithms are described and the performance of the developed toolkit is demonstrated by applying it to the experimentally obtained CT volume data.

[†] Corresponding Author: E-mail: hokyung@pusan.ac.kr

2. Materials and Methods

2.1. *Algorithms*

All the algorithms described in this study have been implemented as an integrated graphic user interface form for the purpose of computer-aided fault diagnosis. For realization of the GUI, we coded basically using Microsoft Visual C++^{TM} and VTK^{TM} and OpenGL^{TM} were used for convenience and rapid implementation. Main functions involved in the GUI are three-dimensional (3D) image reconstruction, volume rendering, segmentation, conversion of voxel data into STL format, decimation and smoothing, and variance mapping between original and converted CAD files.

Among various 3D reconstruction algorithms, we have employed the Feldkamp's method[1]. The Feldkamp algorithm is a simple extended version of the conventional filtered backprojection (FBP) method in longitudinal direction by weighting the cone angles. Thus, the Feldkamp algorithm is approximate and may cause large distortions when the cone angle is wide. When small parts are, however, inspected, this method is powerful because it is very fast and easily applicable.

Volume rendering is a discrete representation and visualization of objects as sampled data in three dimensions not only the surface but also the entire inner of an object. We have employed two different methods in the developmental toolkit; ray casting and maximum intensity projection (MIP)[2]. Ray casting is a direct volume rendering to sum the density values of voxels and calculate a brightness based on light being absorbed as it propagated from back to front through the 3D voxel data set. In MIP methods, the shade of gray of an MIP voxel is chosen to be the brightest voxel intensity in the 3D volume data encountered along the projection line.

The STL file is a mesh data containing geometrical information describing object details. It consists of vectors designating three vertices of a triangle and its surface normal vector. The procedure to extract a STL file from the voxel data is mainly consists of two steps; segmentation of voxel data in binary form and triangulation of the segmented volume data[3]. Segmentation is the most important procedure in this study because it is very sensitive to the reliability of the data information and measurement property. We have employed thresholding methods based on histogram[4]. The threshold is determined by a simple calculation that maximizes the variance between background and object data in histogram. This approach is intuitive and can be easily realized. Besides the

computational effort is effective. However, it may not be proper for a data having complicate structures, such as most medical images.

To generate meshes with triangles, we employed the well-known marching cube algorithm, which is the successive comparison of the segmented image data with a look-up table[5]. A virtual cube is produced and its eight vertices are defined from two slices of vertically consecutive segmented data. Therefore, it is determined how the slice surfaces intersect the cube by comparing the prescribed vertices (256 cases) with the value of slice voxel data. Since possible triangles are already prepared as a look-up table, the triangulation is automatic. The cube marches to the next location and the process is repeated. However, due to the limited 256 cases the marching cube algorithm is tackled to the free-curved surfaces. Reducing the gap between slices might be a way to overcome this restriction sacrificing computational cost. It is completed that the triangulated meshes are exported according to the STL file format.

The size of STL files extracted by the marching cube algorithm is typically large, hence it is essential to remove unnecessary meshes and merge the meshes in coplanar planes. This data reduction process should be applied to preserve the original topology and to get a good approximation of the original geometry. For data reduction procedures, we have employed various well-known algorithms such as mesh decimation, quadric decimation, and quadric clustering[6].

For the computer-aided fault diagnosis, we have incorporated a function that maps differences in geometries between the original object CAD data and the voxel data generated by CT scans. In order to realize this difference mapping, voxelization of the original CAD data is necessary.

2.2. *Experimental Simulation*

In order to implement the developed toolkit, we designed a chessman, bishop in STL file format based on commercial CAD software (Pro/Engineering^{TM}) and manufactured an RP sample by using an optical stereolithography (SLA 350, 3D Systems, USA) with SL-51902 resin. The manufactured RP bishop sample was then scanned by the laboratory miniaturized CT system. The system consists of an x-ray source with small focal spot of 35 μm, a rotational stage with a minimum step of 0.036°, and an x-ray imaging detector with a pixel pitch of 48 μm and an active area of 50×50 mm^2[7]. By using the developed toolkit, we have extracted the STL file from the scanned CT voxel data and performed the utilization of the developed toolkit by comparing the extracted with the original STL files.
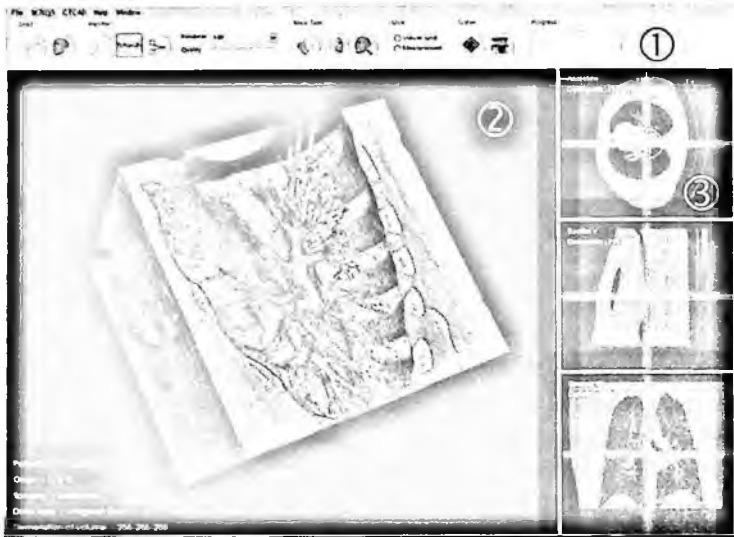
Figure 1. Screenshot of a main window describing the developed toolkit.

3. Results and Discussion

Figure 1 shows a main window of the developed toolkit. Panel ① describes toolbar in which each symbolic button indicates the corresponding function, such as loading of volume data or STL data, handling of visualization and cropping, extracting STL files from volume data including segmentation and triangulation, and difference map procedures. Panel ② describes a partial window to describe 3D visualization. Panel ③ describes subdivided windows to describe three image planes of 3D data, i.e., axial, sagittal, and coronal views.

Figure 2 shows the results of experimental simulation. Figure 2(a) shows the original CAD file utilized as an input file for the RP machine and the photograph of the manufactured RP bishop sample. 3D-rendered images of the CT scanned voxel data are shown in Fig. 2(b). Two different visualizations, i.e., ray casting and MIP are shown. Figure 2(c) shows the extracted CAD files from the developed toolkit and two images are distinguished each other by the degree of decimation. The difference map between the original and extracted CAD files is demonstrated in Fig. 2(d).
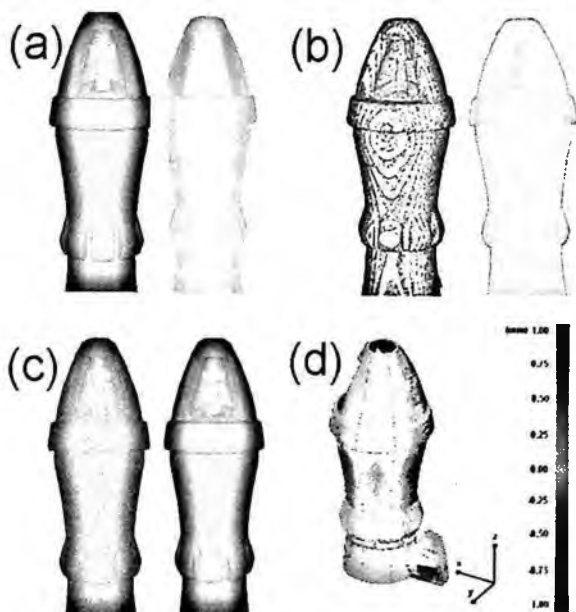
Figure 2. Experimental simulation with a chessman, bishop, for the utilization of the developed toolkit. (a) Original CAD data, which was used as an input file for the RP machine, and the manufactured RP bishop sample. (b) 3D-rendered images of voxel data obtained from the CT scan. Two different visualizations, ray casting and MIP, are shown. (c) Extracted CAD files from the voxel data by using the developed toolkit. Left is the extracted as is and right is after decimation and smoothing processes. (d) A map describing the difference between the original and the extracted CAD files.

4. Summary

A series of algorithms to realize computer-aided fault diagnosis has been integrated in a graphical user interface form. The utilization of the developed graphical toolkit was demonstrated by extracting CAD files from the scanned CT volume data of an RP sample. In the serial procedures, the most important procedure is the segmentation. An object containing various inner structures with similar but definitely different materials requires more elaborate segmentation algorithms. However, the segmentation algorithm used in this study is reasonable to be used in typical industrial applications because most industrial parts are composed of a few materials. It is expected that this study will provide useful tool in computer-aided detection.

References

1. L. A. Feldkamp, L. C. Davis and J. W. Kress, *J. Opt. Soc. Am. A* **1**, 612 (1984).
2. B. Lichtenbelt, R. Crane, *"Introduction to Volume Rendering" Hewlett Packard.*(1998)
3. D. Ma, F. Lin, C. K. Chua, *Int. J. Adv. Manuf. Tech.*, *Vol. 18. pp. 118-127.*(2001)
4. N. Otsu, *IEEE Trans. Sys. Man Cyber*, *vol. SMC-9, no. 1, pp.62~66* (1979).
5. W. E. Lorensen, H. E. Cline, *J. Comp. Gra.*, *Vol. 21.pp.163-169 (proc. of SIGGRAPH).*(1987)
6. P. Cignoni, C. Montani, R. Scopigno, *Comput. Graph. Vol. 22 pp. 37~54.*(1997)
7. M.K Cho, H.K. Kim, Thorsten Graeve, J.M. Kim, *Key Eng. Mater.* 321-323, 1052(2006)

THE ESTIMATION OF KNEE VARUS TORQUE BY AN ACCELEROMETER IN OSTEOARTHRITIS PATIENTS AND HEALTHY ADULTS

SEONHONG HWANG

Dept. of Biomedical Engineering, Yonsei University, 234 Maeji Heungeop Wonju City, Gangwon-do 220-710, KOREA

SI-BOK PARK

Dept. of Rehabilitation Medicine, Hanyang University College of Medicine, Haengdang-dong 17, Sungdong-gu, Seoul City 133-792, KOREA

YOUNGHO KIM[†]

Dept. of Biomedical Engineering and Institute of Medical Engineering, Yonsei University, 234 Maeji Heungeop Wonju City, Gangwondo 220-710, KOREA

To investigate and describe the acceleration of the knee during walking in patients with osteoarthritis of knee and healthy adults, 22 patients with osteoarthritis of knee and 22 healthy adults participated in this study. The accelerometer fixed at left fibular head was used to record anterior-posterior, medio-lateral and superior-inferior accelerations of the knee during walking. There was significant increase in lateral and anterior 1st peak of acceleration at loading response in the patients with osteoarthritis of knee compared to healthy adults ($P<0.01$). There was significant decrease in cadence in the patients with osteoarthritis of knee compared to healthy adults ($P<0.01$), but there was no significant correlation between cadence and 1st peak of acceleration at loading response. The anterior acceleration correlated with the lateral acceleration in all subjects ($P<0.01$). Also there was relationship between anterior-posterior, medio-lateral and superior-inferior acceleration in all subjects ($P<0.01$). The accelerometer could be an easy and useful way to evaluate patients with osteoarthritis of knee.

1. Introduction

Osteoarthritis(OA) and other rheumatic conditions comprise the leading cause of disability among adults in the United States and the estimated U.S. prevalence of arthritis was 70 millions during 2001[1,2]. The medical costs for persons with this disease are increasing in the present aging society. Disability due to the arthritis is revealed especially in dynamic situation, but there are little diagnosis and assessment tools for dynamic analysis. More accurate analysis and diagnosis could be possible by using the three dimensional motion analysis systems especially for patients. However, the 3D motion analysis systems are, in general, too expensive and require highly skilled operators. Recently, the accelerometry has been suggested as a useful method for the gait analysis because of the operational simplicity and economical efficiency[3-5].

In this study, knee joint accelerations of osteoarthritis patients were measured and compared with the normal to describe the patients' biomechanical characteristics of knee joint during gait.

2. Methods

2.1. *Subjects*

Twenty two healthy females and twenty two female patients with knee joint arthritis were selected for this study. Medically compromised patients, peripheral neuropathic patients, patients with fracture history in vertebrae and lower limbs, and gait disabilities were not included.

Table 1. Characteristics of subjects.

	Osteoarthritis group	Non-osteoarthritis group
Age (years)	60.5±5.5	57.3±3.4
OA duration (years)	5.3±3.2	0
Height (cm)	163.7±6.0	164.3±5.2
Weight (kg)	58.7±6.0	59.3±5.6
Cadence (steps/min)	98.2±21.0	108.5±6.0

Values are mean±S.D. OA: osteoarthritis.

2.2. *Methods*

Three axial accelerometer(CXL04LP1Z, Crossbow Ltd, USA) was mounted on the subjects' left fibular head and they were asked to walk 10m straightly as their own comfortable speed.

Mean values of acceleration were subtracted from measured values to calibrate the effect of gravity with respect to the inclination of sensors. The first maximum values were considered as the first maximum acceleration of the knee joint during gait cycles[7].

2.3. *Statistical Analysis*

SPSS v. 11.0 was used for the statistical analysis and paired t-test was performed to compare the acceleration characteristics between normal persons and osteoarthritis patients. Correlation coefficients were analyzed by using the Spearman's rho correlation test($p<0.05$).
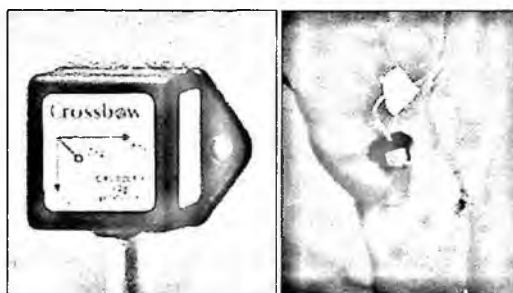
Figure 1. Accelerometer (left) mounted on the left fibular head (right).
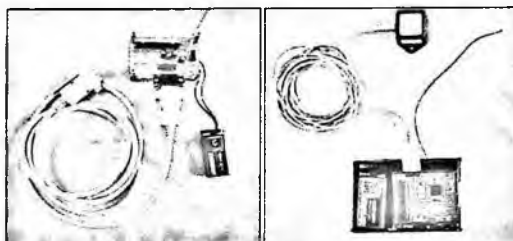
Figure 2. Acceleration measurement system composed of receiver (left) and transmitter (right).

3. Results

3.1. *Comparison of knee joint acceleration between normal and patients*

There was a significant increase in the lateral and the anterior 1st peak of the acceleration during loading response in patients with knee osteoarthritis ($P < 0.01$)(Table 2).

3.2. *The relationship between cadence and knee acceleration*

The cadences of patients decreased significantly compared to the healthy adults' ones($P < 0.01$), but there was no significant correlation between cadence and the 1st peak of the acceleration during loading response.

3.3. *The relationship of three directional knee joint acceleration*

There was a good correlation with the anterior and the lateral acceleration in all subjects($P < 0.01$)(Table 3). In addition, there was a strong relationship among the anterior-posterior, medio-lateral and superior-inferior acceleration in all subjects ($P < 0.01$)(Table 4).
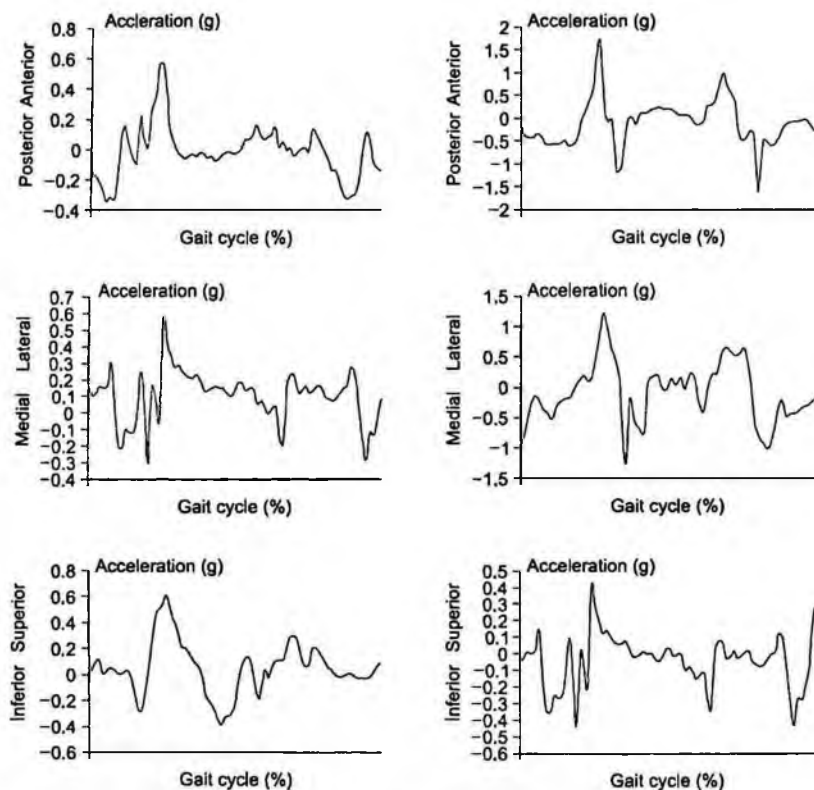
Figure 3. The accelerations at the knee joint (left: non-osteoarthritis group, right: osteoarthritis group)

Table 2. 1st peak of acceleration at loading response of gait cycle in osteoarthritis and non-osteoarthritis group.

	Osteoarthritis group	Non-osteoarthritis group
Ant	1.07±0.40 g	1.40±0.32 g*
Sup	0.86±0.22 g	0.94±0.34 g
Lat	0.81±0.26 g	0.57±0.14 g*

Values are mean±S.D. Paired t-test. Ant: 1st peak of anterior acceleration, Sup: 1st peak of superior acceleration, Lat: 1st peak of lateral acceleration. *P<0.01

Table 3. Correlation of 1st peak of acceleration at loading response of gait cycle between different axis.

	Spearman's rho correlation coefficient		
	Ant	Sup	Lat
Ant		.263	.540*
Sup	.263		.276
Lat	.540*	.276	

Spearman's rho correlation. Ant: 1st peak of anterior acceleration, Sup: 1st peak of superior acceleration, Lat: 1st peak of lateral acceleration. *P<0.01

Table 4. Correlation of 1st peak of acceleration at loading response of gait cycle between different axis.

	Spearman's rho correlation coefficient		
	AP	SI	ML
AP		.476*	.513*
SI	.476*		.633*
ML	.513*	.633*	

Spearman's rho correlation. AP: anterior-posterior acceleration, SI: superior-inferior acceleration, ML: mediolateral acceleration. *P<0.01

4. Conclusions

The peak of the medio-lateral acceleration during loading response significantly increased in knee osteoarthritis patients, and there was a good correlation with the anterior and the lateral acceleration in patients with osteoarthritis. These results showed there were larger varus torques on the osteoarthritis patients' knee joint, and another force on the anterior knee joint. The first peak of knee joint acceleration in loading-response had significant correlations with all three directions. That means knee joint suffers stress from the three-directions. Therefore, we can't help being given the limited information with only radiographs. Accelerometer gives three-dimensional kinetic information as well as the ease of use. This useful method has to be studied continuously and widely to propose the numerical standards or the clinical guidelines.

Acknowledgments

References

1. CDC, *Morb Mortal Wkly Rep.* **50**, 120 (2001).
2. CDC, *Morb Mortal Wkly Rep.* **51**, 948 (2002).
3. Andriacchi TP, Alexander EJ, *J Biomech.* 33, 1217 (2000).
4. Moe-Nilssen R. *Clin Biomech.* 13, 320 (1998).
5. Moe-Nilssen R. *Arch Phys Med Rehabil.* 79, 1377 (1998).
6. Van den Bogert A, Read L, Nigg BM, *J Biomech.* **29**, 949 (1996).
7. Im-sook Jeong, Sa-yup Kim, Youngho Kim, Do-young Jung, Oh-yun Kwon, *J KOSOMBE.* **25**, 289-93 (2004).

DEVELOPMENT OF THE HEALTH AGE FORMULAR AND EXAMINATION FOR WOMEN

JEONGHUN SHIN[†]

Department of Health and Human Performance, Middle Tennessee State University, Murfreesboro, TN, 37132, USA

The purpose of this study was threefold: to analyze factors influencing health and aging, to develop an equation to estimate model for health age, and to help facilitate healthy aging through its cross-validation. A total of 218 middle-aged women of thirty and over participated in this study. General variables affecting prediction variable of health age included cardiovascular function VC(Vital Capacity), body composition BMI(Body Mass Index) and abdominal fat%, such strength variables as grip strength, reaction time, sit-up, close-eyes balance, trunk extension, Vo2max(Maximal Oxygen Uptake), and such measurement variables as triglyceride and total cholesterol. The new estimating equation model for health age is suggested as follows. New Health Age = -0.0039 * VC + 0.151 * Abdominal Fat% + 47.231 * Sit-up + 0.135 * Closed-Eye Foot Balance + 0.347 * Total Cholesterol - 0.037 * Triglycerides - 21.796. As a result of analyzing obesity and cardiovascular group (27) and control group (191), it was found that the difference of health age was 15.75 and the decline in health and strength was rapid in progress, suggesting the significance of this estimating equation model.

1. Introduction

With the improvement of living standards and the development of advanced and medical technology in the 21st century, the number of elderly Koreans increased to 8.3% in 2003 and will increase to 10.3% in 2010, predicting the onset of Korea's super-aged society [1]. This suggests that we will experience a rapidly aged society unparalleled in the world.

With age, the decline in physiological functions accelerates and cardiovascular diseases caused by a lack of exercise such as hypertension and myocardial infarction increase [2]. Thus, concern over exercise is increasing to maintain and improve health. Furthermore, discussions and interest about successful aging have increased [3]. Although comparative research focusing on physical functions, not on real functions are in progress by elucidating a large number of factors changing with age [4-7], few studies focus on the changes in

---

[†] Corresponding Author: shin1014@nate.com

strength and blood composition caused by a decrease in physical activity in relation to actual aging, and the physical measurement factors caused by fat accumulation.

The purpose of this study was threefold: to analyze factors influencing health and aging, to develop an equation to estimate model for health age, and to help facilitate healthy aging through its cross-validation.

2. Method

2.1. Subjects

A total of 218 middle-aged women of thirty and over participated in this study. They were divided into a control group (n=191) who Fulfilled less than four of the following items BMI(Body Mass Index) > 30 kg/m^2, abdominal fat > 0.85, SBP(Systolic Blood Pressure)>140 mmHg, total cholesterol > 250ml/dl, a diagnosis of cardiovascular diseases, and HR(Heart Rate)/min > 90 times, and comparative group (n=27) who Fulfilled more than four of the above items for cross-validation after developing the health age model. All participants were informed of the study objectives and given a detailed explanation of this study and their consent was obtained Table 1.

Table 1. Subjects' physical characteristics.

Age Group	N	Age		Height(cm)		Weight(kg)		BMI(kg/m^2)	
		M	SD	M	SD	M	SD	M	SD
S.G	191	43.20	7.91	159.01	4.81	58.91	6.21	23.30	2.15
C.V.G	27	42.74	6.95	157.49	3.41	64.90	6.07	26.19	2.53
Total	218	42.97	7.43	158.25	4.11	61.91	6.14	24.75	2.34

S.G : Sample group   C.V.G : Cross-validation group,   M : Mean   SD : Standard Deviation

2.2. Method of measurement and Data analysis

Measurement items included vital capacity and blood pressure SBP, DBP(Diastolic Blood Pressure), HR, body composition (body water, muscle mass, %body fat, fat mass, fat free mass, abdominal fat%, B.M.I), anthropometry (skinfolds, girths), fitness (strength, muscular endurance, agility, reaction time, flexibility, power, balance, Vo$_2$max), and blood parameters (Total-cholesterol, High Density Lipoprotein-cholesterol, Low Density Lipoprotein-cholesterol, triglycerides, glucose). To estimate factors influencing health with actual age as a dependent factor, the stepwise method of regression analysis was used. To examine cross-validation of the estimating equation model for health age,

subjects were divided into a sample group and validation group using the random sampling procedure in SPSS12.0 which is statistical analysis program. Finally, the health age of the obesity group and cardiovascular group was compared using the estimating equation.

3. Results

3.1. *Regression analysis for constructing an estimating equation for health age*

As shown in Table 2, the actual age was set up as a reference factor out of 40 items measured to identify the estimating equation for health age. Using the stepwise method, independent variables were optimized according to their significance to construct the regression model. The multiple regression coefficient, R, was .807, the explanatory power of the regression coefficient, R2, was .652 which represented 65.2%, and the F-test of ANOVA was 57.340. It was significant at $p<.001$.

Based on factors derived from regression analysis using the stepwise method, the estimating equation for health age was given by: New Health Age = -0.0039 * VC + 0.151 * Abdominal Fat% + 47.231 * Sit-up + 0.135 * Closed-Eye Foot Balance + 0.347 * Total Cholesterol - 0.037 * Triglycerides - 21.796

Table 2. Result of regression analysis for arriving at a health age

Factor	B	Std. error	t	Sig	R^2	SEE
(Constant)	-21.796	10.633	-2.050	.042		
VC	-3.887E-03	.001	-6.239	.000	.315	6.521
Abdominal fat%	47.231	10.082	4.685	.000	.548	5.297
Sit-up	-.347	.084	-4.134	.000	.616	4.881
Closed-eye balance	-3.698E-02	.010	-3.651	.000	.640	4.726
Total cholesterol	.135	.026	5.273	.000	.591	5.039
Triglycerides	.151	.022	6.951	.000	.506	5.540

R: .807, R^2: .652, F=57.340***, SEE: Standard Error of the Estimate, R: R Square

3.2. *Correlation analysis between the sample group and cross-validation group*

As shown in Table 3, cross-validation between the sample group and cross-validation group showed that the size of constants, the size of explanatory power according to coefficient of determination, health age obtained by the estimating equation, and the error size were nearly identical.

Table 3. Cross-validation of the estimating equation for health age

	Sample group (n=102)	R^2	Cross-validation group (n=89)	R^2
VC	-3.5E-03	.290	-3.5E-03	.310
Abdominal fat%	45.814	.456	57.665	.450
Sit-up	-.457	.559	-.442	.561
Closed-eye balance	-3.3E-02	.619	-3.3E-02	.641
Total cholesterol	.200	.658	.164	.689
Triglycerides	.134	.675	.098	.711
(Constant)	-29.529		-30.010	
SEE	4.626		4.150	
R	.822		.843	
Correlation(r)	.824		.807	
Age(age)	42.98 ± 6.60		43.34 ± 6.11	
Health age(age)	42.96 ± 7.66		43.45 ± 8.16	
Mean difference	0.2		0.11	

SEE: Standard Error of the Estimate, R: R Square

3.3. *Comparison between general subjects and the obesity and cardiovascular group*

As shown in Table 4, while general subjects showed an actual age of were 43.19±7.88, the obesity and cardiovascular group 42.74±6.95. However, on comparison of the health age using the new health age equation, general subjects were 43.15±6.36 whereas the obesity and cardiovascular group was 58.90±8.05, suggesting a marked difference of 15.75years. Examination of the group differences suggested their significance ($p < .001$), strongly validating estimation of the health age.

Table 4. Comparison between general subjects and the obesity and cardiovascular group

	G.S (n=191) M	SD	O.C.G(n=27) M	SD	Mean difference	Std. error	t	p
Age(age)	43.19	7.88	42.74	6.95	.45	1.598	.280	.780
Health age(age)	43.15	6.36	58.90	8.05	-15.75	1.354	-11.630	.001***
Correlation(r)	.807		.179					
Mean difference	0.4		-16.16					
t	-.103		8.698					
p	.897		.001***					

*** p<.001, G.S: General subjects, O.C.G: Obesity and cardiovascular group
M : Mean, SD: Standard Deviation, t: t-test for Equality of Means, p: p-value

4. Discussion

Since it is very common to judge subjects on the basis of the in actual age, it is persuasive to refer to the actual age of subjects as well as several measures as an index of measuring aging [8].

The purpose of this study was to develop a new health age model. To achieve this goal, this study intended to identify factors influencing body aging by measuring cardiovascular performance which is the most basic of the physiological phenomena, anthropometry (girth and abdominal fat) which shows the standards of fatness and body shape, physical fitness which indicates the ability to enjoy daily life without fatigue, and blood.

Previous researchers also suggested some factors associated with health age. Lim et al. selected 184 subjects between 32 and 63 years old residing in Seoul, Gyeonggi, Daegu, and Gyeongbuk and measured 35 items [9]. They finally produced factors influencing health age such as abdominal girth, waist girth, % body fat, FVC, side step, vertical jump, SBP, VO2LT, HDLC/TC, VELT, Vo2max, and HRmax. Kiyoji Tanata selected 134 Japanese women between 32 and 77 years old and measured 58 items identifying produced factors influencing health age such as abdominal girth, systolic blood pressure at rest, VO2LT, HRLT, total cholesterol, LDL-cholesterol, tryglycerides, hematocrit, side to side, single leg balance with eyes closed, forced expiratory volume for one second, and the calcaneal speed of sound [10].

This study produced factors influencing aging such as VC, tryglycerides, abdominal fat %, total cholesterol, reaction time, Vo2max, sit-up, balance with eyes closed, gluteal girth, BMI, trunk extension, grip strength, iliac crest skinfold, front thigh skinfold, biceps skinfold, and abdominal girth and some of them were consistent those of with previous researchers'.

5. Conclusion

1. Factors influencing the estimating equation of health age include balance with the eyes closed foot balance, sit-up, total cholesterol, abdominal fat %, triglycerides, and VC. The new estimating equation model of health age is suggested as follows: New Health Age = -0.0039 * VC + 0.151 * Abdominal fat% + 47.231 * Sit-up + 0.135 * Close-Eye Foot Balance + 0.347 * Total Cholesterol - 0.037 * Triglycerides - 21.796

2. Cross-validation between the actual age and health age shows that the size of constants, the size of explanatory was according to the coefficient of determination, health age obtained in the estimating equation, and the error size were nearly identical in the two groups.

3. As a result of analyzing the obesity and cardiovascular group (n=27) and control group (n=191), it was found that the difference in the health age was 15.75 and the decline in health and strength progressed rapidly, suggesting the significance of this estimating equation model.

References

1. The National Statistics Office, *Statistics of older people*. (2004).
2. A. Z. La Croix, J. M. Guralnik, L. F. Berkman, R. B. Wallace and S. Satterfield, *American Journal of Epidemiololy*. **137**, 88-869 (1993).
3. K. Tanaka and J. C. Z. Wojtk, *Bulletin of Institute of Health and sport sciences University of Tsukuba*. **21**, 1-13 (1998).
4. H. S. Kim and K. Tanaka, *Journal of Aging and Physical Activity*. **3**, 39-53. (1995).
5. M. S. Lee, K. Tanaka, F. Nakadomo, K. Watanabe, N. Takeshima and H. Teruo, *Applied Human Science*. **15**, 97-104 (1996).
6. E. Nakamura, T. Moritani and A. Kanetaka, *European Jounal of Applied Physiology*. **78**, 195-200 (1998).
7. K. Tanaka, Y. Matsuara, F. Nakaclomo and E. Nakamura, *Japan Journal of Physical Education*. **35**, 121-131 (1990).
8. K. Lim, H. Nho, S. N. Lee, S. K. Choi and K. Tanaka, *The Korean Jounal of Exercise Nutrition*. **6**, 247-252 (2002a).
9. K. Lim, H. Nho, S. N. Lee, K. Tanaka and S. K. Choi, *Korean Journal of Physical Education*. **41**, 617-626 (2002b).
10. K. Tanaka, R. Shigematsu, N. Vmecla, Y. Nakata and E. Nakamara, *Medicine and Science in Sports and Exercise*. **36**, S29 (2004).

RECONSTRUCTION OF IMAGES OF SPEED OF SOUND FROM MEDICAL ULTRASOUND IMAGES

MOK-KUN JEONG, SUNG-JAE KWON

Department of Electronic and Communication Engineering, Daejin University, Pocheon, Kyeonggi, 487-711, Republic of Korea

MIN JOO CHOI[1,2,3], ANDREW J COLEMAN[3]

[1]*Interdisciplinary Graduate Program of Biomedical Engineering, [2]Department of Medicine, Cheju National University, Jeju, Republic of Korea, [3]Dept. of Medical Physics, Guy's & St Thomas' NHS Foundation Trust, London, UK*

Medical ultrasonic imaging systems make use of focusing to enhance the resolution in images. The speed of sound (SOS) of a medium should be known in order to achieve precise focusing. The brightness of the image increases as focusing becomes better. Accordingly, the SOS of media can be estimated using relationships between the brightness of images and SOS. The present study has used compounding images to estimate SOS even in speckle images. Phantom tests were carried to measure the average SOS of the tissue and eventually to have images of SOS distribution constructed.

1. Algorithm for Measuring Speed of Sound

Medical ultrasonic imaging systems make use of focusing to improve the resolution of their images. Signals returned from a location of image arrive at receiving elements at different times, but 'receiving focusing' makes the echoed signals look like those returned at the same time [1,2]. The focusing time delay applied to each receiving element can be calculated from the distance that ultrasound propagates when the speed of sound (SOS) of media is known. Current medical ultrasonic imaging systems assume that the SOS of the human body is usually 1,540 m/s. However, errors in the delay time for focusing are inevitable because the SOS varies from 1,450 m/s to 1,600 m/s depending on constituents of the human body [3]. Therefore, the SOS value must be known so that the time delay required for focusing can be accurately calculated.

Explained is a method to experimentally measure an accurate SOS in a medical ultrasonic imaging system. Since ultrasonic images result from a coherent imaging system, the best image of an object is obtained when it is precisely focused. Therefore, unless SOS is accurately known, performance in focusing deteriorates and thus the resolution and average brightness of images

drop. An approximative SOS is preassumed for making focusing. If an image focused was obtained as SOS alters, the brightness of the image changes according to the SOS of the medium. Therefore, the SOS, when the brightness of images reaches its maximum, is regarded as the average SOS value of the medium. The method proposed works well for the case that the image is made on a point target [4].

In a speckle image, however, the brightness of image does not increase proportionally to the performance of focusing, even if the SOS is accurately known. In order to measure accurately the SOS even in speckle images, it was measured in compound images. In a compound image, the constituent images each are obtained by steering at different angles and are coherently superposed each other. In the case of steering a scan line at angle θ, the steering time delay $\tau(x)$ of an element of an ultrasonic probe located at x is calculated by Eq. (1).

$$\Delta \tau_\theta(x) = \frac{x \cdot \sin(\theta)}{c} \tag{1}$$

where c is SOS. This equation indicates that the time delay is influenced by SOS.

Unless an accurate SOS is known, the steering angle changes, with the result that the resolution of compound images is more adversely affected by SOS errors. Therefore, the proposed method to measure SOS using compound images becomes a viable technique that can measure SOS relatively accurately even in speckle patterns as in ultrasonic images of the human body.

2. Simulations

Computer simulation was carried out for a focusing system to verify the effect of SOS. The simulation has the condition that 128 channels of a 7.5-MHz, 192-element, 40-mm wide linear transducer array are activated simultaneously to achieve transmit focusing at a depth of 20 mm as well as dynamic receive focusing.

Figure 1 shows the brightness variation of an imaging point against SOS at a depth of 20 mm in the medium with an SOS of 1,550 m/s. Focusing was performed by varying the SOS in the range from 1,500 to 1,600 m/s and the maximum value of brightness was obtained for an SOS of 1,550m/s. The solid line shows changes in brightness against SOS resulting from compound images constructed by five images obtained at angular intervals of seven degrees, and

the dotted line represents those in a conventional B-mode. The SOS errors are more pronounced in the compound image.
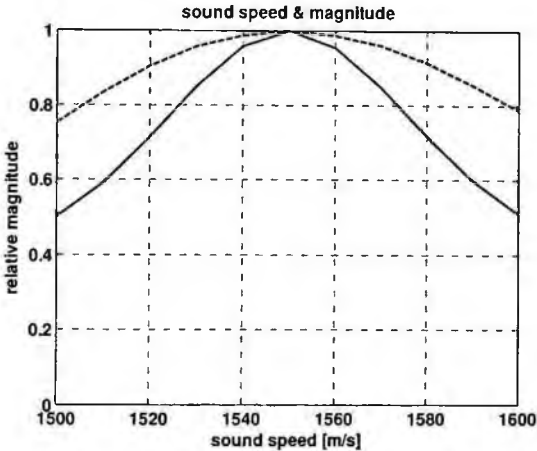
Figure 1. Variation of the brightness of a wire target versus SOS when the true SOS value is 1,550 m/s. The solid and dashed lines represent results from compounding and conventional B-mode images, respectively.

3. Experiments

Figure 2 is the image obtained for wires spaced by 5 mm in a water tank. Averaging SOS values for which the brightness of the image of each reflecting object is maximum, we obtain a measured SOS value of 1,464 m/s with a standard deviation of 18 m/s at a room temperature of 22°C. Therefore, the measured SOS reflects well that of water in which the ultrasound wave propagates.

Figure 3 shows the variations in brightness against SOS for one point reflector. As we obtained curves of brightness against SOS using experimental data, a clear relationship between the two is difficult to identify. However, by curve fitting to a quadratic function we were able to easily find the maximum point. In Figure 3, the dotted line represents the experimental data and the solid line is the result from the curve fitting. We presume the peak point of the quadric to give the SOS of the medium.
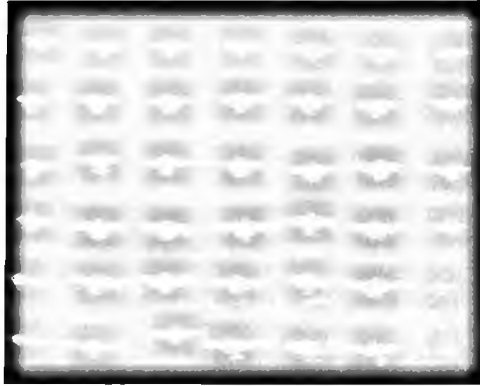
Figure 2. Compound ultrasonic image obtained for the wires spaced by 5 mm in water. Calculation gives the SOS of the water to be 1,464 m/s on average at a room temperature of 22°C.
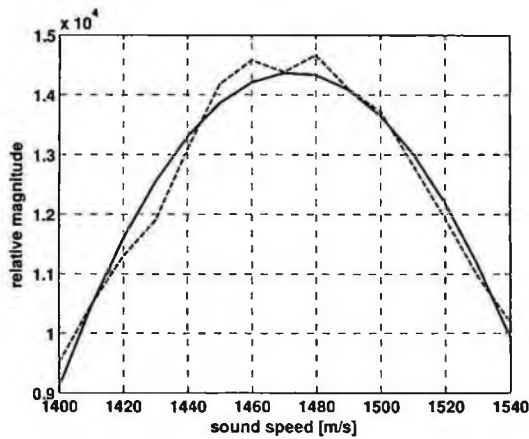
Figure 3. Brightness against SOS calculated for a point reflector in water. The dotted and solid lines represent the experimentally obtained relationship and its curve fitting to a quadratic function, respectively.

4. Speed of Sound Image

In order to measure SOS in speckle images, we constructed a phantom containing a 10-mm diameter cylinder. The SOS was 1,544 m/s in the background medium and 1,450 m/s within the cylinder. We carried out experiments and obtained compounding images, by altering SOS in the range between 1,400 m/s and 1,640 m/s. The left and right panels of Figure 4 show ultrasonic images obtained using an SOS of 1,520 m/s and the measured SOS, respectively. In ultrasonic images, dark regions resulting from large errors in calculation were excluded in the measurement of SOS.

In images of SOS, since ultrasound that propagates in the part of the cylinder is transmitted through the background medium, the SOS calculated in the cylinder was higher than the its true SOS. However, the SOS was calculated to be lower in the region of the cylinder compared to that in background, and we were able to easily differentiate the cylinder from the background in the image of SOS. In particular, the region near the border of the cylinder which has large focusing errors arising from differences in SOS shows large differences in brightness. As a result, the boundary of the cylinder is clearly delineated in the image of SOS.
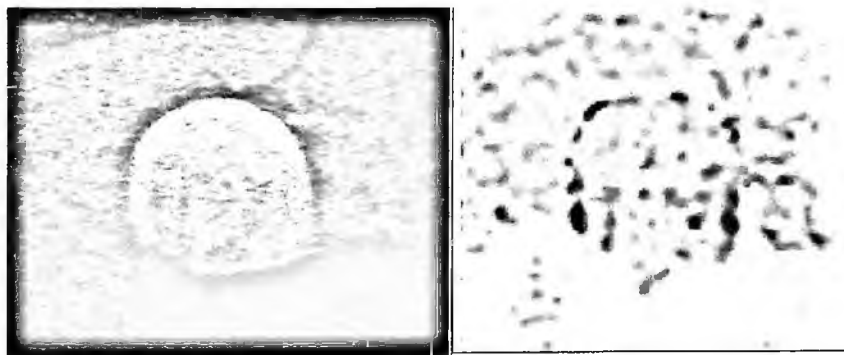
Figure 4. Conventional ultrasonic B-mode compound image (left) and SOS image (right) of the phantom containing a cylinder in uniform background whose SOS is different from that of the embedded cylinder.

5. Conclusion

The study has proposed a simple yet effective method to measure SOS in a medium in an echo mode in a medical ultrasonic imaging system. We obtained SOS of a tissue from compounding images utilizing properties of focusing in the ultrasonic imaging system. Performing experiments on a phantom containing cylinders having a different SOS, we were able to distinguish the cylinder from the background. We expect that the image of SOS can be applied to tissue characterization or lesion monitoring during surgery by high intensity focused ultrasound.

Acknowledgments

References

1. J. H. Kim, T. K. Song, and S. B. Park, Ultrason. Imag. 9, 75 (1987).
2. H. J. Kim, M. H. Bae, and M. K. Jeong, J. Biomed. Eng. 19, 9 (1998).
3. D. Zaho and G. E. Trahey, IEEE Trans. Ultrason. Ferroelect. Freq. Contr. 38, 125 (1991).
4. M. K. Jeong and, S. J. Kwon, J, Biomed. Eng. 19, 321(1998).
5. J. E. Wilhjelm, M. S. Jensen, T. Brandt, B. Sahl, S. K. Jespersen, and E. Falk, Proc. IEEE Ultrason. Sympo.(2000).

MEASUREMENT AND EVALUATION OF IMPULSE FORCE WHICH HUMAN BODY RECEIVES BY CONTACT OF MACHINE AND STRUCTURE

YASUMI ITOH

Department of Gerontechnology, National Institute for Longevity Sciences, 36-3 Morioka, Obu, Aichi 474-8522, Japan

TETSUYA NEMOTO, SHUICHI YANAI, KAZUHARU KOIDE, AKIRA INAMORI, HIROYUKI MATSUURA

Department of Gerontechnology, National Institute for Longevity Sciences, 36-3 Morioka, Obu, Aichi 474-8522, Japan

AKIRA SHIMAMOTO

Advanced Science Laboratory, Saitama Institute of Technology, 1690 Fusaiji Fukaya, Saitama, 369-0293, Japan

In this research, the hit experiment was conducted using the metal baseball bat, the wooden sword, and the aluminum pipe. We considered the evaluation method of impact load using the maximum of impact load, and hit speed. Furthermore, it compared by investigating the impact absorption characteristic of organism soft tissues and buffer material in order to select the buffer material (organism soft tissue substitution object) used when measuring the impact load generated by contact with an assisted living instrument and a human body.

1. Introduction

By development of a robotics technique, the assisted living instruments, which have intelligent functions, are being developed. As a result, there is a possibility that the accident to which the assisted living instrument under actuation contacts a human body may occur. Therefore, preparation of the safety standards of an assisted living instrument is hurried.

However, since many parameters, which should be taken into consideration in order to evaluate the strength of impact force from a viewpoint of personal injury, exist, quantification is difficult.

Moreover, the relationship between an impact load and an injury level has been eagerly studied in the police, in order to clarify existence of the murderous intent in murder cases and injury cases [1, 2]. As a result, it has turned out that

the injury levels by an impact load differ in the situation of organism soft tissues, such as the skin and muscles.

In this research, the impact force measurement system, which used three load cells, was built. Then, we conducted the hit tests by hit objects, such as a pipe made from aluminum, a wooden sword, and a metal baseball bat, and performed study about the measuring method and appraisal method of impact force. Moreover, the impact absorption characteristic of organism soft tissues and buffer material was investigated in order to select the buffer material (organism soft tissue substitution object) used when measuring the impact load which a bone receives by hit.

2. Impact Force Measurement System

The impact force measurement system is the structure which measures the impact load which the upside sheet steel receives by three load cells placed between the sheet steel (300×300×35 mm) of two sheets as shown in Figure 1. As shown in Figure 2, we have placed the center of three load cells at equal intervals (120-degree spacing) in position of 120 mm from the center of the sheet steel, respectively. A system figuration is shown in Figure 3 and a list of instruments is shown in Table 1.

Figure 1. Three load cells are placed between two sheet steel.
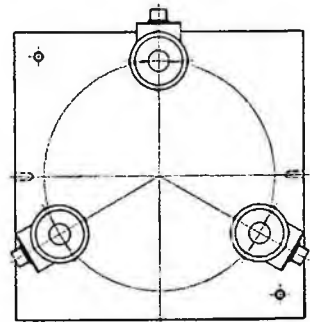
Figure 2. Layout of three load cells.
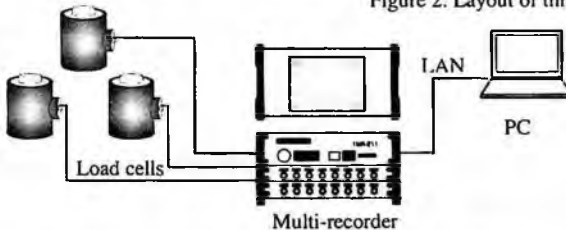
Figure 3. Component of an impulse-force measurement system.

Table 1. Instrument list of an impulse-force measurement system.

Device name	Manufacturer	Type
Load cell	Tokyo Sokki Kenkyujo	CLP-10KNB
Multi-recorder	Tokyo Sokki Kenkyujo	TMR-211
Notebook PC	Epson	EndeavorNT2850

3. Hit Experiment

3.1. *Experimental Procedure*

The impact loads by hit were measured using the sheet steel with a lunar projection shown in Figure 4 instead of the upper steel plate of an impact force measurement system. Experiments were photoed by 500 frames per second using the high-speed video camera (Memory Cam: made by Nac) for measurement of hit speed. The hit objects used for the hit experiment are shown in Table 2. The hit method was made into free fall except for the experiment by human power. Moreover, the experiments in the condition of having covered the sheet steel with buffer material, such as rubber, cell sponge, and soft sponge, were also conducted. The situation of an experiment is shown in Figure 5. Image express (made by Nac) was used for the analyses of high-speed video images. As shown in Figure 5, in order to make image analysis easy, target marks were beforehand stuck on the hit object.
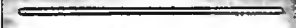
Figure 4. Component of an impulse-force measurement system.

Figure 5. Situation of a hit.

Table 2. Hit objects.

Hit object	Length (mm)	Weight (kg)	Shape
Aluminum pipe	1000	0.3450	
Wooden sword	1150	0.8863	
Metal baseball bat	850	0.7935	

3.2. *Experimental Result and Discussion*

3.2.1. *Comparison by Hit Methods*

The comparative experiments of the hit by human power and the hit by free fall were conducted. The hit object used for this experiment is a pipe made from aluminum. The experimental result is shown in Figure 6. In addition, a hit position is 0.1 m in position from the head of a pipe. There was no difference of the impact load according to the hit method. Moreover, in the range where impact speed is slower than 5 m/sec, it disclosed that impact speed and a maximum-load value were proportionality relation. However, the maximum-load value was decreasing in the range where impact speed is faster than 5 m/sec. It seems that the reason for a maximum-load decrease is deformation of a pipe.
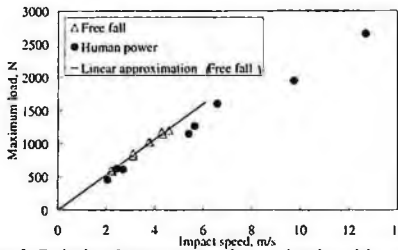
Figure 6. Relation between maximum load and impact speed.

3.2.2. *Comparison by Hit Objects*

Hit experiments were conducted using three kinds of hit objects, an aluminum pipe, a wooden sword, and a metal baseball bat. Experimental results are shown in Figure 7. By all the hit objects, it turned out that impact speed and a maximum-load value are proportionality relation. Moreover, it also turned out that the difference in a hit part does not affect the relationship between hit speed and a maximum-load value. In figure 7, hit positions (distance from an end distant from a hit part) are shown following the name of a hit object.
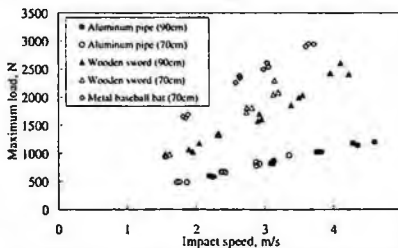
Figure 7. Relation between maximum load and impact speed.

4. Impact Absorption Characteristic Evaluation of Organism Soft Tissue and Buffer Material

4.1. *Experimental Procedure*

The organism soft tissues and buffer material, which were used for this experiment, are shown in Table 3. As shown in Figure 8, organism soft tissue or buffer material was placed on the sheet steel on three load cells of an impact force measurement system, and the experiments which drop 0.5 kg weight on it from height 0.25, 0.5, 0.75, and 1.0 m were conducted. The situation of experiments is shown in Figure 9.

Table 3. Test material.

(a) Organism soft tissue

Name	Thickness (mm)
Pork tenderloin	31.5
Pork loin	57.0
Beef tenderloin	25.0
Chicken breast	21.0
Chicken thighs	11.4
Left arm (human body)	64.1
Right arm (human body)	73.9

(b) Buffer material

Name	Thickness (mm)
Cell sponge	5, 10, 20, 30
Soft sponge	5, 10, 20
Rubber	5, 10, 20
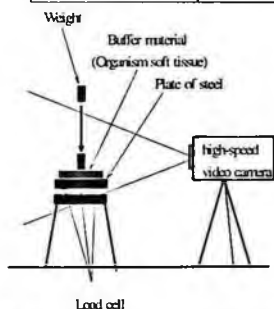
Figure 8. Mimetic diagram of a test situation.

Figure 9. Photograph of test situations.

4.2. *Experimental Result and Discussion*

The experimental results of the buffer material near the impact absorption characteristic of organism soft tissue and typical organism soft tissue are shown in Figure 10. As shown in Figure 10, in organism soft tissue, the relationship between weight falling height and a maximum-load value is not based on the type of soft tissue, but is expressed with the straight line of the same inclination. Moreover, it was confirmed that the measured maximum-load value is also in

102

inverse proportion to the thickness of organism soft tissue. On the other hand, in buffer material, the relationship between weight falling height and a maximum-load value changed greatly with types.

Then, the impact absorption characteristic of buffer materials and organism soft tissues were compared. As a result, it was confirmed on all the conditions (weight falling height, buffer material thickness) that the impact absorption characteristic of organism soft tissue and cell sponge is nearly the same.
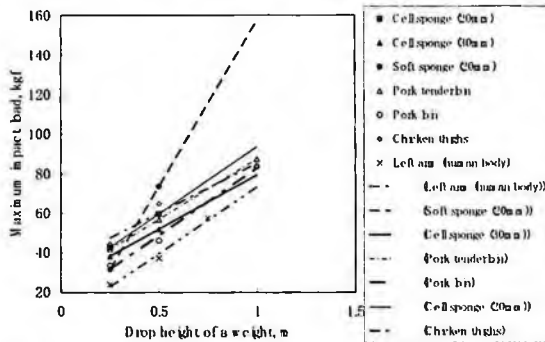
Figure 10. Relationship between weight drop height and maximum load.

5. Conclusions

1. In the range which a hit object does not transform, it was confirmed that it is not based on the type of the hit method and hit object, but impact speed and a maximum-load value show good proportionality relation.
2. We discovered that the differences of the impact absorption characteristic of the organism soft tissue of a different type were few.
3. The impact absorption characteristic of cell sponge is nearly the same as that of the characteristic of organism soft tissue. Therefore, it is confirmed that cell sponge can be used instead of organism soft tissue.

Acknowledgments

References

1. Y. Itoh, T. Ogura, K. Mogami, T. Nemoto and H. Matsuura, *JCOSSAR Paper*, 157 (2007).
2. Y. Itoh, K. Mogami, T. Nemoto and H. Matsuura, *AAFS 59th Annual Meeting, Proceedings*, 156 (2007).

EVALUATION OF HAND FUNCTION RECOVERY IN CHRONIC HEMIPARETIC PATIENTS USING ELECTROMYOGRAPHIC RESPONSES

KISIK TAE[†]

Department of Biomedical Engineering, Konyang University,
119 Daehangro, Nonsan, Chungnam 320-711, South Korea

SUNGJAE SONG

Department of Mechanical Engineering, Kangnung University,
901 Namwonro, Wonju, Gangwon 220-711, South Korea

YOUNGHO KIM

Department of Biomedical Engineering, Yonsei University,
234 Maeji, Heungup, Wonju, Gangwon 220-710, South Korea

The aim of this study was to evaluate the motor recovery in 4 chronic hemiparetic patients with Fugl-Meyer (FM) and EMG characteristics before and after the training program. The training was performed at 1 hr/day, 5 days/week during 6 weeks in 4 chronic stroke patients. Electromyographic activities of the affected hand were recorded during isometric wrist flexion/ extension movements. In all patients, FM was significantly improved after the 6-week training. Onset/offset delay of muscle contraction significantly decreased in the affected wrist after the training. The co-contraction ratio of flexor/extensor muscles decreased significantly. Also, onset/offset delay of muscle contraction and co-contraction ratio correlates significantly with upper limb motor impairment and motor recovery. This EMG technique allows an objective evaluation of changes in muscle activity in post-stroke patients, providing easily measurable, quantitative indices of muscle characteristics.

1. Introduction

Spasticity is attributed to increased muscle tone associated with hyperreflexia [1]. Previous efforts to quantify spastic hypertonia have concentrated on clinical scales [2, 3] and electromyographic analysis of limb resistance to passive or voluntary movements [4]. In spite of this broad range of techniques, no uniformly useful objective measurements have emerged in the clinical practice.

An objective, quantitative measure would achieve widespread clinical acceptance only if its variations broadly paralleled an accepted clinical scale. An important criterion that objective parameters have to fulfill to gain everyday

clinical acceptance is consistency and sensitivity [5]. Clinical scales, such as those proposed by Ashworth [2], offer qualitative information, but lack temporal reproducibility and suffer from a clustering effect in that most of the patients are grouped within the middle grades [5].

In order to expand treatment strategies, the nature of hemiparesis and its relationship to motor recovery must to be further elucidated using quantifiable methods. Prior electomyographic (EMG) studies among stroke patients demonstrated significant onset/offset delay of muscle contraction [6], gaps in EMG interference patterns [7], abnormal co-contraction of agonist and antagonist muscles [8] and abnormal co-activation of synergistic muscles [9].

The purpose of this study is to describe the relationship between characteristics of muscle contraction and motor recovery in chronic hemiparetic subjects after rehabilitative training by designed arm trainer.

2. Method

A. Subjects

As a control group, six of them were right-handed healthy male subjects (age: 34±5, ranging 24~38 years) without any history of neurological or psychiatric disease. Other four were hemiparetic patients (age: 40.8±7 years) in chronic state, 24 months elapsed since hemiparesis; with no severe spasticity (modified Ashworth's Scale: MAS<3) or tremor on affected upper extremity; and no serious cognitive problems, aphasia, attention deficits (Table 1).

Table 1. Demographics of 4 patients with stroke.

Patient No.	Age/ Sex	Lesson type	Paretic hand	Time of stroke (months)
1	44/M	ICH in right BG, TH	Lt.	38
2	37/M	ICH in right BG, TH	Lt.	58
3	49/M	ICH in left BG, IC	Rt.	24
4	33/M	ICH in left TH, IC	Rt.	58

ICH = Intracerebral hemorrhage, BG = basal ganglia, TH = thalamus, IC = internal capsule.

B. Intervention

For the rehabilitative training of patients, we designed the arm trainer [10], which consists of 2 independent handles that move symmetrically. The system provides both handles with symmetric motions such as forearm pronation/ supination or wrist flexion/extension. The affected side can be passively controlled with the symmetrical movement according to the active motion of the unaffected side. Each the training with arm trainer was performed 5 times

per week during 6 weeks. Patients trained both forearm pronation/supination or wrist flexion/extension each 30 minutes, respectively.

C. Fugl-Meyer (FM) Assessment

Fugl-Meyer (FM) assessment has been shown to be valid and reliable and it correlates well with inter-joint upper-limb coordination measurements in the upper-limb of patients after stroke [11]. During the 6-week training, FM in participated patients was measured every two weeks. The initial analyses were one-way t-test to compare measures on the dependent reliables before and after training at 6 weeks of training. An alpha level of <0.05 was used as the level of significance. All statistical analyses were performed by SPSS 10.0 (SPSS, Chicago, USA).

D. EMG Measurement

Surface EMGs (Noraxon, AZ, USA) were recorded from the flexor carpi radialis (FCR) and the extensor carpi radialis (ECR) muscles. During the experiment, the subject's arm was placed on an apparatus that stabilized the wrist in a neutral position (Figure 1). Each subject was instructed to contract the wrist flexor or extensor as forcefully and quickly as possible against the confinement of the apparatus in response to an audible beep, and relax the muscle as quickly as possible as soon as the 3s beep terminated. The procedure was repeated for wrist extension.
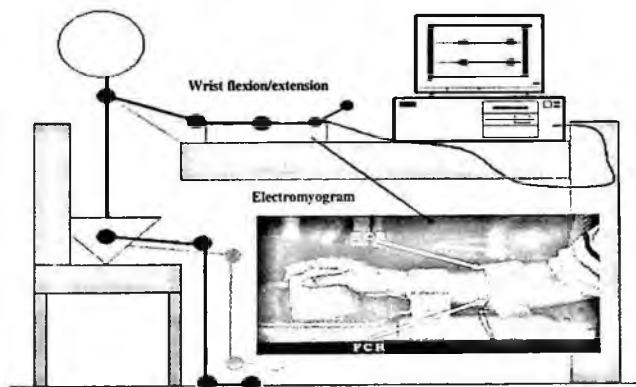
Figure 1. The setting for positioning of the arm and forearm for EMG recording during isometric wrist flexion and extension.

Onset/Offset Delay
Onset delay of the EMG signals was defined at the time interval between onset of the audible beep and onset the of the EMG signal. Offset delay of the EMG signal was defined as the time interval between termination of the audible beep and termination of the EMG signal. Data acquisition hardware included MP 150 system (Biopac system, Inc., CA, USA). Amplifier gain was set at 1,000 with sampling frequency of 1,080 Hz was used. For determination of the delay of muscle contraction, EMG signals were band-pass filtered (10-1000Hz) and full-wave rectified. The baseline of the EMG signal was defined as the average activation level for 3 seconds prior to muscle contraction and maintained the above baseline at least during 25 milliseconds. Then, the onset was defined when the rectified signals first exceeded the baseline plus two standard deviations.

Co-Contraction Ratio
Since the muscle force is almost proportional to the integrated EMG (*IEMG*) [12], we first measured muscle activations in agonist and antagonist during wrist movements.

$$EMG_N = \frac{EMG_m}{EMG_{m\_rest}} \tag{1}$$

where EMG_N represents a normalized value of EMG signals during wrist movements. EMG_m indicates muscle activations during wrist movements; and EMG_{m_rest} indicates a value of EMG_m measured during relaxation.

$$IEMG = \sum_{n=0}^{N} \overline{\left(EMG_{Nn}\right)} \Delta t \tag{2}$$

where N indicates the number of sampled data in experimental trials and Δt is a wrist contraction time.

$$Co-contraction\ ratio = \frac{IEMG_n^{ANTA}}{IEMG_n^{AGO}} \tag{3}$$

where $IEMG_n^{AGO}$ indicates a IEMG of agonist and $IEMG_n^{ANTA}$ is a IEMG of antagonist during wrist movements. During the 6-week training, we measured EMG parameters in patients were measured every two weeks.

E. Data Analysis
EMG data was analyzed using two separate *t*-tests. The second test determined the differences between delay in onset/offset included arm side (control, unaffected and affected), direction of wrist movement (flexion and extension) using in paired *t*-test. One-way repeated ANOVA was used to compare before and after training. Finally, Spearman's correlation coefficients describing the

relationship between EMG parameters and FM scores, were obtained. All statistical analyses were performed with SPSS 10.0 (SPSS, Chicago, USA).

3. Results and Discussions

A. Fugl-Meyer (FM) Assessment
FM score during the 6-week training. In all four patients, FM (range: 0-66) of the affected hands were significantly improved after the 6-week training program ($p < 0.05$).

B. Onset/Offset Delay
After the 6-week training, the unaffected hands, as well as the control group, did not show significant changes in onset/offset delays for wrist flexion/extension. However, affected hands showed significantly decreased onset/offset delays in muscle contraction after the 6-week training in both wrist flexion and extension ($p < 0.05$). Before the training, onset/offset delay on the affected side was significantly larger than those in the control group and unaffected side. Onset/offset delay in the unaffected side was significantly larger than those on the control group. Offset delay of affected sides was significantly larger than onset delay in both wrist flexion and extension ($p < 0.05$). In unaffected side, offset delay was significantly larger than onset time in wrist extension.

C. Co-Contraction Ratio
Co-contraction ratio of muscle contraction in the affected side was significantly larger than those in the control group ($p < 0.05$). After the training, the unaffected
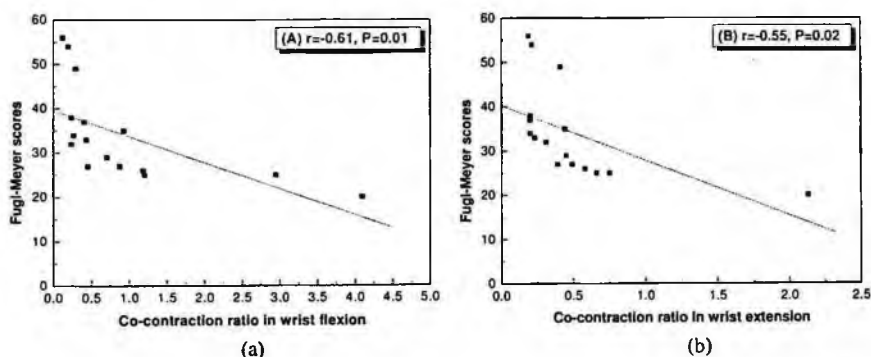
Figure 2. Correlations between co-contraction ratio of wrist movement and FM score. (a) Co-contraction ratio of wrist flexion versus FM scores, (b) Co-contraction ratio of wrist extension versus FM scores.

hands, as well as the control group, did not show significant changes in co-contraction ratio for wrist flexion/extension. However, affected hands showed significantly decreased co-contraction ratio in muscle contraction ($p<0.05$).

D. Correlations between EMG Parameters and Motor Recoveries

Spearman's correlation coefficients were determined, relating each EMG parameter from wrist flexion and extension of the affected hand to FM scores. Onset/offset delays in muscle contraction correlated well with FM scores, except for offset delay in wrist flexion. Figure 2 shows the co-contraction ratio in wrist movements correlated well with FM scores.

4. Conclusion

Major findings in this paper are: (1) there is a significant difference in onset/offset delay of muscles contraction between the affected and unaffected upper limbs; (2) there is a significant decrease in co-contraction ratio of affected hand of chronic stroke patients after 6-week training program; and (3) onset/offset delay and co-contraction ratio correlates significantly with upper limb motor impairment and motor recovery.

In this study, EMG responses allow an objective evaluation of changes in muscle activity in post-stroke patients, providing easily measurable, quantitative indices of muscle characteristics.

References

1. J. W. Lance, *Neurology* **30**, 1303(1980).
2. B. Ashworth, *Practitioner* **192**, 540(1964).
3. R. W. Bohannon and M. B. Smith, *Phys Ther.* **67**, 206(1987).
4. S. J. Fellows, C. Kaus and H. F. Ross, *Electroencephal Clin Neurophsiol.* **93**, 106(1994).
5. R. Katz, G. P. Rovai and C. Brait, *Arch Phys Med Rehabil.* **73**, 339(1992).
6. M. Hammond, G. H. Kraft and S. S. Fitts, *Arch Phys Med Rehablil.* **69**, 106(1988).
7. S. S. Fius, M. Hammond and G. H. Kraft, *Electroencephal Clin Neurophsiol.* **73**, 225(1989).
8. D. G Kamper and W. Z. Rymer, *Muslce Nerve* **24**, 673(2001).
9. J. P. Deward, P. S. Pope and D. J. Given, *Brain* **118**, 495(1995).
10. K. S. Tae, S. J. Song and Y. H. Kim, *J Biomed Eng Res.* **28**, 139(2007).
11. J. Filiatraut, A. Arsenault and Dutil E, *Am J Occup Ther.* **45**, 806(1991).
12. C. A. M. Doorenbosch and J. Harlaar, *Clinical Biomechanics* **18**, 142(2003).

THE BALANCE RECOVERY MECHANISMS AGAINST THE FORWARD PERTURBATION[*]

SUNGJAE HWANG

*Department of Biomedical Engineering, Yonsei University, 234 Maeji-ri, Heungup-myun
Wonju-si, Gangwon-do 220-710, South Korea*

HUESEOK CHOI

*Department of Biomedical Engineering, Yonsei University, 234 Maeji-ri, Heungup-myun
Wonju-si, Gangwon-do 220-710, South Korea*

KISIK TAE

*Department of Biomedical Engineering, Konyang University, 119 Daehang-ro
Nonsan-si, ChungNam 320-711, South Korea*

YOUNGHO KIM[†]

*Department of Biomedical Engineering, Institute of Medical Engineering,
Yonsei University, 234 Maeji-ri, Heungup-myun
Wonju-si, Gangwon-do 220-710, South Korea*

Falls are one of the main concerns among the elderly population. Proper postural
adjustments to recover the balance involve the activation of appropriate muscles to
produce force and relocate CoM. In this paper, biomechanical aspects of dynamic
postural responses against forward perturbations were experimentally determined
simultaneous measurements of joint angles and EMG activations. Thirteen young healthy
volunteers, stood on a flat platform, were translated into the forward direction by an AC
servo-motor at two separate velocities(0.1m/s, 0.2m/s). Joint motions in the sequence of
the ankle dorsiflexion, the knee flexion and then the hip flexion during the later
acceleration phase were noted in order to recover postural balance against the forward
perturbation. Tibialis anterior(TA) for the ankle dorsiflexion and biceps femoris(BF) for
the knee flexion, the primary muscle to recover the forward perturbation, was activated
during the half of acceleration phase. The ankle strategy was used for slow-velocity
perturbation, but the mixed strategy of both ankle and hip for the fast-velocity
perturbation.

1. Introduction

Generally, the balance is maintained by making postural adjustments to recover the center of mass (CoM) over the base of support. Proper postural adjustments involve the activation of appropriate muscles to produce force and relocate CoM. Balance assessments should evaluate how balance strategies cope with changes in support and sensory conditions, in an individual's expectation and experience and with changes in task constraints. In 1985, Nashner *et al.* [1] found that the existence of two discrete strategies that could either be used separately or be combined by the nervous system to produce adaptable control of the horizontal position of the CoM in the sagittal plane. The ankle strategy repositioned the CoM by moving the whole body as a single-segment inverted pendulum by production of ankle torque. The hip strategy, in contrast, moved the body as a double-segment inverted pendulum with counter phase motion at ankle and hip [1-2]. Balance assessments should also differentiate among different types of balance control including the ability to response to external stimulations, the ability to anticipate postural demands associated with voluntary movements, and the ability to move the CoM voluntarily and efficiently because patients may be differentially affected in these different types of balance control [2]. Nashner *et al.* [1] reported that the ankle strategy was used to response to translations during stance on a flat support surface, while Winter *et al.* [2] supported the mixed ankle and hip strategies in an increased platform speed. The mixed postural control strategy is better explained in patient with Parkinson's disease [3].

Several researchers have performed experiments of artificial slip perturbation in upright standing or walking to understand the procedure of protective postural control [4-6]. Cham *et al.* [4] performed slip experiments during walking and compared displacements of CoM and CoP in normal gait, slip recovery and falling conditions. They reported that knee flexion moment was the dominant response to generate corrective reactions against slips. Hughes *et al.* [5] reported that the postural balance was obtained against the forward perturbation in quiet standing by lowering the body with ankle and knee flexions. Feber *et al.* [6] also induced forward perturbations on healthy adults and patients with chronic anterior cruciate ligament deficiency. They found that hip muscles are important to control trunk and to prevent collapse against the forward perturbation.

The purpose of the present study was to determine how the postural balance recovery was obtained against the forward perturbation at two different speeds using motion analysis and electromyography measurement system.

2. Methods

Thirteen young healthy adult volunteers (10 men, 3 women) were chosen for subjects. Their ages ranged from 23 to 30 years (24.5±1.8years), height from 158 to 182cm (171.2±7.6cm) and weight from 50 to 84kg (66±12.2kg). Any subject with orthopedic abnormality or neurological impairment was excluded in the study. A three-dimensional force plate (Kistler Ltd., Switzerland) was mounted on the platform controlled by an AC servo motor (Yaskawa Ltd., Japan).

Joint angles of the lower extremity were measured by a sampling rate of 20Hz using an ultrasonic motion analysis system (Zebris, Germany). Five active markers were placed on the subject's lower extremity: the fifth metatarsal head, the lateral malleolus, the lateral femoral condyle, the great trochanter, and the lateral side of acromion of the scapula. EMG data were collected using bipolar surface electrodes (Delsys Inc., USA) at 1,000Hz. Surface electrodes were placed on muscle bellies of tibialis anterior (TA) and gluteous maximus (GM), medial head of the gastrocnemius (GAS), biceps femoris (BF) and rectus femoris (RF). EMG signals were band-pass filltered (60-120Hz) and full-wave rectified. The baseline of EMG signals was defined as the average activation level during 1sec prior to perturbation and maintained the above baseline at least for 25ms. Then, EMG onset time was defined when the rectified signals first exceeded the baseline plus two standard deviations.

Subjects stood on the platform on bare foot with their self-chosen feet positioning. The platform moved forward by 15cm with three different phases: acceleration phase (AP), constant speed phase (CP) and deceleration phase (DP). Two different speeds of 0.1m/s(Case 1) and 0.2m/s(Case 2) were applied on the platform during CP. For each subject, two trials were performed. Table 1 shows two perturbation methods for the present study. All apparatuses were in the study were synchronized in time with the perturbation system. Pearson correlation coefficients were obtained using SPSS 10.0 (SPSS, Chicago, USA) in order to evaluate correlations between joint motions and the onset timing of activations.

Table 1. Two perturbation conditions in this study.

Setting Parameters	Case 1	Case 2
Platform speed(m/s)	0.1	0.2
Acceleration (m/s^2)	1	2
Displacement (cm)	15	15
Acceleration phase(AP) (ms)	300	300
Constant speed phase(CP) (ms)	900	200
Deceleration phase(DP)(ms)	300	300

3. Results

Figure 1 shows joint angles of ankle, knee and hip in the sagittal plane for Case 1 and Case 2. Lines in the graph represent the average and one standard deviation. Movements consisted of an early passive component due to the platform translation, and a later active component, a corrective response against the platform translation. In Case 1, slight ankle plantarflexion, knee extension and hip extension occurred as passive movements during AP. For corrective movements, ankle dorsiflexion (1-8°), knee flexion (1-3°), and hip flexion (1-3°) were observed sequentially during later AP. Then, ankle plantarflexion, knee extension and hip extension were repeated from early CP to the end of the perturbation, returning to the equilibrium. In Case 2, ankle dorsiflexion (1-12°), knee flexion (2-6°), and hip flexion (3-14°) were observed during later AP. Ankle plantarflexion, knee extension and hip extension prolonged even after the end of the perturbation. In both cases, the sequence of joint motions for balance recovery was ankle dorsiflexion (A1R), knee flexion (K1R), hip flexion (H1R), ankle plantarflexion (A2R), knee extension (K2R) and then hip extension (H2R). In Case 1, A1R (251.7 ± 11.3ms) and K1R (260.7 ± 12.3ms) occurred during later AP, but H1R (401.2 ± 15.2ms), AR2 (647.7 ± 22.5ms), K2R (678.3 ± 119.9ms) and H2R (826.7 ±130.8ms) occurred sequentially during CP. While, in Case 2, A1R (237.2 ± 11.1ms) and K1R (250.3 ± 11.7ms) occurred during later AP, but the H1R (395.8 ± 14.3ms) occurred during the middle of CP. AR2 (725.8 ± 17.3ms) and K2R (740.3 ± 83.4ms) occurred during later DP. H2R (845.0 ±120.5ms) followed after the end of perturbation.

Figure 2 represents the mean timing of joint motions and the EMG onset time against forward perturbations. In Case 1, immediately after the perturbation, ankle plantarflexion and then knee extension appeared as passive movements. This initial response to the plate movement is mechanical in nature, rather than a neuromuscular response. TA (233.7 ± 13.2ms) was activated, followed by the activation of BF (254.2 ± 13.2ms) in later AP. The onset time of TA activation precedes the reversal of the ankle movement, so TA may work at first eccentrically to decelerate the plantarflexion, and then concentrically to reverse it. The onset time of TA and BF activations was found to be strongly correlated with the timing of A1R ($r = 0.89$, $p = 0.016$) and K1R ($r = 0.96$, $p = 0.002$). GAS (507.8 ± 19.5ms) and RF (559.7 ± 19.4ms) were activated sequentially in early CP. Then, ankle plantarflexion and knee extension were repeated. The onset time of GAS and RF activations was found to be correlated with the timing of A2R ($r = 0.86$, $p = 0.002$) and K2R ($r = 0.69$, $p = 0.12$). In Case 2, onset time sequences of muscle activation were corresponded with those of the Case 1.
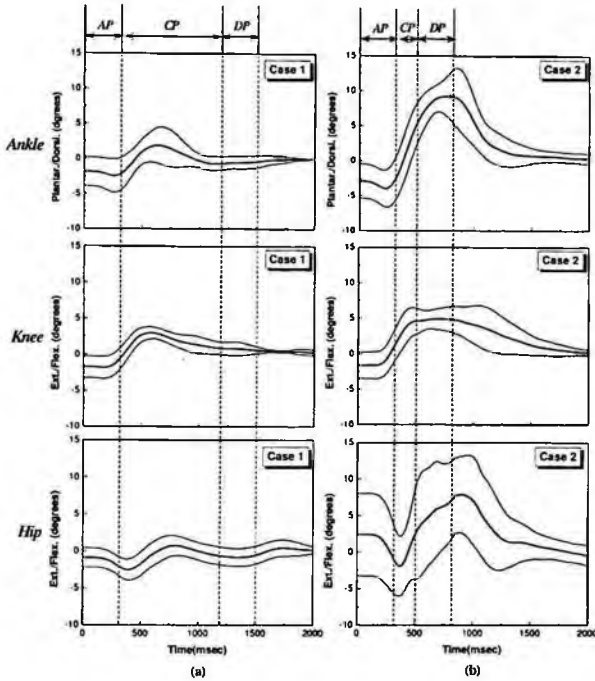
Figure 1. Joint angles in the sagittal plane at ankle, knee and hip against the forward perturbation. (a) Case 1, (b) Case 2. positive values indicate flexion and negative values indicate extension. Lines are mean ± SD.

TA (214.2 ± 8.9ms) and BF (244.0 ± 21.8ms) were activated sequentially in the middle of AP. Then, GAS (503.8 ± 18.6 ms) and RF (544.5 ± 20.4ms) were activated sequentially in early DP. Activations of TA, BF, GAS and RF were significant correlated with A1R ($r = 0.87$, $p = 0.025$), K1R ($r = 0.90$, $p = 0.014$), A2R ($r = 0.97$, $p = 0.001$) and K2R ($r = 0.87$, $p = 0.024$), respectively. GM was continuously activated from AP to DP.
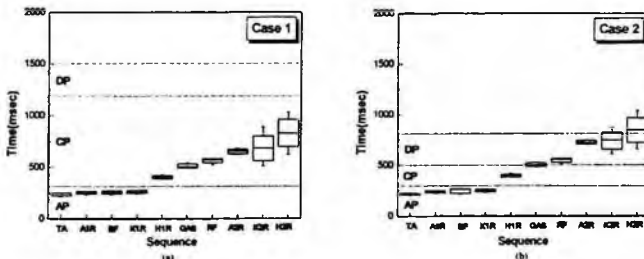
Figure 2. The timing of the joint motions and EMG onset. (a) Case 1, (b) Case 2.

4. Discussion & Conclusion

Researches in the last 20 years have provided many new insights into how balance is controlled by the sensory motor system. Kinematic data alone can not give enough information on muscle activities, and thus it is impossible to distinguish between active and passive motions. Information on muscle activation patterns from EMG recordings could provide additional insights into the cause of body movement. The present study explained that ankle strategy was used for the slow-speed perturbation, but mixed strategy of both ankle and hip used for the fast-speed perturbation. Our results also verified that the mixed strategy was more employed against perturbations on a flat surface as the perturbation speed increased. However, future studies should examine the nature of this variation since recovery responses are likely to be dependent of the platform speed. Perturbation methods such as speed and duration play a role in the postural response.

In conclusion, the present study showed that the sequence of lower extremity motions to regain balance against the expected forward perturbation is ankle-knee-hip response and joint flexions in the lower extremity are important in balance recovery against the forward perturbation. Future studies on elderly subjects including the effect of upper extremity motions would be helpful to understand the balance recovery mechanism.

Acknowledgments

References

1. L. Nashner and G. McCollum, *Behav. Brain Sci.* **8**, 135 (1985).
2. D. Winter, *Biomechanics Inc.,* 177 (1990).
3. F. Horak, *Gait and Posture* **6**, 76 (1997).
4. R. Cham and M. Redfern, *J. Biomechanics* **34**, 1439 (2001).
5. M. Hughes, M. Schenkman, J. Chandler and S. Studenski, *Clinical Biomech.* **10**, 318(1995).
6. R. Ferber, L. Osterning, M. Woollacott, N. Wasielewski and J. Lee, *Clinical Biomech.* **18**, 132 (2003).

EMG PATTERN RECOGNITION USING NEURAL NETWORKS DURING THE POSTURAL BALANCE CONTROL OF HUMAN BODY [*]

HYEONKI CHOI[†]

School of Mechanical Engineering, Sungkyunkwan University
Suwon, 440-746, Republic of Korea

JAEHOON JEONG

School of Mechanical Engineering, Sungkyunkwan University
Suwon 440-746, Republic of Korea

WONHAK CHO

School of Mechanical Engineering, Sungkyunkwan University
Suwon 440-746, Republic of Korea

The purpose of the study was to recognize EMG signal patterns of lower limb muscles by using neural networks during the recovery of postural balance of human body. EMG signals were collected from lower limb muscles during the balance recovery process from a perturbation without permitting compensatory stepping. A multi-directional moving platform was used to apply transient perturbations in five horizontal directions. Twenty features were extracted from EMG signals of one event and feature evaluation was performed by using Davies-Bouldin Index. The features were classified into five categories, such as forward perturbation, backward perturbation, lateral perturbation and two oblique perturbations. A neural network classifier using 10 hidden units was trained by back-propagation algorithm for 100 epochs from five classes with 40 patterns each. As results, motions were recognized with mean success rates of 75 percent. With the neural networks classifier of this study, the EMG patterns of lower limb muscles during the recovery of postural balance can be classified with high accuracy of recognition.

1. Introduction

Balance recovery is the most basic human movement during gait and dynamic activities of daily life and the complex process to adjust body posture by various joints, muscles and bones. Loss of balance caused by the degeneration of the

---

[†] Corresponding Author: hkchoi@skku.edu.

balance recovery control system is becoming ever more critical with the increase in our ageing population [1]. Virtually it has been estimated that one third of older people 65 years and over experience one or more falls each year. And older people are hospitalized for fall-related injuries 5 times more often than they are for injuries from other causes [2]. A serious health threat facing the older adult population is an increasing susceptibility to loss of balance resulting in a fall and possible injury. On the one hand, several system using bio-signals that assist humans for their incomplete activities and lost senses have been developing.

There are various bio-signals, such as EMG, EEG, EOG and ECG. Recently, bio-signals have been paid a great deal of attention due to their potentiality to provide new communication and control channels between human and machine, or, more specifically, between the disabled and the computer/robot in rehabilitation engineering [3]. The EMG signal reflects the level of electrical activity of muscles and therefore provides insight in their coordination in movement and in their role in a specific task. The studies on EMG signal can be classified into two groups: the control of human-assisting robots and rehabilitation systems by using EMG pattern recognition; and an automatic diagnosis in a clinic. As examples of the former, Sankai [4] developed HAL (Hybrid Assistive Leg) which was performed according to the operator's intention by using EMG signal as the primary command signal. Later, there are researches on diagnosis of neuromuscular system by evaluating the degree of muscle fatigue [5].

Studies concerning falls and balance recovery mechanisms have been developed using surface sway, slipping, waist pulling, pushing and setting an obstacle artificially [6-8]. Especially, surface sway has been most frequently used for understanding postural balance recovery mechanism [6]. One of the researcher, Runge et al. presented a fact that movement analysis by using joint torque is useful method for understanding of postural balance recovery mechanism [7]. Recently, Pai et al. and Rosers et al. compared postural balance recovery mechanism between the older adults and the young during waist pulling at standing [8].

Many studies on using EMG signal pattern recognition have been reported [10]. During the first stage of this research, linear prediction models for EMG signal, such as the autoregressive (AR) model, were frequently used. Graupe et al. [10] reported on discriminating EMG signal measured from one pair of electrodes using this model. In pattern recognition problems, neural networks are

of particular significance because of their learning capability and have already been successfully applied to a wide range of bio-signal analysis and classification problems. As examples of application, there are the research of Michael [9] and Fukuda et al. [3]. In this study we recognized EMG signal patterns of lower limb muscles by using neural networks during the recovery of postural balance of human body.

2. Methods

Ten male adults (age range: 23-30; height range: 167-181cm; weight range: 59-86kg) participated who have no history of otologic, neurologic, or orthopedic abnormality. We used EMG system (MyoSystem 1400, Noraxon USA, Inc.) and waist pulling system. Waist pulling system consisted of air cylinder, compressor and switching module. The waist pulling system pulls and pushes the rope, which is connected to subject's waist, with, respectively, from 8psi to 12psi for applying transient perturbations in five horizontal directions, such as forward, backward, oblique (45°), oblique (135°) and lateral perturbation. We used switching module to develop natural sway of subjects. In the experiments, we used eight surface electrode attached to lower limb (ch. 1 Tibialis anterior m.; ch. 2 Castrocnemius m.; ch. 3 Peroneus longus m.; ch. 4 Vastus medialis m.; ch. 5 Rectus femoris m.; ch. 6 Vastus lateralis m.; ch. 7 Biceps femoris m.; ch. 8 Gluteus m.) (Figure 1).
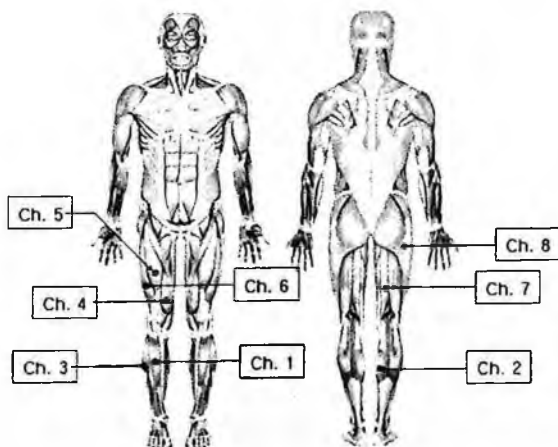
Figure 1. The sites of surface EMG electrodes.

Experimental procedure, which is followed, is that first, subjects stood with bare feet on the ground. They loosely tethered at the waist to the perturbation system. To initiate the perturbation, the air cylinder was activated by a compressor. EMG signals were collected during the balance recovery process form a perturbation without permitting compensatory stepping. EMG signals of fifty repetitions of five motions were analyzed for five subjects. Data collection was started from the balance recovery of the subject after the onset of pulling for 1 second.

Feature extraction is an important step in process of pattern recognition. Generally, there are two major approaches to extracting feature: temporal approach and spectral approach. Temporal approach in feature extraction identifies the attributes of the raw EMG signal that characterize it temporal structure relative to a specific muscular function [11]. Spectrum analysis is applied to EMG studies. Various feature extraction methods based on the spectral analysis are experimented [14]. The using of information contained in frequency domain could lead to a better solution for encoding the EMG signal.

3. Results and Discussion

We conducted experiments with waist pulling system on ten subjects. EMG signal is amplified by 1000 times, and filtered by using sixth Butterworth band pass filter (10-500 Hz). Because the usable frequency range is 0-500 Hz with most energy concentrated from 50-150 Hz, the sampling rate set up to 1 KHz.

Biceps femoris m. and Gluteus m., corresponding respectively to ch. 7 and ch. 8, rarely activated and peroneus longus m., corresponding to ch. 3, simultaneously activated with gastrocnemius m. (ch. 2). So, three muscles mentioned above, such as Biceps femoris m., gluteus m. and peroneus longus m. were excepted from the process of feature extraction. Twenty features, such as IAV, SE, CF and VCF, were extracted from EMG signals of one event and used as input parameter of classifier. MATLAB (Math Works, V 7.0) was used for programming feature extraction and classification.

The classifier system consisted of 20 neurons in input layer, 10 neurons in hidden layer and 5 neurons in output layer. Training of neural network was able to be finished with 100 patterns in the training set and within a few hundred epochs by error-back-propagation algorithm. Test set size is fixed at 150 patterns. Then the classifier after learning could identify distinct types of EMG signals that were generated by five perturbations.

Table 1. Mean recognition rates (%). FP, BP, LP, OP1 and OP2 is forward, backward, lateral, oblique 45° and oblique 135° perturbation, respectively.

Motion Subject	FP	BP	LP	OP1	OP2
a	87	85	86	84	83
b	83	77	78	75	73
c	74	79	69	60	63
d	77	74	70	63	61
e	76	71	77	72	70
f	81	84	74	75	70
g	79	80	81	70	60
h	84	81	82	75	74
i	84	80	82	70	65
j	71	73	70	62	64

Mean recognition rate during forward, backward and lateral perturbation is 80%, 78% and 77%, respectively, but mean recognition rate is 71% in case of oblique (45°) perturbation and 69% in case of oblique (135°) perturbation (Table 1). Although training database size is small, we considered that there was not a large difference in activation pattern of EMG signal by oblique perturbations direction in comparison with the others perturbations.

By subject, there is the variation of mean recognition rate. In case of subject a as shown in Table 1, mean recognition rate is 85%. Whereas, in case of subject j, mean recognition rate is 68%. We considered the causes of results are that the EMG patterns are changed according to differences among individuals, different locations of the electrodes and time variation caused by fatigue or sweat. Mean recognition rate on total subjects is 75%. For further recognition rate improvement of the system, several techniques such as feature selection method for reducing feature space dimension and combining multiple classifiers must be applied.

4. Conclusion

The goal of this research was to perform the EMG pattern recognition during postural balance control of human body. We proposed an EMG pattern recognition method to classify motions of lower limb. Mean recognition rate during forward, backward and lateral perturbation is 80%, 78% and 77%, respectively, but in case of oblique perturbations, mean recognition rate is 70%. And mean recognition rate on ten subjects is 75%. For more accurate results, a

larger training database is required and further improvement of the system may be achieved by several techniques such as feature selection method for reducing feature space dimension and combining multiple classifiers.

Acknowledgments

References

1. P. Kannus, J. Parkkari, S. Koskinen, S. Niemi, M. Palvanen, M. Jarvinen, and I. Vuori, *JAMA* **281**, 1895–1899 (1999).
2. M. E. Tinetti, M. Speechley, and S. F. Ginter, *N. Engl. J. Med.*, 319-26, 1701-1707 (1998).
3. O. Fukuda and T. Tsuji, *IEEE Transactions on Robotics and Automation*, **19-2**, 210-222 (2003).
4. H. Kawamoto and Y. Sankai, *IEEE International Conference on System, Man, and Cybernetics*, 3877-3882 (2002).
5. M. Maranzana Figini and M. Fabbro, *Electroencephalography and clin. Neurophys.*, **52-4**, 378-381 (1981).
6. C. F. Runge, C. L. Shupert, F. B. Horak, and F. E. Zajac, *Gait and Posure*, **10**, 161-170 (1999).
7. Y. C. Pai, M. W. Rogers, J. Patton, T. D. Cain, and T. A. Hanke, *J. Biomechanics*, **31**, 1111-1118 (1998).
8. M. W. Rosers, L. D. Hedman, M. E. Johnson, K. M. Martinez, and M. L. Mille, *Cognitive Brain Research*, **16**, 192-198 (2003).
9. M. F. Kelly, P. A. Parker, R. N. Scott, *IEEE Trans. On Biomed. Eng.*, **37-3** (1990).
10. D. Graupe, J. Magnussen, A. A. Beex, *IEEE Trans. On Automatic control*, **23-4** (1978).
11. B. Hudgins, P. Parker, *IEEE Transactions on Biomed. Eng.*, **40-1** (1993).
12. W. J. Tonpkins, *Biomedical Digital Signal Processing*, Prentice Hall International Editions (1993).
13. D. L. Davies, D. W. Bouldin, *IEEE Trans. Pattern Anal. Machine Intell.*, **PAMI-1**, 224-227 (1979).
14. B. Hannaford, S. Lehman, *IEEE Transactions on Biomed. Eng.*, **BME-33**, 1173-1181 (1986).
15. O. Omid, D. Judith, *Neural networks and pattern recognition*, Academic Press, Inc. (1998).

PASSIVE ELASTIC CHARACTERISTICS AND MUSCULOSKELETAL KINEMATICS OF HUMAN FOOT FOR BIOMECHANICAL ANALYSIS[*]

HYEONKI CHOI[†]

School of Mechanical Engineering, Sungkyunkwan University
Suwon, 440-746, Republic of Korea

SIYEOL KIM

School of Mechanical Engineering, Sungkyunkwan University
Suwon 440-746, Republic of Korea

WONHAK CHO

School of Mechanical Engineering, Sungkyunkwan University
Suwon 440-746, Republic of Korea

In this study we investigated the relationship between kinematic and kinetic characteristics of foot joints resisting ground reaction force (GRF). Passive elastic characteristics of joint were obtained from the experiment using three cameras and one force plate. With the mathematical models that relates joint angle and plantar pressure, we could get the kinematic data of the joints which are not available from conventional motion analysis. During the calculation process we used approximate equations and partial plantar pressures. The maximum angular displacements of each tarsometatarsal joint ranged from 4° to 7° and the maximum moments were from 200N·cm to 1500N·cm. Foot kinematic data calculated from the approximated equations, which were represented by the correlation between moment and angular displacement, and the data from motion analysis were very similar. We found that the movements of foot joints were decided by the passive characteristics of the joints when ground reaction force acts.

1. Introduction

Human foot is a multi-joint mechanism which determines the critical interaction between the lower limb and the ground during locomotion [1]. The kinematic and kinetic data of foot joints that were obtained from gait analysis have provided useful information for diagnosis of musculoskeletal foot diseases [1, 2]. The movements of joints are determined by the complicated interaction of many

---

[†] Corresponding Author: hkchoi@skku.edu.

factors that include muscle, ligament, external force and the shape of bones which are comprised in the joint. Furthermore any injury, lesion or neuromuscular disorder of these factors of foot will cause degradation, instability or disability of locomotion. The characterization of the kinematics and kinetics of specific segments of foot complex is therefore one of the major goals in clinical evaluation of many foot pathologies as well as in biomechanical investigations of foot [1, 3, 4].

Although many researchers have proposed biomechanical models for the kinematic and kinetic analysis of foot, there have been many limitations in precisely describing the very complicated structure of foot. Scott and Winter [2] proposed a three dimensional, eight-segment biomechanical foot model and implemented the kinematic and kinetic analysis for TM (tarsometatarsal), TT (transverse tarsal) and MP (metatarsophalangeal) joints. But, their analysis using the deformation of plantar soft tissue and the rotation of metatarsal heads of TM and TT joints did not provide satisfactory results [2].

In this study we assumed that the kinematic characteristics mainly depend on the passive components of joints which are against the ground reaction forces. To overcome the limitations of the conventional motion analysis using cameras and skin makers., we present a mathematical model that represent the correlation between the kinetic data (joint moment) and kinematic data (angular displacement) by using the passive elastic characteristics of foot joints. To validate the results, we compared the angular displacements measured from motion capture experiments and those calculated by using passive elastic moments. Finally, we showed that the kinematic behavior of foot joint is governed by ground reaction forces and passive elastic characteristics of joints.

2. Methods

Three young healthy male were recruited for the experiment. To measure the plantar pressure, EMED system (Novel, Germany) was used. The plantar contact area was dissected into seven sub-areas like heel, hallux, and five metatarsal heads etc. The ground reaction forces of four toes were not included because of their relatively small quantities.

X-ray image and MPP (maximum pressure picture) were used to find the correct location of metatarsal head. To calculate the sub-area forces, a mesh was used. The partial pressure was measured by a sensor located inside a mesh. We obtained the force by multiplying the measured pressure and mesh area. Three measurements were made for each subject. To calculate the average values of the measurements, cubic spline interpolation method was used. To synchronize the ground reaction force data and motion data, the time period from heel-striking to toe-off was normalized.

Six skin makers were used to specify the local reference frames. The foot model used in this study was adopted from Scott and Winter's [2]. The X-axis of

the each reference frame was aligned to the longitudinal direction and the Z-axis was aligned to the axis of the joint (Figure 1). Three skin makers were used to define the local reference frame of heel. Vectors were defined from maker 1 to makers 2 and 3. One of these two vectors was used to define X-axis of frame {Heel}. From the cross product of the two vectors Y-axis of the frame {Heel} is defined. And from the cross product of the pre-defined X, Y axes Z-axis was defined.

(a)

(b)
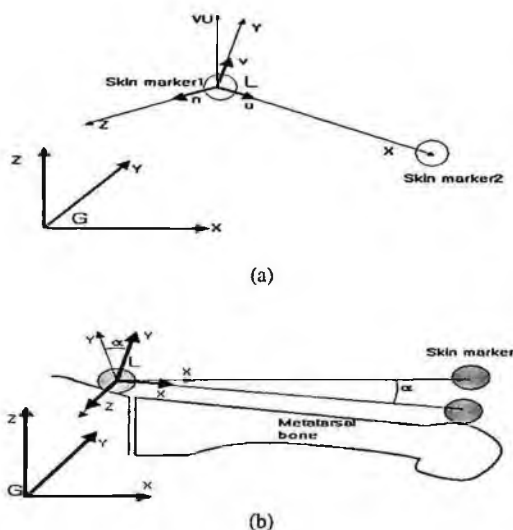
Figure 1. (a) Definition of the global and local reference frame. (b) Angular displacement of MT bone. (α: the angular displacement with respect to local reference frame, G: global reference frame, L: local reference frame)

(a)

(b)
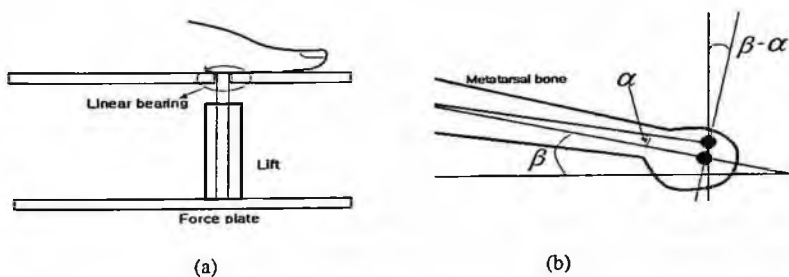
Figure 2. (a) Lift system for pushing up foot joint. (b) Angle between metatarsal bone and ground reaction force (β: the angle between ground reaction force vector and bone segments in the situation of no external force).

These vectors were defined as unit vectors to define part of transformation matrix of reference frames. To define the frames of medial cuneiform and cuboid, two markers were used. X-axis was selected as the line connecting these two markers. By performing the cross product with Z-axis of the reference frame, Z-axes of {Cun1} and {Cub} were defined. By performing cross product of X-axis and Z-axis, Y-axis was defined. X, Y, Z axes of each frame were defined as unit vectors and the rotation part of transformation matrix was also defined.

In the experiment, we used three cameras and one force plate and laboratory-made lift system (Figure 2(a)). Lift system touches force plate and allows only vertical translational movement. For that purpose we used linear bearing whose friction can be disregarded. When the lift system pushes up a bone, as ground reaction force applies during the gait, the Z direction force of force plate increases. As the lifting force increases, the displacement of foot joint increases, too. The cameras catch the changes of coordinates of makers as the displacement of foot joint (Figure 2(b)) increases. Ground reaction force (GRF) data was interpolated by using cubic spline interpolation function. And the result was fitted to a curve by using least square method.

The motion analysis was done by using four 60Hz cameras. To transform the images into 3 dimensional coordinates, KWON 3D (Bisol Inc., Korea) software was used which adopts DLT (direct linear transformation) method. Gait experiments were implemented three times for each subject. The final data obtained from the motion analysis is 3 dimensional coordinates with respect to the global reference frame. To synchronize ground reaction force (GRF) exerting on the foot and motion data the period from heel strike to toe-off was normalized.

3. Results and Discussion

As the joint moment increased the angular displacement of TM and TT joints increased with 2 degree function relationship, and that of TM increased with 3 degree function relationship (Figure 3). The joint moments did not increase when they reached certain values. This means that the ligaments around the joint reached physiologic load condition. If the loads surpass the limits of physiologic load the micro-failure of collagen fibers might happen [5].

The data from the approximate equations is the results considering only the passive elastic characteristics of joint moments by ground reaction forces. We proposed a mathematical model that represents the relationship between foot joint moment and joint angular displacement by using the passive elastic characteristics of joint. And we also presented the ranges of joint angular displacements (Table 1). The maximal movements of TM joints were $4°\sim7°$ except the big toe. Each subject showed quite different results. This difference is considered because of the differences of individual gait characteristics, body weight and the passive characteristics of joints.

(a) TM joint 3   (b) MP joint 1
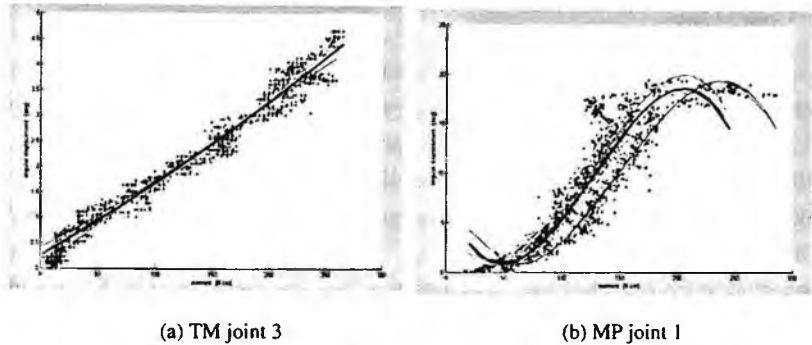
Figure 3. Examples of the moment and angular displacement curve of subject DW (thick line is the averaged curve. X-axis: Joint moment, Y-axis: Angular displacement).

During the gait the maximal moments were 200~1500N·cm. It showed quite wide variation in accordance with each individual subject. This variation is considered due to the combination of many factors affecting to moments like, the characteristics of individual subject, the velocity of gait, the passive characteristics of joints, etc. For example, the viscoelastic nature of joint which is one of the passive characteristics of joints cause the change of friction coefficient and furthermore the change of kinetic energy of joint. Consequently, the kinematics of the joint changes as much as the change of kinetic energy of joint.

To calculate the exact joint moments, we needed to exactly calculate the angles between the bone segment and the ground and to exactly select the boundary of the local area of foot when we measure the GRF. With EMED system we can not calculate the direction of force vectors because we can not measure the shear forces but the vertical forces. Generally TT joints had bigger moments this is because TT joints has relatively longer moment arms and the local force applied to the second metatarsal head is big.

Table 1. The coefficients of curve and the range of joint motion for one selected subject (DW).

Joint	Coefficient of curve				Available range	
	3order $\times 10^{-5}$	2order $\times 10^{-5}$	1order $\times 10^{-2}$	Constant	Moment [N.cm]	Angle [deg]
TM1		2	1.1	0.2	20<M<280	0<A<5.5
TT		-0.4	0.8	0.2	20<M<425	0<A<3.2
TM3		0.9	1.3	0.3	10<M<270	0<A<4.5
TM4		1.3	1.2	0.4	20<M<350	0<A<5.8
TM5		-2.2	2.7	-0.02	20<M<300	0<A<5.7
MP1	-0.9	352	-28	7	50<M<200	0<A<20

4. Conclusion

By defining the relationship between kinematic data and kinetic data, we could approximate the joint angular displacement from the joint moment which is calculated from plantar pressure. The notable limitations of this study are as follows. Firstly, we did not consider the effects of movements of the neighboring joints when we calculate moments or angular displacements of joints. Secondly, unlike the independent joints (knee or elbow), each foot joint is intricately connected to the neighboring joints with muscles, ligaments or skin. So, we must consider their effects when we deal with the joint kinematics of foot joints. Finally, a larger subject group is required to have statistically more meaningful results. The mathematical model presented in this study can be usefully applied to the analysis of foot joint movement during gait and to the diagnosis of foot-related diseases.

Acknowledgments

References

1. A. Leardini, M.G. Benedetti, F. Catani, L. Simoncini and S. Giannini, *Clin. Biomech.*, **14**, 528-36 (1999).
2. S. H. Scott and D. A. Winter, *J. Biomech.* **26**, 1091-1104 (1993).
3. J. R. Gage, P. A. Deluca and T. S. Renshaw, *J. Bone Joint Surg.*, **77**-A, 1607-23 (1995).
4. S. H. Scott and D. A. Winter, *J. Biomech.*, **24**, 743-52 (1991).
5. R. Riener and T. Edrich, *J. Biomech.*, **32**, 539-44 (1999).

EMG ANALYSIS OF MUSCULAR FATIGUE AND MUSCLE ACTIVITY DUE TO TURTLE NECK SYNDROME

WONHAK CHO

School of Mechanical Engineering, Sungkyunkwan University
Suwon, 440-746, Republic of Korea

WOOYONG LEE

School of Mechanical Engineering, Sungkyunkwan University
Suwon 440-746, Republic of Korea

SANGHOON YOON

School of Mechanical Engineering, Sungkyunkwan University
Suwon 440-746, Republic of Korea

CHEONHO JEONG

School of Mechanical Engineering, Sungkyunkwan University
Suwon 440-746, Republic of Korea

HYEONKI CHOI[†]

School of Mechanical Engineering, Sungkyunkwan University
Suwon 440-746, Republic of Korea

An experimental study was conducted to determine the effect of turtle neck syndrome on muscular fatigue and muscle activity. Six subjects (males) participated in the study. They had performed the casual computer work for three hours just before the experiment. Electromyography (EMG) was recorded from 6 muscles of the dominant neck-back region using a computerized data recording and analysis system. Root-mean-squared (RMS) values of muscle activity were computed to compare the influence of experimental conditions on muscle strain. Static, dynamic and mean components of muscle activities were obtained. The power spectrum function of muscles was calculated off-line by means of a signal processing software package. The power spectrum functions calculated by using FFT analysis were smoothed with a moving average filter of 21 points and normalized with respect to the maximal value achieved during trials. Median frequency (MF) of the EMG power spectrum from 6 muscles was reduced more rapidly turtle neck posture than normal neck posture. Sternocleidomastoid showed the biggest decrease in MF. Muscle fatigue can be quantified by following the shift in the

† Corresponding Author: hkchoi@skku.edu

EMG spectral density towards lower frequencies using MF of the power spectrum as a guiding parameter. The shift towards the lower band has been correlated with several physiological reactions of muscle tissue to fatigue. The results of the present study have been compared with other published studies and suggestions for future work have been given. Moreover, we considered that the results can be usefully applied to physical therapy.

1. Introduction

Turtle neck syndrome is a serious health problem in life. It affects the mobility of the neck-back region and adjacent muscles leading to functional disabilities. It is clinically important to increase our understanding of the effects of turtle neck syndrome on the relationship between the movements of the cervical spine and adjacent muscles.

The primary function of the cervical spine is to orientate the head against the opposing forces of gravity whilst permitting multi-directional movement. To accomplish this task the cervical spine must be mechanically stable, both in static and dynamic postures. In neutral postures, passive resistance to cervical spine motion is minimal [1] and destabilizing gravitational forces are counteracted by moments of the anterior and posterior cervical muscles. In particular, the deep more segmental cervical muscles such as the deep cervical flexors, are important for the control and support of the cervical lordosis and maintenance of cervical spine postural form [2, 3].

Localized muscle fatigue can be quantified by following the shift in the EMG spectral density towards lower frequencies, using MF (medium frequency) of the power spectrum as a guiding parameter [4]. The shift towards the lower band has been correlated with several physiological reactions of muscle tissue to fatigue [5]. Mannion and Dolan [6] have shown a nearly linear relation between a decrease of MF and the force output of skeletal muscles during fatigue.

The purpose of the present study was to examine the effects of turtle neck syndrome on muscular fatigue and muscle activity during they had performed the casual computer work.

2. Methods

Six subjects (males) with mean ages of 26-28 years were recruited to the experiment. Subjects' height ranged from 168 to 170 cm, their mass was 65–70 kg, and their neck circumference ranged from 32 to 36 cm. They were divided into two groups: group 1 – three normal subjects who were in good health with

no history of neck or back pain within the last 12 months, group 2 – three subjects with current turtle neck syndrome. These subjects had pain over the neck-back during prolonged casual computer work. There were no significant differences among the two groups of subjects regarding age, weight and height. Subjects were excluded if they had inflammatory joint disease, fracture/dislocation of the vertebral column, history of spinal surgery, neurological signs or unable to perform trunk movements due to unbearable pain. Subjects were informed about the experimental procedure and any potential risks prior to the attainment of written consent.

Subjects had performed the casual computer work for three hours just before the experiment. EMG signals from 6 muscles were acquired and recorded for 10 s. The EMG data were acquired simultaneously from both heads of six muscles, using an eight-channel portable system of EMG amplifiers connected in parallel (MyoSystem 1400, Noraxon USA, Inc.). After having and scrubbing the skin with alcohol, disposable Ag/AgCl surface electrodediscs with a diameter of 9 mm (Noraxon Dual Electrodes) were attached to the subject's skin at locations recommended by Perotto and Delagi [7]. For each muscle, two electrodes were placed at a distance of approximately 30 mm in the direction of the muscle fibers. A reference electrode, shared by the six measurement channels, was placed on the bony part of the lateral aspect of the knee joint. Cables and interfaces were shielded to eliminate interferences.

EMG was recorded from 6 muscles of the dominant neck-back region using a computerized data recording and analysis system. EMG signals were pre-amplified by factors in the range of 1000–4000 (depending on the subject) and captured by a 12-bit A/D board (PLC 818, Scientific Solution Lab, USA) at a sampling rate of 1 kHz. The evolution of the power spectrum function of each of the six muscles of interest was calculated off-line by means of a signal processing software package. Signal envelopes were calculated using a digital band, 10-80Hz band pass filter and six-order Butterworth 7–11 Hz filter [8] to evaluate the activity time frames of the EMG bursts and to locate the mid-time values of their duration. The power spectrum functions that were calculated by using the FFT analysis were smoothed with a 'moving average' filter of 21 points and normalized with respect to the maximal value achieved during trials. The evolution of the MF of muscle was then derived from its set of power spectra in terms of percent decrease from the initial value.

3. Results and Discussion

Table 1, 2 show the muscular fatigue of each muscles and we can compare the differences between turtle and normal neck posture. MF of the EMG power spectrum from 6 muscles was reduced more rapidly turtle neck posture than normal neck posture. In particular, Sternocleidomastoid showed the biggest decrease in MF. In turtle neck posture, fatigue of Thoracolumbar Paraspinal, Sternocleidomastoid, Upper Trapezius, Middle Trapezius, Nfraspinatus, Latissimus dorsi is approximately 53%, 137%, 37%, 67%, 25%, 61% more than normal neck posture.

Table 1. Median frequencies of the selected muscles in turtle neck posture.

Time Muscle	0 (MF)	3 hour later (MF)	MF Decrease
Thoracolumbar Paraspinal	27.22 Hz	20.26 Hz	26%
Sternocleidomastoid	40.25 Hz	25.11 Hz	38%
Upper Trapezius	39.57 Hz	27.51 Hz	30%
Middle Trapezius	31.94 Hz	22.39 Hz	30%
Nfraspinatus	36.54 Hz	27.20 Hz	25%
Latissimus dorsi	25.91 Hz	18.47 Hz	29%

Table 2. Median frequencies of the selected muscles in normal neck posture.

Time Muscle	0 (MF)	3 hour later (MF)	MF Decrease
Thoracolumbar Paraspinal	60.23 Hz	50.17 Hz	17%
Sternocleidomastoid	63.85 Hz	53.65 Hz	16%
Upper Trapezius	60.68 Hz	47.40 Hz	22%
Middle Trapezius	54.80 Hz	45.25 Hz	18%
Nfraspinatus	64.23 Hz	51.80 Hz	20%
Latissimus dorsi	60.98 Hz	50.34 Hz	18%
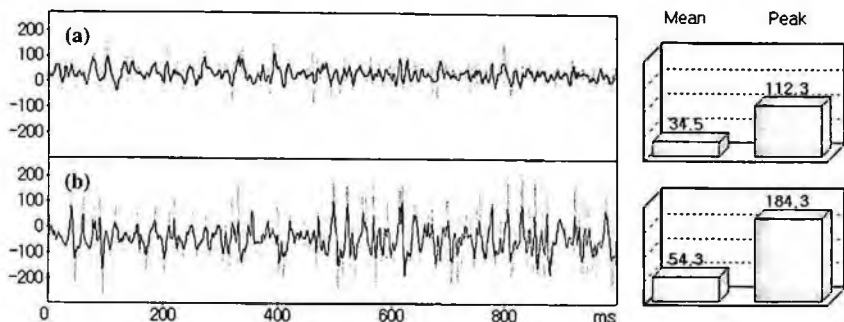
Figure 1. The EMG activities of sternocleidomastoid in turtle neck (a) and normal neck (b) postures.

As shown in the Figure 1, the EMG activity of sternocleidomastoid decreased in turtle neck posture. Mean and peak value of muscle activity in turtle neck posture is approximately 37%, 40% less than those in normal neck posture. Turtle neck syndrome showed significant decrease in MF and muscular activity.

4. Conclusion

The purposes of this study were to objectively quantify the muscular fatigue and muscle activity of 6 muscles of the dominant neck-back region during casual computer work and to compare the differences between normal neck posture and turtle neck posture. Also this study was conducted to identify the effects of turtle neck syndrome on EMG activities and muscular fatigue. Muscle fatigue can be quantified by following the shift in the EMG spectral density towards lower frequencies using MF of the power spectrum as a guiding parameter. The shift towards the lower band has been correlated with several physiological reactions of muscle tissue to fatigue. MF of the EMG power spectrum from 6 muscles of the dominant neck-back region was reduced more rapidly turtle neck posture than normal neck posture. Sternocleidomastoid showed the biggest decrease in MF. The results will provide insight into the neck-back functions of turtle neck patients, in particular, they will be helpful in developing rehabilitation programs for restoring patients' neck-back functions.

References

1. C. A. Oatis, *Lippincott Williams & Wilkins: Philadelphia* (2004).
2. L. C. Boyd Clark, C. A. Briggs, and M. P. Galea, *Spine* **27**, 694–701 (2002).
3. A. N. Vasavada, S. Li, and S. L. Delp, *Spine,* **23**, 412–22 (1998).
4. U. Rattanaprasert, R. Smith, M. Sullivan and W. Gilleard, *Clinical Biomechanics*, **13**, 85-92 (1992).
5. E. S. Rebecca and R. W. Kelth, B. H. George. *Foot and Ankle*, **13**, 85-92 (1992)
6. M. LeClair and D. Riach, *Postural stability Measures,* **11**, 176-178 (1996).
7. T. E. Prieto, J.B. Myklebust, R. G. Hoffmann, E. G. Lovett, and B. E. Myklebust, *IEEE. Transactions on Biomedical engineering*, **43**, 956-966 (1996).
8. D. A. Winter. *Elsevier Science B. V* (1995).

THE RELATIONSHIP AMONG THE CENTER OF PRESSURE, THE CENTER OF MASS AND THE HORIZONTAL ACCELERATION OF THE BODY IN POSTURAL SWAY, FALLING AND WALKING*

HUE-SEOK CHOI

Department of Biomedical Engineering, Graduate School, Yonsei University,
234, Maeji-Ri, Heungeop-Myoen, Wonju-Si, Gangwon-Do, 220-710, South of Korea

YOUNG-HO KIM[†]

Department of Biomedical Engineering, Graduate School,
Institute of Medical Engineering, Yonsei University,
234, Maeji-Ri, Heungeop-Myoen, Wonju-Si, Gangwon-Do, 220-710, South of Korea

Many researchers have referred to the human body as an inverted pendulum. The inverted pendulum model, relating the center of mass (COM), the controlled variable, with the center of pressure (COP), the controlling variable, shows that the differences between COP and COM are proportional to the horizontal accelerations of the body. Using the three-dimensional motion analysis synchronized with three force plates, the inverted pendulum model was applied to four different movements (quiet standing, intended postural sway, falling and walking) in twenty healthy volunteers who have no musculoskeletal problems and balance disorders in order to investigate the relationship among COP, COM and the horizontal acceleration of the body. We also performed the cross-correlation analysis between (COP-COM) and the horizontal acceleration of the body. Results revealed that (COP-COM) had high negative correlations with the horizontal acceleration in quiet standing and postural sway. In addition, high negative correlations between (COP-COM) and horizontal accelerations of the body were found before falling occurs, but high positive correlations were found once falling occurs. However, during walking, high negative correlations between (COP-COM) and midial/lateral accelerations of the body were found. Therefore, the correlation between (COP-COM) and horizontal accelerations of the body based on the inverted pendulum model can be used to determine the postural stability in falling.

1. Introduction

Falls are a major health problem in elderly people. Especially, accidental falls are the main cause of injury in people over the age 65 and result in accidental death in people over the age of 85 [1]. Postural instability has been identified as one of the most common causes of falls in the elderly [2].

The postural control is maintained by a complex sensorimotor system, which integrates information from the visual and somatosensory system [3]. To examine postural control, many studies have used movements of the whole body center of mass (COM) and its relative position to the center of pressure (COP) of the supporting foot. Winter [4] suggested that the vertical projection of COM should be within the base of support during locomotion for balance to be maintained. Also, the maximum horizontal separation distance between COM and COP during single limb stance was reported to sensitively quantify gait instability in patients with cerebellar ataxia [5]. In addition, dynamic stability during locomotion has been assessed using COM momentum, and an excessive lateral momentum was identified in imbalance of elderly [6].

The most common model used to characterize the postural control is the inverted pendulum. Many researchers have referred to the human body as an inverted pendulum. In this model, the postural control is defined by the relation between COP and the whole body COM. Especially, the difference between the COP and the whole body COM, (COP-COM), was highly correlated to the horizontal acceleration of the whole body COM during postural sway and was reported as the 'error' of the postural control system and provided important insight into the postural control mechanism [7, 8, 9]. Recently, Corriveau et al. [10] has been shown that the root mean square (RMS) error of the (COP-COM) is greater in elderly with neurological impairments compared with healthy.

Although the most falls occur during locomotion, many studies into balance during quiet and perturbed standing had evolved. In this study, we investigated the relationship among COP, COM and the horizontal acceleration of the whole body COM and the feasibility of the inverted pendulum model in postural sway, falling and walking.

2. Methods

2.1. *Subjects and Motion Analysis*

Using the 3D motion analysis system (VICON Motion Systems Ltd., England) with six infrared cameras synchronized with three force plates (AMTI, U.S.A.), the inverted pendulum model was applied to four different motions (quiet

standing, intended postural sway, falling and walking) in twenty male volunteers (age: 24.7±1.3yrs, height: 169.8±5.9cm, weight: 66.7±7.2kg) who have no musculoskeletal problems and balance disorders in order to investigate the relationship among COP, COM and the horizontal acceleration of the body. Whole body COM position data were calculated as the weighted sum of all body segments [4]. In order to calculate 3D locations of segmental COMs, we attached 38 reflective markers on feet, legs, pelvis and upper extremities based on Helen-Hayes marker set [11]. COP position data were calculated using the ground reaction forces and moments measured with three force plates. During the double stance phase, the COP position data were calculated for both feet using the COP and vertical ground reaction force from each foot [9].

2.2. The Inverted Pendulum Model

Figure 1 shows the inverted pendulum model of the human body in the sagittal plane. In the inverted pendulum model, we can estimate the horizontal linear acceleration ($\ddot{x}$) of the whole body COM is related as if Eq.(3) using the ground reaction force (GRF), the body weight (W), the location of COP (u) and the whole body COM (x).

$$u(GRF) - xW = I\frac{\ddot{x}}{l} \tag{1}$$

$$GRF = W = mg \tag{2}$$

$$u - x = -\frac{l}{g}\ddot{x} = K\ddot{x} \tag{3}$$

where K is constant. Thus the difference between the COP and the whole body COM is proportional to the horizontal acceleration of the whole body COM.
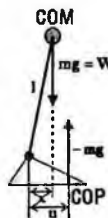
Figure 1. An inverted pendulum model of the human body in the sagittal plane.

To compare with (COP-COM) and the acceleration of the whole body COM in both anterior/posterior (A/P) and medial/lateral (M/L) directions, (COP-COM) was cross correlated with the acceleration of the whole body COM in each direction using Matlab 6.5 (Mathworks, U.S.A.).

3. Results

Figure 2(a) shows data of time series of COP and the whole body COM for one subject in the postural sway. The features of COP and the whole body COM resembled each other closely in both directions. However, COP was slightly larger than the whole body COM as it fluctuated around the whole body COM in both directions. Figure 2(b) shows data of time series (COP-COM) and the horizontal acceleration of the whole body COM for one subject in the postural sway. The features of (COP-COM) resembled the inverse form of the acceleration of the whole body COM well. As a result of cross correlation, (COP-COM) had high negative correlations with the acceleration of the whole body COM as -0.96 ± 0.02 in the A/P direction and -0.95 ± 0.03 in the M/L direction. This result shows that (COP-COM) can be directly related to the horizontal acceleration of the whole body COM in postural sway based on the inverted pendulum model.
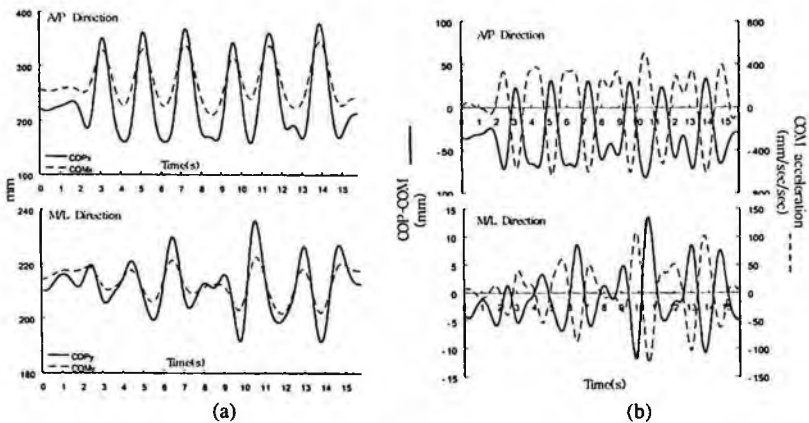
Figure 2. COP and COM in the A/P and M/L sway
(a) COP and COM fluctuations (b) (COP-COM) and the acceleration of the whole body COM

Figure 3(a) shows data of time series (COP-COM) and the acceleration of the whole body COM for one subject in the falling. The features of (COP-COM) resembled the inverse form of the acceleration of the whole body COM before

falling occurs. As a result of cross correlation, (COP-COM) had high negative correlations with the acceleration of the whole body COM as -0.92±0.06 in the A/P direction and -0.89±0.13 in the M/L direction before falling occurs, but high positive correlations were found as 0.81±0.05 in the A/P direction and 0.77±0.24 in the M/L direction once falling occurs. In addition, during walking, (COP-COM) had low negative correlations with the acceleration of the whole body COM as -0.21±0.12 in the A/P direction, whereas high negative correlations were found as -0.87±0.11 in the M/L direction (figure 3(b)). This result shows that (COP-COM) can be directly related to the horizontal acceleration of the whole body COM before falling occurs based on the inverted pendulum model.
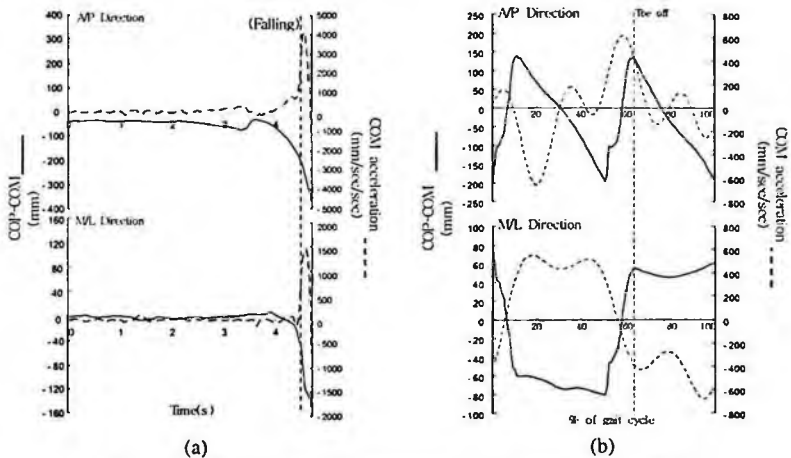
Figure 3. (COP-COM) and the acceleration of the whole body COM
(a) falling (b) gait

4. Discussion

This study investigated the relationship among the center of pressure, the center of mass and the acceleration of the whole body COM in postural sway, falling and walking using the 3D motion analysis system synchronized with three force plates. Results revealed that (COP-COM) had high negative correlations with the acceleration of the whole body COM in postural sway. In addition, high negative correlations between (COP-COM) and the acceleration of the whole body COM were found before falling occurs, but high positive correlations were found once falling occurs. However, during walking, high negative correlations between (COP-COM) and the acceleration of the whole body COM were found in M/L

138

direction. Therefore, the correlation between (COP-COM) and the acceleration of the whole body COM based on the inverted pendulum model can be used to determine the postural stability in falling. Furthermore, a better understanding of biomechanical challenges and new method imposed on whole body dynamic stability during locomotion will provide an opportunity to reduce the incidence of falls in the elderly through early detection and intervention.

Acknowledgments

References

1. B. J. Vellas, S. J. Wayne, P. J. Garry and R. N. Baumgartner, *The Journals of Gerontology.* 53A, M264 (1998).
2. A. J. Blake, M. J. Morga, H. Dallosso, S. B. Ebrahim, T. H. Arie, P. H. Fentem and E. J. Bassey, *Age and Ageing.* 17, 365 (1988).
3. R. Johansson and M. Magnusson, *CRC Crtical Reviews in Biomedical Engineering.* 18, 413 (1991).
4. D. A. Winter, *John Wiley & Sons.* (1990).
5. D. E. Krebs, C. A. McGibbon and D. Goldvasser, *IEEE Transactions Neural System Rehabilitation Engineering.* 9, 76 (2001).
6. B. K. Kaya, D. E. Krebs and P. O. Riley, *The Journals of Gerontology.* 53A, M126 (1998).
7. D. A. Winter, *Gait and Posture.* 13, 193 (1995)
8. P. G. Morasso, G. Spada and R. Capra, *Human movement Science.* 18, 759 (1999)
9. D. A. Winter, A. E. Patla, F. Prince and M. Ishac, *Journal of Neurophysiol.* 80, 1211 (1998)
10. H. Corriveau, R. Hebert, M. Raiche, M. F. Dubois, F. Prince, A. E. Patla and F. Prince, *Archives of Gerontology and Geriatrics.* 39, 163 (2004)
11. M. Kadaba, H. Ramakrishnan and M. Wootten, *Journal of Orthopaedic Research.* 10, 383 (1990).

JOINT MOMENTS AND LUMBAR CURVATURES DURING SYMMETRICAL LIFTING[*]

SEONHONG HWANG

*Dept. of Biomedical Engineering, Yonsei University, 234 Maeji Heungeop
Wonju City, Gangwon-do 220-710, KOREA*

SUNGJAE HWANG

*Dept. of Biomedical Engineering, Yonsei University, 234 Maeji Heungeop
Wonju City, Gangwon-do 220-710, KOREA*

YOUNGEUN KIM

*Dept. of Mechanical Engineering, Dankook University, San44-1 Jukjeon-dong, Suji-gu,
Youngin City, Gyeonggi-do 448-160, KOREA*

YOUNGHO KIM[†]

*Dept. of Biomedical Engineering and Institute of Medical Engineering, Yonsei
University, 234 Maeji Heungeop
Wonju City, Gangwondo 220-710, KOREA*

Each lower extremity joint has specific strategy to minimize and support the lumbar load in different lifting techniques. In the present study, joint angles and moments and lumbar spinal curvatures were analyzed in two different symmetrical lifting(squat and stoop) using the three-dimensional motion analysis system. Thirteen male volunteers participated in the study, lifting three different boxes(5, 10 and 15kg). There were no significant differences in peak moments in the lumbar joint between squat and stoop lifting. Rather, the peak moment in squat lifting was larger than that in stoop lifting, when 15kg was lifted. The analysis of support moment during lifting showed that extension moments of hip and ankle joints contributed the most to support the body in squat lifting, and the knee flexion moment played an important role in stoop lifting. There were individual differences in joint angles and moments when the lordotic curvature occurs. However, there might be some strategies to minimize mechanical stress on the waist by the change in lordotic curvature of the lumbar spine for the safe lifting.

1. Introduction

Lifting an object from the floor is a complex movement that requires the whole body coordination and various movement strategies. It is proposed that the safest lifting strategy is the squat lifting that does not harm on the back. But, van Dieen[2] conducted a comprehensive review of 27 biomechanical studies comparing stoop and squat techniques, and concluded that no justification existed for advocating a squat technique. Jager and Luttman[4] used a three-dimensional dynamic model to estimate lumbar compression and found that compression was not influenced by lumbar curvature. By observations of physiologic, psychologic, biomechanical and clinical evidence on three lifting techniques(squat, semi-squat, stoop) Leon Straker[6] reported that all those lifting techniques had both advantages and disadvantages. These recent studies have shown that many variables exist depending on different lifting methods. Accordingly, various lifting strategies must be analyzed quantitatively and precisely, considering the coordination between lumbar and lower limb joints. In this study, lumbar, hip, knee, and ankle joint motions and lumbar spine curvatures were analyzed using the 3-D motion analysis during squat and stoop lifting with three different weights to find out relations between lower limb motions and lumbar joint motion.

2. Methods

Thirteen young male volunteers who have no problems in both lifting and walking were selected for the subjects in this study. Two forceplates were synchronized with the 3D motion analysis system. Totally 31 reflective markers were attached on the anatomical locations based on the VICON Plug-in-Gait marker placement protocol. Besides, additional four markers(V1~V4) were mounted on the back along the spinous process to define the spinal curvature. The boxes weighed 5, 10 and 15kg and had the same side handles. Subjects were asked to lift those boxes in two different techniques(squat and stoop) as their own comfortable speed. Joint moments in the lower extremities were determined using the inverse dynamics and the support moment was also calculated as a summation of all lower extremity joint moments. Paired t-tests were used to determine the statistical difference in the maximum lumbar moments in squat and stoop techniques and the Kruskal-Wallis test was used to compare the joint angles and moments with respect to the increase of weight when the lumbar lordosis appears.

3. Results

3.1. *Joint Angles*

The mean lifting speeds were 0.59m/s(±0.14) in squat lifting and 0.60m/s(±0.10) in stoop lifting. Figure 1 (a),(b) represents the lower extremity joint angles on the sagittal plane during lifting. Though the different weights were lifted, the range of motions(ROMs) were not different significantly. However, between two techniques, ROMs for the same joints showed significant difference. Remarkable difference was shown especially in the knee joint.
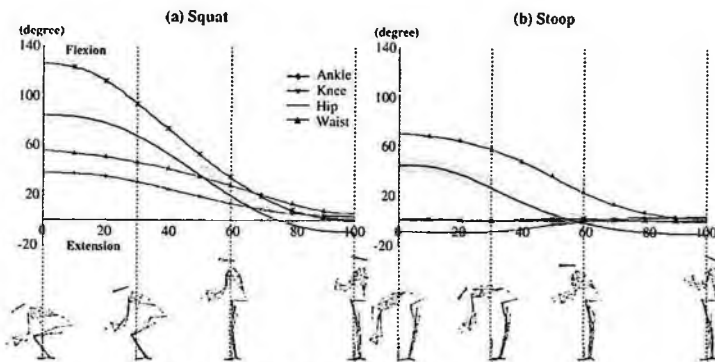
Figure 1. Joint angles of lower extremities during lifting.

3.2. *Joint Moments*

Joint moments in two techniques were plotted in Fig. 2 for different object weights. The ankle joint moment was larger in squat than in stoop except initial time at 5kg and 10kg. The knee joint moment was flexion moment in stoop, but in squat it was changed from extension moment to flexion moment. As the object weight increased, the knee extension moment changed quickly to the flexion moment in squat. The hip extension moment increased to its maximum value as soon as lifting started, and then it decreased nearly to zero. The maximum hip extension moment in the stoop technique was always larger than that in squat for all weights. The differences of the maximum waist extension moments between squat and stoop were negligible at 5kg and 10kg. Rather, it was larger in squat than in stoop when 15kg was lifted($p<0.05$).
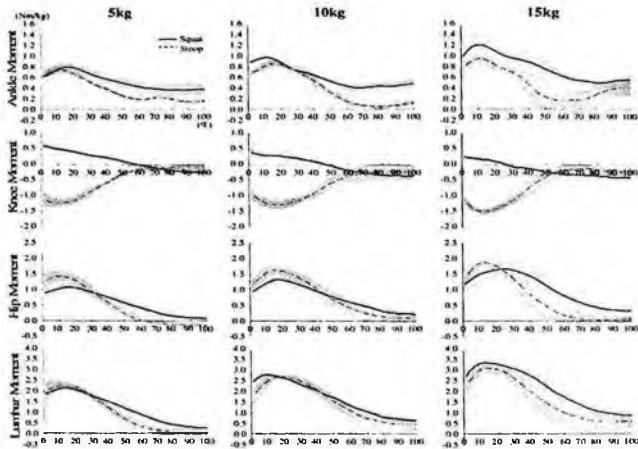
Figure 2. Joint moments during squat and stoop lifting.

Table 1. The maximum lumbar moment in squat and stoop lifting. (Nm/kg).

	Mean (SD)		P
	Squat	Stoop	
5kg	2.19 (0.08)	2.29 (0.19)	0.21
10kg	2.85 (0.07)	2.73 (0.13)	0.11
15kg	3.48 (0.17)	3.13 (0.22)	0.02*

3.3. Support Moments

Joint moments of the lower extremity could be analyzed with the concept of 'support moment'. Fig. 3 shows that the each joint's supporting ratio during lifting. At any time, the areas between two curves represent the support moment on that joint. The extension moments of hip and ankle joint contributes largely on the support moment in both lifting technique. However, in stoop lifting, flexion moment of knee joint played an important role in supporting.
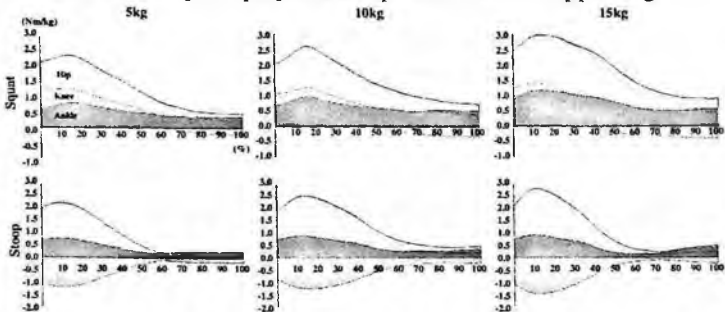
Figure 3. Contributions of lower extremity joints on the support moment during squat and stoop lifting.

3.4. *Lumbar Curvature*

Fig. 4. represents the spine curvature when the lumbar lordosis appeared. Table 2 shows results of the nonparametric central tendency test in three groups(5kg, 10kg, and 15kg). In squat lifting, knee angle, ankle angle, lumbar moment had significant differences as the lifting weight increased. And in stoop lifting, lumbar angle, lumbar moment and hip moment had significant differences as the lifting weight increased ($p<0.05$). Table 3 shows results of the correlation coefficient test between lumbar and L/E, comparative parameters were angle and moment. The knee angle in squat and hip and the ankle angle in stoop showed strong correlation with the lumbar angle. In squat lifting, all three joint moments(hip, knee, ankle) showed correlation with the lumbar moment. However, in stoop, only hip moment had relation to the lumbar moment($p<0.01$).
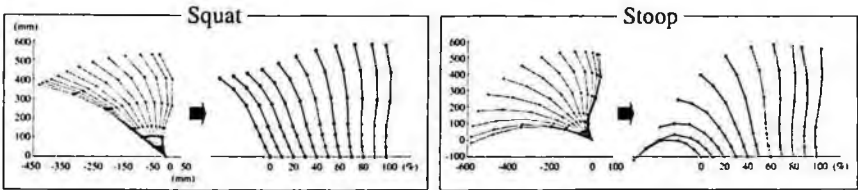
Figure 4. Lumbar spine curvatures during squat and stoop lifting.

Table 2. Joint angles and moments when the lumbar lordosis appears during lifting (Kruskal Wallis)

Mean (SD)		Squat			Stoop		
		5kg	10kg	15kg	5kg	10kg	15kg
Joint Angle (deg)	Lumbar	31.32(3.41)	31.14(4.05)	28.01(3.71)	28.19(1.96)*	25.96(2.14)*	24.79(4.53)*
	Hip	18.23(22.16)	13.55(20.55)	5.67(15.49)	-1.90(5.11)	-1.89(6.23)	-6.05(4.79)
	Knee	23.06(18.41)*	18.65(13.54)*	8.15(6.30)*	-0.83(3.95)	-1.18(2.81)	-2.15(2.38)
	Ankle	10.28(6.71)*	7.32(4.71)*	2.80(2.28)*	1.25(2.58)	0.09(2.12)	-0.25(2.93)
Joint Moment (Nm/kg)	Lumbar	0.89(0.33)*	1.17(0.33)*	1.19(0.21)*	0.60(0.09)*	0.85(0.12)*	0.97(0.09)*
	Hip	0.51(0.26)	0.62(0.28)	0.61(0.20)	0.32(0.07)*	0.42(0.10)*	0.46(0.11)*
	Knee	-0.20(0.10)	-0.36(0.14)	-0.47(0.11)	-0.38(0.13)	-0.43(0.12)	-0.48(0.11)
	Ankle	0.48(0.20)	0.57(0.20)	0.54(0.15)	0.42(0.17)	0.43(0.18)	0.45(0.24)

* : There is significant difference in angle or moment with respect to the weight increase ($p<0.05$)

Table 3. Correlation coefficients between lumbar and lower extremity joint.

Correlation coefficient (p)		Squat		Stoop	
		lumbar angle	lumbar moment	lumbar angle	lumbar moment
L/E joint Angle	Hip angle	0.22(0.40)	-0.33(0.19)	0.82(0.00)*	0.04(0.86)
	Knee angle	0.65 (0.01)*	0.02(0.95)	0.38(0.13)	0.53(0.03)
	Ankle angle	0.15(0.57)	-0.30(0.25)	-0.75(0.00)*	-0.28(0.26)
L/E joint Moment	Hip moment	0.38(0.13)	0.98(0.00)*	0.29(0.25)	0.88(0.000)*
	Knee moment	0.35(0.17)	-0.62(0.01)*	0.67(0.00)*	-0.12(0.65)
	Ankle moment	-0.35(0.16)	0.67(0.00)*	-0.80(0.00)*	-0.20(0.43)

* : The correlation coefficient has a statistical significance at $p<0.01$

4. Conclusion

The characteristics of the lower extremity joint moments during lifting under the three different weights and two different position techniques could be summarized as follows: There were no significant differences in the maximum lumbar joint moments between two techniques. Rather, the maximum lumbar extension moment was larger in squat than in stoop when 15kg was lifted (p <0.05) Hip and ankle contributed the most part of the support moment during squat lifting, and the knee flexion moment played an important role in stoop lifting. At the time of lordotic curvature appearance in squat lifting, strong correlations were found in knee angle and all three L/E joint moments with the lumbar joint. Differently, in stoop lifting, strong correlations existed in hip and ankle angles and hip moment with the lumbar joint. The present preliminary results suggested that lower limbs contribute to minimize mechanical loading on the waist by the change of lordotic curvature in the lumbar spine for the safe lifting.

Acknowledgments

References

1. Y.L. Chen, *Int. J. Ind. Ergon.*, **25**, 611-619 (2000).
2. J.H. van Dieen, M.J.M Hoozemans, H.M. Toussaint, *Clin. Biomech.* **14**, 685 (2000).
3. R. Burgess-Limerick, J. Shemmell, B.K. Barry, R.G. Carson, B. Abernethy, *Hum. Mov. Sci.* **20**, 549 (2001).
4. M. Jager, A. Luttman, *Eronomics* **32**, 93 (1989).
5. J. Matt Maines, Raul F. Riser, *Int. J. Ind. Ergon.* **36**, 109 (2006).
6. Leon Straker, *Int. J. Ind. Ergon.* **31**, 149 (2003).
7. R. Burgess-Limerick, *Int. J. Ind. Ergon.* **31**, 143 (2003).

DETERMINATION OF THE MATERIAL PROPERTY FOR THE REAR FIXATION DEVICE OF THE VERTEBRAE BY FEM*

DAE JIN OH, SEUNG HYUN YOO, JOON HO SONG, DHANESHWAR MISHRA

Mechanical Engineering, Ajou University, 209 East-Hall WonChun-dong PalDal-gu, Suwon 442-749, Korea

SEONG CHEOL HWANG

U&I corporation, 519-1, YougHyun-dong, Uijungbu Kyunggi-do 480-050, Korea

Since Boucher technique used pedicle screw for the fixation of the spine in 1959, various kinds of pedicle screws have been developed continuously. The treatments of degenerative spine disease include spinal fusion and fixation using spinal devices. Spinal fusion surgery is classified into fusion and non fusion. The spine device market in which pedicle screws are used is getting bigger. However, it is one of the most challenging fields because of lack of the experimental and analytic data. In this study, a finite element model which includes non fusion device of human lumbar is developed and studied to understand the stability of the technique. The material property of the non fusion device is decided through comparison of intact model with fixed model. This result can be used as a basic source to new apparatus. This dynamic device offers a system that may alter the motion preservation and load sharing of a spinal segment without sacrificing stability.

1. Introduction

In modern society, spinal illnesses have greatly increased due to the wrong posture and life styles of the moderns. Various therapeutic methods are being developed in accordance to this phenomenon. Currently, treatments such as the artificial disc replacement and the vertebral fixation using pedicle screws are given. This research compared the in-vitro test of Yamamoto et al.[1] with a newly made model of the 3rd to 5th lumbar vertebra. Also, the model was verified in comparison with the earlier lumbar vertebra model of Chen et al.[2] and Yoon[3]. Generally for patients that received the vertebral fixation treatment, side effects occur to the vertebras adjacent to the fixed ones, because they repeatedly have to endure pressure. Therefore, the current fixation treatment using rear fusion device needs to be amended. This view does not focus only on attempting to fix the vertebras together. It actually focuses on the two vertebral

---

bodies placed between the problematic discs, so they can endure the load and have some capacity to move at the same time. We compared the intact model without the rear fusion device and the lumbar vertebra model with the non fusion device which allows some movement in this research. The amount of the disc displacement of the intact model without the device was measured. Then the mechanical property of the rod in the device was changed and accordingly analyzed. The mechanical property of the rod for the desired motion value was found in this way. The result of this research can be used as a factor of the basic design of the non fusion fixation device which is a step more developed than the former entirely fixed pedicle screw.

2. Methods

2.1. *Intact FE Model*

A finite element model was made by making a three dimensional CAD file from the CT film used in the pre-existing model [4].
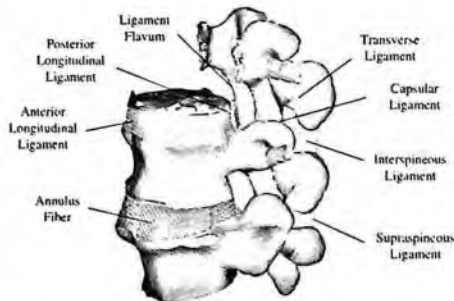
Figure 1. Developed finite element model with ligaments.

Fig. 1 shows the 3rd to 5th lumbar vertebra model of a normal spine used in this research. It shows the curvature of the spine when there is no outer force applied to it. The upper and lower part of the vertebral body consists of an 0.5mm thick endplate. The disc is composed of the annulus fibrosus, nucleus pulposus, and the annulus fibre, which is at an average angle of 30 degrees with the horizontal plane. The disc especially connects two adjacent vertebral bodies together. At the same time, it moves in a complex manner between the bodies, and it supports or absorbs the pressure load. If compressive force is applied to the disc, pressure builds up at the nucleus pulposus. This pressure pushes the annulus fibrosus, which surrounds the nucleus pulposus, to the side. This force on the annulus fibrosus in turn applies tension force to the annulus fibre attached

to it. This makes a very stable structure for bearing the pressure caused by compressive force. The C3D10 element which is the 2nd order tetrahedral element was used for the annulus fibrosus and nucleus pulposus in this model. This enabled a more realistic analysis by describing a more flexible movement. And the T3D2 element was used for the annulus fibre. This was also used for the ligaments. A total of seven kinds of ligaments were described as shown in Fig. 1. ABAQUS 6.4 was used and the total number of elements in this model is 180,379

2.2. FE Model with rear fixation device

Normally the rear fixation device has been inserted to entirely fix the adjacent vertebral bodies. The operation involved removing the facet joint and inserting pedicle screws in replacement in this case. However the facet joint was not removed, but avoided in this research. The spinal movement needs to be preserved.
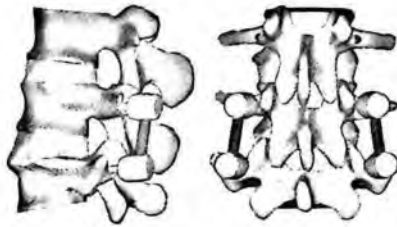
Figure 2. The fixed model between 4th and 5th lumbar by rear fixation device.

When the spine moves, the facet joint is essential to control the displacement amount of the vertebral bodies. Therefore, the purpose of this research was not an entire fixation, but the insertion of screws while preserving the original form of the spine as much as possible. The result of the Hartl et al. [5] research was referred to because the location and direction of the screws are also important variables in this research.

Table 1. Material properties in this model.

Component	Young's modulus, E (MPa)	Poisson's ratio, ν
Cortical bone[6][7]	12,000	0.3
Cancellous bone[7][8]	100	0.2
Endplate[6]	12,000	0.3
Disc-annulus[9]	2	0.45
Disc-nucleus[8]	1	0.4999
Annulus fibre[7]	175	0.3

The diameters of the pedicle screws and rods are is 4.5mm and 6mm respectively. As shown in Fig. 2., the rear fixation device consists of pedicle screws, rod, and housing which connects the rod and screw. The device is inserted as a pair at the left and right, with the posterior in the middle. It was designed to make that most of the movement occurs at the rod. The rear fixation device was inserted at the 4th and 5th vertebra in this model. And an expanded model of the 3rd vertebra was prepared for further research.

2.3. *Loading and boundary condition*

As shown in Fig. 3, vertical pressure of 150N was applied to the upper end plate of the 3rd vertebra, followed by the a 10 N-m moment of flexion and extension to the central part of the end plate. This was to compare with the in-vitro experiments of other researches [1,2,3]. The lower end plate of the 5th vertebra was fixed.
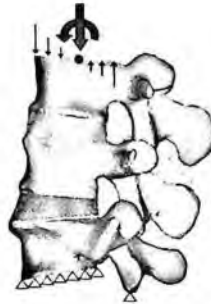
Figure 3. Loading and boundary condition in flexion.

3. Results and conclusions

The results of former researches and the intact model of this research was compared with and verified before the analysis to find the property of the rod. The results of the experiment of applying the flexion and extension moment using the same boundary condition as the Yamamto et al.[1] experiment are on Fig. 4. The displacement of L34 in this model is slightly higher when extension is applied. This is due to the fact that the facet joint of each model differs in shape. This research is on the 3rd to 5th vertebra, whereas the former analysis results were on the 1st to 5th vertebra. This causes small differences. The extension cases result in a smaller amount of displacement compared to flexion cases as shown in Fig. 4. This is because of the influence of interference at the facet joint. This is already a known fact in anatomy. Generally the movement inclination is similar to former research results.
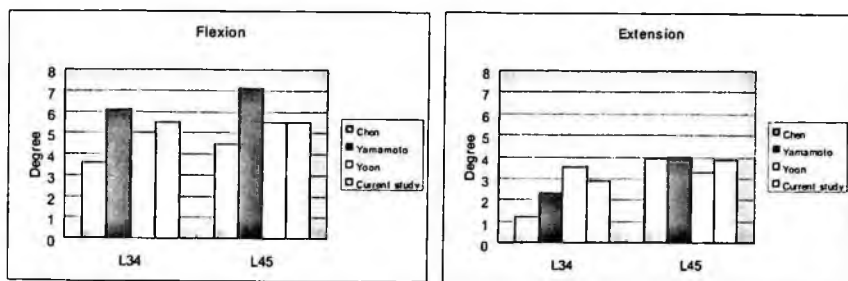
Figure 4. The result of verification with recent researches.
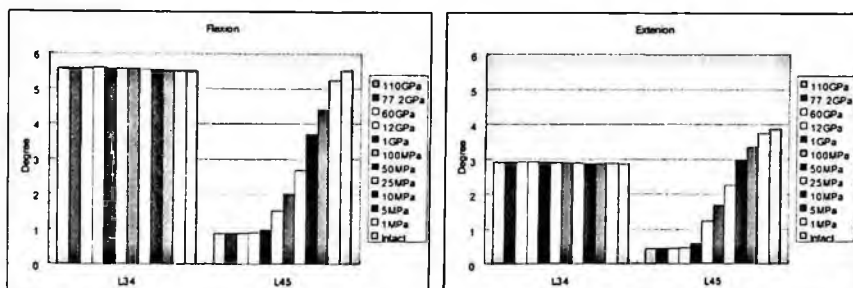
Figure 5. Flexion and extension angular motion in disc L34, L45.

After verifying the model, the rear fixation device was inserted in the 4th and 5th lumbar vertebra to compare the result with the intact model. Especially, the mechanical property value of the rear fixation rod needs to be constantly changed. The movement range of each disc was measured. The Young's modulus of the rod was selected out of the range of 1MPa ~ 110000MPa and the Poisson's ratio was fixed to 0.3. Titanium was used for the pedicle screws and housings. Titanium in the fixation device had been used in the human body without any side effects for long time. As shown in the Fig. 5, most of the spine motion preservation for extension and flexion occurred when the rod's Young's modulus was below 1000MPa. According to the analysis result, if the rod's Young's modulus is over 1000MPa, the movement of spine is limited to less than 1 degree. Therefore fixation devices that fix the spine in this way can be classified as a fusion device. Regarding that the motion range of an intact L45 disc is 5.5 degrees, a device that can preserve a minimum of 50% of the motion range of an intact spine was defined non fusion device. When the extension model can motion up to 50% of an intact model, the modulus is 25MPa. As for the flexion model, it is 35MPa. The minimum Young's modulus of the rod in designing a non fusion device is below 25MPa, when the extension and flexion model can move 50% of an intact model. As shown in the result above, the

displacement amount between the 3rd and 4th lumbar vertebra is almost same with the intact model regardless of whether the device is fusion or non fusion if the 4th and 5th lumbar vertebra is connected to a rear fusion device. However, this result does not run counter to the former research result that fusion device will impose needless pressure on adjacent discs causing degenerative diseases in discs that did not have any problems in the first place. The stress analysis is needed to prove this. It cannot be judged with only the angular motion in the result above. In this analysis, the pedicle screws used for the rear fixation device had a diameter of 4.5mm, and the circular rod, 6mm. This rod is bent to correspond to the curvature of the spine.

The result of this research can be used as basic data for the development of a new non fusion device. It will also be used as one of the specific design factors. Specific standards on the device rod have been presented. Furthermore, research on various sizes and shapes of the non fusion fixation device will be progressed.

References

1. Yamamoto, I., Panjabi, M. M. and Crisco, T., Three-Dimensional Movement of the Whole Lumbar Spine and Lumbosacral Joint, *Spine*, Vol. 14 (1989), p.1256-1260.
2. Chen, C. S., Cheng, C. K., Liu, C. L. and Lo, W. H., Stress Analysis of the Disc Adjacent to Interbody Fusion in Lumbar Spine, *Medical Engineering & Physics*, Vol. 23 (2001), p.483-491.
3. Yoon S. S., Biomechanical analysis of artificial disc using FE model, *Master's thesis, Dankook Univ.*, Korea (2006)
4. S. H. Yoo, Annotated bibliography of mechanical properties of a human body, *Ajou Univ. Press*, Korea (2004)
5. Hartl R, Theodore N, Dickman CA and Sonntag VKH, Technique of Thoracic Pedicle Screw Fixation for Trauma. *Operative Techniques in Neurosurgery*, Vol. 7 (2004), p.22-30
6. Brown N, Saputa C and Black J, Young's modulus of living human bone. *Transaction of the orthopaedic research society*, Vol. 6 (1981)
7. Goel VK, Park H and Kong W, Investigation of vibration characteristics of the ligamentous lumbar spine using the finite element approach. *J Biomech Eng*, Vol. 116 (1994), p.377–383
8. Koji T, Naoya T, Etsuo C, A biomechanical study of posterolateral lumbar fusion using a three-dimensional nonlinear finite element method, *J Orthop Sci*, Vol. 4 (1999), p.115-126
9. Robin S, Skalli W, Lavaste F, Influence of geometrical factors on the behaviour of lumbar spine segments: a finite element analysis. *Eur Spine J*, Vol. 3 (1994), p.84–90

A FES SENSOR SYSTEM USING A TILT SENSOR FOR IMPROVING HEMIPLEGIC GAIT[*]

SUNWOO PARK

Department of Biomedical Engineering, Yonsei University, 234 Maeji-ri, Heungup-myun Wonju-si, Gangwon-do 220-710, South Korea

JONGSANG SON

Department of Biomedical Engineering, Yonsei University, 234 Maeji-ri, Heungup-myun Wonju-si, Gangwon-do 220-710, South Korea

SUNGJAE KANG

Department of Biomedical Engineering, Yonsei University, 234 Maeji-ri, Heungup-myun Wonju-si, Gangwon-do 220-710, South Korea

YOUNGHO KIM[†]

Department of Biomedical Engineering, Institute of Medical Engineering, Yonsei University, 234 Maeji-ri, Heungup-myun Wonju-si, Gangwon-do 220-710, South Korea

Simple, accurate gait phase detection is essential for the efficient application of the automatic FES walking system. In this paper, a preliminary FES sensor system was developed to correct foot drop in hemiplegic patients. Twelve healthy volunteers and five hemiplegic patients whose cadence was 30steps/min with circumduction gait pattern participated in this study. We attached a miniature tilt sensor with the hardware filter system on a shank to acquire segment angles during gait. For healthy volunteers, TO(toe-off) and IC(initial contact) were defined as the time with 87.8±7.3% and 58.4±9.5% from the offset voltage, respectively. For hemiplegic patients, IC was defined by the negative peak, HO(heel off) by the second positive peak, TO by the third positive peak and the TV(tibia vertical) by the offset voltage in sensor signals. In healthy volunteers, IC and TV were 100% successfully detected, but in the hemiplegic patients HO and TO were detected approximately 85% and 79% respectively. The algorithm to provide trigger signals to the main FES system was also tested. Two channel trigger signals were generated by the voltage from the tilt sensor which was filtered by the hardware filter

152

system. The Ch1 trigger signal controlled FES stimulation on the ankle and knee joints during stance phase by turning ON at IC and turning OFF at the 1st TV. The Ch2 trigger signal controlled FES stimulation during swing phase by turning ON at HO and turning OFF at the 2nd TV. This study would be helpful to develop an efficient FES walking system to correct drop foot in hemiplegic patients.

1. Introduction

FES(Functional Electrical System) is being applied to prevent foot drop and foot drag of patients whose central nerve systems have been damaged due to industrial disaster, traffic accident, and stroke [1]. To apply this FES system effectively, we need a system that can accurately estimate gait cycles and send immediate input signals. In general, 3-dimensional movement analysis system is widely used in analyzing gait cycles, which is very accurate in analyzing but very expensive. Besides, it is difficult to apply this system to a patient's daily life and analyze his and her gait cycle because it can only be used inside the laboratory. Hence, there have been studies conducted on sensors which can be applied effectively and easily to a FES system, and also on composite sensor systems, where merits of various sensors are used selectively to detect gait cycles more accurately. In general, when giving functional electric stimulus on legs to restore walking ability, patients themselves had to use hand-switches to set the stimulating time and foot-switches to detect gait cycles[2]. This method had limitations because it had to be operated by hand, connected by wires, and not applicable to bear foot. Tong and Grant[3] succeeded in detecting the angular speed of shank and thigh using two gyrosensors, and gait cycles by measuring the gradient to the gyrosensor's shaft. Seung Chan An *et al.*[4] developed a gait cycle detecting system which uses FSR sensors and gyrosensor. Ju Hyeon Lee *et al.*[5] analyzed stroke patients' gait cycles using accelerometers. Dai *et al.*[6] attached tilt sensors on shank and thigh, and analyzed gait cycles by measuring the angle of each volume.

In this research, we attached the tilt sensor along with the FES stimulating pad on the shank, and detected gait cycles of a normal person and a hemiplegic patient. In addition, we experimented whether 2-channel FES stimulus trigger signals are generated, using the voltage of gait cycles detected from the normal walking.

2. Methods

In this study, we conducted experiments on twenty healthy volunteers (male and female), and five hemiplegic patients (male), who was generated right-partial

paralysis, walking very slowly and unbalanced right and left and showing the characteristics of circumduction gait.

A SMD-type tilt sensor (SCA100T, VTI, Finland) has been used, which has the measurement range of ±90° and sensitivity of 2V/g. A flexible PCB with the tilt sensor equipped with a hardware filter was designed, and then integrated into a FES stimulating pad, as shown in figure 2(a). As shown in figure 2(b), the stimulating pad was placed on the motor point of tibialis anterior (TA), the main ankle dorsiflexor. The positive output was defined when the tibia makes an acute angle with respect to the anterior direction. two channel FES stimulation trigger signal generating system was designed and the sensor output signals were processed using a microprocessor (ATmega128). We synchronized the sensor output with the three-dimensional movement analysis device and four force-plates through datastation, and compared and analyzed the gait cycles detected from the sensor.

(a)   (b)
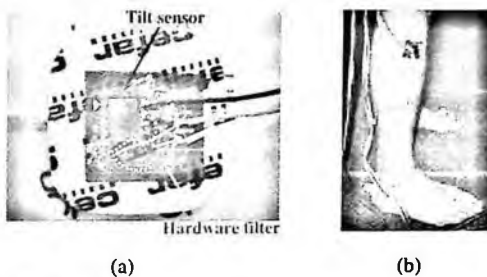
Figure 1. Stimulating pad(a) and its application on TA(b)

3. Results

The output voltage of the tilt sensor attached on the shank is illustrated in figure 2. The output signal of the sensor has been processed in 2nd low-pass filter of cutoff frequency 1Hz through frequency analysis (main frequency: 0.29Hz). During a normal walking (Fig 2 (a)), two negative peaks and one positive peak appeared during a gait cycle, and two offset voltage was generated. Heel contact (HC) was detected for negative peak, and toe off (TO) was detected for positive peak. And using the sensor's characteristic of generating offset voltage when the shaft of the sensor meets vertically with the ground, we detected tibia vertical (1st TV, 2nd TV), which is when the shank meets vertically with the ground for once in the stance phase and swing phase. On a scale of 100% from a offset voltage to peak voltage, TO appeared in 87.8±7.3%, and IC appeared in 58.4±9.5%.

During a hemiplegic patient's walking where cadence was 30steps/min (Fig. 2 (b)), two negative peaks and four positive peaks appeared in a gait cycle, and two offset voltage was generated same as in a normal walk. HC was detected for negative peak, heel off (HO) was detected for 2nd positive peak, and TO was detected for the 3rd positive peak, and 1st TV 와 2nd TV was detected as the point generating offset voltage.
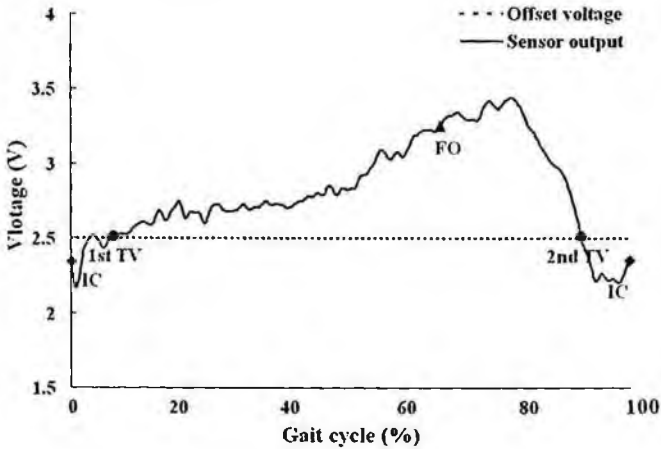
(a)
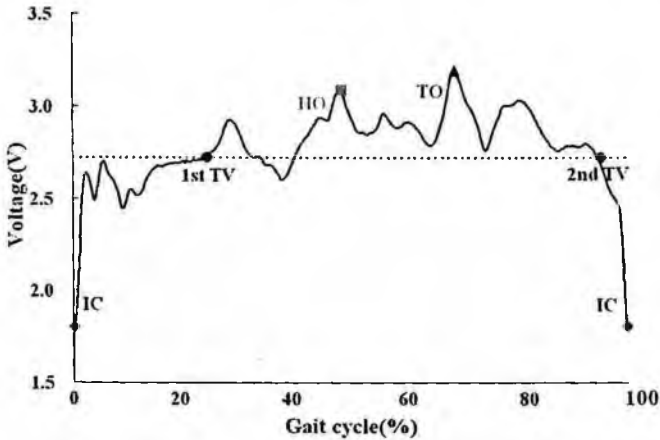
(b)

Figure 2. The output signals of tilt sensor in normal walking (a) and hemiplegic patient's walking (b)

We developed a two channel FES stimulation trigger signal generating system based on the output voltage of each gait cycle detected by the tilt sensor system used in this experiment (Fig. 3).
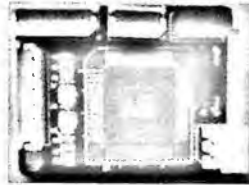
Figure 3. 2Ch FES stimulation trigger signals system

When the voltage that generated gait cycle were 0.9V for IC, 2.5V for TV, and 3.2V for HO, we programmed each voltage value as the triggering signal's base ON / OFF value. The Ch1 trigger signal controlled FES stimulation on the ankle and knee joints during stance phase by turning ON at IC and turning OFF at the 1st TV. The Ch2 trigger signal controlled FES stimulation during swing phase by turning ON at HO and turning OFF at the 2nd TV. Sensor's output curve and the output of 2ch trigger signal were illustrated in figure 4.
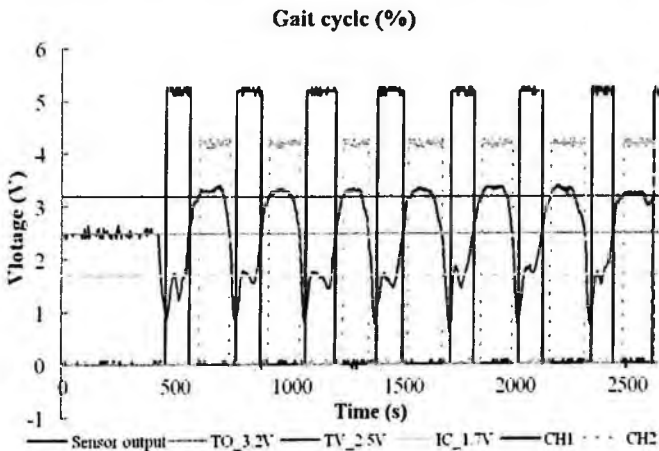
Figure 4. Output signals of the tilt sensor system and 2ch trigger signals

4. Discussion & Conclusion

In this study, gait cycles of normal person and hemiplegic patients have been detected using the tilt sensor output in shanks, through the tilt sensor system

attached on the electrode. Even though the tilt sensor system which is used in this study has simple advantage, in the case of hemiplegic patient's walking we showed lower success rate than the normal walking. Gait cycles have been detected using the offset voltage and peak voltage of the tilt sensor, and as a result, in healthy volunteers, IC and TV were 100% successfully detected, but in the hemiplegic patients HO and TO were detected approximately 85% and 79% respectively. We made 2ch FES stimulation trigger signals to be generated using the voltage of the gait cycles detected from this sensor system, and as a result, we confirmed that trigger signals are turned ON / OFF depending on the base voltage value. Further study, we need the method to increase the success rate that additional application of the sensor or the calibration step to be able to determine the reference values compare with realtime sensor output voltage. This study would be helpful to develop an efficient FES walking system to correct drop foot in hemiplegic patients.

References

1. W. T. Liberson, H. J. Holmquest, D. Scott and M. Dow, *Arch. Phys. Med. Rehab.* **42**, 101-105 (1961)
2. B. R. Brandell, *Am. J. Phys. Med. Rehab.* **6**, 279-301 (1982).
3. K. Tong and H. M. Grant, *Med. Eng. Phys.* **21**, 87-94 (1999).
4. S.C. Ahn, S. J. Hwang, S. J. Kang, Y.H. Kim, *J. KSPE* **21**, 196-203 (2004)
5. J. H. Lee, S. W. Park, D. A. Kim, S. J. Jang, Y. H. Kim and J. B. Lee, *J. KARM* **28**, 488-493 (2004)
6. R. Dai, R. B. Stein, B. J. Andrews, K. B. James and M. Wieler, *IEEE Trans. Rehab. Eng.* **4**, 63-72 (1999)

HOMOGENEIYT AND RANKLET BASED MASS-TYPE CANCER DETECTION IN DENSE MAMMOGRAPHIC IMAGES[*]

WONHA KIM

School of Electronics and Information, Kyunghee University
Yongin-si, Gyeonggi-do 446-701, Republic of Korea

SUNGMIN KIM

Department of Biomedical Engr., KonKuk University
Choongju-si, Chungchung-namdo, Republic of Korea

In dense mammographic images usually obtained from oriental women, mass-type cancer tissues have the appearance of severely entangled tissues associated with screwed tissues. Thus, it is much more difficult to detect mass-type cancers in dense breast mammographies. For the better detection of mass-type cancers in dense breast mamographies, we propose a multi-feature function integrating homogeneity and the Ranklet. We constructed a Maximum Likelihood based homogeneity classifier for extracting cancerous masses from mixtures of mass tissues and screwed tissues. We also design a Support Vector Machine based Ranklet classifier for selecting mass-type cancers.

1. Introduction

In mass-type cancers in dense breast, cancer tissues tend to become severely entangled with normal tissue. Such dense breast mammographic images are commonly observed in Asian women. Therefore, the detection rates of current cancer detection systems developed for western women are not satisfactory when they are applied to the dense mammographies [1]. In this paper, we developed a mass type breast cancer detection system for dense breast mammographic images.

Most previous methods for detecting mass-type cancer calculated the statistical gradient and and identified mass-type cancer based on the direction of textures gradient [2][3][4]. Due to the severe microscopic changes that usually occur in dense mammographic images, these methods are difficult to use to identify the direction of the statistical gradients in dense breast images.

To overcome the shortcomings of the previous methods, we propose a multi-feature function that analyzes the homogeneity and Ranklet [5][6]. The homogeneity measures the tissue uniformity. The Ranklet coefficients provide more reliable texture directions in mass areas. We design a homogeneity classifier using the Maximum Likelihood (ML) estimation. The developed homogeneity classifier efficiently distinguishes cancerous masses from miscellaneous screwed tissues. Then, we use the Support Vector Machine (SVM) to design the Ranklet classifier. The Ranklet classifier identifies mass-type cancers by choosing masses whose texture gradient directions are toward the center. We exploit a hierarchical decision mechanism. The developed homogeneity classifier extracts masses among mixtures of cancerous mass tissues and entangled tissues. Then, the Ranklet classifier selects mass-type cancers from masses passing through the homogeneity classifier.

2. Homogeneity Classification

2.1. *Cancerous Mass extraction via Homogeneity*

In dense breast images, tissues associated with masses and other miscellaneous tissues such as capillary vessels are severely mixed and bright at their centers. A difference between mass tissues and miscellaneous tissues is that mass tissues have more uniformity textures at their centers. We exploit the homogeneity to quantify the texture uniformity [5]. The homogeneity is calculated using

$$H = \sum_{i \leq M} \sum_{j \leq M} \frac{P(i,j)}{1+|i-j|}$$

where $P(i,j)$ is the Co-occurrence value whose horizontal and vertical distance are 1, and M defines the size of the tissue centers. In this paper, M is set to 20% of tissue area to be tested.

Figure 1.(a) compares the homogeneities among various tissues. As seen in the figure, the tissues with large Homogeneity values contain the uniform textures and are more likely to be cancers, while the tissues with low homogeneity values are more likely to be miscellaneous tissues.

2.2. *Designing homogeneity classifier*

Figure 1.(b) overlays two probability distributions of the homogeneity values of mass-type cancer tissues and miscellaneous screwed tissues. The samples sizes
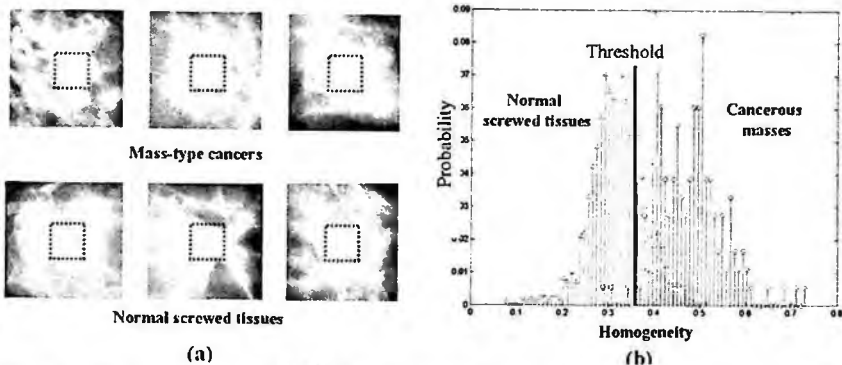
Figure 1. (a) Mass-type cancers and Normal screwed tissues. (b) Probability density functions of homogeneity values for normal screwed tissues and cancerous masses and decision threshold.

of the mass-type cancer tissues and miscellaneous screwed tissues are 182 and 96, respectively.

We exploit the Maximum Likelihood Estimation (MLE) to determine the threshold value used to classify potentially cancerous masses and miscellaneous screwed tissues. As seen in the probability distributions, the optimal threshold by MLE estimation is 0.4. However, a threshold value of 0.4 results in a missing rate of about 10 %. To reduce the missing rate, we bias the threshold to 0.35. With this threshold value, the true alarm rate improved to be about 95%, but the false alarm rate is increased up to about 12%.

3. Ranklet based classification

3.1. *Texture gradient direction measure via Ranklet*

Although the central areas of masses have uniform textures, most of them are classified as benign masses which are not relevant to cancer. Thus, homogeneity alone is insufficient to distinguish the cancerous masses from the benign masses. However, mass-type cancer tissues generally diffuse outward from their centers radially. Therefore, the texture gradient directions of cancerous masses tend to point toward their centers. To exploit this phenomenon, we developed a gradient direction classifier using Ranklet coefficients [6].

Ranklet developed in 2002 estimates underlying texture directions by analyzing the relative brightness of pixels in vertical, horizontal and diagonal directions. Figure 2 illustrates the separated regions used for calculating the pixel
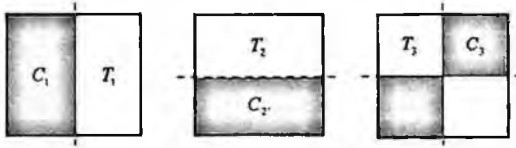
Figure 2. Vertical, horizontal and diagonal regions for calculating relative pixel brightness.

brightness. The relative brightness coefficient W^i_{YX} for a region T_i is calculates as follows:

$$W^i_{YX} = \sum_{x \in T_i} \left\{ \pi(x) - \frac{N(N+1)}{2} \right\}$$

where x is the value of pixel belonging to a region, π is the rank transform that transforms pixel values to relative brightness, N is number of pixels in T_i. Then, Ranklets corresponding to horizontal (h), vertical (v) and diagonal (d) directions are obtained as follows:

$$R_i = \frac{2W^i_{YX}}{N^2/4} - 1, \qquad i = v, h, d$$

We used 40% of the mass areas for calculating Ranklets. Since the variations among adjacent pixels are difficult to observe in mammographic images with a high resolution, we down-sampled our mammographic images to decrease their resolution to 400um/pixel from 100um/pixel. In this resolution, we could more easily observe the texture due to relatively apparent variations among pixels and also reduce about 80% of computation load.

Figure 3 shows examples of malignant masses containing cancers and benign masses. The texture gradients of the masses containing cancers direct toward mass centers, and the Ranklet values for all directions are small. However, the centers of the masses of entangled tissues often elongates in a certain direction. Thus, at least one of their Ranklet values is large. Table 1 compares the Ranklet values obtained from the masses of cancers and the masses of the entangled tissues.

3.2. *Designing Ranklet classifier via SVM*

We adopt the Support Vector Machine (SVM) to design a Ranklet classifier. The SVM developed in 1995, is a statistical learning model popularly used for designing pattern classifiers [7]. The learning data supplied to the SVM training include 90 masses containing cancers and 120 benign masses.

Table 1.. Raklets values for masses shown in Figure 3.

Rankles	Mass-type cancer			Benign mass		
	(a)	(b)	(c)	(d)	(e)	(f)
Vertical	0.17	0.12	0.04	0.51	0.61	0.66
Horizontal	0.25	0.20	0.25	0.07	0.22	0.14
Diagonal	0.26	0.35	0.18	0.66	0.18	0.12
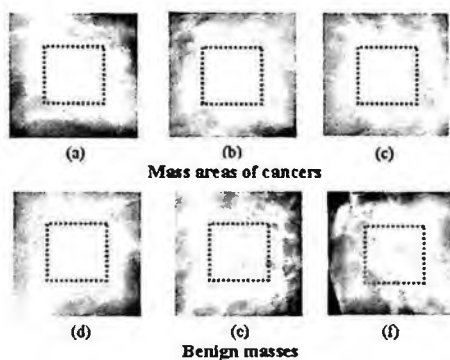
Figure 3. Mass-type cancers and benign masses.

For our SVM classification, the weight parameters are 1.389, 1.294 and 1.065, respectively, and the bias is 0.8467.

4. Experiments and Discussions

We applied the developed multi-feature function to 230 mammography images provided by Samsung Medical Center. These images obtained from Korean patients show typical dense mammographies. The resolution and color depth of the images are 100um/pixel and 12bits/pixel, respectively.

The proposed multi-feature function detects 75% of the mass-type cancers and produces 2.3 false alarms per image, while an existing commercial system is reported to detect about 67% of mass-type cancers and produce less than 1 false alarm per image [1]. The analysis of the experimental results verifies that the homogeneity classifier is useful, especially in distinguishing masses from cross veins, and that the Ranklet classifier detects at least 20% more mass-type cancers than the existing methods based on the texture gradient orientation. Figure 4 shows the actual detections of cancers.
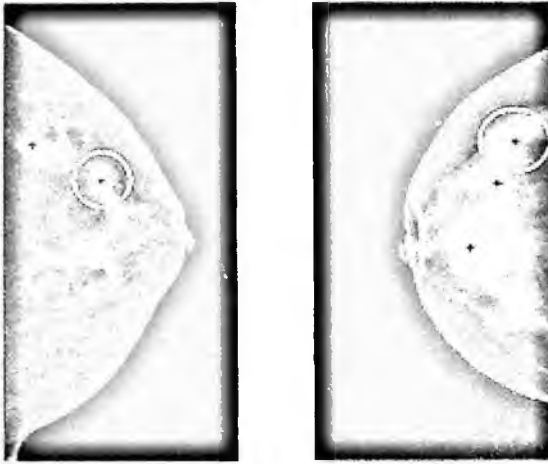
Figure 4. Actual mass detections. '+' indicates the cancerous masses detected by the proposed feature function. The circled masses are cancers.

It should be also noted that the developed system only makes use of homogeneity and Ranklet. Thus, a direct comparison between the proposed system and commercial systems may not be fair. With the addition of other features such as the irregularity of the mass, the performance of the proposed system would be improved.

References

1. S. J. Kim, W.K Moon, N. Cho, J. H. Cha, S.M. Kim and J.G. Im, *Radiology*, Vol. **241**, 695, (2006)
1. R. M. Rangayyan, *Biomedical Analysis*, CRC press, (2005)
2. N.Karssemeijer, *Image-Processing Techniques for Tumor Detection (ed. R. N. Strickland)*, Marcel Dekker, New York, 187, (2002).
3. Brake, G. M., Karssemeijer, N, *IEEE Trans. Medical Imaging*, **Vol.18**, 628 (1999).
4. N.R.Mudigonda, *IEEE Trans. Med. Imag.*, **Vol. 20**, 7 (2001).
5. R. Jain, R. Kasturi and B. Schunck, *Machin Vision*, McGraw Hill, (1995).
6. F.Smeraldi, J. Bigun, *Pattern Recognition Letters*, **Vol.23**, 475 (2002).
7. Chang, C.-C. and C.-J. Lin, *A library for support vector machine*, http://www.csie.ntu.edu.tw/~cjlin/libsvm/. (2001)

THE EVALUATION OF USEFULNESS OF THE FEA AND RELATIONSHIP BETWEEN TRABECULAR MICROSTRUCTURAL AND BIOMECHANICAL PROPERTIES IN HUMAN FEMORAL HEAD

MYONG-HYUN BAEK

Clinical Trial Center, Ajou University Hospital, San 5 Wonchon-dong Youngtong-gu
Suwon-City, 443-721, KOREA

WEN-QUAN CUI

Orthopaedic surgery, Ajou University Hospital, San 5 Wonchon-dong Youngtong-gu
Suwon-city, 443-721, KOREA

KEYOUNG JIN CHUN

Medical Health Team, KITECH, Hongcheon-ri Ipjang-myeon
Cheonan-city, 330-825, KOREA

YOUNG EUM KIM

Mechanical Eng., Dankook University, 44-1, Jukjeon-dong
Yongin-city, 448-701, KOREA

YE-YEON WON[†]

Orthopaedic Surgery, Ajou University School of Medicine, San 5 Wonchon-dong
Youngtong-gu
Suwon-city, 443-721, KOREA

JUNE HUYCK HUR

Orthopaedic Surgery, Lee Chun Tek Orthopaedic Hospital, 130-1 Kyo-Dong, Paldal-Gu,
Suwon-city, 442-130, KOREA

To evaluate the usefulness of the finite element analysis and the relationship between trabecular bone microstructural and its biomechanical properties, the micro image-based FEA and the experimental test were performed in the same bone cores from the primary compressive trabecular system of human femoral head.

---

† Corresponding author.

1. Introduction

Bone quality is one of the factors to assessment bone fracture risk. It is refers to architecture, geometry, bone turnover and damage accumulation[1]. As for the trabecular bone, its micro-structural properties play a very important role in bone quality. Deterioration of the bone quality caused trabeculae thinning, perforation. It is lead to mechanically weaker, ultimately disconnection or fracture. In the past, traditional method to assessment of bone quality is bone mineral density and experimental test (e.g. Instron or MTS machine). Evidently, BMD measurement alone is not possible to clarify the trabecular skeletal structure adaptive to mechanical stresses, as one of the bone quantity indices. Additionally, the direct assessment of the mechanical properties of bone from experiments is subject to large error and significant uncertainties, mostly due to the small sample sizes and the relatively large length scales of the non-homogeneities [2-3]. Recently, following development of non-invasive technique and application of finite element analysis on bone research field, bone morphological and biomechanical study has been progressing [4-6]. Recently, high-resolution micro-computed tomography (micro-CT) reconstruction of trabecular bone has been introduced which allows for noninvasive assessment of the bone microstructure in three dimensions [7]. Furthermore, based on the micro-CT images, micro-structural finite element models can be created to simulate real mechanical tests, and to evaluate the elastic properties of trabecular bone specimens, thereby eliminating experimental artifacts [8].

The purposes of this study were to evaluate the usefulness of the finite element analysis(FEA) and the relationship between trabecular bone microstructural and its biomechanical properties, the micro image-based FEA and the experimental test were performed in the same bone cores from the primary compressive trabecular system of human femoral head.

2. Materials and Methods

Twenty-one human trabecular bone samples obtained from the femoral head region of 11 patients and 10 cadavers (mean age 62 years, age range 45 to 79) were studied. Cylindrical trabecular bone cores were obtained from primary compressive trabecular system of femoral head in human (Fig. 1).
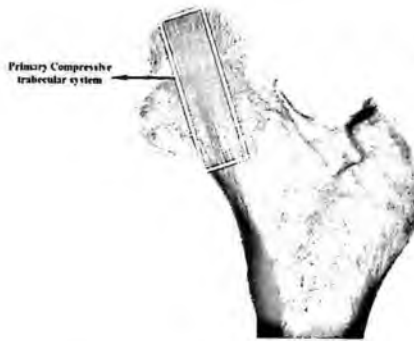
Fig. 1. The pattern of primary compressive trabecular system in the proximal femur.

Size of cored samples was 19 ㎜ of diameter, 15 ㎜ of height. All samples were stored in 70 % ethanol at −20 °C until use.

Micro-CT Scanning

All samples were scanned with a micro computed tomography (SKYSCAN, Antwerp, Belgium) at a spatial resolution of 21.31 μm (Fig. 2). Based on the serial micro-CT images, a volume of interest (VOI) was 9.50 ㎜ of diameter and 7.50 ㎜ of side length. The histomorphometry indices were determined by ANT software (Skyscan, Belgium) such as trabecular thickness (Tb.Th), trabecular seperation (Tb.Sp), bone surface to volume ratio (S/V), bone volume fraction (BV/TV), degree of anisotropy (DA), structure model index (SMI) and trabecular number (Tb.N) [Table. 1], [9].
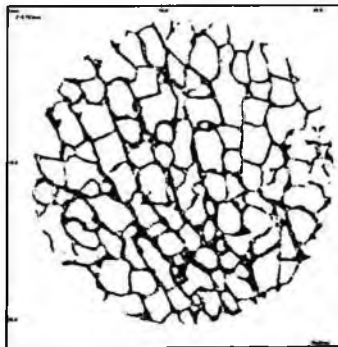
Fig. 2. 2D cross-section image of the primary compressive trabecular bone.

Finite Element Analysis

Finite element(FE) models having from 175,840(±38,258) elements and 336,397(±56,359) nodes were created from diameter 9.5mm and height 7.5 mm region of each cylindrical samples. FE models were converted by BioNix^{TM} software that represent bone tissue to equally shaped 8-node brick elements using the hexahedron meshing technique. A specified threshold level was chosen to ensure the best possible agreement between BV/TV in the histomorphometry and BV/TV$_E$ in the FE-model during conversion. FE-model reconstruction reflects bone microstructure that modulated of element number to same BV/TV and BV/TV$_E$ [8]. The voxel conversion method is as follows.

$$BV/TV=BV/TV_E = E_N/T_N \qquad (1)$$

(BV/TV = bone volume fraction, BV/TV$_E$ =element volume fraction, E$_N$ = element number, T$_N$ = total number).

For all models, element material properties were assumed to be isotropic, linear elastic, and uniform with a tissue modulus of 1 GPa and a tissue Poisson's ratio of 0.3. The FE-solving for the FE models were calculated using a commercial software package (ANSYS 9.0, Inc). The mechanical parameters calculated were yield stress (σ_y) and modulus of elasticity (E).

Destructive Mechanical Test

Samples were stored at room temperature for 24 hours prior to being tested in compressive tests using a servo-hydraulic testing machine (INSTRON 8501, Instron Corp., US). Load was applied perpendicular to the longitudinal axis of each bone at a displacement rate of 0.017 mm/sec for the samples. Load and deformation during the compressive test were obtained. The yield point defined by 0.2% offset (Fig. 3). The biomechanical properties including σ_y and E were determined.

Statistical Analysis

All statistical tests were performed using SPSS 10.0 for Windows (SPSS Inc, Chicago, IL), and a P value of <0.05 was used to judge significance. Pearson correlation coefficients were used to express relationships between the parameters.
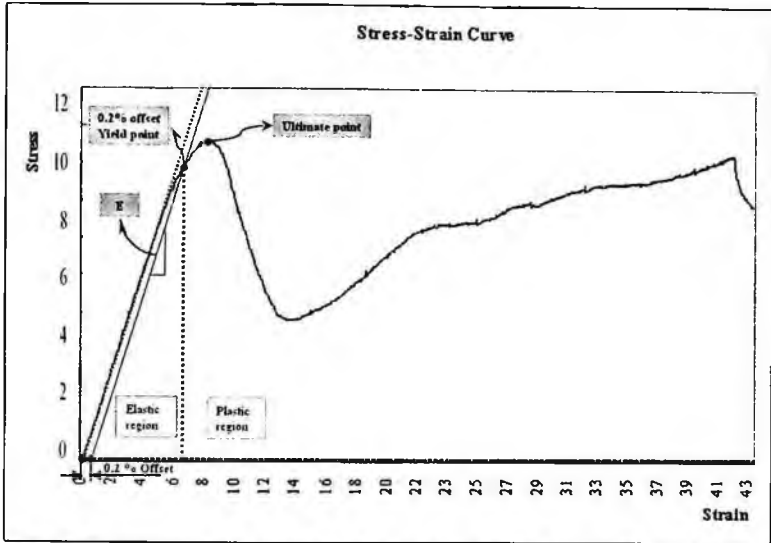
Fig. 3. Stress-strain curve using Instron system in human femoral head.

3. Results

The average and standard deviation of histomometry is listed in Table. 1.

Table 1. Histomorphometry of the primary compressive trabecular system in human femoral head

	Tb.Th(mm)	Tb.Sp(mm)	S/V(mm²/mm³)	BV/TV(%)	DA	SMI	Tb.N(1/mm)
AVE	0.173	0.395	11.449	28.489	0.359	0.851	1.858
STDEV	0.027	0.140	1.616	6.460	0.041	0.328	0.436

The average σ_y and E from FEA and Instron system were 13.04 MPa and 1.30 GPa, 13.06 MPa and 0.11 GPa, respectively (Table. 2). Pearson correlations between of the histomorphometry indices, Tb.Th, Tb.Sp, S/V, BV/TV and Tb.N were significantly correlated with from FEA, while only BV/TV and Tb.N were significantly correlated with the σ_y and E from Instron system. The correlations between the σ_y calculated from FEA and Instron were significant ($P = 0.001$) and $P = 0.055$ for the E.

Table 2. Biomechanical data in finite element analysis and Instron machine

	FEA	Instron
σ_y (MPA)	9.839(±5.031)	9.928(±3.419)
E (MPA)	303.994(±149.236)	282.977(±112.482)

4. Discussions

The results showed a significant correlation between the trabecular microstructure and its biomechanical properties(Table. 3). It supports the concept that bone strength is not only depended on bone quantity, but also depended on bone quality. The biomechanical properties of trabecular bone calculated from FEA are well correlated with those from the mechanical test, suggesting that the micro-image-based finite element analysis as a substitute of the mechanical test can be a useful tool to predict the fracture risk.

Table 3. Correlations (r) between bone morphology indices and biomechanical properties (FEA and Instron)

P value		Tb.Th	Tb.Sp	S/V	BV/TV	DA	SMI	Tb.N
FEA	σ_y	0.413	0.688†	0.599$\ddagger$	0.821$\ddagger$	0.317	0.083	0.643$\ddagger$
	E	0.404	0.544†	0.366	0.408	0.349	0.367	0.406
Instron	σ_y	0.215	0.510†	0.351	0.543†	0.325	0.195	0.441†
	E	0.083	0.222	0.021	0.054	0.285	0.144	0.062

† and‡ mean significant and very significant, respectively.

References

1. NIH Consensus Development Panel on Osteoporosis Prevention, Diagnosis, and Therapy, *JAMA*. 185: 785-795 (2001).
2. T.M. Keaveny, T.P. Pinilla, R.P. Crawford, D.L. Kopperdahl, and A. Lou: *J Orthop Res*. 15: 101-110 (1997).
3. A. Odgaard and F. Linde: *J Biomech*. 24: 691-698 (1991).
4. D. Ulrich, B.V. Rietvergen, A. Laib and P. Ruegsegger. *Bone*. 25: 55-60 (1999).
5. H.H. Bayraktar and T.M. Keaveny, *J Biomech*. 37: 1671-1678 (2004).
6. J. Homminga, B.R. Mccreadie, H Weinans and R. Huikes, *J Biomech*. 36: 1461-1467 (2003).
7. T. Hildebrand, A. Laib, T. Muller, J. Dequeker and P. Ruegsegger, *J Bone Miner Res*, 14: 1167-1174 (1999).
8. B. van Rietbergen, H. Weinans, R. Huiskes and A. Odgaard, *J. Biomech*, 28: 69-81 (1995).
9. A. Parfitt, M. Drezner, F. Glorieux, J. Kanis J Malluche, P. Meunier, S Ott and R. Recker, *J Bone and Miner Res*, 2: 595-608 (1987).

EVALUATION ALGORITHM BASED ON AUTOMATIC IMAGE ANALYSIS FOR MALARIAL BLOOD CELL IMAGES[*]

CHANG-HYUN KIM[†]

School of Electronics, & Computer Engineering, Chonnam University,
300 Yongbong-dong, Buk-gu, Gwang-ju, 500-757, South Korea

JAE-YEOL KIM

Department of Mechatronics Engineering, Chosun University
375 Seosuk-dong, Dong-gu, Gwang-ju, 501-759, South Korea

SUNG-HOON HONG

School of Electronic, & Computer Engineering, Chonnam University
300 Yongbong-dong, Buk-gu, Gwang-ju, 500-757, South Korea

Malaria is most serious and widespread parasitic dieses of humans. Therefore, rapid and precise evaluation of parasitemia is necessary for malaria research. Manual test is the most widely used method for parasitemia evaluation but it is a time-consuming process and relies on the expertise of the techinician. This paper describes a algorithm for detecting and classifying malaria parasites in images Giemsa stained blood slides in order to evaluate the parasitemia of blood. A major point of this algorithm is an efficient method to segment cell images. So we introduce morphological and clamp splitting methods to cell images segmentation, that is, more accurate than classical segmentation algorithms.

1. Introduction

Malaria is the most serious and widespread parasitic disease of humans. Therefore, rapid and precise evaluation of parasitemia is necessary for malaria research. Manual test is the most widely used method for parasitemia evaluation but it is a time-consuming process and relies on the expertise of the technician. Now, light microscopy is the most used art for parasitemia evaluation. However, microscopy is a time-consuming process and relies on the expertise of the techinician. A standardized automated image analysis algorithm would envir-onment these limitations associated with manual parasitemia determinations.

This paper describes a algorithm for detecting and classifying malaria parasites in images Giemsa stained blood slides in order to evaluate the parasitemia of blood. A major point of this algorithm is an efficient method to segment cell images. So we introduce morphological and clamp splitting methods to cell images segmentation, that is, more accurate than classical segmentation algorithms

2. Processing methods

Automatic image analysis tool, evaluation algorithm, using MATLAB, was designed. Its algorithm can be divided into following 6 sequential steps : (1) preprocessing, (2) edge detection, (3) edge link, (4) morphological operation, (5) clump split, (6) parasite detection

2.1. *Edge detection*

The images are first subjected to a preprocessing step which involves the enhancement of the image contrast via adaptive histogram equalization. And then we used Canny edge detector for edge detection process.

2.2. *Edge link*

The resultant edge contours need to be linked together at their terminal points to form closed boundaries around the RBCs. The terminal points are form closed boundaries using 20 different 3×3 masks shown in Figure 1.
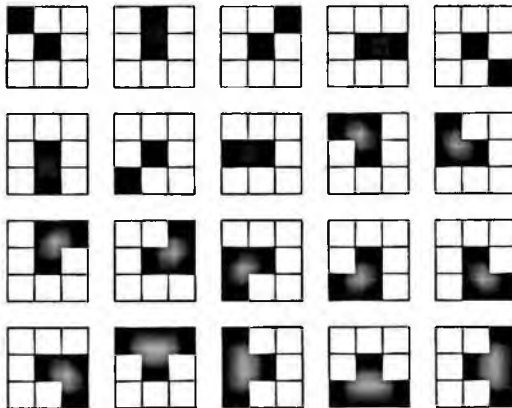
Figure 1. The mask of edge linking

2.3. *Clump split*

The clumping together of RBCs adversely affects the accuracy of the parasitemia. First, the deepest boundary pixels, i.e., the concavity pixels in a clump, are detected using a fast and accurate scheme. Next, concavity based rules are applied to generate the candidate split lines that join pairs of concavity pixels.

2.4. *Parasites detection*

First, a binary filling operation is performed on the closed contour of the RBCs to yield results. Next, the filled regions are eroded by applying a disk-shaped structural element of radius two, in order to obtain the inner regions of RBCs where the parasites are located.

3. Experimental results

Automatic image analysis tool, evaluation algorithm, was designed using MAT-LAB platform with the main steps outlined in Figure 2. Briefly, this involved the detection of RBCs using edge detection, binary morphology and clump splitting routines. Subsequently, parasite infection within each RBCs is identified based on the characteristic edge properties of the parasites. The graphical and textual results are shown in Figure 3.
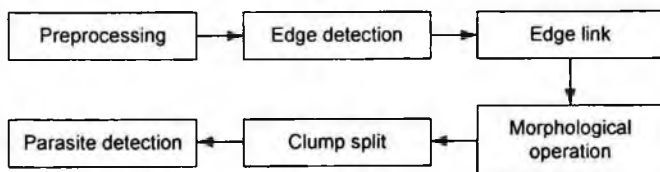
Figure 2. Block diagram of main process
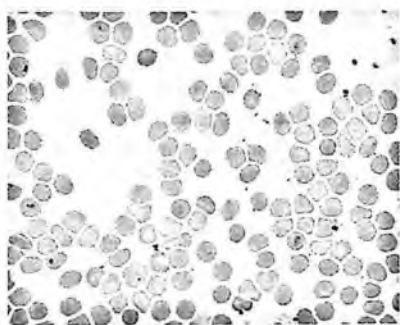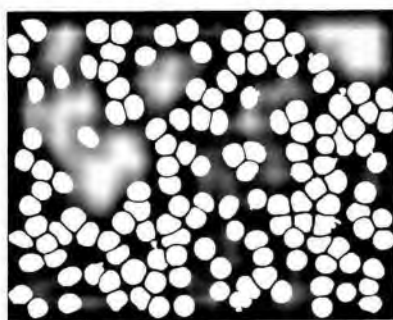
(a) Origin image   (b) Filling Image

Figure 3. Graphical and textual results
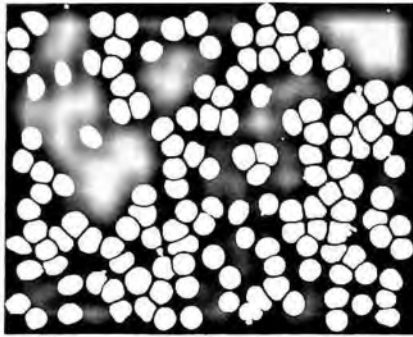
(c) Clump split image

(d) Parasite detect image
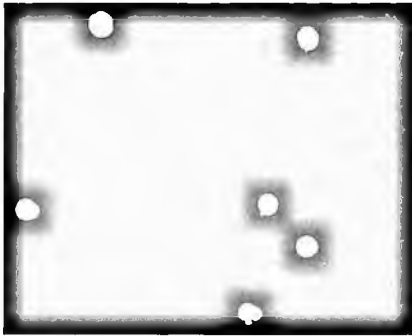
(e) Infected RBCs

(f) Detail image of clump split

Figure 3. *Continued*

4. Discussion

The preprocessing steps involve the enhancement of the image contrast via adaptive histogram equalization. The next process, edge detection, serves to obtain the boundaries (or contours) of all RBC objects in each image (field). The resultant contours may be broken, and therefore, an edge-linking process is applied in order to form a set of closed cell contours. Subsequently, binary Morphological techniques are used to ensure that enclosed regions with distinctly different sizes and shapes from those of RBC are removed. Irregularities due to image artifacts along the contours of RBC regions are also smoothened. The regions enclosed by these contours may comprise clumps of overlapping RBC. Hence, this tool has a clump splitting routine that separates these regions into their constituent objects. Finally, the edge function and binary morphology serve to differentiate infected from uninfected RBCs.

This tool could be run from MATLAB. With the current setup, and depending on the complexity of the image, it takes approximately 200 s to process a single image. While this paper was being reviewed, a report describing an automated image processing method for the speciation of malaria on thin smears was published. We have developed an image based tool that characterizes malaria-infected RBC via edge based parameters.

References

1. S. Kumar, S.H. Ong, S. Ranganath, T.C. Ong, F.T. Chew, *Pattern Recogn.* 39, 1088-1098 (2005)
2. J.C. Olivo-Martin, *Pattern Recogn.* 35, 1989-1996 (2002)
3. N. Tasumi, R.V. Pierre, *Clin. Lab. Med.* 22, 299-315 (2002)
4   F. Murtagh, J.L. Stack, *Stat. Comput.* 10, 95-103 (2000)
5   T. Hanscheid, *Clin. Lab. Haematol* 21, 235-245 (1999)
6. Z. Karel, *Graphics Gems IV* 474-485 (1994)

A STUDY ON THE PERFORMANCE OF 3D ACOUSTIC FIELD ANALYSIS METHOD FOR THE EVALUATION OF MEDICAL ULTRASONIC PROBE[*]

W.J. YU, S.C. NOH, H.G. MIN. M. K.PARK, H.H.CHOI

Dept. of Biomedical Engineering, College of Bioscience Engineering, Inje University, Obang-dong, Gimhae-si, Gyeongsangnam-do,621-749, Korea

The quality of ultrasonic images is crucially affected by the applied ultrasonic probe, thus it is necessary to evaluate the ultrasonic probe to achieve optimal performance. Currently the evaluation methods of the probe are insufficient to evaluate ultrasonic probe for it has the spatial beam pattern and the nonlinear characteristics. In this paper, the 3D acoustic field analysis method, one of the probe evaluation methods, is suggested. The 3D acoustic analysis using a hydrophone is performed and the usage about this evaluation method is estimated. According to the result of impulse response, the signal of each channel of normal parts and abnormal parts was acquired and analyzed with MATLAB R2006a. The acoustic field distribution of each signal of channels was displayed and some parameters were calculated. By comparing each acoustic field characteristics of each channel, it was confirmed that the 3D acoustic field analysis method proposed in this paper was useful to evaluate the performance of ultrasonic probe.

1. Introduction

In the diagnostic sonography, the ultrasonic probe is a critical factor in quality of diagnostic images. The performance of Ultrasonic probe has been improved constantly with growing the technique of materials, fabrication, signal processing etc. However, mechanical vibration lead to probe's poor or dead. Another factor is dead element, cable down, alignment error, pitch error. This facts need to regular estimation of performance. It is a decisive factor that falling-off in image quality and disturbs efficient diagnosis. Therefore, a performance by the ultrasonic probe should be evaluated in a process of manufacture even after when applied to diagnosis instruments.

Nowadays, evaluating method for performance of probe in clinical use is; detecting the radiation force from target for measurement and analysis of received acoustic pulse wave from hydrophone and live image test after applied to clinical using. Especially, evaluation method in progress of fabrication and

application is analysis of impulse response characteristics for each elements and test with phantom image and live image test etc. But, because array probe has the characteristic of spatial transmit pattern, the established evaluating method can't express definitely. In addition, the distortion of diagnostic image by alignment error, unbalance of pitch dose not reveals with test of impulse response characteristics. On the other hand, the acoustic field evaluating method for sensitivity calibration of ultrasonic transducer can describe the distribution of spatial acoustic pressure. This benefit said that detecting the defeats of elements is possible to predict by checking the distortion of acoustic field.

Consequently, to evaluate the overall transmit characteristics, measurement method of acoustic field is needed. In this study, we performed acoustic field analysis measurement experiment for quantitative evaluation of ultrasonic probe, displayed acoustic field in 3-dimension, calculated some parameters such as the volume of above -3dB, symmestry and the maximum pressure and confirmed usefulness of those parameters.
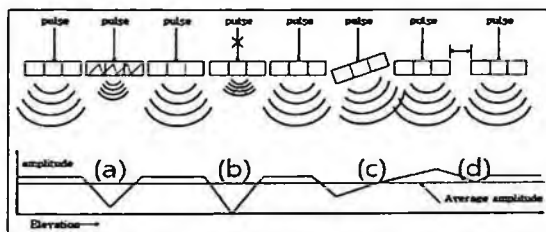
Figure 1. Typical defects of elements affecting the probe performance

2. Materials and Method

2.1. *Setup and Experiments*

The Figure 2 shows experimental setup using in this study. After arranging the hydrophone with sample probe, impulse response data are acquired. According to the result of impulse response, the acoustic field's data of normal and abnormal is measured by channel division. The distance between hydrophone and sample probe is 3mm. The data is acquired at intervals of 0.13mm for elevation axis, 1mm for azimuth axis and 2.5mm for axial axis. The axial axis is set limit to 60mm. Hence the number of data is 3,125(5*25*25). One channel consists of 8 elements. The peak-to-peak value of acquired data are stored and

transferred automatically from digital oscilloscope to computer through GPIB communication. The specification of experimental setup is stated in table 1.

Table 1. The specification of experimental setup

Experimental	Specification
Probe	CF=7.5MHz, 128 elements, linear probe
Hydrophone	PVDF(Generex Inc.), dia = 1 mm
Control Board	DAQ6016 Pad, NI Inc.
Pulse Board	Vpp = -150V, PD=1us
Oscilloscope	Wave runner 6100(Lecroy Inc.)
Stepping Motor	Type 103-781-0814, Sanyo Denki Inc.
Motor Driver	2D24M, Prime Driver Inc.
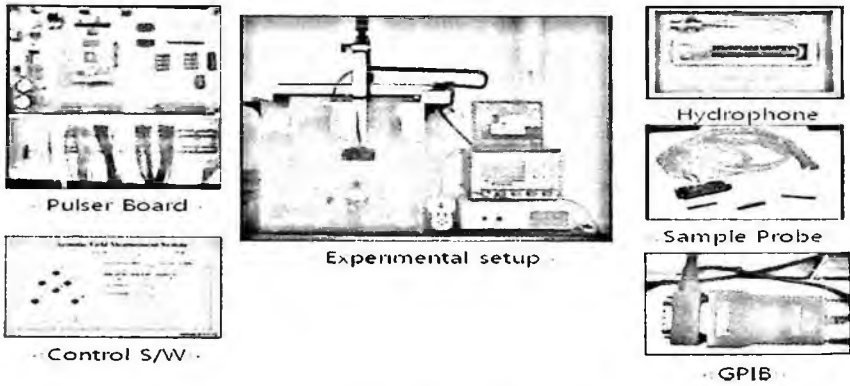
Figure 2. Experimental Setup

2.2. Data Analysis

After the acoustic field distribution data of probe which were acquired in experiment had had the procedures of normalizing and interpolation, the highest acoustic pressure point was extracted and cross section, longitudinal section, frontal section and 3-dimension image were displayed with the highest acoustic pressure point as standard. 3-dimension display is consist of 'Normal mode' and '-3B mode' by using MATLAB R2006a. The volume of field more than -3dB of the highest value ,the volume symmetry in aximuth and elevation axis, the maximum pressure, distance symmetry of each axis, angle and beam width were calculated.

3. Result

3.1. *Impulse Response*

Figure 3. shows the result of impulse response of each elements. There is one defect element in this probe. According to the result of impulse response, we performed 2 abnormal channels including number 67 element(65-72) and 2 normal channels(91-98).
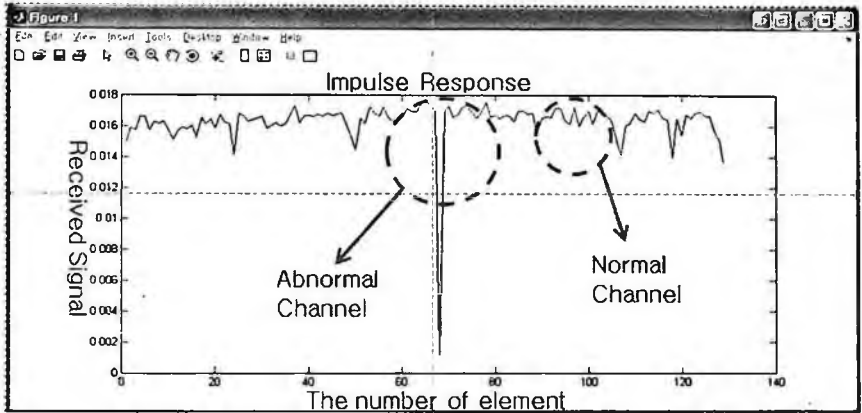
Figure 3. The result of impulse response

3.2. *Acoustic field of channels*

Figure 4. shows acoustic field of normal channels, whereas figure 5. denotes that of abnormal channels. Each results have cross section, longitudinal section, front section and 3-dimension images in each modes, named 'Normal mode' and '-3dB mode'. 'Normal mode' shows whole acoustic field, but '-3dB mode' shows only the part of more than 0.707. Cross section, longitudinal section and frontal section is based on the highest acoustic pressure point. And 3-dimension display is consist of a lot of slices of 2-dimension image. As all images can be rotated by using mouse, each part of acoustic field can be evaluated with every direction by observer.

In acoustic field data, the volume of above -3dB, beam width, angle(directivity), distance symmetry, volume symmetry and maximum pressure were calculated and displayed. Table 2. shows the value of each parameters in both normal channel and abnormal channel and reference value to compare with. Reference value means the ideal value for ideal normal ultrasonic probe.
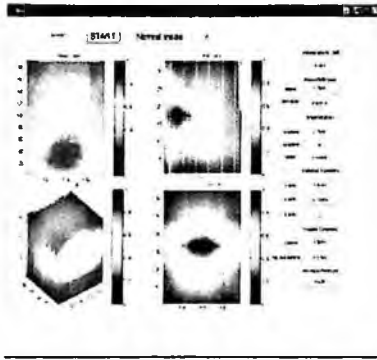
Figure 4. Acoustic Field of Normal Channel   Figure 5. Acoustic Field of Abnormal Channel
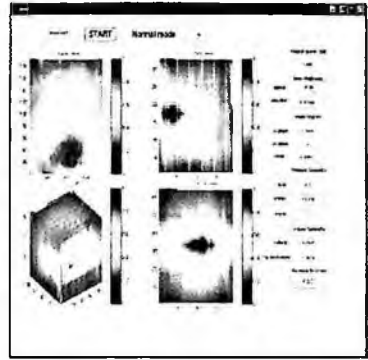
Table 2. Calculate parameters to evaluate ultrasonic probe in this study

Parameters	Normal Channel	Abnormal Channel	Reference
Volume of above -3dB(%)	3.424	3.456	-
Lateral Beam Width(mm)	1.7691	1.4796	0.077
Elevation Beam Width(mm)	0.94118	0.70588	0.077
Angle(xy-plane) (degree)	0.7448	1.1916	0
Angle(yz-plane) (degree)	0	0	0
Angle(rotate) (degree)	0.64469	0.59957	0
Distance Symmetry(x)	1.4545	1.5	1
Distance Symmetry(y)	0.73684	1.1333	1
Distance Symmetry(z)	2	1	1
Volume Symmetry(Lateral)	1.8091	2.2322	1
Volume Symmetry(Top and Bottom)	1.1745	1.3054	1
Maximum Pressure (mV)	0.028	0.023	-

4. Discussion and Conclusion

By comparing normal channels and abnormal channels, the volume of -3dB is higher in abnormal channels. It seems because the maximum pressure is lower as acoustic field cannot be focused but dispersed widely. For dispersed ultrasonic beam results in the decrease of resolution, it will affect to the image quality of ultrasonic equipment. As angle means the directivity of beam, near '0' is good. Distance symmetry is calculated the ratio of both side of each axis based on the maximum pressure point. Volume symmetry shows the ratio of both side separated by the slice which includes the maximum pressure. As acoustic field is focused, normal channel has higher maximum pressure.

In this study, we performed acoustic field analysis to evaluate the performance of ultrasonic probe and suggested some parameters. From those parameters, the possibility of quantitative evaluation for ultrasonic probe using acoustic field analysis is shown. As difference in those parameters between normal and abnormal channels is confirmed, we will perform study for quantitative evaluation in the future.

Acknowledgments

References

1. R. Krimholtz, J.D. Fraser and G.S. Kino (1970): 'New Equivalent Circuits for Elementary Piezoelectric Transducer', *Electronics Letters* 6, pp. 398-399
2. G. R. Harris (1988): Hydrophone measurement in diagnostic ultrasonic fields', *IEEE trans. Ultrason. , Ferroelec. , Freq. Contr.* , UFFC-35, pp. 87
3. J. A. Jensen (1999): A new calculation procedure for spatial impulse responses in ultrasound'. In press, JASA
4. D. R. Bacon (1971): 'Ultrasonic Schlieren using a pulsed gaslaser', IEEE trans. Sonics Ultrason. , 43, pp 282-285
5. Luis G. Ullate, Antonio Ramos, Jose Luis San Emeterio(1994), Analysis of the Ultrasonic Field Radiated by Time-Delay Cylindrically Focused Linear Arrays, IEEE TRANSACIIONS ON ULTRASONICS, FERROELECTRICS, AND FREQUENCY CONTROL, VOL. 41, NO. 5, 1994

MEASUREMENT OF SHAKING FOR THE SACRAL-REGION CIRCUMFERENCE SKIN UNDER STATE OF DECUBITUS

TETSUYA NEMOTO
YASUMI ITO, LEE CHEONGCHEON ZENZO ISOGAI
KAZUHARU KOIDE, NOBUO NODA, HIROYUKI MATSUURA
Dept. of Gerontechnology, National Institute for Longevity Sciences
36-3 Gengo, Morioka, Obu, 474-8522 Aichi, Japan

HISAE ISOE, HIROYASU YAMASHITA, HARUKI OKANO

Tokyo Measurement Laboratory Co., ltd.
6-8-2, MinamiO, Shinagawa, 140-8560 tokyo, Japan

FUMIO NOGATA

Dept. of Human & Information Systems, Gifu University
1-1 Yanagido Gifu, 501-1193, Japan.

The pressure sore is a trouble by the mechanical loading. As for this, the stress concentration occurs to the skin surface, next, sphacelation is meant by the skin. For example, the external stress which people receive is eased by the skin. That is, the viscoelasticity effect of skin structure is important. However, there is a case where the pressure sore is not improved even if the stress is removed. For this case, defective fixation of the skin is more remarkable than the general person. As a result, we proposed the model of the mechanism where the skin received the shear stress and the pressure sore was generated. To verify this model experimenting, it examined it in pathology. First of all, to measure the viscoelastic property of the skin with in vivo, the measuring instrument using the rheometer was developed. Next, it made comparative study with the state of pathology of the pressure sore with this measuring instrument. Moreover, the model (pocket) of people's bedsore was created. The newly created distortion gauge was attached to this model. From the result, it was distorted with the model and the validity of the gauge was examined. As a result, it was able to be suggested that defective fixation of the skin decide the form of the pressure sore. In addition, it has understood though the state of the therapeutic approach and the prognosis can be evaluated. It reports on these results in this paper.

1. Introduction

The engineering of human tissue represents a major technique in clinical medicine. Material evaluation of skin is important as preventive medicine. Decubitus originates in pressure and the rub. However, shearing in the skin has

exerted the influences on the sore pressures most. This paper examines one demand of crucial importance, namely the real time in vivo monitoring of the shearing characteristics skin tissue. Rheometer is a technology developed to measure viscoelasticity of solid and liquid. To measure viscoelasticity of the skin in the noninvasive with this device, we remodeled it. It is ideal for the continuous monitoring of tissues in vivo. Moreover, the model (pocket) of people's bedsore was created. The newly created distortion gauge was attached to this model. From the result, it was distorted with the model and the validity of the gauge was examined.

2. Experimental Device and Experimental Method

The rheometer used by this research. This measuring instrument machine is AR550 made by TA Instruments, and the angular velocity is 100rad/s, and the situs perversus resolution ability is 0.62 micro rad. As a result, stress distribution and frequency distribution can perform viscoelasticity measurement.

The photograph under measurement is shown in Fig.1. The photograph of Fig.1 is in the measurement status of the palmar upper part. It was performed as follows so that the disk of a probe and operation of the skin might be in agreement. A probe disk and the skin attached the fixed jig on the measurement stage so that it might become isofacies. In this research, it measured by the stress distribution and displacement distribution which agitation of the skin tends to measure. What must be careful of tends to receive the position of the bone part under the skin, and the influence of form in viscoelasticity measurement of the skin. In this experiment, there is distance from an outer cover to a bone part, and near the forearm part center where which indirect operation part cannot be found on the outskirts, and the stable agitation is obtained was made into the measurement part. An experimental condition is shown in Table 1.

Fig. 1. Photograph at viscoelasticity determination of forearm part

3. Results and discussion

3.1. *Relation between skin agitation and phase difference*

The viscoelasticity determination result of the forearm palmar part of 24 years old, 36 years old, and a 50 years old male is shown in Fig.2. M24-01 is 24 years old, M36-01 is 36 years old, and M50-03 is 50 years old. Moreover, all measurement persons are male. As for the phase angle delta, a big change was not seen although storage modulus G' and loss modulus G" changed with measurement conditions, such as a measured region and forcing power, a lot during measurement. Here, when its attention is paid to delta, in M50-03, it understands that agitation of the skin becomes large and it is impossible to follow to displacement near the amplitude stress 10KPa.

Table 1. Experimental method

Dispersion type	Dispersion	Forcing power	Frequency
Stress	0 to 40 KPa	3.0 N	10 Hz
Frequency	$10^{-3 \text{ to } 0}$ rad		
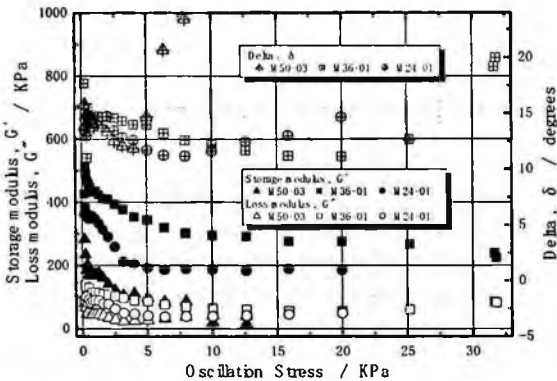
M50-03 is 50 years old, male, M36-01 is 36 years old, male and M24-01 is 24years old, male. Blacklacquered symbol are strage modulus G'. White symbol are loss modulus G". Cross overlapped symbol are phase difference (Delta).

Fig. 2. Viscoelasticity determination result of male forearm part

However, in M36-01 and M24-01, most agitation was not seen (20KPa or more), but was understood that displacement of a probe and the skin is almost the same. Moreover, change was not accepted in the range until a phase progresses with the increase in stress in all the measurement results of whose were about 13 degrees in 5KPa or less, however M50-03 and a phase angle results in 20KPa in M36-01 and M24-01.

3.2. *Part characteristic of a skin viscoelasticity characteristic value*

The viscoelasticity measurement result of a 34 yearsold male's forearm back side part is shown in Fig.3. M34-P01 to P03 expresses the measured segment. The wrist side is P01, the elbow side is P03, and these middle is set to P02. The position of the measurement segment of P01 to P03 is shown in Fig.4. In the case of measurement of P01. Measured value is not stabilized near a joint part. Therefore, in P01, near the central part in which measured value is stabilized was measured, and in P03 which is a joint part like P01, it was the measured value stabilized on the whole elbow.

If Tan (δ) of Fig.3 is observed, Tan (δ) will increase most to the increase in displacement of the wrist side. Next, the elbow part was large and the intermediate part was the lowest value. G' and the difference over displacement of G" did not almost have the elastic modulus of an intermediate part, and they were about 100 KPa(s) (G') and 250KPa (G"). However, the elbow part had the large agitation to displacement, and G' decreased rapidly with the increase in displacement. It seems that this is because flexibility changes a lot with the distance from the bone part used as the base of the skin, or composition.

3.3. *Influence that muscular turgescence exerts on viscoelasticity value*

To examine the influence of the muscular tension, viscoelasticity of the core of the arm (P2 part) was measured. Fig.4 shows the result. When Fig.4 was seen, both of G'G' were almost the same tendencies. The steady price did not obtain δ when slackening. This is bad the adhesion of probe and the skin, and seems no influence by the gap. It has been understood that a muscular state is not related from these in the shake of the skin. In a word, viscoelasticity of the skin seems movement of the surface side from the fascia.

3.4. *Relation between a viscoelasticity observed value and the skin*

From the above result, it seems by measurement by stress distribution that the phase difference delta is what can show the correspondence to the external force

of the skin, i.e., the degree of agitation of skin structure. This understands that the result of M50-03 is going up rapidly from about 5 KPa, and the viscous clause is dominant so that clearly from Fig.2. On the other hand, it is possible that M36-01 and M24-01 are understood that an elastic clause is dominant, and express the relation of agitation between external force and the skin clearly since change is not seen to 20KPa. Next, in measurement by displacement distribution, it seems that it is what can see a move of the whole skin structure from a bone part to the skin. This is considered to express the degree of movement of the whole organization so that viscoelasticity measurement of a polymer material etc. may also be the same. These results have suggested the possibility of the soundness evaluation of the skin considered to become a cause of generating of the bedsore by viscoelasticity measurement of the skin.
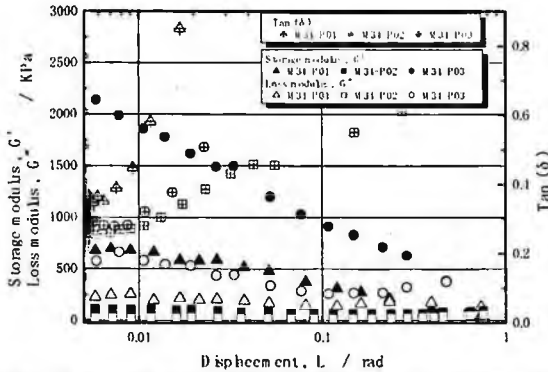
M50-03 is 50 years old, male, M36-01 is 36 years old, male and M24-01 is 24years old, male. Blacklacquered symbol are strage modulus G'. White symbol are loss modulus G". Cross overlapped symbol are phase difference (Delta) .

Fig. 3. Viscoelasticity determination result of part dependability
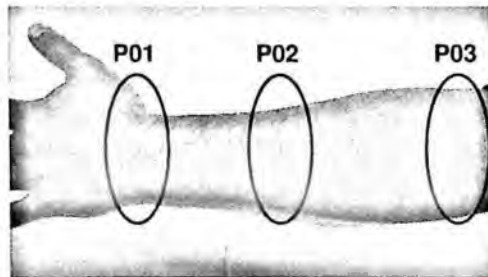
P01 is wrist part. A measurement part is the central part without a joint.
P02 is upper arm part, It does not have the influence by a measurement part.
P03 is elbow part, It does not have the influence by a measurement part.

Fig. 4. Position of the measurement segment of P01 to P03

4. Conclusion

The following things became clear as a result of doing research by viscoelasticity measurement of the skin.

1. Stress distribution measurement showed that agitation of skin structure could be evaluated.

2. Displacement distribution measurement showed that the movement state of the whole skin structure could be evaluated.

3. Viscoelasticity measurement of the skin, it has suggested that soundness evaluation could be performed.

4. Viscoelasticity of the skin seems movement of the surface side from the fascia.

5. Bedsore model was able to be created and the distortion state of the pocket was able to be reproduced.

6. Distortion gauge for the skins was able to be created and it was able to respond to the form very much.

References

1. Tetsuya Nemoto, Zenzo Isogai, Kazuharu Koide, Fumio Nogata, Akira Shimamoto and Hiroyuki Matsuura, *J. Achivements materials and manufacturing engineering*, 21(2), 33-36 (2006).
2. Ghosh Peter and Guidolin Diego, *Semin Arthritis Rheum*, 32(1), 10-37 (2002).
3. Powell, Courtney A; Smiley, Beth L; Mills, John; *Am J Physiol Cell Physiol*, 283(5), 1557-1565 (2002).
4. Xisto Debora G, Farias Luciana L, Ferreira Halina C, Picanco Miguel R, Amitrano Daniel, Lapa E Silva Jose R, Negri Elnara M, Mauad Thais, Carnielli Denise, Silva Luiz Fernando F, Capelozzi Vera L, Faffe Debora S, Zin Walter A and Rocco Patricia R M, *Am J Respir Crit Care Med*, 171(8), 829-837 (2005).
5. Linder Ganz E., Gefen A., *Proc. Annu. Int. Conf. IEEE Eng. Med. Biol. Soc.*, 25(2),1839-1842 (2003).
6. Stefaniak, Aleksandr B; Harvey, Christopher J, *Toxicol In Vitro*, 20(8), 1265-1283 (2006).
7. Chen, Qin Sheng; Russell, John L Jr; Macklis, Roger R; Weinhous, Martin S; Blair, Henry F, *Med Phys*, 33(7), 2384-2390 (2006).
8. Bosboom E M H, Oomens C W J, Bouten C V C, Janssen J D, *ASME BED (Am Soc Mech Eng Bioeng Div.)*, 42, 299-300 (1999).

MECHANICAL PROPERTIES OF THE HUMAN CAROTID ARTERY USING ULTRASONOGRAPHY AND PRESUMPTION OF ARTERIOSCLEROSIS*

TETSUYA NEMOTO

Dept. of Gerontechnology, National Institute for Longevity Sciences
36-3 Gengo, Morioka, Obu, 474-8522 Aichi, Japan

YASUMI ITO, HIROYUKI MATSUURA

Dept. of Gerontechnology, National Institute for Longevity Sciences
36-3 Gengo, Morioka, Obu, 474-8522 Aichi, Japan

YASUNARI YOKOTA, YOKO KAWAMURA MARIKO MARUYAMA
FUMIO NOGATA

Dept. of Human & Information Systems, Gifu University
1-1 Yanagido Gifu, 501-1193, Japan

Every year, a quite large number of people die from cardiac and cerebrovascular diseases that are related to arteriosclerosis. Arteriosclerosis shows symptoms only in the advance stage, and hence it is vital to diagnosis it at an early stage to prevent diseases like cerebral infraction, myocardial infraction, etc. In this study, a new technique has been proposed for measuring the in vivo elastic modulus of human common carotid artery using ultrasound. This method is based on the in vivo elastic modulus calculated from the dynamic changes in the diameter of the common carotid artery and the systolic and diastolic blood pressures. It is found that the in vivo elastic modulus of common carotid artery is a useful marker of the development of the arteriosclerosis.

1. Introduction

Hypertension, hypercholesterolemia, smoking, etc. cause several changes of arterial wall, both morphologically and mechanically. Mechanical changes include thickening of arterial wall, alteration of arterial elasticity, contraction of smooth muscle, increase in sensitivity to pharmacological stimulation and increase in arterial viscoelasticity, i.e., arteriosclerosis (Matsumoto and Hayashi, 1996). A recent report of Japan Ministry of Health, Labor and Welfare indicates that cardiac and cerebrovascular diseases are the main cause of one-third death

---

in Japan in 2002 (Japan Ministry of Health, Labor and Welfare, 2003). Cardiac disease like myocardial infraction, and cerebrovascular disease are directly related to the arteriosclerosis (Hayashi, 2000). Arteriosclerosis is a disease of the arterial wall of which the particularity is to give clinical symptoms only when advanced. Therefore it is indispensably required to discover arteriosclerosis by an early diagnosis method to prevent such a disease beforehand. In this study, in vivo elastic modulus of common carotid artery is considered as a useful marker of the development of the carotid arteriosclerosis, and a new technique for measuring it by using ultrasound has been proposed. Ultrasound is a relatively inexpensive and safe diagnosis method that can non invasively visualize the lumen and walls of selected arteries. The proposed technique is based on the in vivo elastic modulus that is calculated from the dynamic changes in the diameter of the common carotid artery and the systolic and diastolic blood pressures. The diameter changes of the common carotid artery were measured using B-mode ultrasonic images. Besides, the systolic and diastolic blood pressures were obtained from a sphygmomanometer. The in vivo elastic modulus of the common carotid artery was then calculated using these data. The results indicate that the in vivo elastic modulus is a useful symptom index for carotid arteriosclerosis.

2. Experimental Methods

2.1. *Calculation of in vivo elastic modulus of human common carotid artery*

Due to the viscoelastic property of blood vessel, the elasticity of human artery shows a non-linear relation when subjects to a pressure. Figure 1 represents schematical stress-strain relationship of human artery. The curves for both younger and older adults exhibit non-linear relation as a whole. Besides, with the increase of age, the curve becomes steeper. For this nonlinear relationship, a generalized mathematical expression for calculating the in vivo elastic modulus of human artery is difficult to obtain. However, a linear stress-strain relationship within the physiological blood pressure range was considered in this study for facilitating the formulation process.

Several reports describing the mechanical property of in vivo artery have been published (Peterson and Jensen, 1960; Hudetz, 1979; Imura et al., 1986; Hansen et al., 1995). In this study, the mechanical property (i.e., in vivo elastic modulus) of human common carotid has been calculated utilizing the equation

for a hollow cylinder experiencing uniform internal pressure. The equation is given by

$$E_{\text{in vivo}} = 2\frac{R_o}{R_o^2 - R_i^2}\frac{\Delta P_i R_i^2}{\Delta R_o} \tag{1}$$

Here Ro and Ri are the outer and inner diameters of the carotid artery, ΔRo is the difference between maximum and minimum value of Ro, and ΔPi is the difference between systolic and diastolic blood pressures.

Next, as a preliminary experiment, the mechanical properties of the thoracic aorta of an ox (two and a half years old castrated ox) were examined with the help of inner pressure testing and tensile testing. The inner-pressure testing was conducted with a portion of thoracic having inner and outer diameters of 20.5 mm and 25.3 mm, respectively, while the tensile testing was conducted with a portion of thoracic having a size of 18.6 x 17.7 x 3.2 mm. In determining Ein vivo of the thoracic aorta of ox, the change in the specimen's diameter and length during conducting the inner-pressure testing and tensile testing were noted, and then Eq. (1) was utilized. Figure 2 represents the relationship between stress and strain of thoracic aorta of ox. It is observed that a linear stress-strain relationship takes place within the normal blood pressure range for the both inner-pressure testing and tensile testing, and Ein vivo of the thoracic aorta of ox within the normal blood pressure range was measured as 0.48 MPa. The same equation is considered to be applicable in calculating Ein vivo of human common carotid artery within the normal blood pressure range.
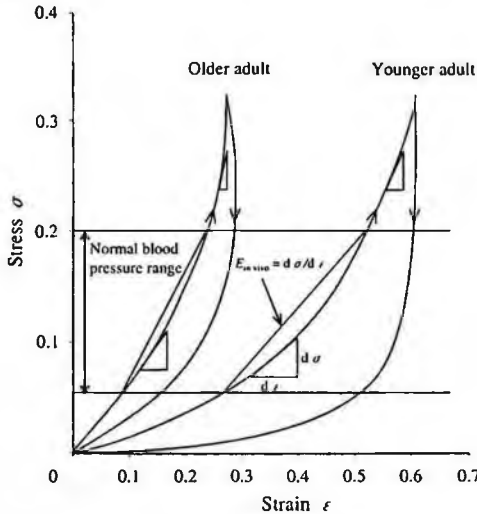
Fig. 1. Stress-strain relationship of human artery

2.2. List Measurement of elastic modulus of human right and left common carotid artery

Figure 3 represents the experimental layout of this study. Firstly, the subject to be examined, lay down on a bed in a relaxed mood keeping its chin slightly upward and turning 30o in a direction opposite to the side where carotid artery to be viewed. Then ultrasound gel was applied on the skin surface of the subject's neck and a linear-type ultrasound transducer (7.5 MHz) was placed. Subsequently, the B-mode image of the subject's common carotid artery appeared on the monitor of the ultrasound equipment. Real-time A-mode wave was also obtained from the screen of the oscilloscope attached to the ultrasound equipment. Besides, systolic and diastolic blood pressures of the subject were measured using a sphygmomanometer. Furthermore, to obtain the shape of the common carotid artery, the ultrasound transducer was displaced linearly with a regular interval of 5 mm with the help of a scale previously sticked to the neck of the subject. The same technique was applied during examining the common carotid artery on the opposite side of the subject's neck.
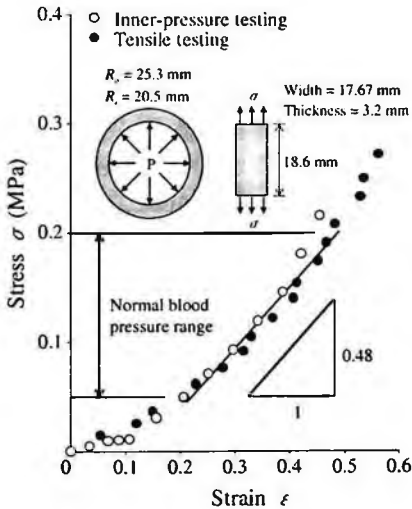
Fig. 2. Relationship between stress and strain of thoracic aorta of ox
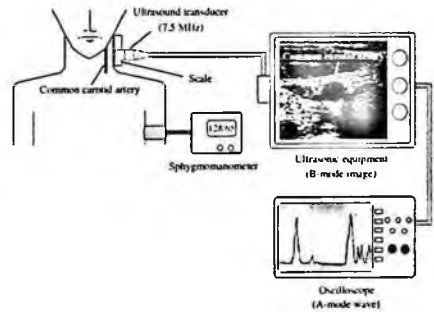
Fig. 3. Experimental layout

3. Results and discussion

3.1. *Variations in diameter of the human common carotid artery with time*

Figure 4 represents the comparison between variations in diameter of pulsating common carotid arteries with time of a 54-years old (an older adult) and a 21-years old (a younger adult) males. The ordinate of this figure is the normalized common carotid artery diameter ratio D/Dmin (Dmin for the older and younger adults are 6.88 mm and 7.46 mm, respectively), and the abscissa is the time in second.

3.2. *Difference in elastic modulus of the right and left common carotid arteries*

Figure 5 represents the dependency of E in vivo on the age of test subjects (10 male and 10 female) for right and left common carotid arteries. Besides, this figure represents the magnitudes of E in vivo at the 3rd section of the right common carotid artery of the 21-years old subject (Fig.4) and at the 2nd section of the right common carotid artery (not shown in this report) of the 54- years old subject. The differences in E in vivo for right and left common carotid arteries are visible for both younger adults and older adults, but the tendency is prominent for the later group. According to this figure, it can not be summarized that E in vivo for a particular side's (right or left) artery is always larger; it rather varies with person. Similarly, it is not always true that the difference in magnitudes of E in vivo for the right and left common carotid arteries is always larger for a particular sex (male or female) of same age, but the difference in magnitudes of E in vivo increases with age for both male and female. Thus, it is not appropriate to measure E in vivo for only right or left common carotid artery during diagnosis of arteriosclerosis.
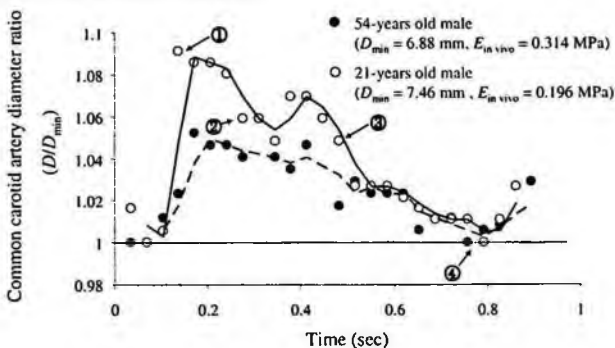
Fig. 4. Variations of diameter of pulsating common carotid arteries with time of two different aged subjects
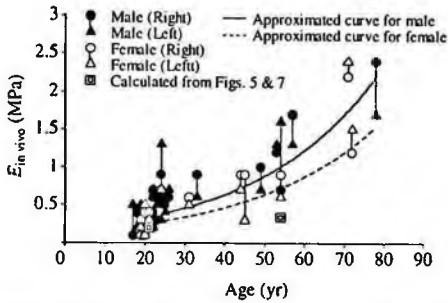
Fig. 5. Dependence of Ein vivo on age of test subjects for right and left common carotid arteries

4. Conclusion

(1) A new technique for investigating the risk of arteriosclerosis beforehand by measuring the in vivo elastic modulus of human common carotid artery has been proposed.

(2) Knowledge of E in vivo and the parameters required for its determination can provide important insight into structural differences occurring with age and sex, and possibly with the onset of very early arterial disease.

(3) The diameter of the pulsating common carotid artery varies with time. The difference between the maximum and minimum diameters decreases with the increase of age of the test subject.

(4) The structure, as well as the magnitudes of Ein vivo of the right and left common carotid arteries are different at different sections. The The differences in Ein vivo between the right and left common carotid arteries increases with the increase of age.

References

1. Matsumoto, T. and Hayashi, K., *Response of arterial wall to hypertension and residual stress, Biomechanics,* Springer, 93-119 (1996).
2. Annual report of Ministry of Health, Labor and Welfare, Japan (2003).
3. Hayashi, K., *Biomechanics,* Corona, 71-213, (2000).
4. Peterson, H.L. and Jensen, R.E., *Circulation Research,* 8, 622-639, (1960).
5. Hudetz, A.G., *J. Biomechanics,* 12, 651-655, (1979).
6. Imura, T., et al., *Cardiavascular Research,* 20, 208-214 (1986).
7. Hansen, F., et al., *Ultrasound in Med. & Bio.,* 21, 1-9, (1995).
8. Gamble, G., et al., *Atherosclerosis,* 102, 163-173, (1993).
9. Kudo, N., et al., *The Japan Society of Ultrasonics in Medicine,* 25, 3, 155-166, (1998).

CHARACTERIZATION OF STRUCTURAL PERFORMANCE IN CERAMIC MATRIX COMPOSITES

JEONGGUK KIM[†]

Railroad Safety Research and Testing Center, Korea Railroad Research Institute, 360-1 Uiwang, Kyunggi, 437-757, Korea

JOON-HYUN LEE

School of Mechanical Engineering, Pusan National University, Busan, Korea

Several nondestructive evaluation (NDE) techniques, such as ultrasonic testing (UT), acoustic emission (AE), and infrared (IR) thermography, were employed on ceramic matrix composites (CMCs) to illustrate defect information that might affect mechanical behavior and to analyze structural performance of CMCs. Before and after mechanical testing, UT was used to characterize the defect distribution of the CMC samples. During mechanical testing, AE sensors and an IR camera were used for in-situ monitoring of the damage evolution in terms of the AE intensity and/or energy and temperature changes, respectively. After tensile testing, microstructural characterization using scanning electron microscopy (SEM) was performed to investigate the fracture mechanisms and modes of CMC samples. This paper describes the employment of nondestructive evaluation (NDE) techniques to facilitate the understanding on structural performance of CMCs during tensile testing.

1. Introduction

Ceramic matrix composites (CMCs) have been identified as promising materials for high-temperature structural applications because of their high-temperature strength, light weight, and excellent corrosion and wear resistance [1]. Due to those advantages, CMCs have been widely used for high-temperature structural and aerospace applications, such as heat exchangers, gas turbines, and space shuttle engine components.

In order to encourage the expanded application of engineering ceramics, the use of appropriate nondestructive evaluation (NDE) approaches is critical to effective process control and the assurance of high-quality products and reliable performance in service [2-5]. NDE techniques, such as ultrasonic testing (UT), acoustic emission (AE), and infrared (IR) imaging, are powerful methods to investigate the fracture behavior and defect distribution in the composite [2-8].

[†] Corresponding Author: Jeongguk Kim, jkim@krri.re.kr

The objectives of the current research are to introduce and apply NDE techniques to assure the quality and structural integrity of CMCs, perform NDE using UT, AE, and IR thermography methods for the analyses of defect distributions that may affect mechanical properties, and investigate tension behavior of CMC samples with the aid of NDE methods.

2. Materials and Experimental Procedures

2.1. *Ceramic Matrix Composites (CMCs)*

In this investigation, several different types of continuous fiber reinforced ceramic matrix composites (CFCCs) were used for the understanding of structural performance during tensile testing with NDE signatures, i.e., continuous Nicalon (manufactured by Nippon Carbon Co. Ltd., Japan) fiber-reinforced silicon carbide (SiC) matrix composites designated as Nicalon/SiC, continuous Nicalon fiber-reinforced calcium aluminosilicate glass-ceramic matrix composites, designated as Nicalon/CAS, and continuous Nextel (manufactured by 3M) fiber-reinforced Blackglas matrix composites, designated as Nextel/Blackglas.

2.2. *Nondestructive Evaluation (NDE) Techniques for CMCs*

Several NDE techniques are available for assessing the integrity of composite materials [5-8]. In particular, the UT method is frequently used for such measurements. UT has been successfully applied to characterize composites based on variations in transmitted ultrasonic amplitudes [5-7]. The transmitted ultrasonic waves can be related to the presence of defects and anomalies in the composites.

AE can be a very powerful NDE technique for the in-situ monitoring of damage evolution during mechanical testing [8]. When a material is subjected to stress, it experiences plastic deformation, the formation of flaws, or fracture; these conditions produce small stresses or ultrasonic waves in the material and acoustic emissions are generated. For ceramics, an increase in acoustic emissions occurs before fracture, providing a potential means of either detecting crack initiation or predicting when failure is imminent.

The infrared (IR) thermography is another possible NDE method for characterizing of CMCs. This technique is based on the concept that after applying a uniform heat pulse to the sample surface, a localized disruption of the heat flow will occur when defects and/or flaws are present [6,7]. In this study,

the IR thermography was used to measure the temperature changes of CMC samples during mechanical tests.

3. Results and Discussion

3.1. *Structural Performance during Tensile Testing*

Monotonic tensile tests were conducted using a computer-controlled Material Test System (MTS) 810 servohydraulic frame equipped with hydraulic grips. The tensile tests were performed at room temperature under displacement control at a cross-head speed of 0.5 mm per minute. In this study, dog-bone type flat specimens were used to investigate the damage evolution during the tests.

Figure 1 shows the tensile behavior of different types of CMC samples. The ultimate tensile strength (UTS) values were determined about 290 MPa, 197 MPa, and 89 MPa for Nicalon/SiC, Nicalon/CAS, and Nextel/Blackglas, respectively, as shown in Fig. 1. The tensile stress-strain behavior for the composites exhibits very similar except showing different UTS values. After proportional limit, the stress-strain behavior of both Nicalon/CAS and Nicalon/SiC composites shows plastic deformation-like behavior due to the subsequent fiber breakage and fiber pullout, and presents enhanced fracture toughness as compared with monolithic ceramics, which show only linear elastic behavior followed by catastrophic failure.
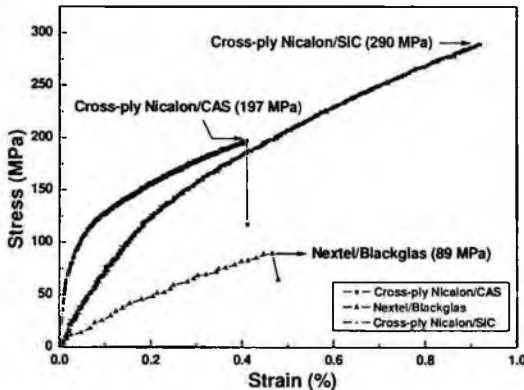
Figure 1. The stress-strain behavior of several CMC specimens with values of ultimate tensile strength.

3.2. *Ultrasonic Investigation*

Figure 2 shows UT C-scans results for a Nextel/Blackglas composite specimen

before and after mechanical testing. The range of the ultrasonic transmitted amplitude is Min (minimum) to Max (maximum). The dashed lines in Figure 2 indicate the final fracture positions, i.e., the final ruptures occurred along the dashed lines. The failures occurred at lower UT transmitted amplitude values. Note that the sample was not separated completely after tensile testing stopped. The 90° warp bundles still held the testing coupons without a separation into two pieces although the final rupture achieved.

The damage evolutions in terms of UT transmitted amplitude after tensile testing are shown in Figure 2(b). This means that the damage and/or crack propagation areas are showing much lower UT amplitude values than those before testing with light colors. This is mainly due to the presence of macro and micro-cracks, and fiber pullout around fracture surfaces.

(a) Before testing   (b) After testing
Min   Max

UT Transmitted Amplitude
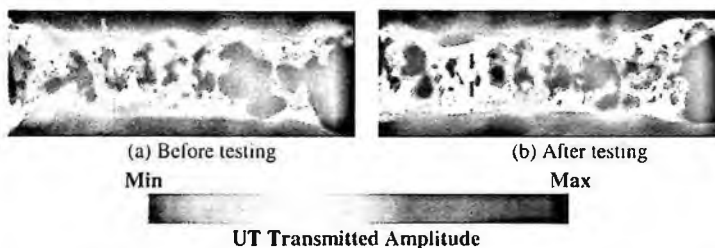
Figure 2. UT C-scans for (a) before tensile testing, and (b) after testing. Note that the lines indicate the locations of final failure.
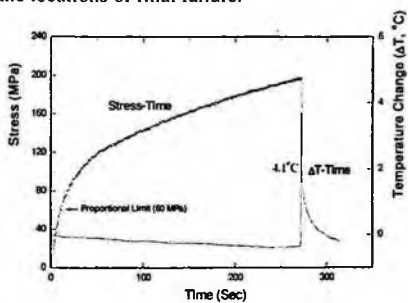
Figure 3. Stress vs. temperature evolution during tensile testing for a cross-ply Nicalon/CAS composite.
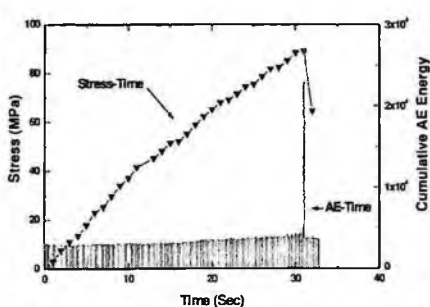
Figure 4. Stress responses vs. AE energy during tensile testing for a Nextel/Blackglas composite.

3.3. *IR Thermography during Tensile Testing*

Figure 3 shows a direct comparison between the stress-strain behavior and temperature evolution behavior during monotonic tensile testing. The speed of the IR camera was 7 Hz for both samples, and the individual data points in

Figure 3 indicate one frame of IR image, i.e., every frame was obtained every 1/7 second (about 0.143 sec). The number of frames at the time of failure shows more than 6 frames. This means that the failures of the Nicalon/CAS composites were achieved by more fiber pullout and breakage at the time of failure, which indicates the toughening mechanisms in the composites. The sample exhibits the temperature peaks, especially, at the time of failure. From these results, it is understandable that the main temperature changes for the composites during tensile testing seem to result from the final fiber pullout and breakage. The fiber pullout and breakage at the final moment of failure generate severe heating between the fiber and matrix, and the temperature increases seem to be developed from the final fractures of fibers.

3.4. *Acoustic Emission (AE) Investigation*

Figure 4 shows another evidence of failure mode in a Nextel/Blackglas composite using AE methods. Figure 4 presents the cumulative acoustic emission (AE) energy-time relationship during tensile testing, and also, stress-strain curves are juxtaposed with AE results. Only one significant peak has been found during the tensile testing, which indicates instant failure of the composite specimen. The main purpose of the use of AE method for this investigation is to detect and investigate damage initiation and the associated evolution process. The failure mode was instant brittle failure right after crack initiation in Nextel/Blackglas samples.

3.5. *SEM Characterization of Structural Performance in CMCs*

After mechanical testing, microstructural characterization was conducted to investigate fracture mechanisms in CMC samples using scanning electron microscopy (SEM). Figure 5(a) presents the entire cross-sectional view of failure area in a Nextel/Blackglas composite. The SEM micrograph shows that initial cracks/damages start at 0° fiber bundle and propagated with debonding at the interface between fiber and matrix. The 90° fiber bundle plays a role to retard the crack propagation, and the bundle provides a toughening mechanism of Nextel/Blackglas composites.

Figure 5(b) presents the summary of the failure mechanisms in Nextel/Blackglas composites showing the fracture surface. The initial cracks start from the intersection of 0° and 90° fiber bundles due to the stress concentration, and crack propagates along 0° fiber bundle and matrix region, and final rupture occurs at 90° fiber bundle with fiber/matrix debonding and fiber pullout. Figure 5(b) also shows limited fiber pullout.

<center>(a)   (b)</center>
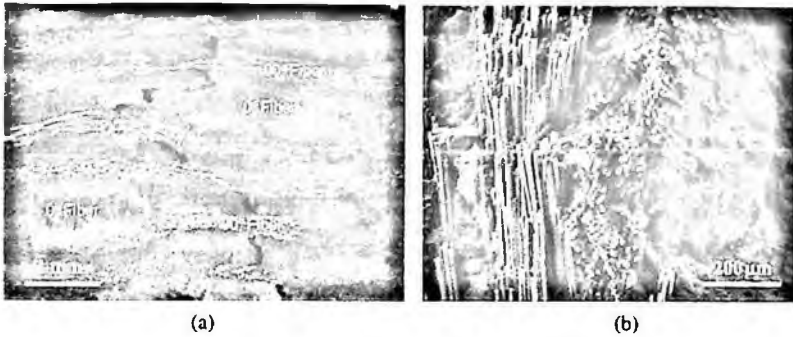
Figure 5. The micrographs showing (a) the cross-sectional view of fracture area, and (b) fracture surface of Nextel/Blackglas composite.

4. Conclusions

The tensile behavior of CMCs was investigated with the aid of several NDE techniques, such as ultrasonic testing, acoustic emission, and infrared thermography methods. Various types of NDE methods provided the possible ways to predict and interpret structural performances of CMCs. The combination of several NDE techniques could assure greater level of reliability for ceramic composites evaluation to investigate the fracture behavior of CMCs.

The failure mode (mechanism) of CMCs was provided through the microstructural characterizaion with SEM micrographs. The fractures of CMC samples were shown brittle failure manners for all testing samples. The strong interfaces between continuous fibers and ceramic matrices provides brittle fracture modes with extensive fiber pullout.

References

1. K. K. Chawla, Ceramic Matrix Composites, Chapman & Hall, London, 4 (1993).
2. ASM Handbook, vol. 17, ASM International, 284 (1992).
3. Nondestructive Testing Handbook, 2nd ed., vol. 10, Nondestructive Testing Overview, American Society for Nondestructive Testing, Inc., (1996).
4. P.K. Liaw, JOM, 38 (1995).
5. J. Kim and P.K. Liaw, JOM, 50, 11 (1998).
6. J. Kim and P.K. Liaw, Met Transactions A, 38A(13), 2203 (2007).
7. J. Kim and P.K. Liaw, MSE A, Vol. 409, 302 (2005).
8. J. Luo, S. Wooh, and I.M. Daniel, Journal of Composite Materials, 29(15), 1946 (1995).

A STUDY ON NATURAL FREQUENCY DETECTION OF VEHICLE COMPONENTS; SENSORS AND ACTUATORS

BEOM-SEOK KIM, KI-CHUL SHIN, JUN-SEOK YOON AND HYUN-JU PARK

Test Center Team, Engineering and Technology Institute, KEFICO Corporation,
410, Dangjeong-dong, Gunpo-si, Gyeonggi-do, 435-716, Korea

All kind of sensors and actuators used in real vehicle must pass vibration endurance test for mass production. Since there are lots of rotating and moving parts in vehicle, the components mounted on the vehicle also experiences complicated vibrations during whole life. If the frequency of vibration gets closer to the natural frequency of the components, they may suffer from malfunction or break down. That's why lots of engineers try to know the natural frequency of their products and the vibration environment surroundings of them in early stage of design phase. But it is a hard and difficult job to acquire natural frequencies of sensors and actuators on vehicle components because they are small sized, consisted of many parts, and lots of their parts and housing are made of polymer materials. In this paper, we want to share our trial, effort and results of topics related above.

1. Introduction

Since reliability of vehicle and its components are directly related to the human life, securing safety is the most important part in the automotive industry. In addition, lots of efforts are given to secure the safety in more active position and attitude. We can easily find evidence converging to support this fact in emerging industry field like IVSS(Intelligent Vehicle Safety Systems). In accordance with this mood, reliability test specifications and conditions in the automotive industry are getting more severe. Test time and duration has been extended, test level has become more severe and analysis of the test result has become more close and detail.

Vibration test of a vehicle component is one of important tests to secure reliability and safety of its life. Generally, vibration tests on shaker are adapted to reduce time and cost. The most biggest disadvantage of shaker test is that it is difficult to induce the same condition to the DUT(Device under test) as in or on the vehicle. The mounting condition of the DUT is different and incoming vibration characteristics are also different. That's why our test engineers have to give every effort to check if the tests are performed properly.

Before performing a vibration test, we must know the natural frequencies of components(i.e. shaker, jig and fixture) which can give effects to the DUT. That's because if we do not take those components' behavior into account, we cannot induce proper test profile to the DUT and it finally can lead to improper reliability test.

2. Specimens

A vehicle consists of over than 20,000 components. In this paper, we chose two types of components. One is a sensor, the other is an actuator. CMP(Camshaft Position sensor) is chosen for sensor, PCSV(Purge Control Solenoid Valve) is chosen for actuator[1].

(a) CMP sensor   (b) PCSV
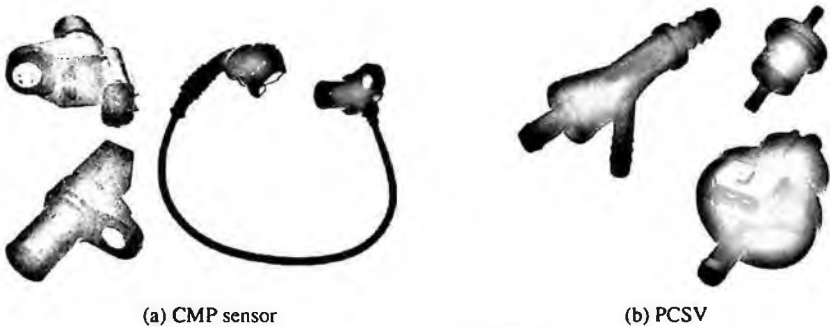
Figure 1. CMP and PCSV [2]

The CMP sensor can also be referred to as the CID(Cylinder Identification) sensor. As the engine rotates the sensor will signal to the ECU(Electronic Control Unit) that cylinder number one is approaching Top Dead Center(TDC) and the timing of the injection pulse can be determined. On an inductive sensor, a resistance value should be seen between its terminals with these terminating back at ECU. The output signal from these units can be in either analogue or digital format(sine wave or square wave) and will depend on the manufacturer concerned [3].

The PCSV, which also can be referred to as the canister purge valve, is in-line with the evaporative emissions canister and controls the flow of fuel vapors out of the evaporative emissions canister. The PCSV is normally closed. When the engine is shut OFF, vapors from the fuel tank flow into the evaporative emissions canister. After the engine is started, the evaporative emission canister purge valve is engaged and opens, purging the fuel vapors into the engine. With

the evaporative emission canister purge valve open, vapors from the fuel tank are routed directly into the engine [4].

3. Result of natural frequency investigation

3.1. *PCSV Jig and Fixture(Difference by measuring point)*

(a) Response point #1

Control   Response
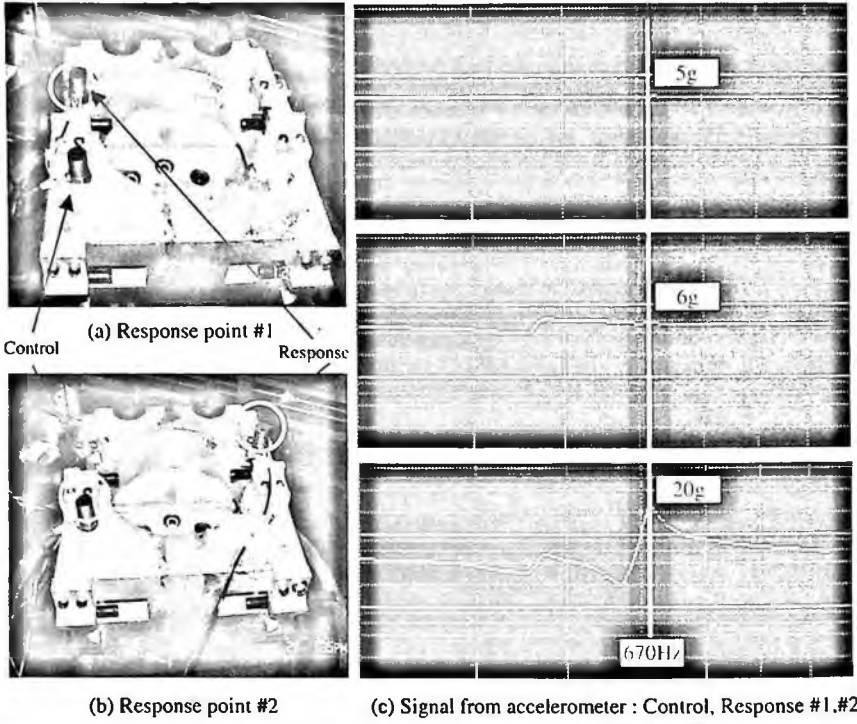
(b) Response point #2   (c) Signal from accelerometer : Control, Response #1,#2,
                          (respectively from top to bottom)
Figure 2. Test setup and FRF result of PCSV jig and fixture

As shown in Figure 2(c), we could find that the acceleration value and vibration profile is influenced by the location. Of course it is nothing special to vibration engineers but it was hard to guess that the magnitude can be more than 4 times bigger comparing with some other points of rigid fixture. This means all DUTs mounted on different location, although they are on the same jig and fixture, are exposed to very different vibration condition. And in natural way, we have to consider if the vibration reliability test can be performed in proper way.

3.2. *Natural Frequency of CMP, Jig and Fixture*

(a) Test setup   (b) FRF of jig and fixture
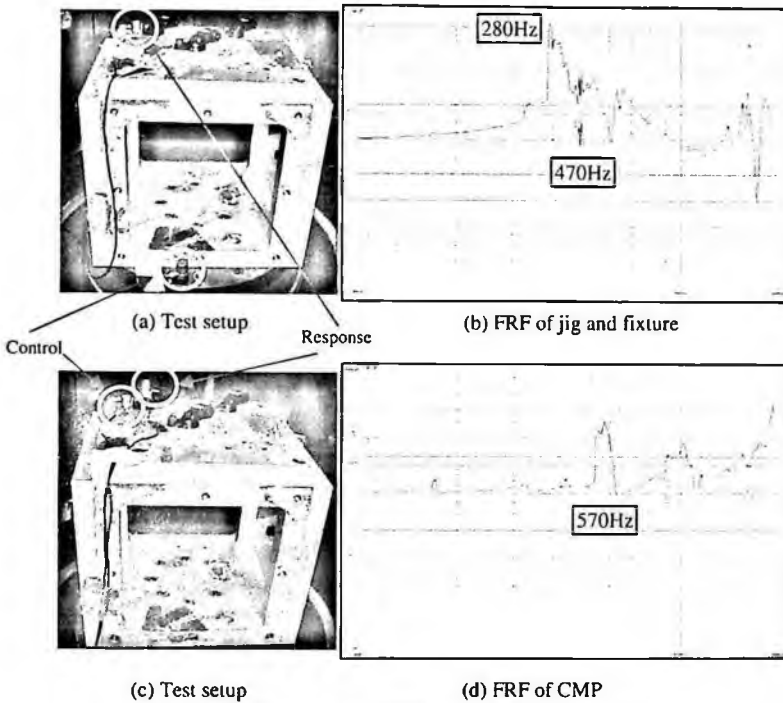
(c) Test setup   (d) FRF of CMP
Figure 3. Test setup and FRF result of CMP, jig and fixture

As shown in Figure 2(b), we could find the natural frequency of jig and fixture for CMP. The green line shows signal from the control accelerometer and the magenta line shows signal from the response accelerometer. The first two natural frequencies lay about 280Hz and 470Hz. It is not a surprise that control accelerometer shows noisy signal at about those frequencies because the shaker also can be affected by resonance of heavy jig and fixture. Comparing Figure 2(b) with Figure 2(d), we could find the natural frequency of CMP at about 570Hz.

4. Conclusion

As shown in Figure 2, we experienced that every point on the jig and fixture are exposed to different acceleration and vibration profile. This is a big drawback of shaker test. The basic aiming of shaker test is to ensure that the DUT is robust enough to survive through its target life time. If the vibration profile is much

different from the real condition, nobody can ensure if the DUT can survive or not. That's why we must try to find out the optimal control point of the test.

As shown in Figure 3, we found the natural frequency of CMP sensor, jig and fixture. We must try to avoid testing in the resonance area of jig and fixture (e.g. setting the control point to optimal location, stiffening the jig and fixture, putting additional mass on it).

Acknowledgments

References

1. KETI/ KEFICO Corporation, *Automotive electronic control.* 90 (2001).
2. *http://www.innerauto.com/.*
3. *http://www.auto-solve.com/cid.htm.*
4. *http://autorepair.about.com/library/a/1c/bl646c.htm.*

A STUDY ON THE FIRE RESISTANCE CAPACITY OF ASYMMETRIC SLIMFLOR BEAM MEMBERS

SANG-HOON HAN[†]

Korea Institute of Construction Technology, Fire & Engineering Services Research Center, 451-1 Baekgok-ri, Mado-Myeon Hwaseong-Si, Gyeonggi-Do 455-861, Korea

SENGKWAN CHOI

Korea Institute of Construction Technology, Fire & Engineering Services Research Center, 451-1 Baekgok-ri, Mado-Myeon Hwaseong-Si, Gyeonggi-Do 455-861, Korea

This paper is a pilot study regarding an experimental and parametric study to investigate the structural behavior of slimfloor beam in fire. The objective of this research is to obtain the rational fire resistance design method through understanding the moment capacity and structural behavior of composite members, especially using asymmetric H beam (ASB), in fire. The flexural capacity of slimfloor section under various thermal conditions is examined on a basis of the strength retention of the materials at elevated temperatures and full bonding assumption. The moment capacity is calculated with heat transfer analysis and material's properties under standard fire conditions. The effect of web thickness and ASB depth is also examined.

1. Introduction

In the composite beam which is used in the steel structure, the steel section part was inserted in concrete slab, the slim floor system(Figure 1.), which improves a composite effect and fire resistance efficiency was developed from 1970's Europe. Recently the slimfloor beam which uses hot-rolled asymmetric H beam is introduced in design and construction in Korea. The domestic research about the slim floor is various according to the strengthen type of bottom flange to the H beams, attachment of shear connector and shape of the deck slab and it mainly evaluated the flexural capacity and synthesis ability of the composite beam as the test of room temperature conditions. But the research about the fire-resistance or

---

[†] Corresponding Author, E-mail: hans @ kict.re.kr
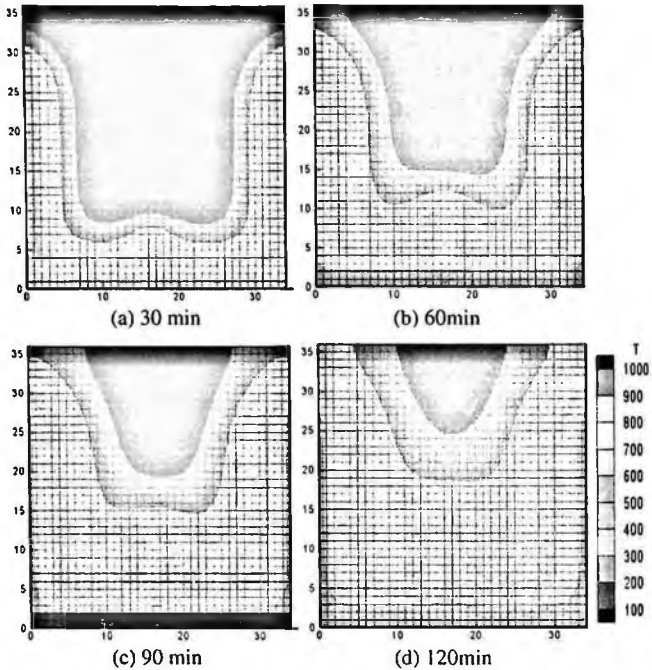
Figure 3. Temperature distribution of beam section at exposure time (unit : ℃)

2.3. *Moment Capacity at Elevated Temperature*

Moment capacity of the section which is exposed to high temperature calculated with input the remained strength of the material at corresponding point of mesh in temperature distribution. Moment strength is calculated by combine the every stress which it gets from the stress-strain relationships in the elevated temperature for the small curvature increment from the neutral axis location. From here, the rib portion of the slab is not accepted.

It shows the maximum moment of the model in the table 1 and the strength retention ratio in Figure 4. When it tries to observe the strength retention ratio, in the 30minutes of standard fire, only the Model-C is 50% remains, also it passes over 60 minutes, the sections except the Model-C are showing the ratio below 30%. The case which increases the thickness of the web from retention ratio of fire strength appeared with the more effectiveness.

Table 1. Analytic results for moment resistance at standard fire with different web thickness of steel section. (kNm)

	Model A (tw : 7mm)	Model B (tw : 14mm)	Model C (tw : 28mm)
Non-heated	694.41	727.95	791.30
30 min	175.24	263.60	407.86
60 min	67.96	127.68	248.40
90 min	52.07	96.40	183.68
120 min	39.52	71.98	136.31

Authors' names are set in 9 pt and in upper case. Addresses are in 9 pt italics. The abstract, figure and table captions should be in 8 pt.

It is also important to reproduce the spacing of the text and headings as shown here. Text should be slightly more than single-spaced; use a leading (which is the average distance from the base of one line of text to the base of an adjacent line) of 13 pt and 10 pt for footnotes. All headings should be separated from the text preceding it by a vertical space of about 12 pt and by 6 pt from the subsequent text.
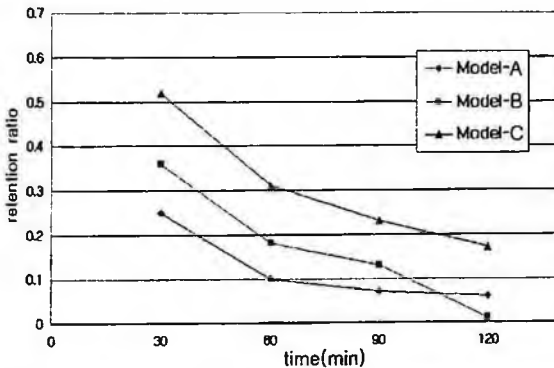
Figure 4. Strength retention ratio of specimen at exposure time

2.4. *List*

The basic model makes the following assumptions:

1. Environmental fluctuations may have a negative effect on the number of species. This effect is due to physiological stress, which may even cause the extinction of some species.
2. Environmental variability may have a positive effect on richness because it relaxes interespecific competition.
3. Both effects are independent and additive.
4. Both effects, stress and competence, can be represented by average values in two different parameters, which may be considered as constants.

To analyze the model behavior under different scenarios we consider three cases. First, the competitive effect is bigger than the stress one; second, both effects have a similar magnitude; third, the effect of stress is the biggest:

Acknowledgments

References

1. The Steel Construction Institute, Design of Asymmetric Slimflor Beams using Deep Composite Decking, SCI P175 (1997).
2. D. Hosser, T. Dorn and O. El-Nesr, Experimental and Numerical Studies of Composite Beams Exposed to Fire, *Journal of Structural Engineering*, Vol. 120, No. 10 (1994).
3. American Society for Testing and Materials, ASTM E 119-83, Standard Methods of Fire Tests of Building Construction and Materials (1985).
4. Y.C. Wang, Deflection of Steel-concrete Composite Beams with Partial Shear Interaction, *Journal of Structural Engineering* (1998).
5. British Standards Institution, BS 5950: Part8: Code of Practice for the Fire Protection of Structural Steelwork, UK (1990).
6. European Committee for Standardization, ENV1994-1-2:Eurocode4: Design of Composite Steel and Concrete Structures. Part 1.2

A STUDY ON STRESS ANALYSIS AND EXPERIMENTAL EVALUATION FOR THE ALL COMPOSITE STRUCTURE OF WIG VEHICLE

JAE-DO HAN

HU Solutions inc., Dasangwan Venture Town, Daeduck-Gu, Daejeon, 306-230, Korea

YOUNG-SHIN LEE[*]

Dept. of Mechanical Design Engineering, Chungnam National Univ., Daejeon, Korea

KUK-JIN KANG, HAN-KOO JEONG

WIG Craft Research Div., Korea Ocean Research & Development Institute, Daejeon, Korea

A structural analysis and semi-structural experimental evaluation of all composite WIG vehicle structure in order to verify major load path and structural stability were studied and presented in this paper. Semi-experimental evaluation was conducted to confirm the stress analysis result. As a result of comparison between analysis and test results, it was verified that these results were coincided with well. Stress and stiffness analyses on the maneuvering load case were conducted to confirm the structural healthiness of all composite WIG vehicle by using the verified applicable FE model on the basis of this comparison result. The healthiness of this WIG vehicle structure on the maneuvering load was good in global without local skin buckling. WIG structure is safe for the Tsai-Wu failure criterion and wing skin design change is proposed to improve the stiffness to avoid the skin buckling found in this study.

1. Introduction

High effective transportation tool is required as a major economic one in modern industry. Many industries are interested in Wing-In-Ground Effect(WIG) vehicle as a new high effective, fast and safe transportation tool[1]. WIG vehicle has an advantage of airvehicle and ship simultaneously and it can be called technology complex. In this paper, a study of static structural analysis for static structural test and full scale static semi-test on the small(6-seat) WIG vehicle which is composed of full composite material to reduce the weight is conducted to confirm the structural stability and applicable FE model. Full scale static semi-test is done to verify the major load path on the wing-to-fuselage joint.

---

[*] Corresponding author. Tel: +82-42-821-6644; Fax: +82-42-821-8894; e-mail: leeys@cnu.ac.kr

Simplified load is applied to conduct the test. Structural analysis is done in order to check strength and stiffness on ultimate load case of the 6-seats WIG vehicle by using the verified applicable FE model. Maneuvering load is calculated and distributed according to traditional load distribution method[1],[2].

2. Static Structural Test

2.1. *Static Structural Test*

Purpose of this test is to verify the major load path of small WIG vehicle. Static structural test is limited of applied load because of test article which will be used operational flight test. Thus, maximum applied load of this test is about 40% of 1.0-gravity(1.0g) on each wing. Semi-static test which is very simplified test method is done. It is considered because of limited test condition. Table 1 shows the design characteristic. Figure 1 shows the configuration of small WIG vehicle. The test set-up photograph is presented in Figure 2. Simplified test load applied just 2-point on each wing to match bending moment at wing root. Bending moment at the wing root is most important to match calculated one. Total number of channel for this test is 120. Strain gage and LVDT are used to static test.

Table 1. Design characteristics of small WIG vehicle

Length	12.25 m
Width	11.0 m
Take-off Weight	1500 kg
Maximum Velocity	137 km/hr
Engine Thrust	204 HP
Material	Carbon-Epoxy
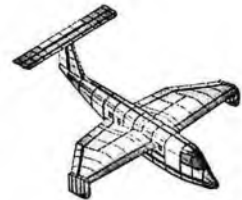
Figure 1. Configuration of small WIG vehicle
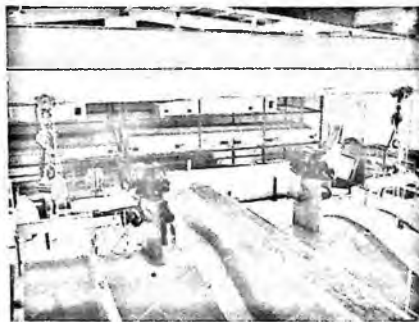
Figure 2. Photograph of wing static test set-up

2.2. FE Analysis for Static Structural Test

FE analysis is conducted to correlate with test results. NASTRAN is used to analyze the small WIG vehicle. FE model is considered half structure as shown in Figure 3 and laminated composite shell element is applied. Displacement symmetry boundary condition is applied and self weight is considered. Concentrated test load and engine load are applied one point by using rigid beam element to match test loading condition.

Figure 3. Finite element modeling for structural analysis of wing-to-fuselage

(a) Displacement

(b) Global von-Mises stress contour

(c) Fuselage stress contour

(d) Wing spar stress contour
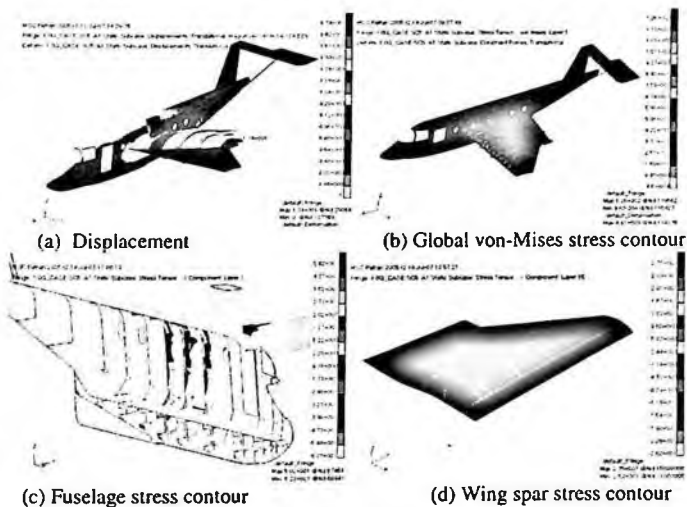
Figure 4. Stress analysis result for 1.0g load case

Two nodes of fuselage lower side are fixed three directional displacements to avoid rigid body motion. Materials are classified carbon-epoxy fabric, carbon-epoxy UD, glass-epoxy fabric and nomex honeycomb. Figure 4 shows the stress analysis results on wing-to-fuselage joint of small WIG vehicle. Maximum displacement is 17.4 mm at wing tip as shown in Figure 4(a). Figure 4(b)~(d)

show the stress contours. Maximum von-Mises stress is occurred the wing root as shown in Figure 4(b). Figure 4(c) shows fuselage stress contour. Stress is concentrated around 3-bulkheads which are jointed with wing major spars and skin around wing root. Figure 4(d) shows the spar flange stress level.

2.3. *Result Review of Static Structural Test and Analysis*

Correlation result between static test and stress analysis is presented in this section. Objectives of this correlation are to verify of suitability of FE model for structural analysis of WIG and to check stress level between test result and analysis. If load correlation result between test and analysis match well than it mean that this FE model is very useful to analyze WIG vehicle for other load conditions such as maximum maneuvering load cases which couldn't verify by the test because of test load limitation.
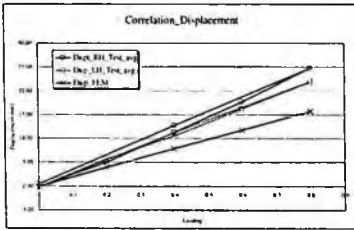
Figure 5. Displacement correlation result   Figure 6. Stress correlation result
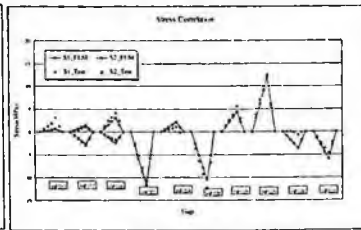
Test result is accord with test one because load path of wing-to-fuselage joint is very clear. Figure 5 shows the hysteretic displacement correlation result between test and analysis. Displacement result is comparatively matched at the lower load case but tolerance is bigger for the higher load case as shown in Figure 5. Tolerance is about 27 % at 0.8 g load case. Figure 6 is presented stress comparison between analytical and experimental results on the ten channels among the 120 channels. From this correlation, globally consistent with each other as shown in Figure 6. The reason of these difference can be predicted the manufacturing tolerance.

3. Structural Static Analysis for the Maneuvering Load

The FE model is confirmed through the structural analysis and test. Structural analysis for the critical maneuvering load case is conducted and presented in this section by using the verified FE model at forward section. Applied maneuvering load distribution method is according to traditional load distribution method[1,2]. Load factor 2.0 as a critical load case and safety factor 1.5 assigned in FAR are

considered. Structural strength and stability is studied and results are presented in this section.

Figure 7. FE model for structural snalysis
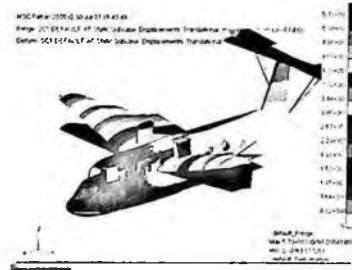
Figure 8. Displacement analysis result for maneuvering load case

Full FE model is considered on this analysis because of unsymmetrical load condition at vertical tail(see Figure 7). Figure 7 shows the FE model and load distribution. Displacement analysis result for 2.0g load case is shown in Figure 8. Maximum Displacement is 57.3mm at wing tip as shown in Figure 8. Figure 9 shows the equivalent stress contour and Figure 10 shows the Tsai-Wu failure index. Maximum stress is 376 MPa at wing root area. This stress level very low compare with Carbon-Epoxy Yield strength, thus WIG structure is safe for strength. Maximum Failure Index 3.44 is found at wing-to-fuselage local joint area, but this index can be ignored because FE model is a perversion of the fact like piling one on another of metal and composite. Composite skin is modeled as a cutout skin although skin has no cutout there as shown in Figure 10. For this reason WIG structure is safe under Tsai-Wu criterion. Figure 11 shows the first buckling mode. Maximum buckling load factor of 0.387 is found at fuselage skin. It means that WIG skin is locally weak for the buckle.

Figure 9. Stress contour for maneuvering load case
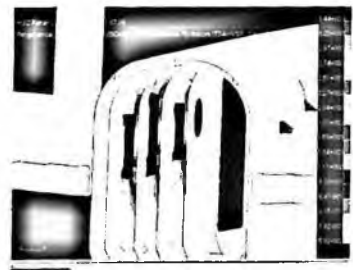
Figure 10. Failure index for maneuvering load case

Figure 11. Buckling analysis result for maneuvering load case

4. Conclusions

A static structural test and analysis of small scale WIG vehicle for the simplified test load is done in this study. Major load path is verified and applicable FE model is evaluated from comparison of these results. Static structural analysis for ultimate maneuvering load is done with this applicable FE model to achieve safety and stability of this WIG structure. The major findings from this study are as follows,

(1) Major load path is verified through experimental & analytical methods.

(2) Semi static test method is developed for the small scale WIG vehicle.

(3) The finite element for the all composite WIG vehicle static model is developed.

(4) Strength & stability for maneuvering load are verified using proven FE method and strength of small scale WIG for maneuvering load(2.0g) is sufficient.

(5) Small scale WIG is safe for the Tsai-Wu failure criterion.

(6) Local buckling problem is found for the present wing and tail skin laminates and sandwich design could be an option to avoid the local buckling.

References

1. C. D. Kong, H. B. Park and J. I. Kim, *A Study on Structural Design and Analysis for Composite Main Wing and Horizontal Tail od a Small Scale WIG Vehicle*, The Korean Society for Aeronautical & Space Science, Vol.35, No.2, pp.149~156 (2007)

2. F. Wojewodka, *Design of Simple Light Airvehicle* (1973)

3. M. S. Shin, Y. S. Kim, G. J. Lee, K. J. Kang, Y. H. Park and Y.Y. Lee, *Conceptual Design of Small WIG Craft*, Journal of the Society of Naval Architects of Korea, Vol.43, No.1, pp. 134~146 (2006)

4. C. D. Kong, H. B. Park and K. J. Kang, *Structural Design and analysis for Carbon/Epoxy Composite Wing of A Small Scale WIG Vehicle*, Journal of the Society for Composite Materials , Vol.19, No.5, pp. 12~19 (2006)

5. R. F. Gibson, *Principles of Composite material Mechanics* (1994)

AN ELASTIC-PLASTIC FINITE ELEMENT ANALSYS OF THE INTERFACE WITH PERPENDICULAR CRACK USING THE PROPERTY GRADIENT IN FIBER REINFORCED MMC[*]

JI-WOONG KANG[†]

Department of safety engineering, Pukyong National University, San100, Yong-dang dong, Nam-gu, Busan 608-739, Korea

OH-HEON KWON

Division of safety engineering, Pukyong National University, San100, Yong-dang dong, Nam-gu, Busan 608-739, Korea

The effective utilization of the strength and stiffness of the fiber reinforced MMCs depends on efficient load transfers from the matrix to fibers through the interfacial region. However, during the fabrication and afterward utilization of composites, so many numbers of micro crack may extend, especially at the interface, even before any load has been applied. Thus, in this study, the interfacial perpendicular crack behavior and stress state of the unidirectional fiber reinforced MMCs are investigated by using FEA under the transverse loading. The fiber/matrix interface is modeled as multi thin layer with different linear material properties. The behavior of perpendicular crack to the interface according to the change of the interface characteristics and thickness are evaluated.

1. Introduction

The low transverse property of unidirectional composites can be regarded as one of the major limitations in the application of composite materials [1]. Such composites possess a pronounced anisotropy given the large differences in fiber and matrix properties, and especially the performances in transverse direction are poor. The interfacial region between fiber and matrix in a fiber reinforced MMC and its properties play a great role in the stiffness and strength of the composite [2, 3]. Moreover, during the fabrication of composites, micro cracks may extend, especially at the interface, even before any load has been applied [4]. Therefore, the objective is to evaluate the interfacial characteristic and the interfacial perpendicular crack behavior focused on the interfacial characteristic changes when the MMC is loaded transversely.

[†] Ji-Woong Kang, slashjw@paran.com

Table 1. Mechanical properties of SiC fiber reinforced MMC.

	Elastic Modulus (GPa)	Tangential Modulus (Gpa)	Poisson's Ratio	Yield Strength (MPa)
SiC	364	-	0.23	-
Layer 1	284	-	0.26	-
Layer 2	224	5	0.28	1882.5
Layer 3	164	5	0.3	1334.4
Ti-15-3	88	5	0.32	716

2. Elastic-Plastic Finite Element Analysis

2.1. *Material property and modeling*

Table 1 shows the mechanical properties of SiC fiber, Ti-15-3 matrix and the multi thin layer with variable properties. The metal matrix composite consists of an elastic- plastic matrix with continuous elastic fiber. The fiber is assumed as a silicon carbide SiC and the matrix as Ti-15-3 Titanium alloy. Square fiber arrangement was used to estimate the interfacial stress state and the perpendicular crack behavior of MMC. The numerical analysis are based on a 2-D generalized plain strain model of cross-section of a unidirectional fiber reinforced MMC. Four fiber volume fractions were selected from 5% to 40% (5%, 10%, 20% and 40%) by changing the radius of the SiC fiber.

2.2. *Multi thin layer interface and perpendicular crack*

The finite element analysis is used for solving a
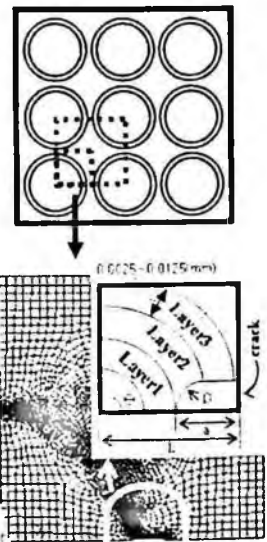
Figure 1. Finite element model for the fiber reinforced metal matrix composite with multi thin layers.

perpendicular cracked model to the interface shown in Figure 1. In the region of the interface, high stress variability is expected, and besides, bonding capability of the fiber/matrix interface is considered. Therefore, we suggested multi thin layer interface model with different linear material properties. Five layer thicknesses were selected from 2.5μm to 12.5μm (2.5μm, 5μm, 7.5μm, 10μm and 12.5μm). The perpendicular crack with round tip is positioned on the interface between the fiber and the matrix. The behavior of perpendicular crack to the interface according to the interfacial characteristic changes is evaluated.

Crack ratio (a/L) is 0.125. The load level is 2GPa. The analyses of the interfacial stress state and the perpendicular crack behavior of MMC was carried out using the commercial finite element code ANSYS.

3. Result and discussion

Figure 2 shows the variation of the normalized von Mises stresses at the interface of multi thin layer model according to the layer thickness and orientation θ. Interfacial stress state have nothing to do with the changes of layer thickness. However, the maximum normalized stress values in round notch tip gradually decreased from 1.42 to 1.20 according to increasing layer thickness (1.42, 1.30, 1.25, 1.22 and 0.17).

The variation of the normalized von Mises stresses at the interface of multi thin layer model (layer thickness is 7.5μm) for different fiber volume fraction and orientation θ is shown in Figure 3. The maximum normalized von Mises stresses at the interface, which are 1.42, 1.24, 1.19 and 1.28, respectively for different fiber volume fraction 5-40%, have not so difference in a value. However, the maximum normalized stress values in round notch gradually increased from 1.25 to 1.37 according to increasing fiber volume fraction (1.25, 1.26, 1.30 and 1.37).

Figure 4 shows the variation of the equivalent plastic strain at the interface of multi thin layer model according to the layer thickness and orientation θ. Interfacial equivalent plastic strain have nothing to do with the changes of layer thickness. However, the maximum equivalent plastic strain values in round notch
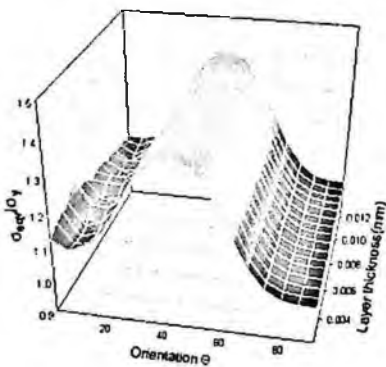
Figure 2. The variation of the normalized von Mises stresses at the interface of multi thin layer model according to the layer thickness and θ (Volume fraction is 5%).
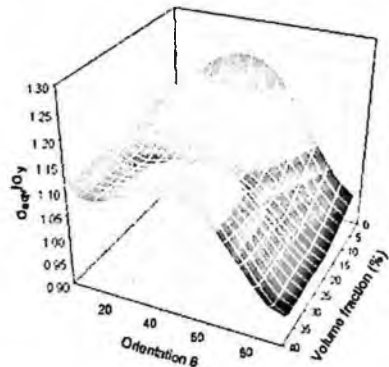
Figure 3. The variation of the normalized von Mises stresses at the interface of multi thin layer model according to the volume fraction and θ (Layer thickness is 7.5μm).
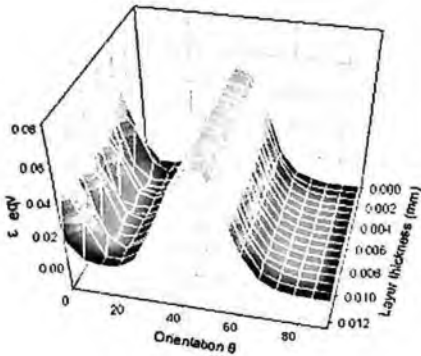
Figure 4. The variation of the equivalent plastic strain at the multi thin layer interface according to the layer thickness and θ (Volume fraction is 20%).
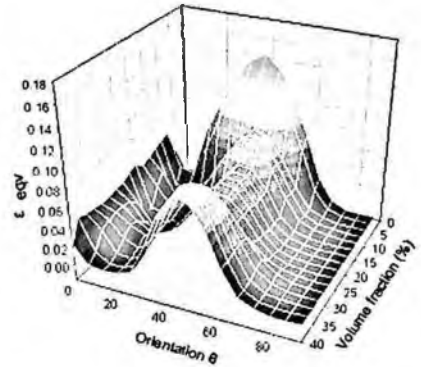
Figure 5. The variation of the equivalent plastic strain at the multi thin layer interface according to the volume fraction and orientation θ (Layer thickness is 5μm).
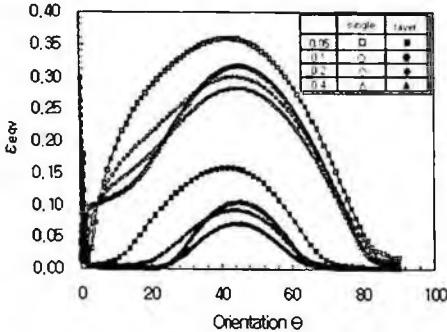
Figure 6. The variation of the equivalent plastic strain at interface according to the interfacial characteristic changes.
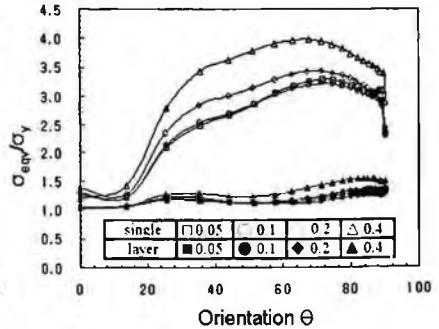
Figure 7. The variation of the normalized von Mises stresses at the round notch-tip according to the interfacial characteristics.

tip gradually decreased from 0.19 to 0.087 according to increasing layer thickness (0.19, 0.13, 0.11, 0.098 and 0.087).

The variation of the equivalent plastic strain at the interface of multi thin layer model (layer thickness is 5μm) for different fiber volume fraction and orientation θ is shown in Figure 5. The maximum equivalent plastic strain values at the interface have not so difference in a value. However, the maximum equivalent plastic strain values in round notch gradually increased from 0.11 to 0.17 according to increasing fiber volume fraction (0.11, 0.12, 0.13 and 0.17).

Figure 6 shows the variation of the equivalent plastic strain at the interface of single and multi thin layer model according to the different fiber volume fraction and orientation θ. Maximum equivalent plastic strain at the interface of the single interface model, which are 0.36, 0.30, 0.28 and 0.31, respectively for
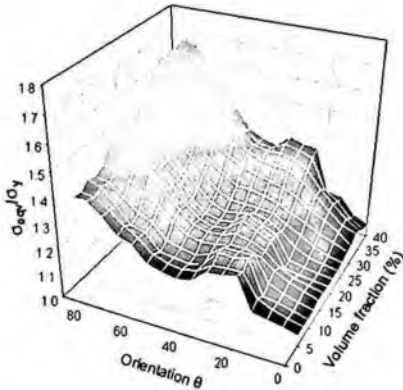
Figure 8. The variation of the normalized von Mises stresses at the round notch-tip of multi thin layer model according to the volume fraction and θ (Layer thickness is 7.5μm).
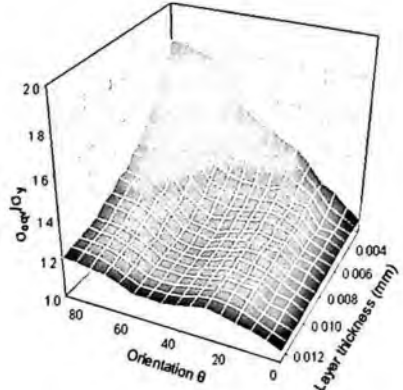
Figure 9. The variation of the normalized von Mises stresses at the round notch-tip of multi thin layer model according to the layer thickness and θ.

the different fiber volume fraction, have not so difference in a value. Those of multi thin layer model for different fiber volume fraction are 0.16, 0.09 0.07 and 0.1 respectively, under 2Gpa. It shows that the introduction of multi thin layer adjacent to the interface leads to reduce in the maximum equivalent plastic strain values at the interface.

Figure 7 shows the variation of the normalized von Mises stresses at the round notch-tip for the single and multi thin layer model. In the case of single interface model, the normalized von Mises stress along the round notch tip shows rapid variation, while those of a multi thin layer model shows gentle variation. The maximum normalized von Mises stresses in a single interface model are somewhat as large as a multi layer interface model under the same volume fraction. Those of multi layer interface model are 1.34, 1.27, 1.36 and 1.54, respectively for different fiber volume fraction. Those of single interface model are 3.28, 3.20, 3.42 and 3.98, respectively. The maximum normalized von Mises stresses positions of multi layer model gradually decreased from 90° to 83° according to increasing fiber volume fraction. However, those of single interface model located in about 70°.

Figure 8 shows the variation of the normalized von Mises stresses at the round notch-tip for multi thin layer model. Its layer thickness is 7.5μm. The normalized stress values along the round notch-tip gradually increased according to increasing fiber volume fraction. The maximum normalized von Mises stresses values in round notch gradually increased from 1.35 to 1.67 according to increasing fiber volume fraction (1.35, 1.38, 1.48 and 1.67).

Figure 9 shows the variation of the normalized von Mises stresses at the round notch-tip of multi thin layer model according to the layer thickness and orientation θ. The normalized von Mises stress values along the round notch-tip gradually decreased according to increasing layer thickness. The maximum normalized von Mises stresses values in round notch gradually decreased from 1.84 to 1.21 according to increasing layer thickness (1.84, 1.51, 1.27 and 1.21).

4. Conclusions

Using the proposed model, the effects of the interfacial characteristic changes in MMCs on the distribution of stress and strain, characteristics of the interfacial crack behavior are estimated.

Interfacial stress state has nothing to do with the changes of layer thickness. However, the maximum normalized stress values in round notch tip gradually decreased according to increasing layer thickness.

Normalized von Mises stresses of the single interface model have precipitous changes at the interface. On the contrary, the stress distributions of a multi thin layer interface model have much less changes compared with those of conventional perfect bonding interface, because it has multi thin layer with different properties.

The equivalent plastic strain of the single interface model occurred in the overall interface and maximum values are located in interface, but those of layer model partially occurred in the interface. It shows that the introduction of multi thin layer adjacent to the interface leads to reduce in the maximum equivalent plastic strain values at the interface.

In the case of single interface model, the normalized von Mises stress along the round notch-tip shows rapid variation, while those of a multi thin layer model shows gentle variation. The normalized stress values along the round notch-tip gradually increased according to increasing fiber volume fraction. The normalized von Mises stress values along the round notch-tip gradually decreased according to increasing layer thickness.

References

1. Ji-Woong Kang and Oh-Heon Kwon, Key engineering materials. 297-300. pp. 148-153. (2005).
2. J. M. M. de Kok, t. Peijs, Composites. Part A. 30. pp. 917-932. (1999).
3. S.A. Meguid, G.Shagal, R.Paskaramoorthy, composites. Part A. 33. pp. 1629-1640. (2002).
4. B. Fiedler, M.Hojo, composites. Part A. 33. pp. 1323-1326. (2002).

A STUDY FOR LOAD BEARING CAPABILITY OF LAMINATES WITH EMBEDDED SHAPE MEMORY ALLOY SUBJECTED TO LOW VELOCITY IMPACT

KI-WEON KANG

Ph.D., Dept. of Sports Eng. Korea Institute of Sport Science, Seoul, Korea

JUNG-KYU KIM[†]

Professor, School of Mech. Eng., Hanyang University, Seoul, Korea

The paper aims to identify the damage behavior and load bearing capability of the glass/epoxy laminates with embedded SMA (shape memory alloy) subjected to low velocity impact at various temperatures. For these, impact tests were performed by using an instrumented impact-testing machine at three temperatures (293K, 263K and 233K). Then, static tests are conducted under flexural loading to identify the strength reduction behavior of the SMA laminates with the impact-induced damage. The SMA behaves as a discontinuity at ambient temperature: but, as the temperature decreases, it appears that the SMA plays a role of reinforcement at lower temperatures. Also, the strength of SMA laminates is greatly decreased by the impact damage to reach a plateau and this behavior can be predicted by Caprino's model that was proposed on the unidirectional laminates. Finally, their load bearing capability is affected by test temperature.

1. Introduction

Impact damage is one of the main problems that composite structures face [1]; hence, there needs to be a way of reducing that damage when it occurs, reducing it enough so that the integrity of structure is not compromised [1]. One possible way to increase the impact damage resistance of composite structure is by embedding shape memory alloy (SMA) into structures [2]. Although the embedded SMA can enhance their resistance to the low velocity impact, the impact resistance and strength reduction behavior are greatly influence by the constituent materials, their lay-ups and environment conditions [3 4]. Therefore, more research is of necessity to understand the impact damage and strength reduction behavior when the SMA is embedded into composite laminates.

Many pieces of research have performed on the impact response and resultant damage behavior of SMA laminates [4~6]. Birman [5] has presented an

---

[†] To whom correspondence should be addressed. Fax: 82-2-2291-6707; E-mail:kimj@haynag.ac.kr

approach to the problem of optimum design in the impact resistance to low-velocity impact for SMA hybrid plates. And Meo et al. [6] have shown that embedding SMA wires into composites lead to an increase of the damage resistance of hybrid composites structures. However, since the impact damage is quite sensitive to constituent materials of laminates and moreover, it cannot be avoided that the structures are subjected to severe environmental conditions such as low temperature; thus more extensive research is necessary to identify the damage behavior of the SMA laminates under severe environmental condition.

When the composite structures are loaded, the impact damage behaves as a discontinuity: hence, several researches have focused on the load-bearing capability of the impacted laminates [7, 8]. Zhang et al. [7] have investigated the damage severities and residual properties of the impacted laminates. Also, the study by Ibekwe et al. [8] has illustrated the impact and residual strength of laminates at low temperatures. From this literature survey, almost all the previous studies were focused on strength reduction behavior of monolithic laminates at ambient or elevated temperature; there is currently a lack of understanding of the load-carrying capability of the impacted SMA laminates under low temperatures.

The paper aims to identify the damage behavior and load bearing capability of SMA laminates subjected to the low velocity impact at various temperatures. For these, the impact are performed on the SMA laminates (glass/epoxy laminates with embedded SMA) under temperatures of 293K, 263K and 233K. The resulting impact damage is measured by using a scanning acoustic microscope (SAM). Then, three point flexural tests are conducted to identify the strength reduction behavior of the SMA laminates with the impact-induced damage at the aforementioned temperatures.

2. Experimental Procedure

2.1. *Material and specimens*

The composite material was 24ply glass/epoxy laminates (TBCarbon SGP 125NS) obtained from a prepreg with a thickness of about 0.2mm. The shape memory alloy was the Ni-Ti SMA wire with 0.4 mm-diameters and inserted every 5mm at the neutral plane of the laminates with a stacking sequence of $[0_6/90_{12}/0_6]$. The plates (250mm×500mm) with volume fraction of $v_f \approx 50\%$ were processed in an autoclave according to manufacturer's recommendation and then cut into specimens with a dimension of 90mm×120mm. Their detail mechanical properties are shown in the previous study [4].

2.2. Impact and flexural tests

The Dynatup 9250HV impact test machine was used for the low velocity impact tests. The specimens were round-clamped with the opening of 76.2 mm-diameters. The radius and mass of the hemispherical impactor were 6.35mm and 6.45kg, respectively. The specimens were inspected by the scanning acoustic microscope (SONIX HS1000, 5MHz). And then, the 3-point static tests were conducted by an Instron model 5581 according to ASTM D 7264M [9]. The specimens were simply supported on 12.7mm diameter rollers with a span length of 80mm, put the impacted surface upward at crosshead speed of 3mm/min. Prior to each test, the specimens were cooled to temperatures (293K, 263K and 233K) in the environmental conditioning chamber for 3 hours.

3. Results and Discussion

3.1. Impact damage behavior

To identify the damage configurations of the SMA laminates with test temperature, the impact tests were made at the plate center at the temperatures of 293K, 263K and 233K. Fig. 1 shows the typical damage states, which were observed by the SAM. Here the damage was captured at the 2nd interface from the impact point. The figure shows that the impact damage is mainly delamination and peanut-shaped with major axis along their lower fiber orientation, the same as reported [1, 2]. And, though it seems that the damage is affected by temperature, it is hard to identify the effects of temperature on the damage behavior.

For further understanding of the damage behavior of SMA laminates with temperatures, the peak impact force against the incident energy is plotted in Fig. 2. The figure shows the rising trends in loads with an increase in incident energy for all the temperatures. As the temperature decreases, however, the SMA laminates have slightly different behavior from ambient temperature: the loads under lower temperatures slightly get lower at higher incident energy compared to the ambient temperature and this behavior is more remarkably in the lowest temperature. Similar behavior can be found on the load-deflection curves in Fig. 3. The delamination areas obtained by the SAM, against the incident energy are shown in Fig. 4. The damage areas are rapidly increased with increasing of incident energy for all the temperature as expected, but it is hard to identify the temperature effect on the impact damage behavior of the SMA laminates. To identify the temperature effect on damage behavior, the damage area against the peak load is presented in Fig. 5. As the temperature decreases, the severity of the

impact damage in the SMA laminates is changed, especially at the lowest temperature. From the above results, it is, therefore, inferred that the impact response of the SMA laminates is affected by the temperatures and also, the SMA plays a role of reinforcement in laminates, especially under lower temperatures.

(a) Result at 293K   (b) Result at 263K   (c) Result at 233K
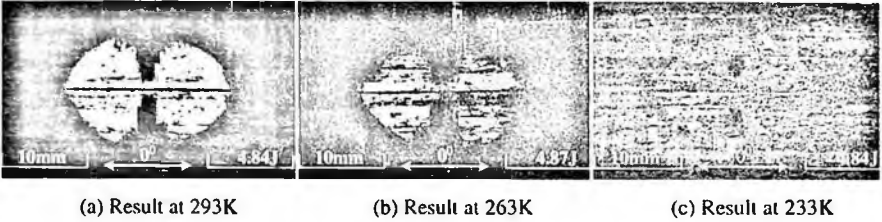
Fig. 1 Impact damage configuration of SMA laminates
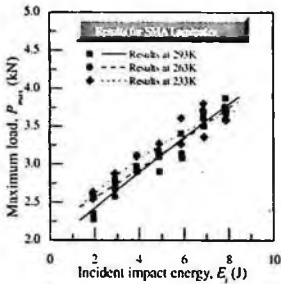
Fig. 2 Peak load vs. incident energy
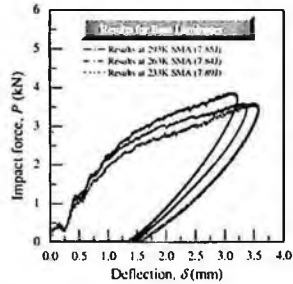
Fig. 3 Load-deflection curves
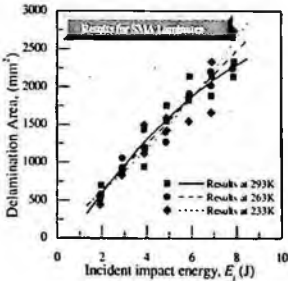
Fig. 4 Damage area vs. incident energy
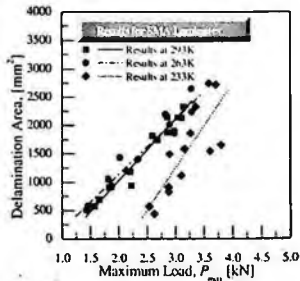
Fig. 5 Damage area vs. peak load

3.2. *Residual flexural properties*

The damage behaves as a discontinuity when the composite structures are loaded and then it causes a large drop in load bearing capabilities of composite structures: hence, it is of particular interest to understand to what extent the impacted materials can sustain further loading [7, 8]. In this study, flexural

testing was carried out to investigate the post impact properties, namely the flexural strength and modulus at the temperatures of 293K, 263K and 233K.

The relationship of residual flexural secant modulus [9], normalized by the modulus of the unimpacted laminates, with incident energy is illustrated in Fig. 6. It indicates that impact events result in reductions in the modulus to varying degrees and the maximum reduction is approximately 20%: the flexural modulus is not particularly sensitive to the damage presence, as expected. Also, it is hard to identify the effect of temperature on the flexural modulus. These may result from the fact that the impact damage is localised in most cases and therefore it has less effect on the global properties such as the modulus. The calculation of modulus only involves the initial linear part of force-deflection curves [7].

(a) Result at 293K   (b) Result at 263K   (c) Result at 233K
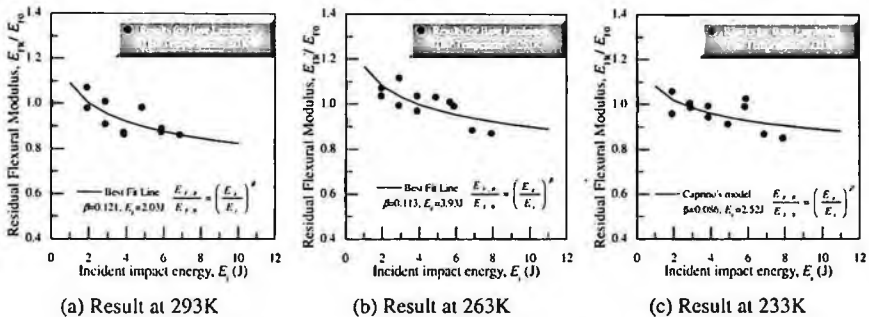
Fig. 6 Residual flexural modulus of impacted SMA laminates

And the residual strength data, normalized by the strength of the unimpacted laminates, are plotted against the impact energy in Fig. 7. Here the solid lines are drawn according to Caprino's model [10], which was proposed on the unidirectional laminates under tensile loading. From the figure, Caprino's model can be used to predict the residual strength of SMA laminates with the impact-induced damage under flexural loading for all the temperatures. And the residual strength is not influenced by the incident impact energy up to some energy level(1.89J at 293K, 1.73J at 263K and 1.58J at 233K): thus, this level can be defined as the strength threshold energy, which is the minimum energy to cause strength reduction in structures. Above these energy levels, the residual strength is rapidly reduced with the incident energy and reaches at about 50% of strength in the unimpacted laminates for all the laminates. Compared to the residual modulus, the flexural strength is more severely affected by the impact damage, leading to higher reductions. This higher sensitivity can be explained by the fact that the damage is localized as aforementioned and this has the adverse effect on the load bearing capability of laminates. Also, the strength reduction behavior is affected by the temperatures, especially in the strength threshold energy and

dispersion in strength. These are consistent with the aforementioned behaviors that the impact response of SMA laminates is affected by the temperatures.

(a) Result at 293K　　　　(b) Result at 263K　　　　(c) Result at 233K
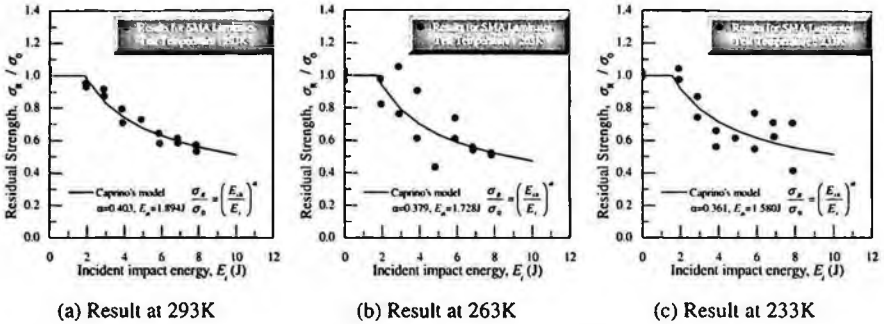
Fig. 7 Residual flexural strength of impacted SMA laminates

4. Conclusions

1. The impact damage of SMA laminates is mainly delamination and its configuration is peanut-shaped with major axis along their lower fiber orientation. Also, their damage behavior is affected by the temperatures.

2. The impact events result in reductions in the modulus and strength to varying degrees and the flexural strength is more severely affected by the impact damage, leading to higher reduction.

3. The strength is greatly reduced with the impact energy and well described by Caprino's model. The strength reduction behavior is affected by temperatures, especially in the strength threshold energy and dispersion in strength.

References

1. K.W. Kang and J.K. Kim, *Compos. Part A*, **37**, 1451 (2006)
2. J.H. Roh and J.H. Kim, *Compos. Struc.* **56**, 175 (2002)
3. K.A. Tsoi, R. Stalmans, J. Schrooten, M. Wevers and Y.W. *Mai, Mater. Sci. Eng.* A342,207 (2003)
4. K.W. Kang, H.J. Kim and J.K. Kim, *J. Mech. Sci. Tech.* (to be published)
5. V. Birman, *Compos. Part B*, **27**, 439 (1996)
6. M. Meo, E. Antonucci, P. Duclaux and M. Giordano, *Compos. Struc.* **71**, 337 (2005)
7. Z.Y. Zhang and M.O. Richardson, *Compos. Struc.* **81**, 195 (2007)
8. S.I., Ibekwe, P.F. Mensah, G. Li, S.S. Pang and M.A. Stubblefield, *Compos. Struc.* **79**, 12 (2007)
9. ASTM, D **7264M** (2007)
10. G. Caprino, and R. Teti, *Compos. Struc.* **29**, 47 (1994)

NONDESTRUCTIVE TESTING AND STRENGTH PREDICTION OF ADHESIVE BONDED JOINTS USING THE SCAN TYPE MAGNETIC CAMERA

HO-CHEL YOON[†]

Division of Mechanical & Automotive Engineering, Wonkwang University,
344-2 Shinyong, Iksan, Jeonbuk, 570-749, Republic of Korea

JINYI LEE

Department of Information and Comunication Engineering, Chosun University,
375, Seosuk, Gwangju, 501-756, Republic of Korea

Adhesive bonded Structures have become an important part of manufacturing. It is easy to join two different materials together by adhesive bonding, and this method is well used in the aircraft, automotive, marine, architecture and space industries. The integrity and reliability of the bonds are extremely important to the quality of the end products. The flaws or inner defects are potential problem in adhesive bonding especially in the position of high stress intensity. In this paper, scan type magnetic camera with complex induced current and magnetic flux leakage (CIC-MFL) is proposed to detect and evaluate flaws inside adhesive bonded part. The manmade cracks, such as slits and hollow air bubbles, are used to verify the effectiveness of the test result. Specimens which contained flaws are tested to evaluate the failure strength of single-lap-joined in tensile-shear tests. The Finite Element Method (FEM) simulates the same condition of adhesive bond testing. The test results are presented by tensile-shear strength comparing with FEM and analysis. The strength prediction is discussed in order to explain the effect on the position of defects. Finite element method gives good explain how strength evaluated in adhesive bonded joint containing the flaws.

1. Introduction

Adhesive bonding has a different characteristic comparing with other welding method. Especially, in some cases higher strength of adhesive bonding is able to be expected than spot welding, because there is no damage to the high temperature and there is less remaining stress [1]. Adhesive joining method is able to be suggested for the assembling; it is easy to join two different materials together by the adhesive joining method, and this method is well used in the fields of aircraft, automotive, marine, architecture and space industries etc [2]. In

---

[†] Corresponding Author : yoonhc@wonkwang.ac.kr.

this paper, Aluminum (Al 5052) was selected and joined using adhesive bonding. The specimens are made of single-lap type with different thickness and contain the manmade flaws, such as slits and holes. In this paper, a scan type magnetic camera, which uses a complex induced current - magnetic flux leakage (CIC-MFL) method as a magnetic source and a linearly integrated Hall sensor array (LIHaS) on a wafer as the magnetic sensors, was examined for its ability to detect flaws on the combined material (Al and SPC) [3]. Magnetic camera by using CIC-MFL is proposed to detect and evaluate flaws inside adhesive bonded part. In this research, a nondestructive testing technique using linearly integrated Hall sensor array (LIHaS) is proposed to detect and evaluate defects in the adhesive bonded area. The nondestructive testing system using the technique has merits such as lightness because it does not have to use a weighty yoke type magnetizer and an economic merit because it does not use magnetic particles. Several slits and holes, which were introduced on a in the adhesive bonded area by using cold-rolled steel sheet (SPC) piece made by punching, were used to verify the effectiveness of the novel technique.

2. Material and Method

The Aluminum (Al 5052) was used for the specimen. The single lap adhesive joint specimens were also manufactured according to ASTM D 1002. The structural epoxy adhesive (3M, DP-460), two-liquid-state mixture type, was used and it is able to be hardened at the room temperature. The adhesive joining part was polished with the sand paper of #1000 and washed several times with acetone. The adhesive thickness was maintained with jig and the steel wire of 0.5mm. The adhesive was hardened at the room temperature to have enough strength. The same conditions of the surface toughness were maintained for all specimens.
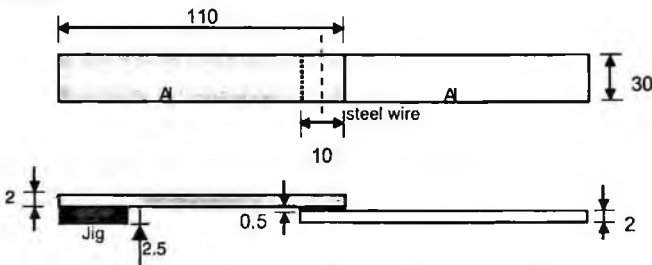
Figure 1. Schematic diagram of specimen.

The length of the lap joint part was 10mm was manufactured. And Al adherends have the inner flaws. SPC piece was coated to avoid bonding and

inserted as outer flaws in the adhesive bonded area. The effects of the manmade flaws were evaluated by tensile-shear test. Figure 1 shows the schematics for the single lap adhesive tensile-shear specimen. The fracture from the tensile-shear load was led with the universal testing machine (Instron 4206). The cross-head speed of 1mm/min. was maintained.
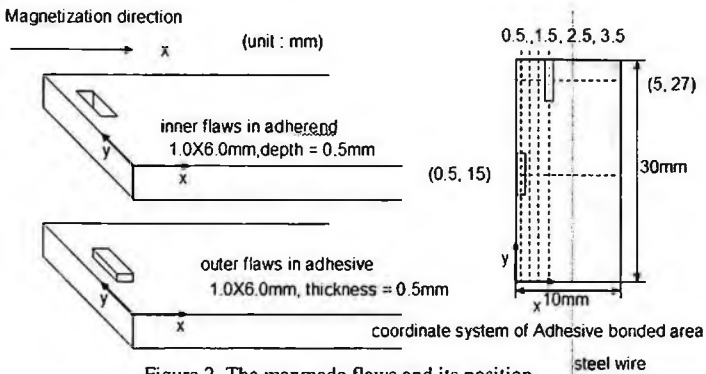
Figure 2. The manmade flaws and its position.

Finite element method (FEM) model was used to get the information about the stress distribution of the adhesive joining part [4]. The non-linear analysis method, increasing the load from 0N to 980N (ramped), was used. Figure 3 shows the analytical model and the boundary conditions used for the FE analysis.

Table 1. Mechanical properties of material.

	Young's modulus	Poisson's ratio	Yeld strength	Ultimate strength
Al	70.3GPa	0.33	89.6MPa	193MPa
Epoxy adhesive	30MPa	0.30		
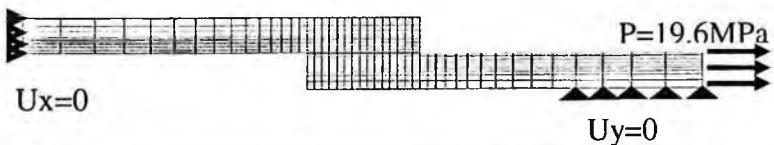
Figure 3. Mesh model and boundary condition for finite element method.

In nondestructive test, magnetic camera by using CIC-LMF and LIHaS is proposed to detect and evaluate flaws inside adhesive bonded part. The CIC-LMF permitted the crack detection of the ambient material, such as ferromagnetic and paramagnetic metal. The eddy current and magnetic field

were distorted at the tips of crack and the strength of magnetic field was maximized at the same location. Hence, the two peaks were appeared at both tips of slits or holes. Also, the height of the peak has a deep relationship with the slits and holes sizes.

3. Results and Discussion

The results of the tensile-shear test for the 16 specimen types, such as inner (Figure 4 (a)) or outer (Figure 4 (b)) flaws, and position (0.5,15), (1.5,15), (2.5,15), (3.5,15), (0.5,27), (1.5,27), (2.5,27) (3.5,27), were showed.
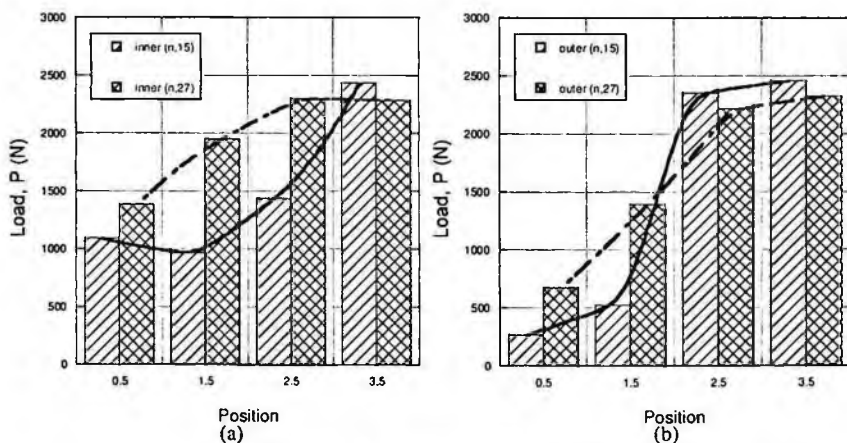
Figure 4. The result of tensile-shear test.
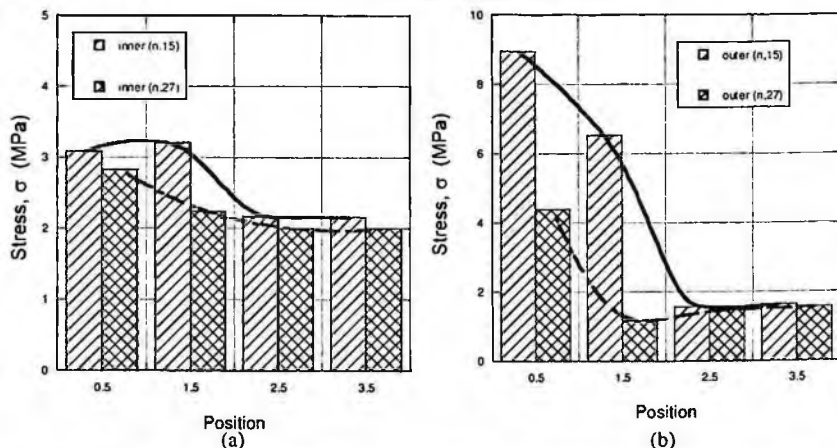
Figure 5. The result of stress intensity(maximum von Mises stress) from FEM.

The relationship between stress intensity (maximum von Mises stress) from FEM and adhesive bond strength is in inverse proportion. If stress intensity is very high and work on the edge of joining part, crack propagation is made easily. therefore, the failures of specimens were observed at the lower tensile load. If we know flaws position and size exactly, FEM result is helpful to predict adhesive strength. In nondestructive test, magnetic camera is proposed to detect flaws position. The NDT results according to distinguish inner and outer were shown in Figure 6. Flaws can be detected on the combined material of Al plate with SPC outer flaws, which are paramagnetic and ferromagnetic material respectively. And If we detect flaws at the position (2, 21), Adhesive strength of this specimen is predicted 1750N using FEM results (Figure 8(a)) and acquired test result 1680N (Figure 8(b)).

(a) inner flaw   (b) outer flaws
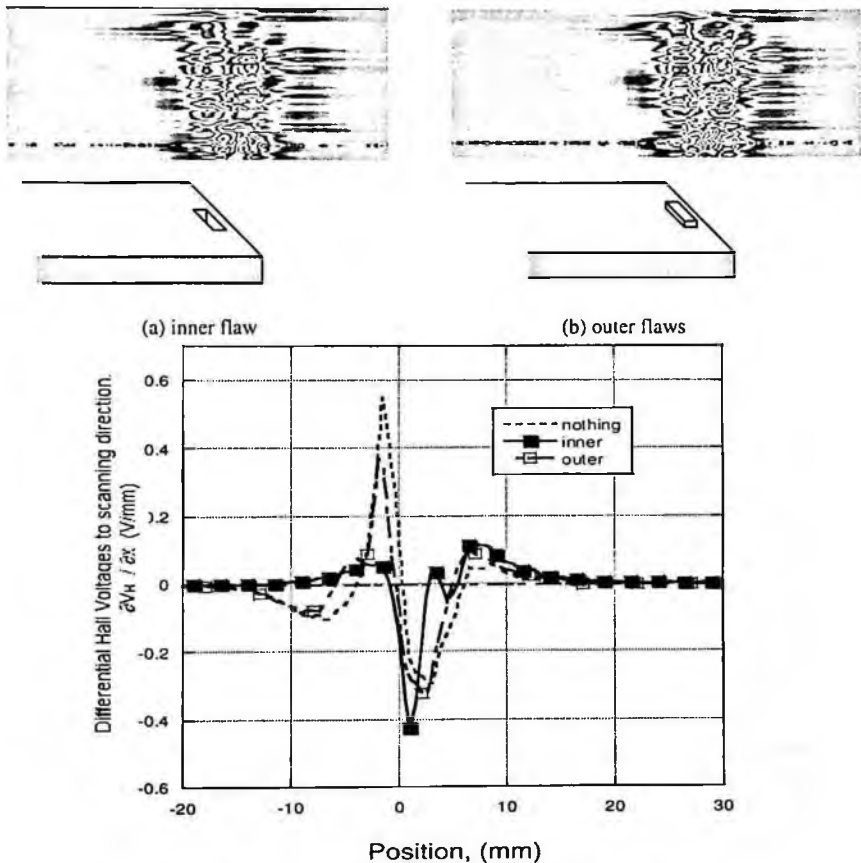
Figure 6. The $\partial V_H / \partial x$ sectional distributions on the flaws.
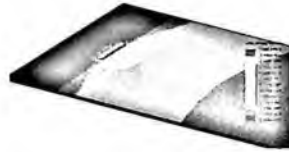
(a) inner flaws model   (b) outer flaws model

Figure 7. The stress distribution (von Mises stress) in FEM.
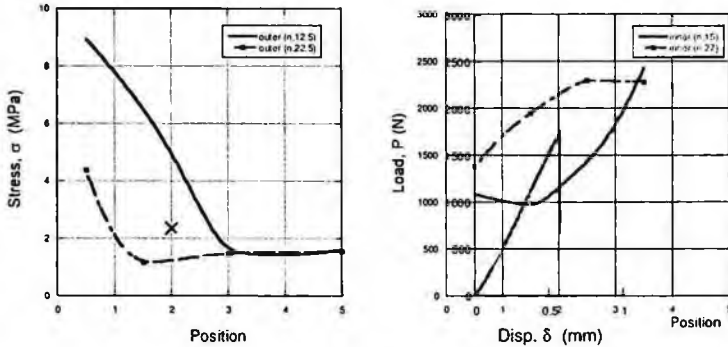
Figure 8. The relation between the prediction and test result.

4. Conclusions

The relationship between stress intensity (maximum von Mises stress) from FEM and adhesive bond strength is in inverse proportion. If stress intensity is very high and work on the edge of joining part, crack propagation is made easily. therefore the failures of specimens were observed at the lower tensile load. NDT help to find flaws position and size exactly. NDT and FEM results are useful to predict adhesive strength.

References

1. Robert W. messler Jr. : Joining of advanced materials, Butterworth Heinemann Ltd, (1993) p108-180.
2. L. E. Meade : Adhesives for aerospace, Joining Technologies for the 1990's, eds., Noyes Data Coporation (1986).
3. J. Hwang, J. Lee, J. Jun, R. Wang, S. Choi and S. Hong, "Scan type magnetic camera images with a high spatial resolution for NDT obtained by using a linea interated hall senosr array", Proceedings of IEEE International Workshop on Imaging Systems and Techniques, pp. 1-6, (2007)
4. T. Cheuk, Liyong Tong : Failure of Adhesive Bonded Composite Lap Shear Joints with Embedded Precrack, Composites Science and Technology 62 (2002), 1079-1095

A STUDY ON THE LIGHT-WEIGHT THIN-WALLED MEMBER FOR OPTIMUM CRASHWORTHINESS DESIGN

KIL SUNG LEE, HYEON KYEONG SEO, WOO CHE HWANG
AND IN YOUNG YANG[†]

*BK21 Education Center of Mould Technology for Advanced Materials & Parts,
Chosun University, Gwangju 501-759, Korea*

KWANG HEE IM

*Department of Automotive Engineering,
Woosuk University, 490 Hujung-ri, Samrae-up, Wanju-kun, Chunbuk, 565-701, Korea*

In automotive industry, the need for weight reduction of a car body has been growing in order to solve the environmental problems in recent years. It is very important for the crashworthiness designs to ensure safety of passengers as well as light-weight. The side members are the mainly absorb the energy at the frontal and rear collisions. Therefore, it is important to investigate their energy absorption and optimize their behavior. It is more efficient that the energy is absorbed by the progressive collapse of members in order to decrease the acceleration transferred to the passengers. Most side members consist of a single-hat-section shape by spot welding. In this study, based on the collapse characteristics of simplified aluminum square section member, the collapse characteristics of Square and hat shaped section member were analyzed. The simplified square section members consist of aluminum, CFRP (carbon fiber reinforced plastics) and aluminum/CFRP members, and the hat shaped section members consist of CFRP and aluminum/CFRP hat shaped members. The aluminum/CFRP members were designed to reinforce the inside of the CFRP member with an aluminum member. Axial collapse tests have been carried out on each of the section members. Test results showed that the aluminum/CFRP member were the most effective energy absorption characteristic among square section members. However CFRP and aluminum/CFRP hat section members were not effective on the energy absorption.

1. Introduction

Currently, the most important objective in designing automobiles is to focus on environment-friendly aspects and safety performance aspects. The requirement of improving fuel efficiency and hence reducing CO_2 emission pushes the automobile industry to use light-weight components. However, the requirement of safety performance such as crash safety, comfort level and multi-functional

---

[†] Corresponding Author: E-mail: iyyang@chosun.ac.kr

program demands tend to increase automobile weights. Therefore, the design of automobile components is should be more concerned on the aspect of securing safety performance, but at the same time, it also should consider reducing weight of automobile structural member.

Side members of automobile front parts are structural members which absorb energy under axial load. The structural members absorb more energy in collision if they have higher strength and stiffness, and stable folding capacity (local buckling). Using the above characteristics on energy absorption, automobiles should be designed lightweight to improve fuel efficiency.

Researches on collapse characteristics of structural member is conducted with numerous materials and various sectional shapes [1-4]. Many studies have been conducted to analyze the collapse characteristics for spot welded hat shaped section member which is nearer to the actual automobile side member[1] and for the simplified seamless section member which made of representative lightweight materials, such as aluminum and composite [2, 3].

In this study, based on the collapse characteristics of simplified aluminum square section member, the collapse characteristics of square and hat shaped section member were analyzed. The simplified square section members consist of aluminum, CFRP (Carbon Fiber Reinforced Plastics) and aluminum/CFRP square member, and the hat shaped section members consist of CFRP and aluminum/CFRP hat shaped member. The axial static collapse tests were performed for each section members.

2. Experimental

2.1. *Specimen*

The aluminum square members were manufactured using a sheet metal of 6063-T5 type with thickness of 1.0mm, and the width of outside of members was 30mm. The CFRP members were made of 8 plies (about 1.0mm) of unidirectional prepreg sheets of carbon/Epoxy (HANKUK Fiber co.) at 90 fiber orientation angle of CFRP and the width of outside of members was 32mm. The aluminum/CFRP compound members were manufactured by wrapping CFRP prepreg sheets outside the aluminum member, were stacked to $[90]_8$ using unidirectional prepreg sheets of carbon fiber where the $0°$ direction coincides with the axis of the members.

During manufacturing by the autoclave, it was manufactured by a heater located inside the circumference of chamber by setting caving temperature of $130°C$ and caving time of 90 minutes. It was manufactured by providing about

0.3MPa compression from outside of vacuum bag with a compressor after vacuuming inside of vacuum bag up to 0.1 Pa by vacuum pump during molding.

All the specimens were cut using a diamond cutter to have the specimen length of 120mm.

2.2. Collapse Test

An axial static collapse test was performed by using universal testing machine. All specimens were compressed to 50% (60 mm) of the whole length (120 mm) in axial direction at a rate of 10 mm/min.

(a) Square section member   (b) Hat shaped section member
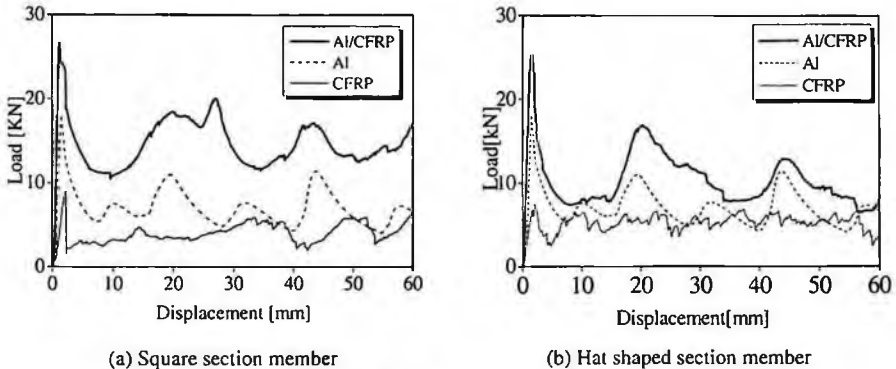
Figure 1. Load-displacement curves of specimens

The absorbed energy is represented by the area under the load-displacement curve shown in Figure 1, and thus obtained by integrating as in Equation (1).

$$E_a = \int_0^S P dS \tag{1}$$

Where, E_a, P and S indicate the absorbed energy, the collapse load, and the length of specimen at collapse, respectively.

The absorbed energy per unit volume is calculated by dividing the absorbed energy with the volume of the collapsed part, as in Equation (2). The absorbed energy per unit mass is calculated similarly by dividing with mass of the collapsed part as in Equation (3).

$$E_v = \frac{E_a}{A\,S} \tag{2}$$

$$E_m = \frac{E_a}{\rho\,A\,S} \tag{3}$$

Where, E_v and E_m are the absorbed energy per unit volume, and the absorbed energy per unit mass, respectively. A and ρ are the cross sectional areas and density of the specimen, respectively.

3. Results and Discussion - *Collapse Characteristics*

The aluminum square member absorbed energy by stable plastic deformation with axis-symmetric mode, and the CFRP square member absorbed energy by unstable brittle failure with folding mode. The aluminum/CFRP square member was stably collapsed with compound folding mode combined two modes as shown Figure 2(c); compound folding mode is defined as a mode that the CFRP member is held between folding of the aluminum member.

(a) Aluminum square member　　(b) CFRP square member　　(c) Aluminum/CFRP square member
Figure 2. Collapse modes of square member

The CFRP hat shaped member was collapsed by matrix crack of transverse with fragmentation mode. This type of collapse mode absorbs most of the energy by matrix crack due to transverse shearing. The aluminum/CFRP hat shaped member was collapsed as the following: the initial collapse, outer CFRP hat shaped member was collapsed stably by entering the fiber in the folding of aluminum member. While the collapse is progressing, the " $\cap$ " shaped part and flat part were split.

(a) CFRP hat shaped member　　　　(b) Aluminum/CFRP hat shaped member
Figure 3. Collapse modes of hat shaped member

Figure 4 and 5 shows the absorbed energy, the absorbed energy per unit volume and the absorbed energy per unit mass for the square and hat shaped

member, the CFRP member with 90° fiber orientation angle of 8 plies, and the aluminum/CFRP member with 90° fiber orientation angle of 8 plies.
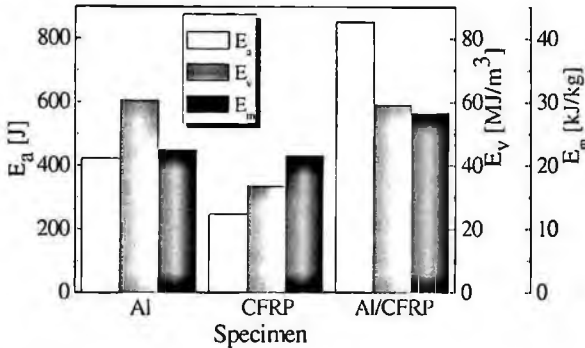
Figure 4. Absorbed energy of the square section member

In the Figure 4, the absorbed energy for aluminum/CFRP member is higher than sum of that for the CFRP and the aluminum member alone. The interaction effect was caused by combining energy absorption due to stable collapse of aluminum member with high collapse loads of CFRP member.

The aluminum and the aluminum/CFRP square member have similar absorbed energy per unit volume, while the CFRP member has the smallest value. Considering that the aluminum member has higher density than the CFRP member, it is worthy to notice that the absorbed energy per unit mass of the aluminum/CFRP member is larger than that of the aluminum member or the CFRP member.
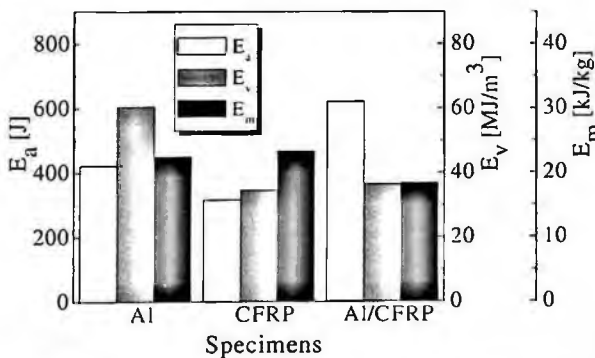
Figure 5. Absorbed energy of the hat shaped section member

In the Figure 5, the absorbed energy for aluminum/CFRP member is lower than sum of that for the CFRP and the aluminum member alone. The interaction effect

was not shown because inner aluminum member applied load to the outer CFRP hat shaped section member in the form of hoop stress therefore they were split each other.

4. Conclusion

We researched collapse mode and energy absorption capability of aluminum, CFRP and aluminum/CFRP square section members and based on the collapse of square section, the collapse characteristics energy absorption capability of hat-shaped section members were analyzed.

The test results are as follows:

1. The aluminum square section member had stable plastic deformation with axis-symmetric mode, and the CFRP square section member had unstable brittle failure with folding mode. The aluminum/CFRP square member had compound folding mode.

2. The absorbed energy for aluminum/CFRP square member is higher than sum of that for the CFRP and the aluminum square member alone. The interaction effect was caused by combining energy absorption due to stable collapse of aluminum member with high collapse loads of CFRP member.

3. In the simplified square section member, the most effective energy absorption characteristic was shown aluminum/CFRP member. However CFRP and aluminum/CFRP hat section member is not effective on the energy absorption because inner aluminum square member and outer CFRP hat shaped section member were split each other.

4. The Light-weight aspect, aluminum/CFRP members are more efficient than CFRP members.

References

1. M. D. White and N. Jones, *Int. J. of Mechanical Science*, Vol. 41, pp. 179-208(1999).
2. M. Avalle and G. Belingardi, *Int. J. of Mechanical Science*, Vol. 39, pp. 575-583(1997).
3. G. L. Farley and R. M. Jones, *Journal of composite Materials*, Vol. 26, pp. 37-50(1992).
4. I. Y. Yang, K. S. Lee, Y. N. Kim, J. O. Chung and C. S. Cha, *Key Engineering Materials*, Vols. 297-300, pp. 183-188(2006).

INFLUENCE OF STACKING CONDITION ON AXIAL COMPRESSION AND BENDING COLLAPSE OF THE HYBRID HAT SHAPED MEMBER

JI HOON KIM

Department of Mechanical Design Engineering, Chosun University, 375 Seosuk-dong Dong-gu Gwang-ju, 501-750, Korea

JUNG HO KIM

Department of Advanced Parts and Materials Engineering, Chosun University, 375 Seosuk-dong Dong-gu Gwang-ju, 501-750, Korea

JUN WOO PARK

Department of Mechanical Design Engineering, Chosun University, 375 Seosuk-dong Dong-gu Gwang-ju, 501-750, Korea

YONG JUN YANG

Department of Advanced Parts and Materials Engineering, Chosun University, 375 Seosuk-dong Dong-gu Gwang-ju, 501-750, Korea

IN YOUNG YANG[†]

Department of Mechanical Design Engineering, Chosun University, 375 Seosuk-dong Dong-gu Gwang-ju, 501-750, Korea

Recently, the structural material which is used mainly in automobile and aircraft industries is changed the Al alloy or composite. The front side members of automobile which supports engine mount and suspension absorb the materials energy during the front-end collision. Generally, when an automobile crashes front-end, axial compression and bending collapse take place on the front side members.

In the study, the hybrid hat shaped members reinforced the inside of the CFRP hat shaped member with the Al member were manufactured. The stacking condition related to the energy absorption besides strength of composite material (CFRP for an anisotropic material) is being considered as an issue for the structure efficiency. So the energy absorption besides strength characteristic of the hybrid hat shaped member under the axial compressive load and the bending collapse load were experimentally investigate. The kinds according to stacking condition(orientation angles) are five [15°, 45°, 90°, 0°/90°, 90°/0°]. Same experiment was performed for the Al member and the CFRP hat

† Corrensponding Auther : E-mail: iyyang@chosun.ac.kr

shaped member to find comparative characteristics of energy absorption besides strength with hybrid hat shaped member. The energy absorption according to stacking condition under axial compression load was most effective when the orientation angle of 90°/0°, 0°/90°. The energy absorption according to stacking condition under bending collapse load was most effective when the orientation angle of 45°. The absorbed energy of hybrid hat shaped member is higher than that the CFRP hat shaped or the Al member.

1. Introduction

Works on the absorption of collision energy in the structural members are carried out widely with various material and cross-sections. And, with ever increasing safety concerns, they are presently applied in various fields including railroad trains, air crafts and automobiles. In addition to this, problem of lighting structural members became important subject by control of exhaust gas emission, fuel economy and energy efficiency. In order to meet these requirements of safety against collision and lighting the members, study on the collision energy absorption characteristics of light weight materials including aluminum and composite material is very active throughout the world.

Collision energy absorption characteristics differ depending upon the material and sectional shape of the structural members; composite material absorbs energy by brittle fracture, while metals absorb it by stable plastic deformation [1-8].

Front-end side members of the automobiles are made of structural members having property of high energy absorption and are generally in the sectional shape of hat type. This side member is receiving axial collapse as well as bending collapse when collided. Therefore, it is important to consider simultaneously axial compression and bending collapse characteristics of side member when the automobiles collide. Shin et al. has studied on collision energy absorption characteristics under axial compression and bending collapse load [8]. In this study, the hybrid hat shaped members reinforced the inside of the CFRP hat shaped member with the aluminum member were manufactured. The stacking condition related to the energy absorption besides strength of composite material (CFRP for an anisotropic material) is being considered as an issue for the structure efficiency. So the energy absorption besides strength characteristic of the hybrid hat shaped member under the axial compressive load and the bending collapse load were experimentally investigate. The kinds according to stacking condition(orientation angles) are five [15°, 45°, 90°, 0°/90°, 90°/0°]. Same experiment was performed for the aluminum member and the CFRP hat shaped member to find comparative characteristics of energy absorption besides strength with hybrid hat shaped member. The energy absorption according to stacking condition under axial compression load was most effective when the orientation

angle of 90°/0°, 0°/90°. The energy absorption according to stacking condition under bending collapse load was most effective when the orientation angle of 45°. The absorbed energy of hybrid hat shaped member is higher than that the CFRP hat shaped or the aluminum member.

2. Experimental

2.1. *Axial Compression Test*

The hybrid side member was made of CFRP hat type sectional shape reinforced by aluminum member inside. Outside of the aluminum reinforcement, CFRP prepreg sheets were laminated and compression formed under vacuum using autoclave.

The specimen for axial compression test was prepared in size of width (horizontal $\times$ vertical) = 30 $\times$ 30 mm^2, flange length = 12 mm and length 120 mm using 1mm thick aluminum and CFRP.

For axial compression test, UTM was used, where two compression zigs were installed in parallel between load cell and actuator. Strain speed was controlled at 10 mm/min for uniform compression to perform quasi-static collapse test. The collapse test was performed with axial displacement controlled to 50% (60 mm) of total length (120 mm).

Absorbed energy in the specimen was calculated by measuring the area of load-displacement curve and integrating it by following eq. (1)

(1) $E_a = \int_0^\delta P dS$

Where, E_a is absorbed energy, P is applied load and S is collapsed specimen length.

In addition, each same axial compression test for aluminum used hybrid side member and CFRP side member were carried out respectively and the axial compression characteristic of hybrid structures that have combine the two materials were compare and examined.

2.2. *Bending Test*

Specimen for bending test was prepared, like in the case of axial compression test, in size of width (horizontal $\times$ vertical) = 30 $\times$ 30 mm^2 ,flange length = 12 mm and length = 490mm using 1mm thick aluminum and CFRP.

4 point bending test was performed in order to make uniform bending moment, to prevent compression fracture by concentrated stress at load points and to prevent fracture by pure bending at all portions of the specimen. In accordance

with ASTM D 6272, specimen length was made in 490 mm, and bending test was performed in speed of 10 mm/min.

Because the weakest characteristic of CFRP is the brittle failure, the initial collapse, resulting in the maximum load, causes rapid destruction and the overall load drops, as a result, there is a decrease in overall absorption energy after the initial collapse. Therefore, the absorbed energy was calculated by integrating the load-displacement curve up to maximum load (fracture point).

In addition, each same bending test for aluminum used hybrid side member and CFRP side member were carried out respectively and the bending collapse characteristic of hybrid structures that have combine the two materials were compare and examined.

3. Results and Discussion

Figure 1. and Figure 2. are shown energy absorption capability under axial compression and under bending collapse for each specimen- aluminum, CFRP, hybrid side member. And figure 3. is shown energy absorption characteristics considered simultaneously axial compression and bending collapse.

The absorbed energy of hybrid side member is higher than that of CFRP side or aluminum member but is lower than that of combined effect of the CFRP side and the aluminum member alone under axial compression loads as shown Figure 1.. The interaction effect was not shown because inner aluminum member applied load to the outer CFRP side member in the form of hoop stress therefore the CFRP side and the aluminum member were split each other. But if the member is stacked so as not to be split each other, it is considered that the energy absorption capability of hybrid member will be improved by interaction effect [4].

The absorbed energy of hybrid side member is higher than that of CFRP side or aluminum member, also is higher than that of combined effect of the CFRP side and the aluminum member alone under bending collapse loads as shown Figure 2.. It is worth noticing that the hybrid side member absorb energy effectively under bending collapse loads. The reason why the synergy effect was interacted by combing energy absorption due to stable plastic deformation of aluminum member with energy absorption due to high load of CFRP side member.

In the energy absorption characteristics considered simultaneously axial compression and bending collapse (Figure 3.), the most effective energy absorption characteristics was shown hybrid side member.
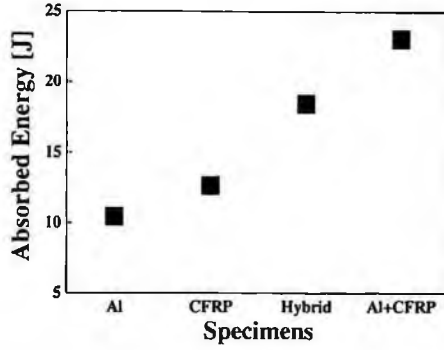
Figure 1. Comparison absorption capability under axial compression test
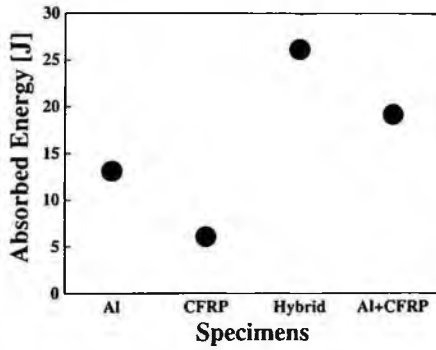
Figure 2. Comparison absorption capability under bending test
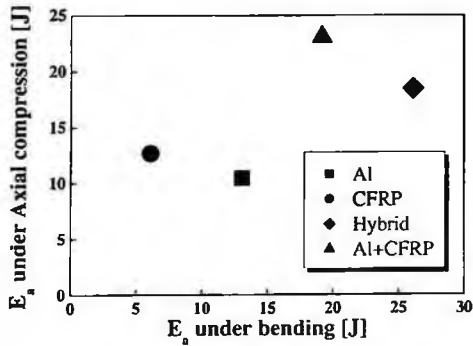
Figure 3. Relationship between Absorbed energy under axial compression and bending loads

4. Summary

In this study, energy absorption characteristics of hybrid side member under static axial compression and bending collapse loads was experimentally investigated. Also same experiment was performed for pure aluminum and composite material to find comparative characteristics of energy absorption with the hybrid side member up to maximum load (fracture point). The results are as follows:

1. The absorbed energy of hybrid side member is higher than that of CFRP side or aluminum member but is lower than that of combined effect of the CFRP side and the aluminum member alone under axial compression loads.
2. The absorbed energy of hybrid side member is higher than that of combined effect of the CFRP side and the aluminum member alone by synergy effect was interacted by combing energy absorption due to stable plastic deformation of aluminum member with energy absorption due to high load of CFRP side member under bending collapse loads.
3. In the energy absorption characteristics considered simultaneously axial compression and bending collapse, the most effective energy absorption characteristics was shown hybrid side member.

References

1. M. D. White and N. Jones, *International Journal of Mechanical Science* Vol. 41, pp. 179-208, (1999a).
2. M. D. White, N. Jones and W. Abramowicz, *International Journal of Mechanical Science* Vol. 41, pp. 209-233, (1999b).
3. C. S. Cha, J. O. Chung, J. W. Park, Y. N. Kim and I.Y. Yang, *KSME International Journal* Vol. 17, pp. 501-510, (2003).
4. I. Y. Yang, K. S. Lee, Y. N. Kim, J. O. Chung and C. S. Cha, *Key Engineering Materials* Vols. 297-300, pp. 183-188, (2006).
5. A. A. Singace, *International Journal of Mechanical Science* Vol. 41, pp. 865-890, (1999).
6. S. K. Kim, K. H. Im, Y. N. Kim, J. W. Park, I. Y. Yang and T. Adachi, *Key Engineering Materials* Vols. 233-236, pp. 239-244, (2003).
7. Y. N. Kim, J. J. Hwang, K. Y. Baek, C. S. Cha and I. Y. Yang, *KSME International Journal* Vol. 17, pp. 48-56, (2003).
8. C. Shin, J. J. Lee, K. H. Kim, M. C. Song and J. S. Huh, *Composite Structures* Vol. 57, pp. 279-287, (2003).

A STUDY ON THE DRILLING CHARACTERISTICS ACCORDING TO DRILL DIAMETER OF LAMINATE COMPOSITE

SEUNG CHUL LEE*

Department of Mechanical Engineering, Chosun University, Graduate School Gwangju, Korea

SEONG TAEK JEONG

Small Business Corporation, Gwangju, Korea

JONG NAM PARK

Department of Computer Mechanic, Chosun College of Science & Technology Gwangju, Korea

GYU JAE CHO[†]

Department of Mechanical Engineering, Chosun University Gwangju, Korea

The purpose of this paper is to examine the drilling characteristics of laminated carbon fiber reinforced composite based on its drilling diameter. Carbon fiber reinforced plastic is characterized by super light weight, high non-rigidity and specific strength, and excellent fatigue characteristics, vibration attenuation and dimensional stability. In this study, the effect of feed speed on cutting force was measured and analyzed for three carbide drill whose diameters were φ 8, φ 10 and φ 12mm respectively at two different cutting speeds of 25.12m/min and 47.1m/min. In addition, roughness of the internal surface of the drilled hole was examined using the surface roughness surface test. It was shown that when the lamination thickness was small, the effect of feed speed on cutting force was small but under the thickness of 32 plies or more, cutting force increased significantly as the feed speed was increased. At the drill diameter of φ 8mm, thrust hardly changed but as the diameter got bigger, it also increased noticeably.

1. Introduction

In today's rapidly developing and highly specialized industrial society, it is most important to develop new materials and properly apply and use those materials[1~3]. For the automobile industry in particular, it is considered the

---

[†] Corresponding Author: kjcho@chosun.ac.kr

most effective alternative for improving fuel efficiency to make the car body lightweight. The most representative technology that has been developed so far to make the car body lightweight is to make the structure with such lightweight materials as super lightweight steel and aluminum composites[4].

Performance of structures like car body is significantly influenced by the joint. Once their surfaces are processed, separately manufactured structures are either bonded together using the adhesive or mechanically tightened together using bolts and nuts. In order to use bolts, it is necessary to make holes.

In this research, drilling characteristics of CFRP composite were examined based on lamination thickness and drilling diameter, in order to propose qualitative drilling conditions for optimum drilling techniques which are practical and highly efficient.

2. Experimental Setup and Experiment Method

The specimens used for this study were unidirectional Carbon Fiber/Epoxy Resin Prepreg sheets (CU125NS). They were laminated using the method shown in Fig. 1. The specimen with 48 plies was laminated by $[0°/45°/90°/-45°]6s$, the one with 32 plies by $[0°/45°/90°/-45°]4s$, and the other with 16 plies by $[0°/45°/90°/-45°]2s$. The forms of the specimens were made using the autoclave. In order to be fixed to test jigs for experiment, the specimens were cut into 30mm × 30mm sizes using the diamond wheel cutter.

Fig. 2 shows the schematic of the experimental setup. The device used for the experiment was a vertical machining center (Hwachon, HIPLUS-V4). On its vise, a jig manufactured for the experiment was fixed and on that jig, the object to be cut was fixed. The cutting force was measured using a real-time monitoring system, a rotary tool dynamometer (Kistler, Type 9123c), in wireless data transmission mode. At the time of cutting, the force applied to the tool and its cutting edge was amplified by the charge amplifier and recorded on the data logger. The recorded signal was once again amplified, and went through A/D conversion at Dynoware (Kistler, Type 2825A). The converted data was analyzed for torque and thrust.
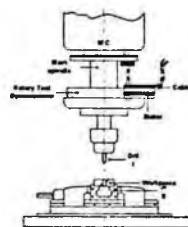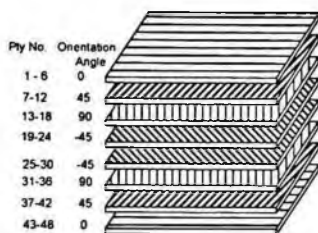
Fig. 1 Stacking sequences of multi-direction hand lay-up.
set up

Fig. 2 Schematic of experimental

In this experiment, the effect of drill diameter and lamination thickness on the drilling characteristics was examined using the carbide drill of which point angle is 118°, relief angle 11° and twist angle 30°. For this, three types of drills whose diameters were φ 8, φ 10 and φ 12mm were used and the cutting speed was fixed to 25.12m/min and 47.1m/min. In addition, in order to examine the effect of feed speed on the cutting speed, drilling was carried out at four drilling speeds of 5, 10, 40 and 60mm/min.

3. Experiment Results and Considerations

3.1. Relationship between cutting force and feed speed with respect to specimen thickness and drill diameter

Fig. 3 (a), (b) and (c) show the relationship between cutting force and feed speed with respect to specimen thickness and drill diameter at the fixed cutting speed of 25.12m/min.

As shown in Fig. 3 (a), for the laminate whose thickness was 16 plies, cutting force did not change significantly when the drill diameter changed. In other words, thrust changed by about 40N because of the feed speed difference.

Fig. 3 (b) and (c) show the specimens of the laminate composites whose thicknesses were 32 plies and 48 plies respectively. Unlike the 16-ply thick specimen, thrust rapidly increased when the feed speed became higher than 10mm/min, resulting in a considerable difference of thrust as about 170N.
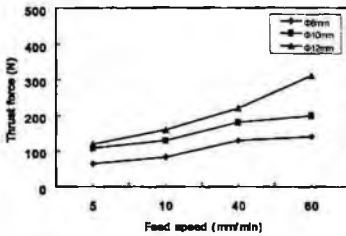
(a) Stacking sequences of specimens ([0°/45°/90°/-45°]2s)
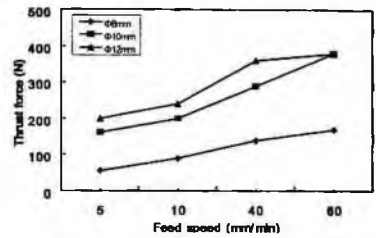
(b) Stacking sequences of specimens ([0°/45°/90°/-45°]4s)
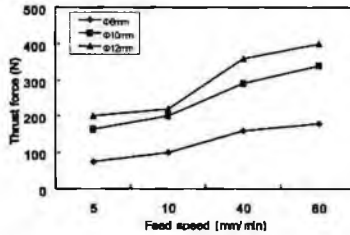
(c) Stacking sequences of specimens ([0°/45°/90°/-45°]6s)

Fig. 3 Relationship between cutting resistance and feed speed with respect to thickness of specimens (V: 25.12m/min)

When the feed speed was increased, thrust also increased. The cutting force for the drill diameter of φ 8mm was greatly different from thrusts for the drill diameters of φ 10 and φ 12mm. It seems to be because as the drill diameter gets smaller, drilling space becomes smaller and thus smaller cutting force is generated.

Fig. 4 shows the relationship between cutting force and feed speed with respect to specimen thickness and drill diameter at the fixed cutting speed of 47.1m/min. As shown in Fig. 4 (a), when the feed speed was 5mm/min, thrust of about 40N was generated but there was hardly a difference in thrust with regard to the drill diameter.

In Fig. 4 (b) and (c), at the drill diameters of φ 10mm and φ 12mm, thrusts were almost the same but about 40N larger than the one for the drill diameter of φ 8mm, which were much smaller than those generated when the specimens were drilled at the cutting speed of 25.12m/min.

With regard to the drill diameter, less cutting force was generated as the feed speed was increased, when the cutting speed was 47.1m/min rather than when it was 25.12m/min. When the specimen was drilled with φ 8mm drill, cutting force was hardly influenced by the specimen thickness. But, when it was

drilled with φ 10mm and φ 12mm drills, cutting force was significantly influenced by the specimen thickness. When the specimen was 16-ply laminate composite, the difference of cutting force was big but when the specimens were 32- and 48-ply laminate composites, there was hardly any difference in cutting force. This tendency existed in the relationship between specimen thickness and drill diameter, regardless of cutting speed.
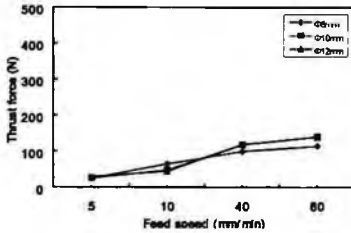
(a) Stacking sequences of specimens ([0°/45°/90°/-45°]2s)
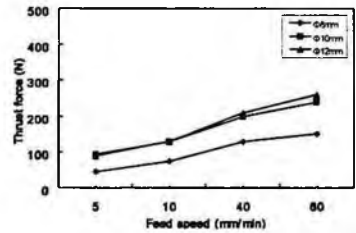
(b) Stacking sequences of specimens ([0°/45°/90°/-45°]4s)
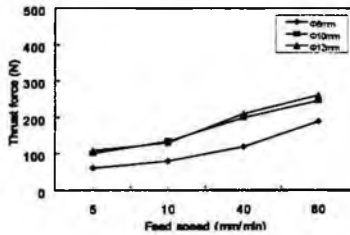
(c) Stacking sequences of specimens ([0°/45°/90°/-45°]6s)

Fig. 4 Relationship between cutting resistance and feed speed with respect to thickness of specimens (V: 47.1m/min)

3.2. Effects of drill diameter and specimen thickness on surface roughness

Fig. 5 shows the average of surface roughness values measured for the laminate composed as [0°/45°/90°/-45°]6s, with changing the feed speed to 5, 10, 40 and 60 mm/min at the fixed cutting speed of 25.2m/min. Measurement was done for the length of 4mm, leaving 1mm respectively at the beginning and at the end of total drilling length, in consideration of the specimen thickness of 6mm. The measurement range was 20 μm, and the average value of 3 Ra measurements was used for analysis

As shown in the figure, surface roughness was measured as 0.4 μm when the feed speed was 5mm/min but it increased significantly to 1.7 μm when the feed speed was increased to 60mm/min.

The value of roughness measured inside the hole drilled with φ 8mm drill was smaller than those of the holes drilled with φ 10mm and φ 12mm drills.

Surface roughness had a shape of periodic ruggedness, which probably resulted from joints in the laminate which was made as plies were glued to each other. This phenomenon became more noticeable at the feed speed of 60mm/min and when the drill diameter was larger, the value of roughness between ply surfaces became larger.

Fig. 6 shows the surface roughness measured inside the hole drilled at the cutting speed of 47.1m/min. As shown in the figure, surface roughness had almost the same shape as that of the hole drilled at the cutting speed of 25.12m/min. However, when the feed speed became higher than 10mm/min, the value showed a difference of about 0.3 μm depending on the drill diameter.

Comparison between Fig. 5 and Fig. 6 shows that the surface of a hole became smoother when it was drilled at the cutting speed of 47.1m/m than at 25.12m/min under the same drilling conditions. It is because, under the same feed speed, when the rotation per minute (rpm) is faster, the surface area to be drilled per cutting nose of the drill becomes smaller.

It was also shown that when the hole was drilled with the drill of the smallest diameter (φ 8mm), surface roughness was the least. However, the thickness of the specimen appeared to hardly influence the surface roughness.
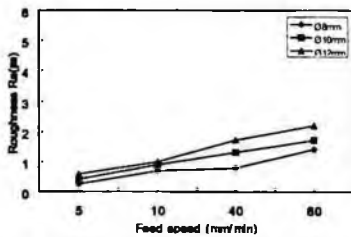
Fig. 5 Surface roughness of holes (V: 25.12m/min)   Fig. 6 Surface roughness of holes (V: 47.1m/min)
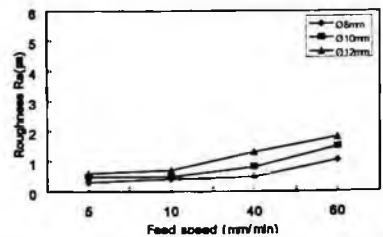
4. Conclusion

Through the study of mechanical characteristics with regard to lamination composition and drill diameter, the following results were obtained.

1. With the drill whose diameter was φ 8mm, thrust hardly changed with regard to the feed speed but as the drill diameter became larger, it also increased remarkably.

2. The value of surface roughness inside the drilled hole was 0.4 μm when the feed speed was 5mm/min but it increased to 1.7 μm at the feed speed of

60mm/min. When the drill diameter was the smallest as φ 8mm, the surface roughness had the smallest value.

References

1. P. K. Malick, Marcel Dekker, Inc, 3~4 1988
2. Jcantwell W. J. and Morton J., *Composites Structures*, Vol. **3**, 241~257 (1985)
2. C. Reugg and J. Habermeir, *Processings of ICCM 3*, Vol. **2**, 1740~1755 (1980)
3. M. Ramulu and D. Arola, *Int. J. Mach Tools. Manufact*, Vol. **34**, 295~313 (1994)
4. W. S. Lau, M. Wang and W. B. Lee, *Int. J. Mach. Tools. Manufact.* Vol. 30, 297~308 (1990)

EFFECT OF WEAR TO THE FATIGUE LIFE OF SHAFT BASED ON PRODUCT LIFECYCLE MANAGEMENT

YOU-TANG LI, YAO-BING WEI, MING SONG

Key Laboratory of Digital Manufacturing Technology and Application,
Ministry of Education, Lanzhou University of Technology,
Lanzhou, Gansu 730050, China

Product lifecycle management is one of the main developmental aspects of advanced manufacturing technology. Anti-fatigue design is a key content in product lifecycle management and there are many factors to affect the fatigue life of parts. The mechanics model for assessing the fatigue life of shaft is set up, and the main factors that affect the fatigue life of shaft are summarized. The assessment method of fatigue life for shaft is set up according to the traditional fatigue life estimation and the effect factor. The effect of wearing parameter to fatigue life is analyzed and the results show that the wear is an important factor to affect the fatigue life.

1. Introduction

The Product lifecycle management (PLM) concept holds the promise of seamlessly integrating all the information produced throughout all phases of a product's life cycle to everyone in an organization at every managerial and technical level, along with key suppliers and customers[1]. A lifecycle assessment (LCA) gives a general overview of resource consumption and environmental stress in the entire lifecycle of the product[2].

Anti-fatigue design is a key content in product lifecycle management. The shaft is used in engineering widely, such as machine tool, automobile, steamship and so on. There are many factors to affect the fatigue life of component. Therefore, it is very difficulty for determining a designed criterion exactly. An anti-fatigued criterion of annularly breached spindle on mechanical design[3] and an uniform model and fracture criteria of annularly breached bars under bending[4] have been put forward, respectively. The cumulative damnification is the effective method in limited lifecycle design, and Miner's rule, modified Miner's rule, relative Miner's rule, Manson's bilinear theory and Corten-Dolan's theory are applied in actual design at present and the precisions of lifecycle estimate are between 1/3 and 3[5]. These methods are suit to the strength assessment and life estimation of finite life under variable amplitude loading. An assessment rule of fatigue life of shaft based Corten-Dolan's theory and modified Miner's rule has been put forward[6], but the influencing factors that considered

in the rule is not roundly. For designing the fatigue life of shaft exactly and putting forward an effective assessment method, the influencing factors must be analyzed completely. The mechanics model for assessing the fatigue life of shaft is set up, the main factors that affect the fatigue life of shaft are summarized, the assessment method of fatigue life for shaft is put forward according to the traditional fatigue life estimation and the effect factor, and the effect of wearing parameter to fatigue life is analyzed in this paper.

2. Influencing Factors of Fatigue Life and Mechanical Model

2.1. *Influencing Factors of Fatigue Life of Shaft*

There are many factors, which include materials property, geometrical factors, notched factors, boundary conditions, environmental conditions and loading conditions, to affect the fatigue life of shaft. The main factors can be classified as Fig.1. The every factors are affected each other in the cycle life of machine.
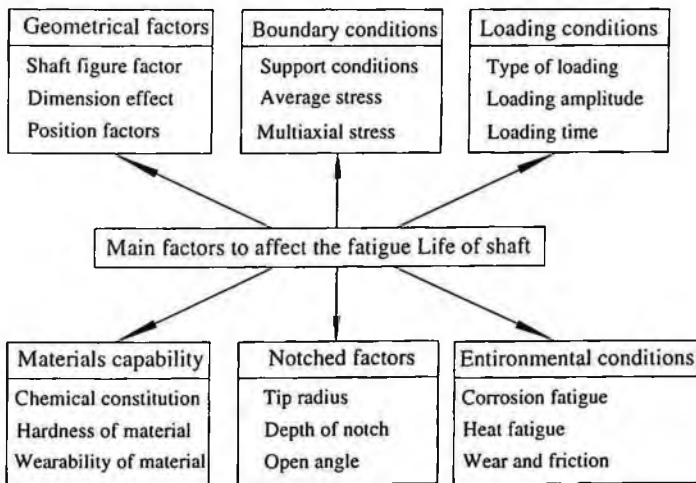
Fig.1 Factors to affect the fatigue life of shaft

2.2. *Mechanical Model of Shaft for Life Estimation*

The annular notch is the main factor to affect the fatigue life of shaft in engineering practice. The annular notches such as tool back groove and installation groove are existed usually in shaft and the stress concentration is existed at the tip field of notch. On the other hand, the crack may be existed in the shaft and the singularity at the tip of crack should be expressed by stress intensity factor. If we regard tip radius, depth and field angle of notch or crack as descriptive parameter, the crack and notch can be served as breach uniformly.

The mechanical model of shaft for life estimation can be shown as Fig.2.
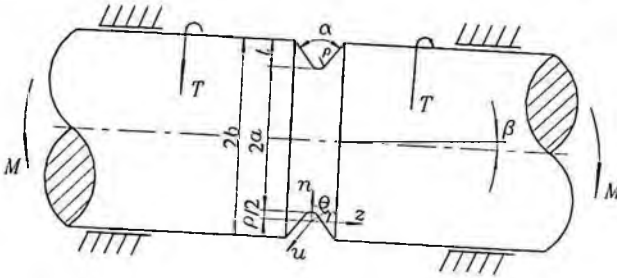
Fig.2 Mechanical model of shaft for life estimation

The notch can be synthesized to a unitive notch in anti-fatigue life design and the description parameters of unitive notch are tip radius, depth and open angle. All the breaches according to the change of parameters are shown in Fig.3.
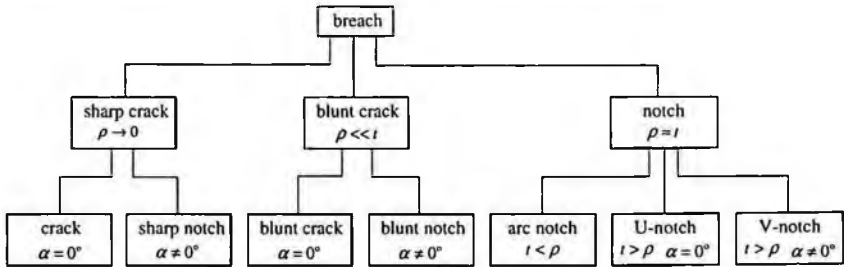
Fig.3 All kinds of breaches according to the change of parameters

3. Fatigue Strength and Fatigue Life Estimation

3.1. *Fatigue Strength*

The strength criterions of modified miner's rule can be shown as following

$$n = \frac{\sigma_{-1D}}{\left(\sum_{i=1}^{l} n_i \sigma_i^m / aN_0\right)^{1/m}} \geq [n] \tag{1}$$

When a is elected to the test value of cumulative damnification in loading chart, D_f, the modified miner's rule is called relative Miner's rule. The strength criterion of Corten-Dolan's theory can be written as following

$$n = \frac{\sigma_1}{\sigma_q} = \frac{\sigma_1}{\left(\sum_{i=1}^{l} n_i \sigma_i^d\right)^{1/d}} \geq [n] \tag{2}$$

where σ_1 is the maximal stress (MPa), N_1 fatigue life in maximal stress(c), d the exponential of Dortem-Dolan express, m the exponential of S-N curve.

3.2. Traditional Fatigue Life Estimation

For every circular loading, the damnification can be calculated according to the loading chart method and the fatigue life can be estimated according to certain cumulative damnification theory. For modified miner's rule and Corten-Dolan's theory, the fatigue life of shaft can be written as followings[6].

$$N = a\sum_{i=1}^{i} n_{0i} \left/ \sum_{i=1}^{i} \frac{n_{0i}}{N_i} \right. \tag{3}$$

$$N = N_1 \left/ \sum_{i=1}^{i} \alpha_i \left(\frac{\sigma_i}{\sigma_1}\right) \frac{n_{0i}}{N_i} \right. \tag{4}$$

where α_i is the ratio of cycle times in ith stress level than total cycle times.

3.3. Modified Fatigue Life Estimation

The precisions of fatigue life estimation of traditional fatigue life estimation are between 1/3 and 3. The errors are caused by the every complicated condition, such as materials capability, geometrical factors, notched parameters, boundary, environmental conditions and loading conditions. The equation of fatigue life estimation for modified miner's rule and Corten-Dolan's theory can be modified as following, respectively.

$$N = K_1 K_2 K_3 K_4 K_5 K_6 a \sum_{i=1}^{i} n_{0i} \left/ \sum_{i=1}^{i} \frac{n_{0i}}{N_i} \right. \tag{5}$$

$$N = K_1 K_2 K_3 K_4 K_5 K_6 N_1 \left/ \sum_{i=1}^{i} \alpha_i \left(\frac{\sigma_i}{\sigma_1}\right) \frac{n_{0i}}{N_i} \right. \tag{6}$$

where K_1, K_2, K_3, K_4, K_5 and K_6 are the influencing coefficients for materials capability, geometrical factors, notched parameters, boundary conditions and environmental conditions and loading conditions, respectively. The influencing coefficient of notched parameters, K_3, can be estimated by the chart of tip radius, depth and open angle of notch to stress concentration factor[7].

4. Effect of Wear to Fatigue Life of Shaft

The effect of wear to the fatigue life of shaft includes two ways. The first one is the deflection, β, will be changed which affect the influencing coefficient, K_4, because the wear quantities between front and back support place are different. The second one is the environmental conditions will be changed which affect the influencing coefficient, K_5. The wear quantities of front and back support place

should be known for determining the influencing coefficients, K_4 and K_5.

4.1. *Wear Quantities of Shaft*

The directions of wear of front and back support place are different, which induce the change of the deflection, β. The wear quantities of the principal axis of a lathe (The serial number is C6140 and made in Shenyang Machine Tool Plant) have been measured from 1999 every year. The wear quantities of front and back support place are shown in Tab.1.

Table 1. Wear quantities of a principal axis

Year	Front	Back	Deflection	Year	Front	Back	Deflection
1999	0.055	0.035	0.00619	2003	0.266	0.161	0.02948
2000	0.108	0.067	0.01203	2004	0.315	0.189	0.03479
2001	0.156	0.102	0.01781	2005	0.363	0.217	0.04003
2002	0.207	0.134	0.02354	2006	0.411	0.245	0.04529

4.2. *Effect of Wear to Fatigue Life of Shaft*

The influencing coefficient, K_4, is affected by support condition, average and multi-axial stress, which can be written as following

$$K_4 = k_1 k_2 k_3 \tag{7}$$

where k_1, k_2, k_3 are the influencing coefficient of support condition, average and multi-axial stress, respectively. The influencing coefficient of multi-axial stress, k_3, in I-III mode can be written as following

$$k_3 = f_{3,\alpha} / \sqrt{(f_{1,\alpha}^2 + f_{3,\alpha}^2)(1 - \nu^2)} \tag{8}$$

where $f_{1,\alpha}$ and $f_{3,\alpha}$ are the dimensionless factor near the tip of notch of bending stress, σ_1, and torsional stress, σ_3. The $f_{1,\alpha}$ and $f_{3,\alpha}$ can be calculated with finite element method and the results in different deflection, β, when $\rho/b=0.2$, $a/b=0.85$ and $\alpha=60^0$, are shown in Fig.4. We can know from Fig.4 that dimensionless factor, $f_{1,\alpha}$, increase with the increase of deflection, β, and $f_{3,\alpha}$ are not changed nearly. The results of influencing coefficient, k_3, with different deflection, β, are shown in Table 2.

We can know from Table 2 that the influencing coefficient, k_3, will decrease gradually with the increase of deflection, β, i.e. the fatigue life will decrease gradually with the increase of wear quantities of the shaft. In the process of design, the average value of influencing coefficient, k_3, should be considered. The effect of wear to the environmental conditions, K_5, and other influencing coefficient, can be determined by experiment or other method.
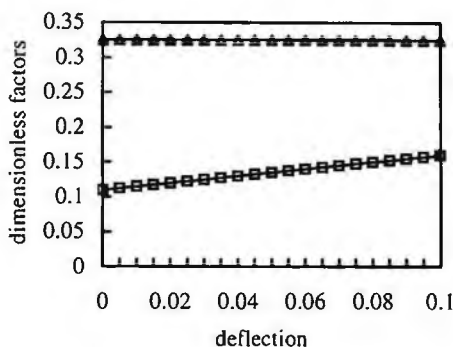
Fig.4 Dimensionless factor vs deflection, β,

Table 2. The influencing coefficient, k_3, vs deflection

Deflection	0.01	0.02	0.03	0.04	0.05	0.06	0.07	0.08
$f_{1,a}$	0.116	0.121	0.126	0.132	0.137	0.142	0.148	0.153
$f_{3,a}$	0.325	0.326	0.327	0.328	0.329	0.330	0.330	0.331
k_3	0.981	0.977	0.972	0.966	0.962	0.957	0.951	0.945

5. Conclusions

(1) The fatigue life of shaft is affected by many factors, such as materials capability, geometrical factors, notched parameters, boundary conditions, environmental conditions and loading conditions.

(2) The fatigue life can be estimated by modified rule, in which the effect of materials capability, geometrical factors, notched parameters, boundary, environmental conditions and loading conditions have been considered.

(3) The wear affects the fatigue life, and which will decrease gradually with the increase of wear quantities. In the process of design, the average value of influencing coefficient, k_3, should be considered.

References

1. R.Sudarsan, S.J.Fenves, R.D.Sriram. *Computer-Aided Design*, 37, 1319 (2005)
2. J. Glahn, K. Heydenreich. *Corporate Environmental Strategy*. 8,186 (2001)
3. Y.T.Li, P.Ma, C. F. Yan. *Key Engineering Materials*. 321-323, 755 (2006)
4. Y.T.Li, Z.Y.Rui, C.F.Yan. *Key Engineering Materials*. 321-323, 751 (2006)
5. S. B. Zhao. *J. of machine design*.17(6), 5 (2000)
6. Y.T.Li, P.Ma, J.T.Zhao. *Materials Science Forum* 561-565, 2253 (2007)
7. Y.T.Li, Z.Y.Rui, C.F.Yan. *Key Engineering Materials*. 274-276, 211 (2004)

COMPRESSIVE FATIGUE STENGTH OF AL-ALLOY FOAM WITH DIFFERENT THICKNESSES

MYNUL HOSSAIN, ILHYUN KIM, KWAN-WOO SHIN, AMKEE KIM[†]

Division of Mechanical and Automotive Engineering, Kongju National University,
kongju, Chungnam 314-701, Korea

Aluminum foam filled composite panels have enormous potential for application as light weight structural members as well as the energy absorber during crushing. In such applications the mechanical properties of foams are of paramount importance. The compressive fatigue tests on the closed cell Al-Si-Ca alloy foams with different thicknesses were performed using a load ratio of 0.1 in this study. The quasi-static and cyclic compressive behaviors were obtained respectively. The fatigue stress-life (S-N) curves were evaluated from the obtained cyclic compressive behaviors. It turned out that the onset of shortening of thinner foam took place earlier and the fatigue strength showed the higher value for the thicker foam. In addition, the seven times the cell size criterion was not valid in the fatigue strength.

1. Introduction

Metallic foams, especially aluminum (Al) alloy foams have received a considerable amount of attention in recent years because of their extremely low density and unique functional properties such as impacting energy absorption, sound absorption, flame resistance and heat resistance. They are growing in use in sandwich structure for panels, tubes, shells, packaging, crash protection devices and the weight sensitive construction parts in transportation and aerospace industries. Parts in vehicles and components in airplanes or helicopters are frequently subjected to vibrations and repeated strains, more commonly the cyclic compressions. In many potential applications such as in sandwich panels, the foam core is loaded in compression [1].

The monotonic compressive mechanical properties of Al-alloy foams have been extensively studied [2-6] during last few decades. One of main findings from mechanical properties studied by the static test is in that the strength dependency on the size of specimen disappears if the dimension is chosen so that the edge length in all cases was more than seven times the cell size [7-10].

[†] Corresponding author: E-mail: amkee@kongju.ac.kr Phone: +82-41-550-0258 Fax: +82-41-555-9123

The apparent maximum values of nominal stresses in such vibrations and/or cyclic compressions are often much less than the static yield stress of the material. Even though these cyclic loadings do not cause any instant failure, in long run they may lead to fatigue damage of the materials which causes catastrophic consequences. Thus the cyclic stress-strain response of metallic foams has become at the center of attention for many of the metal foam researchers recently, showing that the foam structures subjected to repeated load rapidly lose their strength after a certain number of cycles depending on the stress amplitude and the mean stress. However, the size dependency of the cyclic stress-strain response and strength of metallic foams have not been investigated so far.

In this paper, we studied the size effect on the cyclic compression fatigue properties of closed cell Al-alloy foam by performing the compression-compression fatigue test. As result, the seven times the cell size criterion turned out to be invalid for the fatigue test.

2. Experimental

2.1. *Materials and specimens*

The material used in this study was closed cell Al-Si-Ca foam obtained from commercial manufacturer (FOAMTECH Korea). The material was produced using the melt-based process and was obtained in a form of panel. The foam had a relatively uniform microstructure. The foam used in this study had the cell diameter of about 3~4 mm and the relative density (density of foam / density of constitute material) of about 0.11. The specimens of three different sizes, 40x40x40 mm^3, 40x40x60 mm^3 and 40x40x80 mm^3 were machined from the foam panel for static and fatigue tests.

2.2. *Test method*

All the cyclic and static compression tests on specimens with different thicknesses (40mm, 60mm, 80mm) along the thickness direction were performed using an MTS 858 servo-hydraulic test machine at a load ratio of R = 0.1 and four different endurance ratios ($|\sigma_{max}|/ \sigma_{pl}$) in the range of 0.6 to 0.9. Here, σ_{max} is the maximum stress in the fatigue cycle and σ_{pl} is plateau stress taken as an average within plateau region. The frequency of cyclic load was 50 Hz. The conditions for fatigue test are shown in Table 1.

Table 1. Specification of the fatigue test

Thickness (mm)	Endurance ratio ($|\sigma_{max}/\sigma_{pl}|$)	Relative density (ρ^*/ρ_s)	σ_{pl} (MPa)
40	0.6	0.106	2.1
	0.7	0.114	
	0.8	0.105	
	0.9	0.110	
60	0.6	0.109	2.1
	0.7	0.109	
	0.8	0.109	
	0.9	0.105	
80	0.6	0.110	2.1
	0.7	0.113	
	0.8	0.107	
	0.9	0.108	

3. Results and Discussion

3.1. *Quasi-static compression behavior*

In general, when foam is compressed, the stress-strain curve shows three regions. At low strains, the foam deforms in a linear elastic way. There is then a plateau of deformation at almost constant stress and finally there is a region of densification as the cell was crushed together. Figure 1 shows the static stress-strain curves of Al-Si-Ca foam having different thicknesses in this study. From the stress-strain curves, it is found that the linear elasticity only appears at a very low compressive strain (about -0.03 <) where partially reversible cell walls bending occurs, followed by a plastic plateau stress at which successive bands of cells collapse, buckle and yield, and finally densification appears after a strain of approximately -0.45 where the stress rises sharply as the compaction commences.

For different thicknesses, the curves were similar to each other having approximately same values of Young's modulus, yield stress and plateau stress. In fact, the effect of thickness on the compressive properties was not manifest implying that the strength dependency on the size of specimen disappears if the dimensions of edge in all cases are more than seven times the cell size [7-10]. The obtained plateau stress for specimens with different thicknesses of 40 mm, 60 mm and 80 mm was about -2.1 MPa.
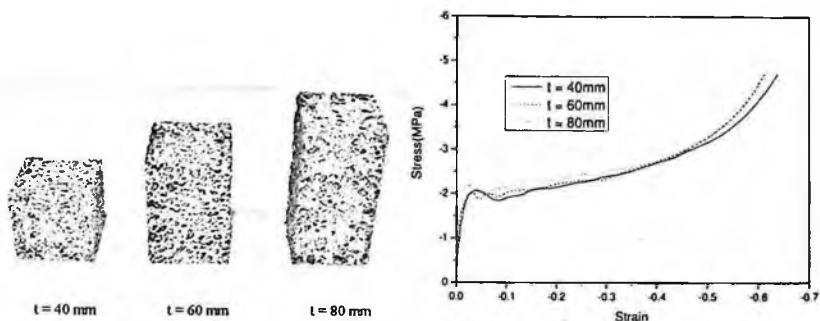
Figure 1. The static compressive stress-strain curve of Al-Si-Ca foam

3.2. Compressive fatigue behavior

The strain versus number of cycle curves of Al-Si-Ca foams with different thicknesses are shown in Figure 2. All the figures show that the compressive strain increases with number of cycle which means that progressive shortening of the specimen takes place with increasing number of cycle. However, a transition is evident, at a strain of about -0.05 for all endurance ratios, where the rate of shortening is accelerated abruptly. This sudden rise of the rate of progressive shortening takes place at a strain level of about -0.04 which is equal to the static yield strain of the foam. The numbers of cycles at which the abrupt increase of shortening takes place were taken as the fatigue life at that stress in this study.

Figure 3 represents the S-N curves of Al-Si-Ca foam based on Figure 2. For the specimens with thicknesses of 40 mm, 60 mm and 80 mm, all failures of specimens were observed before 10^7 cycles for endurance ratios of 0.6~0.9. The endurance strengths for the specimens with thickness of 80 mm, 60mm and 40 mm extrapolated to 10^7 cycles [11-13] are about -0.57, -0.52 and -0.33 respectively. From Figure 3 it is evident that the fatigue life is increased with increasing specimen thickness.

It is also noticed that the endurance strength of the foam at 10^7 cycles decreases as the thickness of foam decreases although the static strength such as yield stress and plateau stress of different thickness specimens were almost same.

(a)

(b)

(c)
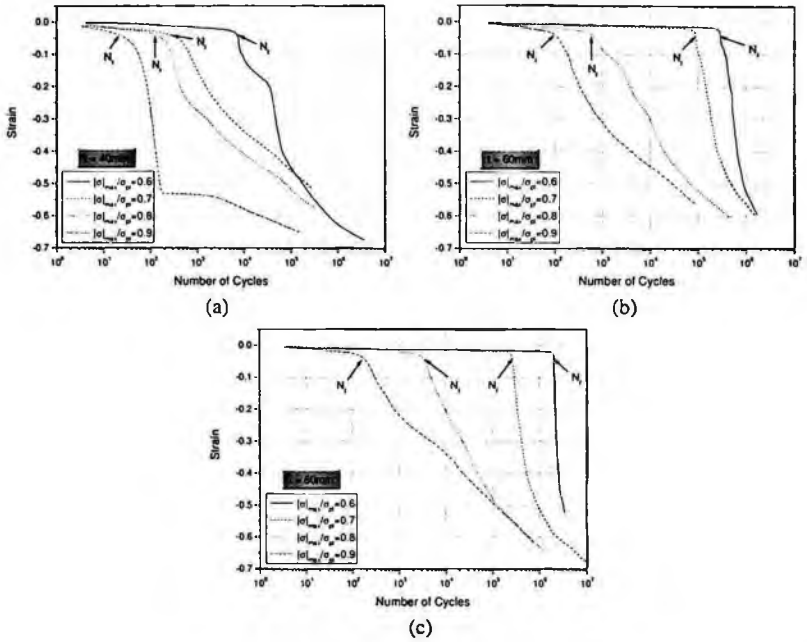
Figure 2. The strain versus number of cycle curves of Al-Si-Ca foams showing the progressive shortening of specimens with (a) t = 40mm, (b) t = 60mm and (c) t = 80mm
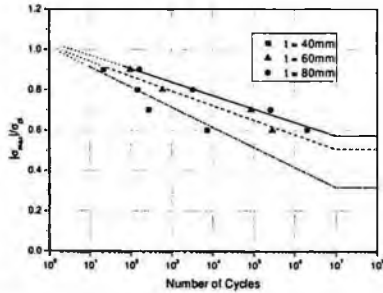
Figure 3. The S-N curves of Al-Si-Ca foams in case of compressive fatigue test

4. Conclusions

The quasi-static and fatigue behavior of closed cell Al-Si-Ca foam with different thicknesses produced by melt-based method were studied. The results can be summarized as follows:

1. Fatigue failure in Al-Si-Ca foams occurred at the quasi-static yield strain of the foams where the value was -0.04.
2. The same yield stress and plateau stress were obtained from specimens with difference thicknesses (40 mm, 60 mm and 80 mm).
3. The endurance strength of Al-Si-Ca foams, however, was increased as the characteristic thickness of the foam was increased although all the dimensions of specimen were satisfactory with the seven times the cell size criterion.

Acknowledgments

References

1. O.B. Olurin, N.A. Fleck and M.F. Ashby, *Metal foam and porous metal structures, Verlag MIT Publishing.* 365 (1999).
2. E. Andrew, W. Sanders and L.J. Gibson, *Mat. Sci. and Engg.* **270**, 113 (1999).
3. T.G. Nieh, K. Higashi and J. Wadsworth, *Mat. Sci. and Engg.* **283**, 105 (2000).
4. D. Ruan, G. Lu, F.L. Chen and E. Siros, *Comp. Struct.* **57**, 331 (2002).
5. E. Koza, M. Leonowicz, S. Wojciechowski and F. Simancik, *Mat. Lett.* 58, 132 (2003).
6. Y. Sugimura, J. Meyer, M.Y. He, H. Bart-Smith, J. Grenestedt and A. G. Evans, *Acta Mater.* **45**, 5245 (1997).
7. Insu Jeon, Tadashi Asahina, *Acta Mater.* **53**, 3415 (2005).
8. U. Ramamurty, A. Paul, *Acta Mater.* **52**, 869 (2004).
9. A-F. Bastawros, H. Bart-Smith, A. G. Evans, *J. Mech. Phys. of Solids.* **48**, 301 (2000).
10. E.W. Andrews, G. Gioux, P. Onck, L.J. Gibson, *Int. J. of Mech. Sci.* **43**, 701 (2001).
11. A-M Harte, N.A. Fleck and M.F. Ashby, *Acta Mater.* **47**, 2511 (1999).
12. Y. Sugimura, A. Rabiei, A.G. Evans, A. M. Harte and N.A. Fleck, *Mat. Sci. and Engg.* **269**, 38 (1999).
13. M.F. Ashby, A.G. Evans, L.J. Gibson, J.W. Hutchinson, N.A. Fleck, H.G.N. Wadley, *Cellular Metals: A Design Guide, Butterworth Heinemann.* 92 (1998)

STUDY OF EXPERIMENTAL EXAMINATION ON STRENGTH EVALUATION IN THE DESIGN OF DOUBLE COLUMN FOR

Syuutei SASAKI

Applied Dynamics laboratory, Shibaura Institute of Technology, 3-7-5 Toyosu Koto-ku, Tokyo, 135-8548, Japan

Keiiti HAGIWARA

Applied Dynamics laboratory, Shibaura Institute of Technology, 3-7-5 Toyosu Koto-ku, Tokyo, 135-8548, Japan

Tsutomu EZUMI

Applied Dynamics laboratory, Shibaura Institute of Technology, 3-7-5 Toyosu Koto-ku, Tokyo, 135-8548, Japan

A double column made of that has the important problem of a three-dimensional crack existed in interfacial vicinity on a surface crack was modeled by using the difference of the rigidity by mixing the curing agent of epoxy resin for this resin, and the experiment analysis by means of the stress freezing method through the photoelastic method and was done. After the freezing stress was observed about K_I and K_{II}, the specimen of a model was obtained by the photoelastic method and K_{III} was obtained by the reflection type of causitics method. The difference of the modulus of Yong modulus effects to the rigidity, the value of the K_I has a significant impact on the rigidity, but that of K_{II} has an insignificant effect. As the difference of an inner diameter and an outer diameter of the double column has the effort, it is possible to save the rigidity.

1.1. *Introduction*

A double column made of that has the important problem of a three-dimensional crack existed in interfacial vicinity on a surface crack was modeled by using the difference of the rigidity by mixing the curing agent of epoxy resin for this resin, and the experiment analysis by means of the stress freezing method through the photoelastic method and was done. After the freezing stress was observed about K_I and K_{II}, the sample of a model was obtained by the photoelastic method and K_{III} was obtained by the reflection type of causitic method. The difference of the

modulus of Yong modulus effects to the rigidity, the value of the K_{I} has a significant impact on the rigidity, but that of K_{II} has an insignificant effect[1][2]. As the difference of an inner diameter and an outer diameter of the double column has the effort, it is possible to save the rigidity[3]

1.2. *Test piece and experiment method*

In this research, the one that the Young's modulus of epoxy resin was changed as a dissimilar kind material was used. It was used that the Young's modulus changed by varying the mixture ratio of the weight for the curing agent to epoxy resin. Each mixture ratio in four kinds and mechanical properties are shown in Table 1 Moreover, each mixing rate, the outside diameter of a double column, and the inside diameter size are shown in Table 2. The crack was inserted in a vertical direction axially on the cast columnar for the test piece. Epoxy resin is used to see the influence given to K value of an interfacial position, and it is outside diameter D out $=50$ (constancy)mm, and length. It did $L=200$, the machine was processed like the column of the mm, joint boundary radius R in$=10$ mm, and 12.5mm, and the crack inserted depth $D=5$ mm of width $W=0.15$ mm and Crack and length $L=100$ mm in the direction of the hand of the length of the axis with the miller cutter of 0.15mm in the thickness of the blade. After the specimen was experimented for the photoelastic method, it was tried to apply the method of caustics to the slice splinter of a three-dimensional model that the stress is frozen, the freezing stress was opened the annealing doing when the stress froze the slice splinter without the surface transformation finished up and almost the same cycle. It recovers in the state before the slice splinter freezes, and the surface transformation is caused. It takes a picture of the caustic image of K_{III} with a reflection type caustic image formation device after the transformation corresponding to the torque at the load is caused in the slice splinter. The figure 1 is the static torsion tester that newly produced it was used for the experimental apparatus. It is a load examination machine that fixes the right side so that the test piece should not receive a stress axially, makes free axially left, rotates only on the other hand, and adds the load by the couple of force.

Table 1. Property of epoxy resin by ultrasonic inspection.

Mixture ratio	100 : 25	100 : 30	100 : 35	100 : 40
Modulus of longitudinal elasticity E (GPa)	3.93	4.06	4.13	4.25
Modulus of transverse elasticity G (GPa)	1.45	1.48	1.51	1.55

Table 2. Epoxy resin mixture ratio and relation of bond interface radius.

| | Araldite: Hardner | | | | | |
	Inner Phase	Outer Phase	G_{in}/G_{out}	R_{in} [mm]	R_{out} [mm]	R_{in}/R_{out}
Type A	100 : 40	100 : 30	1.05	12.5	25	0.5
Type B	100 : 35	100 : 30	1.02	12.5	25	0.5
Type C	100 : 30	100 : 30	1.00	12.5	25	0.5
Type D	100 : 25	100 : 30	0.98	12.5	25	0.5
Type E	100 : 30	100 : 30	1.00	10.0	25	0.4
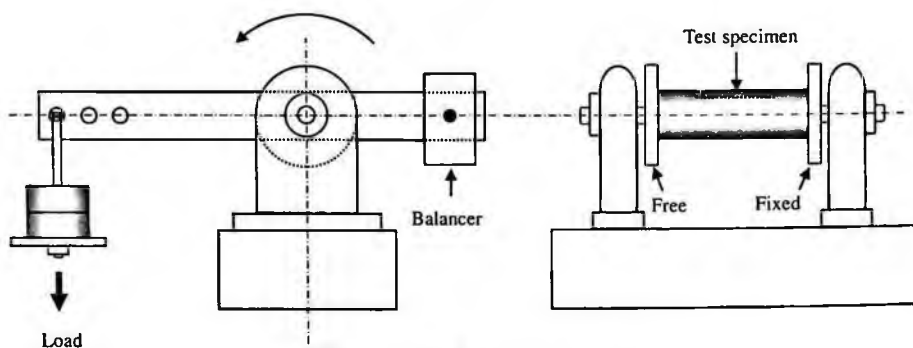
Figure 1. Static torsion tester

1.3. *Experiment result and consideration*

Figure 2 and Figure 3 are the image of isochromatic fringe for the photoelasitic method. Slice 2 is the magnified image of the center of a slice 1. These are type C and type D. Figure 4 is the relation between of K_{III} and dimensionless distance for type A. As for the K_{III} value of other types, they resemble the tendency of type A.

Figure 4 is the result of type C in 5 types, there is the tendency that the K_{III} is small at the crack tip and grows at the part of center of the crack. This means that the stress of the center of the crack is growing and very dangerous.

Slice No.1   Slice No.2   Slice No.1   Slice No.2

Figure 2. Isochromatic fringe pattern (Type C)   Figure 3. Isochromatic fringe pattern
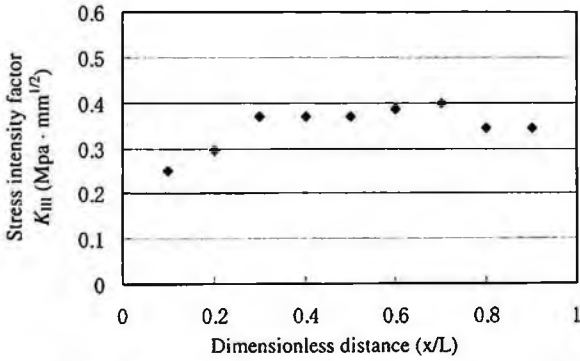
Figure 4. Relation between K_{III} and dimensionless
Distance (Type C)
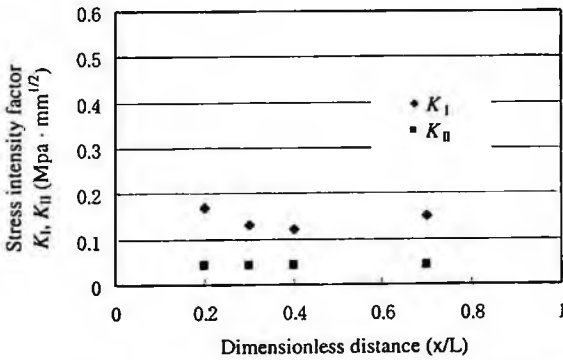
Figure 5. Relation between K_{I}, K_{II} and dimensionless
Distance (Type C)

As for the K_{III}, each type is almost in the tendency to type C. The edge of the crack is small, a center of the crack grows.

Figure 5 is the result of the relation between K_{I}, K_{II} and dimensionless distance of type C. As for the K_{I} and K_{II} is different from other typeis. Therefore, it is understood to be greatly related th diameter and the Young modulus of the double column for the dissimilar materials.

Figure 6 is the result of K_{I}, K_{II} and interface radius ratio $R_{\text{in}}/R_{\text{out}}$ (TypeB,C,D). Figure 7 is the result of various of the stress intensity factor K_{III} and interface radius ratio $R_{\text{in}}/R_{\text{out}}$ (Type A,B,C, D, E)
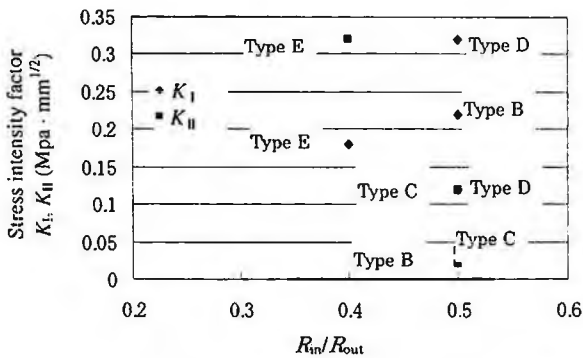
Figure 6. Variations of the stress intensity factor K_{I}, K_{II} and interface radius ratio $Ri_{\text{n}}/Ro_{\text{ut}}$ (Type B,C,D,E)
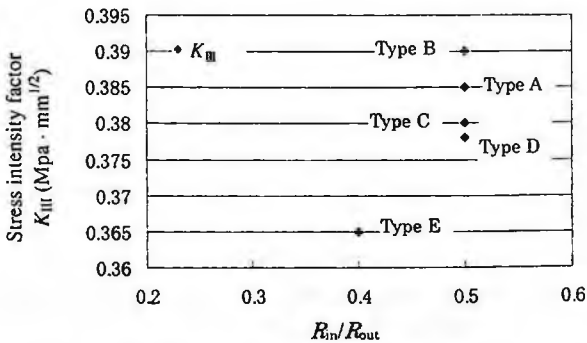
Figure 7. Variations of the stress intensity factor K_{III} and interface radius ratio $Ri_{\text{n}}/Ro_{\text{ut}}$ (Type B,C,D,E)

In a double column under the twist load, the annealing is given to the test piece to which the photoelastic experiment is finished, therefore the transformation outside respect is confirmed to the crack tip. The obtained Caustics image was corresponding to the theory image of mode Ⅲ transformation well.

The difference compared with the rigidity of the material that composes a double column understands and it has been understood that the influence by the difference of an inside, outside rigidity is large of influence by causing for the transformation style of the crack of the joint field side neighborhood in mode Ⅰ.

1.4. *Conclusion*

In this research of the influence of the surface axially crack on the double column, the good result ware obtained by the the photoelastic method and caustic method as follows:

1. Young modulus gives the influence for the K_I about the axially crack on the surface of the dissimilar double column.

2. In a double column that has the surface axially crack, it has been understood the value of K_I is to be able to control by putting the material with different degree of elasticity internally.

3. In a double column that has the surface axially crack, as for the value of K_I, K_{II}, and K_{III} it has been understood that the influence by varing R in/R out compared with an inside and outside radius is large.

References

1. Hisashi Shibuya and Akihiro Otomo, Twist of double cylinder which has Akihiro one outer toroidal crack, *Japan Society Of Mechanical Engineers* **A, 59-567**(1993), pp. 2510-2516.

2. Hisashi Someya and Akihiro Ootomo, Twist of double cylinder which has outer toroidal crack, *Japan Society Of Mechanical Engineers thesis collection* **A, 590-567**(1993), pp. 2510-2516.

3. Zhengmei L . Pings, Photoelastic Determination of Mixed-mode Stress Intensity Factor K_I, K_{II}, and K_{III}, *Experimental Mechanics*, **23-2**(1983-6), pp. 228-235.

EVALUATION OF FRACTURE TOUGHNESS OF INTERFACIAL CRACKS SUBJECTED TO MECHANICAL AND THERMAL LOAD USING FINITE ELEMENT METHOD

DHANESHWAR MISHRA, SEUNG HYUN YOO, DAE JIN OH, JOON HO SONG, YOUNG TAE LEE

Mechanical Engineering, Ajou University, 209 East-Hall WonChun-dong PalDal-gu, Suwon 442-749, Korea

Stress Intensity factor has been evaluated using virtual crack extension method for Fiber Reinforced Metal Laminate (FRML) with interfacial crack at the bond of aluminum sheet and carbon/epoxy fiber composite subjected to mechanical and thermal load. Stress intensity factor has been evaluated for varying thickness of fiber reinforce composite and studied the effect of thickness change on stress intensity factor using finite element analysis.

1. Introduction

Fiber reinforced epoxy resin composites are promising materials for different applications such as aerospace industries, automotive industries and so on. Presently Aluminum is mostly used by such industries but due to shortage of aluminum ore, it will be difficult to fulfill the demand of various industries in future. So multidimensional research is going on to develop newer materials which can replace or substitute fully or partially. Due to some disadvantages of fiber reinforce epoxy composites like sensitive towards impact and suffer sever degradation under some environmental conditions such as moisture, lighting and so on. Fiber reinforced metal laminates (FRML), consists of alternating layers of metal sheets and fiber reinforced composites as shown in fig. 1 have been developed to overcome the drawbacks of Fiber reinforced composites and enhance its properties.

Cracks and its subsequent growth leads to fracture at interfaces (bonds) are inevitable due to precipitation or segregation of grain boundaries which leads to transition from ductile to cleavage fracture concomitant loss in ductility and toughness. In composite polycrystalline intermetallic alloys; interfacial and inter angular fracture are common and in large part determine material overall response.

This work is focused on evaluating energy release rate and thus stress intensity factor at various tensile mode loading for FRML composed of (2024-T3) Aluminum sheet attached with carbon fiber/epoxy composite (prepeg) with initial crack at the interface of metal/fiber against mechanical load and thermal load using virtual crack extension method.
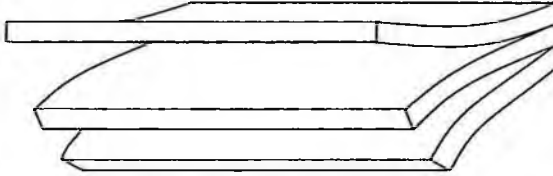
Figure 1.(a) Schematic representation of fiber reinforced metal laminate

2. Method

2.1. *Virtual crack extension method*

Virtual crack extension method as proposed by Irwin (Ref.5) can be utilized to calculate energy release rate for crack opening mode and shearing mode I and II respectively can be written as

$$G_1 = \lim_{\Delta a \to 0} \int_0^{\Delta a} \sigma_y \left[u_y \right] dx \tag{1}$$

$$G_2 = \lim_{\Delta a \to 0} \int_0^{\Delta a} \sigma_{xy} \left[u_x \right] dx \tag{2}$$

Where σ_{yy} and σ_{xy} are normal and shear stress components where as $[u_y]$ and $[u_x]$ represents displacement discontinuities at the crack face in x and y direction respectively.
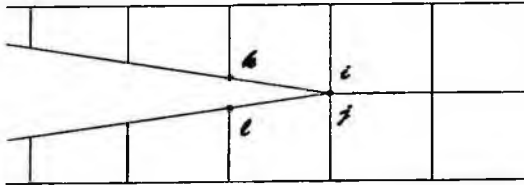
Figure 1.(b) Calculation of energy release rate for virtual crack

In the direction of crack growth a double row of nodes (i and j) tied together. The above equation for energy release rate can be written as

$$G_1 \quad = \quad (1/2\Delta a)\, F_y^i\, (u_y^k - u_y^l) \tag{3}$$

$$G_2 \quad = \quad (1/2\Delta a)\, F_{xy}^i\, (u_x^k - u_x^l) \tag{4}$$

$$G_{tot.} \quad = \quad G_1 + G_2 \tag{5}$$

Where F_y^i and F_{xy}^i are traction related to stresses in normal and shear directions.

2.2. *Extraction of stress intensity factors*

Mixed mode (complex) stress intensity factor can be calculated from equation below using energy release rate

$$K = K_1 + iK_2 = G_{total} / \{E^*\, \mathrm{Cosh}\,(\pi \varepsilon /2)\} \tag{6}$$

Where E^* is young's modulus at interface = 13.14GPa and ε is bi-material constant = 0.40.

2.3. *Finite Element Model*

A FRML (fiber reinforced metal laminate) is modeled as shown in fig. 2 with two T024T3 Aluminum sheets joined by carbon epoxy composite (prepeg).

Carbon epoxy prepeg of different thickness have been used to join 2 aluminum sheets of 50mm width and 10mm thickness to make FRLM.
Thickness direction of FRLM has been modeled with plane82 and plane77 elements for structural and thermal application with isotropic material property for aluminum and shell91 and shell132 elements with 2 layers (0/90) and orthotropic material property using ANSYS10.0. Material properties are shown in Table 1.
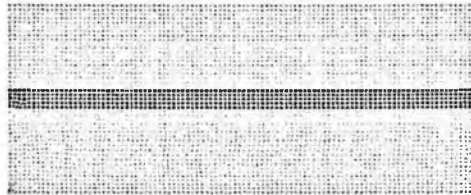
Figure 2. Finite Element model

Nonlinear transient thermal and static structural analysis has been performed. Thermal analysis results have been superimposed on structural analysis to get temperature effect on the model.

Table 1. Material Property

Material 1 (Aluminum)	Material 2(Carbon Epoxy composite)
Linear Isotropic	Linear Orthotropic
$E = 70$GPa, Poison's ratio(v) =0.3 Density = 2300kg/m^3 Thermal Conductivity = 260W/mK Coefficient of Thermal Expansion $\alpha = 8$e-6/K	$E_{xx} = 71.3$GPa, $E_{yy} = 5$GPa, $(v_{12}) = 0.03$ Density = 1300kg/m^3 Thermal Conductivity $K_{xx} = K_{yy} = 36$W/mK Coefficient of Thermal Expansion $\alpha_{xx} = \alpha_{yy} = 1.47$e-7/K

3. Results

3.1. *Thermal Analysis*

Transient thermal analysis has been performed on the model and result is superimposed to the static analysis along with mechanical load. Temperature distribution in thermal analysis is shown in fig. 3.1. We can see the temperature distribution in aluminum layer and composite layer are different. It is due to mismatch in thermal property of both the materials.
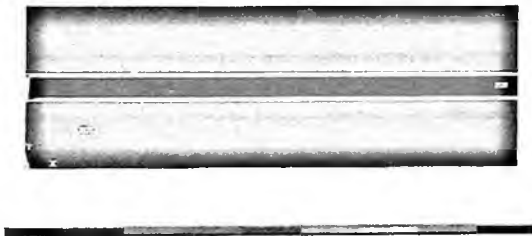
Figure 3.1 Thermal Analysis

3.2. *Energy release rate calculation*

Energy release rate has been calculated using equations 3, 4 & 5 with proper displacement and stress values at particular nodes for both opening and shearing modes for different values of tensile loads with varying thickness of carbon/epoxy (prepeg) composite for different crack lengths with virtual crack extensions.

Results for variation in energy release rate with variation in prepeg thickness, variation in loads (mechanical/thermal) and variation in crack lengths have been plotted as shown in figures below.
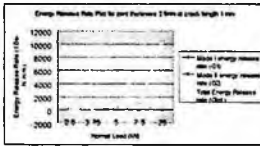
Figure 3.2. (a)
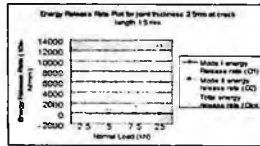
Figure 3.2. (b)
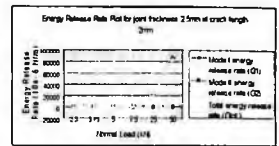
Figure 3.2. (c)
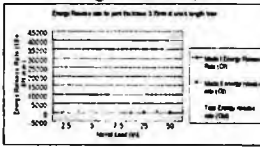
Figure 3.2. (d)
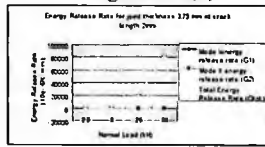
Figure 3.2. (e)
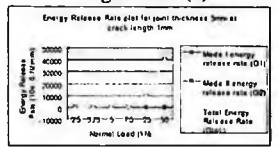
Figure 3.2. (f)

Figure 3.2. (g)

3.3. Stress Intensity Factor Calculation

Mixed mode (Complex) Stress intensity factor has been calculated by using equation 6. Results of variation in complex stress intensity factor with variation in prepeg thickness, variations in loads (mechanical-thermal combined) and variation in crack lengths have been plotted as shown in figure below.
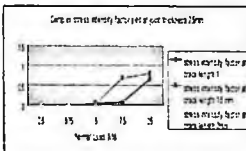
Figure 3.3. (a)
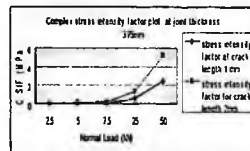
Figure 3.3. (b)
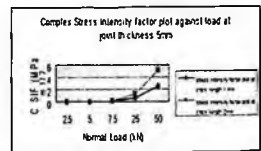
Figure 3.3. (c)

4. Discussion and conclusion

The results presented here shows that there is increase in energy release rate at increase in crack length which implies the need of more energy release for crack to open and grow. Though in present analysis energy release has not cross the critical value so at present load applied the crack will not grow but if load is increased further there is chance of growth in crack which can be seen from higher values of stress intensity factor at higher load. Once the energy release rate reaches its critical value and the crack is opened, it should decrease drastically.

Thermal analysis suggests that due to higher temperature, the cohesive force between the elements is decreased which can cause early crack growth at higher temperatures.

The correlation between energy release rate and joint thickness shows that, the energy release rate increases sharply at lower value of loads for smaller thickness of prepeg in comparison to higher prepeg thickness, which implies the fracture toughness of joint is increased with increase in prepeg thickness. It needs further examination as testing it at critical load where the energy release rate attains critical value with varying thickness of prepeg (here carbon fiber reinforced epoxy composite)

Complex Stress intensity factor plots show effect of load variation, increase in crack length and adhesive thickness on it. Stress intensity factor is increasing with increase in load, which suggests that at certain load, it can attain its critical value and further increase in load can cause damage growth and finally fracture failure.

Acknowledgments

References

1. Akbar Afaghi-Khatibi, Glyn Lawcock, Lin Ye, Yiu- Wing Mai, Computer methods in applied mechanics and engineering **185,** 173-190 (2000)
2. Alireza Asadpoure, Soheil Mohammadi, Abolhasan Vafai, Thin Walled Structures **44,** 1031-1038 (2006).
3. Axel Muller, Wilfried Becker, Detlef Stolten, Jorg Hohe, *Engineering Fracture Mechanics* **73,** 994-1008 (2006)
4. Edson Cocchieri Botelho, Rogerio Almeida Silva, Luiz Claudio Pardini, Mirabel Corqueria Rezende, Materials Research Review **No. 3,** 247-256, (2006)
5. Irwin GR. Analysis J Appl Mech **24(3)**:361-4, (1957).
6. Jeong- Ho Kim, GlaucioH. Paulino, Journal of Applied Mechanics **72,** 351-364 (2005).
7. Masaki Nagai, Toru Ikeda, Noriyuki Miyazaki, Engineering Fracture Mechanics **74,** 2481-2497 (2007).
8. X. Q. Shi, X. R. Zhang, J. H. L. Pang, International Journal of Adhesion and Adhesives **26,** 249-260 (2006)

HIGH-VELOCITY IMPACT CHARACTERISTIC
OF CFRP COMPOSITE*

RYO KUBOTA†*, DAIJI NUMATA**, MASAYUKI ANYOUJI**
AKIRA SHIMAMOTO*, KAZUYOSHI TAKAYAMA**

* *Saitama Institute of Technology, 1690, Fusaiji, Fukaya, Saitama, 369-0293, Japan*
** *Tohoku University, 2-1-1, Katahira, Aoba-Ku, Sendai, Miyagi, 980-8577, Japan*

The CFRP composite is positively used as aeronautical and spacecraft material, material for the main structure of the ground structure and public welfare parts. Therefore, the CFRP composite is used in a wide speed region. In this research, it has aimed to clarify the impact and the flexural property of the CFRP composite in such a condition.

1. Introduction

The CFRP composite material has exquisite mechanical properties such as high specific tensile strength and high specific elastic modulus as well as the characteristic such as low density, low thermal expansion coefficient, heat resistance and chemical stability and self-lubrication property [1]. The CFRP now becomes the substitution for the aluminum alloy, which is the main light metal material for air- and space crafts, vehicles and sporting goods, because of environmental preservation and energy conservation points of view. However, the CFRP has the anisotropy because of laminating carbon fiber in one direction. To give the material property which suits for the specific use, the direction of laminating fiber and the thickness of plate have to be changed. When the CFRP receives the external force from the antiplane it results in delamination and/or fiber breakage; thus caused the devastating damage to structure, environment, as well as human life. From previous studies, it has been clarified that there is a linear relationship between the delaminating area and the impact energy under the room temperature environment [2-6].

The space debris impacts in the space environment are the one of the severest environments where the CFRP receives the external force from the antiplane. The relative velocity of the space debris of less than 1mm in the diameter can become 10 km/s on the average and has enormous kinetic energy.

It is necessary to elucidate the fracture behavior by a hypervelocity impact under the cryogenic temperature for defend the space structure from the space debris.

On this research the effect of laminating fiber direction on the penetration resistance and the fracture behavior was studied by using ballistic range. Several different conditions in temperature, which is room, low, and cryogenic temperature and impact velocity, which divides penetration/non-penetration of objects were considered.

2. Specimen and Experimental method

To evaluate the effect of laminated direction of CFRP composite materials on their fracture resistance, impact tests were conducted.

2.1. *Specimen*

The direction of the prepreg fiber (8131 TORECA by Toray Industries, Inc.) was set to be $[0°/90°]_6$ and $[0°/45°]_6$. The fiber METSUKE of CFRP prepreg was 175 g/m^2, and resin content rate was 33%. The CFRP specimen as the bumper shield was processed with the hot press. For processing, it would be heated and pressurized up to 120°C and 0.7 MPa in 24 minutes, and maintained the state for 120 minutes. Then, it was cooled down to the room temperature and depressurized till 0 MPa in 80 minutes. The specimen's shape and the size were; 110×100 mm square plate with 2.0mm thickness. It was shaped with a diamond cutter. The projectile as the space debris was the sphere of aluminum alloy (Al 2017-T4) with 7.938 mm in the diameter, and 0.74 g in mass. The metallic plate as the main structural wall of the space structure was the plate of aluminum alloy (Al 2024-T3) with 5.0 mm thickness.

2.2. *Experimental method*

Fig. 1 shows the ballistic range (Two-stage light gas gun. Shock wave research in the Institute of Fluid Science, Tohoku University) used by the examination.

The ballistic range contained a propellant chamber, a compression tube, a high-pressure coupling, the lunch tube, and the test section. The specimen was fixed in the cryogenic chamber, and the main structure wall, which was the aluminum alloy plate, was placed 104 mm behind and parallel to the CFRP specimen (Refer to Fig.2).The projectile was stored in the polycarbonate sabot. When the projectile was launched, the polycarbonate sabot was divided into four parts, and fell from the projectile. We made the impact phenomenon visible by using the shadowgraph method and took a picture with ultra high speed camera (DRS Hadland Co. Ltd.,.Imacon200).

On the impact test, three different temperatures and three different impact velocities were considered. Such velocity was deduced based on the

penetration/non-penetration of a structural wall after it penetrated through the CFRP specimen. Those velocity levels were 0.5, 1.0 and 1.7 km/s. The temperature was either room temperature, 25°C, low temperature, -50°C or cryogenic temperature -120°C.
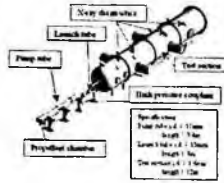
Fig.1 Schematic drawing of Ballistic range   Fig.2 Installed Specimen in chamber

3. Experimental result and consideration

Influence of the temperature and impact velocity to the CFRP was partly clarified in the temperature from -30 to 180°C and impact velocity from 0.06 to 1.0km/s. In the case of Carbon fiber/PEEK composite, impact energy and the total area of delamination approximately showed linear relationship in the low temperature environment. There has been, however, no study for the carbon fiber/epoxy yet [7]. Therefore, the hypervelocity impact experiment was conducted on the CFRP specimen in various experimental conditions on this research.

Table 1 Result of projectile penetration

		Impact Velocity v (km/s)					
		[0°/90°]$_6$			[0°/45°]$_6$		
		0.5	1.0	1.7	0.5	1.0	1.7
Experimental temperature (°C)	25	P / NP	P / NP	P / P	P / NP	P / P	P / P
	-50	P / NP	P / P	P / P	P / NP	P / NP	P / P
	-120	P / NP	P / P	P / P	P / NP	P / NP	P / P

*P: Penetration, NP: Non Penetration. It writes as CFRP composite specimen / aluminum alloy plate

The results were shown in Table1. It indicated whether the projectile penetrated through CFRP specimen and/or structural wall. In the case of impact velocity 0.5 km/s the projectile did not penetrate through the structural wall on every temperature. In the case of impact velocity 1.0 km/s the results differed for the direction of prepreg fiber. For the specimen [0°/90°]$_6$ the projectile did not penetrate through the structural wall when 25°C. For [0°/45°]$_6$ it did not penetrated the structural wall when -50 and -120 °C.

Fig. 3 shows one example of debris cloud by impact with 1.0 km/s velocity and [0°/45°]$_6$ specimen. Fig. 4 shows the relationship between the size of the penetration hole and the impact velocity. Fig. 3 indicates that the debris cloud

was formed symmetric around the injection shaft, and the influence of temperature was not admitted on the formed debris cloud. Fig. 4 shows the size of the penetration hole increased as the velocity increased. It was confirmed that there was an excellent liner relationship between the size of the penetration hole and impact velocity for the specimen (a) $[0°/90°]_6$. The relation shows the increase with the increasing rate with the specimen (b) $[0°/45°]_6$. The difference comes from the difference in the laminated fiber direction.

(a) Experimental Temperature 25°C (Room Temp.)

(b) Experimental Temperature -50°C (Low Temp.)

(c) Experimental Temperature -120°C (Cryogenic Temp.)
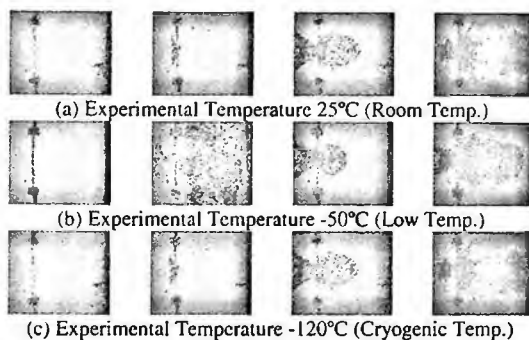
Fig.3 formation process of debris cloud
([0°/45°]$_6$, v = 1.0km/s, inter flame 54μs)

(a) [0°/90°]$_6$ CFRP composite specimen

(b) [0°/45°]$_6$ CFRP composite specimen
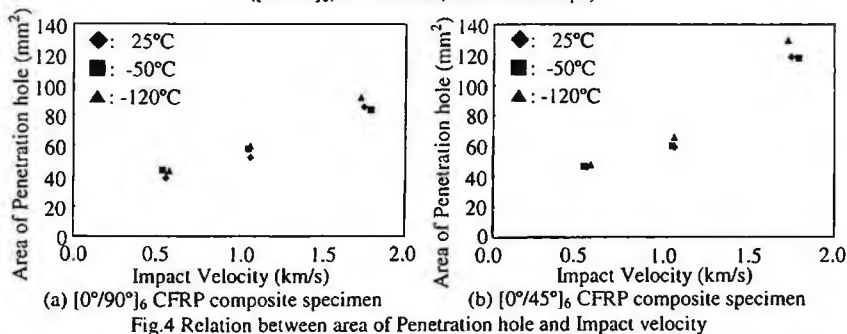
Fig.4 Relation between area of Penetration hole and Impact velocity

Fig. 5 and 6 are the photos of the specimens $[0°/90°]_6$ and $[0°/45°]_6$ after penetration. When the velocity was 1.0 and 1.7 km/s, the shock wave generated on the surface of the specimen caused the delamination of prepreg, and it was extended to the edge of the specimen along the direction of the fiber [8].

The size of the penetration hole expanded as the impact velocity increased. The fiber near the penetration hole were cut and created rectangular destructive area as the result of penetration for the specimen $[0°/90°]_6$. The fiber around the penetration hole delaminated and created the rhombus destructive are on the front of the specimen $[0°/45°]_6$. On the back of the specimen the fiber was broken and shot. The area of delamination in fact expanded on the front as the impact velocity increased while the amount of the broken fiber decreased on the

back for $[0°/45°]_6$. As Fig. 7 shows the damage around the penetration hole occurred from the edge of the penetration hole, and shock wave propagated along the fiber direction. Considering this, the specimen $[0°/45°]_6$ had the wider area to receive the damage of penetration than the specimen $[0°/90°]_6$ since the lingth of $[0°/45°]_6$ fiber was longer than the one for $[0°/90°]_6$. Therefore more energy was necessary to break and delaminate the fiber, and delaminate the fiber, and the penetration hole kept near circle.

(a-1) $v = 0.5$km/s   (a-2) $v = 1.0$km/s   (a-3) $v = 1.7$km/s

(a) Experimental temperature 25°C (front and rear face)

(b-1) $v = 0.5$km/s   (b-2) $v = 1.0$km/s   (b-3) $v = 1.7$km/s

(b) Experimental temperature -50°C (front and rear face)

(c-1) $v = 0.5$km/s   (c-2) $v = 1.0$km/s   (c-3) $v = 1.7$km/s

(c) Experimental temperature -120°C (front and rear face)

Fig.5 $[0°/90°]_6$ CFRP composite specimen

(d-1) $v = 0.5$km/s   (d-2) $v = 1.0$km/s   (d-3) $v = 1.7$km/s

(d) Experimental temperature 25°C (front and rear face)

(e-1) $v = 0.5$km/s   (e-2) $v = 1.0$km/s   (e-3) $v = 1.7$km/s

(e) Experimental temperature -50°C (front and rear face)

(f-1) $v = 0.5$km/s   (f-2) $v = 1.0$km/s   (f-3) $v = 1.7$km/s

(f) Experimental temperature -120°C (front and rear face)

Fig.6 $[0°/45°]_6$ CFRP composite specimen

Fig.7 Failure zone image around Penetration hole

4. Conclusion

The difference in penetration resistance due to the lamination of different fiber direction was studied in this research. Using the ballistic range, impact test was conducted for three impact velocity of projectile; 0.5, 1.0, 1.7 km/s, and three temperature level; room temperature (25°C), low temperature (-50°C) and cryogenic temperature (-120°C). As the results:

1. The temperature effect was not admitted on the shape of debris cloud and the area of penetration hole by the hypervelocity impact to the CFRP composite material.
2. When the impact velocity of the projectile was 1.0km/s, penetration of the structural wall was not occurred at 25 °C in specimen $[0°/90°]_6$, and at -50 and -120 °C in $[0°/45°]_6$.
3. The size of the penetration hole and the impact velocity showed excellent liner relationship for the specimen $[0°/90°]_6$, and was almost a liner relationship for the specimen $[0°/45°]_6$.
4. The magnitude of delamination and breaking of the fiber around the penetration hole depended on the fiber direction. It has been understood that the shape of penetration hole changed from circle into rectangle for the specimen $[0°/90°]_6$ because of an increase of the impact velocity. The delaminating zone of the fiber on the front of the specimen increased and shaped like diamond while the amount of the broken fiber on the back decreased for the specimen $[0°/45°]_6$.

References

1. Kiyoshi Uzawa, *Journal of the Society of Materials Science (in Japanese)* 55-1, 131(2006).
2. Hiroyuki MATSUMOTO, Masahiro ARAI, Tadaharu ADACHI and Sadayuki UJIHASHI, *Transactions of the Japan Society of Mechanical Engineers Series A* 57-535, 583(1991).
3. Hideo MORITA and Hiroyuki MATSUMOTO, *Transactions of the Japan Society of Mechanical Engineers Series A* 61-581, 127(1995).
4. Sadayuki UJIHASHI, Katsunori TANAKA, Hiroyuki MATSUMOTO and Tadaharu ADACHI, *Transactions of the Japan Society of Mechanical Engineers Series A* 63-616, 2560(1997).
5. R. C. Tennyson and C. Lamontagne, *Composites PartA* 31, 785(2000).
6. E. A. TAYLOR, M. K. HERBERT, B. A. M. VAUGHAN and J. A. M. MCDONNELL, *Int. J. Impact Engng,* 23, 883(1999).
7. Masayosi Shimizu, *Proceedings of 11th International Conference on Experimental Mechanics* Oxford, 1387(1998).
8. V. V. Silvestrov, A. V. Plastinin and N. N. Gorshkov, *Int. J. Impact Engng,* 17, 751(1995).

WEAR AMOUNT PREDICTION OF AUTOMOBILE TIRE BY FINITE ELEMENT ANALYSIS[*]

JAE-HOON LEE, JIN-RAE CHO[†], JOO-HYOUNG CHOI

School of Mechanical Engineering, Pusan National University
Kumjung-Ku, Busan 609-735, Korea

Recently, the development of high wear-resisting tire has become a great challenging subject to both tire and automobile makers due to the intensification of the environmental protection regulation. The wear amount of a tire manufactured already has been traditionally measured by experiment, but the design of a new tire model satisfying the target wear life-time should be made on the wear prediction. In this context, this paper proposes a numerical technique for predicting the tire wear amount by utilizing the finite element method. The power function wear model is adopted and a 3-D full patterned tire model is used to compute the tire frictional energy loss.

1. Introduction

The main ingredient of automobile tire is rubber, as depicted in Figure 1(a), and the tire wear is caused by the frictional slip of the tread rubber against the abrasive ground. The tire wear not only degrades the tire running performance and durability [1] but also becomes a critical source of the air pollution because the size of rubber particles is less than $10\mu m$. In this situation, the development of high wear-resisting tire becomes essential nowadays, owing to the intensification of the environmental protection regulation as well as the high mileage warranty. In order for this goal, most tire makers are now focusing their research efforts on the development of the wear prediction technique [2].

In general, the wear depth and amount produced after a tire was driven along the specific field test course can be measured by experimental methods such as one shown in Figure 1(b) [3]. But, the wear prediction of a new tire model under the design consideration is not so simple owing to the complexities of the running conditions and the material and structural composition of the tire, so that the numerical technique making use of the finite element method and a suitable wear model is attractable. In fact, the major driving modes of the tire in

[†] Corresponding author, *E-mail:* jrcho@pusan.ac.kr.

running along the specified field test course can be classified according to the virtual driving simulation by the commercial ADAMS program, and the detailed material properties and tread geometry can be fully reflected by employing the 3-D patterned tire model [4].

1. TREAD   6. INNER LINER
2. BODY PLY   7. CAPPLY
3. BELT   8. FLIPPER
4. SIDEWALL   9. APEX
5. BEAD
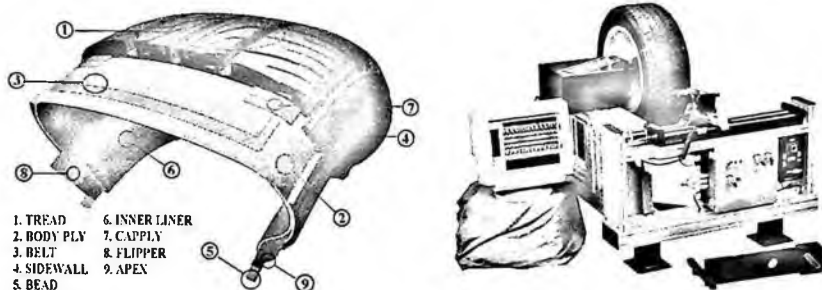
Fig. 1. Automobile tire: (a) material composition; (b) indoor wear experiment.

The purpose of this paper is to present a numerical technique for predicting the wear depth and amount of an automobile tire under the design consideration by utilizing the frictional dynamic rolling analysis of the 3-D patterned tire model. The power function wear model [5] is adopted and the tire running condition is classified into nine weighted modes. And, the frictional energy loss during a tire revolution is computed by the commercial ABAQUS code. The validity of the proposed technique is examined through the numerical experiment.

2. Wear Model and Driving Modes

The wear phenomenon is classified largely into corrosive, adhesive, abrasive and fatigue wears according to the physical cause, but the wear of rubber-like materials is characterized by the abrasive wear. In the wear prediction of the specific material at hand, the prediction reliability is definitely influenced by the suitability of the wear model chosen. The Archard's law has been widely and successfully used to describe the wear phenomenon for several decades, but the power function model, which is modified from the Archard's law,

$$\dot{W}\left(m^3 / sec \cdot m^2\right) = 6C_{EA}\left[\overline{E}\left(F_f, \dot{\gamma}\right)\right]^m \tag{1}$$

is widely used for the rubber-like materials. It is because the slip rate is not uniform within the contact region and rubbers show the highly nonlinear deformation. In Eq. (1), $\dot{W}$ is the volumetric wear rate, $\overline{E}\left(J / m^2\right)$ the averaged frictional energy density expressed in terms of the contact shear force F_f and the slip rate $\dot{\gamma}$. The abradability C_{EA} and the exponent m, which are in

function of the material type and the slip condition, are determined by the specific wear experiment apparatus shown in Figure 2(a).
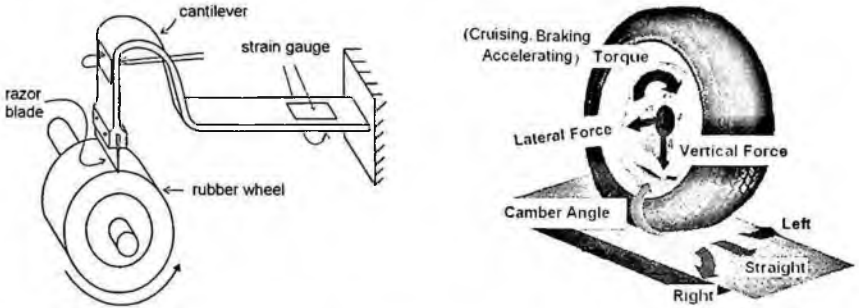
Fig. 2. Wear experiment of tire: (a) schematic view of blade abrader: (b) driving modes.

The tire wear performance is usually evaluated through the field test, for which the specified test car equipped with the test model tires is forced to be driven along the preset driving course which was constructed according to the traffic regulation. Referring to Figure 2(b), the driving conditions are generally classified into nine weighted driving modes: cruising, acceleration and braking modes in the straight, right and left directions, and the relative driving time spent for each driving mode is defined as the mode weight. The driving direction is numerically implemented by the camber angle θ_c and the lateral force F_H, while the tire velocity is controlled by the torque T_W. For the current study, we use the weights w_I and the kinematic and loading conditions, for individual driving modes, given in a paper by Zheng [6]. Letting N be the total rotation number of the tire that is required for the specified traveling mileage, the total wear amount W and wear depth H of the tire are predicted as

$$W = 6NC_{EA} \left\{ w_1 \overline{E}_1^m A_1 \Delta t_1 + \cdots + w_9 \overline{E}_9^m A_9 \Delta t_9 \right\}, \quad \overline{E}_I = E_I / A_I \qquad (2)$$

$$H = W / \overline{A}, \quad \overline{A} = w_1 A_1 + \cdots + w_9 A_9. \qquad (3)$$

Here, A_I and Δt_I are respectively the contact area of the tire and the time spent per revolution. The total frictional energy loss E_I of the tire per revolution in driving mode I is computed by the frictional dynamic rolling analysis [7].

3. Numerical Experiment

A non-symmetric tire P205/60R15 is considered for the numerical experiment, and its FEM mesh shown in Figure 3(a) was generated by our in-house program [4] with 35,363 tri-linear elements. Two steel belts and a single-ply polyester carcass embedded in rubber matrix are modeled using composite shell elements,

while steel cords in the bead region are treated as homogenized solid elements [7]. Referring to Figure 3(b), the internal pressure p of $30\,psi$ is applied to the tire, and then W, F_H and θ_c of the specific driving mode are specified [6]. After that, it is accelerated linearly to reach the uniform tire velocity $V = 60km/h$ in $0.6\,sec$ and then the specified torque T_w is applied during a single revolution of the tire with the frictional coefficient μ of 0.8.
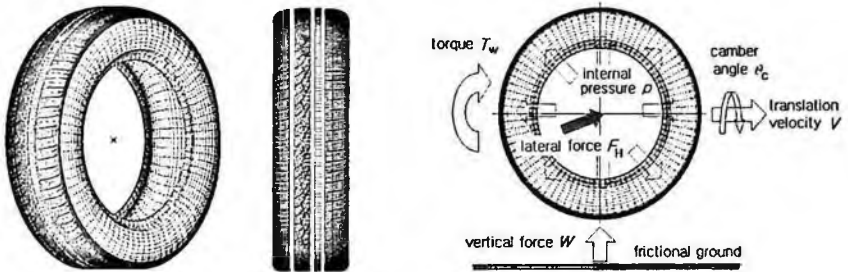
Fig. 3. A simulation model: (a) FEM mesh of the patterned tire; (b) simulation conditions.

Figures 4(a) and 4(b) represent the distributions of the nodal shear force and the nodal slip amount within the footprint, respectively. Since ABAQUS provides the nodal shear force F_f^N and the nodal slip rate $\dot{\gamma}^N$ at each finite element node N, one can compute the nodal slip amount γ^N during the specific time interval δt by time-integrating the nodal slip rate $\dot{\gamma}^N$. In the straight cruising mode, the contact shear force is higher in the rear left contact region, while the slip is bigger in the center contact region. But, both distributions become different for different driving modes.
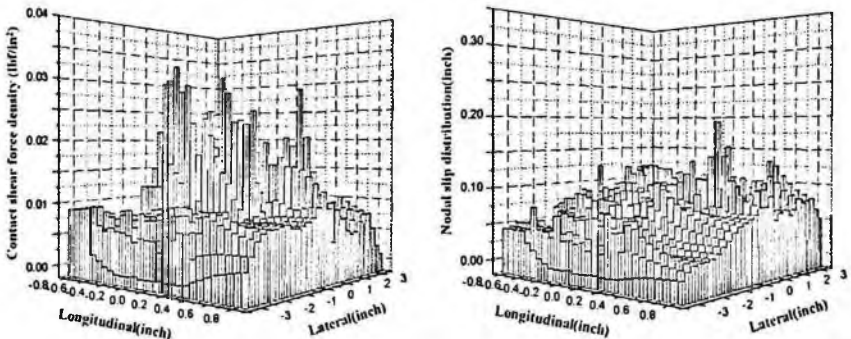
Fig. 4. Straight cruising mode: (a) nodal shear force; (b) nodal slip amount ($\delta t = 0.01\,sec$).

Figure 5 compares the nodal frictional energy distributions within the footprint in four driving modes. In each driving mode, the total frictional energy

E_I produced during a single revolution in each driving mode, after the torque T_w is applied, is computed through

$$E_I = \sum_{N=1}^{Node} \int_0^{\Delta t_I} \left(T_{f,x}^N \times \dot{\gamma}_x^N + T_{f,y}^N \times \dot{\gamma}_y^N \right) dt, \quad I = 1, 2, \cdots, 9 . \qquad (4)$$

Here, *Node* is the total node number within the footprint and the time period Δt_I taken for a single revolution can be found from the ABAQUS analysis.
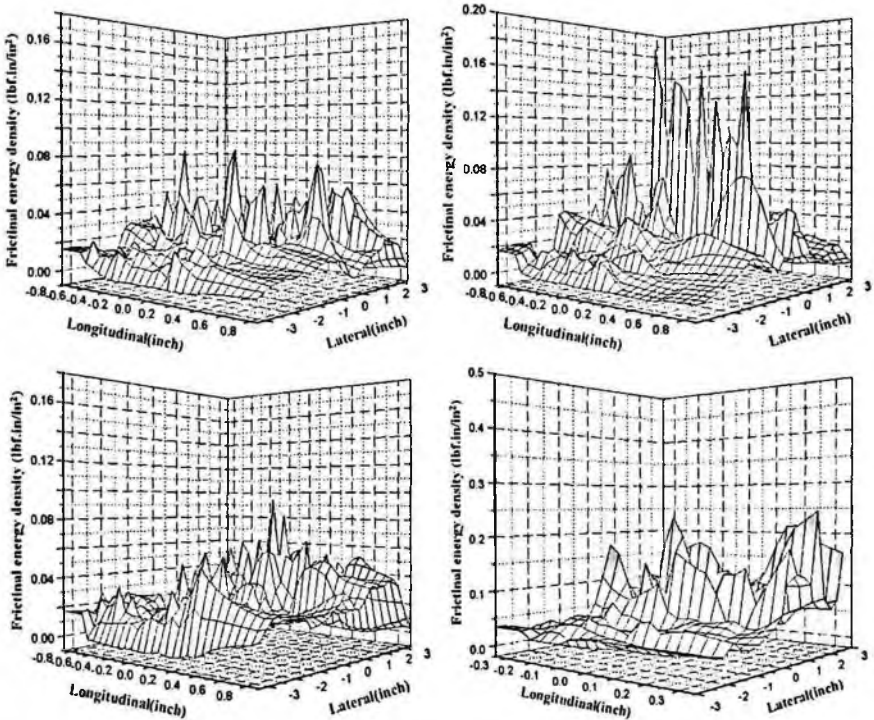
Fig. 5. Comparison of the frictional energy density distributions (during $\delta t = 0.01 \, sec$): (a) straight cruising; (b) straight acceleration; (c) straight braking; (d) right cruising.

Table 1 contains the computed total frictional energies E_I produced during a single tire revolution and the relative weights w_I for nine driving modes. In each driving direction, the total frictional energy is highest in the braking mode and lowest in the cruising mode. On the other hand, the straight cruising mode appears by almost three quarters (75%) during the entire test driving period.

Based upon the computed frictional energies and weights, the wear amount W and the wear depth H were calculated using Eqs. (2) and (3). Two wear coefficients C_{EA} and m for carbon-black-filled PB (propylene butadiene) may

be referred to the paper by Gent and Pulford [5], and the total driving distance are set by $80,000km$. It is worth to note that the driving mode weights become different depending on the road conditions and the driver's driving style, but the wear amount of the tire can be predicted by the proposed method in an extremely short period time once the driving and load conditions are specified. Thus, this method can be a useful tool for designing the high wear-resistance tire with the minimum design cost and time.

Table 1. Frictional energies E_I per revolution and weights w_I of nine driving modes.

Driving modes (C: Cruising, A: Acceleration, and B: Braking)	Left			Straight			Right		
	C	A	B	C	A	B	C	A	B
Frictional energy $E_I(N \cdot m/rev)$	11.2	12.4	16.3	19.6	23.7	25.0	58.6	63.1	81.8
Weight $w_I(\%)$ [6]	6.35	1.20	0.97	74.32	6.48	4.65	4.41	0.99	0.63

Table 2. The predicted wear depth H and wear amount W after driven $80,000km$.

Rubber material	Carbon-black-filled PB
Wear coefficients	$C_{EA} = 4.0\times10^{-14}$, $m = 1.9$
Averaged contact area $\overline{A}(mm^2/rev)$	2.89×10^5
Wear amount $W(mm^3)$ and wear depth $H(mm)$	1.50×10^6, 5.19

4. Summary

A numerical technique for predicting the tire wear amount has been proposed by making use of the frictional dynamic rolling analysis and the power function wear model. The frictional energies produced during a single tire revolution in the weighted nine driving modes were computed using the 3-D patterned tire model. Through the illustrative numerical experiment, the validity of the proposed numerical technique was justified.

References

[1] J.R.Cho, S.W. Shin and W.S. Yoo, *Comput. Struct.* **83**, 920 (2005).
[2] H. Lupker, F. Cheli, F. Braqhin, E. Gelosa and A. Keckman, *Tire Sci. Technol.* **32**, 164 (2004).
[3] S.R. Chung, K.S. Lee and H.J. Yu, *Tire Sci. Technol.* **26**, 120 (1998).
[4] J.R. Cho, K.W. Kim and W.S. Yoo, *Int. J. Adv. Eng. Softw.* **35**, 105 (2004).
[5] A.N. Gent and C.T.R. Pulford, *J. Appl. Polymer Sci.* **28**, 943 (1983).
[6] D. Zheng, *Tire Sci. Technol.* **31**, 189 (2003).
[7] J.R. Cho, K.W. Kim, D.H. Jeon and W.S. Yoo, *Eur. J. Mech. A/Solids* **24**, 519 (2005).

TRANSFORMED SOLUTION FOR FIXED SPECIMEN WITH NOTCHES BY INFINITELY SIMILAR ELEMENT METHOD

YOU-TANG LI, WU-YIN JIN, CHANG-FENG YAN

Key Laboratory of Digital Manufacturing Technology and Application,
Ministry of Education, Lanzhou University of Technology,
Lanzhou, Gansu 730050, China

The dynamics stress intensity factor of fixed specimen with several notches was analyzed by semi-analytic method. The semi-analytic formula was taken as the interpolation function near notch tip in this method and the degrees of freedom near notch tip were transformed into a small set of generalized coordinates by means of the series expansion formulas of the displacement field. The dynamics stress intensity factor for fixed specimen with two notches or cracks under centralized loading and well-proportioned loading was obtained. The results show that the K_I and K_{II} are existed at the same time for fixed specimen with several notches under dynamics loading.

1. Introduction

The fixed beam with several notches or cracks usually is used in engineering. This is very important to calculate the stress intensity of fixed specimen with several notches or cracks.

Geometrically similar elements have been used to calculate the stress intensity factor. The use of the stress intensity factor (SIF) in examining crack stability requires an accurate prediction or estimation of the stress field in the vicinity of the notch or crack tip for the given structural geometry, loading and boundary conditions. However, analytical solutions only exist for certain relatively simple cases due to the complicated boundary conditions associated with the governing equations. A number of techniques have been suggested for the evaluation of SIF from the finite element results but adequate representation of the crack tip singularity remains a common problem to most of these methods. Fractal finite elements is originated with Panagiotopoulos[1]. He adopted the iterated function system to model fractal boundaries and fractal bodies, obtaining asymptotic results for stresses and strains in elastic bodies by classical finite element method. Geometrically similar elements have been used to calculate the static stress intensity factor[2-4]. The stiffness matrix of the super element is formulated by the concept of matrix condensation. The use of fractal geometry to

generate infinite number of finite elements around the crack tips has been adopted widely[5-6]. The transition methods of geometrically similar element to calculated the dynamic stress intensity factor (DSIF) of crack[7] and notch[8] have been put forward, respectively. The DSIF for fixed specimen with two notches or cracks under centralized load and well-proportioned loading was calculated by the transition method of geometrically similar element in this paper. The results show that the K_I and K_{II} are existed at the same time for fixed specimen with two notches under dynamics loading.

2. Dynamics Stress Intensity Factor and Equation of Strain Energy

2.1. *Stiffness and Inertia Matrix*

In order to study the effect of V-notch on the dynamic behavior of elastic structure, an area Ω is divided around the tip of V-notch which boundary is polygon L_1. The polygons L_2, L_3, $\cdots\cdots L_n$ are made around the tip of notch, the proportional coefficient between near polygons is constant, $c(0<c<1)$. A super element is established (Fig. 1). For the jth and $j+1$th similar element, there are the following relations.
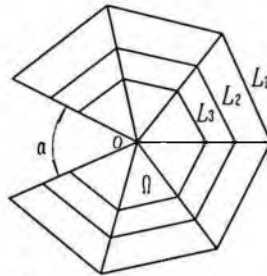
Fig. 1. Similar shape element

$$[N]_j = [N]_{j+1} \qquad\qquad [B]_{j+1} = [B]_j / c \tag{1}$$

$$A_{j+1} = c^2 A_j \qquad [K]_{j+1}^e = [K]_j^e \qquad [M]_{j+1}^e = c^2 [M]_j^e \tag{2}$$

The above equations show that the stiffness matrix of similar element is only depend on the shape, and no the size and position of element. That can be said that there is the same stiffness matrix for similar element. The inertia matrix of similar element is only depend on the proportional coefficient, and no the position of similar element.

2.2. *Dynamics Stress Intensity Factor and Equation of Strain Energy*

The stress intensity factor of V-notch can be written as following according to displacement field of dynamics V-notched[8].

$$K_I^V(t) = \sqrt{2\pi}\lambda_1^I(\lambda_1^I + 1 - \lambda_1^I \cos 2\alpha - \cos 2\lambda_1^I \alpha)a_1^R(t)$$
$$K_{II}^V(t) = \sqrt{2\pi}\lambda_1^{II}(\lambda_1^{II} - 1 - \lambda_1^{II} \cos 2\alpha + \cos 2\lambda_1^{II}\alpha)a_1^I(t) \tag{3}$$

It is obvious that the dynamics stress intensity factor of V-notch is involved to the angle of V-notch. If the combined stiffness and inertia matrix of area Ω is assembled to that of another elements, the global stiffness and inertia matrix will be obtained. The displacement, velocity and acceleration of all nodes can be obtained as following through solving the equation of dynamics finite element.

$$\{u\} = [T]\{a\} \quad \{\dot{u}\} = [T]\{\dot{a}\} \quad \{\ddot{u}\} = [T]\{\ddot{a}\} \tag{4}$$

There is an equation as follows according to conservation of strain energy.

$$[T]^T[K][T]\{a\} + [T]^T[C][T]\{\dot{a}\} + [T]^T[M][T]\{\ddot{a}\} = [T]^T\{R\} \tag{5}$$

3. Transformation Method

3.1. *First layer transformation*

Let the degrees of freedom on the boundary polygon L_1 be master nodes and another be slave nodes. To carry out the transformation, the formula of dynamic FEM can be written as follows with respect to 'm' and 's'.

$$[\hat{K}]\begin{Bmatrix} u_m \\ a \end{Bmatrix} + [\hat{C}]\begin{Bmatrix} \dot{u}_m \\ \dot{a} \end{Bmatrix} + [\hat{M}]\begin{Bmatrix} \ddot{u}_m \\ \ddot{a} \end{Bmatrix} = \begin{Bmatrix} f_1 \\ 0 \end{Bmatrix} \tag{6}$$

where

$$[\hat{K}] = \begin{bmatrix} K_{mm} & K_{ms}T^f A \\ A^T(T^f)^T K_{sm} & A^T(T^f)^T K_{ss}T^f A \end{bmatrix}$$
$$[\hat{C}] = \begin{bmatrix} C_{mm} & C_{ms}T^f A \\ A^T(T^f)^T C_{sm} & A^T(T^f)^T C_{ss}T^f A \end{bmatrix}$$
$$[\hat{M}] = \begin{bmatrix} M_{mm} & M_{ms}T^f A \\ A^T(T^f)^T M_{sm} & A^T(T^f)^T M_{ss}T^f A \end{bmatrix} \tag{7}$$

where $[A]$ is the diagonal matrix about a^{λ_i}, $a^{\lambda_i''}$ and the different elements of $[T^f]$ can be written as following, respectively.

$$T^f(2i-1,2j-1) = \frac{(r_i)^{\lambda_j'}}{2\mu}[(\kappa + \lambda_j' \cos 2\alpha + \cos 2\lambda_j'\alpha)\cos \lambda_j'\theta - \lambda_j' \cos(\lambda_j' - 2)\theta]$$

$$T^f(2i,2j-1) = \frac{(r_i)^{\lambda_j'}}{2\mu}[(\kappa - \lambda_j' \cos 2\alpha - \cos 2\lambda_j'\alpha)\sin \lambda_j'\theta + \lambda_j' \sin(\lambda_j' - 2)\theta]$$

$$T^J(2i-1,2j) = \frac{(r_i)^{\lambda_j^{ll}}}{2\mu}[(\kappa + \lambda_j^{ll}\cos 2\alpha - \cos 2\lambda_j^{ll}\alpha)\sin \lambda_j^l\theta + \lambda_j^l\sin(\lambda_j^l - 2)\theta]$$

$$T^J(2i,2j) = \frac{(r_i)^{\lambda_j^{ll}}}{2\mu}[-(\kappa - \lambda_j^{ll}\cos 2\alpha + \cos 2\lambda_j^{ll}\alpha)\cos \lambda_j^{ll}\theta - \lambda_j^{ll}\cos(\lambda_j^{ll} - 2)\theta]$$

$$i = 1,2,\cdots,2m \ j = 1,2,\cdots,n \tag{8}$$

where r_i, θ_i are the radius vector and polar angle of L_1, respectively.

3.2. *Inner layers transformation*

All the nodal degrees of freedom after the second layers should be transformed and assembled to the global matrices. For the nth layer, the three matrices after being transformed can be written as following, respectively.

$$[K^n] = [\tilde{T}^n]^T[\tilde{K}][\tilde{T}^n] \qquad [C^n] = [\tilde{T}^n]^T[\tilde{C}][\tilde{T}^n] \qquad [M^n] = [\tilde{T}^n]^T[\tilde{M}][\tilde{T}^n] \tag{9}$$

where $[\tilde{T}^n]$ is the transition matrix of the nth layer, it can be divided into blocks according to inner and outer boundary nodes, i.e. $[\tilde{T}^n]^T = [T^n \quad T^{n+1}]$, where $[T^n]$ and $[T^{n+1}]$ are the transition matrix of polygon L_n and L_{n+1}, respectively. Therefore the entry at row i and column j of the transformed global stiffness, damping and mass matrices can be written as follows

$$K_{ij}^n = \begin{bmatrix}(T_i^n)^T & (T_i^{n+1})^T\end{bmatrix}\begin{bmatrix}\tilde{K}_{11} & \tilde{K}_{12} \\ \tilde{K}_{21} & \tilde{K}_{22}\end{bmatrix}\begin{bmatrix}T_j^n \\ T_j^{n+1}\end{bmatrix} \tag{10}$$

$$C_{ij}^n = \begin{bmatrix}(T_i^n)^T & (T_i^{n+1})^T\end{bmatrix}\begin{bmatrix}\tilde{C}_{11} & \tilde{C}_{12} \\ \tilde{C}_{21} & \tilde{C}_{22}\end{bmatrix}\begin{bmatrix}T_j^n \\ T_j^{n+1}\end{bmatrix} \tag{11}$$

$$M_{ij}^n = \begin{bmatrix}(T_i^n)^T & (T_i^{n+1})^T\end{bmatrix}\begin{bmatrix}\tilde{M}_{11} & \tilde{M}_{12} \\ \tilde{M}_{21} & \tilde{M}_{22}\end{bmatrix}\begin{bmatrix}T_j^n \\ T_j^{n+1}\end{bmatrix} \tag{12}$$

where $T_{ij}^n = c^{k_j(n-1)}T_{ij}^1$ and $k_j = \lambda_{(j+1)/2}^l$ when j is odd and $k_j = \lambda_{j/2}^{ll}$ when j is even. We can know from above equations that the K_{ij}, C_{ij} and M_{ij} of different layers form geometric progression. Therefore, the following equations can be obtained.

$$\sum_{n=2}^{\infty} K_{ij}^n = \frac{R_{ij}}{1 - R_{ij}}\begin{bmatrix}(T_i^1)^T & c^{k_i}(T_j^1)^T\end{bmatrix}\begin{bmatrix}\tilde{K}_{11} & \tilde{K}_{12} \\ \tilde{K}_{21} & \tilde{K}_{22}\end{bmatrix}\begin{bmatrix}T_j^1 \\ c^{k_j}T_j^1\end{bmatrix} \tag{13}$$

$$\sum_{n=2}^{\infty} C_{ij}^n = \frac{S_{ij}}{1 - S_{ij}}\begin{bmatrix}(T_i^1)^T & c^{k_i}(T_j^1)^T\end{bmatrix}\begin{bmatrix}\tilde{C}_{11} & \tilde{C}_{12} \\ \tilde{C}_{21} & \tilde{C}_{22}\end{bmatrix}\begin{bmatrix}T_j^1 \\ c^{k_j}T_j^1\end{bmatrix} \tag{14}$$

$$\sum_{n=2}^{\infty} M_{ij}^n = \frac{S_{ij}}{1 - S_{ij}}\begin{bmatrix}(T_i^1)^T & c^{k_i}(T_j^1)^T\end{bmatrix}\begin{bmatrix}\tilde{M}_{11} & \tilde{M}_{12} \\ \tilde{M}_{21} & \tilde{M}_{22}\end{bmatrix}\begin{bmatrix}T_j^1 \\ c^{k_j}T_j^1\end{bmatrix} \tag{15}$$

where

$$R_{ij} = c^{(k_i + k_j)} < 1 \qquad S_{ij} = c^{(k_i + k_j + 4)} < 1 \qquad i, j \geq 1 \tag{16}$$

Using eq.(7) and eqs. (13)~(16), the global stiffness, damping and mass matrices for area Ω can be assembled.

4. Numerical Result and Discussion

The structure of fixed specimen with two notches under centralized loading and well-proportioned loading was shown in Fig.2, a) and b), respectively. The loading is put on the inside of the center line of V-notch exactly for model a). The normalized dynamic stress intensity factors with two notches in dynamics loading can be defined as following

a) Two centralized loading   b) Well-proportioned loading
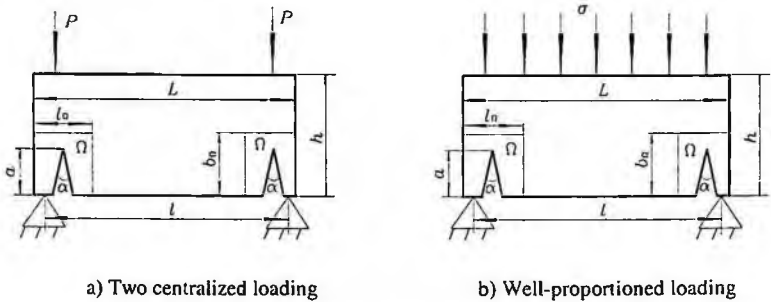
Fig. 2. Model with double notches

$$K_I^V = K_I^V(t) / K_{IS}^V \qquad K_{II}^V = K_{II}^V(t) / K_{IIS}^V \tag{17}$$

where K_{IS}^V and K_{IIS}^V are static stress intensity factors of mode I and II notches, respectively. For the pure shearing model, K_{IS}^V is zero and $K_{IS}^V(t)$ isn't always zero because the effect of stress wave. Therefore, the first of equation (17) is meaningless. For the convenience of analysis, the normalized dynamic stress intensity factors can be defined as following

$$K_I^V = K_I^V(t) / K_{IIS}^V \qquad K_{II}^V = K_{II}^V(t) / K_{IIS}^V \tag{18}$$

The explosive shock loading is put on the model and the loading can be expressed as

$$F(t) = t F_{max} / t_f \qquad\qquad t \leq t_f \tag{19}$$
$$F(t) = (t_m - t) F_{max} / (t_m - t_f) \qquad t > t_f$$

where $t_m \approx 4t_f$ and $t_f \approx 100 us$. The similar shape elements are used in two areas, Ω, and the ordinary eight nodes quadrilateral element is used in other area.

The parameters of the model are as following: a/b=0.3, L/b=2.4, l/L=0.9, $\alpha = 60°$. The parameters of area Ω are: b_Ω/b=0.6 and l_Ω/l=0.4. The results of normalized dynamic stress intensity factors under centralized loading and well-proportioned loading was shown in Fig.3, a) and b), respectively.

a) Two centralized loading   b) Well-proportioned loading
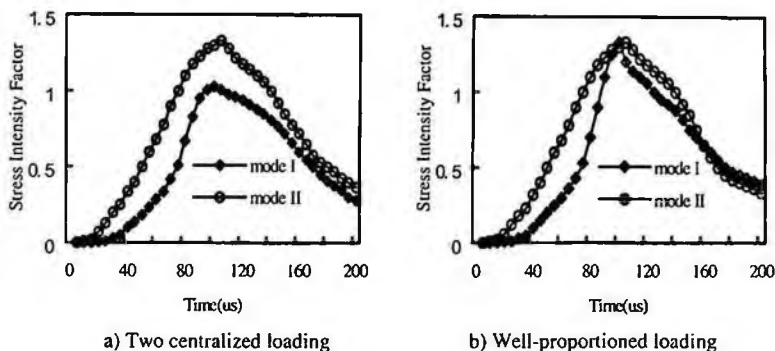
Fig. 3. Curves of normalized dynamic stress intensity factors

The model a) is the pure shear state and K_I should be zero in static loading. We can know from Fig.3 that $K_I^V(t)$ and $K_{II}^V(t)$ are existed at the same time for fixed specimen with two notches and the propagation of mode I crack plays an important role under centralized loading and well-proportioned loading.

5. Conclusions

The elements are automatically generated around the tip of V-notch in area Ω for the method. Taken an analytical solution of displacement as the global interpolation function, a row matrix of coefficient is obtained and DSIF can be evaluated directly. K_I and K_{II} are existed at the same time for fixed specimen with two notches and the propagation of mode I crack plays an important role under dynamics loading. The results show that the transition method of geometrically similar element to calculated DSIF of V-notch are feasible.

References

1. K.Kishimoto, S.Aoki and M.Sakata, *Engng Fracture Mech.* 13, 501 (1980)
2. A.D.Dimargonas and G.Grounaris, *Comput. Structures* 28,309 (1988)
3. N.Miyazaki, *Engng Fracture Mech.* 38,320 (1991)
4. C.Germ and Y.S.Lin, *Engng Fracture Mech.* 48,475 (1994)
5. A.Y.T.Leung, R.K.L.Su, *Engng Fracture Mech.* 48,847 (1994)
6. A.Y.T.Leung and R.K.L.Su, *Engng Fracture Mech.* 51,879 (1995)
7. C.B.Hu, Y.T.Li and J.Gong. *Key Engineering Materials.* 145, 267 (1998)
8. Y.T.Li, C.F.Yan and Y.P.Kang. *Key Engineering Materials.* 306, 61 (2006)

STRESS ANALYSIS ON DISCONTINUOUS FINITE-WIDTH PLATE BY HYBRID METHOD

LEI CHEN

Department of Mechanical Engineering, Graduate School, Kunsan National University
#68, Mirong-dong, Gunsan City, Jeonbuk, 573-701, Korea

TAE HYUN BAEK[†]

School of Mechanical Engineering, Kunsan National University
#68, Mirong-dong, Gunsan City, Jeonbuk, 573-701, Korea

Combining the advantages of mathematical analysis and experimental methods, the hybrid method is developed. A fairly accurate picture of stress distribution is given even around abrupt discontinuities in a material. In this paper, specimens containing a crack and some typical holes are chosen. By complex-series type stress equations, the stress distribution fields in the vicinity of the cracks and holes are obtained and the stress concentration/intensity factors can be calculated. With the help of some image processing software, the stress fields can be represented by the reconstructed isochromatic fringe image and directly compared with the fringe patterns taken from photoelasticity experiments. Good agreement of the isochromatic fringe patterns indicates that the hybrid method utilized in this paper is properly reliable and the results can be used as bench mark in theoretical simulations and experiments.

1. Introduction

The occurrence of holes and/or cracks in mechanical parts makes the parts discontinuous and causes the stress around them much higher than those in the region far away from themselves. The discontinuous parts may fracture at the stress which is much lower than the ultimate strength. Even though their size may be very small, it should be a concern in the design. But it is hard to observe the cracks and holes in the parts straightforwardly and more hard to evaluate the crack propagation. Lots of theoretical and experimental studies [1, 2] show that the stress concentration and intensity factors are most important parameters for the stress field distribution and crack propagation. But for complicated problems, with irregular geometries and the boundary conditions, mathematical methods become quite cumbersome and experimental methods, such as photoelasticity method, are usually applied for them. In general case, however, it is difficult to

---

Email of corresponding author: thbaek@kunsan.ac.kr

measure directly mechanical quantities very near the region of geometric discontinuity. In such case, the hybrid method which combines the advantages of mathematic analysis and experimental measurements far away from them is one of good alternatives [3, 4].

In this paper, specimens with a crack and some typical holes are chosen. The hybrid method is employed to calculate full-field stress distributions and the stress concentration/intensity factors for discontinuous finite-width plates subjected to uni-axial tension and to compare with experimental and FEM results. With the help of some image processing software, the stress fields were represented by the reconstructed isochromatic fringe image and directly compared with the fringe patterns taken from photoelasticity experiments.

2. Theoretical Formulation

The present technique employs general expressions for the stress functions with traction-free conditions which are satisfied at the geometric discontinuity using conformal mapping and analytical continuation. In the absence of body forces and rigid body motion, the stresses under plane and rectilinear isotropy can be written as [1, 3]

$$\sigma_x = 2\operatorname{Re}\left[\mu_1^2 \frac{\phi'(\zeta_1)}{\omega_1'(\zeta_1)} + \mu_2^2 \frac{\psi'(\zeta_2)}{\omega_2'(\zeta_2)}\right]; \quad \sigma_y = 2\operatorname{Re}\left[\frac{\phi'(\zeta_1)}{\omega_1'(\zeta_1)} + \frac{\psi'(\zeta_2)}{\omega_2'(\zeta_2)}\right]; \quad \tau_{xy} = -2\operatorname{Re}\left[\mu_1 \frac{\phi'(\zeta_1)}{\omega_1'(\zeta_1)} + \mu_2 \frac{\psi'(\zeta_2)}{\omega_2'(\zeta_2)}\right] \quad (1)$$

where complex material parameters $\mu_j \, (j = 1, 2)$ are the roots of the characteristic equation for an orthotropic material under plane stress [3].
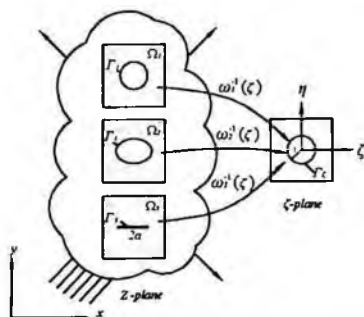
Fig. 1. Conformal mapping from the physical z-plane into the ζ-plane.

The two complex stress functions $\phi(\zeta_1)$ and $\psi(\zeta_2)$ are related to each other by the conformal mapping and analytic continuation. For a traction-free physical boundary, the two functions within sub-region Ω of Figure 1 can be written as

Laurent expansions, respectively [1, 3]

$$\phi(\zeta_1) = \sum_{k=-m}^{m} \beta_k \zeta_1^k \; ; \qquad \psi(\zeta_2) = \sum_{k=-m}^{m} (\overline{\beta_k} B \zeta_2^k + \beta_k C \zeta_2^k) \quad (k \neq 0) \tag{2}$$

In Eq. (1), complex quantities B and C depend on material properties [3]. The inverse of the mapping function ω namely ω^{-1}, maps the geometry of interest from the physical z-plane into the ζ-plane ($\zeta_1 = \xi_1 + \mu_1 \eta$). For isotropic materials, the conformal transformation from a simple geometry, a unit circle, in the ζ-plane to multiple geometric discontinuities can be shown as in Figure 1.

Combining Eqs. (1) and (2) gives the following expression for the stress through regions Ω of Fig. 1. In matrix form

$$\{\sigma\} = [V]\{\beta\} \tag{3}$$

where $\{\sigma\} = \{\sigma_x, \sigma_y, \tau_{xy}\}^T$, $\{\beta\}^T = \{b_{-m}, c_{-m}, \cdots, b_m, c_m\}$ and $[V]$ is a rectangular coefficient matrix whose size depends on material properties, positions and the number of terms m of the power series expansions of Eqs. (1).

3. Experiment and Analysis

3.1. *Photoelasticity Experiment*
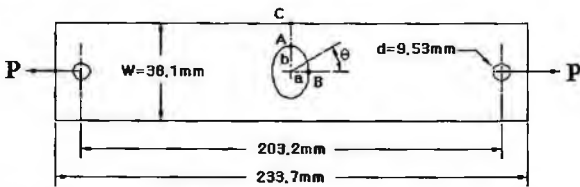
Circular hole: a=b=6.35 mm   Elliptical hole: a=4.763 mm b=9.525 mm

(a) Specimen containing a hole.
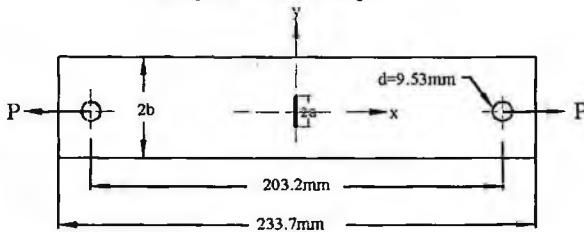
(b) Specimen containing a crack (2a=12.7 mm).

Fig. 2. Finite-width uni-axially loaded tensile plate.

In this experiment, three PSM-1 [5] plates shown in Figure 2 are subjected to the uni-axial tension $\sigma = 3.27MPa$, the thickness of specimen is 3.175 *mm*, material fringe constant $f_\sigma = 7005N/m$, Young's modulus $E=2482\ MPa$, Poisson's ratio $v= 0.38$. The radius of circular hole $r=6.35mm$, and for elliptical hole $a = 4.763mm$, $b = 9.525mm$. The length of crack is $2a = 12.7mm$.

3.2. FEM Analysis

In this paper, a commercial FEM software ABAQUS is used to discretize the specimen into two kinds of elements, CPS3 (3-node linear plane stress triangle element) and CPS4R (4-node bilinear plane stress quadrilateral element). Stress concentration factors (K_t) and stress intensity factor (K_I) for the plates shown in Figure 2 were calculated by ABAQUS [6].

3.3. Hybrid Photoelasticity

In order to obtain accurate fringe data, fringes are twice multiplied and sharpened by digital image processing [4]. The isochromatic data at the cross marks (+) on the sharpened fringes in Figure 3 are obtained. Isochromatic data on the edge of the hole and/or the crack are excluded since fringes near the edge may be affected by machining stresses. References [3, 7] discuss about determining the size of the region for data acquisition.
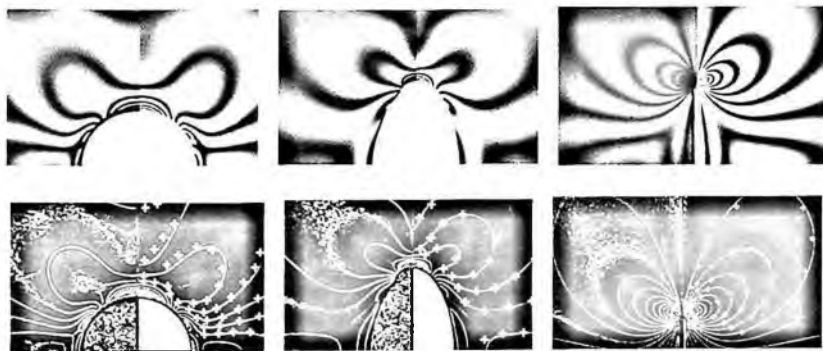
Fig. 4. Two times multiplied and sharpened actual fringe pattern (left half) and reconstructed (right half) fringes using m=9 of Eq. (2).

For measured fringe orders and a predetermined value of "m" in Eq. (2), coefficients $\{\beta\}$ are obtained by nonlinear least-sqaures [8]. Then, stress components are calculated by substituting $\{\beta\}$ into Eq. (3). To show the physical effect, full fringes are reconstructed using the results of $\{\beta\}$ obtained from the analyses, as shown in the right halves of Figure 4. The left halves of the images

in Figure 4 are twice-multiplied fringes from an actual measured isochromatic pattern.

A quantitative check on the quality of fit between input and calculated fringes is made by using a simple type of statistical parameter, the standard deviation (SD) of percentage error. For a predetermined point, the input fringe value (N_{inp}) is known. The calculated fringe value (N_{cal}) is also determined at the same point. Then, the percentage error (E) between the calculated and the input fringes at any point is $E=(N_{cal}-N_{inp})/N_{inp}\times100(\%)$. For "$n$" data points, the standard deviation of the percentage error can be calculated [4]. The standard deviations of percentage error with different number of terms are shown in Figure 5. Figure 5 shows that standard deviation tends to converge to constant values when "m" is greater than or equal to nine.
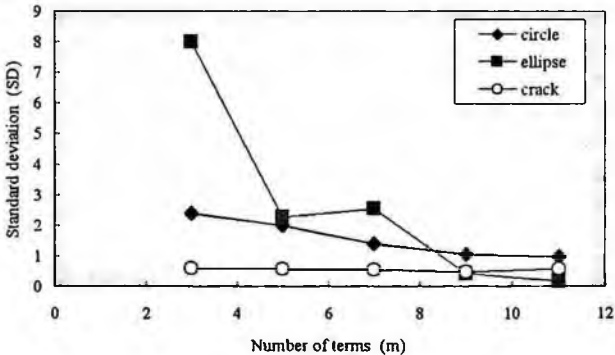
Fig. 5. Variation of standard deviation for different number of terms (m).

Table 1. Comparison of stress concentration factors (K_t) and stress intensity factor (K_I) from hybrid photoelasticity, FEM and empirical approximation for the plates of Figure 2.

(a) Circular and elliptical holes (Figure 2(a))

2a/W	a/b	Hybrid Photoelasticity		FEM	Equation [9]
		Load (N)	K_t		
0.333	1.00	490	3.44	3.47	3.44
0.250	0.50	153	6.43	6.48	6.50

(b) Central crack (Figure 2(b))

2a/W	Hybrid Photoelasticity		FEM	Equation [10]
	Load (N)	K_I		
0.333	90	1.039	1.060	1.065

From Figure 4, we can see that the reconstructed fringes of hybrid method are quite comparable to actual fringes when "m" is greater than or equal to nine.

The normalized stress concentration factors (K_t) by applied stress (σ_o) and normalized stress intensity factor of Mode I (K_I) by $\sigma_o\sqrt{\pi a}$ are obtained by hybrid photoelasticity, FEM and empirical approximate equations and compared in Table 1. For hybrid photoelasticity, $m=9$ in Eq. (2) was used.

4. Discussion and Conclusion

The figures and table presented above show that the hybrid method employed in this paper is an efficient method for calculating stress field for a discontinuous isotropic tensile-loaded plate. The stress of interest region is calculated through isochromatic fringe order of given points. This calculation has been made handy through least-squares method integrated with complex power series representation (Laurent series) implemented on a computer program for high-speed processing. The advantages of this method underscore the use of relatively small amount of data which are conveniently determined from the fringe loops.

In this study, we use only isochromatic data with their respective coordinates. By this information we can easily obtain stress distribution, stress concentration and intensity factors at the geometric discontinuity. Excellent results were obtained with number of terms "m" is greater than nine. We can see that the technique is very effective and reliable. The use of hybrid method has a potential future and the results attained in this study can be used for bench mark test in theoretical simulation and experiment.

References

1. G. N. Savin, *Stress Concentration Around Holes*, Pergamon Press (1961).
2. T. H. Baek and R. E. Rowlands, *J. of Strain Analysis*, **34** (2), 69 (1999).
3. G. D. Gerhardt, *ASME J. of Applied Mech.*, **51**, 804 (1984).
4. T. H. Baek, M. S. Kim, J. Rhee and R. E. Rowlands, *JSME Int. J, Series A*, **43** (4), 327 (2000).
5. Photoelastic Division, Measurement Group, Inc., Raleigh, NC 27611, USA.
6. *ABAQUS Analysis User's Manual*, ABAQUS Inc., Providence, RI 02909, USA.
7. J. Rhee, *Ph. D Dissertation*, Dept. of Engrg. Mech. and Astronautics, University of Wisconsin-Madison, USA (1995).
8. R. J. Sanford, *Exper. Mech.*, **20** (6), 192 (1980).
9. R. E. Peterson, *Stress Concentration Factors*, John Wiley & Sons, Inc., 150-196 (1973).
10. T. L. Anderson, *Fracture Mechanics Fundamentals and Applications*, 2nd ed. CRC Press Inc., 53-64 (1995).

FATIGUE ANALYSIS OF THE CERVICAL PLATE SYSTEM INSTALLED IN CERVICAL SPINE USING FINITE ELEMENT METHOD

IN CHUL YANG

Department of Advanced Technology Fusion, Konkuk University
1, Hwayang-dong, Gwangjin-Gu, Seoul 143-701, Korea

SUNG MIN KIM

Department of Biomedical Engineering, Konkuk University
322, Danwol-dong, Chungju-city, Chungcheongbuk-do 380-701, Korea

SUNG YOUN CHO

R&D Center, U&I Corporation
529-1, Yonghyun-dong, Uijungbu, Kyunggi-do 480-050, Korea

In this study, we performed finite element analysis for the cervical plate system installed in cervical spine. In our daily life, cervical spine or lumbar spine fractures, result from car accidents or falls or severely ligaments damaged, often causing radicular injuries or neuromuscular injuries. Thus, this study performed the biomechanical analysis of cervical plate systems by using a computer simulation based on finite element method to derive reliable model by analysis of design variables and fatigue behavior. The result of computer simulation is compared with experimented test.

1. Introduction

Cervical spine or lumbar spine fractures often result from car accidents or falls or severely ligaments damaged, causing radicular injuries or nerve root injuries. Therefore, spondylodesis is considered when relatively simple treatments, such as medication, orthopedic therapy, injections, and/or operations prove ineffective.

Thus, this study performed a biomechanical study of cervical plate system to anticipate its available life and to develop a more durable cervical plate system. We compared the mechanical properties of a cervical plate system and the results of computer simulations using the finite element method in order to examine the usability of the finite element method and to obtain design variables, fatigue yield, available life, and many other data needed to develop a new model.

2. Finite Element Models

To simulate the cervical spine movement in-vivo state by surgery, we modeled the cervical plate system which consisted of screws, rings, rivets, and plate and Ultra High Molecular Weight Polyethylene (UHMWPE) Block. The cervical plate system was installed to the UHMWPE Block (Fig. 1).

(a) Implanted System   (b) The Mesh of FE Model   (c) The Cervical Plate System
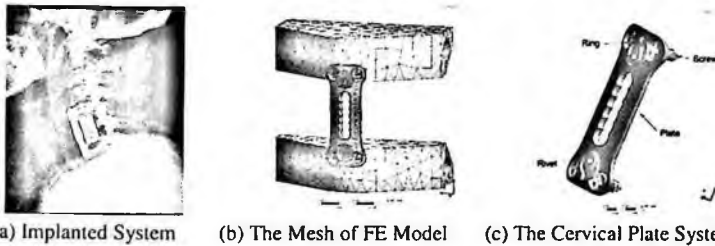
Fig. 1. Finite element model of implanted Cervical Plate System

The commercially available finite element program ANSYS Workbench 10.0 was applied to model the Ultra High Molecular Weight Polyethylene (UHMWPE). The UHMWPE test block eliminates the effects of the variability of bone properties and morphometry. Alternate designs of test blocks may be used as long as equivalent performance is demonstrated. This FE Model of the cervical plate system consisted of 21,378 elements and 37,406 nodes (Fig. 1(b)).

3. Materials and Methods

The material properties were assumed to be homogeneous and isotropic, and the data were adopted from the ASTM F136-02a and ASTM D638-00 (Table 1) [1].

Table 1 Material properties of Cervical Plate System and UHMWPE Block

Part	Material	Young's Modulus (MPa)	Poisson's ratio	Yield Strength (MPa)
Block	UHMWPE	1.11e+3	0.42	-
Cervical Plate System	Ti6Al4VELI	1.1e+5	0.33	795

3.1. *Procedure for Static Tests*

The experiment of cervical plate system followed the ASTM F1717 standards that covered the materials and methods for the static and fatigue testing [2].

We selected appropriate UHMWPE Blocks for the spinal implant assembly and then installed the screws. We placed the UHMWPE Blocks into the test apparatus such that the positions of the hinge pins are external to the screws. Then we completed the spinal implant assembly in a standard construct. We

applied the load to the test apparatus at 9mm/min and recorded the load displacement curves.

In the simulation, we kept the procedure for Static Test of experiment. as, we designed forthe UHMWPE and Cervical Plate System. Amounting plate for each side supports were free to rotate about the X-axis for the compression bending, and fatigue tests. The UHMWPE Blocks were connected to the side supports via hinge pins and allowed to rotate around the X-axis of the hinge pin during the compression bending and fatigue test.

The compression bending test and fatigue tests applied load to the Z direction without constraining rotation in the X-Y plane (Fig. 2). The compression bending fatigue test used the same test configuration as static compressive bending.

| (a) Set-up | (b) Compression | (a) Front view | (b) Side view |
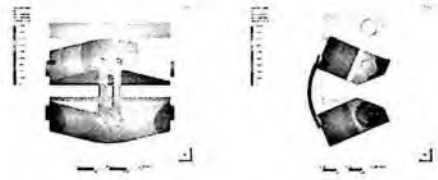
Fig. 2. Test set-up   Fig. 3. Deformation of simulation

3.2. Boundary and Loading Condition

In this analysis, we restricted any displacements about X-axis and Y-axis except the Z-direction. For this purpose, we applied load to the Z direction with 200 N. There were two types of FEM contact condition. The first one was no separation and the others was Bonded. No separation contact condition means that contact setting is similar to the bonded case. It only applies to regions of faces. Separation of faces in contact is not allowed, but small amounts of frictionless sliding can occur along contact faces. The bonded was allowed to be no sliding or separation between faces or edges. Meanwhile, the rotation of UHMWPE Blocks about X-axis was not restricted. Therefore, we could get the deformation in experiment (Fig. 3).

4. Results

This study presents the results in two parts. The first one is experimental result. Second one is the analysis of biomechanical behavior of cervical spine with the cervical plate system using Finite Element Methods based on linear anaysis. We compared these two types of results.

The results show a little deviation from the experiment. However, the simulation and experiment results show similar tendencies.

4.1. *Compressive Bending Test*

4.1.1. *Experimental Results*

The number of specimens for compressive bending test was six spicemens. In the experiment, the mean ultimate displacement was 23.5 mm and mean ultimate force was 145.3 N (Table 2, Fig. 4).

Table 2 Test summary of Compression bending test

Parameters	Ultimate displacement (mm)	Ultimate force (N)
1	25.3	155.2
2	23.8	146.7
3	23.3	134.9
4	24.5	142.7
5	23.2	123.7
6	21.0	168.8
Mean	23.5	145.3
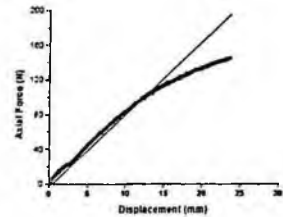
Fig. 4. Result of the compression bending test

4.1.2. *Biomechanical analysis using FEM*

The results of the simulation were compared with the experiment results as showing Table 3, Fig.5. Meanwhile, the exact result through the non-linear analysis would be obtainable.

Table 3 Simulation Results of Compressive bending test

Load (N)	Displacement (mm)	Load (N)	Displacement (mm)
40	1.328	200	6.644
80	2.657	400	13.288
120	3.986	800	26.576
160	5.315	-	-
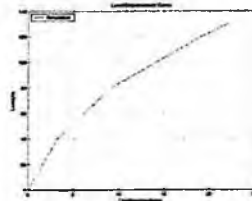
Fig. 5. The diagram of the compressive bending test

4.2. Compressive Fatigue Test

4.2.1. Experimental Results

The fatigue test applied a sinusoidal load to the spinal construct. The loading should be maintained via a constant sinusoidal load amplitude control. The cycle rate was five cycles per second for the spinal construct from the test apparatus.

When the compressive bending load was 59.6N, the available life was infinite life. But we loaded higher than 59.6N, the available life was decreased and also cracks were generated in mechanical experiments.
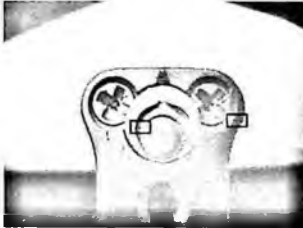
Fig. 6. Cracks at 118.666 cycles
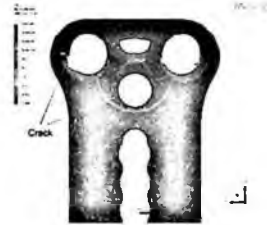
Fig. 7. The Position of the Crack

4.2.2. Biomechanical analysis using FEM

For the fatigue analysis, we used Goodman theory and S-N curve of Ti-6Al-4V (Fig. 8, Fig. 9). The fatigue test applied a sinusoidal load which is similar to experiment. Through the fatigue analysis, we got the results of Life, Damage, and Fatigue Sensitivity. The critical position of the plate was quite similar with experiment.
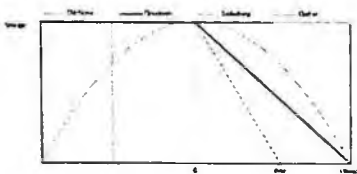
Fig. 8. The Diagram of the Goodman Theory
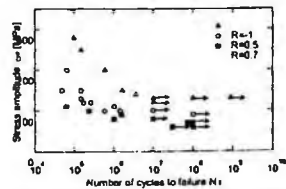
Fig. 9. S-N curve of Ti-6Al-4V9

Fatigue Sensitivity described the available life of the FE models. 1.1e+8 means that the infinite life. As a loading history increased, the available life was decreasing. When we compressive bending loaded with 54.1N, available life was 1.1e+8 cycles. That means infinite life as we explained before. But we loaded higher than 54.1N, the available life was decreased. The result was similar with experimental result. If the available life reached "0", the position of cracks would be the position as shown Fig. 7.
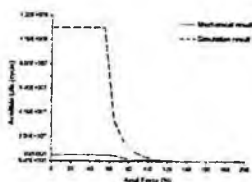
Figure 15. Fatigue Curve of the Plate

5. Conclusion

As a result of the simulation by linear analysis, it was verified that mechanical results were similar to general tendencies of experiments as shown in Fig. 15. This results satisfied FDA (Need : 100 N / Result : 145.3 N) requirements. Because of fatigue analysis using FEM had not be performed by nonlinear analysis. However the result of simulation was same as experimental results. In conclusion, it will be more effective to apply non-linear model for development of reliable model with less error in the future study.

Acknowledgment

References

1. STM international, *Designation F 136-02a* (2002).
2. ASTM international, *Designation F 1717-01* (2002).
3. Heo, S., Son, K., Park, J. H., Lee, S. J., "Biomechanical analysis of lumbar interspinous process fixators", *KSPE*, Vol. 23, No. 3 (2006).
4. Hao-Che Chuang, Der-Yang Cho, Cheng-Siu Chang, Wen-Yuen Lee, Chen Jung-Chung, Han-Chung Lee, Chun-Chung Chen., "Efficacy and safety of the use of titanium mesh cages and anterior cervical plates for interbody fusion after anterior cervical corpectomy", *Surgical Eurology*, 65, 464–471 (2006).
5. Virany H. Hillard, Ronald I. Apfelbaum., "Surgical management of cervical myelopathy: indications and techniques for multilevel cervical discectomy", *The Spine Journal*, 6, 242S–251S (2006).
6. D. K. Kim, S. C. Hwang, Maxima Cervical Plate System Report, *U&I Corporation*, (2004).
7. S. Shirai, K. Kumuthini, Y. Mutoh, K. Nagata, "Fretting Fatigue Characteristics of Titanium Alloy Ti-6Al-4V in Ultra High Cycle Regime", Fretting Fatigue: Advances of Basic Understanding and Applications, *ASTM STP 1425*, 353-365 (2003).

DURABILITY ANALYSIS OF RUBBER DIAPHRAGM FOR VEHICLE SUSPENSION DAMPER SYSTEM

SEUNGKEE KOH

School of Mechanical Engineering, Kunsan National University
Kunsan, Chonbuk, 573-701, Korea

TAEHYUN BAEK

School of Mechanical Engineering, Kunsan National University
Kunsan, Chonbuk, 573-701, Korea

HANYOUNG HWANG

Graduate School of Kunsan National University
Kunsan, Chonbuk, 573-701, Korea

Durability analysis of a diaphragm made of hydrogenated nitrile butadiene rubber(HNBR) used for a vehicle suspension damper was done. The rubber diaphragm contracts and expands repeatedly along with road profiles. Durability life of the rubber diaphragm was estimated by using strain distributions of the diaphragm and fatigue properties of the HNBR. Finite element method was used for the stress and strain analysis of the rubber diaphragms with two different shapes, i.e. SR and SS types. It was found from the finite element analysis that high stresses and strains occurred at the end regions of both types of diaphragm. Durability of the rubber diaphragm was estimated using the Green-Lagrange strain damage parameters. SR- and SS-type rubber diaphragms were expected to have infinite lives for the operation loads.

1. Introduction

A rubber diaphragm is used for a self-leveling suspension damper. The self-leveling system attached in the damper has been developed to maintain the height of the vehicle regardless of the carrying loads in the vehicle. As shown in Figure 1, the rubber diaphragm is inserted between the base shell and outer tube of the damper assembly, being held by the lower and upper holders at the ends. Inside and outside of the diaphragm are filled with oil and nitrogen, respectively.

The diaphragm is made of HNBR(hydrogenated nitrile butadiene rubber), which has very good mechanical and thermal properties, including wear and oil resistances [1]. The rubber diaphragm used in this research has two different types to investigate the better performance and durability. Figure 2 shows SR and SS types of the rubber diaphragm, depending on the shapes of diaphragms.

In this research, deformation and stress analyses of the rubber diaphragm in the vehicle damper system were performed using the finite element method. The first stage of analysis was to assemble the diaphragm into the system and the second stage of the analysis was to applying the operating pressure on the diaphragm. Based on the fatigue damage parameters of the HNBR material determined from the load-controlled fatigue test and the finite element stress analysis of the diaphragm, durability life of the rubber diaphragm was estimated.
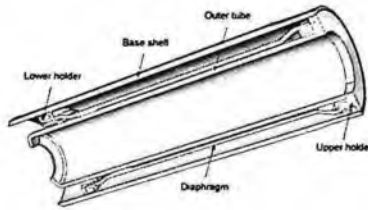
Fig. 1. Cross-section of a self-leveling vehicle suspension damper.
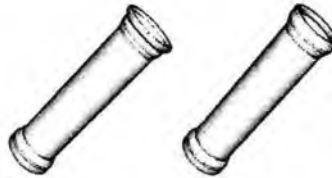
Fig. 2. Rubber diaphragms of SR(left) and SS(right) types.

2. Material Characterization of Rubber Diaphragm

Rubber can be considered as a hyperelastic material, showing highly nonlinear elastic isotropic behavior with incompressibility. A relationship between stress and strain in the hyperelastic material, generally characterized by strain energy potentials, is essential for the finite element analysis of rubber components [2]. In order to define the hyperelastic material behavior, i.e. a constitutive relation, experimental test data are required to determine material parameters in the strain energy potential.

Strain energy potential, U, in terms of Mooney-Rivlin model can be represented by the following equation [2].

$$
\begin{aligned}
U = U(I_1, I_2, I_3) &= C_{10}(I_1 - 3) + C_{01}(I_2 - 3) \\
I_1 &= \lambda_1^2 + \lambda_2^2 + \lambda_3^2 \\
I_2 &= \lambda_1^2 \lambda_2^2 + \lambda_2^2 \lambda_3^2 + \lambda_3^2 \lambda_1^2 \\
I_3 &= \lambda_1^2 \lambda_2^2 \lambda_3^2
\end{aligned}
\tag{1}
$$

where C_{10}, C_{01} are material parameters. I_i and λ_i are invariants and principal stretch ratios, respectively. Material parameters in Mooney-Rivlin model can be determined from the experimental stress-strain data. The stretch ratio is defined as the ratio of the extended length of a specimen, L, to the original length, L_o. The nominal strain, ε, can be expressed in terms of the principal stretch ratio as $\varepsilon = \lambda - 1$.

In this study, the material constants were obtained by curve fitting of uniaxial tension, pure shear and equi-biaxial tension test data. C_{10}, C_{01} were determined as 0.6196 and 0.0291 for the strain range less than 100%, respectively. Typical nominal stress-strain curves for uniaxial tension and equi-biaxial tension loadings of HNBR rubber are shown in Fig. 3.
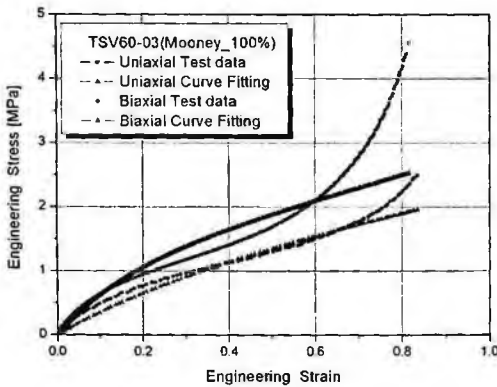
Fig. 3. Stress-strain curves of HNBR rubber material.

3. Finite Element Analysis

The vehicle suspension damper system for self-leveling the vehicle consists of many components such as lower holder, upper holder, base shell, and outer tube, including the rubber diaphragm, as shown in Figure 1. The lower and upper holders clamp the diaphragm ends. There are pin holes in the lower holder, through which oil passes between the outer tube and diaphragm.

The assembled damper system in Figure 1 is not completely axisymmetric, but the rubber diaphragm in Figure 2 is axisymmetric. Therefore, the assembled damper with the diaphragm inserted was assumed to be symmetric, performing the finite element stress analysis of the diaphragm. For simplifying the finite element model of the self-leveling damper system, the diaphragm, base shell, and the outer tube with lower and upper holders are modeled as shown in Figure 4.

Fig. 4. Axisymmetric model of a damper system.

A finite element program of ABAQUS Version 6.5 was employed for the stress analysis. The 8-noded axisymmetric element(CAX8H) was used for the rubber diaphragm [3]. The base shell, outer tube and holders were, however, modeled as rigid bodies since the deformations and stresses due to the assemblage and internal pressure loadings were negligible, compared to those of rubber diaphragm, exhibiting a hyperelastic material behavior. Total numbers of elements were 19,065 and 20,616 for the SR and SS types, respectively. No friction between the diaphragm and the contacting bodies was assumed due to the lubrication during the assemblage process of the damper.

The vehicle damper system is assembled in the procedure that the diaphragm is placed on the lower and upper holders attached in the outer tube, followed by the fitting the base shell. Sequential analysis was done by assembling the diaphragm into the damper, followed by internal pressurization of the diaphragm. Loadings applied to the diaphragm were due to the assemblage and pressurization. The diaphragm was expanded to fit its ends on the lower and upper holders during the assemblage process. Cyclic pressure of 20 MPa loading was applied to the inside of the diaphragm during the vehicle operation.

(a) Stress contour   (b) Strain contour

Fig. 5. Stress and strain contours at lower and upper ends of SR type diaphragm.

Figures 5 and 6 show stress and strain distributions near the lower and upper end regions of SR and SS type diaphragms, respectively. Significantly high stress and strain could be seen near the diaphragm ends of the sealing region contacting the lower and upper holders. Stress and strain concentrations at the lower end region were remarkable, compared to the upper end region. Similar behavior can be observed for the SS type diaphragm as shown in Figure 6. It should be noted that quite high magnitudes of stress and strain were already observed just after assemblage. Since the high stress concentrations at the region was attributed to the squeezing the diaphragm ends into the holders while

assembling, the failure due to the fluctuation of operating internal pressure might not occur at the inside corner of the diaphragm ends. Instead, the outside regions of the diaphragm ends were expected to be vulnerable to fatigue cracking.

(a) Stress contour   (b) Strain contour

Fig. 6. Stress and strain contours at lower and upper ends of SS type diaphragm.

(a) SR type   (b) SS type
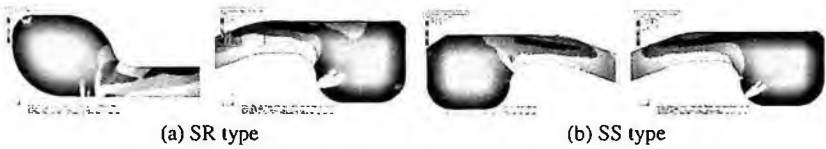
Fig. 7. Green-Lagrange strain contours at lower and upper ends of diaphragms(undeformed shape).

4. Durability Life Estimation

Durability life of the diaphragm can be estimated by applying the local damage value to the fatigue life curve of the diaphragm rubber material. In this research, the maximum Green-Lagrange strain was used for the local damage parameter, which was determined from the finite element analysis. The fatigue life curve of the HNBR was represented by the damage parameter in terms of cycles to failure. Relationships between the nominal strain(ε_N), Green-Lagrange strain(ε_{GL}), and stretch ratio(λ) are as follows.

$$\varepsilon_N = \lambda - 1, \quad \varepsilon_{GL} = \frac{1}{2}(\lambda^2 - 1) \tag{2}$$

The Green-Lagrange strain distributions for both types of diaphragm are shown in Figure 7, by subtracting the initial assemblage strain from the final strain in the finite element analysis. Fatigue life curve shown in Figure 8 was obtained from the load-controlled fatigue test using 3-dimensional dumbbell specimen made of HNBR material [4]. The maximum Green-Lagrange strain takes the mean load, P_m, into account, as shown in Figure 9, which can be expressed as the following equation.

$$\varepsilon_{GL,\max} = 6.332(N_f)^{-0.1876} \tag{3}$$

The maximum Green-Lagrange strain was found at the outside regions of diaphragm ends, ranging from 0.05 to 0.34. Durability life was calculated by using Eq. (3) and the calculated maximum Green-Lagrange strain, resulting in lifetimes of 10^7 to 10^{11} cycles. Therefore, the diaphragms of both types were expected to have infinite lives for the cyclic internal pressure loading.
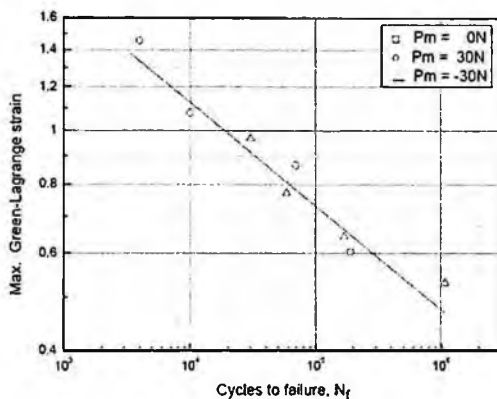
Fig. 8. Maximum Green-Lagrange strain versus cycles to failure curve of HNBR material.

5. Conclusions

In order to estimate the durability of HNBR rubber diaphragm used for a vehicle self-leveling suspension damper system, the finite element stress analysis of the diaphragm and material characterization of HNBR material were performed. High stress and strain were observed near the regions of diaphragm ends, being attributed to the assemblage of the diaphragm into the lower and upper holders. Durability lives of two different type of diaphragms subjected to the fluctuating internal pressure loading were estimated by using the maximum Green-Lagrange strain at the diaphragm and fatigue damage equation of the rubber material, resulting in lifetimes of 10^7 to 10^{11} cycles. The rubber diaphragms used for vehicle suspension damper system were expected to have infinite lives.

References

1. J. E. Mark, B. Erman and F. R. Eirich, *Science and Technology of Rubber*, Elsevier (2005)
2. A. N. Gent, *Engineering with Rubber*, Hanser Publishers (2001).
3. *ABAQUS Analysis User's Manual*, ABAQUS Inc. (2004).
4. W. D. Kim, H. J. Lee, J. Y. Kim and S. K. Koh, *Int. J. Fatigue.* 26, 553 (2003)

FAILURE ASSESSMENT ANALYSIS TO API 5L X65 PIPELINE SUBJECTED TO LARGE PLASTIC DEFORMATION

JONGHYUN BAEK

R&D Division, Korea Gas Corporation, 638-1, Il-dong, Sangnok-gu, Ansan, Gyeonggi-do, 425-790, Korea
jhbaek@kogas.re.kr

YOUNGPYO KIM

R&D Division, Korea Gas Corporation, 638-1, Il-dong, Sangnok-gu, Ansan, Gyeonggi-do, 425-790, Korea
ypkim@kogas.re.kr

WOOSIK KIM

R&D Division, Korea Gas Corporation, 638-1, Il-dong, Sangnok-gu, Ansan, Gyeonggi-do, 425-790, Korea
wskim@kogas.re.kr

CHANGSUNG SEOK

School of Mechanical Engineering, Sungkyunkwan University, 300, Chunchun-dong, Jangan-gu, Suwon, 440-746, Korea
seok@skku.edu

This paper prescribed the structural integrity of the API 5L X65 pipeline subjected to large plastic deformation. A series of experimental procedures have been carried out to study the effects of the plastic deformation on the API 5L X65 pipeline. Pipelines may be deformed by outside force such as ground subsidence, ground liquefaction, cold bending and mechanical damage. The effects of plastic deformation on the mechanical properties of API 5L X65 pipe were substantially investigated through a variety of the experimental procedures. Axial tensile pre-strain of 1.5, 5 and 10% was applied to plate-type tensile specimens cut from the pipe body prior to mechanical testing. Tensile test revealed that yield strength and tensile strength were increased with increasing tensile pre-strain. However, Fracture toughness for crack initiation decreased with increasing tensile pre-strain. The structural integrity of the API 5L X65 pipeline subjected to large plastic deformation was evaluated through the fitness-for service code.

1. Introduction

Pipelines have been used as one of the most economical and safety ways for transmitting natural gas which are still being constructed around the world. Pipelines for natural gas transmission may be subjected to plastic deformation by outside force such as ground subsidence, ground liquefaction, cold bending and mechanical damage [1, 2].

The integrity assessment of the pipeline is the most important problem to be solved first of all for prevention of any fracture accident of the pipeline. As a result of considerable effort on the integrity assessment, a criterion of fitness for service (FFS) based on the engineering critical analysis (ECA) has been suggested. Codes as BS 7910 [3], API RP 579 [4] and WES 2805 [5] have been widely used for analysis of the fracture behavior of the pipeline in the gas and oil industry, and these codes suggest that fracture assessment using a failure assessment diagram (FAD) should be performed.

In this study, structural integrity evaluation of the API 5L X65 pipe was assessed by using the BS 7910 procedure. There are 3 levels in the BS 7910 code for evaluating crack-like flaws. The fracture toughness and strength of the components are employed to assess the level 1. However, the level 2 requires a stress-strain curve data for the material containing the flaw at the assessment temperature in addition to employed data in the level 1. Tensile test, CTOD test and Charpy impact test over the temperature range from room temperature to -40 ℃ were performed to evaluate the integrity of the deformed pipeline up to tensile strain by using the BS 7910 code and its results are discussed in this paper.

2. Experimental Procedure

The material used in this study was the API 5L X65 pipe having a wall thickness of 17.5 *mm* and a outer diameter of 762 *mm* for natural gas transmission. The API 5L X65 pipe has a minimum specified yield strength of 448 MPa and a ultimate tensile strength of 530 MPa according to API 5L specifications. Axial tensile pre-strains of 1.5%, 5% and 10% were applied to the plate-type tensile specimens extracted from the pipe body prior to mechanical testing to evaluate the pre-strain effect on the material properties of the API 5L X65 pipe. The CTOD specimens for fracture toughness test were prepared from the pre-strained plate-type tensile specimen. The CTOD test was performed at four different temperatures between 20° and -40°C in accordance with the BS 7448. The Charpy V-notch specimens were extracted from the pre-

strained plate-type tensile specimen with the notch of the LS direction. All tests were conducted in triplicate at the different temperature
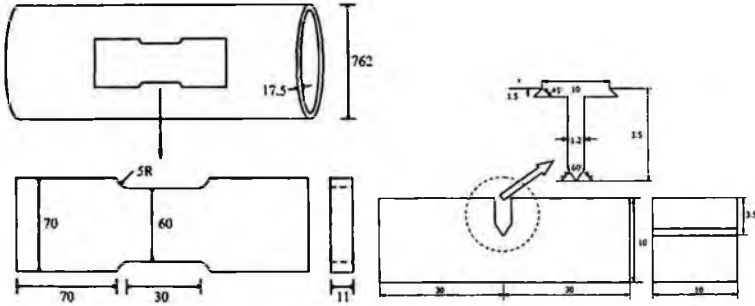
Fig. 1. Plate-type tensile specimen for pre-strain and 3-point bend specimen for the CTOD test.

3. Result and Discussion

Yield strength, tensile strength and elongation on the material without pre-strain (virgin material) and with tensile pre-strain of 1.5, 5 and 10% are shown in Fig. 2. The yield strength and tensile strength of tensile pre-strained material of 5% and 10% considerably increased as compared with the virgin material. The increasing rate of the yield strength owing to the pre-strain is greater than that of the tensile strength. It is indicated from Fig. 2 that the tensile pre-strain has a significant effect on the yield strength. However, the yield strength and tensile strength of tensile pre-strained material of 1.5% somewhat decreased as compared with the virgin material except yield strength at -20 and -40 °C. The pre-strain of 1.5% is corresponds to the yield drop zone in carbon steels without pre-strain. Prediction equations of the yield strength with variation of the temperature were given by the WES 2805 and the BS 7448 as follows

$$YS_{(L)} = YS_{(R)} + \frac{100000}{(491+1.8T)} - 189 \tag{3}$$

$$YS_{(L)} = YS_{(R)} \exp\left[(481.4 - 66.6 \ln YS_{(R)})(\frac{1}{T+273} - \frac{1}{293}) \right] \tag{4}$$

where YS(L) denotes the yield strength (MPa) at the target temperature, YS(R) indicates the yield strength at room temperature and T is the target temperature (°C) [5, 6]. Eq. (1) and (2) are employed to estimate the yield strength when we have no the yield strength at the target temperature. However, above the equation can not apply to estimate the yield strength of the pre-strained material because there is no a term to express the quantity of the pre-

strain. Fig. 2 reveals that the yield strength and the tensile strength rise in proportion with the quantity of the pre-strain. We propose in this paper that the estimating equations of the yield strength and the tensile strength with variation of the pre-strain (1.5~10%) and temperature are given in Eq. (3) and (4).

$$YS_{(T)} = YS_{(VR)} - 20.58 + 16.609 \text{Prestrain}\% + 6.465(-0.05T + 1) \tag{3}$$

$$UTS_{(T)} = UTS_{(VR)} - 16.07 + 7.021 \text{Prestrain}\% + 11.4(-0.05T + 1) \tag{4}$$

where $YS_{(T)}$ is the yield strength (MPa) at the target temperature, $YS_{(VR)}$ is the yield strength without pre-strain at room temperature, $UTS_{(T)}$ is the tensile strength at the target temperature, $UTS_{(VR)}$ is the tensile strength without pre-strain at room temperature and T is the target temperature (°C).

Pre-strain effect on the CTOD and Charpy V-notch energy (CVN) is shown in Fig. 3. The pre-strain had a little influence upon the CTOD up to pre-strain of 5% however the pre-strain of over 5% had a reasonable effect to the fracture toughness. The API 1104 provided the CTOD value for the weld metal to estimate the critical crack size [7]. The minimum CTOD value obtained at or below the lowest anticipated service temperature is 0.127 *mm* or 0.254 *mm* according to the API 1104. The minimum CTOD value obtained at the pre-strain of 10% and -40℃ is 0.245 *mm*. The pre-strain had a slight effect on the CVN up to pre-strain of 10%. The CVN values decreased with decreasing the temperature just as the published results [1, 2]. There is hardly a change of the CVN with variation of the quantity of the pre-strain in case of below -40℃, however. The average CVN value prescribed on the pipe body in the API 5L specification is 27 J for transverse specimens or 41 J for longitudinal specimens below the API X70 grade pipe [8]. It is indicated from Fig. 3 that the pre-strain of 10% has a little effect on the decreasing of ductility of the material employed in this study.
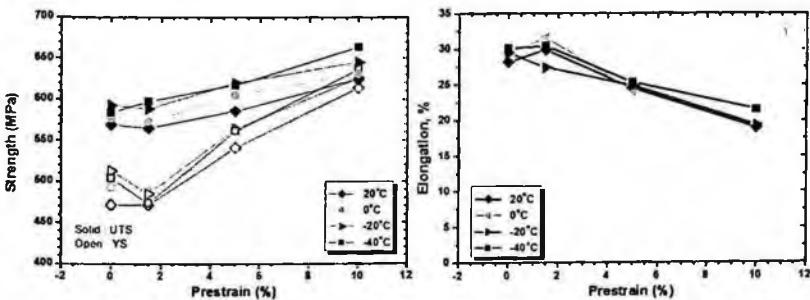
Fig. 2. Yield strength, tensile strength and elongation for the virgin and pre-strained material.
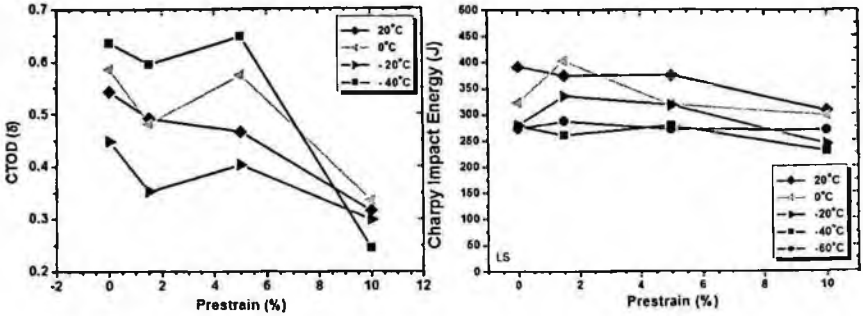
Fig. 3. CTOD and (b) Charpy energy for the virgin and pre-strained material.

Integrity assessment of the deformed pipeline by using the level 2 in the BS 7910 code was performed for axial surface crack in pipeline. Internal pressure of 8 MPa as a primary stress is employed to assess the integrity of the pipeline having a flaw. The primary stress is applied to assess the L_r ratio of the horizontal axis. Table 1 presents the fracture toughness and CTOD values for the virgin material and pre-strain material of 10%. Fig. 4 shows a level 2 FAD by means of the BS 7910 code for pipeline having a crack length of 600mm and crack depth range from 25 to 75% of wall thickness under internal pressure of 8 MPa at room temperature and -40°C. Defects having a crack depth up to 50% of wall thickness are assessed safe under internal pressure of 8 MPa. Defects having a 75% crack depth of wall thickness are appraised unsafe at room temperature. However, defects assessed with mechanical properties obtained at -40°C are evaluated as safe state. FAD is comprised of the brittle fracture ratio, K_r and plastic collapse ratio, L_r. In case of API 5L X65, fracture toughness is less susceptible to temperature variation regardless of pre-strain. Fig. 1 presents that the yield strength and tensile strength are considerably increased as decreased with temperature. So, plastic collapse ratio, Lr is decreased as decreased with temperature in Fig. 4.

Table 1. CTOD and K_{IC} values.

Materials	Temp.	CTOD (mm)	K_{IC} ($MPa\sqrt{m}$)	Temp.	CTOD (mm)	K_{IC} ($MPa\sqrt{m}$)
Virgin	0°C	0.5430	282.38	-40°C	0.3158	237.92
10% Pre-strain		0.6362	316.10		0.2445	214.12
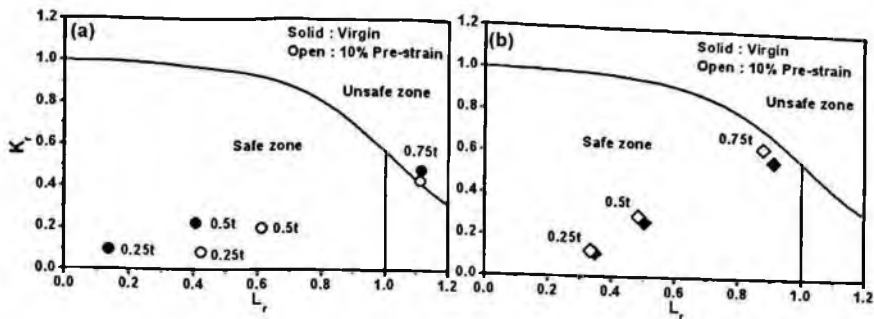
Fig. 4. Level 2 FAD for pipeline having a crack at (a) room temperature (b) and -40 ℃.

4. Conclusion

Axial tensile pre-strain up to approximately 10% was applied to the plate-type tensile specimens. Tensile test revealed that the yield strength and the tensile strength increased with increasing the tensile pre-strain. However, the CTOD and CVN values decreased with the increasing tensile pre-strain. However, the pre-strain up to 10% had a little effect on the decreasing of the fracture toughness. In case of defect having a crack depth of 75% of the wall thickness, plastic collapse ratio, L_r, is decreased as decreased with temperature due to increasing yield strength.

References

1. N. Hagiwara, M. Masuda and N. Oguchi, *J. of Pressure Vessel Technology* **Vol. 123**, 355 (2001).
2. A. Cosham and P. Hopkins, *Proc. ICPVT-10*, 357 (2003).
3. Guidance on Methods for the Assessing the Acceptability of Flaws in Fusion Welded Structures, *BS 7910*, British Standards Institution, 1997.
4. Fitness for Service, *API RP 579*, American Petroleum Institute, 2000.
5. Japan Welding Engineering Society, "Method of Assessment for Flaws in Fusion Welded Joints with Respect to Brittle Fracture And Fatigue Crack Growth", *WES 2805*, 1997.
6. Fracture Mechanics Toughness Tests, *BS 7448*, 1997.
7. Welding of Pipelines and Related Facilities, *API 1104*, 1999.
8. Specification for Line Pipe, *API 5L*, 2000.

FATIGUE CRACK GROWTH BEHAVIOR FOR WELDED JOINT OF X80 PIPELINE STEEL

YOUNGPYO KIM

R&D Division, Korea Gas Corporation, 638-1, Il-dong Sangnok-gu, Ansan, Gyeonggi-do, 425-790, Korea

CHEOLMAN KIM

R&D Division, Korea Gas Corporation, 638-1, Il-dong Sangnok-gu, Ansan, Gyeonggi-do, 425-790, Korea

WOOSIK KIM

R&D Division, Korea Gas Corporation, 638-1, Il-dong Sangnok-gu, Ansan, Gyeonggi-do, 425-790, Korea

KWANGSEON SHIN

School of Material Science and Engineering, Seoul National University, San 56-1, Sillim-dong, Gwanak-gu, Seoul, 151-742, Korea

The fatigue crack growth behavior of high strength X80 pipeline steel was investigated with compact tension specimens that crack growth directions were aligned either parallel or normal to the rolling direction of the pipeline. Also, the fatigue crack growth rates for welded joint of X80 pipeline steel were investigated with compact tension specimens that crack growth directions were aligned either parallel or normal to the welding line. The experimental results indicated the fatigue crack growth behavior was markedly different in three zones, weld metal, heat affected zone and base metal of welded joints. There was a trend toward increment in the fatigue life of weld metal and heat affected zone as compared with the X80 pipeline steel.

1. Introduction

In order to reduce the total construction cost of long distance pipeline, need for high strength pipelines has been increased because material and welding cost can be reduced by thinner pipe wall and gas transportation efficiency can be improved by increased operation pressure. Low grade line pipe below API 5L X65 has been widely used in the 1980s. The application of high strength pipeline such as API 5L X70 and X80 grade has been increased for natural gas transmission since 1990s to raise the operating efficiency. Gas pipelines have

established an impressive safety record over the years. However, fatigue failure can be occurred on the gas pipeline because of undergoing operating pressure fluctuation [1]. The girth weld in the gas pipeline especially is the most likely sites for fatigue crack initiation. Some efforts have been made to characterize the behavior of cracks in welded pipeline steels [2-3]. However, little information is available on the behavior of the fatigue cracks in welded joints of X80 pipelines. Therefore, this study was undertaken to characterize propagation of fatigue cracks in X80 pipeline steel, heat affected zone (HAZ) and weld metal over a wide range of stress intensities in laboratory air.

2. Experimental Procedure

The materials used in this study are X80 pipeline steel having 25.0 mm in wall thickness and 1,067 mm in outside diameter. The V-bevel butt joint configuration has been prepared for joining the pipeline in accordance with API standard 1104. The girth weld of this pipeline steel was welded by gas tungsten arc welding (GTAW) with ER70S-G filler metal for the root and hot pass, and shielded arc metal welding (SMAW) with low hydrogen E10016-G electrode for the remaining passes. The chemical compositions and the tensile properties of X80 pipeline steel and SMAW weld metal are summarized in Table 1 and 2, respectively.

Table 1. Chemical compositions of X80 steel and SMAW weld metal.

Element (wt%)	C	Mn	Si	P	S	Ni	Cr	Mo	Nb	V	Ti
X80 steel	0.06	1.82	0.23	0.0040	0.0001	0.28	0.01	0.26	0.039	0.010	0.010
SMAW weld metal	0.05	1.42	0.58	-	-	1.30	0.17	0.13	0.012	0.010	0.023

Table 2. Tensile properties of X80 steel and SMAW weld metal.

Test position (orientation)	Yield strength [MPa]	Tensile strength [MPa]	Elongation [%]
X80 steel (parallel to rolling direction)	601	651	25.2
SMAW weld metal (parallel to welding direction)	549	700	25.7

The microstructure of X80 pipeline steel mainly consists of bainite. Figure 1 shows the microstructures of weld metal and HAZ obtained by the welding process employed in this study. The microsturcture of SMAW weld metal consisted of grain boundary ferrite and acicular ferrite. And the microstructure of coarse grained HAZ (CGHAZ) near fusion line was coarsened by the welding thermal cycle and mainly consisted of upper and lower bainite, together with minor amount of Widmanstatten ferrite. On the other hand, the microstructure of

the fine grained HAZ (FGHAZ) near base metal was a very fine grain and mainly consisted of equaxed ferrite and pearlite.

(a) SMAW weld metal / CGHAZ   (b) FGHAZ

Fig. 1. Microstructures in girth weld of X80 pipeline.

Figure 2 shows the schematic representation of the compact tension (CT) specimens sectioned from the welded pipeline. The crack growth directions for CT specimens of X80 pipeline steel were aligned either parallel or normal to the rolling direction of the pipeline, which were designated as X80(TL) and X80(LT) specimens according to ASTM E647, respectively. The notch was put at the center of weld metal and such specimens with the crack growth direction parallel to the welding direction were named as the parallel-weld specimens, X80(PW). The effect of various microstructures in the girth weld on the fatigue crack growth behavior was investigated by making the crack growth direction normal to the welding direction. Such specimens were named as the normal-weld specimens, X80(NW). All CT specimens were cut near the outside surface of the pipeline. Therefore, X80(PW) and X80(NW) specimens were not included GTAW weld metal.
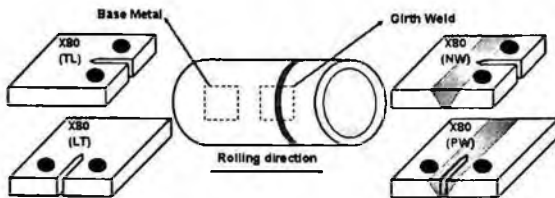
Fig. 2. Schematic representation showing the CT specimens sectioned from the welded pipeline.

The CT specimens were machined with 6.35 mm of thickness and 50.8 mm of width according to ASTM E647. All fatigue crack growth tests were performed with 2.5 ton servo-hydraulic testing machine at room temperature in air of 50~60 % relative humidity. The loading frequency was 20 Hz with a constant amplitude sinusoidal waveform of the applied load at stress ratio of 0.1.

The crack length was measured by the direct observation with traveling microscope.

3. Results and Discussion

Figure 3 shows fatigue crack growth behavior of X80 pipeline steel according to the crack growth directions and weld metal with the crack growth direction parallel to the welding direction. The fatigue crack growth rates of X80(TL) specimen were lower than those of X80(LT) specimen at the same stress intensity factor range (ΔK) value. The fatigue threshold stress intensity factor ranges (ΔK_{th}) of the X80(TL) and X80(LT) were respectively 4.62 and 2.65 $MPa\sqrt{m}$ and the Paris exponents (m) of the X80(TL) and X80(LT) were respectively 3.51 and 2.70. The weld metal had the lower fatigue crack growth rates as compared to the X80 pipeline steel at the same ΔK value. And, the weld metal had higher threshold stress intensity factor range as compared to the X80 pipeline steel at stress ratio of 0.1. The fatigue threshold stress intensity factor range and Paris exponent of the X80(PW) specimen was respectively 17.03 $MPa\sqrt{m}$ and 5.42. It is indicated that the weld metal in the X80 pipeline possesses higher extrinsic resistance against fatigue crack growth as compared to the X80 pipeline steel.
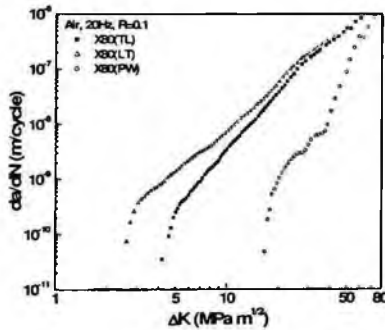
Fig. 3. Fatigue crack growth rates of X80(TL), X80(LT) and X80(PW) specimens as a function of ΔK.

The welded joint of X80 pipeline has shown a gradient of microstructure and mechanical properties from the weld metal to the unaffected base metal in Figure 1 and Table 2. Significant researches regarding the microstructure change and the mechanical properties of X80 pipelines have been performed [4-5]. The evaluation of fatigue crack growth behavior in weld, especially in narrow HAZ, however, is one of the most difficult research fields. Figure 4 shows the results

of fatigue crack growth test for the X80(NW) specimens and weld geometry of CT specimen used. As the crack propagated cross the weld metal, a mixed region with weld metal and HAZ, HAZ, and a mixed region HAZ and base metal into the base metal at the constant ΔK value, the fatigue crack growth rates are continuously increased at all tested ΔK values. The fatigue crack growth rates of HAZ are lower than those of base metal at all tested ΔK value. The results demonstrated that HAZ have a significant higher resistance to crack propagation than base metal.

The fatigue crack growth rates of weld metal, HAZ and base metal in the X80(NW) specimen in Figure 4 are replotted in Figure 5(a) as a function of ΔK. Also, the test results of X80(TL) and X80(PW) specimens are redrawn as the reference fatigue crack growth rate curves from Figure 3. Figure 5(b) shows the average fatigue crack growth rates of weld metal, HAZ and base metal in the X80(NW) specimen at each ΔK value. The average fatigue crack growth rates of weld metal, HAZ and base metal in the X80(NW) specimen, as shown in Figure 5(b) are fitted by linear least square lines to the following equation;

for weld metal, $da/dN = 2.42 \times 10^{-35} (\Delta K)^{18.57}$

for HAZ, $da/dN = 1.86 \times 10^{-23} (\Delta K)^{10.40}$

and for base metal, $da/dN = 1.73 \times 10^{-11} (\Delta K)^{2.56}$

for ΔK in $MPa\sqrt{m}$ and da/dN in m/cycle.

4. Summary

From the results of the fatigue crack growth test for X80 pipeline and its weld, it is indicated that the weld metal and HAZ in the X80 weld joint possesses higher resistance against fatigue crack growth as compared to the X80 pipeline steel. Also, the constant of Paris law, C and m for HAZ in the weld of X80 pipeline steel were obtained by linear least square lines.

References

1. M. D. Chapetti, J. L. Otegui and J. Motylicki, *International Journal of Fatigue* **24**, 21 (2002).
2. Y. W. Shi, B. Y. Chen and J. X. Zhang, *Engineering Fracture Mechanics* **36(6)**, 893 (1990).
3. L. W. Tsay, T. S. Chen and S. K. I. Chan, *International Journal of Fatigue* **23**, 103 (2001).
4. S. Y. Shin, B. Hwang, S. Lee, N. J. Kim and S. S. Ahn, *Materials Science and Engineering* **A458**, 281 (2007).
5. K. Junhua, Z. Lin, G. Bin, L. Pinghe, W, Aihua and X. Changseung, *Materials and Design* **25**, 723 (2004).

(a) $\Delta K = 23\ MPa\sqrt{m}$

(b) $\Delta K = 25\ MPa\sqrt{m}$

(c) $\Delta K = 27\ MPa\sqrt{m}$

(d) $\Delta K = 29\ MPa\sqrt{m}$
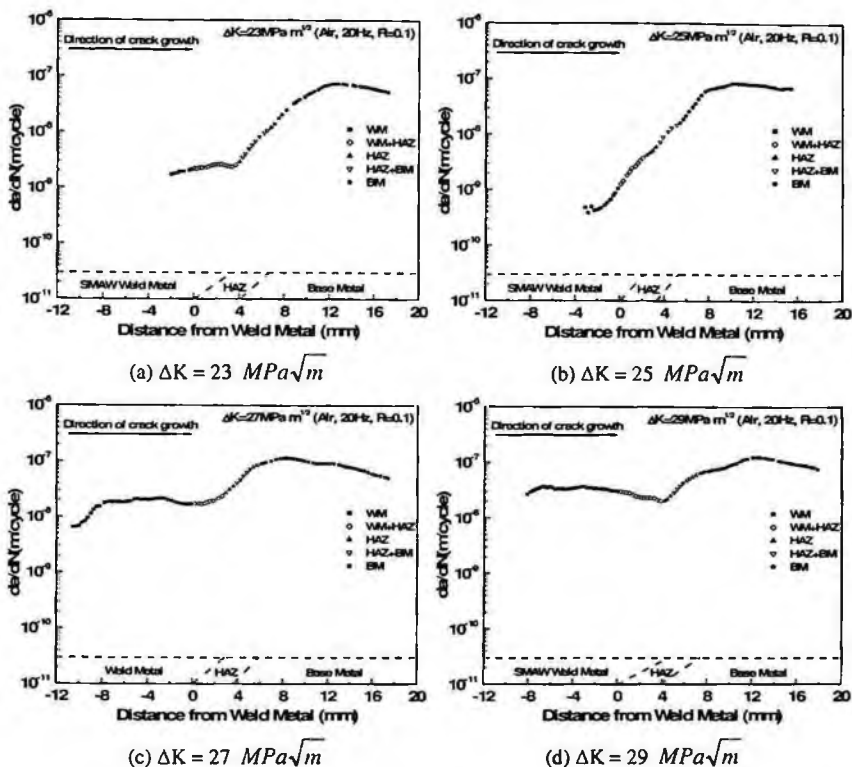
Fig. 4. Fatigue crack growth rates of X80(NW) specimen at the constant ΔK.

(a)

(b)
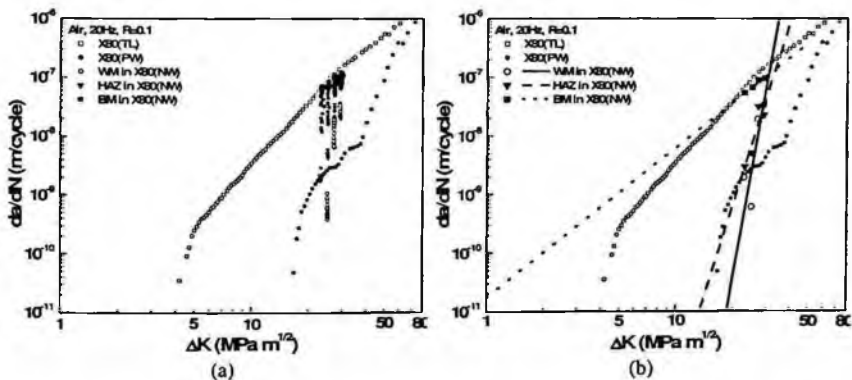
Fig. 5. (a) Fatigue crack growth rates and (b) average fatigue crack growth rates with best fit lines of weld metal, HAZ and base metal in the X80(NW) specimens as a function of ΔK. The fatigue crack growth rate curves of X80(TL) and X80(PW) are redrawn from Figure 3.

AN ANALYSIS FOR FATIGUE BEHAVIOR OF THE BRAZED JOINTS

HEE-JIN SHIM

Graduate Student, Department of Mechanical Engineering, Hanyang University, 17 Haengdang-dong, Seoungdong-gu, Seoul, 133-791, Korea

KI-WEON KANG

Ph.D., Department of Sports Engineering, Korea Institute of Sport Science, 223-19, Kongneung-dong, Nowon-gu, Seoul, 139-272, Korea

JUNG-KYU KIM[†]

Professor, School of Mechanical Engineering, Hanyang University, 17 Haengdang-dong, Seoungdong-gu, Seoul, 133-791, Korea

This paper aims to identify the fatigue behavior of brazed joints used in household electronics. For this goal, the fatigue tests are performed under cyclic internal pressure due to refrigerant in brazed joints. A durability analysis is performed to evaluate the fatigue life with the internal flaws through the finite element analysis and is verified by the fatigue tests. Also, the fatigue strength reduction factor is introduced to identify the strength reduction of brazed joints with the internal flaws. And then, based on the results, the fatigue life prediction model is developed through the fatigue strength reduction factor.

1. Introduction

Brazing is distinguished from welding in that the process is done at temperatures below the melting points of the materials to be joined and from soldering by the temperature of processing above method 450°C [1]. This method is commonly in practice in electronics or refrigerating machines due to its advantages of diminution of heat influence and easy manufacturing [1].

Unfortunately, the brazing method used in household air conditioners has some demerits that the copper alloy is susceptible to heat and there is a remarkable possibility of internal flaws due to design or manufacturing faults [2]. These may cause a deterioration of strength or slow leakage of refrigerant and then may bring premature failures due to growth of flaws under cyclic internal

---

† Corresponding Author, Fax:82-2-2291-6707; E-mail:kimj@hanyang.ac.kr

pressure of refrigerant, caused by operations and suspensions of the compressor. To improve the reliability, therefore, it is of necessity to identify the flaws and their failure mechanisms of the brazed joints. Moreover, it is vital to understand the fatigue behavior of the brazed joints under service operating condition. The previous researche on the brazing method [3~5] is, however, mainly focused on the brazing process to improve the function of various materials or ability to join dissimilar materials with differing physical and chemical properties.

This paper aims to evaluate the fatigue behavior of brazed joints used in household electronics. For the goal, the fatigue tests are performed under cyclic internal pressure due to a refrigerant by using a of the self-designed internal pressure testing machine. Also, a durability analysis was performed to evaluate the fatigue life with respect to the heat and the internal flaws. Also, the effect of an internal flaw on fatigue behavior is analyzed by the finite element method. Finally, the fatigue life prediction model is derived from the fatigue strength reduction factor.

2. Experimental and Analysis Procedure

2.1. *Material and Specimens*

The base and brazing materials are C1220-OL and BCuP-6, respectively and their properties are reported in a previous study [6]. The brazed joints are identical to the parts that are utilized in an air conditioner heat exchanger and fabricated according to the manufacturer's recommended torch brazing method. The diameter and thickness of the pipes are 15.88mm and 0.8mm, respectively. Their brazing length and gap are 7.0mm and 0.2mm, respectively.

2.2. *Experiments and Finite Element Analysis*

The static bursting and fatigue tests were performed by the hydraulic bursting pressure testing machine [6]. The static bursting tests were performed under the pressure control mode with a pressure rate of 8MPa/min. The fatigue test condition was the periodic internal pressure condition as shown in Fig. 1. The flaws were captured at a 0.03mm interval along the longitudinal direction of the joints by the computed tomography (3-D X-ray) and then the flaw volume fraction V_f (flawed volume/total joined volume) was calculated according to process in Fig. 2. Also, a 3-D finite element model was generated by means of the commercial software MSC.PATRAN [7] and incorporated an 8-node hexahedron element and the total elements were 158,880. The stress distribution

and fatigue behavior of the joints were analyzed by the MSC.NASTRAN [8] and MSC.FATIGUE [9].
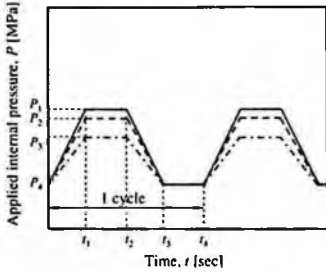
Fig. 1 Loading condition
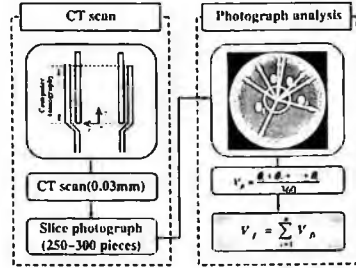
Fig. 2 Flow chart for flaw fraction measurement

3. Results and Discussion

3.1. *Fatigue Behavior of Brazed Joints*

The authors have already identified that the failure mechanism of brazed joint is influenced by the heat and aforementioned internal flaws [6]. It is also shown that the stress distribution is governed by the flaw fraction. It can, therefore, be inferred that the fatigue behavior of brazed joint is mainly governed by the flaw fraction. To identify the effect of the internal flaw fraction on fatigue behavior, the fatigue tests are first performed under cyclic internal pressure by the self-designed internal pressure testing machine. Fig. 3 shows the fatigue behavior of brazed joints under cyclic internal pressure in semi-log scale. From Fig. 3, the fatigue life of brazed joints can be related to the internal pressure as follows:

$$S = m + n \log t_f \tag{1}$$

Here symbols of S and N_f indicate the normalized internal pressure and time-to-failure (fatigue life), respectively. And m and n are the material constants. Also, the flaw fraction in brazed joints is about 20%, which is calculated by using the 3-D X-ray technique according to the process shown in Fig. 2.

The fatigue failure under cyclic pressure occurred at the HAZ (heat affected zone) and this result is consistent with the failure mechanism under static pressure condition, which is reported in a previous study [6]. It can, therefore, be deduced that the internal flaw affects the stress distribution, consequently the fatigue behavior is influenced by the internal flaw.

For understanding of the effect of the internal flaw on fatigue behavior, the durability analysis is performed with the increase of the flaw fraction. Fig. 4 shows the analyzed result for the brazed joint with $V_f = 20\%$. In this figure, the

analyzed result is well in conformance with the experiments: hence, the analysis result is reasonable. Based on this result, the fatigue behavior is analyzed for the brazed joint with V_f=40, 60 and 80%. Fig. 5 shows the overall analyzed results and the fatigue behavior is greatly influenced by the internal flaw fraction.
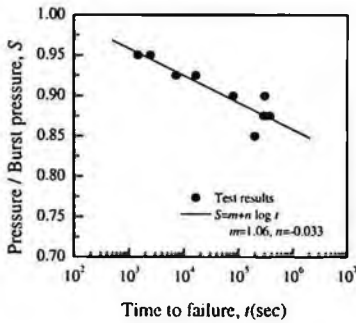
Fig. 3 S-N curve of brazed joints
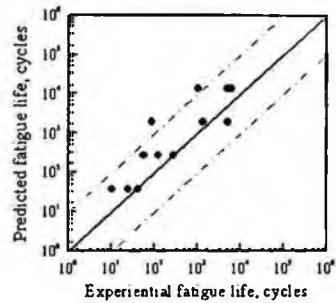
Fig. 4 Analyzed result for V_f=20%
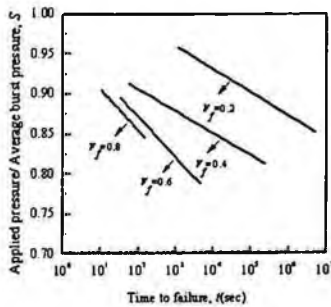
Fig. 5 S-N curves according to V_f

3.2. Fatigue Life Prediction Model

As aforementioned, the fatigue behavior of the brazed joint is greatly affected by the flaw fraction: therefore, it is necessary to develop the fatigue life prediction model in order to evaluate the effect of internal flaws on fatigue behavior. For this, first the authors have defined the fatigue strength reduction factor K_D as follows:

$$K_D = \sigma_o / \sigma_D \qquad (2)$$

in which symbols of σ_0 and σ_D are the fatigue strength of flawless and flawed joints, respectively.

And the K_D can be obtained from the relation between the flaw fraction and loading cycles by the following procedure. From Fig. 5, the P-N(pressure-life) curve with flaw fraction can be obtained as shown in Fig. 6. From Fig. 6, the applied pressure at the specific loading cycles $(3\times10^1, 3\times10^2, 3\times10^3)$ is plotted as a function of the flaw fraction in Fig. 7. Therefore, the K_D can be expressed as a function of flaw fraction as shown in Fig. 8 and is given by:

$$K_D - 1 = AV_f^\alpha \tag{3}$$

in which A and α are the material constants, respectively. Here, since the constant A means the relation of K_D and flaw fraction, it was assumed to be related to the fatigue life by power law as follows:

$$A = CN_f^\beta \tag{4}$$

Fig. 9 indicates that A can be expressed as a function of fatigue life. And the constants C and β are $1.5\times10^{10-3}$ and -0.0597, respectively.

Combining Eq. (3) and Eq. (4) leads to
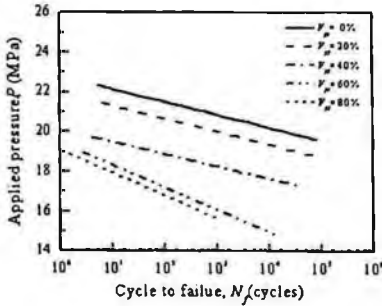
Fig. 6 P-N curves according to V_f
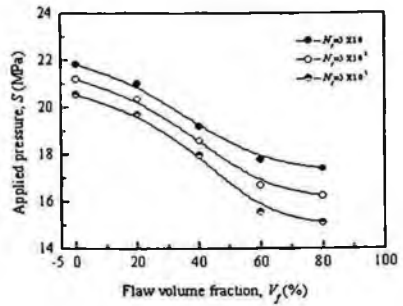
Fig. 7 Applied pressure vs. V_f
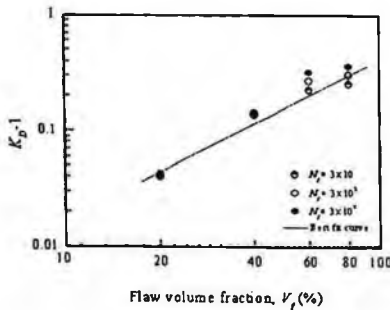
Fig. 8 K_D-1 vs. V_f
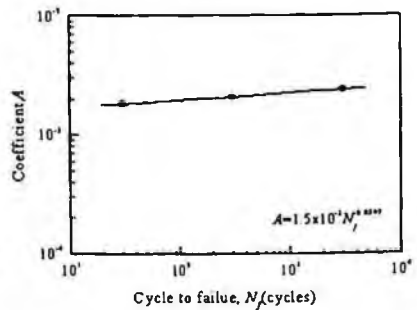
Fig. 9 Relationship of coefficient-life

$$K_D = 1 + CV_f^\alpha N_f^\beta \tag{5}$$

By substituting Eq. (5) into Eq. (2), the fatigue strength of a brazed joint with an internal flaw is given by:

$$\sigma_D = \sigma_0 / \left(1 + CV_f^\alpha N_f^\beta\right) \tag{6}$$

$$C = 1.5 \times 10^3, \ \alpha = -1.5036, \ \beta = -0.0597$$

4. Conclusion

To identify the fatigue behavior of brazed joints used in household electronics, the fatigue tests were performed under cyclic internal pressure due to the refrigerant by the use of a self-designed internal pressure testing machine. Also, a durability analysis was performed to evaluate the fatigue life with respect to the heat and the internal flaws. The following conclusions have been drawn.

[1] The fatigue behavior of the brazed joint can be directly related to the applied internal pressure. And from the results by durability analysis, the fatigue life of the brazed joint is greatly affected by internal flaw volume fraction.

[2] To describe the fatigue life of brazed joints affected by both the applied pressure and flaw fraction, the fatigue strength reduction factor and resulting life prediction model are presented as a function of internal pressure and flaw fraction.

Acknowledgment

References

1. American Welding Society, Welding Handbook, 2, Eighth edition
2. C.Y. Kang, J. *Korean Welding Soc.*, **18**, 672 (2000)
3. S. Mandal, A.K. Ray and A.K. Ray, *Mate. Sci. Eng. A*, **383(2)**, 235~244 (2004)
4. P. He, J. C. Feng and H. Zhou, *Mate. Charac.*, **52(4~5)**, 309 (2004)
5. S. Wang, H. Zhou and Y. Kang, *J. Alloys Com.*, **352(1~2)**, 79 (2003)
6. K.W. Kang, H.J. Shim, C.M. Kim and J.K. Kim, *Key Eng. Mater.* **326-328** 1043 (2006)
7. Mac Neal-Schwendler Corp., *MSC.PATRAN.* (Los Angeles, USA 2001)
8. Mac Neal-Schwendler Corp., *MSC.NASTRAN.* (Los Angeles, USA 2001)
9. Mac Neal-Schwendler Corp., *MSC.FATIGUE.*(Los Angeles, UAS 2001)

EVALUATION OF FATIGUE STRENGTH OF THE BOGIE FRAME FOR ELECTRICAL MULTIPLE UNIT

SUNG-CHEOL YOON[†]

Railroad Testing & Certification Research Center, Korea Railroad Research Institute,
#360-1, Woulam-Dong, Uiwang-City, Gyeonggi-Do, 437-757, Korea

JEONGGUK KIM

Railroad Testing & Certification Research Center, Korea Railroad Research Institute,
#360-1, Woulam-Dong, Uiwang-City, Gyeonggi-Do, 437-757, Korea

This paper describes the results of structural analysis and loading test of a bogie frame. The purpose of the analysis and test is to evaluate the safety and functionality of the bogie frame under maximum load. The bogie system consist of the bogie frame, suspensions, wheel-sets, a brake system and a transmission system. Of these components, the bogie frame is the major component subjected to the vehicle and passenger loads. The evaluation method used the JIS E 4207 specifications throughout the FEM analysis and static load test. The test results have shown the bogie frame to be safe and stable under design load conditions.

1. Introduction

The bogie frame, which is a running system for railway rolling stock, is a key structural part that supports the car body's load, and significantly influences the safety of the passengers and the railway vehicle, running performance, and riding comfort. The running system mainly consists of the bogie frame, wheel, axle, primary and secondary suspension systems, braking system, motor, and transmission gear. The bogie frame, which designates the structure of the bogie, has a complex configuration, directly supports the loads. It involves complex application of both static and dynamic loads, and is subject to the static load due to the car body's empty weight and passenger weight, and the dynamic load due to irregular rail tracks, and the motion mode of the car body, running system, and wheel axle [1]. The bogie used in this study was a bolster-less air spring bogie of the heavy electrical multiple unit that is in operation in Seoul, Korea, with 1,435 ㎜ in gauge, and 860 ㎜ in wheel diameter, and uses tread braking. First, a structural analysis was conducted for the bogie frame, a major component of the running system, and then structural safety was evaluated. The characteristics of the bogie were analyzed by confirming its strength through a load test based on this structural analysis.

[†] Corresponding Author:Sung cheol Yoon, scyoon1@krri.re.kr

The structural analysis was conducted for the test loads of the vertical load, twist load, longitudinal load, lateral load, driving gear load, traction motor load, and brake load, primarily in accordance with the standard for conducting performance tests for urban railway rolling stocks [2-4].
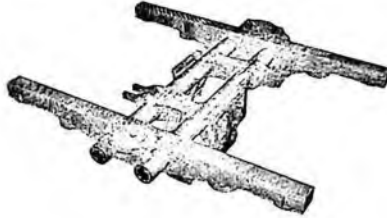
Fig. 1. Analysis model of the bogie frame

Strength analysis was conducted for the bogie frame with a bolster-less welding structure, the roll rubber spring of the primary suspension system, and the air spring of the secondary suspension system by using the finite element method. Shell and solid elements were used for analysis, and the spring element was used for the roll rubber spring. Fig. 1 presents the analysis model.

Table 1. Weight of the bogie frame

No.	Type	Weight	Remarks (unit: kg)
1	Empty weight	37,000	
2	Max. passenger weight	30,000	
3	Bogie weight	14,830	2 sets
4	Spring bottom weight	7,880	2 sets
5	Weight per bogie	29,560	[①+②-④]/2

The calculated weight of the bogie of the electric rail car is shown in Table 1, and each test load, including the vertical load, is calculated in Table 1. The loads applied on the bogie frame are calculated based on the bogie test in the performance test, and are as follows. The structural analysis and the load test were conducted by applying the load conditions as presented in Table 3 [2-5].

Table 2. Mechanical property of the bogie frame

Material	Yield strength	Tensile strength	Fatigue Limit Base metal	G/R	Welding	Remarks (unit: kg f/mm²)
SM490A	33	50	16			side frame, transom support bracket
STKM18B	32	50	14	11	7	transom pipe
SS400	25	41	14			stiffener, seat

Table 3. Load conditions of the bogie frame

No.	Load condition	Load (kg)	Direction of the Load	Remarks	No.	Load condition	Load (kg)	Direction of the Load	Remarks
1	Vertical load	29,560	Down	1.0 g	5	Driving gear load	3,780	Up & down	Forward
		38,428	Down	1.3 g			3,780	Up & down	Back ward
2	Twist load	29,560	Down	2 and 3 position	6	Traction motor load	3,792	Down (5.0g)	
		29,560	Down	1 and 4 position			2,492	Up (3.0g)	
3	Longitudinal load	8,868	Forward		7	Brake load	5,000+	Forward	1 and 2 position
		8,868	Backward				1,250	Backward	
4	Lateral load	8,868	Left				5,000+	Forward	3 and 4 position
		8,868	Right				1,250	Backward	

The strength of the bogie must be less than the yield stress of the materials for each part of the bogie frame in Table 2 [5], and is converted into combined stress to evaluate safety, depending on the fatigue endurance diagram.

2. Structural analysis of the bogie

The stress distributions of each load condition are shown in Table 4 and Figs. 2 to 3. In Table 4, the maximum stress was 14.73 kg f/mm² at the air spring seat when it was subject to the vertical load, and was within the yield stress, 33.0 kg f/mm², of the material used for this part, SWS490A.

Table 4. Maximum stress of the load condition   (unit: kg f/mm²)

No.	Load condition	Max. stress	Yield stress	Material	Remarks
1	Vertical load	14.73	33.0	SWS490A	Side frame
2	Twist load	12.10	33.0	SWS490A	Brake hanger bracket
3	Longitudinal load	8.21	33.0	SWS490A	T/M mounting bracket
4	Lateral load	10.47	33.0	SWS490A	Transom support bracket
5	Driving gear load	5.31	33.0	SWS490A	Gear hanger bracket
6	Traction motor load	8.86	32.0	STKM18B	T/M mounting bracket
7	Brake load	2.76	33.0	SWS490A	Brake hanger bracket
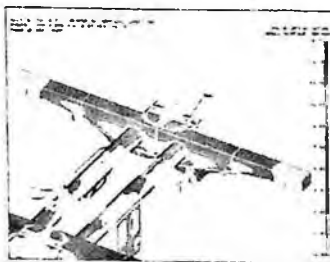
Fig. 2. vertical load   Fig. 3. Longitudinal load

3. Load tests of the bogie

The vertical load, twist load, longitudinal load, lateral load, etc. were measured by strain gauges where high stress is expected under each load condition [6].

3.1. *Vertical load*

The stress was measured after 38.5 tons was added while considering the 0.3 g dynamic effect to the vertical load. The maximum load was produced above the air spring seat (strain gage no. 5), and the value is 14.06 kg f/mm² to make it within the yield stress 33 kg f/mm², of the used materials (SWS490A).

3.2. *Twist load*

Twist load is produced by the rail imbalance, and the stress is measured by inserting the linear load in the lower platform of the primary spring and adding 29.5 tons of the vertical load. The maximum stress is shown above the air spring seat, in the 2nd and 3rd positions tests (strain gage no. 6), with the value being 11.04 kg f/mm², which is within the yield stress, 33 kg f/mm².

3.3. *Longitudinal load*

Longitudinal load is produced by the longitudinal vibration where the stress was measured after 8.9 tons, where 30% of the vertical load was added. The maximum stress appears in the mono link bracket (strain gage no. 39) and is seen when it moves forward. The value is 6.31 kg f/mm², which is within the yield stress, 33 kg f/mm².

3.4. *Lateral load*

For the lateral load, the stress was measured after 8.9 tons which are 30% of the vertical load was added. The maximum stress is shown in the transom support bracket (strain gage no. 64) in the right side load test, and the value is -7.16 kg f/mm², which is within the yield stress, 33 kg f/mm², of the used materials (SWS490A).

3.5. *Driving gear load*

Driving gear load is a reaction on the gear mounting bracket for the maximum torque of the driving motor when a vehicle is driven. The maximum stress is shown in the driving gear bracket (strain gage no. 11) in the reverse travel load test, and the value is -5.82 kg f/mm², which is within the yield stress, 33 kg f/mm².

3.6. *Traction motor load*

The traction motor load produced by the up and down vibration of the motor is 3.0g to the upward direction and 5.0g to the downward direction given the self-load (650 kg). The maximum stress is shown in the transom pipe (strain gage no.

35) in the downward direction load test, and the value is 6.40 kg f/mm² which is within the yield stress 33 kg f/mm².

3.7. *Brake load*

For the brake road, there is a brake reaction by the block force of the piston and the couple of brake force by the friction between the brake shoe and the wheel. The maximum stress is shown in the brake bracket (strain gage no. 50) in the reverse travel direction load test, and the value is 4.05 kg f/mm² which is within the yield stress 33 kg f/mm².

Table 5. Vertical load

S/G No.	Load step (kg)				
	0	29560	38428	29560	0
5	-0.26	-10.83	-14.06	-10.91	-0.50
6	-0.14	-10.71	-13.64	-10.43	-0.06

Table 6. Twist load

S/G No.	Load step (kg)				
	0	22170	29560	22170	0
6	0.04	-8.46	-11.04	-8.18	0.50
48	0.30	8.01	10.55	8.11	0.16

3.8. *Combined stress*

The test results helped compute the combined stress and the fatigue endurance. The measurements point that the average stress is over 9.9 kg f/mm² and the stress amplitude is over 6.8 kg f/mm², as shown in Table 7 and 8 and drawn as Fatigue Endurance Diagram in the Fig 4 and 5. Considering these results, the fact that the average stress is high in the combined stress, with the air spring seat (strain gage no. 6, welding part) while driving reaching -10.85 kg f/mm², and the part where the stress amplitude is shown high is mono link bracket (strain gage no. 39, base

Table 7. Combined stress result(mean stress)

S/G No.	Combined stress (driving)		Combined stress (braking)		Remarks
	Mean stress	Stress amplitude	Mean stress	Stress amplitude	
6	-10.85	4.00	-9.31	3.39	Welding
5	-10.12	3.90	-8.68	3.36	Welding
48	9.90	3.46	7.04	3.17	Base metal

Table 8. Combined stress result(stress amplitude)

S/G No.	Combined stress (driving)		Combined stress (braking)		Remarks
	Mean stress	Stress amplitude	Mean stress	Stress amplitude	
39	-2.54	7.73	-3.15	6.75	Base metal
42	-0.69	6.91	-0.38	6.54	Base Metal
31	-1.10	6.88	-0.91	4.98	Base metal

metal part) while driving at 7.73 kg f/mm², reflects that they are all located in the safety zone of each welding, grinding and base metal part [5, 6].
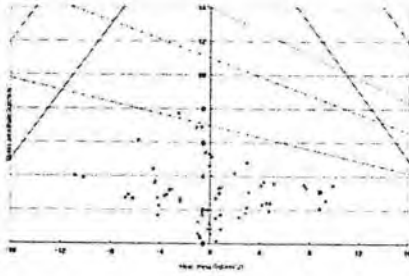
Fig. 4. Fatigue endurance diagram for
driving mode
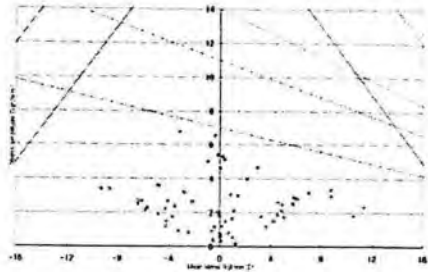
Fig. 5. Fatigue endurance diagram for
braking mode

4. Conclusions

The results of the structural analysis and load tests on the bogie frame are as follows.

1) Comparing the structural analysis and the load test, they occured within the yield stress of each material under each load condition.

2) Regarding maximum stress production, 14.73 kg f/㎟ was produced in the air spring seat of side frame in the vertical load with the respect to the structural analysis, and 14.06 kg f/㎟ was produced in the air spring seat (strain gage no. 5) in the vertical load with the respect of the load test.

3) As a result of the computation of the combined stress, the maximum average stress was -10.85 kg f/㎟ in the air spring seat (strain gage no.6, welding part) while driving, and the maximum stress amplitude produced 7.73 kg f/㎟ in the mono link bracket (strain gage no. 39, base metal part) while driving.

4) As a result of the tests, all the combined stresses are located within the safety zone on the fatigue endurance diagram. Thus, the bogie frame has sufficient static strength and fatigue strength.

References

1. Kijun Park, Hoyong Lee, et al, *Evaluation of fatigue strength of the bogie frame of the standard electrical multiple unit*, Journal of the Korean Society for Railways, **Vol. 3, No. 3**, pp.170-176(2000).
2. MOCT, *Standard for performance tests for urban railway rolling stocks*, load tests for the bogie(2000).
3. Japanese Industrial Standards, *Truck Frames for Railway Rolling Stock-General Rules for Design*, E 4207(1992).
4. Japanese Industrial Standards, *Test Methods of Static Load for Truck Frames and Truck Bolsters of Railway Rolling Stock*, E 4208(1988).
5. Korea Standard Association, *General code of design for bogie stock for railway rolling stock*, R 9210(1996).
6. Sungcheol Yoon, Wonkyung Kim, A *Study on the Structural Analysis and Loading Test of Bogie Frame*, Journal of the Korean Society for Railways, **Vol. 8, No. 6**, pp.101-107(2005).

AN EVALUATION OF RESIDUAL STRESS REDISTRIBUTION CAUSED BY FATIGUE CRACK PROPAGATION BY FINITE ELEMENT METHOD

EUNG-JOON PARK

College of Mechanical Engineering, Ajou Univ. San 5, Wonchun-Dong, Yeongtong- Gu, Suwon, Korea

EUNG-JOON KIM

College of Advanced Material Engineering, Hanbat Univ. San16-1,Duckmyoung-Dong, Yuseong-Gu, Daejeon, Korea

SEUNG-HYUN YOO

College of Mechanical Engineering, Ajou Univ. San 5, Wonchun-Dong, Yeongtong- Gu, Suwon, Korea

An investigation was performed to predict residual stress redistribution for the crack propagation initially through tensile residual stress field. The analytical method to estimate the redistribution of residual stress caused by crack propagation was proposed, on the basis of Dugdale model, by finite element analysis using elastic analysis method considering superposition principle. It is verified that the residual stress redistribution caused by crack propagation depends on configuration of the initial residual stress distribution. The variation aspect of redistribution of residual stress caused by crack propagation was examined based on the equilibrium condition of residual stresses.

1. Introduction

Many researches have been conducted for the evaluation of the fatigue crack propagation behavior in welding residual stress field. Early research for the fatigue crack propagation behavior of welding residual stress was began with the consideration that propagation rate of fatigue crack initiated from tensile residual stress field adjacent to the welding joint is greater than the crack propagation rate in base material at the same applied load condition. After that, for the case that fatigue crack propagates initial tensile residual stress field, and the influence of residual stress on the propagation behavior of fatigue crack is evaluated by the effect of mean stress, that is the effect of stress ratio [1-5].

However, for the residual stresses are those stresses that exist with a distribution, the effect of mean stress changes as the crack propagates. Therefore,

the effect of welding residual stress on fatigue crack propagation behavior is evaluated as the effective stress intensity factor calculated by the stress range at which the crack tip opens. Meanwhile, if fatigue crack propagates from initial tensile residual stress field, residual stress distributed ahead of crack tip changes as the crack propagation. The common feature of redistributed residual stress is recognized that residual stress concentration consecutively occurred in the vicinity of crack tip even the situation that the crack propagated to the region initially compressive residual stress existed. However, the effect of residual stress on stress ratio during the full propagation process of fatigue crack from initial tensile residual stress field to the region initially compressive residual stress existed with relation to the configuration of initial residual stress distributions is not clarified yet.

In this study, to evaluate the effect of welding residual stress on fatigue crack propagation behavior for the case that fatigue crack propagates from initial tensile residual stress field, an analysis method using finite element method based on Dugdale model is proposed to estimate redistributed residual stress caused by crack propagation. And the relation between the configuration of initial residual stress distribution and the variation aspect of residual stress distributed ahead of crack tip during crack propagation depends on the configuration of initial residual stress distribution.

2. Finite Element Analysis

2.1. *Analysis Method*

When a specimen containing a crack of length 2c is subjected to a tensile loading, the stress distribution near the crack can be explained by the principle of superposition as shown in Fig. 1 [6].
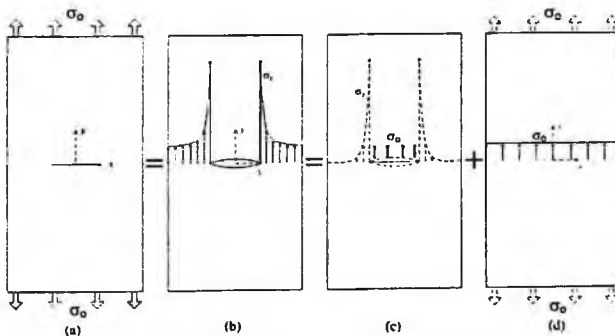
Fig. 1. Illustration of Superposition principle.

Fig. 1(a) shows a plate with a central crack under uniaxial tensile stress σ_0 and Fig. 1(b) shows the stresses distributed ahead of crack tip at the state of Fig. 1(a). Fig. 1(b) is a superposition of a plate with a crack having distributed internal pressure σ_0 (Fig. 1(c)) and a plate without a crack under uniaxial tensile stress σ_0 (Fig. 1(d)). The internal pressure σ_0 of Fig. 1(c) acts in a direction opposite to the applied uniaxial tensile stress σ_0.

Fig. 2 shows the Dugdale model applied in this study to estimate residual stress redistributed ahead of crack tip during crack propagation from initial tensile residual stress field considering plastic zone at crack tip [7].
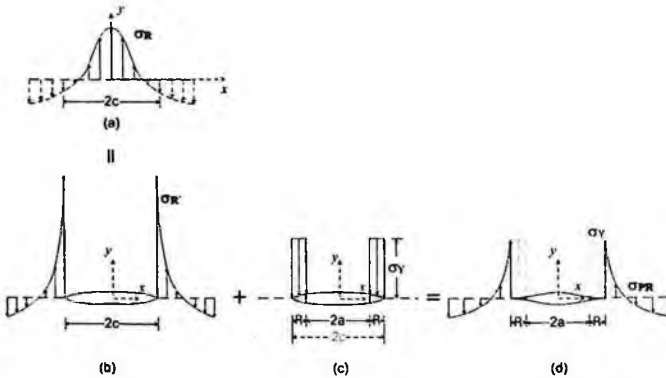
Fig. 2. Modified Dugdale Model.

The application of Dugdale model was carried out in a method that makes compressive stress equivalent to yield stress of material act on a certain region from crack tip to the direction of crack center, to make the stress value at crack tip become under the yield stress of material, using the result of elastic analysis on the distribution of residual stress, which was redistributed in a form that tensile stress is concentrated at crack tip. In this study, a certain region, from crack tip to the direction of crack center, where compressive yield stress act to make the stress value at crack tip become under the yield stress of material, was considered as the plastic zone in Dugdale model.

Fig. 2(a) shows initial distribution of longitudinal residual stress adjacent to welding line y. Where, if the length of 2c is assumed as crack, crack is opened and stress concentration occurs at the crack tips by the tensile residual stresses existed at the range of 2c. Fig 2(c) shows plastic zone size R to make the stress value at crack tip become yield stress of the material. By the superposition of Fig. 2(b) and Fig 2(c), the distribution of residual stress of Fig 2(d) can be acquired.

2.2. *Analysis Model*

The finite element model consisting of center cracked plate with through-thickness crack surrounded by welding residual stress field was applied. The geometry of the finite element model is 250mm long, 200mm wide and 10mm thick. The material properties were for a mild steel and the Young's modulus is 210Gpa and the Poisson's ratio is 0.3 and yield stress is 240MPa. The analysis was executed by elastic analysis on the redistribution of residual stress caused by crack propagation in the residual stress field. Analysis was performed by elastic method using ABAQUS(ver.6.4). The elements used for analysis are contact element for crack plane to prevent the overlapping of the crack surface due to the compressive residual stress, and plane stress element (CPS4; 4-node bilinear element) for the remaining part of base metal [8].

3. Analysis Results and Discussions

Fig. 3 shows the variation of plastic zone size at crack tip during crack propagation obtained by finite element analysis based on Dugdale model as shown in Fig. 2. Distribution of initial residual stress is assumed as a stress distribution obtained from butt weld of two steel plates without constraint.

By considering the equilibrium condition of residual stresses, the area of tensile stress field is almost same that of compressive stress field. At the early stage of crack propagation, plastic zone size increase gradually due to the uniform tensile residual stress equivalent to the yield stress material. However plastic zone size begins to decrease as the crack tip enters initial compressive residual stress field.
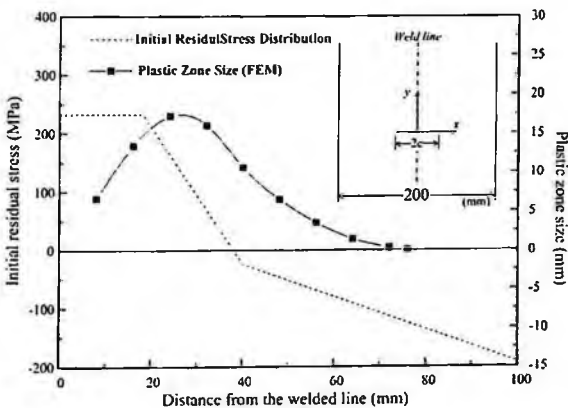
Fig. 3. Plastic zone size caused by crack propagation in the residual stress field by FEM.

Fig. 4 shows the relation between the configuration of initial residual stress distribution and the variation aspect of residual stress distributed ahead of crack tip during crack propagation.

(a)

(b)
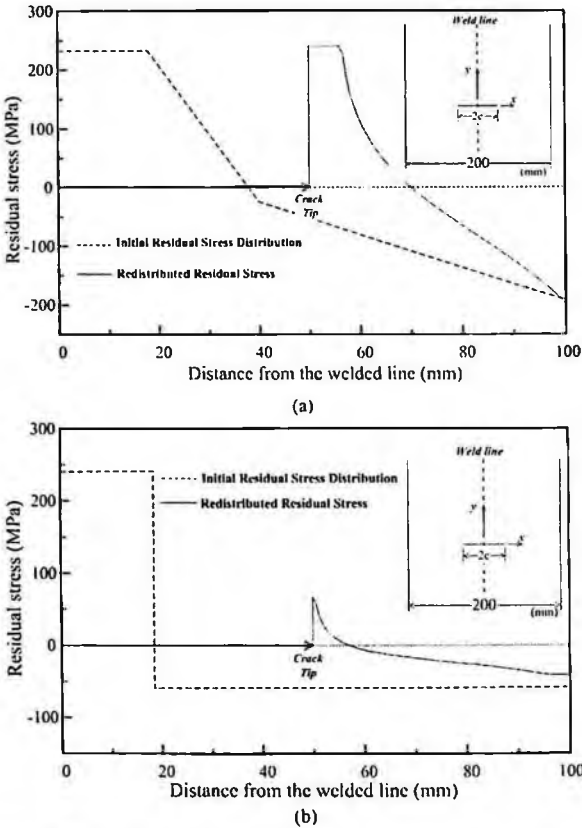
Fig. 4. Redistribution of residual stress depends on the initial residual stress distribution.

For the both initial distributions of residual stress shown in Fig. 4(a) and Fig. 4(b), each area of tensile residual stress field and compressive stress field is configured to be almost same to reflect equilibrium condition, that is, the resultant force and resultant moment produced by the residual stresses must vanish in an unconstrained material. Therefore, in consideration of equilibrium condition of residual stresses, the configuration of residual stress redistributed ahead of crack tip due to crack propagation should have the same area of tensile residual stress field and the compressive one.

However, in spite of the distribution of initial residual stresses both in Fig. 4(a) and Fig. 4(b) seems to be feasible theoretically, the configuration of redistributed residual stress shown in Fig. 4(b) does not comply to the equilibrium condition of residual stresses. Therefore, it is recognized that variation aspect of redistributed residual stresses depends on the configuration of initial residual stress distribution. In regard to this matter, additional examination which is based on fracture mechanics is required to prove the reasonability of initial residual stress distribution.

4. Conclusion

In this study, an analysis method using finite element method was proposed to examine the redistributed residual stress caused by crack propagation initially through tensile residual stress field. And the reasonability of residual stress distribution was examined.

The results of the study are as follows.

1). Using finite element analysis method, redistributed residual stress caused by crack propagation can be estimated by the superposition principle based on Dugdale model.

2). The variation aspect of residual stress distributed ahead of crack tip during crack propagation depends on the configuration of initial residual stress distribution.

3). Additional examination which is based on fracture mechanics is required to prove the reasonability of initial residual stress distribution.

References

1. R. J. Bucci, *ASTM STP.* **743**, 28 (1981).
2. D. V. Nelson, *ASTM STP.* **776**, 172 (1982).
3. A. Ohta, E. Sasaki, M. Kamakura and M. Nihei, *Trans. Japan Welding Soc.* **12-1**, 31 (1981).
4. K. Nihei, H. Ono and T. Tsunenari, *J.of Japan N. A.* **152**, 390 (1982).
5. Y. Mukai, A. Nishimura and E. J. Kim, *J. of the Japan Welding Soc.* **4-1**, 154 (1986).
6. K. Masubuchi, *Monthly Report of Transportion Technical Research Institute.* **8**, 12 (1959).
7. D. S. Dugdale, *Int. J. Mech. Phys. Solids.* **8-100**, 100 (1960).
8. ABAQUS User's Manual for revision 6.4 Vol II . Hibbits, Karlsson & Sorensen, Inc. (2004).

FATIGUE STRENGTH ANALYSIS OF THE WEB PLATE OF WHEELS USING CRITICAL PLANE APPROACH

JUNGWON SEO[†], SEOKJIN KWON, SUNGTAE KWON

Korea Railroad Research Institute, Railroad Testing & Certification Research Center
Uiwang, Kyonggi-do, 437-755, South Korea

Railway wheels have been one of the most critical components in a railway vehicle. Fatigue design of railway wheel is one of the most important factors, because wheel failure can cause derailment with loss of life and property. Damage on the wheel can be divided into three types, such as the contact fatigue of the tread, the thermal fatigue of the rim due to braking and the mechanical fatigue of the web plate. The fatigue strength analysis of wheels has been performed using the method described in the UIC Leaflet 510-5 "Technical Approval of Solid Wheels". This method is based on an assumption that the applied loads for wheels are mono-axial condition. However, the recent application involving the use of a wheel disc with drilled holes has shown that the principle stress field directions vary during the wheel rotation. In this study, the effect of the multi-axial load on the fatigue life for a railway wheel is evaluated through the employment of the critical plane approach. Finite element analysis was carried out to obtain stress-strain fields and to ascertain fatigue behaviors in the multi-axial zone according to wheel rotation.

1. Introduction

Railway wheels have been one of the most critical components in a railway vehicle. The service conditions of railway vehicles have became more severe in recent years due to the increase of the speed. Fatigue design of railway wheel is one of the most important factors, because wheel failure can cause derailment with loss of life and property. The main factors which must be taken into consideration for the fatigue design of wheel are the contact fatigue of the tread, the thermal fatigue of the rim due to braking and the mechanical fatigue

Researches on the thermal fatigue of the rim due to braking among the fatigue strength evaluation of wheel have extensively been performed[1,2,3]. A couple of case studies on the contact fatigue of the tread due to wheel and rail contact has been reported[4,5,6,7].

Up to now, the fatigue strength analysis of the web plate of wheels has been performed using the method described in the UIC Leaflet 510-5 "Technical

---

Approval of Solid Wheels"[8]. This method is based on an assumption that the applied loads for wheels are mono-axial condition. However, the recent application involving the use of a wheel disc with drilled holes has shown that the principle stress field directions vary during the wheel rotation[9]. The UIC does not define a calculation method that is to meet the requirements of the multi-axial stress and other influence parameter. Thoma[10] estimated effects of the centrifugal-force and other parameter on fatigue strength of wheels for the high speed train. Yoshinori[11] proposed the fatigue design method of high speed railway wheel by considering the effect of manufacturing conditions and the volume factor on the fatigue strength of the material. Cocheteux[12] proposed the fatigue strength evaluation method of wheel disc with drilled hole under multi-axial load. However, the effect of residual stress due to manufacturing process was not considered in their simulation.

In this study, the effect of the multi-axial load and the residual stress on the fatigue life for a railway wheel is evaluated through the employment of the critical plane approach. Finite element analysis was carried out to obtain stress-strain fields and to ascertain fatigue behaviors in the multi-axial zone according to wheel rotation.

2. Fatigue strength evaluation

2.1. *F.E. Model and Load condition*

A wheel with drilled holes by using a wheel disc for high speed train is chosen for the analysis. The two type models are used. One is a model for new wheel. The other is a model for wheel with thin rim thickness due to wear during operation and reprofiling for maintenance.
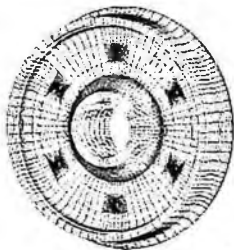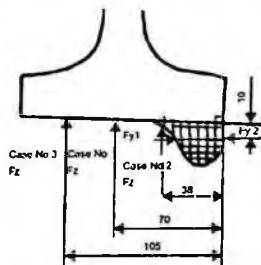
Fig. 1 F.E. model   Fig. 2 Load condition according to UIC

Fig. 1 shows a finite element model used for stress analysis. The UIC reduced the load case to three. These three load cases and the locatons of load are shown

in Fig. 2. Loadcase 1 corresponds to straight track where vertical force($Fz = -1.25*Q*g$, Q : mass of vehicle per wheel, g : accerlation due to gravity) is present. Loadcase 2 corresponds to full curve track where vertical force and transverse force($Fy1 = 0.7 *Q*g$) are included and loadcase 3 in the passing through negotiation of crossings and points where vertical force and transeverse force($Fy2 = 0.42 *Q*g$) are applied to another location.

2.2. *Analysis method and stress state of the web plate surface*

To obtain stress histories for wheel loads which rotate, it is considered that the center of the wheel is fixed and loading locations vary on the wheel at equal angle intervals. Fig. 3 shows the stress history for one wheel rotation at a point of the hole from finite element analysis. To evaluate multi-axial characters, Variations of biaxial ratio which are the ratios of the principle stress with the minor absolute amplitude and that with the major absolute amplitude were calculated. As shown in Fig. 4, the biaxial ratios vary from 0 to -1 and shows multi-axial states at that point.
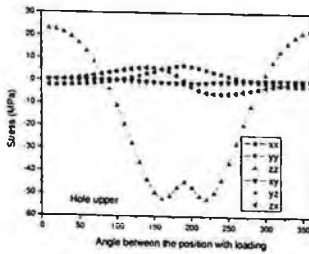
Fig. 3 Stress history at a point of hole
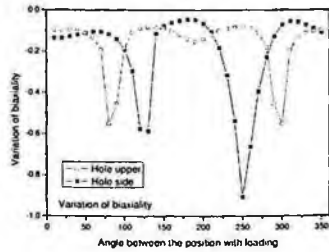
Fig. 4 Variation of biaxial ratio

3. Results and discussion

In the process of the railway wheel manufacturing, the residual stress is created by a heat treatment which is performed to reduce the wear rate by increasing the hardness of the tread. The residual stress on the wheel has been reported to be changed its distributions due to the shape of the plate. The effect of residual stress variations due to the manufacturing process should be included in evaluating the fatigue behavior.

3.1. *Residual stress during manufacturing process*

Fig. 5 shows a typical wheel manufacturing process; cooling after rolling, quenching at the contact zone, and tempering, consequently. A axisymmetric model is used to adopt the symmetric characteristics of the wheel geometry and the loading condition. The heat transfer analysis on the basis of convection

conditions are followed by the thermal stress analysis simulating the heat treatment process of heating, cooling, quenching and tempering, consequently. Fig. 6 shows the residual stress evaluation results according to the distance from a axle part at surface of the web plate. The resulting residual stress in the radial direction is observed at the center of the web plate, the highest stress appears to 50 mm from the axle part. The circumferential residual stress appears to be 180MPa at axle part and gradually changes along the distance and turns to be compressive stress over 80mm from the axle part.
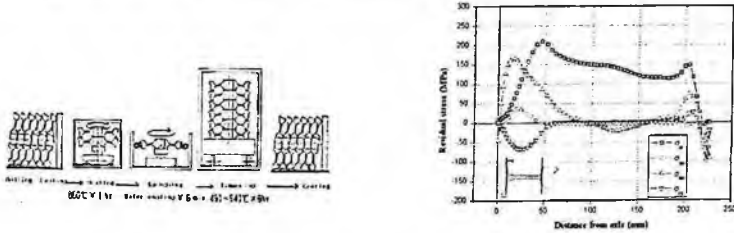
Fig. 5 Manufacturing process of wheel[13]   Fig. 6 Residual stress distribution at web plate

3.2. *Multi-axial fatigue analysis considering residual stress*

The fatigue strength analysis was performed by using the UIC method and the critical plane approach which is one of the methods account for multi-axial fatigue damages. In the procedure of the UIC, the principal stresses should be calculated at all points in the nodes for each of the three load cases. The maximum and the minimum stresses for the three load cases for each node are determined. Finally, the mean stress and the dynamic stress are calculated by using the following equations.

$$\sigma_{mean} = \frac{\sigma_{\max} + \sigma_{\min}}{2} \quad (1) \qquad \sigma_{dyn} = \frac{\sigma_{\max} - \sigma_{\min}}{2} \qquad (2)$$

where σ_{mean}, σ_{dyn}, $\sigma_{\max}$, $\sigma_{\min}$ are the mean stress, the dynamic stress, the maximum stress and the minimum stress, respectively. Many researchers have proposed multi-axial fatigue criteria suitable to different loadings and different materials. In this paper, the Dang van's criterion based on the shear stress for the high-cycle fatigue is applied as follows[14]:

$$\tau_{\max}(t) + a_{DV}\sigma_H(t) = \tau_w \quad (3) \qquad a_{DV} = 3(\frac{\tau_w}{\sigma_w} - \frac{1}{2}) \qquad (4)$$

where, $\tau_{\max}(t)$, $\sigma_H(t)$ are the maximum shear stress and hydrostatic stress evaluated at each time of the load cycle, a_{DV} and τ_{DV} are constants for loads and materials determined by tension-compression and torsion fatigue tests. According to the criterion, damage occurs if the combination of the shear stress amplitude and the hydrostatic stress considered on a shear plane. Fig. 7 shows

the fatigue strength evaluation results according to the UIC. All of the results were within the allowable stress. In the case of without the consideration of the residual stress, the mean stress is seems to be almost a constant value of -10 MPa. While, in the case considering the residual stress, the maximum mean stress was 250MPa and the dynamic stress was 120MPa at the web plate of the wear wheel. Fig. 8 shows the fatigue strength results according to the Dang van's criterion. The results predicted by no considering the residual stress were within the allowable stress. The safety factor(S_f)of the new wheel was 1.4 and that of the wear wheel was 1.3, which was calculated from the following formula.

$$S_f = \cfrac{1}{\cfrac{a_{DV}\sigma_h}{\tau_w} + \cfrac{\tau_{max}}{\tau_w}} \tag{5}$$

While, in the case considering the residual stress, the results of the wear wheel were over the allowable stress at the web plate. However, if the residual stress is relaxed by repeated loadings in service operation, it seems to be within the allowable stress.
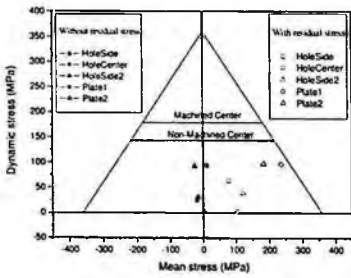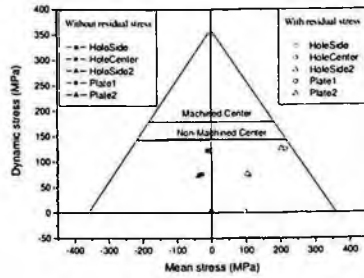
a) New wheel   b) Wear wheel

Fig. 7 Fatigue strength evaluation according to the UIC
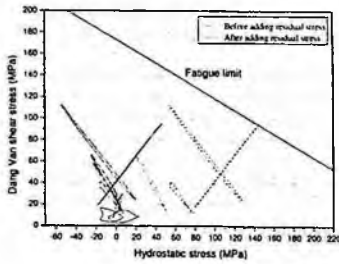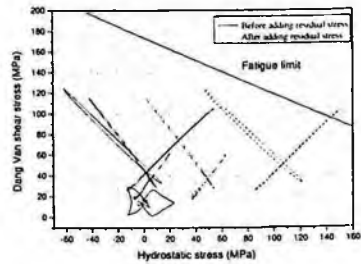
a) New wheel   b) Wear wheel

Fig. 8 Fatigue strength evaluation according to the Dang van's criterion

4. Conclusions

In this paper, the fatigue strength evaluations are performed to investigate the effect of the residual stress and the multi-axial load through the employment of the critical plane approach. The following conclusions are obtained.

1. It is observed that the principle stress field directions vary during the wheel rotation from stress histories obtained the Finite Element analysis.
2. The results predicted by no considering the residual stress were within the allowable stress. The safety factor of the new wheel was 1.4 and that of the wear wheel was 1.3.
3. In the case considering the residual stress, the fatigue analysis results of the wear wheel according to the UIC were within the allowable stress. While, the results according to the Dang van's criterion were over the allowable stress However, if the residual stress is relaxed by repeated loadings in service operation, it seems to be within the allowable stress.

Acknowledgments

References

1. J. Gordon, A. Perlman, *ASME IMECE RTD*,(1998).
2. J. W. Seo, C. S. Suk, Y. J. Kim, *the KSME Mat. And Frac. part*,176(2002).
3. G. Donzella, M. Scepi, *IMechE*, 145(1998).
4. R. Lundin, *wear 144*, 57(1991).
5. P. Mutton, *wear 144*, 193(1991)
6. A. Bernasconi, M. Filippini, S. Foletti, D. Vaudo, *Int. J. of Fat.*, 663(2006)
7. Y. Liu, B. Stratman, S. Mahadevan, *Int. J. of Fat.*, 747(2006).
8. UIC leaflet 510-5, (2003)
9. L. Degang, L. Huiying, W. Fenzhou, *14th wheelset congress*,(2004)
10. G. Thomas, H. Andreas, *14th wheelset congress*, (2004).
11. O. Yoshinori, Y. Yamamoto, H. Kenji, *14th wheelset congress*,(2004).
12. F. Cocheteux, J. Benades, T. Palin-luc, 7th *WCRR*, (2006)
13. H. Desimone, A. Bernasconi, S. Beretta, *wear 206*, 567(2006)
14. T. Noda, *Forum Vol. 7 No. 7*, 9(2002)

FATIGUE BEHAVIOR OF INCONEL ALLOYS DUE TO FRETTING AND HIGH TEMPERATURE

SEUNG-WAN WOO, JAE-DO KWON[†], DAE-KYU PARK, CHOON-YEOL LEE

Department of Mechanical Engineering, Yeungnam University, 214-1 Dae-dong Gyongsan City, Gyongbuk 712-749, Republic of Korea

Inconel 600 and 690, which are high-nickel chromium (Ni-Cr) alloys that exhibit excellent resistance against aqueous corrosion, are generally used in steam generator tubes in unclear power plants. In this paper, the effects of high temperatures such as an operating temperature of 320°C on the fatigue behavior of inconel 600 and 690 were studied. Through these experiments, it was observed that the plain fatigue limit at high temperatures slightly decreases as compared to that in room temperature. Furthermore, the fretting fatigue tests at room temperature were performed by considering the effect of the fretting damage on the fatigue behavior of the inconel alloys. Through fretting fatigue tests, the variations in the frictional forces and relative slips with cycles were obtained. After each test, the fatigue mechanisms were studied through SEM observations. These results can be used as data in structural integrity evaluations under high temperatures and fretting damage in nuclear power plant systems.

1. Introduction

The safety assessment of current industrial facilities has been recognized as a top priority issue. In the case of application of these facilities under conditions of repetitive stresses, a guarantee of their reliability from an early stage in design is required based on the theory of fatigue damage [1].

Fretting is a type of damage that occurs in structural materials according to the local relative slip in a contact region [2]. The major impact factors that impact fretting are the amount of relative slip, contact pressure, friction force, temperature, and humidity. With the occurrence of fretting in structural materials, fatigues including wear are developed according to the initiation and growth of cracks. Furthermore, it has been known that fretting significantly decreases the integrity and economy of material usability because it shortens the service life of such materials [3].

Inconel alloys are a type of high-nickel chromium (Ni-Cr) alloys that represent anti-oxidation and anti-corrosion properties at high temperatures; these alloys are applied in steam generator tubes in nuclear power plants [4]. However, it is necessary to conduct studies on the assessment of their service life because

of the lack of information on the status of theses alloys when they are exposed to certain fatigues under high temperatures and pressures such as the conditions in a nuclear power plant.

This study attempts to apply plain and fretting tests at room temperature for the alloys of inconel 600 and 690, and verify the decrease in the fatigue limits under fretting fatigues at room temperature and plain fatigues at high temperature as compared to those at room temperature. In addition, this study analyzes the mechanism of fretting and high-temperature fatigues through an analysis of a fractured surface. Further, the results from this analysis will contribute toward the evaluation of the structural integrity of an industrial facility and provide important information for the assessment of its safety.

2. Preparation of Materials

The alloys of inconel 600 and 690 used in this study are a type of high Ni-Cr alloys that are used as steam generator tubes in nuclear power plants; theses alloys exhibit an excellent property of anti-corrosion at high temperatures [4]. Inconel 600 and 690 contain 73.66 % and 58.05 % of nickel and 15.75 % and 29.44 % of chromium, respectively. In the microstructures of these two alloys, a lot of twins are included in the grains, as shown in Fig. 1, although their grain sizes are different.

Table 1 shows the results of the tension test of these alloys; it can be observed that these two alloys exhibit excellent elongation.

3. Results and Discussion

3.1. *Fretting fatigue tests at room temperatures*

Fig. 2 illustrates the diagram of the test equipment used in the fretting tests. The specimens were fabricated in the shape of a plate with a parallel length of 7 mm and thickness of 4 mm. Further, the contact pads were fabricated in the form of a bridge in order to obtain a face contact between the contact pad and the

Fig. 1. Microstructures of (a) inconel 600 and (b) inconel 690.

Table 1.Results of tension test.

Materials	Inconel 600	Inconel 690
0.2% yield strength	257 MPa	239 MPa
Tensile strength	628 MPa	591 MPa
Elongation	41	49
Young's modulus	189 GPa	199 GPa

specimen [5]. First, an initial contact pressure of 50 MPa was applied to the proving ring at a constant level and then the pressure was applied to the specimen through the arm and contact pad. The frictional force between the specimen and the contact pad was measured by using a strain-gage installed on the surface of the arm [6]. Further, the relative slip amplitude was measured by using an extensometer. The tests were performed by applying a tension-tension load with a stress ratio of R=0.1 and a load frequency of 10 Hz.

Fig. 3 shows the results of the plain and fretting fatigue tests for the alloys of inconel 600 and 690 at room temperature. In the case of inconel 600, the fatigue limits in plain and fretting fatigue tests were approximately 313 MPa and 101 MPa, respectively. This shows a decrease in the fatigue limits by approximately 67 % as compared to the plain fatigue case. In addition, in the case of inconel 690, the fatigue limits in the plain and fretting fatigue tests were approximately 315 MPa and 175 MPa, respectively. This demonstrates a decrease in the fatigue limits by approximately 44 % as compared to the plain fatigue case. Thus, it is evident that the fatigue limits significantly decrease when fretting fatigue occurs in inconel alloys [7].

Fig. 4 shows the change in the frictional forces according to the number of applied cycles from the results of the fretting fatigue tests. The frictional force
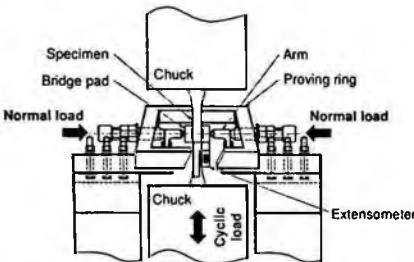
Fig. 2. Fretting fatigue test apparatus.
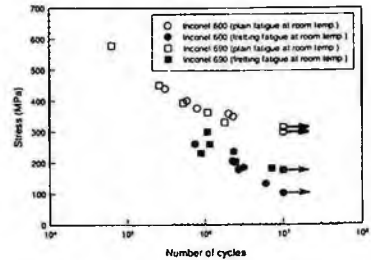
Fig. 3. Results of fatigue tests at room temperature.
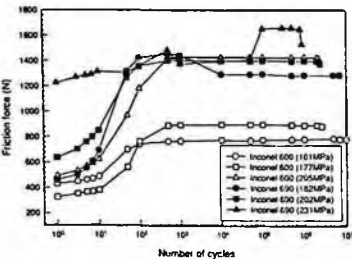
Fig. 4. Variation in the frictional force with increase in the number of cycles.
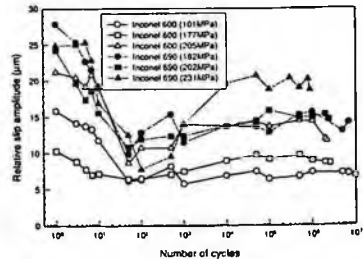
Fig. 5. Variation in the relative slip amplitude with increase in the number of cycles.

shows a rapid increase up to 10^3 cycles for the alloys of inconel 600 and 690, and then maintains a constant level. As shown in Fig. 5, the relative slip amplitude shows a rapid decrease up to 10^3 cycles and then maintains a constant level. It is clear that the behavior of the frictional force contrasts that of the relative slip amplitude according to the variation in the number of applied cycles [8].

Fig. 6 shows the fractographs of the fracture surface after applying the fretting fatigue test on inconel 600. As shown in Fig. 6(a), several wear-damaged areas are observed at the region where the crack begins. The damaged area that occurred due to the frictional force between the contact pad and the specimen was due to the growth of the initial oblique crack, as illustrated in Section A of Fig. 6(a), and this damage is a representative characteristic of fretting fatigues [9]. Further, the crack growth region shown in Fig. 6(b) is largely observed as a quasi-striation pattern.

Fig. 7 illustrates the fractographs of the fracture surface after applying the fretting fatigue test on inconel 690. Fig. 7(a) shows an oblique crack region where the regions at which the cracks begin to occur as well as the damaged regions are observed. Fig. 7(b) shows a stable fatigue crack growth region where ductile striations are largely observed.
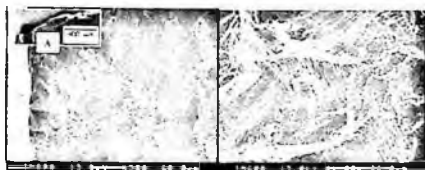
(a) wear damaged area (b) crack growth region
Fig. 6. Fractographs of inconel 600 after fretting fatigue test. (σ_{max} = 177 MPa)
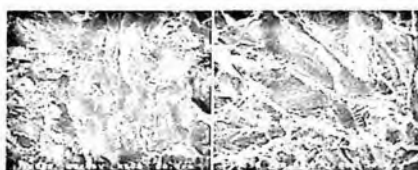
(a) wear damaged area (b) crack growth region
Fig. 7. Fractographs of inconel 690 after fretting fatigue test. (σ_{max} = 182 MPa)

3.2. *Plain fatigue tests at high temperatures*

The high-temperature tests of the inconel alloys were performed at 320°C by considering the operation temperature of a nuclear power plant, which rages from 290 to 330°C. The fatigue tests at high temperatures were performed by using a computer-controlled method while the test temperature was maintained at a proper test temperature by using a heat controller for 30 min after fixing the specimens by using chucks.

Fig. 8 shows the results of the plain fatigue tests at high temperatures. The fatigue limits of the alloys of inconel 600 and 690 at high temperatures were approximately 260 MPa and 271 MPa, respectively. The fatigue limits of these

alloys at high temperatures decreased by approximately 17 % and 14 % as compared to those at room temperature. This shows that the plain fatigue limits slightly decrease at high temperatures as compared to those of the fretting fatigue at room temperature. This occurs due to the fact that these inconel alloys exhibit excellent characteristics at high temperatures. However, it is necessary to consider the factors that affect such inconel alloys when they are used under high-temperature environments because the fatigue limits are found to decrease to a certain level at high-temperatures as compared to those at room temperature.

Fig. 9 shows the fractographs of the fracture surface after applying the fatigue test on inconel 600 at high temperatures. Fig. 9(a) illustrates the initial crack region where some corrosion regions were observed at high temperatures [10]. The crack growth region shown in Fig. 9(b) demonstrates a large distribution of striation that is generally produced in the plain fatigue case.

Fig. 10 illustrates the fractographs of the fracture surface after applying the fatigue test on inconel 690 at high temperatures. The initial crack initiation region shown in Fig. 10(a) and the crack growth region represented in Fig. 10(b) demonstrate similar shapes in the results obtained for inconel 600. Further, the final fractured region shows a type of ductile fracture with dimples. However, it is evident that there were certain influences of the high-temperature fatigue until the final fracture occurred due to the existence of fine striations in the dimpled region.
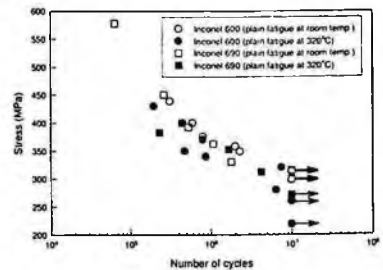
Fig. 8. Results of fatigue tests at high temperature.
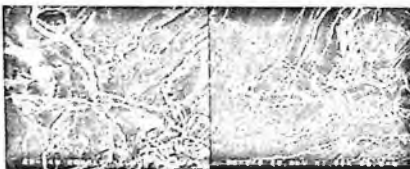
(a) initial crack region (b) crack growth region
Fig. 9. Fractographs of inconel 600 after fatigue test at high temperature.(σ_{max} =280MPa)
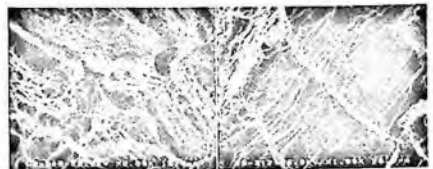
(a) initial crack region (b) crack growth region
Fig. 10. Fractographs of inconel 690 after fatigue test at high temperature.(σ_{max} =312MPa)

4. Conclusion

In this study, fretting and plain fatigue tests were applied at room temperature and high temperatures, respectively, for the alloys of inconel 600 and 690, which

are used in nuclear power plants as steam generation tubes; and the following results were obtained:

(1) From the results of the fretting fatigue tests at room temperature, the fatigue limits of inconel 600 and 690 decreased by approximately 67 % and 44 %, respectively, as compared to those of the plain fatigue tests. Also, the frictional force increased up to 10^3 cycles and then maintained a constant level. The relative slip amplitude decreased up to 10^3 cycles and then maintained a constant level. The oblique cracks were observed in the early stage of the cracks whereas the wear-damaged areas were largely distributed.

(2) From the results of the plain fatigue tests at high temperatures, the fatigue limits of inconel 600 and 690 decreased by approximately 17 % and 14 %, respectively, as compared to those at room temperature. In addition, several corrosion areas were observed in the initial crack region due to the influence of high temperatures.

Acknowledgments

References

1. S. Suresh, *Fat. of Mater.* (1991).
2. Y. H. Lee and H. K. Kim, *Wear*, 255 (2003).
3. M. H. Attia and R. B. Waterhouse, *ASTM STP* 1159 (1992).
4. R. N. Caron and J. T. Staley, *Materials Selection and Design*, *ASM Handbook*, *Vol.* 20 (1997).
5. J. D. Kwon, S. J. Choi and Y. T. Bae, *Key Eng. Mater.*, 261-263 (2004).
6. T. C. Lindley and K. J. Nix, *ASTM STP* 1159, p. 153 (1992).
7. D. K. Park, S. W. Woo, I. S. Chung, Y. S. Chai and J. D. Kwon, *Key Eng. Mater.*, 345-346 (2007).
8. R. B. Waterhouse, *Fretting Corrosion, Fretting Fatigue* (1972).
9. Y. Mutoh, *JSME Int. Journal*, *Vol.* A38 (1995).
10. V. Kerlins and A. Phillips, *Fractography, ASM Handbook. Vol.* 12 (1987).

INFLUENCE OF THE DAMAGED BLADE
OF A MULTIPLE-STAGE AXIAL COMPRESSOR ON TURBINE
COMPONENTS OF THE HEAVY-DUTY GAS TURBINE

MYUNG-SOO KANG, WAN-NO YUN, KAY-YOUN KIM AND JUN-SUNG KIM

Power Generation Laboratory, Korea Electric Power Research Institute
103-16Munji-dong, Yuseong-gu, Daejon, 305-380, Korea

The heavy-duty gas turbine power plants have been known for the high thermal efficiency and the versatility, which can be used for both of base load and cyclic duty utility services. The damaged blade of a multiple-stage axial flow compressor during the operation has an influence on turbine components as well as compressor blades. The ruptured blade which is rotating at high speed can damage blades and turbine components of a all-stage compressor severely. If the shattered blades flow downstream inside turbine parts, then turbine blades and vanes can be damaged. The small parts of shattered blades which flow into the turbine parts can pass through without any damages in the leading edge of the first stage stationary blades. Then, they bump against the convex side of the leading edge of the first stage rotating blades and the trailing edge of the first stage stationary blades repeatedly. Debris of shattered blades may clog cooling holes of turbine blades and vanes. The dent damage and the coating delamination could be also occurred by debris of shattered blades flowing downstream inside the combustion liner and the transition piece. This paper analyzes the influence of the damaged blade of the multiple-stage axial flow compressor on the turbine components, and the damage mechanism and characteristics of the compressor is studied.

1. Introduction

Industrial gas turbine has shown high efficiency even at a peak load as well as a base load, and the machine has been used for many applications. Gas turbines in Korean power industry was started to be utilized in the early 1990s and occupies about 30 percent of total power facilities at present.

A gas turbine is composed of a multiple-stage axial flow compressor and a turbine rotor which are tied into a single rotor. Hot gas path parts are casted with superalloys, and the stainless steel is used as the material of the compressor blade. A compressor blade is designed to withstand the operational fatigue stresses and last throughout the rotor life, but the blade failure happens frequently due to manufacturing defects, casing thermal deformations, tight clearances etc. When the long blades of the front stage fail, the next stage blades are damaged significantly because the compressed air flows from front to next stages in the axial gas turbine. Turbine parts which are tied with compressor in a

single shaft would be influenced by the shattered parts, but debris is not injected to the turbine parts directly because of the configuration characteristics. Therefore turbine blades are not damaged so severely but there could be problems such as plugging of cooling holes, coating delamination and so on. The material for hot gas path parts is very expensive and needs high cost for the repair. The cost would be higher and the damage would be severer unless the effect of compressor blade failure is analyzed and a proper correction is not executed.

In this paper, the effect of the compressor blade failure on hot gas path parts and types of hot gas path parts damage is described.

2. Compressed air and combustion gas flow

2.1. Gas turbine configuration and compressed air flow

A gas turbine is composed of a multiple-stage axial flow compressor and a turbine rotor which are tied into a single rotor. Ambient air is withdrawn and compressed in the compressor. The compressed air induced into a combustor and a combustion gas energy is turn into a mechanical power through a turbine as shown in Figure 1.

In Westinghouse and GE(Generic Electric) gas turbine, 16~20 caned type cylindrical combustors are installed circumferentially. High temperature combustion gas is guided into a turbine by a transition piece which is designed to contact to the first stage nozzle and prevent the ingestion of cold air into a turbine.
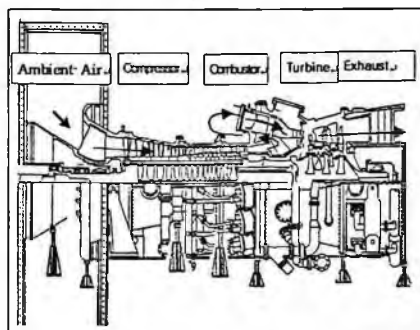
Fig. 1. Air and gas flow in the gas turbine
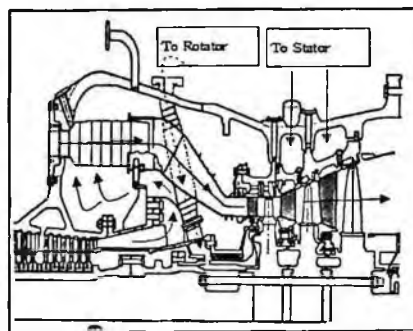
Fig. 2. Cooling air flow from the compressor

2.2. *Flow of compressed air and combustion gas*

Figure 2 describes the compressed air and gas flow through a compressor discharge diffuser and a chamber, a combustor and a turbine. EGV(exit guide vane) at the compressor discharge converts the rotational flow into the directional flow. In diffuser the compressed air velocity converted into the pressure energy. Most of compressed air at the compressor discharge is directed into the combustor through holes at the combustor outer piece. The compressed air is turned 180 degrees while being ingested into the combustor.

Hot gas path parts are cooled by the thermal barrier coating at the outer surface and the internal air flow. The cooling method of the gas turbine rotor and rotational blades is somewhat different depending on design.

Generally the proper fraction of compressed air is extracted, cooled and supplied into the rotor and rotational blades for the purpose of cooling parts. The cooling air for the stationary blades and casing is extracted from compressor middle stages and supplied to each part through pipes installed at the outside of casing.

3. Effect of compressor blade failure on turbine parts

3.1. *Effect of compressor blade failure on turbine rotating blades*

When compressor rotating blade breaks, generally lots of particles are ingested into the turbine by air flow and damage turbine hot gas path parts. Most of the particles ingested into turbine section are very small.

Relatively large particles passed through the compressor hit against the compressor discharge chamber and fall there by an inertial force but small particle flows into the combustor mixed with the air flow which is turned 180°. Small particles pass through the first stage nozzle without inducing any damage and strike against the leading edge convex side of the first stage rotational blade . After the strike, bounced particle strike the trailing edge convex side of the first stage stationary blade again. The action is repeated many times and the particle passes downstream. This mechanism is described in Figure 3 with a velocity triangle.

The compressed air is accelerated by an expansion through the first stage stationary blade and exits the nozzle with the velocity Cs as shown in Figure 3. The accelerated air is injected into the rotating blade with the relative velocity Ws. Small particles ingested with the air flow do not induce any damage at the first stage nozzle but the particle velocity, Cp is lower than the air velocity, Cs

because it does not expand. The relative velocity of the particle to the moving becomes Wp and impacts to the leading edge convex side of the rotating blade.

The particle bounces back to the trailing edge convex side of the first stage stationary blade. Such repetitive actions for many times induce lots of damages at the trailing edge convex side of the stationary blade and the leading edge convex side of the rotating blade, and the particle passes downstream.

As with the mechanism mentioned above, the failure of axial compressor blade makes dents mainly at the rotating blade leading edge and the stationary blade trailing edge. The thermal barrier coating on the rotating blades also spalls.
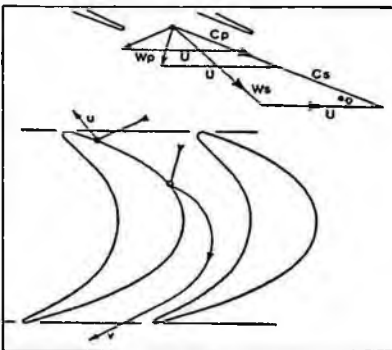
Cs : Gas velocity at stationary blade exit
Cp : Particle velocity at stationary blade exit
U : Blade velocity
Ws : Relative gas velocity at rotating blade inlet
Wp : Relative particle velocity at rotating blade inlet

Fig. 3. Velocity triangle and mechanism of solid material impact in a rotating blade row
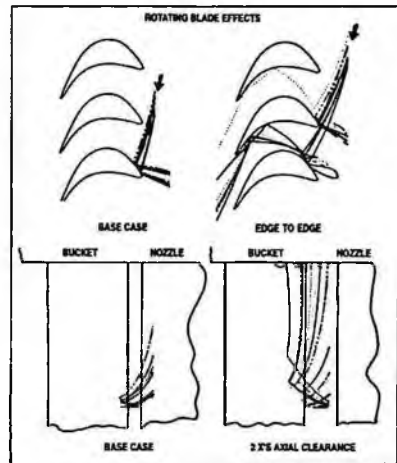
Fig. 4. Particles rebounding in the rotating and stationary blade

3.2. Damage by relatively large particle

The failure of the compressor blade makes fine particles ingested into the turbine section generally.

But sometimes relatively large particles which are sized 5~10 mm diameter are introduced through combustor holes (20~30 mm diameter) into the turbine section and make severe dent damages. Even in that case, there is not any damage at the stationary blade leading edge but there could be one or two dent damage at the trailing edge convex side of the stationary blade.

The particle flows so fast that it could dent the next rotating blade without inducing any dent at the stationary blade. Turbine blade rotates so fast that any

one of the particles sized 5~10 mm could cause lots of dents. This phenomenon happens frequently by the failure of the compressor blade and sometimes it is so severe that the repair of the blade is impossible. Particles could also be introduced into cooling air for turbine casing and turbine rotating blades. So, particles clog cooling holes of the stationary blade, and the stationary blade is overheated enough to liberate the piece of it and the damage is expanded.

Therefore, rotating and stationary blades of the turbine should be repaired when the compressor blade is broken and shattered. Coating of the rotating blades should be removed and thorough non-destructive examination should be performed to judge the condition of the blade because the severely damaged rotating blade cannot be repaired from time to time. And cooling holes of stationary blades and rotating blades should be inspected and there should not be any material in the cooling hole passage.

4. Failure example

4.1. Compressor damage

Compressor blade failures have happened several times in Korea and the gas turbine blade damaged each time as described above. One of failures will be introduced: the first stage rotating blade of a gas turbine compressor was broken at the root section due to the high cycle fatigue.

A blade of multi-stage axial compressor was cut and the cut-out piece rotated for a time between the first stage stationary blade and the first stage rotating blade. The broken piece damaged tip sections of all of the first stage rotating blades while rotating. The shattered fine particles made dents at every surfaces of the blade of stage 1 through stage 19 and some blade were torn.

4.2. Turbine damage

The damage on the turbine are not as severe as that of the compressor because the size of particles was reduced while particles passes through the compressor.

Figure 5 shows the damage on the leading edge convex side of the rotating blade and Figure 6 shows the delamination of a thermal barrier coating on the trailing edge convex side of the stationary blade.

Fig. 5. Thermal barrier coating delamination
in the turbine blades
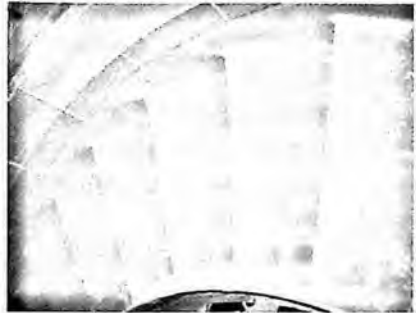
Fig. 6. Dent damage in the turbine
stationary blades

5. Conclusions

The effect, damage type and characteristics on turbine hot gas parts are summarized as follows when the blade of the axial compressor breaks and shatters:

1. When the rotating blade of multi-stage axial compressor breaks, the small pieces generated in the compressor flow into the turbine section and damage the turbine blades. The dents are concentrated at the leading edge of rotating blade and trailing edge of stationary blade. Spalling occurs at the thermal barrier coating on the blades.
2. Relatively large piece could be ingested into turbine sometimes, it could induce so severe dent damage at the rotating blade that the blade cannot be repaired even if the number of large particles is only one or two.
3. The gas turbine stationary blade and the rotating blade are internally cooled by the extracted air from the compressor. So, the particle generated at the compressor could clog cooling holes of blades.
4. Dent damage does not occur inside of the combustion liner and combustor discharge where the flow of compressed air and the flow of particles are parallel. But a coating wear and a spallation occur on the inner surface of combustor. Parts of the combustor should be repaired necessarily when a coating wear and a spallation are found.

References

1. Cotton, K. C., 1998, "Evaluating and Improving Steam Turbine Performance", H. Müller and B. D. Serot, Phys. Rev. C52, 2072 (1995).
2. O'Connor, M. F., Dreier, D. W., 1994, "Upgrade Opportunities for Utility Steam Turbines", 38th GE Turbine State-of-the-Art Technology Seminar, GER-3696C, pp.1-10.
3. Boyce, M. P., 2001, "Gas Turbine Engine Handbook", pp.221-410.

INFLUENCE OF STRESS AND EXCITATION SIZE ON THE VELOCITY OF COMPRESSION WAVEFRONT IN JOINTED ROCK MASSES

MINSU CHA

Dept. of Civil and Environ. Eng., Korea Advanced Institute of Science and Technology (KAIST), Daejeon 305-701, Republic of Korea

EUN-SOO HONG

Geotechnical Engineering Div., Korea Institute of Geoscience & Mineral Resources (KIGAM), Daejeon 305-350, Republic of Korea (esoohong@yahoo.co.kr)

SEUNG-HYUNG BAAK

Dept. of Civil and Environ. Eng., Korea Advanced Institute of Science and Technology (KAIST), Daejeon 305-701, Republic of Korea

GYE-CHUN CHO

Dept. of Civil and Environ. Eng., Korea Advanced Institute of Science and Technology (KAIST), Daejeon 305-701, Republic of Korea

The compression wave velocity of jointed rocks was measured by detecting the arrival time with different stress levels and with different magnitudes of excitation to identify how the two factors affect the wave propagation in jointed rocks. The results show that the compression wave velocity increases with increasing source amplitudes as well as stress levels. Signals received from larger source excitation show an earlier arrival and a steeper rise, which are related to shock wave generation. It is found that the influence of excitation magnitude on the wave velocity decreases as the state of stress in jointed rocks increases. As the source amplitude increases, compression wave velocities become less dependent on stress level. Based on the results, we suggest a method to estimate the farfield wave velocity, which is irrelevant of the source size. Since the compression wave velocity in jointed rocks is governed by the stress level, this should be reflected in rock mass assessments that make use of the compression wave velocity.

1. Introduction

The stress level and the magnitude of source rarely affect elastic wave velocities in homogeneous media, such as an intact rock, while elastic wave velocities are related to those factors in particulate materials. Generally the wave velocity measured from the resonant frequency using steady state vibration decreases as

the strain amplitude increases [1]. But, a compression wave front travels faster with increasing source amplitude in particulate materials, steepening the shape of the wavelet front. The compression front increases the mean stress in the particulate materials, which affect the stiffness of the medium and the velocity of wave propagation, leading to shock waves [2, 3]. Holzlohner and Auersch [4] presented a model to analyze shock wave propagation at the soil surface. Jiao *et al.* [5] numerically found that rock joints act as a filter, through which only low frequency shock waves are allowed to pass, and the amplitude and principal frequency decay faster as the incident angle of shock waves relative to the rock joints becomes larger. Wu *et al.* [6] experimentally proved that the amplitude and principal frequency of shock waves attenuate rapidly with increasing the distance from the charge center and with increasing the incident angle.

Shock wave propagation induced by blasting or large amplitude source has drawn attention in underground mining and engineering. Although the effect of the excitation magnitude and stress level on compression waves is important in seismic investigation, laboratory simulations are rarely performed. This experimental study explores the effects of excitation magnitude and stress level on compression velocity in rock mass and suggests a method to estimate the farfield velocity.

2. Experimental Program

Figure 1 shows the experimental setup for laboratory compression wave measurement in jointed rocks. The 15 rock discs are used as specimens. Gneiss rock cores drilled from a field are cut into identical discs with a center hole. The gneiss discs have an outside diameter of 63.2mm, an inside diameter of 25mm, a thickness of 25.4mm, a density of 2704kg/m^3, and P-wave velocity of 4750 m/s.

The discrete rock discs are stacked up on the steel base to form a jointed rock column. A light metal cap is placed on the top of the rock column, and the axial load can be hung from the cap by means of a thin rod that runs along the center holes of the discs. Weights are hung from the lower end of the rod.

An instrumented hammer and an accelerometer are used to detect the wave signals. An impact is given at the top of the column by the instrumented hammer. An accelerometer is built inside the instrumented hammer so that the impact signals could be directly detected without time delay. The propagated compression wave through the jointed rock column is detected by the accelerometer placed at the bottom of the column. The compression wave velocity is calculated from the travel time and travel length of the propagated waves.
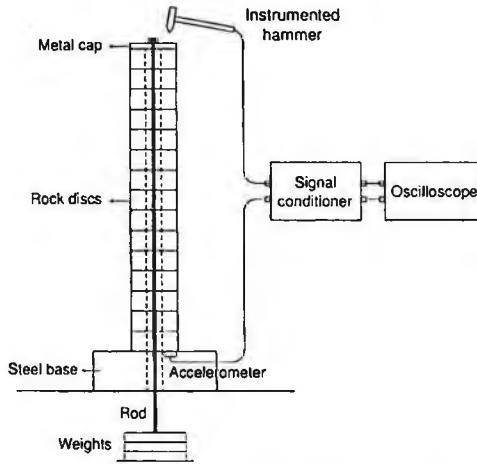
Fig. 1. Test setup: a column of jointed rock discs.

3. Results and Analyses

Figures 2 and 3 show the amplitudes of the source and received signals at two different stress levels of $\sigma_v = 37$ kPa and $\sigma_v = 445$ kPa, respectively. Various amplitudes of sources and their corresponding arrived signals are illustrated together for comparison. The weak amplitude of received signals is pre-amplified by 100 times to observe clear arrivals. Only initial arrivals are shown and their following trails are erased for clarity. The initial upheavals of arrived signals are considered as arrival points. As the amplitude of source excitation becomes larger in compression mode, arrivals are detected earlier and show steeper rise (Figure 2 & Figure 3).

(a) Source signals   (b) Arrived signals
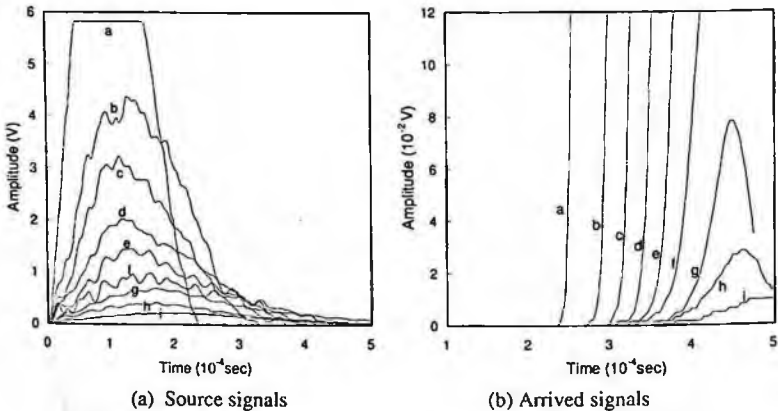
Fig. 2. Amplitudes of sources and corresponding arrivals ($\sigma_v = 37$ kPa).

(a) Source signals   (b) Arrived signals

Fig. 3. Amplitudes of sources and corresponding arrivals (σ_v = 445 kPa).
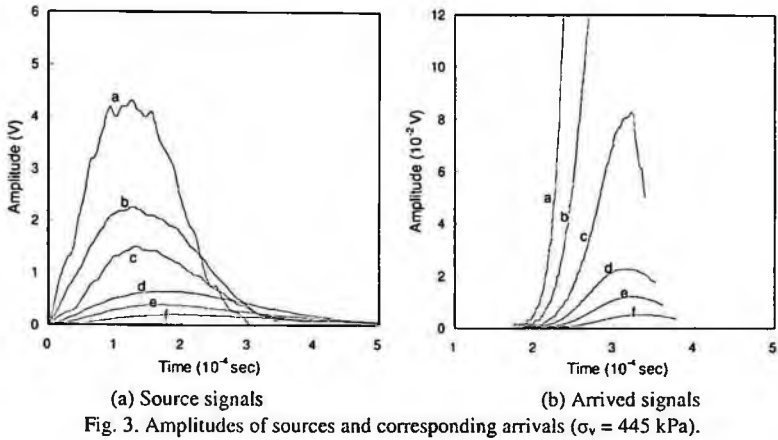
3.1. *Effect of Excitation Magnitude and Determination of Farfield Velocity*

Figure 4 shows the data of compression wave velocities and its quadratic polynomial fitting with respect to the source amplitude at the various stress levels. The compression wave velocity increases with increasing the source amplitude. The increment of the wave velocities by the amplitude increment is nearly the same, regardless of the stress levels applied in this experiment. Because the velocity increases by similar amounts with increasing amplitude for every stress levels, the percentage of velocity changes decreases with increasing stress levels. Thus, the influence of excitation amplitude tends to decrease as the state of stress in jointed rocks increases. Small-strain farfield velocity can be determined from the intercept at zero amplitude in Figure 4.
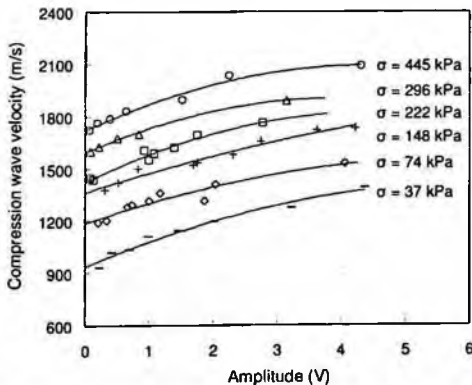
Fig. 4. Compression wave velocity according to source amplitude at different stress levels.

3.2. *Effect of Stress Level*

Figure 5 shows compression wave velocities with respect to stress levels at different amplitudes. The compression wave velocities are obtained from the fitting curves at selected amplitudes in Figure 4. The results show that the compression wave velocity increases with increasing stress levels in jointed rocks. Compression wave velocities are well-fitted by a power function of stress, which is also often used for the wave velocity model for soil-like media:

$$V_C = \alpha \left(\frac{\sigma}{1kPa} \right)^{\beta} \tag{1}$$

From this point of view, the compression wave propagation in jointed rocks reflects the characteristics of wave propagation in soil-like media governed by stress-dependent contact phenomenon.

The model parameters of the fitting curves are listed for different amplitudes in Figure 5 as well. It is found that the β-exponent decreases a little with increasing the source amplitude. Therefore, the stress dependency of the wave velocity slightly decreases with increasing the source amplitude.
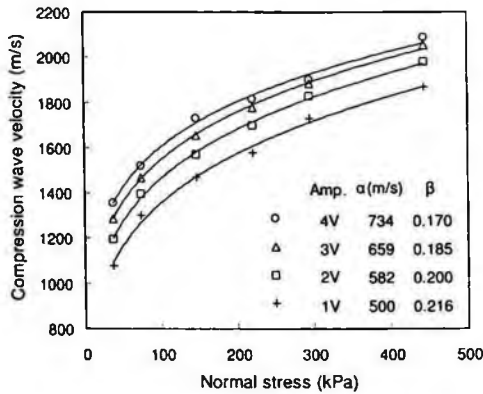
Fig. 5. Compression wave velocity according to normal stress at different amplitudes.

4. Conclusions

The effects of magnitude of excitation and stress levels on the compression wave velocity in jointed rock were explored by laboratory experiments. Following observations are made:

- As the amplitude of excitation becomes larger, an earlier and steeper arrival is detected.

- Compression wave velocity increases with increasing the amplitude of excitation and stress levels.
- The influence of source amplitude on compression wave velocities decreases as the stress in jointed rock increases.
- Data of compression wave velocities at a certain source amplitude are well-fitted by a power function of stress.
- The stress dependency of compression wave velocities slightly decreases with increasing source amplitude.
- Small-strain farfield velocity can be determined from laboratory testing procedure.

It is expected from the experimental results that this non-linear behavior is more prominent near the surface, while it is relatively less influential in deeper underground due to the effect of confining stress. Since the compression wave velocity in jointed rocks is governed by the stress level, this effect should be reflected in rock mass assessments that make use of the in-situ compression wave velocity.

Acknowledgments

References

1. F.E. Richart, J.R. Hall, and R.D. Woods, *Vibrations of Soils and Foundations*, Englewood Cliffs, N.J., Prentice-Hall (1970).
2. H. Kolsky, *Stress Waves in Solids*, Dover, New York (1963).
3. J.C. Santamarina, K.A. Klein, and M.A. Fam, *Soils and Waves*, New York: John Wiley & Sons (2001).
4. U. Holzlohner and L. Auersch, *Int. J. Numer. Anal. Meth. Geomech.* **8**, 57 (1984).
5. Y.Y. Jiao, S.C. Fan, and J. Zhao, *J. Test. Eval.* **33**, 197 (2005).
6. Y.K. Wu, H. Hao, Y.X. Zhou, and K. Chong, *Soil Dyn. Earthq. Eng.* **17**, 407 (1998).

X-RAY DIFFRACTION ANALYSIS ON FATIGUE FRACTURE SURFACE OF SG365 STEEL

MAN-BAE LIM, WON-JO PARK

Department of Mechanical and and Aerospace Engineering, Gyeongsang National University, Tong young, 650/160, Korea
mblim@gnu.ac.kr, wjpark@gnu.ac.kr

JONG-DONG SON, GAB-SONG CHOI

Department of Mechanical Engineering, Tongmyong University, Yongdangdong 535, Busan, 608/711, Korea
dish5@tu.ac.kr, gschoi@tu.ac.kr

This study verified the relationship between fracture mechanics parameters (ΔK, ΔK_{eff}, K_{max}) and X-ray parameters (σ_r, B) for SG365 steel at elevated temperature up to $300\,°C$. The fatigue crack propagation tests were carried out and X-ray diffraction technique according to crack length direction was applied to fatigue fractured surface. The residual stress on the fracture surface was found to increase in low ΔK region, reach to a maximum value at a certain value of K_{max} or ΔK and then decrease. The residual stresses were independent on stress ratio by arrangement of ΔK and full width at half maximums was independent by the arrangement of K_{max}. The equation of σ_r and ΔK was established by the experimental data. Therefore, fracture mechanics parameters could be estimated by the measurement of X-ray parameters.

Keywords: X-ray Diffraction; Fatigue Crack Propagation Rate; Residual Stress; Full Width at Half Maximum; Stress Intensity Factor; Fatigue Fractured Surface.

1. Introduction

The gas pipes for LNG and LPG transmission are subjected to repeated thermal stress as a result of temperature gradients and pressure fluctuation due to changes in operating conditions. It is very important to develop a new stress analysis technique because the materials for pipe line components should have good mechanical properties and fracture characteristic under thermal loading. The material for storage and transmission are generally serviced under thermal loading rather than constant stress amplitude. Therefore, it was suggested that a

prediction model of fatigue crack growth rate at variable stress ratios, amplitude and X-ray diffraction analysis. The fatigue crack growth rate concept has been applied to explain the effect of road ratio and high temperature [1-3]. The fatigue crack growth rate has a tendency to be effected by microstructure fracture mechanics at the crack initiation stage and it was scatters severely in this stage. Such fatigue crack growth rate behavior is similar to shot crack growth rate behavior. The stable growth region of the fatigue crack has been defined as Paris zone. The Paris zone is slightly affected by microstructure, stress ratio and high temperature. The fracture surface analysis becomes information that is influential on cause searching examination of fracture accident, and it was able to assistance for accident prevention and made an accurate estimate.

The fatigue fracture surface analysis is used widely by scanning electron microscope. However, the application of these fracture surfaces has been limited, and these were impossible very useful information in the case of fracture surface oxidized or corrosion. Therefore, X-ray diffraction is appearing information about lattice transformation of fracture surface region. It is very significant to prediction of fatigue crack growth rate and fracture surface information. The X-ray diffraction pattern has a merit that can know microscopic mechanism and stress distribution of destruction. The diffraction patterns were account for spot width of tangential and lattice strain [3-5].

In this research, the fatigue crack growth rate tests were conducted for carbon steel with different stress ratios in order to find the effect of stress ratios and high temperature. The analysis stress distributions were also observed on X-ray diffraction parameters such as half value breadths and residual stresses, and fatigue fracture surfaces of test specimen from scanning electron microscopy.

2. Experimental Procedures

2.1. *Materials and specimens*

The material used in this study was SG365 carbon steel and their chemical compositions were shown in Table 1. After polishing treatment of test specimen, the tensile strength and the fatigue crack growth rate test accomplished according to ASTM E8, E647 regulation [6-7]. The shape and dimensions of standard compact tension (1CT) specimen was shown in Figure 1. The fatigue crack growth rate test was performed using the MTS 810 Test Star testing machine at room temperature, 300°C, and the mechanical properties were shown in Table 2. All of the compact specimens were oriented such that the crack propagation proceeding along the L-T orientation.

2.2. *Fatigue crack growth rate experimental*

The fatigue crack growth rate experiments were accomplished a servo hydraulic dynamic fatigue testing machine. An experimental condition were cyclically loaded repeat tension load under a load control and tested at a frequency of 10Hz with sinusoidal loading waveform, and stress ratio 0.1, 0.5 at room temperature, 300℃. The precrack length is 2mm, a/W=0.26 and crack length was measured using unloading compliance technique by crack opening displacement gauge.

Table 1. Chemical composition of SG 365(wt%)

Material	C	Si	Mn	P	S
SG365	0.14	0.43	1.32	0.001	0.001

Table 2. Mechanical properties of material

Temp. (℃)	Yield stress (MPa)	Tensile stress (MPa)	Elongation (%)	Young's modulus (GPa)	Poisson's ratio
25	386	560	36	196	0.3
300	367	577	37	205	0.3
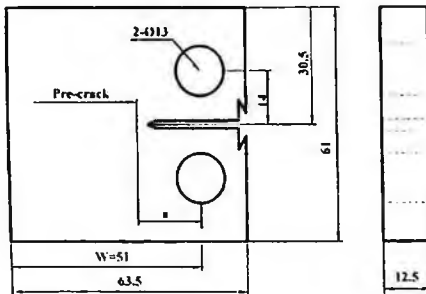
Fig. 1 Geometry and configuration of compact tension specimen
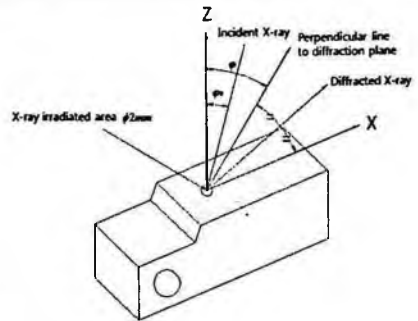
Fig. 2 Schematic illustration of X-ray irradiated area on fatigue fracture surface

The crack opening displacement gauge with 5mm gauge length was attached on to mouth of the specimens, and in order to measure the crack closure, K_{cl} and K_{op} were calculated from the load-displacement curve which was obtained from 1 Hz cyclic loading. The fatigue crack growth rate experiments were predicted from the consideration of the effective stress intensity factor range, $\Delta K_{eff.}$ such as Elber has modified Paris and Erdogan's equation [8-10].

2.3. *X-ray diffraction pattern analysis*

X-ray diffraction techniques to evaluate the macroscopic and microscopic material parameters are presented and approach is demonstrated by exhibiting a case of studies on fatigue crack growth rate of carbon steel. Figure 2 shows schematic illustration of X-ray irradiated area on fatigue fracture surface. The diffraction pattern of small areas in the fracture surface was measured by using the X- ray beam of ϕ 0.2mm and diffraction angle is $156.4°$. The characteristic X- ray of $Cr-K_\alpha$ and the lattice plane (211) of specimens were selected to obtain a middle diffraction angle and Table 3 shown X- ray diffraction condition.

Table 3. X-ray diffraction condition for SG365 Steel

Test condition	Parallel beam method
Characteristic X-ray	$Cr-K_\alpha$
Diffraction plane	(211)
Diffraction angle(2θ)	$156.4°$
Tube voltage	30KV
Tube current	8mA
Irradiated area	ϕ 2mm
Time constant	10sec
Residual stress method	$Sin^2 \phi$
Stress constant(K)	$-30.33kg/mm^2/deg$

3. Results and discussion

3.1. *Fatigues crack growth behavior*

In region II, where da/dN follows a power law, the crack growth rate is relatively to microstructure and tensile properties, while da/dN at either extreme of the curve is highly sensitive to these variables. In this region, fatigue mechanisms are described in flow properties and striation mechanism. The experiments to compare fatigue crack growth rate da/dN and stress intensity factor range in carbon steel were conducted for stress ratio 0.1, 0.5 at various temperatures and the results was presented in Figure 3. The fatigue crack growth rate of stress ratio 0.5 is higher than that of 0.1, which relates to their mechanical properties such as yield strength and stress amplitude. The fatigue crack growth resistance was increased when it is 0.1 more than 0.5 at the room temperature and the difference in fatigue crack growth rate between stress ratio 0.1 and stress ratio 0.5 is large at the low ΔK region. However, the fatigue crack propagation resistance is small at the high ΔK region because stress amplitude was independent of crack driving force. This is primarily due to compressive residual stresses as well as crack close in tension plasticity region. From the above results,

it was confirmed that the increased fatigue crack propagation resistance for this material resulted from the various stress ratio.

In the Figure 3 Paris defined the stress intensity factor range, the equation has da/dN=C(Δ K)^m, where C and m are numerical constants [8]. The slope values, m of the fatigue crack growth rate at room temperature are 3.874, 3.478 in the various stress ratio, and in the case of 300°C, the slope values were estimated 3.394, 2.856 respectively. Elber provided at least a partial explanation for both the fatigue threshold and stress ratio effects. He is noticed an anomaly in the elastic compliance of several fatigue specimens and crack close a phenomenon was believed that this change in compliance was due to the contact between crack surfaces [9-10].
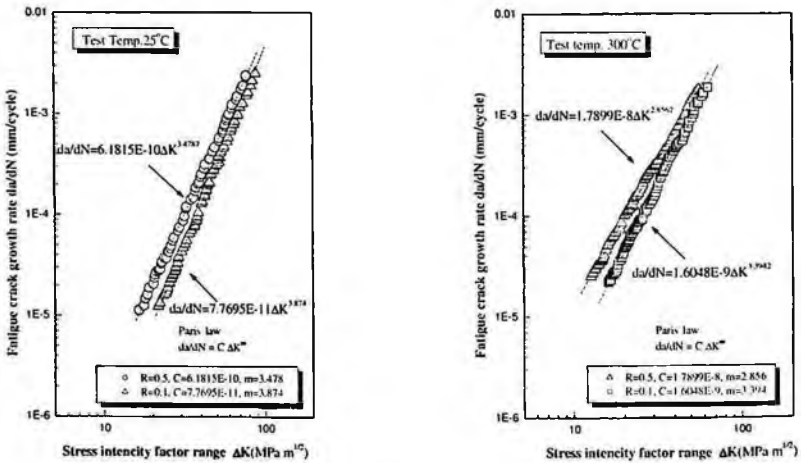
Fig. 3 Relation between stress intensity factor range and fatigue crack growth rate at 25°C and 300°C

In other words, the crack closure concept has been employed to explain the effect of load ratio on fatigue crack growth rate. The experiments to compare fatigue crack growth rate da/dN and effective stress intensity factor range at this material were conducted for stress ratio 0.1, 0.5 at various temperatures and the results was presented in Figure 4. In Elber has modified Paris and Erdogan's equation, the slope values, m of the fatigue crack growth rate at room temperature are 3.898, 3.444 in the various stress ratio, and in the case of 300°C, the slope values were estimated 3.707, 3.3580 respectively. Therefore, the fatigue crack growth rate was retarded with a lower slope due to compressive residual stresses and crack close in the crack tip region.
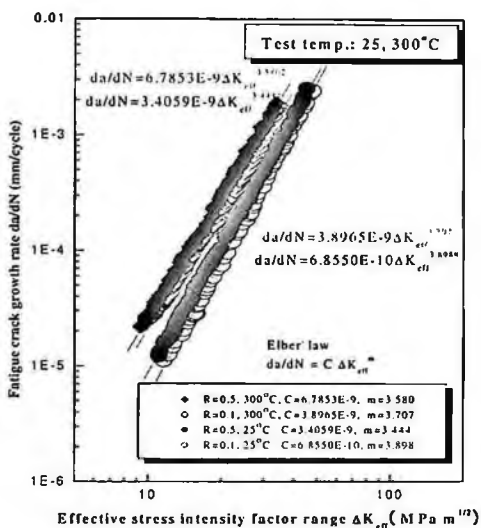
Fig. 4 Relation between effective stress intensity factor range and fatigue crack growth rate at 25 ℃ and 300 ℃

3.2. *X-ray analysis of the fatigue fracture surface*

The distributions of residual stress as well as the full width at half maximum of the diffraction profile, as a function of stress intensity factor range and effective stress intensity factor range measured on the fracture surface of specimens in different stress ratio and at various temperatures was shown in Figure 5 and Figure 6, respectively. From the result of test, residual stress values were found to be tensile stress regardless of stress ratio and test temperatures. They exhibited increasing trends in the fatigue region and decreasing trends in the fast fracture region with maximum stress intensity factor. The relationship between stress intensity factors and the residual stress or full width at half maximum of the steel was almost the same as that of the ferritic cyclic work hardening steels. Therefore the residual stress distributions on the fracture surface of SG365 steel in different test conditions were found to exhibit an increase followed by a decrease with increasing stress intensity factor range and effective stress intensity factor values while the full width at half maximum showed a monotonic increase [3-5].
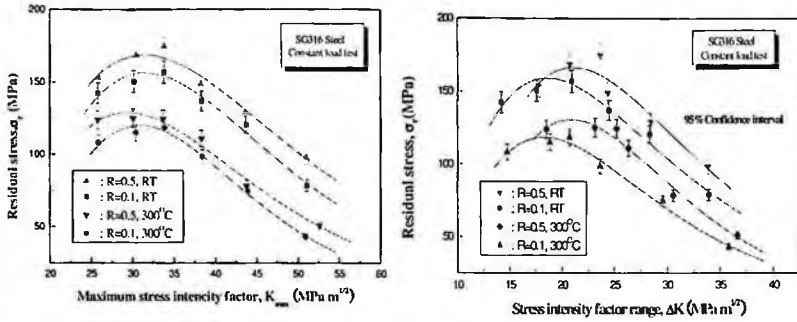
Fig. 5 Relation between the residual stress and maximum stress intensity factor and stress intensity

factor range on fracture surface
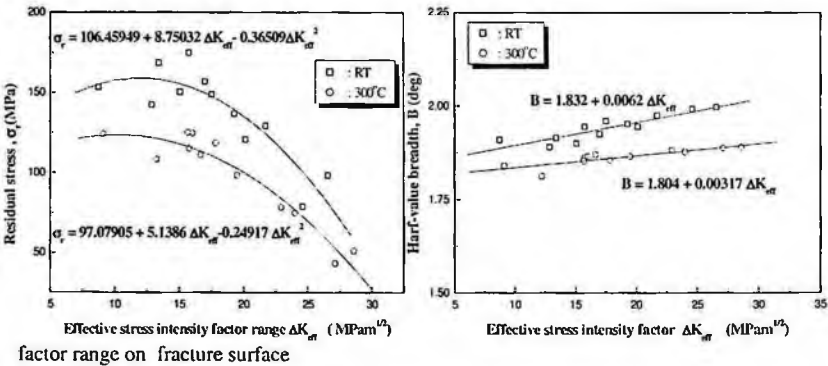
Fig. 6 Linear curve fitting of residual stress, half-value breadth and effective stress intensity factor range on fracture surface

3.3. *Fatigue fracture surface analysis*

Figure 7 shows SEM fracographs on fatigue fracture surface in stress ratio 0.1, 0.5 at room temperature and 300℃. The fatigue fracture pattern and shape showed a typical ductile fracture surface pattern with striation. The striation phenomenon at room temperature observed more definitely than high temperature experimental condition. It was seen that striation size increasing in the ductile material or high strength and it is known that the fatigue crack propagation accelerated quickly when the driving force in crack front sufficiently large. The reason is thought to be the difference in the propagation rate of the fatigue crack or effect of compressive residual stress. Specially the effect of fatigue crack closure on the residual stress of the fracture surface was found to be relatively small and limited in the very thin layer near the fatigue fracture surface. The striation spacing and size depended on repeated stress level,

frequency, stress concentration factors and high temperature. Finally, we think that fatigue crack growth rate increase is the factors and among various factors [11].
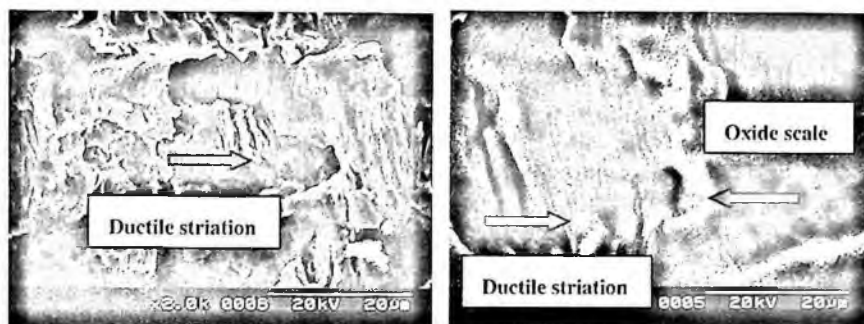
(a) ΔK=30.35(MPa m$^{1/2}$) R=0.1, RT   (b) ΔK=29.97(MPa m$^{1/2}$) R=0.1, 300℃

Fig. 7 SEM fractography showing fracture surface (Direction of crack propagation : left to right)

4. Conclusions

The fatigue crack growth rate tests were carried out under constant load and constant range of stress intensity factor. On the fatigue fracture surface the residual stress along the crack propagation direction was measured by a parallel beam X-ray stress measurement equipment, and the full width at half maximum of the diffraction profile were also measured. The result of the analysis can be summarized as follows;

(1) The fatigue crack growth rate of stress ratio 0.5 is higher than that of 0.1, which relates to their mechanical properties such as yield strength and stress amplitude.

(2) The fatigue crack growth rate behavior of stress ratio and elevated temperature are influenced by crack closure. It was accelerated due to the crack closure and the effect of oxide scale under repeated loading at 300℃

(3) The residual stress of the diffraction profile had a good correlation with maximum stress intensity factor and small decreased with increasing maximum stress intensity factor except for SG365 steel.

(4) The relationship between the half value breadth and stress intensity factor range was represented by a linear line regardless of the stress ratio. Therefore, X-ray diffraction parameters could be explained well with the stress intensity factor range and effective stress intensity factor in the power law region.

References

1. Kazuyuki Matsui, Yukio Hirose, Akiyoshi Chadani and Keisuke Tanaka, "Application of X-ray Fractograpic Technique to Actual Failure Analysis", *JSFM*, Vol. **24**, No. 4, pp. 117-128, (1990).

2. Zenjiro Yajima, Yukio Hirose and Keisuke Tanaka, "X-ray Diffraction Observation of Fracture Surface of Ductile Cast Iron", *Adv. X-ray Anal.* **26**, pp.291-298, (1983).

3. Yuji Sekita, Shotaro Kodama and Hiroshi Misawa, "X-ray Fractography on Fatigue Fracture Surface ", *JSMS*, Vol. **32**, No. 354, pp. 258-263, (1983).

4. Katsu Nagai, Masaki Kitagawa and Akira Ohtomo, "Residual Stress and Half-Value Breadth of Fatigue Fractured Surface of Various Structural Steels Measured by X-ray Diffraction", *JSMS*, Vol. **33**, No. 365, pp. 204-208, (1984).

5. Keiji Ogura, Yoshio Miyoshi, Masahiro Kayama and Yoichi Shoji, "X-Ray Study on Fracture Surface of SM 50A and HT80 Steels", *JSMS*, Vol. **33**, No. 367, pp. 398-404, (1984).

6. *ASTM E8*, "Standard Test Method of Tension Testing of Metallic Materials", pp. 56-76, (2000).

7. *ASTM Standard E647*, "Standard Test Method for Measurement of Fatigue Crack Growth Rates", pp. 1-6, (2000).

8. P.C. Paris and F. Erdogan, J. of Basic Eng. **85**, 528, (1963).

9. W. Elber, Eng. Fracture Mech. **12**, 37 (1970).

10. W. Elber, *ASTM STP* **486**, 37 (1971).

11. Keisuke Tanaka and Nobuo Hatanaka, "X-Ray Fractography of Fatigue Fracture of Steel", *JSMS*, Vol. **33**, No. 366, pp. 324-330, (1984).

THE STUDY OF EVALUATION TENSILE CHARACTERISTICS AND PLANE STRAIN FRACTURE TOUGHNESS IN INDUCTION SURFACE HARDENED OF THE SM53C STEEL

HYUN-BAE JEON

Department of Mechanical and Precision Engineering, Graduate School, Gyeongsang Nat'l., Univ., Tongyoung, Gyeongnam, 650-160, Korea
jhb@gnu.ac.kr

SUN-CHUL HUH[1], WON-JO PARK[†]

[1]*Research Center for Aircraft parts Technology, Gyeongsang Nat'l., Univ., Jinju, Gyeongnam, 660-701, Korea*
schuh@gnu.ac.kr
[†]*Department of Mechanical and Aerospace Engineering, Gyeongsang Nat'l., Univ. Institute of Marine Industry, Tongyoung, Gyeongnam, 650-160, Korea*
wjpark@gnu.ac.kr

Cam shaft which is part of automobile engine is essential part when traveling and significant to fuel injection timing. And also, stiffness and efficiency are component of automobile sash which have a durability of the engine. High hardness and durability are necessary, because engine output is effect by cam shaft directly. So, High-Frequency Induction Hardening is very important. Therefore, in this study here are compared surface hardness characteristic and hardening depth of the SM53C used in the cam shaft. In order to estimate the shape of hardening depth, we investigated hardened structure, hardness, hardening and fracture characteristic of SM53C composed by carbon steel.

1. Introduction

Recently, automobile industry requires that a large output of power, long life and light weight. Therefore parts of an automobile need for high strength, wear resistance and high durability. As part of the countermeasure, use the surface hardening heat treatment.[1-2]

Cam shaft which is part of automobile engine is essential part when traveling and significant to fuel injection timing. And also, stiffness and efficiency are component of automobile sash which have a durability of the engine. High hardness and durability are necessary, because engine output is

---

[†] Corresponding author

affected by cam shaft directly. So, High-Frequency Induction Hardening is very important.

Therefore, in this study here are compared surface hardness characteristic and hardening depth of the SM53C used in the cam shaft. In order to estimate the shape of hardening depth, we investigated hardened structure, hardness, hardening and fracture characteristic of SM53C composed by carbon steel.

2. Material and Method

2.1. *High-Frequency Induction Hardening*

High-Frequency Induction Hardening requires Frequency (Hz), Electric power (kW), Travel Speed etc. In this study Frequency (Hz) and Electric power (kW) are fixed. And Travel speed is different according to hardening depth of material. Table 1 shows condition of High-Frequency Induction Hardening.

Table 1 Experimental Condition for Progressive High Frequency Case Hardened

Working condition	Conditions heat treatment		
	A	B	C
Electric Power	50 kW	50 kW	50 kW
Travel Speed	6.2 mm/sec	7.0 mm/sec	7.3 mm/sec
Layer of Hardened	1.1 mm (HV 500)	0.55 mm (HV 500)	0.35 mm (HV 500)
Hardness	HV : 640-670	HV : 620-640	HV : 635-654
Frequency	200 kHz	200 kHz	200 kHz
Temperature	850℃~870℃	850℃~870℃	850℃~870℃
Tempering	230℃	230℃	230℃

2.2. *Tensile test and Fracture toughness test*

The material used in this study is SM53C whose chemical compositions refer to Table 2. The tensile test was carried out using a MTS 810 machine at room temperature and cross head speed was 0.5 mm/min. Table 3 shows tensile test result after High-Frequency Induction Hardening. The fracture toughness tests were carried out at room temperature and applied cross head speed was 0.05 mm/min.

These tests were conducted on constant amplitude loading in accordance with ASTM E399. The pre-cracking of specimen was conducted under mode I loading with a sinusoidal waveform at a/W=0.48 with a stress ratio R=0.1 at 15 Hz. And it followed in Hardening depth (1 mm and 2 mm) and it was executed, respectively.

Table 2 Chemical compositions of specimen (wt %)

Material	C	Si	Mn	P	S	Ni	Cr	Mo	Cu
SM53C	0.55	0.22	0.63	0.017	0.027	0.02	0.02	-	0.03

Table 3 Mechanical properties of specimen

Material	Type	Hardening Depth [mm]	Tensile Strength [MPa]	Yield Strength[MPa]
SM53C	Base Metal	0	831	447
	A	1.1	873	731
	B	0.55	833	559
	C	0.35	831	547

2.3. *Microstructure and Hardness*

Micro Vickers hardness tester (Mitutoyo MVK-G1) was used in Hardness measurement. Condition load is 500 gf during 10 sec. And, interval of 0.1 mm from surface of hardening depth part and base part were measured. Also, after etching (HNO_3 5% + ethanol 95%), microstructure and hardening depth were observed by Optical microscope.

3. Results and Discussion

3.1. *Hardness distribution*

Figure 1 shows hardness measurement and the result at the surface to 2.0 mm depth by 0.1 mm interval. The hardness of High-Frequency Induction Hardening part average is 717 HV. And, a rapid decrease in boundary of High-Frequency Induction Hardening part and base part. This phenomenon is known from its microstructure because it is hardened by remaining proeutectoid ferrite and imperfection austenite. In martensite the carbon constantly decreases following the depth, also, rapid decrease happen because of martensite quantity. Figure 2 shows verification of Effective Case Depth (ECD). The value of the ECD was computed using following formula

$$DC = d_1 + \frac{(d_2 - d_1)(H_1 - H_s)}{H_1 - H_2}$$

Where,

Hs: Hardness

H_1, H_2: The arithmetical average of measured hardness from d_1 and d_2

Also, $d_2 - d_1$ must be smaller or equal than 0.3 mm.
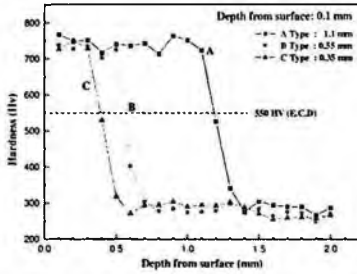
Fig. 1 Nature of hardness with depth from surface
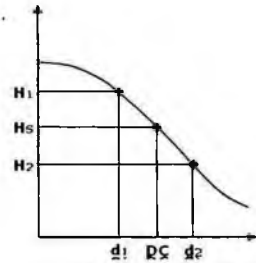
Fig. 2 Verification of ECD.

3.2. Optical microstructure

(a) Surface part in hardened region (0.5 mm from surface)
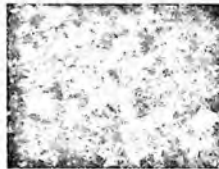
(b) Surface part in hardened region (1 mm from surface)
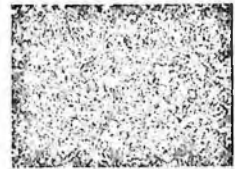
(c) Surface part in hardened Region (1.2 mm fromsurface)
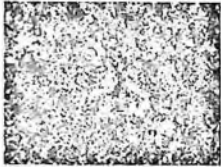
(d) Non-hardened region (Center)

(e) Hardness depth and non-hardness depth

(f) Hardness depth and non-hardness depth

Fig. 3 Optical microstructure of SM53C hardened in ECD 1.1 mm

Figure 3 indicates structure of hardening depth and non-hardening depth of SM53C. Surface part of hardening depth (a) can be seen to be composed generally uniform detailed martensite structure by quick freezing. And some quantity of Residual austenite is still remaining. In case of slow travel speed outside surface of hardening, martensite is known larger size than the surface directly under high temperature heating. But in case of High-Frequency Induction Hardening, the inclination is not indicated. This is happened because of past travel speed (6.2, 7.0, 7.3 mm/sec). Therefore, quantities of carbide decrease for austenite course because structures are short of temperature and time which can completely change by austenite. Also, observed proeutectoid ferrite is kept to be like that. (b and c) In the center by way of a boundary of hardening and non-hardening depth, it composes pearlite and ferrite as original material. (e) indicates a boundary of hardening and non-hardening depth. (f)

indicates a cutting plane after etching. Shaded section indicates heated hardening depth. Bright section indicates non-hardening depth section. [3]

3.3. *Tensile test*
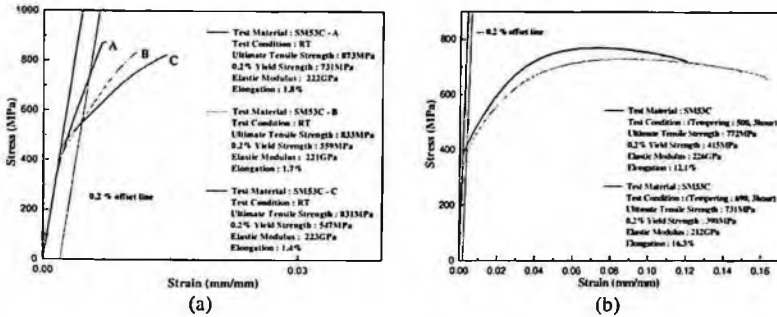
Fig. 4 Stress–Strain diagram for SM53C (a) hardness depth: 1.1, 0.55, and 0.35 mm and (b) tempering at 500 ℃ and 690 ℃

Figure 4(a) shows that the tensile strength of A type, B type and C type are 873 MPa, 833 MPa and 831 MPa, respectively. In case of A type, tensile strength is 873 MPa and Yield strength is 731 MPa. It is highest tensile strength and yield strength. When compare with base metal, B type and C type, tensile strength is similar but yield strength is different. Therefore in case of High-Frequency Induction Hardening specimen, if hardening depth deepens, the tensile strength and yield strength can be improved. Tensile strength increases because of decrease of grain size by High-Frequency Induction Hardening. That is, in compliance with the Hall-Petch Equation ($\sigma_y = \sigma_0 + Kd-0.5$), decreases of grain size (d) brings increasing of the yield strength (σ_y).[4] Figure 4(b) indicates tensile test result after Tempering in order to decrease brittleness and give toughness for heated steel. After tempering, elongation increases altogether, but tensile strength is known shortly decreasing.

3.4. *Fracture toughness test*

Plane strain fracture toughness of SM53C is seen in Figure 5. The values of the plane strain fracture toughness (K_{IC}) was computed using following formula

$$K_{IC} = P_Q \frac{f(a/W)}{B\sqrt{W}}$$

$$f(a/W) = \frac{(2+a/W)(0.886 + 4.64a/W - 13.32a^2/W^2 + 14.72a^3/W^3 - 5.6a^4/W^4)}{(1-a/W)^{3/2}}$$

--- (1)

Where,

P_Q: Load, B: Specimen thickness, a: Crack length, W: Width of the sample.
The plane strain fracture toughness (K_{IC}) was satisfied the Equations (2) and (3)
which are load condition and thickness condition of ASTM E 399 respectively.

$$P_{max} / P_Q \langle 1.10 \text{ --- (2)}$$

$$B, a \langle 2.5 (K_Q / \sigma_{ys})^2 \qquad R_{sc} = 2P_{max}(2W + a) / B(W - a)^2 \sigma_{ys} \text{ ---------------------- (3)}$$

The load-crack opening displacements (COD) curve was recorded, and the
stress intensity at crack propagation (K_Q) was estimated using the 95% secant
line. The criteria for a successful testing, i.e. $K_{IC} = K_Q$. From the results of
fracture toughness tests, K_{IC} value of SM53C (Hardness depth: 1mm) is 26.955
MPa-m$^{0.5}$ and SM53C (Hardness depth: 2mm) is 28.874 MPa-m$^{0.5}$. In case of
SM53C (Hardness depth: 2mm), the value of K_{IC} (28.874 MPa-m$^{0.5}$) is higher
than other SM53C (Hardness depth: 1mm). Fracture toughness values of SM53C
(Hardness depth: 1 mm and 2 mm) is shown in Table 4 and relationship between
Force and COD is shown in Figure 5
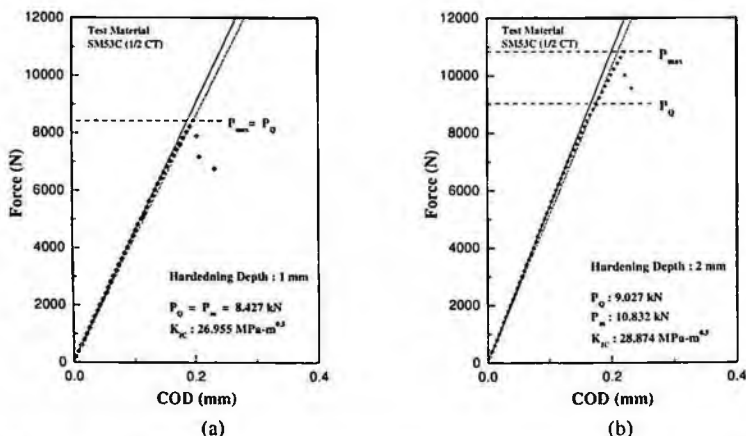
Fig. 5 Variation of force with COD of SM53C for hardening Depth: (a) 1mm and (b) 2 mm

Table 4 Fracture toughness values of SM53C

Material	Hardness Depth [mm]	Critical load P_Q [kN]	Maximal load P_{max} [kN]	Fracture toughness K_{IC} [MPa-m$^{0.5}$]
SM53C	1	$P_Q = P_{max} = 8.427$		26.955
	2	9.027	10.832	28.874

4. Conclusion

In this study are compared with surface hardness characteristic about hardening
depth of the SM53C used in the cam shaft. In order to estimate the shape of

hardening depth, we investigated about hardened structure, hardness, hardening characteristic and fracture characteristic using SM53C composed by carbon steel.
1. The hardness of High-Frequency Induction Hardening part average is 717 HV. And, a rapid decrease in boundary of High-Frequency Induction Hardening part and base part.
2. Surface part of hardening depth can be seen to be composed generally uniform detailed martensite structure by quick freezing. And some quantity of Residual austenite is still remaining. In case of slow travel speed outside surface of hardening, martensite is known larger size than the surface directly under high temperature heating. But in case of High-Frequency Induction Hardening, the inclination is not indicated. This is happened because of past travel speed (6.2, 7.0, 7.3 mm/sec). Therefore, quantities of carbide decrease for austenite course because structures are short of temperature and time which can completely change by austenite. Also, observed proeutectoid ferrite is kept to be like that.
3. In case of High-Frequency Induction Hardening specimen, if hardening depth deepens, the tensile strength and yield strength can be improved.
4. Material heated by High-Frequency Induction Hardening changed from pearlite and ferrite to martensite and increases strength. According to hardening depth, KIC value increased

Acknowledgments

References

1. L. Semiation, D. E. Stutz. Induction Heat Treatment of Steel, American Society for Metals.
2. "Development of Dual Frequency Phase Heat Treatment Technology," KIMM Report BSM235-1637.C, 1991.
3. J. of the Korean Society for Heat Treatment Vol. 3, No.2, June 1990, pp.10~19.
4. Richard. w. Hertzberg, Deformation and Fracture Mechanics of Engineering Materials, 2nd Ed. pp.98-99. 1983.

FRACTURE CHARACTERISTRICS OF CERAMIC PLATES USING SHOCK TUNNEL*

KYOUNG JOO KIM[1], JAE HOON KIM[1,†], YOUNG SHIN LEE[1], JONG HO PARK[1], KEE HYEUK SONG[1]

[1]BK21 Mechatronics Groups, Dept. of Mechanical Design Engineering, Chungnam National University, 220 Kung-Dong, Yuseung, Daejon 305-764, Korea

SONG HOE KOO[2] AND SOON IL MOON[2]

[2]Propulsive Group, Agency for Defense Development, Yuseung P.O.Box 35, Daejon, 305-301, Korea

This study is to evaluate fracture pressure and characteristics using shock tunnel for ceramic plates of dome port cover. Dome port cover has an important role in separation of solid and liquid fuel at ramjet engine system. Dome port cover is a component of the ramjet engine system and is required to have resistance to high temperature. Moreover, the fractured particles of dome port cover must not affect the structure of combustion chamber with damage. Ceramic materials have been considered as one of promising candidate materials for dome port cover of a ramjet engine system. we test the shape of plate and dome by the shape of structure, evaluated sizes and movements of fragments. This experiment presents shock-fracture of dome port cover using shock tube by means of basic study of design of dome port cover. The results which studies on fracture properties of ceramic are used for basic data of developments and structure designs.

1. Introduction

Dome port cover materials have characteristics of frangibility, high pressure resistance and high temperature resistance. The materials also are good at manufacturing about drilling and machining, never have to be deformed before these are fractured [1]. In this study, these experiments are performed to measure fracture pressure and investigate fracture phenomenon.

A theory of dome port cover is that dome port cover is fractured by inlet pressure after all of solid fuel is combusted during resistance about combustion pressure [2]. The concept of this operation is similar to an apparatus of shock tunnel. Compression wave is produced by pressure of driver section that is high

---

† Corresponding author: TEL +82 42 821 6645; FAX 82 42 821 8894
E-mail ; kimjhoon@cnu.ac.kr (Jae Hoon Kim)

pressure according to shock tunnel toward out of a port which is the part of installing specimen. Shock tunnel is an experimental apparatus used for compressive wave and expansion wave. The apparatus is good for compression wave hypersonic aerodynamics. In this present, it is extensively used in dynamic engineering, aerospace engineering, high-temperature physics, high-speed chemistry, and so on [3, 4].

This study is conducted to evaluate fracture pressure and fracture characteristics of ceramic plates and analytic techniques using compression wave of shock tunnel. he results obtained from this study will be utilized as a design database for dome port cover of ramjet engine system.

2. Experimental procedures

Figure 1 shows schematic diagram of shock tunnel used for evaluating fracture pressure and characteristics of ceramic plates. Shock tunnel system consists of driver, driven and Dump tank part. P_1 is driver gas before expansion, P_2 is driven gas behind contact surface, P_3 is driver gas after contact surface, P_4 is driver gas before expansion, P_5 is reflected wave (fractured pressure), M_s is incident wave respectively [5].
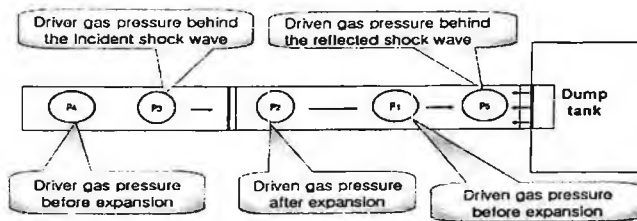
Fig. 1. Schematic diagram of shock tunnel

Mach number of incident wave is determined by P_4/P_1 of pressure ratio, k of specific heat ratio. P_1 is atmospheric pressure. In this test condition, specific heat ratio is 1.4 for air. Speed of sound present α. Parameter α_1 is equal to α_4. This relation is given in Eq. (1).

$$\frac{P_4}{P_1} = \left[\frac{2kM_s^2 - (k-1)}{k+1} \right] \cdot \left[1 - \frac{\alpha_1(k-1)}{\alpha_4(k+1)}(M_s - \frac{1}{M_s}) \right]^{-\frac{2k}{k-1}} \tag{1}$$

The pressure ratio of the driven gas pressure behind reflected shock wave (P_5) and the driven gas pressure before expansion (P_1) is given in Eq. (2)[6,7].

$$\frac{P_5}{P_1} = \left[\frac{2kM_s^2 - (k-1)}{k+1}\right] \cdot \left[\frac{(3k-1)M_s^2 - 2(k-1)}{(k-1)M_s^2 + 2}\right] \tag{2}$$

Air is used for test gas and driving gas in this test.

The materials used in this study are MACOR ceramic of Corning Incorporated, Al_2O_3 ceramics of Duckseung co., Ltd., BN ceramic of Dandan co., Ltd.. The chemical compositions of Al_2O_3 and MACOR ceramics summarize in Table 1 [8]. The diameter of test specimens conducted using shock tunnel is 98 mm and the thickness of that is 2 ~ 6.6 mm.

The shock tunnel used for this test is shown in Fig. 2.

Table 1. Chemical compositions of Al_2O_3 (960A) and MACOR ceramic [8]

Al_2O_3 ceramic		MACOR ceramic	
Composition	Approximate weight (%)	Composition	Approximate weight (%)
Al_2O_3	95	SiO_2	46
SiO_2	2.6	MgO	17
CaO	0.3	Al_2O_3	16
MgO	0.7	K_2O	10
Cr_2O_3	1.4	B_2O_3	7
-	-	F	4
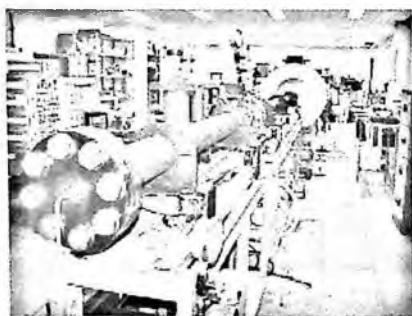
Fig. 2. Experimental apparatus of shock tunnel
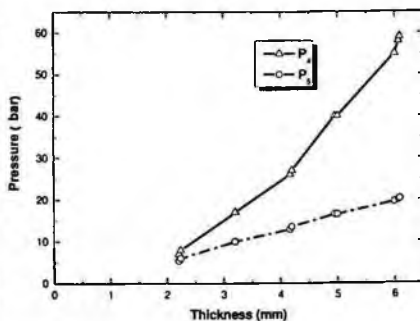
Fig. 3. Experimental pressure data at the thickness for Al_2O_3 ceramics

FEA program is ANSYS 10.0. Inner diameter which is really pressured is modeling in 70 mm. Thickness which is similar with real experiments is modeling in 2 ~ 6.60 mm. The constraints are that the circumference of a circle is clamped. The pressure time applied is 0.001 sec. The FEA results are compared with experimental results in fractured pressure according to the thickness.

3. Results and discussion

The experimental results of the fracture pressures and pressures of driver section used for shock tunnel according to the thickness of ceramics are plotted in Fig. 3.

The fractured pressure is 10 bars at 3 mm and 20 bars at 6 mm for Al_2O_3. Fig. 3 shows that driver section pressures rise in pressure rate according to fractured pressures. This phenomenon is occurred at 30 bars in driver section because an increasing rate of Mach number is very small.

Fig. 4 shows fractured specimens of MACOR, Al_2O_3 and BN ceramics. The cases of Al_2O_3 ceramics are fractured in small fragments and large segments for Al_2O_3 ceramics at 6 ~ 7 mm. This fractured shape of Al_2O_3 ceramics is not suitable for requirements that are the characteristics of small size fractured. MACOR ceramics are fractured to almost small size. These characteristics of MACOR ceramics are adequate for requirements of dome port cover. BN ceramics are fractured to almost large size. BN ceramics are not also suitable for requirements.
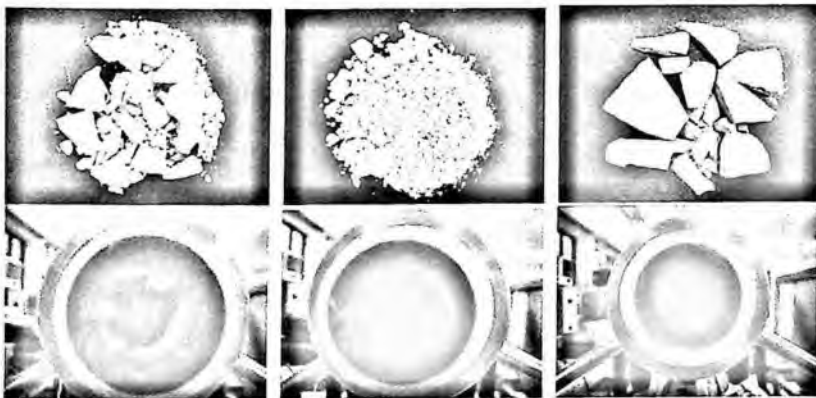
(a) Al_2O_3 (t= 6.10 mm)   (b) MACOR (t= 6.60 mm)   (c) BN (t=6.60 mm)

Fig. 4. Fractured specimens for various ceramics

386
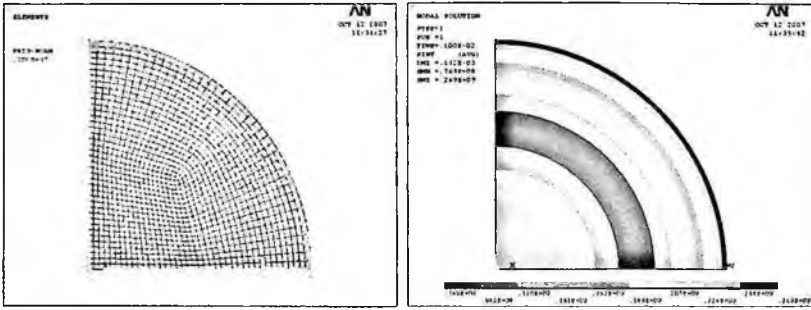
Fig. 5. Analysis of Al₂O₃ ceramics using ANSYS
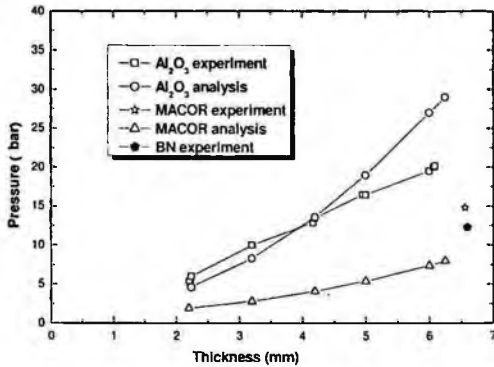
Fig. 6. Results of experimental and FEA data

Fig. 5 represents the results of FEA for Al$_2$O$_3$ ceramics. Al$_2$O$_3$ ceramics of the highest hardness at the inside diameter are not clearly fractured about a phenomenon of the fractured shape. However, MACOR and BN ceramics of the low hardness compared with Al$_2$O$_3$ ceramics are clearly fractured more than Al$_2$O$_3$ ceramics about a phenomenon of the fractured shape.

The materials of fine fractured specimens according to inner diameter correspond with that the specimens are fractured into small pieces. Fig. 6 resents the fracture pressure of various ceramics with the thickness of specimens. The conditions of FEA assume that the model is fractured at the time of over ultimate tensile strength or maximum strain. The ultimate strength and maximum strain are occurred in the circumference of the ceramic plates clamped.

In the FEA and experimental results, Al$_2$O$_3$ ceramics are fractured with 13.5 bar of fractured pressure at 4.2 mm thickness of material, FEA results are 20 % lower than experimental results at 2 ~ 3.2 mm thickness. FEA results are 20 ~

30 % higher than experimental results at 2 ~ 6.25 mm thickness. In the MACOR ceramics, the experimental data is 30 % higher than FEA data at 6 ~7 mm thickness. MACOR ceramics in contrast with Al_2O_3 ceramics are higher than Al_2O_3 ceramics for experimental results. The fractured pressure of BN ceramics with the same thickness of MACOR and Al_2O_3 ceramics are 15 ~ 40 % lower than MACOR and Al_2O_3 ceramics. The reasons of this case expect Mach number. This phenomenon occurs because Mach number, shock energy and a sintering state are considered about FEA.

4. Conclusions

In this study, compressive wave test is performed to evaluate fracture pressure and characteristics using shock tunnel by changing thickness and pressure of materials. FEA is conducted in order to be compared with experimental results. The conclusions of this study are as follows:

1. The fracture pressure of Al_2O_3 ceramic is the highest fracture pressure of ceramics with the same thickness of ceramics.
2. The results of FEA are similar with the results of experiments at 2 ~ 5 mm thickness of Al_2O_3 ceramic.
3. MACOR ceramic is well evaluated among materials that has characteristics of fragility and withstand combustion pressure in the objective of this study according to experimental results.

Acknowledgments

References

1. P. R. Scannell, N. R. Milich and E. O. Kalil, *AIAA*, No. 1980-1279(1980)
2. F. F. Webster, *AIAA*, No. 1978-1108(1978)
3. I. I. Glass & J. G. Hall, *Handbook of Supersonic Aerodynamics*, section 18, Shock tube, Vol.6, pp.317 ~ 522(1959)
4. H. Mirels, *AIAA*, Vol. 2, No 1
5. So. M. S, *Doctoral dissertation, Chungnam national university graduate school* (1997)
6. D. R. Smith and A. J. Smith, *AIAA*, Paper No.94-2227(1994)
7. L. G. Smith, *OSRD Report* 6271(1945)
8. Http://www.Coming.com

AN EVALUATION OF FRACTURE TOUGHNESS FOR CERAMICS*

KYOUNG JOO KIM[1], JAE HOON KIM[1, †], YOUNG SHIN LEE[1], NAM SU NO[1]

[1]BK21 Mechatronics Groups, Dept. of Mechanical Design Engineering, Chungnam National University, 220 Kung-Dong, Yuseung, Daejon 305-764, Korea

SONG HOE KOO[2] AND SOON IL MOON[2]

[2]Propulsive Group, Agency for Defense Development, Yuseung P.O.Box 35, Daejon, 305-301, Korea

The objective of this study is to compare the mechanical properties, static and quasi-dynamic fracture toughness for glass ceramics using dome port cover of ramjet engine system. Static and quasi-dynamic tests were conducted using SENB specimens (Single Edge Notched Beam). Strain rate of static fracture toughness in very low and that of quasi-dynamic fracture toughness is 0.04 m/sec at MTS 810. The specimens of the respective materials are machined according to the various notch radii using SENB method. The static and quasi-dynamic fracture toughness according to the various notch radii are evaluated using the ASTM and straingage method. The evaluation method of static and quasi-dynamic fracture toughness are validated using the straingage method for two materials.

1. Introduction

Ceramics are promising materials having rather high thermal strength characteristics but quite low crack resistance properties. These materials are finding increasing applications and there is a need to design then for resistance to impact loading. Al_2O_3 ceramics are compared with MACOR ceramics that have been considered as one of promising candidate materials for a dome port cover of a ramjet engine system [1, 2]. The materials also are good at manufacturing about drilling and machining, never have to be deformed before these are fractured [3, 4].

---

† Corresponding author: TEL +82 42 821 6645; FAX 82 42 821 8894
  E-mail ; kimjhoon@cnu.ac.kr (Jae Hoon Kim)

In this study, static and quasi-dynamic fracture toughness tests are carried out using two kinds of methods. The fracture toughness was investigated using SENB specimens with various notch radii.

The results obtained from this study will be utilized as a design database for dome port cover of ramjet engine system.

2. Experimental procedures

The materials used in this study are Al_2O_3 ceramics of Dandan co., Ltd., MACOR ceramics of Corning Incorporated. The mechanical properties of Al_2O_3 and MACOR ceramics are reported in Table 1 [5, 6]. An important consideration in the selection of the dome port cover material is the high thermal resistance and crack resistance under the impact loading. MACOR ceramics have been considered as one of promising candidate material satisfying these requirements. Al_2O_3 ceramics also have these characteristics. These materials have some special features such as excellent mechanical and machinable properties. Al_2O_3 ceramic consists of Al_2O_3 (95%), SiO_2 (2.6%), Cr_2O_3 (1.4%), CaO (0.3%) and MgO (0.7%). MACOR ceramic consists of SiO_2 (46%), MgO (17%), Al_2O_3 (16%), K_2O (10%), B_2O_3 (7%) and F (4%).

Fig.1 shows the configurations and dimensions of SENB specimens.

In this study, static and quasi-dynamic fracture toughness tests are carried out using SENB specimens. SENB specimens are fabricated in accordance with ASTM E399 standard [7]. Fracture toughness test of this kind of materials is generally conducted using notched specimens because fatigue pre-cracking of brittle material such as MACOR ceramic is practically impossible. Notch radii of SENB specimens used in this study were machined with 0.25, 0.5, 1.0, 1.5 and 2.0 mm. And notch depth ratio (notch depth/specimen width) is 0.48.

Table 1 Mechanical properties of two kinds of ceramics

Materials		Tensile strength (MPa)	Young's modulus (GPa)	Poisson's Ratio	Compressive strength (MPa)	Hardness (H_{RA})
Al_2O_3 ceramics	Exp.	266.7	371.2	0.22	1283.6	88.49
	Ref [5].	300	300	0.22	2400	88
MACOR ceramics	Exp.	65.0	67.8	0.27	341.7	47.4
	Ref [6].	-	66.9	0.29	345	48
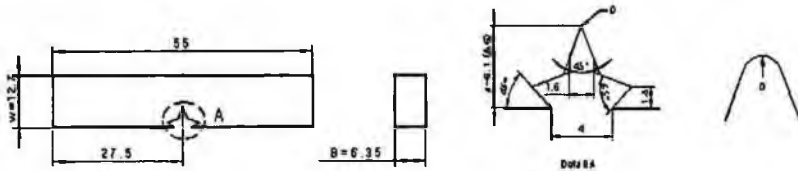
Fig. 1. Shape and dimensions of 3PB specimen (unit: mm)

To compare the results obtained from ASTM E399 standards, stain measurement is performed on equal test conditions. And the comparisons of Al_2O_3 and MACOR ceramics are respectively performed about the static and quasi-dynamic fracture toughness. Loading rate is 1.7×10^{-6} m/sec for the static fracture toughness test and is 0.04 m/sec for the quasi-dynamic fracture toughness test. The static and quasi-dynamic fracture toughness tests are conducted by using the hydraulic universal material testing machine of 10 ton (Model: MTS 810). To obtain the reliable fracture toughness using strain measurement, the strain field near crack tip was defined well enough for properly position and orient the strain gage in advance. A number of strain gages were attached at various positions [8 ~ 10].

3. Results and Discussion

Table 2 shows the results of static fracture toughness test evaluated from ASTM standard and strain method at $\rho = 0.25$ mm. Al_2O_3 ceramic is evaluated higher than MACOR ceramic in the static fracture toughness obtained from ASTM standard and strain method. The results of static fracture toughness are practically corresponding with the methods for MACOR ceramics. However, the strain method is 20 % higher than the ASTM standard method for static fracture toughness.

Table 3 summarizes the results of fracture toughness test under various loading rates at $\rho = 0.25$ mm. In the result of the quasi-dynamic fracture toughness, MACOR ceramic is 50 % lager than Al_2O_3 ceramic. The static fracture toughness of Al_2O_3 ceramic is half of quasi-dynamic fracture toughness. In the case of MACOR ceramic, the static and quasi-dynamic fracture toughness is practically the same results.

Fig. 2 represents a comparison of the static fracture toughness evaluated using ASTM standard and strain measurement for two kinds of ceramics. The static fracture toughness obtained from ASTM standard and strain measurement is nearly constant for Al_2O_3 ceramics, but static fracture toughness of MACOR ceramics shows an increasing trend at over $\rho = 0.6$ mm.

Table 2 Results of static fracture toughness test at ρ = 0.25 mm

Material	Al_2O_3 (Notch radius = 0.25 mm)		MACOR (Notch radius = 0.25 mm)	
Method	ASTM	Strain	ASTM	Strain
Fracture toughness $(MPam^{1/2})$	5.86	8.21	1.73	2.19

Table 3 Results of fracture toughness test under various loading rates at ρ = 0.25 mm

Material	Al_2O_3 (Notch radius = 0.25 mm)				MACOR (Notch radius = 0.25 mm)			
Method (SENB)	ASTM	Strain	ASTM	Strain	ASTM	Strain	ASTM	Strain
Loading rate (m/sec)	1.7×10^{-6} (Static)		0.04 (Quasi-dynamic)		1.7×10^{-6} (Static)		0.04 (Quasi-dynamic)	
Fracture toughness $(MPam^{1/2})$	5.86	8.21	3.32	4.02	1.73	2.19	1.66	1.41

Fig. 3 shows a comparison of the quasi-dynamic fracture toughness evaluated using ASTM standard and strain measurement for two kinds of ceramics. The quasi-dynamic fracture toughness of ASTM standard with ρ = 0.25 ~ 2.5 mm is practically the same that of strain measurement for MACOR ceramics. In the case of Al_2O_3 ceramics, the quasi-dynamic fracture toughness of strain measurement increases about 21 % compared with ASTM standard.

Fig. 4 shows a comparison of the static and quasi-dynamic fracture toughness evaluated using strain measurement for two kinds of ceramics. Quasi-dynamic fracture toughness evaluated using strain measurement decreases about 50 % compared with the static test result for Al_2O_3 ceramics. In the case of Al_2O_3 ceramics, static fracture toughness obtained from strain measurement is constant (average about 8.21 $MPa·m^{1/2}$), quasi-dynamic fracture toughness is constant (average about 5.86 $MPa·m^{1/2}$) As can be seen in Fig. 4, the critical notch radius in the case of static fracture toughness test using strain measurement for MACOR ceramics can be evaluated 0.6 mm, quasi-dynamic fracture toughness test can be evaluated about 0.9 mm.

a) Al_2O_3 ceramics

(b) MACOR ceramics
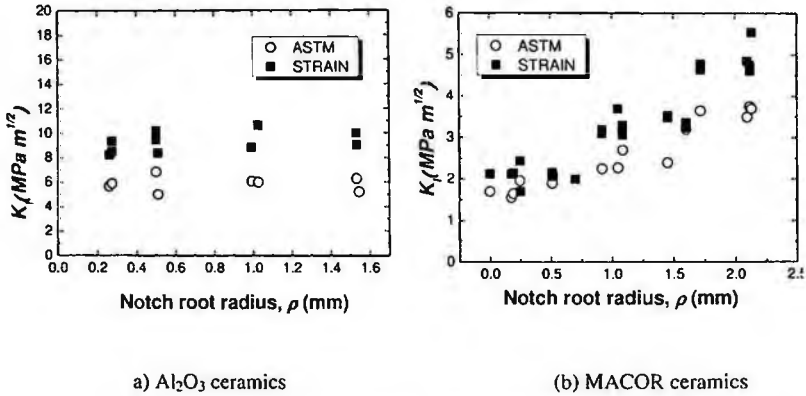
Fig. 2. Comparisons of the static fracture toughness evaluated using ASTM standard and strain measurement for two kinds of ceramics

a) Al_2O_3 ceramics

(b) MACOR ceramics
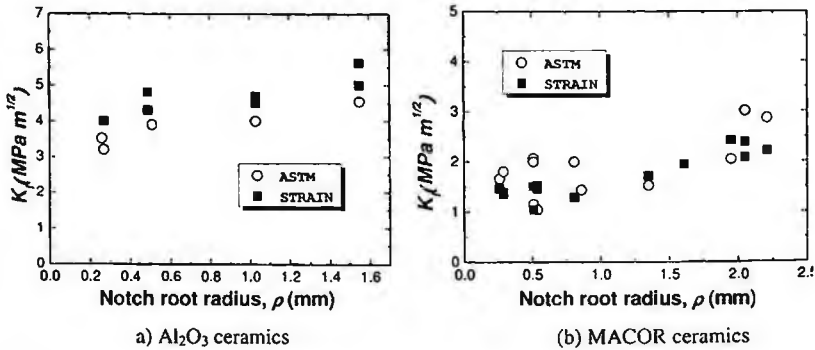
Fig. 3. Comparisons of the quasi-dynamic fracture toughness evaluated using ASTM standard and strain measurement for two kinds of ceramics

(a) Al_2O_3 ceramics

(b) MACOR ceramics
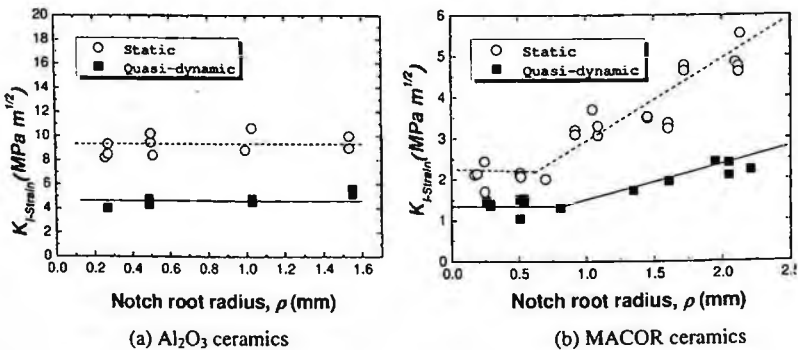
Fig. 4. Comparisons of the static and quasi-dynamic fracture toughness evaluated using strain measurement for two kinds of ceramics

4. Conclusions

In this study, To evaluate the static and quasi-dynamic fracture toughness for the materials of Al_2O_3 and MACOR ceramics, Load based on ASTM standard and strain measurement are performed using SENB specimens. The main results in this study can be concluded as follows:

1. The static fracture toughness obtained from ASTM standard and strain measurement is nearly constant for Al_2O_3 ceramics, but static fracture toughness of MACOR ceramics shows an increasing trend at over $\rho = 0.6$ mm.
2. The quasi-dynamic fracture toughness of ASTM standard with $\rho = 0.25 \sim 2.5$ mm is practically the same that of strain measurement for MACOR ceramics. In the case of Al_2O_3 ceramics, quasi-dynamic fracture toughness of strain measurement increases about 21 % compared with ASTM standard.
3. In the strain measurement, the static and quasi-dynamic fracture toughness obtained from strain measurement for Al_2O_3 ceramics are 8.21 and 4.04 $MPa \cdot m^{1/2}$, these of MACOR ceramics are 1.94 and 1.41 $MPa \cdot m^{1/2}$ respectively.
4. Critical notch radius for static and quasi-dynamic fracture toughness of MACOR ceramics is about 0.6 and 0.9 mm respectively.

Acknowledgments

References

1. S. Karishnan and P. Feorge, *Prog. Aerosp. Sci.*, Vol. 34, p.219(1998)
2. L. Delneste, *AIAA*, No.79-1253(1979)
3. P. Lapp and B. Quesada,1992, *AIAA*, No. 92-3616(1992)
4. T. D. Myers and J. A. Trimble, *AIAA*, No.78-1059, p.2~3
5. http://www.dandan21.com
6. http://www.Corning.com/Lightingmaterials/Products/MACOR.html
7. ASTM: Annual Book of ASTM Standards (ASTM International, USA 2004)
8. J. W. Dally and R. J. Sanford, *Exp. Mech.*, Vol.27, p.381(1978)
9. J. H. Kim, D. H. Kim, S. I. Moon and J. H. Kim, *Key Eng. Mat.*, Vol. 261-263, p. 313(2004)
10. L. S. Nui, C. Chehimi and G. Pluvinage, *Engineeing Fracture Mechanics*, Vol.49, No. 3, pp.325-335(1994)

FATIGUE LIFE OF COMPOUND CYLINDER COMBINING AUTOFRETTAGE AND SHRINK FIT DUE TO THE FIRING

Young-Shin Lee[†]

Department of Mechanical Design Engineering, Chungnam National University, Daejeon, 305-764, Republic of Korea
Corresponding Author, Director of BK21 Mechatronics Group

Jae-Hyun Park, Jae-Hoon Kim, Qiu-Ming Yang

Department of Mechanical Design Engineering, Chungnam National University, Daejeon, 305-764, Republic of Korea
BK21 Mechatronics Group, Daejeon, Republic of Korea

Ki-Up Cha, Suk-Kyun Hong

Agency for Defence Development, Daejeon, Republic of Korea

Autofrettage process is used for internal forming and sizing of cylinder designed to withstand high internal pressures. The compound cylinders can be manufactured with combining autofrettage and shrink fit process to extend fatigue lifetimes. The thermo-mechanical effects of firing induce very considerable stresses on the internal surface of the gun barrel. Consequently, micro-cracks appear very soon in the life of the tube. So it is important to control the propagation of these cracks. This paper presents the fatigue design of an autofrettaged compound and single cylinder for gun barrel which is worked by thermal flash. To ensure the structural integrity of the autofrettaged compound cylinder subjected to cyclic internal pressure and thermal loading, the fatigue crack propagation life of the cylinder was evaluated. Stress intensity factors of the internal cracked cylinder due to internal thermo-mechanical pressure and autofrettage loadings were calculated using the finite element method. As a result, predicted fatigue life of the compound cylinder was about 1.1~1.3 times more than those of the single cylinder depending on the levels of autofrettage.

1. Introduction

Multilayer pressure vessels are widely used in the field of high pressure technology. The compound cylinder can be manufactured with combining autofrettage and shrink fit process. A gun barrel is made of A723 steel. The magnitude of the residual compressive stresses and their distribution for any given geometry of the cylinder and overstressing process is highly dependent on the specific characteristics of the cylinder's material [1].

[†] leeys@cnu.ac.kr.

The internal surface of the barrel is thus subjected to a very high pressure and temperature cycle, which induces a temperature gradient in the surface layer of the barrel with a maximum temperature of more than 1300 ℃ in the internal wall [2]. This gradient is accompanied by differential expansions, which induce thermo-mechanical stresses far greater than the stresses due to the pressure of the gases, greatly exceeding the yield stress of steel. Thus, the thermal flash causes an elasto plastic stress/strain cycle over several tenths of a mm, which the material can withstand only for a few cycles before cracking.

An estimation of the fatigue crack initiation life of cylinders with different levels of autofrettage subjected to pulsating high internal pressure loading has been made by Koh [3] incorporating the finite element stress analysis, low-cycle fatigue testing, and local strain approach. Lee et al.[4] studied analytical analysis and Bauschinger effect about compound cylinder. Petitpas and Campion [5] used weight function methods for crack growth analysis in a gun barrel due to firing considering thermo-mechanical stresses. Adibi-Asl and Livieri [6] investigated analytical approach in autofrettaged spherical pressure vessels considering the bauschinger effect.

This paper focuses on the study of short crack propagation kinetics during firings. Two-dimensional modeling taking into consideration the residual stresses from a hydraulic autofrettage and the thermo-mechanical stresses due to the successive firings is presented. The cyclic plastic behavior of the material is taken into consideration. This makes it possible to observe the effect of loss of the residual stresses at the surface due to the firings. Cracks of increasing length are introduced in the model to calculate the stress intensity factor. The stress intensity factor is calculated using finite element code, ANSYS10.0. A classic Paris law is then used to predict the crack propagation kinetics. Effect of autofrettage on crack propagation of compound cylinder is analyzed.

2. Thermal Damage and Example

To quantify the thermal damage induced by firing, the distribution of transient temperature and residual stress resulting from gunnery is estimated, first. Then the stress intensity factor is calculated using finite element method, which in turn yields the fatigue life estimation. As pointed out earlier the choice of initial crack length is important and will depend on the tensile stress near the bore. in which temperature (T) is measured in Kelvin. Hot gases cause thermal expansion and compression yielding near the bore, resulting in significant tensile residual stress after gun cooling.

Fig. 1 represents sectional diagram of single cylinder and Fig. 2 shows sectional diagram of compound cylinder including tolerance 'δ'. To show the merits of the method described, a numerical example is presented.
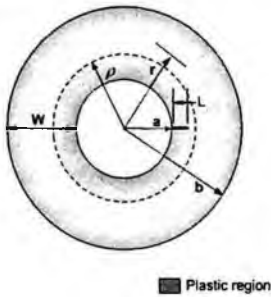
Fig. 1 Sectional diagram of single cylinder   Fig. 2 Sectional diagram of compound cylinder
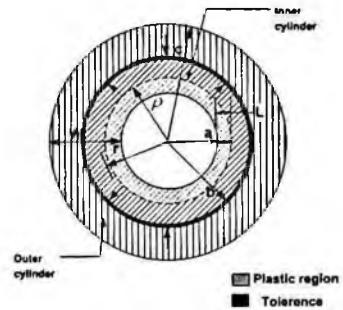
A single cylinder of inner and outer radii of a=78 mm, b=156 mm. A compound cylinder of inner, middle and outer radii of a=78 mm, b=117 mm, c=156 mm, δ =1 mm. Both of single and compound cylinder are with operating pressure of P^{APP} =385 MPa and autofrettage pressure that makes 20 %, 40 %, 60 %, 80 % of the wall thickness plastic, with initial crack length of a_i =0.1 mm is considered. The material is ASTM A723 steel, with following properties [3]:

$$E = 202.2 \; GPa, \quad v = 0.3, \quad \sigma_y = 1129 \; MPa, \quad K_{IC} = 130 \; MPa \cdot m^{1/2}$$

To calculate the residual stress distribution and stresses due to operational load on crack length, the method of Lee et al. [3] is used. It is assumed that temperature reaches its maximum limit in operating period. Thermal expansion coefficient and environment temperature are taken, respectively, as 13.5E-6 K^{-1}, $T_E = 300 \, K$. $T_i = 1611 \, K$ was used as Internal temperature. Thermal conductivity of this steel is 34 W/mK and thermal diffusion factor is 6.63E-6 and 7800 $kg \, / \, m^3$ for density. In the case of compound cylinder, thermal conductivity of contact interface is 20 W/mK [2].

3. Stress Intensity Factor by Thermo-Mechanical Stress and Autofrettage Residual Stress

Fatigue analysis of the autofrettaged compound cylinder with internal crack to cyclic internal thermo-mechanical pressure loading requires a through understanding of the stress distribution in the pressure vessel. A two-dimensional finite element analysises were performed to find the stress intensity factors. Fig.

3 and Fig. 4 are show finite element model of single and compound cylinder containing internal straight crack.
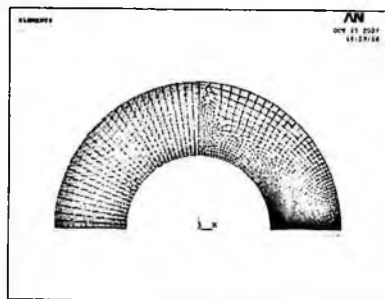
Fig. 3 Temperature distribution near the bore of single cylinder
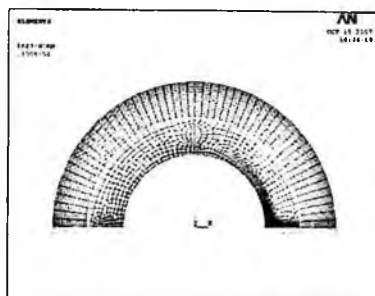
Fig. 4 Temperature distribution near the bore of compound cylinder

Applying the procedure to different crack lengths, stress intensity factor of compound and single cylinder containing internal crack represents following expression.

$$K_I = K_{it} + K_{ip} + K_{res}$$

where K_{it} is the stress intensity factor obtained by thermal stress. K_{ip} is the stress intensity factor under internal pressure, K_{res} is the stress intensity factor under autofrettage residual stress. Stress intensity factors can be obtained using 2-D four node quadrilateral element. Crack tip was obtained by dense mesh. The interface between inner cylinder and outer cylinder was modeled by contact element of ANSYS10.0. The interfered tolerance length is 0.1 mm

4. Fatigue Life Prediction of Autofrettaged Compound Cylinder Under Shrink Fit and SingleCylinder

The pressure vessels are occurring instable fracture, when a stress intensity factor 'K' approaches a critical stress intensity factor 'K$_{IC}$' of the material on the basis of fracture mechanics. The cylinder's material is ASTM A723 steel, a critical stress intensity factor 'K$_{IC}$' is measured about 130 $MPa \cdot m^{1/2}$ which was evaluated using 3 point bending specimens [3]. The measured critical crack lengthes 'Lcr' corresponding to K_{IC} are represented Table 1 according to autofrettage percentages.

To predict fatigue propagation life of autofrettaged compound and single cylinder under receiving internal thermo-mechanical pressure, the following

Paris equation (1) is introduced, the evaluated property values about cylinder's material are applied to the life prediction equation [3].

$$\frac{dc}{dN} = C(\Delta K)^m, \quad C = 4.24 \times 10^{-12}, \quad m = 3.2 \tag{1}$$

where ΔK (= K_{max} - K_{min}) are the range of the stress intensity factor. $\Delta K = K_{max} - K_{min} = [(K_{it} + K_{ip} + K_{res}) - K_{res}] = K_{it} + K_{ip}$ is used for thermo-mechanical pressure. $\Delta K = K_{max} - K_{min} = [(K_{ip} + K_{res}) - K_{res}] = K_{ip}$ is used for only mechanical pressure.

The measured critical crack lengthes 'L_{cr}' corresponding to K_{IC} are represented Table 1 according to autofrettage percentages. Fig. 5 is fatigue life under only mechanical pressure vs thermal mechanical stress following overstrain levels.

Table 1. Critical crack lengthes at the inner surface of cylinder

% O. S	Single cylinder		Compound cylinder	
	Thermo-mechanical L_{cr} (mm)	Mechanical L_{cr} (mm)	Thermo-mechanical L_{cr} (mm)	Mechanical L_{cr} (mm)
20	2.5	3.2	2.8	3.5
40	3.1	4.3	3.5	4.6
60	3.8	5.2	4.5	5.4
80	4.7	6	5.8	6.5
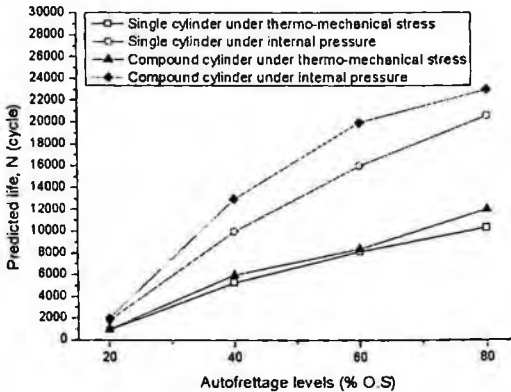
Fig. 5 Fatigue life under only mechanical pressure vs thermo-mechanical stress following overstrain levels

5. Conclusions

The method for calculation of stress intensity factor has been extended to include thermal effects. This method assumes constant firing heat input, effect of heat on an already autofrettaged tube and an initial crack length of 0.1 mm. The method has been applied to a case and studied numerically. As a result, following concluions are obtained.

(1) A compound cylinder have longer critical crack length about 1.1~1.3 times than a single cylinder. Also, critical crack lengthes are gradually increasing with autofrettage levels.

(2) The fatigue life of compound cylinder is about 1.1~1.3 times more than single cylinder. Also, the more autofrettage levels, the more predicted fatigue crack propagation life.

(3) Thermal stresses reduce the life of autofrettaged single and compound cylinder by a factor of 2.

Acknowledgments

References

1. H. Jahed, B. Farshi, M. Karimi, "Optimum Autofrettage and Shrink-Fit Combination in Multi-Layer Cylinder", *Trans. Of ASME Journal of Pressure Vessel Technology*, Vol. 128, pp. 196~200 (2006).
2. H. Jahed, B. Farshi, M. Karimi, "The actual unloading behavior effect on thermo-mechanical stress intensity factor and life of autofrettage tubes", *International Journal of Fatigue*, Vol. 125, pp. 321~325 (2006).
3. S.K. Koh, Y.I. Kim, S.H. Chung, and S.I. Lee, "Stress Analysis and Fatigue Life Prediction of an Autofrettaged Thick Cylinder with Radial Holes," *Trans. Of the KSME*, Vol. 2, No. 1, pp. 73~78, (1995).
4. J.H. Park, Y.S. Lee, J.H. Kim, K.U. Cha and S.K. Hong, "Machining Analysis of the Autofrettaged Compound Cylinder," *Trans. Of the KSME*, Vol. 31, No. 7, pp. 800~807, (2007).
5. E. Petitpas, B. Campion, "Crack Propagation in a Gun Barrel Due to the Firing Thermo-Mechanical Stresses", *Trans. Of ASME Journal of Pressure Vessel Technology*, Vol. 125, pp. 293~298 (2003).
6. R. Adibi-Asl, P. Livieri, "Analytical Approach in Autofrettaged Spherical Pressure Vessels Considering the Baushinger Effect", *Trans. Of ASME Journal of Pressure Vessel Technology*, Vol. 129, pp. 411~419 (2007).

FATIGUE LIFE EVALUATION OF PIPE WELDS IN POWER PLANT USING ADVANCED NONDESTRUCTIVE METHODS

SANG-GUK LEE, SUNG-KEUN PARK, KEUN-BONG YOO

*Korea Electric Power Research Institute, 103-16 Munji-Dong, Yusung-Gu
Daejeon, 305-380, Korea*

DUCK-GUN PARK

*Korea Atomic Energy Research Institute, P.O. Box 105, Yusung-Gu
Daejeon, 305-600, Korea*

The objective of this study is to estimate the feasibility of advanced nondestructive method (X-ray diffraction, AE(acoustic emission) and BN (barkhausen noise) measurement application for fatigue life evaluation of the high-temperature pipeline steel such as main steam pipe, re-heater pipe and header etc. in power plant. In this study, various nondestructive tests using various types of specimen simulated low cycle fatigue damage were performed in order to analyze fatigue properties when fatigue damage conditions become various stages such as 1/4, 1/2 and 3/4 of fatigue life, respectively. As a result of X-ray diffraction tests for specimens simulated fatigue damages, we conformed that the variation of the full width at half maximum intensity decreased in proportion to the increase of fatigue life ratio. And also, AE and BN signal due to fatigue damage has linear relationship with fatigue life ratio algebraically. From this relationship, it was suggested that direct expectation of the life consumption rate was feasible.

1. Introduction

Fatigue damages occur frequently in the high-temperature pipelines such as main steam pipe, re-heater pipe, and header etc. in power plant. If these damages are predicted by maintenance or replacement of parts for prevention, it can be enable to reduce financial loss and spreading accident [1-2]. Mechanical test is required to predict damage condition and fatigue life. But, it is very hard to gather test specimen from the working facilities. So assessment of fatigue life by non-destructive method is urgently needed, but researches on that are insufficient [3-5]. In this paper, artificial fatigue degradation test and advanced methods (X-ray diffraction, AE and BN measurement) for their fatigue degraded specimens (Cr-Mo-V alloy steel) were carried out for the purpose of evaluation for fatigue damage.

2. Experimental Procedures

2.1. *Specimens*

P92 steel using as a high-temperature pipeline steel in ultra super critical power plant was used in this investigation. X-ray diffraction, AE and BN tests using various types of specimen simulated low cycle fatigue damage were performed in order to analyze fatigue properties when fatigue damage conditions become various stages such as 1/4, 1/2 and 3/4 of fatigue life, respectively. The chemical composition of the steel is given in Table 1. Specimen for this investigation was made from the base metal, welds and heat affected zone (HAZ) of P92 steel, respectively. P92 steel has a half Mo content of ASME SA-335 P91 steel and DIN 17175 X20CrMoV12.1 steel to enhance creep strength, was added 1.5~2.0% more W content and has 0.10% lower C content for improvement of welding performance. Figure 1 shows geometry of specimen.

Table 1. Chemical composition of base metals.

C	Si	Mn	P	S	Ni	Cr	Mo	W	V	Nb	B	N
0.10	0.22	0.48	0.017	0.006	0.18	9.11	0.47	1.71	0.18	0.056	0.003	0.041
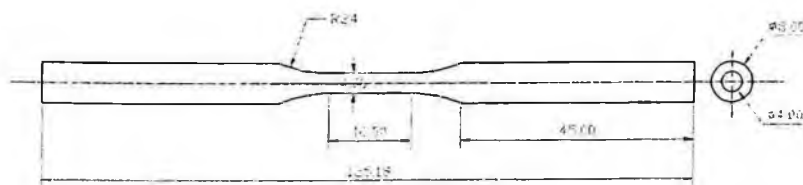
Fig. 1. Geometry of P92 steel specimen.

2.2. *Fatigue Test*

Fatigue tests were conducted in air under strain control mode in an Instron 8500 system using triangular waveform. Measuring conditions of fatigue test are as follows.

Table 2. Measuring conditions of fatigue test.

- Geometry of specimen: gage diameter: 4φ, gage length:16mm - Strain gage: 12.5mm - Strain amplitude: ±0.4%	- Waveform: triangular - Frequency: 1Hz - Fatigue life: 20% load reduction

2.3. *X-Ray Diffraction Test*

X-ray diffraction tests were conducted in XSTRESS 3000(Finland), the portable X-ray diffraction equipment. Residual stress measurements were carried out using $\sin^2\psi$ method. The five ψ angles used for the measurements were 0°, 20.7°, 30°, 37.8° and 45°. Measuring conditions of X-ray diffraction test are as follows.

Table 3. Measuring conditions of X-ray diffraction test.

- Characteristic X-ray: Cr-Kα	- Tube current: 10mA
- Diffraction plane: (211)	- Scanning speed: 2deg. /min
- Tube voltage: 30kV	- Time constant: 3sec

2.4. *AE and BN Test*

The AE properties measuring system used in this study consists of a 1 MHz acoustic emission test system, a 100 MHz spectrum analyzer, a digital oscilloscope and a personal computer for data processing. AE signals were detected by resonant type PZT transducer with nominal center frequency of 1 MHz. The transducer output was fed into 40~60 dB preamplifier and then to a band-pass filter of 1.5 f_c (where f_c is the center frequency of the transducer). The relationships of AE signal properties such as AE cumulative counts versus time, AE cumulative hits versus time, other AE parameters and fatigue properties of each fatigue damage stages were analyzed. BN signal was measured by a surface coil sensor(Φ 9; 100 turns of 0.1 mm enamel coated wire. The filter output was sent to an envelope line detector, followed by an A/D converter and a signal averager. A trigger was gotten at a zero-crossing of H (magnetic field) in order to average a number of signals synchronously.

3. Results and Discussion

3.1. *Fatigue Test*

Full width at half maximum intensity (FWHM) is sensitive to the variation in microstructure and stress-strain accumulation in the material. X-ray diffraction is sensitive to the local phenomenon of grain deformations by the occurrence of the particular slip line as fatigue and crack initiation. In the close of fatigue life, the occurrence of microscopic crack and propagation makes the value of the residual stress decrease exponentially. Therefore, in this investigation, the occurring point of microscopic crack is estimated about 70% stage of the fatigue life ratio. The value of FWHM is sharply decreased by 20% of the fatigue life ratio, and

then shows a gentle decline. The relation between FWHM and life consumption rate is as follows.

$$B_f = k. \ln x + C \qquad (1)$$

B_f means the rate of FWHM, B_0 means the value of FWHM before deformation, k means slope of the FWHM rate, and C means material constant. Material constant, C is the FWHM rate when the life of material runs out. Using equation 1, life consumption rate can be calculated simply. And also, by using the value of the FWHM rate (B/B_0) and measuring the FWHM (B) of materials under fatigue, the range of life consumption rate (Nc) can be predicted directly. The variation of FWHM values versus life consumption rate is shows in Figure 2.
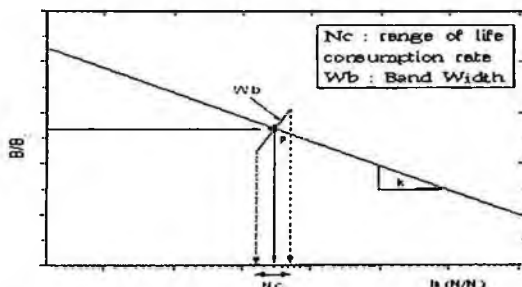
Fig. 2. Calculation of fatigue life consumption rate.

3.2. AE Test

It is considered that the various fatigue damage stages such as 1/4(1st), 1/2(2nd) and 3/4(3rd) of fatigue life, and damage in fatigue curve could be qualitatively related to AE properties such as counts vs. time, hit and vs. time, etc. Fig. 3(a) shows the relationship between AE cumulative counts and fatigue test time during fatigue test. AE cumulative counts mean the total number of signal counts in excess of certain threshold level among AE burst signals acquired during fatigue test. In Fig. 3(a), it is confirmed that AE cumulative counts indicate about 2,000 counts until 1st fatigue stage, about 6,000 counts until 2nd fatigue stage and about 16,000 counts until 3rd fatigue stage, respectively. Fig. 3(b) shows the relationship between AE cumulative hits and fatigue test time during fatigue test. AE cumulative hit means a parameter showing the total numbers of AE burst signals acquired during fatigue test. AE parameters versus fatigue stage can be

analyzed by the same method as Fig. 3(a). From Fig. 3(b), it is confirmed that AE cumulative hits indicate about 22 hits in 1st fatigue stage, about 60 hits in 2nd fatigue stage, and about 150 hits in 3rd fatigue stage, respectively.

(a) cumulative counts vs. time   (b) cumulative hits vs. time
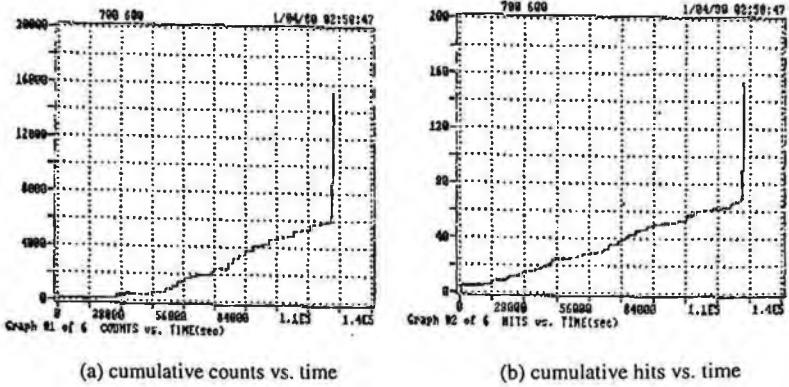
Fig. 3. Relationship between fatigue behavior and AE properties during fatigue test.
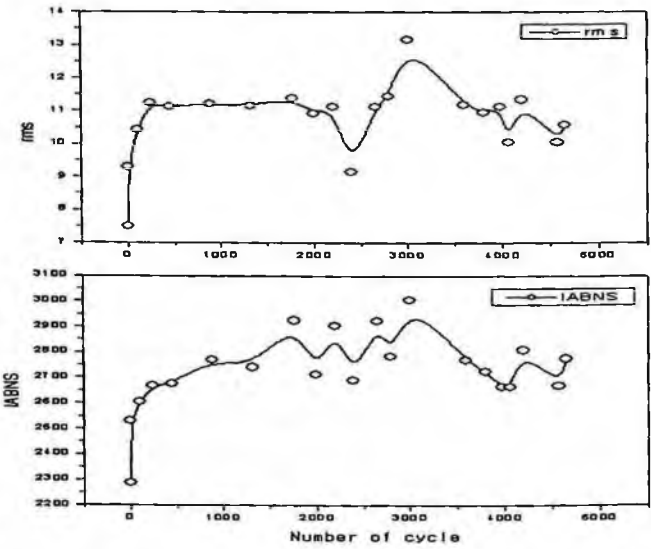
Fig. 4. Variation of RMS and IABNS values of BN signal according to fatigue damage.

3.3. *BN Test*

In order to obtain a more reproducible record of BN events, the envelope mode was used. The BN voltage was taken to be the maximum peak-to-peak value of the envelope. BN measurements were made on the pipe sample under various fatigue damage levels. Figure 4 indicates the relationship between number of cycle of fatigue test and RMS(root mean square) value, and also the relationship between number of cycle of fatigue test and IABNS(initial area barkhausen noise) for fatigue damage specimens. This shows that the RMS values increase as increasing fatigue cycles, and the IAVNS values increase as increasing fatigue cycles.

Summary

In this study, FWHM by X-ray diffraction, AE and BN for fatigue damage have been measured, and conclusions are as follows.
1) The relation between FWHM and life consumption rate is linear, and by using the Eq. (1) the direct prediction of life consumption ratio is enable.
2) AE parameters and fatigue properties of each fatigue damage stages, it was confirmed that AE evaluation for monitoring fatigue properties in real time could be possible qualitatively at present.
3) In BN noise analysis according to increasing fatigue damage, it is conformed that the BN and IABNS are increased with increasing fatigue life fraction.
4) X-ray diffraction, AE and BN measuring method are effective methods of assessing fatigue damage. These methods can be the most suitable nondestructive methods of assessing fatigue condition, as the amount a measured value change in relation to extent of damage is larger and more suitable than other methods.

References

1. Toru Goto, *Advances in X-Ray Analysis*, **35** (1992).
2. Sanjay Rai, *International Journal of Pressure Vessels and Piping* **76**, 275 (1999).
3. Y. Mori and T. Kisi, *Welding Technique*, **34-10**, 24 (1986).
4. G. Dobmann, N. Meyendorf and E. Schneider, *Nucl. Eng. Design*, **171**, 95 (1997).
5. Chennupati Jagadish, Lynann Clapham and David L. Atherton, *IEEE Trans. on Magnetics*, **26-1**, 262 (1990).

A STUDY ON ACCELERATED LIFE TEST UTILIZING FATIGUE DAMAGE THEORY FOR AUTOMOBILE COMPONENTS

DOHYUN JUNG

Korea Automotive Technology Institute, Reliability Division, Cheonan, Korea

YOUNGWOO CHOI

National Institute of Scientific Investigation, Physical Analysis Division, Seoul, Korea

BOKKYU LIM

Small Business Corporation, Training Center, Iansan, Korea

SUNGIN BAE

Changwon National University, Mechanical Engineering, Changwon, Korea

An important factor for guaranteeing the competitiveness in automobile industry is the prompt assessment of a newly developed part and then it is required to develop and obtain its technologies. Therefore, this research aims to propose a new design methodology of accelerated lift test (ALT), which is based on previous theories and various requisites for ALT and to contribute to development of life test of automobile parts. This research proposes ALT of some automobile part. The results are shown to be efficient.

1. Introduction

Having a rapid life test on automobile components is a primary factor in competitiveness; it is very important to acquire and develop this technology.

This study intends to contribute to technological development by providing a guideline to accelerated life test of automobile components applying existing theories. Related studies include Meeker and Hahn[1] who proposed an alternative accelerated life test method to the existing inefficient standard test design method, which alloted the same amount of components in all tests. Nelson[2] put many accelerated life test study results in order, and introduced problems and practical examples which could occur in actual practice.

Meeker, Jr.[3] also provided a fundamental rule in accelerated life test design, while Miller and Nelson[4] conducted a study on minimizing divergence

on time staging tests where the level of testing is increased after a certain amount of time, and a test where the level of testing is increased after a certain amount of malfunction occurs.

2. Accelerated Life Test Method

2.1 *Representative Loading Method*

Formula(3) can be derived by substituting the stress-life formula(1) in N to formula(2).

$$N = S_0^m \cdot S^{-m} \tag{1}$$

$$D = \sum_{i=1}^{k} \frac{n_i}{N_i} \tag{2}$$

$$D = \sum \frac{S_i^{\,m} \cdot n_i}{S_0^m} \tag{3}$$

n_i=number of inputs
N_i=number of damages
D=fatigue damage

Use condition must be measured in order to design an accelerated life test where fatigue damages of both the using condition and testing condition are equal; the fatigue damage is labeled D_{user} as shown in Formula (4). If the fatigue damage for testing is D_{test}, then the two variables should be comparably equal to each other. The S_0^m in the denominator is the same on both sides and is a constant, therefore can eliminate each other when considering the comparative size only.

$$D_{user} = \sum \frac{S_i^{\,m} \cdot n_i}{S_0^m}, \; D_{test} = \sum \frac{S_{Ri}^m \cdot n_{Ri}}{S_o^m} \tag{4}$$

$$D_R = \sum S_i^{\,m} \cdot n_i = \sum S_{Ri}^m \cdot n_{Ri} \tag{5}$$

D_R ; comparative use damage
S ; use load

The test fatigue damage can be expressed as comparative use damage D_R, as shown in formula(5), the cumulative use damage D, and comparative use damage D_R of use condition are set at a same value so that an appropriate testing

condition design can be guaranteed. However, for a more efficient test, it needs to be designed by properly controlling the input load, use load and number of operations. Therefore the introduction of representative stress or loading is necessary. If formula(5) is sorted by introducing a load which can be expressed as a single size, or use load $S_{eq}{}^m$ and the representative number of repetition N_{eq}, we get the formula(6) below.

$$D_R = \sum S_i^m \cdot n_i \fallingdotseq S_{eq}^m \cdot N_{eq}$$

(6)

$S_{eq}{}^m$ in formula(6) can be defined by representative stress and load which expresses the overall fatigue and use damages in a single stress or load.

The comparative use damage was defined as the value expressing the overall use damage in use condition, and this can be viewed as the size of an assumed use damage if the measured value is not a stress or transformation rate, but a measure that is hard to calculate into fatigue damage such as displacement or acceleration.

2.2 Block Cycle Loading Method

This method selects a certain number of loads out of the many inputs, and gives them a number of operations which is equivalent to use condition; in terms of fatigue damage, this method spreads the load more evenly than using a single load repeatedly until breakdown, and it also has a higher acceleration rate.

When considering average stress, the measuring signals are used with the Rainflow cycle counting method to calculate cumulative distribution, and cumulative cycle vs stress are both put to the log axis to calculate the load distribution curve as shown in Figure 1. Then the curve is broken down into segments in a stepwise fashion to calculate and test equivalent block curves.
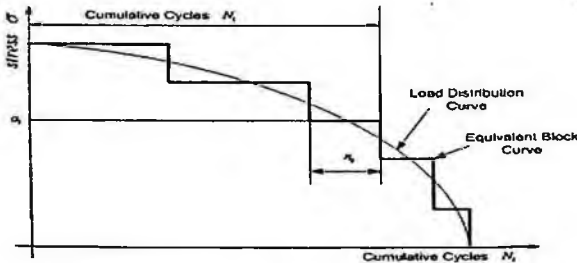
Fig. 1. Block cycle and load distribution curve.

2.3 *An Example of Representative Loading Method (Brake pedal)*

The apparatus for measuring the load of a brake pedal was built by using jigs and load cells. e-DAQ (Somat, USA) was used for the measuring system. As a result, the range of load was within 0~200N; emergency brakes created a load of 200N. The harsh driver A showed a slightly higher load of 108% input rate compared to driver B, and the load distribution was also higher than driver B. The use load history and cumulative equivalent damage level of the measured pedal were set at 22% use on highway, 28% on state roads and 50% on city roads; 50 repetitions of 1,000km runs were made, totalling at an extended target life of 500,000km. SPHC was used for the pedal material.

The overall sum of damage rate was set at 1 as shown in Figure 2., and each load and their respective damage rate are also displayed. Formula(6) was used to calculate the load, which has an equivalent damage rate and number of repetitions; the results are shown in Table 1.
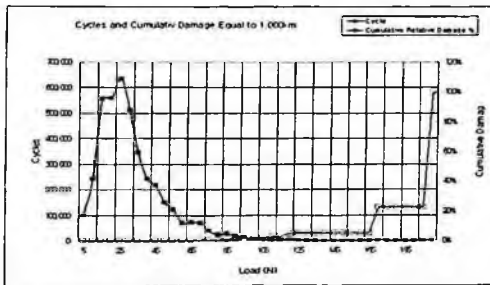
Fig. 2. Cycles and cumulative relative damage of severe user.

Table 1. Cycles and equivalent load for durability test .

	Sum of Damage	Test Cycles	Test Load (N)
Total Condition	8.6E-07	100,000	121
		300,000	107
		700,000	98
Severe Condition	9.9E-06	100,000	157
		300,000	139
		700,000	127

3. Test Results of Various Automobile Components

Figure 3. shows the flow chart of the accelerated life test design process used in this study. Table 2. shows the test results from using a representative loading method and block cycle loading method in both real and test lab conditions,

using sensors and measuring equipment which suits the physical characteristics of the automobile components.

Generally weibull distribution is suitable for automobile components. The analyzed results that use representative stress (load) method are appear that 90% confidence level is suited to test condition. Automobile components are not good to using 6 sigma. Exponent of sensitive life can be derived from existing test standard. When exponent of sensitive life is known, we can compare severity of another test result.
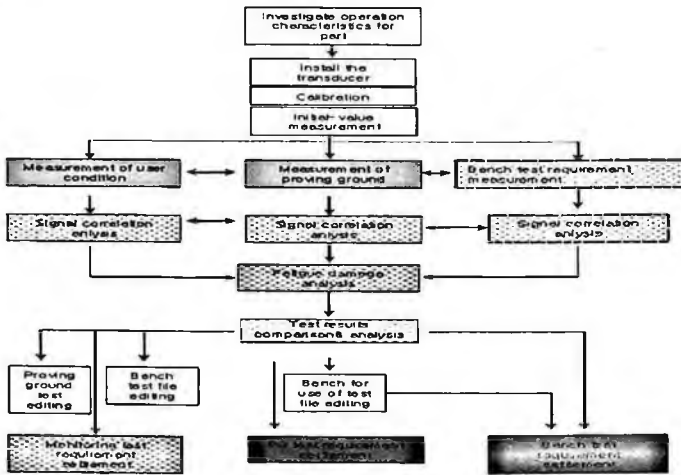
Fig. 3. Flow chart for accelerated test.

Table 2. The test results.

Component	Major Reason for Malfunction	Study Method and Results	Effective Accelerated Test Method
Brake Pedal	Operating Foot Power	- Limited factor method and comparative examination - Use damage is different depending on user, road conditions, region	Representative loading method
Stabilizer Bar	Operating Load	- Comparison of actual signal reproduction, block cycle, and representative loading method	Representative loading method and block cycle method
Shock Absorber	Response Speed	- Comparison of actual signal reproduction, and block cycle method	Block cycle method
Auto Tensioner	Displacement	- Comparative use damage analysis which considers road use frequency and detailed driving conditions	Representative loading method

4. Conclusion

The following conclusions could be drawn from the test results using the proposed accelerated life test method.

1. A representative stress (load) method which calculates the overall fatigue damage level with a single stress size proposed by stress-life linearity and analysis method derived from the Miner method can effectively be used in testing brake pedals, stabilizer bars and auto tensioners.

2. It is appropriate to use the block cycle method for components such as stabilizer bars and shock absorbers.

References

1. G. J. Hahn and W. Q. Meeker, "How to Plan an Accelerated Life Test-Some Practical Guideline," ASQC Basic References in Quality Control: Statistical Techniques, 10 (1986).
2. W. Nelson, "Accelerated Life Testing-Step Stress Models and Data Analysis," IEEE Transctions on Reliability, R-29, pp. 103-108 (1980).
3. W. Q. Meeker, "A Comparison of Accelerated Life Test Plans for Weibull and Lognormal Distributions and Type I Censoring," Technometrics, 26, pp. 157-171 (1984).
4. R. Miller and W. Nelson, "Optimum Simple Step Stress Plans for Accelerated Life Testing," IEEE Transctions on Reliability, R-32, pp. 59-65 (1983).

COMPARISON OF FATIGUE PROPERTIES OF AL ALLOYS
FOR CHASSIS COMPONENTS

CHUNG-YOUB KIM

Division of Mechanical and Automotive Engineering, Chonnam National University,
San 96-1, Dunduck-dong, Yosu, Chonnam, 550-749, Korea

JUN-HYUB PARK

Department of Mechatronics Engineering, College of Engineering, Tongmyong
University, 535, Yongdang-Dong, Nam-Gu, Busan, 608-711, Korea

JI-YOUNG PARK

S&T Daewoo Co., 5 Songjeong-ri, Cheolma-myon, Kijang-goon,
Busan, 619-873, Korea

BYUNG-IK CHOI
HAK-JOO LEE
SEUNG-MIN HYUN

Korea Institute of Machinery and Materials, 171 Jang-dong, Yusong-gu,
Daejeon, 305-343, Korea

JOO-SUNG KIM

Ssangyong Motor Co., 150-3, Chilgoy-dong, Pyongtak, Kyongki, 459-711, Korea

In this study, the mechanical and fatigue properties of two aluminum alloys Al 356-T6 developed to apply to chassis components were compared with FCD 500, and microstructure and components of the two aluminum alloys were analyzed. The two aluminum alloys were manufactured by low pressure and squeeze casting method, respectively. Mechanical properties of the two aluminum alloys are nearly same, but the fatigue strength of the squeezed alloy is higher than the low pressure cast alloy. The squeezed alloy has enough fatigue strength compared to FCD 500.

1. Introduction

Automakers have tried to enhance vehicle performance and safety, and current advances in vehicle technology greatly increase them and customer's expectation for vehicle performance is also increased. Customers desire high fuel economy and vehicle performance in vehicle selection. One of the most effective methods

to improve fuel economy and vehicle performance is weight reduction by using a lightweight material. Among the materials, aluminum alloy is a typical material to replace steel which is most widely used for vehicle components [1,2].

In this study, an aluminum alloy Al 356-T6 was developed to apply to chassis components, and the effects of the casting methods, that is, low pressure and squeeze casting, on the mechanical and fatigue properties of the aluminum alloy were investigated, and the results were compared with FCD 500. In addition, microstructure and components analysis of the two aluminum alloys were performed.

2. Experimental Details

2.1. *Tensile and Fatigue Tests*

The specimens were produced from chassis components made of aluminum alloys Al 356-T6 cast by low pressure and squeeze method and FCD 500. The specimens had a circular cross-section with a diameter of 6.35 mm.

The tests were performed by using a servo-hydraulic testing machine and the strain was measured by using an extensometer at the centre of the specimen. Tensile tests were performed at a stress rate of 5 MPa/s and the gauge length of the specimen was 25.4 mm [3]. The fatigue strength was determined from the strain–life (ε-N) curve, so that fatigue tests were performed under strain control at a frequency of 1 Hz and a strain ratio of -1, and the gauge length of the specimen was 12.5 mm. The fatigue test was continued until a number of cycles, 10^6, has been applied to the specimen [5].

2.2. *Microstructure and Components Analysis*

After tensile and fatigue tests, the specimens of the aluminum alloy were cut to observe the difference in microstructure of cast and squeezed aluminum alloy. A standard metallographic method, which includes mounting, grounding and polishing steps, was used.

A dual beam workstation (FEI Nova 200) was used to observe the structure of aluminum alloys. Elements of Al alloy is detected by energy dispersive spectroscopy (EDX) that was equipped with Scanning electron microscope (FEI Nova nanosem).

3. Results and Discussion

3.1. Test Results

3.1.1. Mechanical properties

Mechanical properties obtained from tensile tests are summarized in Table 1. Tensile strength σ_u, 0.2 % offset yield stress $\sigma_{0.2}$, and elongation δ of the two aluminum alloys are nearly same although the results of squeeze casting are slightly higher. This result indicates that there is no great effect of the two casting methods on the mechanical properties. On the other hand, ductility of the aluminum alloys is less than FCD500.

Table 1. Mechanical properties.

Casting method	E (GPa)	$\sigma_{0.2}$ (MPa)	σ_u (MPa)	δ (%)
Low pressure	68.7	222	287	5.4
Squeeze	71.7	235	298	5.2
FCD500	152	358	600	9.3
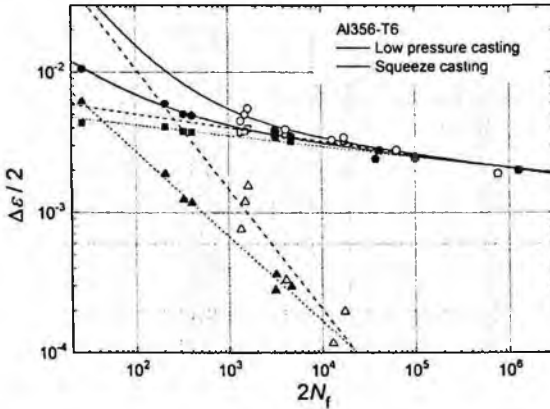
Fig. 1. Strain-life curve for the low pressure and squeeze cast aluminum alloys

3.1.2. Fatigue strength

The strain-life curves for the two aluminum alloys are shown in Figure 1, where solid and open marks represent the result of the low pressure and squeeze cast alloys, respectively. As can be seen from this figure, fatigue strength of the squeezed aluminum alloy is higher than that of the low pressure cast alloy for

low cycle region, while the fatigue strength of the two alloys are nearly same for high cycle region.
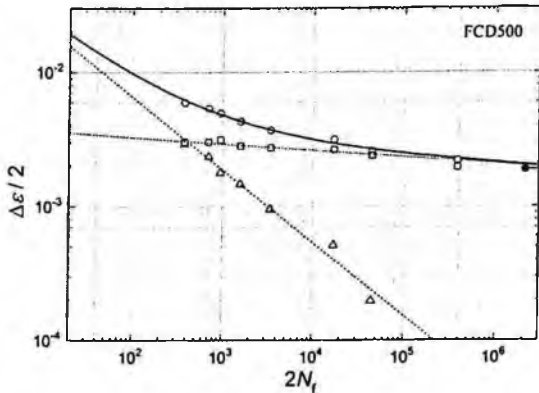
Fig. 2. Strain-life curve for FCD 500.

On the other hand, the strain-life curve for FCD 500 is shown in Figure 2. As can be seen from Figures 1 and 2, for low cycle region, fatigue strength of the squeezed aluminum alloy is higher than that of the FCD500, while fatigue strength of the low pressure cast aluminum alloy is lower than that of the FCD500. For high cycle region, however, fatigue strength for all materials is nearly same. Fatigue strength coefficients are represented in Table 2, where σ_f', ε_f', b, and c represent fatigue strength coefficient, fatigue ductility coefficient, fatigue strength exponent, and fatigue ductility exponent, respectively. From these results, it can be found that the squeezed aluminum alloy has enough fatigue strength compared to FCD 500.

Table 2. Fatigue strength coefficients.

Casting method	σ_f' (MPa)	ε_f'	b	c
Low pressure	411	0.0441	-0.0760	-0.604
Squeeze	562	0.0542	-0.0959	-0.855
FCD500	626	0.0802	-0.0488	-0.543

3.2. *Microstructure and Component Analysis*

Microstructure and components of the two aluminum alloys were observed by scanning electron microscopy and energy dispersive spectrum and the results are shown in Figures 3 and 4. Image was taken at low magnification to identify components in the alloy. Energy dispersive spectrum represented in Figures 3(a)

and 4(a) shows that the two aluminum alloys are mainly composed of aluminum and silicon. The weight percents of Al and Si are 81.6 and 18.4 % for the low pressure cast alloy, and 72.5 and 27.5 % for the squeeze cast alloy. From EDX analysis, it can be seen that there is no great difference of the components between the two Al alloys, and the squeezed alloy shows Si rich component while the low pressure cast alloy has less Si elements. Figures 3(b) and 4(b) shows microstructure of the two alloys. Grey particles shown in Figure 3(b) were known as Si, while white area represents Alpha phase in Al-Si alloy.
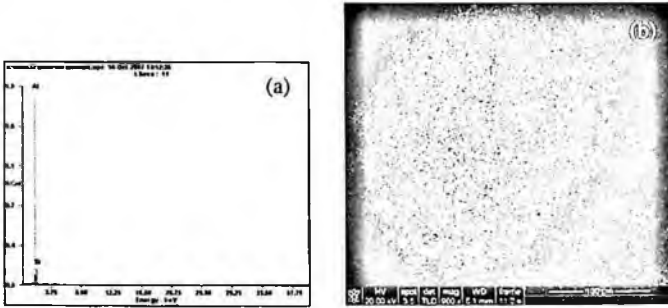
Fig. 3. Components and microstructure of the low pressure cast alloy.
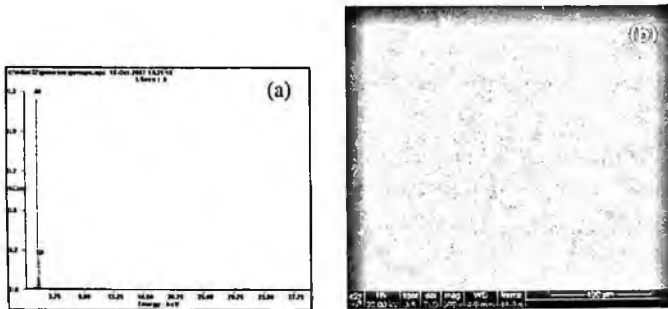
Fig. 4. Components and microstructure of the squeeze cast alloy.

For the squeezed alloy shown in Figure 4(b), the gray and white areas shown in Figure 3(b) were not clear. Therefore, the surface of the specimen was exposed to Ga ion in a short time and then the images were taken by e-beam. After metallogrphically prepared, grey particles and white area on the surface were appeared as shown in Figure 5. The particle size of the squeezed Al alloy shown in Figure 5 is much smaller compared to that of the low pressure cast alloy shown in Figure 3(b). This result indicates that the particle size of the alloy

may be one of reasons for the difference of the fatigue strength between the two alloys.
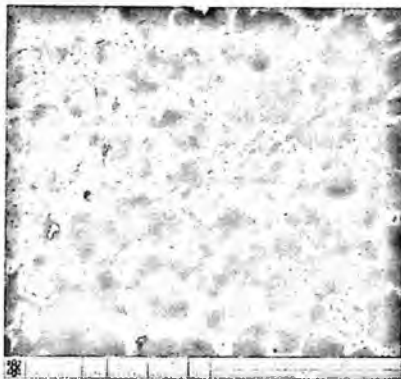
Fig. 5. Microstructure of the squeeze cast alloy.

4. Summary

In this study, the effects of the casting method for the aluminum alloy Al 356-T6 on the mechanical and fatigue strength was investigated. The results are summarized as follows.

Mechanical properties of the two aluminum alloys are nearly same, but the fatigue strength of the squeezed alloy is higher than those of the low pressure cast alloy. Additionally, the squeezed alloy has enough fatigue strength compared to FCD 500.

Acknowledgments

References

1. A.G. Grabowski and A.K. Jaura, *SAE Technical Papers*. SP-1598, 2001-01-0878 (2001).
2. Automotive Technology Handbook, JSAE, (1993).
3. Annual Book of ASTM Standards, V03.01, E8, (2000).
4. Annual Book of ASTM Standards, V03.01, E606, (2000).

ACOUSTIC PERFORMANCE OF A MAGNETOSTRICTIVE STRIP SENSOR FOR A TORSIONAL GUIDED WAVE

YONG-MOO CHEONG AND SHIN KIM

Nuclear Materials Research Center, Korea Atomic Energy Research Institute, Daeduk-daero 1045, Yusong-gu, Daejeon, 305-353, Korea

The magnetostrictive sensor technique has several advantages in practical applications for a long-range guided wave inspection, such as a 100-percent volumetric coverage of a long segment of a structure, a reduced inspection time and cost effectiveness, as well as its' relatively simple sensor structure. One promising feature of this magnetostrictive sensor technique is that the wave patterns are relatively clear and simple when compared to a conventional piezoelectric ultrasonic transducer. If we can characterize the evolution of defect signals with this technique, it could be a promising tool for a structural health monitoring of pipes for a long period of time as well as a flaw identification. In this paper, we attempt to analyze the ultrasonic wave patterns from various artificial defects and geometrical obstacles, such as a support structure in a pipe. Based on the experimental results, the theoretical interaction and superposition of those wave patterns are discussed.

1. Introduction

The presence of damage or defects in pipes or tubes is one of the major problems in nuclear power plants. However, in many cases, it is difficult to inspect all of them by the conventional ultrasonic methods, because of their geometrical complexity and inaccessibility. The magnetostrictive guided wave technique has several advantages in practical applications, such as a 100-percent volumetric coverage of a long segment of a structure, a reduced inspection time and its' cost effectiveness, as well as its' relatively simple structure.

One promising feature of the magnetostrictive sensor technique is that the wave patterns are relatively clear and simple when compared to a conventional piezoelectric ultrasonic transducer. If we can characterize the evolution of defect signals with this technique, it could be a promising tool for a structural health monitoring of pipes for a long period of time as well as a flaw identification[1]. An in-bore guided wave probe was developed for an application to small bore heat exchanger tubes[2].

In this paper, we analyzed the wave patterns reflected from various artificial defects and geometries in a long pipe mockup, which is similar to the field

inspection condition in a nuclear power plant. The Fe-Co-V magnetostrictive strip was used for a generation and reception of a torsional guided wave. The wave patterns from various defects and geometries were analyzed in the time and frequency domains. Unique features from different reflectors were extracted for a classification of the defects.

2. Experimental Method

A carbon steel pipe mockup representing a field inspection condition in a nuclear power plant was fabricated. The dimensions of the pipe have an nominal diameter of 150 mm (6 inch), thickness of 11 mm (sch. No. 80), and a length of 22 m. The pipe mockup contains 3 butt welds and a welded elbow. The Fe-Co-V magnetostrictive strip was attached at 7.5m from the pipe end. A hole was drilled at 9.5 m from the sensor. A circumferential notch at -5.5 m, two axial notches at 3.5 m and -2.5 m, a thinning in an elbow region were fabricated (refer to Fig. 1). A DC bias magnetization along the circumference of a tube is required for a generation of a torsional vibration mode, T(0,1). Generally, a circumferential magnetization of a magnetostrictive strip can be achieved by moving a permanent magnet along a circumference. In order to obtain a clear signal in the time domain, one cycle of a 64 kHz sinusoidal excitation was applied.
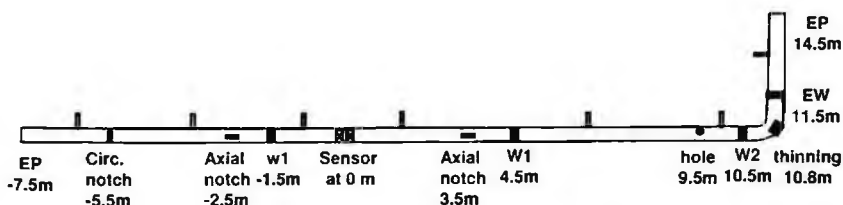
Fig. 1. Schematic drawing of pipe mockup shows location of various defects and elbow.

The torsional guided waves were excited and received from one end of each specimen by using a magnetostrictive sensor and its instrument system [1]. The signals from the various reflectors such as geometries (a weld, directionality, multiples) and artificial defects such as a hole, notch, thinning were acquired and reprocessed for an analysis. Their phases and amplitudes including their waveforms were compared from a variation of the reflector size.

3. Results and Discussion

Fig. 2 shows the guided wave signal obtained from the various reflectors in the piping mockup by a Fe-Co-V strip sensor. Because of the strip sensor location is 7.5 m from a pipe-end, signals from the geometry, such as signals due to a directionality or multiple beam paths are possible, as shown in Fig. 2.
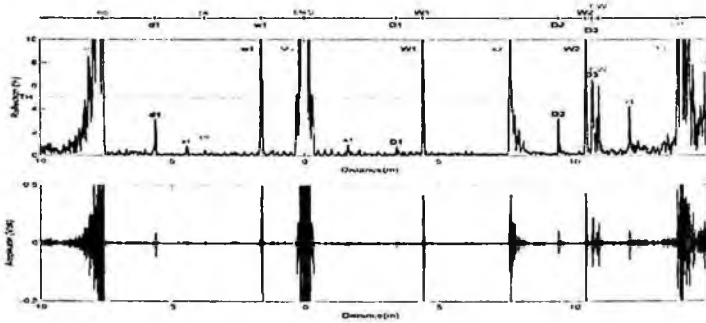
Fig. 2. Guided wave signal obtained from a long pipe mockup with an elbow and welds.

The waveform excited with one cycle from a perfect reflector such as pipe end or weld is very clear, and looks like an ideal oscilloscope signal and is easy to analyze. One of the advantages of this magnetostrictive sensor technique is that the wave patterns are relatively clear and simple when compared to a conventional piezoelectric ultrasonic transducer. There is almost no change or distortion in the waveform structure.

Detail waveforms from various signal sources for a classification of the defects are shown in Fig. 3. A radio frequency(rf) waveform in the time domain and a fast Fourier transformed(fft) signal in the frequency domain make it easy to classify the characteristics of the origin of a reflection. Based on the weld signal shown in Fig 3(a), other defect signals can be compared. The volume in the weld region increases but the other defects, such as a hole or notch reduces in their volume. Therefore when a guided wave propagates in a pipe, the weld signal and defect signal show quite different characteristics. The phase of a reflected signal from an increased thickness is reversed to the signal from a decreased thickness [4]. We can see the phase of the weld signal in Fig. 3(a) is reversed to a hole signal in Fig. 3(b) or notch signal in Fig. 3(c).

Also two waveforms from a weld signal after an elbow are shown in Fig. 3(d). These two waveforms are believed to be signals propagating in a short path and long path in the elbow region. Fig. 4 shows a signal from a simulated thinning at an elbow region. A big signal at 10.4 m marked as 'W2' corresponds to a weld

before an elbow and two signals approximately at 10.8~10.9 m, marked as 'EW' correspond to another weld after an elbow. Two signals marked as 'D2' correspond to the simulated thinning with a diameter of 50 mm and a reduction of the thickness of 2 mm. It is believed that two overlapped signals are due to a path difference in the elbow region.

(a) Weld   (b) Hole   (c) Circumferential notch (d) Weld after elbow
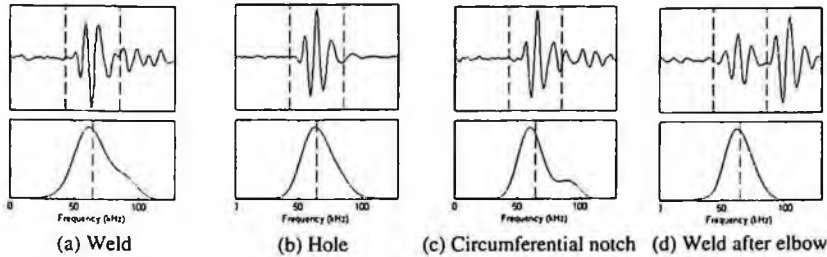
Fig. 3. Detail signal analysis of various signal sources. (top: rf signal in time domain, bottom: FFT signal in frequency domain).
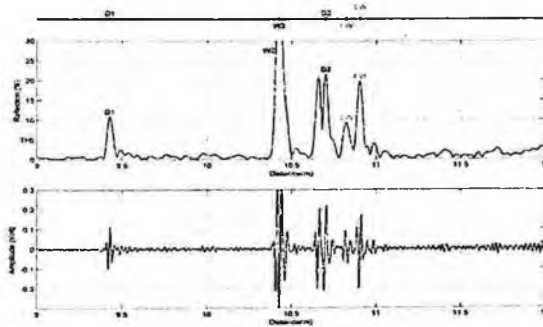
Fig. 4. Guided wave signal from a simulated thinning in an elbow region.

(a) Simulated thinning   (b) elbow-weld-1   (c) elbow-weld-2
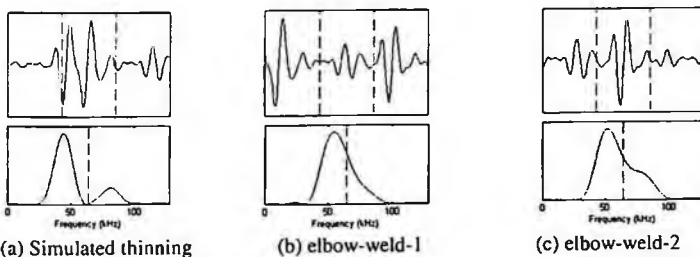
Fig. 5. Detail signal analysis of thinning and elbow-weld. (top: rf signal in time domain, bottom: fft signal in frequency domain).

One extraordinary phenomena of this magnentostrictive sensor technique was that we could detect an as axial notch, shown in Fig. 6. Because the wave vector or propagation direction of the torsional guided wave is parallel to the axial direction of the pipe, the classical wave theory can not explain this experimental fact of detecting an axial flaw. However, when the torsional vibration mode meets a deep axial notch, we believe it encounters a free boundary created by an axial notch and acts as another source of guided wave. The axial notch signal has a periodical repetition and the distance of this repetition matches exactly to the circumferential length, shown in Fig. 6. When there are two notches at 0° and 180° in the circumference, the distance between those signals is reduced by one half of the circumferential length, shown in Fig 7. It seems that the wave is going around the circumference of the pipe and the trailing signals are separated by a certain period of time that is equal to the transit time around the circumference.
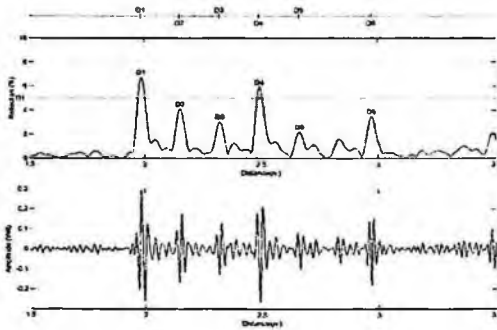
Fig. 6. Guided wave signal from a single-side axial notch.
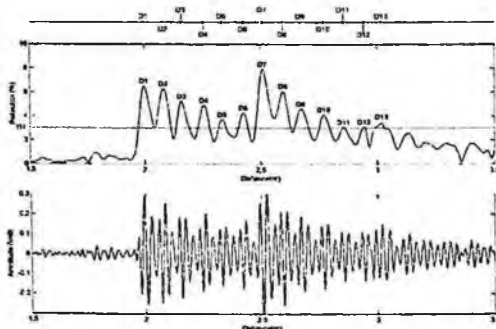
Fig. 7. Guided wave signal from double-side axial notches.

4. Conclusions

We analyzed the wave patterns reflected from various artificial defects and geometries in a long pipe mockup. The Fe-Co-V magnetostrictive strip was used for a generation and reception of a torsional guided wave. The wave patterns from various defects and geometries were analyzed in the time and frequency domains.

The phase of the reflected signal from the weld was reversed to the signal from a defect such as hole, notch or thinning. This phenomenon can be a rule to distinguish a weld or a defect. Also we could clearly detect a thinning defect in the elbow region. The two waveforms from weld after an elbow are believed to be due to the different beam path in the elbow region.

We first reported that an axial notch can be detected with $T(0,1)$ mode. When the torsional vibration mode meets a deep axial crack, we believe the crack, i.e. free boundary acts as a source of a guided wave and generates another guided waves to spread out. The signal pattern from an axial crack shows a periodical repetition and the distance of this repetition matches exactly to the circumferential length. It seems that the wave is going around the circumference of the pipe and the repeated signals are separated by a certain period of time that is equal to the transit time around the circumference.

Acknowledgments

References

1. H. Kwun, S. Y. Kim and G. M. Light, *Mater. Eval.* 61, 80 (2003).
2. H. Kwun, et al., *Mater. Eval.* 62, 430 (2004).
3. Yong-Moo Cheong and Shin Kim, *Trans. Korean Nuclear Society Fall Meeting* (2006).
4. M. S. Choi and S. J. Kim, *J. Korean Phys. Soc.* 49, 1955 (2006).

A STUDY ON TIME DOMAIN COMPUTER SIMULATION OF ULTRASONIC GUIDED WAVE MODE CONVERSION

YOUNHO CHO (CORRESPONDING AUTHOR)

School of Mechanical Engineering, Pusan National University, South Korea

YOUNG-KWUN CHOI

Graduate School, School of Mechanical Engineering, Pusan Natl. Univ., South Korea

NOHYU KIM

Dept. of Mechatronics, Korea University of Technology and Education, South Korea

Ultrasonic guided wave mode conversion was studied for thin-plate defects by using lamb wave scattering. For lamb wave scattering analysis, the phase velocity dispersion curve and group velocity dispersion curve of the material were calculated. A mode conversion was investigated by the boundary element method (BEM) in terms of reflection and the transmission factor. Time domain wave analysis was performed with scattering field modeling and inverse fast Fourier transform (IFFT). The feasibility of the lamb wave technique was discussed for various practical applications, including the classification of defects.

Keywords: Ultrasonic guided wave; Lamb wave; Plate wave; Boundary element method; Inverse fast Fourier transform; Dispersion curve.

1. Introduction

Because of the increase in demand for energy, the construction of wind plants, LNG ships, and plant facilities have increased. Therefore, a quantitative nondestructive evaluation (QNDE) technique is employed nowadays in order to maintain security and life expectancy

Previous methods for the inspection of defects involved the use of longitudinal and transverse waves; however, these methods had problems in large areas and bad conditions. In order to resolve these problems, lamb waves (plate waves), which propagate through mixed vibrations, are used at present[1-4]. The advantage of using these waves is that the measurement sensitivity can be increased by selecting a mode among a large number of modes because lamb waves are affected by material properties, thickness, and frequency. Hence, to apply lamb waves in plate structures and pipes, we should select a proper mode

and know the characteristics of a structure to be able to perform thorough measurements using the lamb wave.

We can measure the type and size of the defective region by analyzing the lamb wave reverse signals that are reflected from the defect. In addition, an affordable measurement of the defect size, type, and length is carried out from the characteristics of a scattering pattern correlated with a mode and a defect geometry. The possibility of applications of lamb waves is well known globally; therefore, knowledge of the theoretical calculation of the phase velocity dispersion curve is required for the selection of modes in order to maintain security and life expectancy. In addition, a subsequent study of the scattering field modeling is also essential. For a plate with a defect, it was shown by the Variational approach and FEM that when the defect is deeper, a better reflection coefficient value is obtained by using the characteristics of the lamb wave[1-3]. The detailed aspects of guided wave fundamentals and applications with BEM were also discussed in one of the authors' earlier works [4].

There are several methods for scattering analysis such as BEM, FEM, and other experimental methods. However, the time domain Lamb wave scattering analysis is still relatively rare in comparison with the ones in frequency domain [1-4]. Therefore, a new nondestructive evaluation method for plate scattering analysis in the time domain by the inverse Fourier transformation and by a superposition of the input modes on the basis of previous studies is introduced.

We studied the analysis of lamb wave scattering and mode expectancy by BEM in a thin plate, which is frequently used in the industry. For the analysis of lamb wave scattering in the thin plate structure, we considered the following procedures. First, in lamb wave scattering analysis, the dispersion curve is obtained from the properties of the material with the defect. The present correlation between the depth and wave length of a defect is obtained by means of a computer simulation of BEM. Secondly, the displacement of the specimen is transformed from the frequency domain to the time domain by using IFFT, defect compared correlation of non defect.

2. Time Domain Modeling of Guided Wave Propagation and Scattering

To compute the field of lamb wave scattering in a non defective model by using BEM, we calculated 64 incident waves. The frequency field of these waves ranged from 0.244~0.752 MHz with an internal frequency of 0.008 MHz in the Gaussian distribution. Figure 1 is based on the dispersion curve. In Fig. 2, it can be observed that the width of the thin plate is 1 mm, length is 100 mm and

the observation points are at distances of 25 mm, 45 mm, and 65 mm. If Fd (F : frequency, d : thickness) is 0.5 MHz, the corresponding value in the group velocity dispersion curve is 2.94 mm/us in the A0 mode. Hence, we attempted to compare the values in the graph and the other values obtained by BEM.
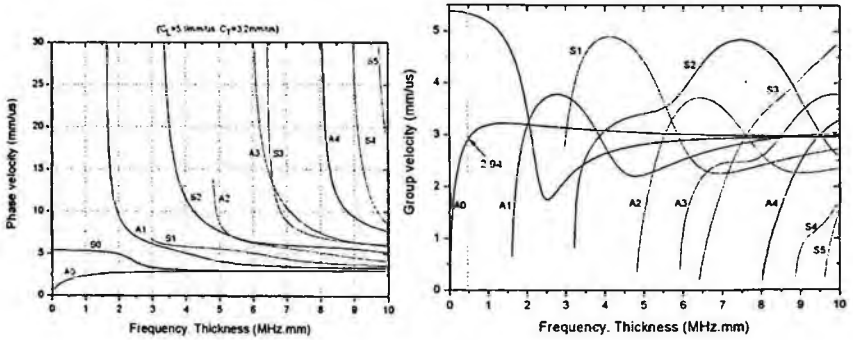
Fig. 1. Phase & Group velocity dispersion curve of Steel
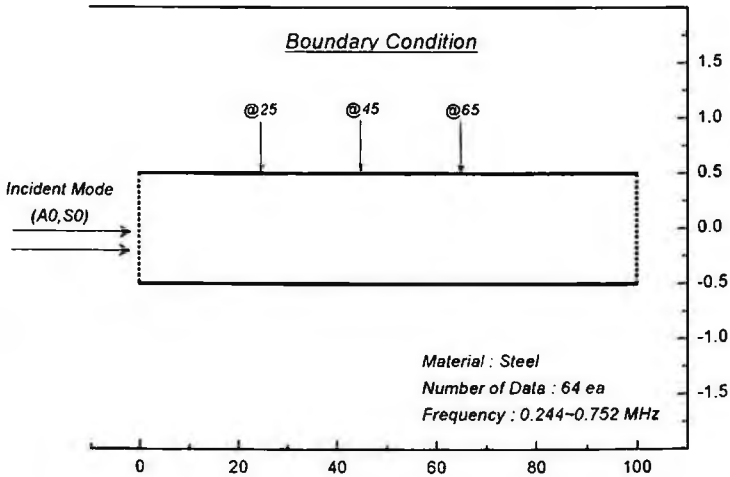
Fig. 2. Boundary Condition of Zero-defect Model

2.1 The time domain modeling of guided wave propagatione

The propagation field of A0 mode was calculated by BEM and IFFT in the time domain. Figs. 3–5 are similar to that in Fig. 2. Product that used by IFFT in 25, 45, and 65mm, is changed with wavy pattern in time domain. 2.94mm/usec had 15% error because of value that 2.94~3.4mm/usec per displacement after

transformed IFFT. And it is 15% error that time gap per displacement is 2.93~3.4mm/usec. Further, it is clear that the field of guided wave scattering is predicted without defects in the observed result.
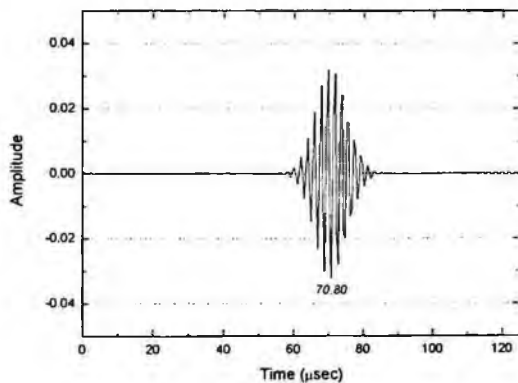
Fig. 3. A0 Mode IFFT result at 25 mm
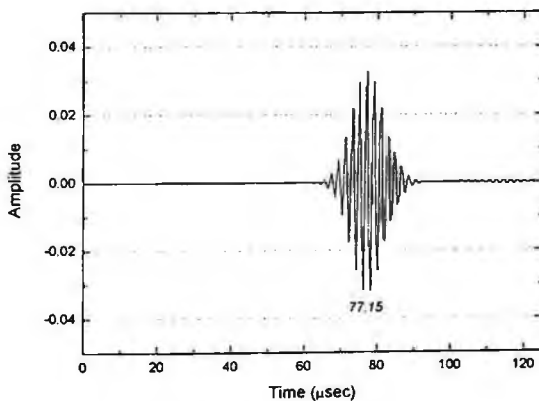
Fig. 4. A0 Mode IFFT result at 45 mm
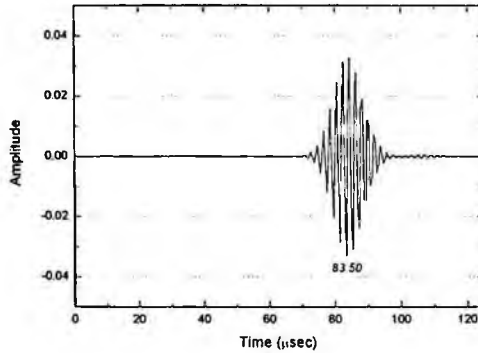
Fig. 5.   A0 Mode IFFT result at 65 mm

2.2   Scattering from a defect

In Fig. 6, the width and depth of the defect are 2 mm and 0.7 mm, respectively. Sixty four incident waves are calculated at intervals of 0.008 MHz and at around 0.5 MHz. These calculations are based on the dispersion of steel. This defect model has a width of 1 mm and length of 140 mm and is transformed through IFFT of BEM, in a view point is 25, 45, and 65mm.
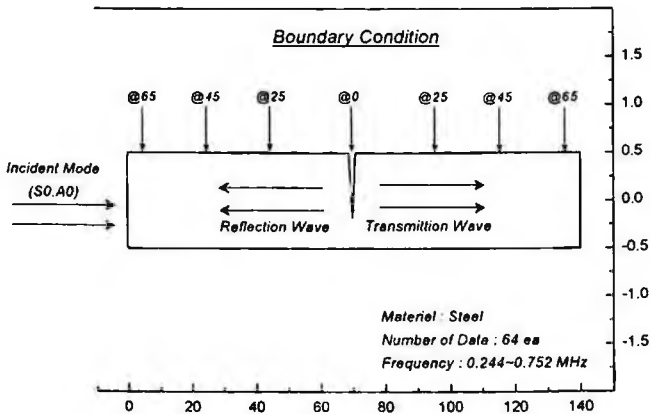
Fig. 6.   Boundary Condition of Defect Model

By using BEM, time domain wave analysis was performed with a scattering field that was transformed through IFFT. Figures 7–8 show that the wave motion is reflected after the A0 mode is inversed. The scattering field's evaluation only

shows three points that are located at the left side of the defect in Fig.6.

In the case of the reverse signal, the direction of propagation of the waves was the opposite. The model was at a distance of 25 mm from the defect, and the incident, S0, and A0 modes were completely separated. The S0 and A0 modes began to separate from 45 mm, and they are thoroughly separated from 60 mm.

From Fig. 8, the amplitudes of the incident and A0 modes were 0.15 and 0.06, respectively. This reveals that the A0 mode's reflection coefficient, which is 0.462, is very close to the BEM's resolution.
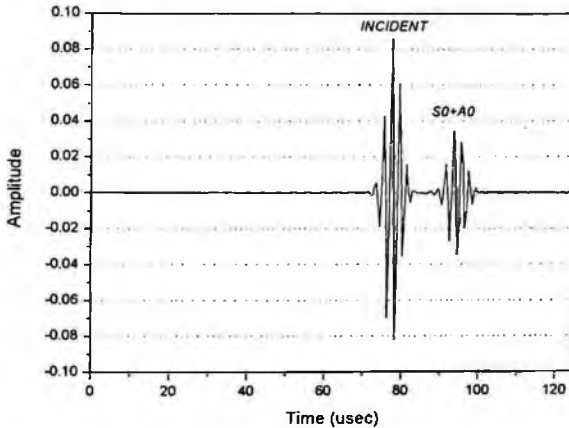
Fig. 7.　A0 Mode IFFT result at 25 mm from the defect
(Reflection, Including Incident mode)
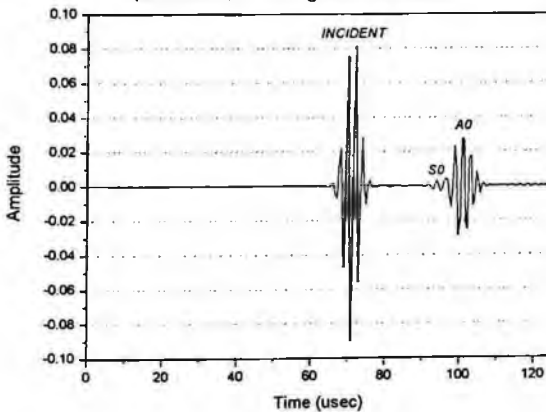
Fig. 8.　A0 Mode IFFT result at 45 mm from the defect
(Reflection, Including Incident mode)
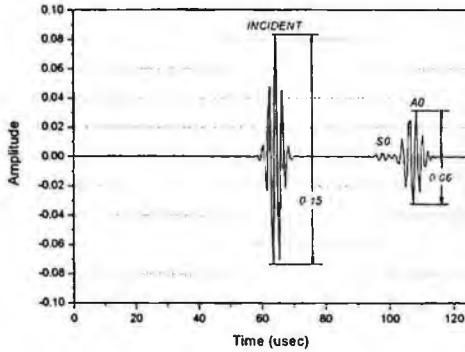
Fig. 9. A0 Mode IFFT result at 65 mm from the defect (Reflection, Including Incident mode)

3. Conclusions

The defect location and a specific characteristic were possible by using BEM. Second, A defect signal was located after the input mode was scattered from defect in the model with the defect, and the transformed signals were further separated as the distance was greater. The defect signal, guided wave transmission, and dispersion could be expected. In addition, the receive methodology was conformed; hence, this technology can be applied in defect monitoring systems.

Acknowledgment

References

1. B. A. Auld and E. M. Tsao, "A Variational Analysis of Edge Resonance in a Semi-infinite Plate," IEEE Transactions on Sonics and Ultrasonics, 24(5), pp. 317-326, 1977.
2. M. Koshiba, M. Karakida, and S. Suzuki, "Finite-Element Analysis of Lamb Wave Scattering in an Elastic Plate Waveguide", IEEE Transactions on Sonics and Ultrasonics, Vol.31(1) pp. 18~24, 1984.
3. S. K. Datta, Y. Al-Nassar and A. H. Shah, "Lamb Wave Scattering by a Surface Breaking Cracks in a Plate," Review of Progress in Quantitative Nondestructive Evaluation, 10A, pp. 97-104, 1991.
4. Younho Cho and Jospeh L. Rose, "An Elastodynamic Hybrid Boundary Element Study for Elastic Guided Wave Interactions with a Surface Breaking Defect," International Journal of Solids and Structures, 37, pp. 4103-4124, 2000.

SIGNALS OF MAGNETOSTRICTIVE SENSORS ON ARTIFICIAL DEFECT PIPES OF CARBON AND STAINLESS STEEL

DAE-SEO KOO

Operational Safety Research Center, Korea Atomic Energy Research Institute, 1045 Daedeok-daero, Yuseong-gu, Daejeon, 305-353, Republic of Korea

SIN KIM, YONG-MOO CHEONG

Nuclear Material Research Center, Korea Atomic Energy Research Institute, 1045 Daedeok-daero, Yuseong-gu, Daejeon, 305-353, Republic of Korea

CHISEUNG PARK

Component Safety Diagonosis Group, Korea Advanced Inspection Tech. Inc., Jeonmin-dong 461-61, Yuseong-gu, Daejeon, 305-811, Republic of Korea

Artificial specimens (diameter 6inch, schedule 80, thickness 11mm) of carbon steel and stainless steel pipes were fabricated with several defect shapes and sizes. The signals of the artificial defects on the specimens were detected at a torsional vibration mode with a frequency of 32 or 64 kHz using a Ni strip or an FeCoV alloy strip sensor. The signals from an elbow of the carbon steel pipe with artificial defects were detected using an FeCoV alloy strip sensor. These results may provide a potential for a guided wave inspection of defects and a degradation of an elbow in a pipe.

1. Introduction

A pipe leak takes place from a corrosion, or erosion of nuclear power plant pipes under a high temperature and pressure. Accurate inspection of a corrosion and cracking in a pipe is required because a leak from primary pipes leads to a diffusion of a radioactive activity. A thinning of a pipe in a nuclear power plant is believed to be due to a flow-accelerated corrosion(FAC). FAC is affected by environmental factors such as the temperature, pressure, and pH. Thus, nondestructive techniques are required for a corrosion inspection of the pipes in a nuclear power plant[1]. All the vibration modes can be generated and received by using a magnetostrictive strip sensor technique. Torsional vibration modes, longitudinal vibration modes and flexural vibration modes are possible by a combination of the direction of a DC magnetic bias and an alternative magnetic

field[2]. T(0,1) mode has a low attenuation for a long-range inspection such as a long pipe including water. A T(0,1)mode indicates that the group velocity does not change with the frequency. A T(0,1) mode has been chosen for a long-range inspection of a long pipe because of these advantages[3].

In order for a demonstration of an effectiveness of the long-range guided wave technique, a real scale piping mock-up with a length of 21 m with an elbow was manufactured. Dimension of this piping mock-up is a diameter of 6 inch, and a thickness of 11mm. An artificial hole was fabricated to locate a defect. The wave-form from a hole and a weldment was analyzed. The wave-form from an elbow was also analyzed. A relationship between the amplitudes and the cross section areas of the holes was obtained and a detectable limit of a hole defect was determined.

2. Examination and Torsional Vibration Mode

Holes with a diameter range of 2 to 5 mm were fabricated at 17 m from the end of an artificial carbon steel pipe. A 49Fe-49Co-2V alloy strip sensor was bonded on to the circumference of the mock-up pipe at 7.5m of it and magnetized along the circumferential direction for a DC bias magnetization. A torsional vibration mode, T(0,1) was generated by a strip sensor with a coil with a alternating current. Figure 1 shows a torsional vibration mode in a pipe. This mode has a low attenuation for a long-range inspection such as a long pipe including water. Figure 2 shows the dispersion curves of the phase velocity and group velocity. A T(0,1)mode indicates that the group velocity does not change with the frequency. A T(0,1) mode has been chosen for a long-range inspection of a long pipe because of these advantages. The signal was analyzed at a frequency of 32, and 64 kHz.

Fig. 1. Torsional vibration mode in a pipe.
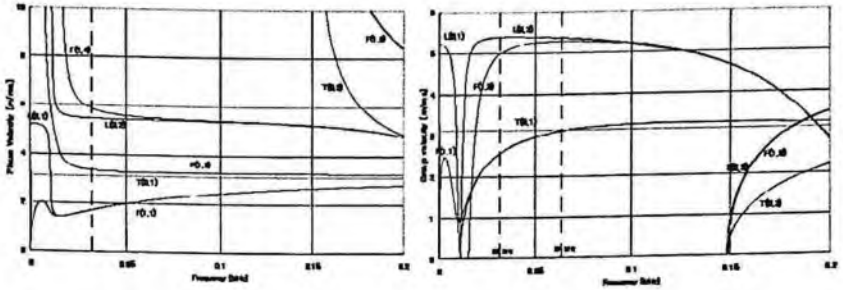
Fig. 2. Dispersion curve of phase velocity and group velocity for an artificial carbon steel mock-up pipe.

3. Results and Discussion

Figure 3 shows the signals from a hole, a weldment and an elbow in a mock-up pipe. From Figure 3, the signals from an elbow show a signal from the intrados and the extrados of an elbow. Figure 4 shows a wave-form from a hole and a weldment. A wave-form from a hole is a step up pattern while a wave-form from a weldment is a step down pattern. Each frequency peak shifts to the left. Figure 5 shows a wave-form from an intrados and an extrados in an elbow. The wave-form from the intrados is a step up pattern while the wave-form from the extrados is a step down pattern. A frequency peak from the extrados shifts to the right.
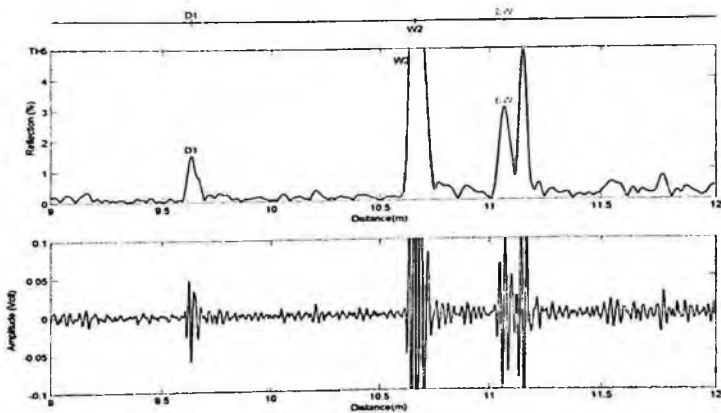
Fig. 3. Signals from an artificial carbon steel mock-up pipe on an FeCoV alloy strip sensor.

434
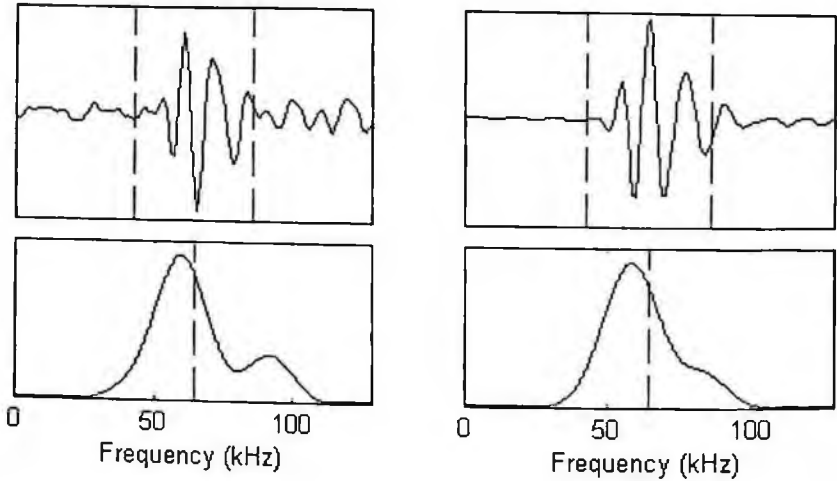
Fig. 4. Wave-form of a hole and a weldment from an artificial carbon steel mock-up pipe.
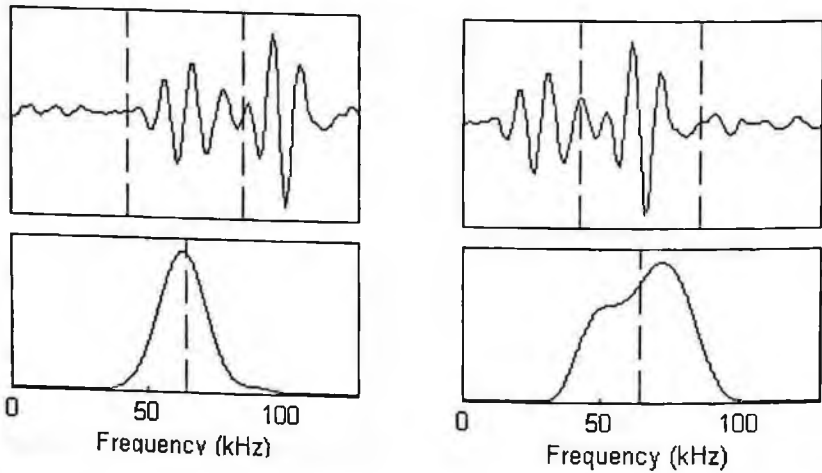
Fig. 5. Wave-form of an intrados and an extrados in an elbow of an artificial carbon steel mock-up pipe.

Figure 6 shows a comparison of the amplitude due to a different hole size in a piping mock-up. As the diameter of the hole increases, the signal amplitude increases. Figure 7 shows the relationship between the amplitude and the cross section area of the hole defects. As the cross section area of the hole defects increase, the amplitude from the hole defects increase, on the whole, linearly with respect to the cross section area of the hole defects. Detectable limit for the

hole defects was about 0.4% with respect to the cross section area of the hole defect.
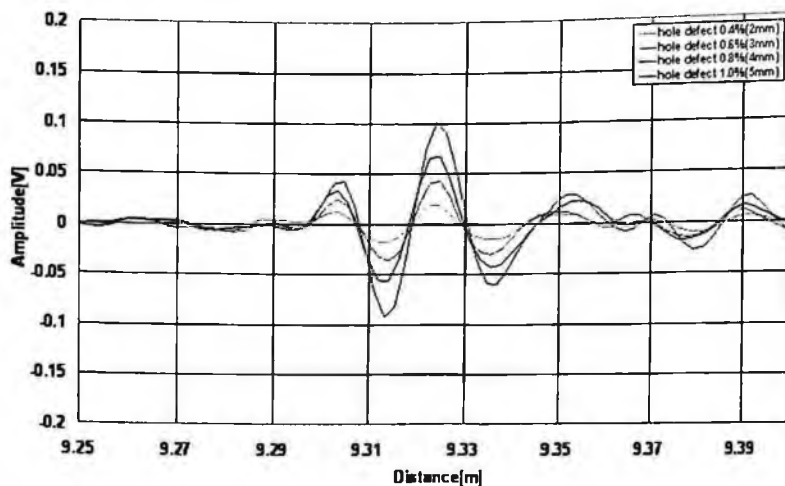
Fig. 6. Signals from several hole sizes in an artificial carbon steel mock-up pipe.
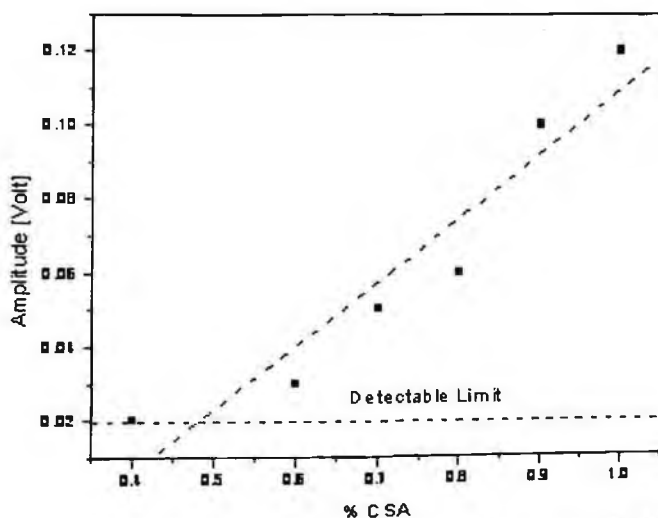
Fig. 7. Signal amplitude vs cross section area of the several hole defects in an artificial carbon steel mock-up pipe.

4. Conclusion

T(0,1) mode has a low attenuation for a long-range inspection such as a long pipe including water. A T(0,1)mode indicates that the group velocity does not change with the frequency. A T(0,1) mode was chosen for the long-range inspection of a long pipe because of these advantages.

The signals from an elbow show a signal from an intrados and an extrados of an elbow. A wave-form from a hole is a step up pattern while a wave-form from a weldment is a step down pattern. Each frequency peak shifts to the left. The wave-form from the intrados is a step up pattern while the wave-form from the extrados is a step down pattern. A frequency peak from the extrados shifts to the right.

A torsional guided wave signal from various hole sizes was obtained and analyzed using an Fe-Co-V alloy strip sensor at a frequency of 64kHz. As the cross section area(CSA) of the hole defects increased, the signal amplitude increased, on the whole, linearly with respect to the cross section area of the hole defects. Detectable limit for the hole defects was estimated as about 0.4% of the CSA.

References

1. Jun-Hyun Lee, "Development of Advanced Ultrasonic Technique for On-line Monitoring of Corrosion under High Temperature and Pressure in Pipeline of Nuclear Power Plant," Busan National University, 7-8(2004).
2. Yong-Moo Cheong, "Propagation Mode Analysis of Long-range Guided Ultrasonic Wave and Application to Inspection of PHWR Feeder Pipe," KAERI/TR-2381/2003, 10-11(2003).
3. Yong-Moo Cheong, "Flaw Detection in Pipe by Magnetostrictive Guided Wave Technique," KAERI/TR-2927/2005, 1-2(2005).

WELDING ZONE DEFECT DETECTION USEFULNESS ESTIMATION OF LASER GUIDED LAMB WAVE

KYUNG SEOK SONG

BK21 Education Center of Mould Technology for Advanced Materials & Part, Chosun University, 375, Seosuk-Dong, Dong-Gu, Gwangju 501-759, South Korea

JAE YEOL KIM

Department of Mechatronics Engineering, Chosun University, 375, Seosuk-Dong, Dong-Gu, Gwangju 501-759, South Korea

This paper aims to study that the defect exploration method to specimen's thickness, using an characteristic of an ultrasonic wave generating in ablation area and thermo elasticity area, has been applied to using a way of receiving it by Air-Coupled Transducer and transmitting it by an ultrasonic wave and a way of non-contact receiving and transmitting ultrasonic wave using a laser. To confirm the possibility of implementation on natural defect existing at real welding part, thickness in 3mm SM45C and STS304 artificial defect specimen has been made and defect detection test using Lamb wave has been executed. Detected signal by signal treatment has been expressed in visual not RF signal. By doing so the convenience of defect detection has been attempted and the effectiveness of defect signal visualization using Lamb wave has been confirmed compare with defect image through SAT.

1. Introduction

To evaluate stability of structures or machinery, a non-destructive method using ultrasonic wave is frequently used. The ultrasonic technique detects internal flaw by reflection and penetration of longitudinal wave, transverse wave and surface wave resulting from difference in density along the propagation path of ultrasonic wave.

However, for ultrasonic inspection using transverse and longitudinal waves, it is technically difficult to detect flaw in a narrow space of plate of several millimeters in thickness. To detect internal flaw inside such a thin plate, it is suitable to use Lamb wave that provides better efficiency and flaw detecting capability than straight beam method or angle beam method. Lamb wave, which is a kind of induced ultrasonic wave propagating through the plate, is effective for inspecting plated structures, cell structures, etc[1,2].

Moreover, as the existing ultrasonic technique requires a contact medium to let ultrasonic wave propagate into an object to be tested, it has difficulties in automating the process, contacting a contact transducer with a small object, an object with a complicated shape or a moving object, and applying to a high temperature environment or harmful environments including radiations or chemicals. Thus, a need for non-contact nondestructive evaluation was inevitable.

2. Lamb wave generation using Laser and Measuring System

Where Laser is radiated onto a spot of a specimen, the ultrasonic wave generated by the Laser propagates radically and the acoustic strength decreases with distance. This effect can be improved by letting the Laser beam pass through slits to convert it from a point source to a liner source. At this time, the ultrasonic wave generated by the linear source also becomes linear and has a directionality to propagate vertical to the linear source. The ultrasonic wave generated like this contains frequency components over a significantly wide range and includes various modes due to the scattering property of the material.

ACT was used to measure the generated Lamb wave in order to ensure that the Laser that has passed through the array slits equally spaced induces an expected frequency mode on the surface of a specimen.

Fig. 1 shows a configuration for generation and measurement of Lamb wave using line array slits. Nd:YAG pulsed Laser of wavelength 1064 nm, pulse duration 20 ns and incident energy 100 mJ was used to generate Lamb wave. The applied Laser energy would be strong enough to damage the surface of specimen. However, before passing through the line array slits, the beam width was enlarged to lower the incident energy per unit area so as to prevent damage on the surface of specimen.

The specimen was made of SM-45C plate of 3 mm thickness. ACT (Air Coupled Transducer) with a receive bandwidth 0.5~2.25 MHz was used to receive Lamb wave induced by the Laser. The received signal was stored and analyzed using an Oscilloscope. The line array slits to get a linear Laser source were linearly aligned with 2 mm interval to generate ultrasonic wave with wavelength 2 mm[3,4]. The characteristics of the pulse Laser and the slit shape and size used for the experiment were given in Table 2.

3. Detecting welding zone flaw of plate using Lamb wave

3.1. *Test Method*

Flaw was basically detected by penetration of ultrasonic wave. The Laser
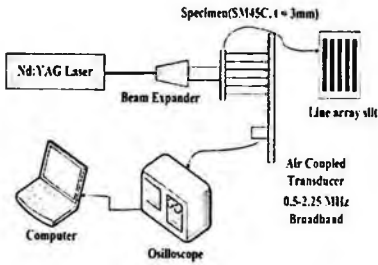
Fig. 1 Experimental Setup for Detecting Lamb Wave
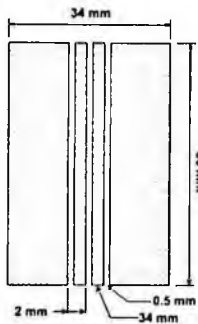
Fig. 2 Line Array Slit of Wavelength

Table 1 Characteristic of Laser and Slit

Item	Characteristics
Laser	Nd:YAG Laser
Wavelength of Laser	1064 nm
Pulse Duration	10 ns
Incident Energy	100mJ
Pulse Repetition Rate	10Hz
Beam Diameter	20 mm
Slit Shape	Line Array
Slit Size	34×56 mm
Wavelength of Lamb Wave	2 mm

that has passed through the line array slits generates a specific mode of Lamb wave, which passes through the welding zone and is received through ACT. The ultrasonic wave can be received from the welding zone provided that there is no flaw. On the other hand, where there is any flaw in the welding zone, the Lamb wave is reflected by the flaw so that the signal received through the ACT would be weakened or lost. Using this mechanism, it is feasible to estimate presence of flaw and its size.

The Laser and the ACT were aligned along propagation of Lamb wave. We detected flaw while moving the specimen vertically against Lamb propagation.

3.2. *Manufacturing Welding Flaw Specimen*

Fig. 3 shows the dimensions of specimens, and Table 2 lists presence of flaw in the welding zone and flaw type when measured under different welding conditions including natural flaw. SAT (Scanning Acoustic Tomography) was used to determine presence of flaw and its type.

To detect internal flaw, which is the purpose of practical non-destructive

evaluation, we introduced circular artificial flaw in the welding zone where no flaw was detected. The circular flaw was 1, 2 and 3 mm in size and thoroughly penetrated through the welding zone using a drilling tool.

Table 2 Existence and Nonexistence and Kind
of Flaw by Welding Condition

| Specimen Number | Welding Condition | | | | Welding Flaw |
	Power	Speed	Focus Length	Material	
LW-1	1800	1.1	0	SM45C	Existence
LW-2	1800	1.1	0	SM45C	Nothing
LW-3	1800	1.1	0	SM45C	Nothing
LW-4	1800	1.3	0	SM45C	Existence
LW-5	1800	0.8	0	SM45C	Nothing
LW-6	1800	0.6	0	SM45C	Existence
LW-7	1400	1.1	0	STS304	Existence
LW-8	1400	1.1	0	STS304	Nothing
LW-9	1400	1.1	0	STS304	Existence
LW-10	1400	1.25	0	STS304	Nothing
LW-11	1400	1.35	0	STS304	Existence
LW-12	1400	1.5	0	STS304	Existence
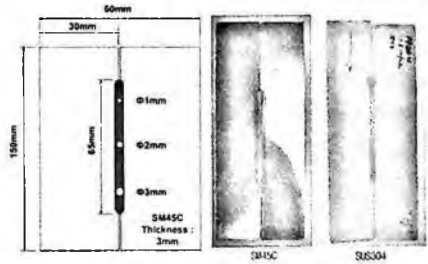
Fig. 3 Dimensions of Specimens

4. Welding Zone Evaluation through Visualization of Welding Flaw

4.1. *Welding Zone Flaw Image by SAT and Lamb Wave*

SAT was used to compare its image with the flaw image of Lamb wave, and the position and the size of flaw were given from the welding start point on the left of the specimen.

This study excluded analysis of flaw type because the flaw image of Lamb wave was obtained by the penetration method. For analysis of flaw type, it is required to analyze the ultrasonic wave reflected from the flaw. Since the reflected ultrasonic information is distinguishable between a cubical flaw and a linear flaw, it is possible to identify the flow shape and type by analyzing the information.

Fig. 4 SAT Image of Specimen LW-1
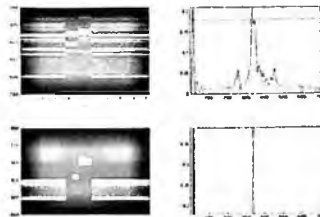
Fig. 5 Ultrasonic Signal for Visualization and Artificial Flaw Image

4.2. *Comparison of SAT Image with Lamb Wave Image*

Fig. 6 compares the SAT image for a natural flaw with the Lamb wave image. The threshold values applied for visualization of flaw using Lamb wave were 0.33 for LW-1, 0.3 for LW-4 and LW-6, 0.08 for LW-7, 0.12 for LW-9, 0.33 for LW-11, and 0.13 for LW-12 respectively.

Comparing the SAT flaw image with the Lamb wave image, we found that the positions of flaw nearly coincide with each other but resolution was not enough to analyze flaw size and others.

As a beam width smaller than the flaw size is required to increase resolution of flaw image, this needs to be studied further. The width of Laser beam transmitted through the slits used in this experiment was 20mm, which is not enough to detect a small flaw even the flaw signal will pass through the flaw zone. In addition, it is more difficult to identify the size and distribution of a natural flaw.

(a) Flaw Image of LW-1

(b) Flaw Image of LW-4

(c) Flaw Image of LW-6

(d) Flaw Image of LW-7

(e) Flaw Image of LW-9

(f) Flaw Image of LW-11

(g) Flaw Image of LW-12
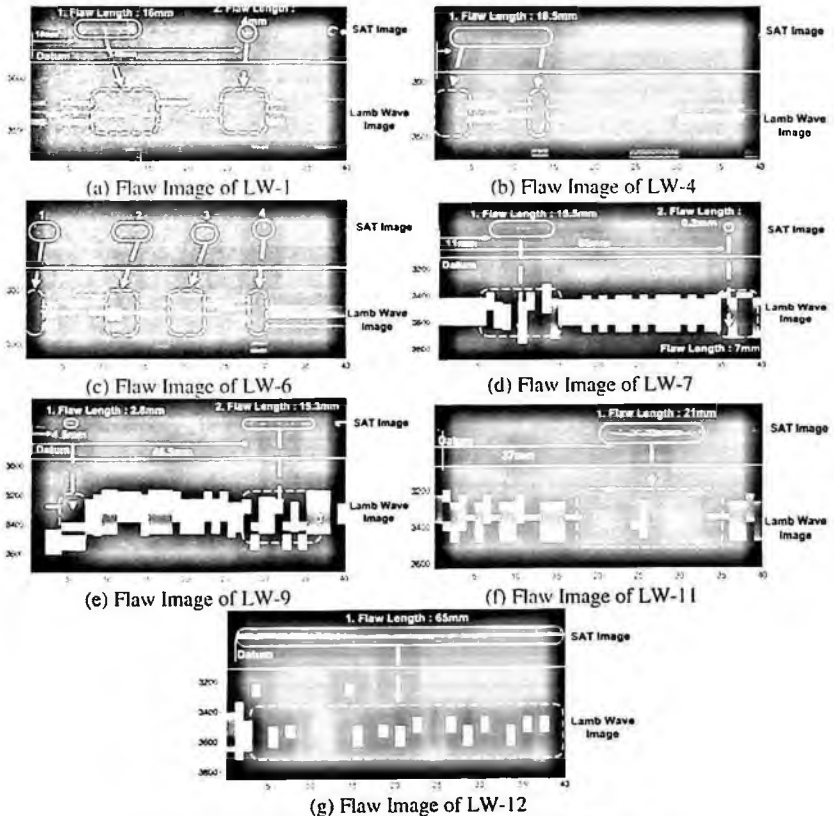
Fig. 6 Flaw Comparison of SAT Image and Lamb Wave Image

5. Conclusion

1. In the experiment to measure distribution of transverse amplitude displacement for artificial flaw, we could identify presence of flaw using the amplitude of ultrasonic signal and estimate the flaw size by plotting the relationship between flaw size and amplitude through the regression analysis.
2. We could see that the existing contact ultrasonic inspection can be replaced by adjusting ultrasonic wave induced zone, Laser incident energy and inspection method depending on the thickness and shape of specimen to be measured.
3. We have verified the efficiency of flaw detection by Lamb wave, Laser induced ultrasonic wave, and could see that it can be replaced by the existing contact non-destructive method.
4. Comparing the SAT image with the Lamb wave image, we could see the flaw image of Lamb wave is useful for detecting artificial flaw and natural flaw, provided that resolution of the flaw image can be improved.

Acknowledgment

References

1. Bork U. and Challis. R.E., *"Nondestructive evaluation of the adhesive fillet size in a t-peel joint using ultrasonic lamb waves and a linear-network for data discrimination"*, Meas. Sci. Technol, Vol6-1, 72-84(1995)
2. Alleyne D.N., and Cawley P., *"The interaction of Lamb waves with defects"*, IEEE Trans. Ultrason. Ferroelectr. Freq. Control, V39-3, 381-397(1992)
3. Gachagan, A., Hayward, G., Kelly, S.P. and Galbraith, W., *"Charaterization of air-coupled transducers"*, *IEEE transactions on ultrasonics*, ferroelectrics, and frequency control, V43-4, 678-689(1996)
4. H-J Kim, K-Y Jhang, M-J Shin and J-Y Kim, *"A noncontact NDE method using a laser generated focused-Lamb wave with enhanced defect-detection ability and spatial resolution"*, NDT&E International 39, 312-319(2006)

A STUDY OF GUIDED ULTRASONIC WAVE APPLICATION FOR HEAT EXCHANGER PERFORMANCE IMPROVEMENT

YOUNHO CHO [1], JIHWAN JUNG [1], JAEHYUN KIM [2]

[1]*School of Mechanical Engineering, Pusan National University, Korea*
[2]*Graduate School School of Mechanical Engineering Pusan National University, Korea*

In this study, a method for improving the heat transfer performance is suggested by using ultrasonic guided wave. An experiment for determining the appropriate angle of incidence is performed on the basis of the theoretical dispersion curve. The obtained data is compared for the following two cases; the presence of ultrasonic vibration and the absence of ultrasonic vibration. It is verified that the ultrasonic wave can improve the heat transfer efficiency by reducing the initial heating time and changing the temperature profile over the entire specimen. The properly tuned angle of incidence with a dispersion curve of the guided wave is a key factor for the success in improving heat transfer performance. It is expected that the present technique can be successfully used for the design of next-generation heat exchangers.

Keywords: Ultrasonic guided wave; selection of incident angle; heat transfer efficiency.

1. Introduction

Since the oil crisis in the 1970s, various heat transfer augmentation technologies have been investigated in the fields such as heat recovery and energy conversion systems. In the case that the temperature difference between two working fluids is small, heat exchanger usually requires large heat transfer area between them. This causes the problem of the increase in production cost and installation space. This acts by important variable in geothermal power plant, seawater's heat energy treatment system, solar energy use system and large size heat pump system. Therefore, a highly effective heat exchanger is a crucial component to solve the energy exchange problem caused by the small temperature difference. The study of the heat transfer augmentation for highly effective heat exchanger development has been of importance since industrial revolution. Heat transfer augmentation technology can be divided into passive methods and active ones[1,2]. Passive methods enhance surface treatment, extension of the heat exchange area. Meanwhile, active methods include an electric field, vibration, and a jet. An example of these methods is a heat transfer enhancement using

ultrasonic vibration[3-5]. This technology has been successfully applied in fields such as welding, washing, and medical treatment.

Recently, ultrasonic waves have attracted considerable attention because of their efficiency and sensitiveness in non-destructive test of large size plate and pipes [6]. This ultrasonic was also used in heat transfer enhancement study. To the authors' knowledge, all the previous research applied the ultrasound to the working fluid. In this case, relatively large power is consumed due to dissipation of ultrasound in the working fluid. The aim of our experiment is to examine whether the ultra-sound traveling through solid material as a guided wave mode is effective onto convective heat transfer enhancement.

2. Fundamental Ultrasonic Theory

An ultrasonic wave provides essential information on the estimation of the safety of structures by measuring the defects and intensities of several types of advanced materials. The frequency of ultrasound is higher than that of sound waves, which are audible to humans (20 Hz~20 KHz).

Ultrasonic wave is divided into longitudinal waves, transverse waves, surface waves, and guided ultrasonic waves. A longitudinal wave, whose motion is in the direction of propagation, is used in the case of normal incidence or immersion incidence. The velocity of the longitudinal waves is the highest among all the ultrasonic waves that can be transmitted in solid, liquid, and gaseous mediums. A transverse wave, whose motion is in the axial direction of the propagation, is mainly used in the case of oblique incidence. It can be transmitted only in liquid or gaseous mediums. A surface wave that propagates along the surface travels slower than the transverse wave. The energy of the surface wave is focused on the surface, and it decreases as go down to thickness direction of material. If a bulk-ultrasonic wave enters a thin structure, a new guided ultrasonic wave is created by a multipath reflection and internal interference phenomenon in the upper and lower surfaces, as shown in Fig.1.

This guided ultrasonic wave possesses a dispersive property, which alters the propagation velocity and propagation mode depending on the material, application frequency, thickness of structure, and ultrasonic incidence angle degree.
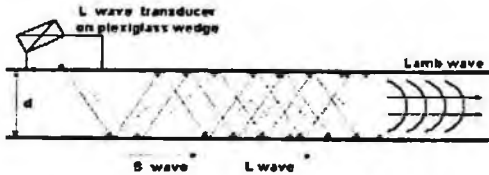
Fig. 1 Oblique incidence method for generation of guided wave

In the case that the ultrasonic wave is obliquely incident on the boundary surface of two mediums, a reflected longitudinal wave and transverse wave are formed. Dispersion is a diagnostic property that changes the type or velocity of the mode of the guided ultrasonic wave. The dispersion curve is displaying various lamb wave modes. It is possible by adjusting the ultrasonic incidence for the required mode. The optimum incidence angle degree for each mode follows Snell's law, which is expressed as follows [6]:

$$\frac{V_1}{\sin \alpha_1} = \frac{V_2}{\sin \alpha_2} \tag{1}$$

The dispersion curve is classified into phase velocity dispersion guidance and group velocity dispersion guidance. Phase velocity is the ratio of the time and space at the area at which the phase of a continuous wave is uniform. The phase velocity dispersion guidance provides the theoretical frequency for a thin plate structure. It also provides the theoretical incidence angle via Eq.(1). Actually, a guided ultrasonic wave consisted of several frequencies is observed in the experiment. The group velocity of dispersion curve is used to distinguish the mode of the guided ultrasonic wave.

3. Experiment

The test piece used in the experiment was a thin aluminum plate whose dimensions were 28 × 330 mm and thickness was 1 mm. We attached a temperature sensor and other sensors were attached at gaps of 30 mm. The temperature sensors were attached in order to determine the temperature and supersonic change depending on the depth of water. A constant-temperature oven was used to generate heat and maintained a constant temperature in the test piece. The temperature in the experiment was maintained at 70 °C. A PC was used to control the cycle and frequency.

To generate the required Lamb wave mode by a 1 MHz probe with a high-power ultrasonic generator, incidence angle control was used. The experimental set-up is shown in Fig.2.
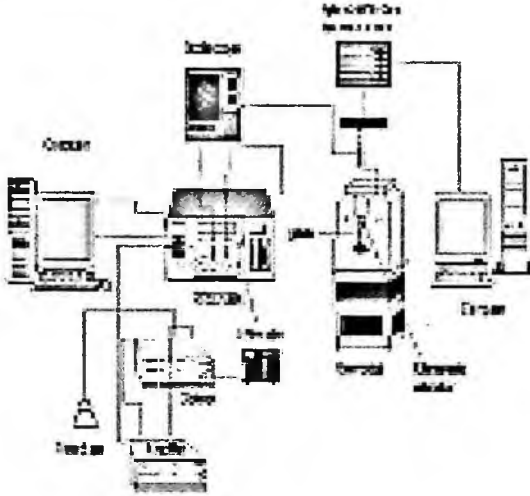
Fig. 2 Experimental set-up

The Lamb wave generated from the probe was transmitted in the test piece. The optimum incidence angle degree that was analyzed from the dispersion curve was used. In this experiment, we used a tone burst system that uses a high-power ultrasonic generator. The sine signal of a short cycle was transmitted to the ultrasonic probe. The duration times can be controlled by unit, and number of vibrators can be controlled in detail. This tone burst system can acquire data receiving automatically with fine frequency control. A thermoscope, which stores data and measures the initial temperature, was used to measure the temperature of the sensors.

Variable angle beam transducer establishes frequency by 1.5 MHz, and Acrylics beam transducers fixed by 1MHz about thickness of aluminum test piece. The Lamb wave mode was fixed and the incidence angle was changed according to Snell's law. Water in constant-temperature oven is always kept titer. The temperature was controlled by a temperature controller. To measure the temperature that is produced in calorification department of heating heater in constant temperature oven, K-Type thermocouples were used.

A sensor was used to measure the temperature of the water and heater. A friction tape was used at all times other than during the temperature measurement

in order to minimize the heat transfer. The temperature measured by the thermocouples was stored in the PC every 10 s by the data measurement device.

To minimize external heat transfer where sensor that water is not touched attaches, we used bridge-building promulgation poly-ethylene form that is a piping thermal insulation lagging and are insulated. An insulation adhesive tape was used in finish coat. The thickness of the test piece was 1 mm. Its frequency was 1.5 MHz and incidence angle was 20°. We compared the difference between having existence and non-existence of ultrasonic excitation.

Next, we examined the temperature change by changing the incidence angle values to 20°, 30°, 35°, and 40° to see the feasibility to optimize the heat transfer enhancement by mode selection.

4. Results and Discussions
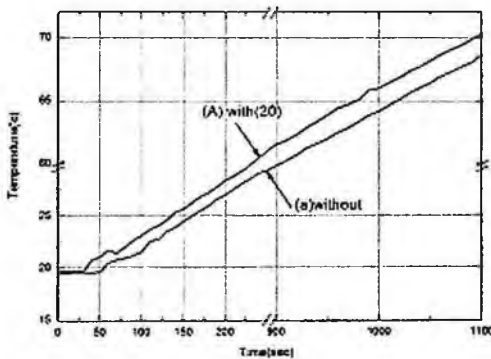
Fig. 3 Aluminum plate expansion graph (20°)

Fig. 3 shows the graph of temperature distribution for the comparison between the cases of the absence ("without") of the ultrasonic wave and presence ("with") of the ultrasonic wave with a frequency of 1.5 MHz, incidence angle of 20° corresponding to S0 mode. The temperature rise in the presence of the ultrasonic wave is greater and steeper than that in the case of the absence of the ultrasonic wave. In particular, temperature delay time of point that temperature rise change is begun at initial temperature of an experiment is shortened due to the ultrasonic excitation. This implies that the heat transfer occurs in most areas where the temperature is measured.
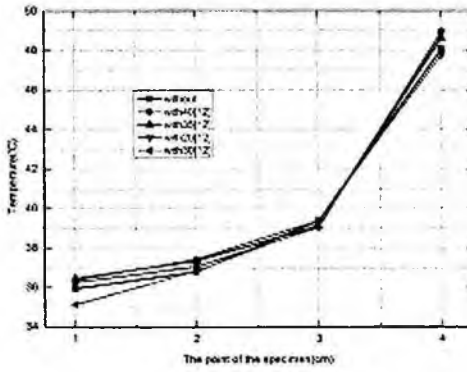
Fig. 4 Comparison of temperatures in aluminum plate (20°~40°)

In Fig. 4, when the incidence angle is 30°, the phase velocity is 3.22 mm/μs. The phase velocity of the A0 mode in the dispersion curve is 3.01 mm/μs. The theoretical incidence angle is 33.2°. When the incidence angle is similar to the theoretical incidence angle, the temperature rise is higher.
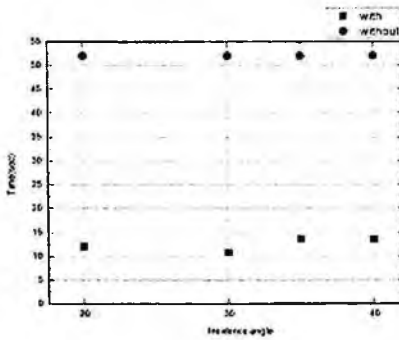
Fig. 5 Temperature rise initiation time (20°~40°)
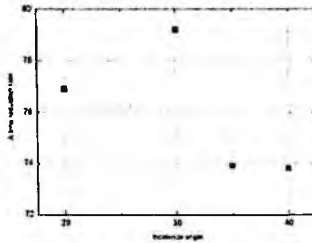
Fig. 6 Time reduction rate (%) (20°~40°)

Figs. 5-6 shows the start time of the temperature rise due to the incidence angles. As observed from Fig.6, the time reduction rates in the cases of the presence and absence of the ultrasonic wave are different. The greatest temperature difference is observed for the incidence angle of 30°. Consequently, as observed in the experiment, the temperature rise in the test piece becomes greater than any other case when it is subjected to a well-tuned ultrasonic guided wave mode.

5. Conclusions

The temperature rise observed in the aluminum test piece in the presence of the ultrasonic wave is higher than that in the absence of the ultrasonic wave. As ultrasonic mode and angle are similar in dispersion curve, temperature rise effect appeared greatly. When the test piece is subjected to the ultrasonic wave, there is a decrease in the temperature rise delay time.

Acknowledgment

6. Reference

1. Oh, Y.K.; Park, S.H. "Acoustic Enhancement of Solid-Liquid Phase Change Heat Transfer" J. of Energy Eng., 2002, 11(3), 262-269
2. Oh, Y.K.; Park, S.H.; Cho, Y.I. "A Study of the effect of ultrasonic vibration on phase-change heat transfer", Int. J. of Heat and Mass Transfer, 2002, 45, 4631-4641
3. Park, K.A.; Bergles, A.E. "Ultrasonic Enhancement of Saturated and Subcooled Pool Boiling", Int. J. of Heat Mass Transfer, 1998, 31, 664-667
4. Kim, Y.G; Kim, H.Y.; Kang, B.H. "Fundamental Mechanism of Boiling Heat Transfer Enhancement via Ultrasonic Vibration", Proceedings of KAMES 2002 Joint Symposium, 2002, 1522-1528
5. Wong, S. W. and Chon, W.Y., 1969, "Effects of Ultrasonic on Heat Transfer to Liquids by Natural Convection and by Boiling and Saturated Liquid," Experimental Thermal Fluid Sci., Vol. 5, pp. 108-115
6. Younho CHO. Journal of the Korean Society for Nondestructive Testing, Vol. 21, No.4(2001. 8)

STUDY ON MODE SWITCHING ALGORITHM AND DAMAGE EVALUATION FOR EFFICIENT AND PRECISION SHM USING SMART SENSOR[*]

YONG HONG[†]

Department of Precision Mechanical Engineering, Chonbuk National University, Jeonju Si, Chonbuk 561-756, South Korea

BYEONG-HEE HAN

Department of Precision Mechanical Engineering, Chonbuk National University, Jeonju Si, Chonbuk 561-756, South Korea

DONG-PYO HONG

Department of Precision Mechanical Engineering, Chonbuk National University, Jeonju Si, Chonbuk 561-756, South Korea

YOUNG-MOON KIM

Department of Architectural Engineering, Chonbuk National University, Jeonju Si, Chonbuk 561-756, South Korea

In this paper, we study the system algorithm that can achieve structural health monitoring more efficiently using the characteristics of two different measurement methods that use a smart sensor. Firstly, the impedance measurement method is used to monitor health conditions of structures in real-time. It changes its mode to the guided wave measurement mode by using the mode switching algorithm upon detection of an abnormal signal. The real-time data is handled efficiently by analyzing the location and shape of the damage through guided wave measurement. We study the construction of database that adopts the statistical analysis algorithm of impedance measurement data and the development of measuring algorithm for achieving our goal.

1. Introduction

As infrastructural facilities and buildings, structures, etc. become bigger, the study of the structural health monitoring (SHM) system, which can measure the health conditions of such facilities, has become important. Especially, many

measurement methods have been studied because nondestructive testing is characterized by convenient testing, low cost maintenance, and wide use. Nondestructive testing using piezoceramic (PZT) patches has many advantages. The PZT can serve as an actuator and a sensor, simultaneously. Therefore, instruments become simple and construction inexpensive. Compared to the PZT-based method, the traditional measurement methods need high efficiency instruments and professional manpower to measure the health conditions of structures. Studies on the development of an efficient monitoring algorithm for large structures, which uses several measurement methods, are presented.

2. Damage Detection Technique

2.1. *E/m Impedance Method*

The interaction between a PZT and its host structure can be described by using a simple 1-D model, as shown in Figure 1. The PZT is normally bonded directly to the surface of the structure using a high-strength adhesive to ensure better mechanical interaction. The bonded PZT is considered as a thin bar undergoing axial vibration in response to an applied alternating voltage. One end of the bar is fixed and the other end is connected to the host structure, which is represented as a single-degree-of-freedom system. This assumption regarding the interaction between the PZT and the host structure at two discrete points is consistent with the mechanism of force transfer from the bonded PZT sensor to the structure. The model of this interaction principle is shown   in Figure 1.
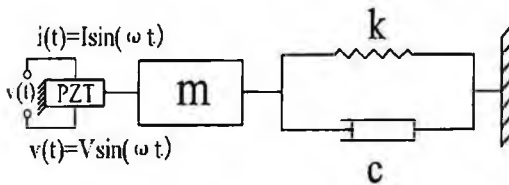
Fig. 1. Degree of freedom model of structure where PZT sensors attached.

2.2. *Guided Wave Technique*

In order to find the damage location, a time domain approach using multiple piezoelectric sensors and actuators is investigated. This approach is based on the pulse-echo method, which is often used in ultrasonic inspection. Instead of ultrasonic transducers, multiple PZT sensors and actuators are used for the feasibility study of identifying the damage location. In this case, we focus on the wave form generated by the PZT patches. The wave speed can be calculated from the length of the test piece and the time difference between the initial echo

and the back echo. Thus, the damage location can be assessed by tracking the flaw echo. However, this method can be applied only to a 1-Dimensional model. Reflection behaviour will become complicated if the wave propagation is not considered as one-dimensional [1].

Waves in one-dimensional longitudinal strain are not the only type of wave motion for a purely longitudinal disturbance. The second type is provided by wave motion in one-dimensional stress, whereby the longitudinal normal stress, say τ_x, which is a function of x and t only, is the one non-vanishing stress component. All other stress components vanish. For the case of one-dimensional stress τ_x and ε_x are related by $\tau_x = E\varepsilon_x$ [2]. So, the longitudinal wave equation can be expressed as:

$$\frac{\partial^2 u(x,t)}{\partial t^2} = c_b^2 \frac{\partial^2 u(x,t)}{\partial x^2} \tag{1}$$

$$c_b = \sqrt{E / \rho} \tag{2}$$

where $u(x, t)$ is the displacement at position x and time t, c_b is the longitudinal wave speed (usually called the bar velocity), E is the Young's modulus, and ρ is the mass density. The longitudinal wave speed calculated by Eq. (2) can be used to check the validity of the wave speed obtained by the experiment.

3. Mode Switching Algorithm

3.1. *Impedance Analysis*
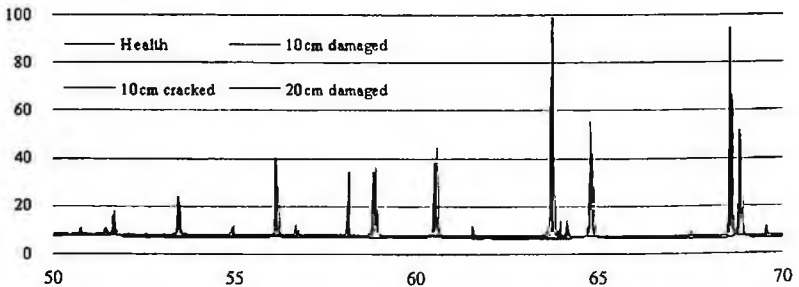
Fig. 2. Impedance response of damaged beam structure

SHM by impedance measurement gives proper results, which can be used to determine the extent of damage. The analyses of impedance measurement use

uses two methods: one uses the amount of peak frequency shift and the other uses the statistical analysis method by choosing a particular frequency band. The method based on the amount of peak frequency shifts is suitable for detecting a local damage. If the natural frequency of a structure alters because of the concentration stress that occurs in the structure by damages, the peak frequency values of the impedance response change.
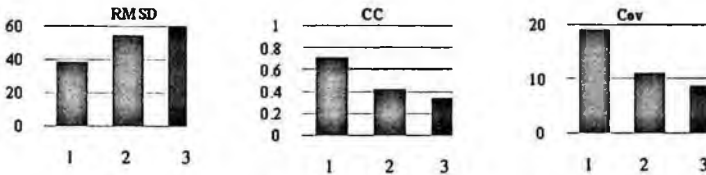
Fig. 3. Statistical Indices of damaged beam structure

The method that analyzes the impedance using statistical indices can give good results in the detection of damages that occur in the whole structure. When the damages propagate in a structure, each index changes quantitatively. Statistical indices can possible to make the algorithm very easy, and the time to analysis of the impedance data can be reduced. Therefore, the use of statistical analysis indices is suitable for real-time monitoring.

3.2. *Guided Wave Analysis*

It is possible to detect damage location by analyzing the guided wave propagation path, which is changed by damage, with time domain data. This analysis method can ascertain the position of the damage with high accuracy. If the sensor networking technique is applied, it is possible to ascertain the damage shape and extent. Also, a short time experiment done several times can prove the reliability of the analysis results.
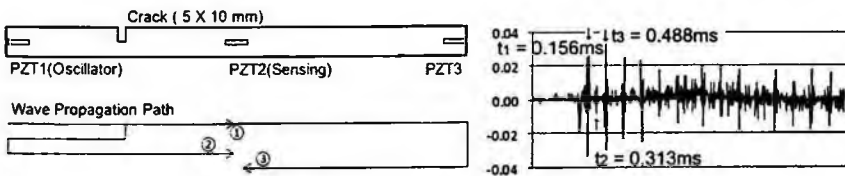
Fig. 4. Guided wave propagation path and time signal.

4. Mode Switching Algorithm

We wrote the program by LabVIEW to execute the SHM efficiently. LabVIEW is one of the most powerful tools to make mode switching program. And when

we develop the hardware, LabVIEW program can be easily embedded into the hardware. The cost is low, as well.

When the program is implemented, first it recognizes the conditions of the structure as a health condition. The program gathers the impedance and guided wave data while the health condition is compared with the damaged conditions. The measured data are saved as spreadsheet format or LabVIEW data file format. Herein, the data were saved as spreadsheet format for the convenience of post processing and modification.
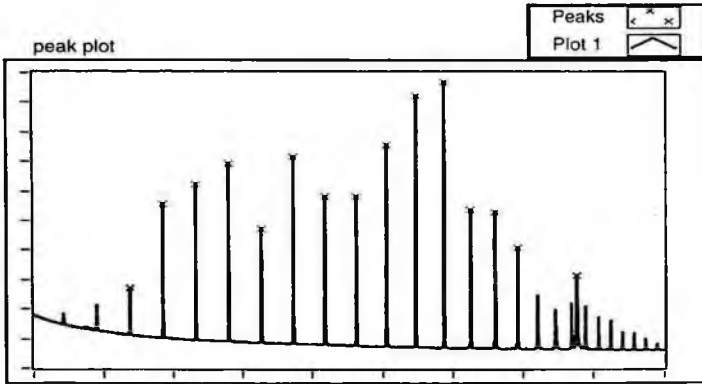
Fig. 5. Impedance response and detected peaks acquired with LabVIEW program.

When program measure the data on a health condition, it measure the impedance data at regular intervals, and monitors the health condition of the structure. The use of the impedance response is proper, because the program ascertains the property of the structure in a wide range. If the program judges the condition as a damaged one, program switches the measurement mode from the impedance mode to the guided wave mode to fine damage location using the guided wave method. The program accurately locates the damage using the guided wave mode effectively.

5. Advantages of Mode Switching Algorithm

The mode switching algorithm is very suitable when measuring the complex or large structures. It is hard to detect damage on such large scale structures accurately by using few sensors, because these structures have complex shapes. To overcome these demerits, we studied the sensory networking method to measure the damage accurately in a considerably wider range over such structures by connecting the sensors organically. Because the method of sensory networking can generate a large number of data, high specification H/W and complex algorithm are needed to process the data.

The data can be reduced by using the mode switching method in large structures. Therefore, the requirements for H/W specifications can be reduced to process the data efficiently. Mode switching algorithm can divides the large structure into several sections, and then it tracks the damage by using the guided wave method. The conditions of objects can be measured accurately by using relatively few sensors in a wider range over such large structures.

6. Conclusions

We presented an efficient measurement algorithm for SHM. The damage status of a structure was determined by using the impedance measurement and the damage was localized efficiently by using the guided wave method. Through the experiment using the mode switching program, damage was detected and tracked efficiently. To develop the method of multi-mode switching more efficiently, we will study the measurement modules, which can simultaneously execute the measurements of impedance and guided wave, and the miniaturization of the modules with much higher reliability.

Acknowledgments

References

1. Kazuhisa K., *Faculty of Virginia Polytechnic Institute*, April (1998)
2. J. D. Achenbach, *North-Holland Publishing company* (1975).
3. V. Giurgiutiu, A.N. Reynolds, and C.A. Rogers., *Journal of Intelligent Material Systems and Structures*, Vol. 10, p802–812. (1999)
4. Victor G. and Andrei N. Z., *Journal of Vibration and Acoustics*, Vol. 124, (2002)
5. Victor G., Andrei N. Z. and Jing J. B., *Sage Publications* (2002)
6. Daniel M. Peairs, Gyuhae Park and Daniel J. Inman., *Journal of Intelligent Material Systems and Structures*, Vol. p129-139, 15-February (2004)
7. Gyuhae Park, Harley H. Cudney and Daniel J. Inman., *Earthquake Engng Struct. Dyn.* 30; 1463-1474 (2001)

BUMPER IMPACT PERCEPTION FOR PEDESTRIAN PROTECTION USING SMART SENSOR[*]

YONG HONG†

Department of Precision Mechanical Engineering, Chonbuk National University, Jeonju Si, Chonbuk 561-756, South Korea

GAO-PING WANG

Department of Precision Mechanical Engineering, Chonbuk National University, Jeonju Si, Chonbuk 561-756, South Korea

HYEN-WOO PARK

Department of Precision Mechanical Engineering, Chonbuk National University, Jeonju Si, Chonbuk 561-756, South Korea

DONG-PYO HONG

Department of Precision Mechanical Engineering, Chonbuk National University, Jeonju Si, Chonbuk 561-756, South Korea

YOUNG-MOON KIM

Department of Architectural Engineering, Chonbuk National University, Jeonju Si, Chonbuk 561-756, South Korea

In this paper, a pendulum system is constructed to perform the fundamental research which is concentrated on the various frequency pattern of impact-object simulation tests are presented. and we confirmed application possibility for the method of discriminable pattern recognition whether impact-object is human-like or not via frequency analysis using smart sensor. Therefore a specific experimental data are compared and analyzed with the above database within a short time period. The impact analysis system, which is based on the above processing, can be developed and then used to recognize the impact information measured by smart sensors.

1. Introduction

According to the publication which is performed by The *Institute of Green city* in South Korea through the OECD IRTAD(International Road Traffic and Accident Database) analysis in 2007, the number of killed pedestrians of car accidents appeared to be 1.58 persons per 100,000 people of average population of member nations of OECD. And also In the U.S., more than 50% of killed pedestrians are involved in an collision with a passenger's car, and between them almost 90% of them are hit by the front of the car.[1]

Actually most of the vehicle manufacturer considered only customers safety system from the accidents. Recently EU took an action for increasing pedestrian safety in case of car to pedestrian accidents. One of the actions, EEVC(European Enhanced Vehicle-safety Committee), revealed the report that is concerned with standard of estimations about pedestrian safety in case of traffic accidents such as, pedestrian protection test standards, safe design solutions. Hence vehicle manufacturers in Europe spontaneously concluded the agreement and decided to apply requirement of pedestrian safety from EEVC to new vehicles by 2010 year.[2] It is mean that henceforth vehicle manufacturers who export to Europe are necessary to comply with the standard of vehicle design for pedestrian's safety.

In this paper, it is aimed to develop a pedestrian protecting system from the car accidents using a smart sensor. As a first step, a pendulum system is constructed to perform the fundamental research which is concentrated on the various frequency pattern of impact-object simulation tests are presented. And we confirmed application possibility for the method of discriminable pattern recognition whether impact-object is human-like or not via frequency analysis using smart sensor. Therefore a specific experimental data are compared and analyzed with the above database within a short time period. The impact analysis system, which is based on the above processing, can be developed and then used to recognize the impact information measured by smart sensors.

2. Principles of Momentum and Impulsive Force

A pendulum system is used to obtain momentums and impulsive forces by using some objects for experiments which is used for discriminating whether collided objects are human-like or not via the methods of pattern recognition.

The pattern consists of frequency data about impact-objects.

The discriminated signals which are containing information about a object are sent to the ECU for a vehicle control such as hood lift-up, Brake system, Air-bag front of the windscreen, etc. however that is only acting on A human-like objects.

Accordingly, we implemented a study of principles of the methods and experiments as below.

According to the conservation of energy

$$mgh = \frac{1}{2}mv^2 \tag{1}$$

Herein, velocity is $\sqrt{2gh}$, also a linear momentum mv obtained through multiply velocity by mass of each object. And also to obtain impulsive impacts

$$mv_1 + \int_{t_1}^{t_2} F\Delta t = mv_2 \tag{2}$$

And initial velocity is zero. therefore we obtain,

$$\int_{t_1}^{t_2} F\Delta t = mv_2 \tag{3}$$

At that time, the impulse is made during very short time. Thus,

$$\sum F\Delta t = mv_2 \tag{4}$$

If Δt is very short time, The Impulsive force is getting

$$\frac{mv_2}{\Delta t} \tag{5}$$

3. Experiment

In this study, the sensory system detects the information of pedestrian through pattern recognition techniques about accurate impact data for pedestrians. And the signals control the ECU which is actuating the brake systems or hood safety devices for reducing pedestrian's injury during short time. Hence, As part of the such study, we implemented the basic experiments using living supplies, such as soccer ball, base ball, water bottle of 500cc, a empty water bucket (18.9ℓ). Those materials weight are 454.44g, 91.96g, 439.42g, 809.72g, respectively.

These impact materials which are hanging on the pendulum system with rope collide to bumper head-on with 90°. At this moment, we could obtain the data.

3.1. Bumper Test Rig

A bumper test Rig was used to discriminate the obtained impact pattern. And as shown the picture, PZT sensors are integrated into front bumper at 3 positions. Figure 2(a) is shown that each part are reassembled again for experiments

(a)   (b)
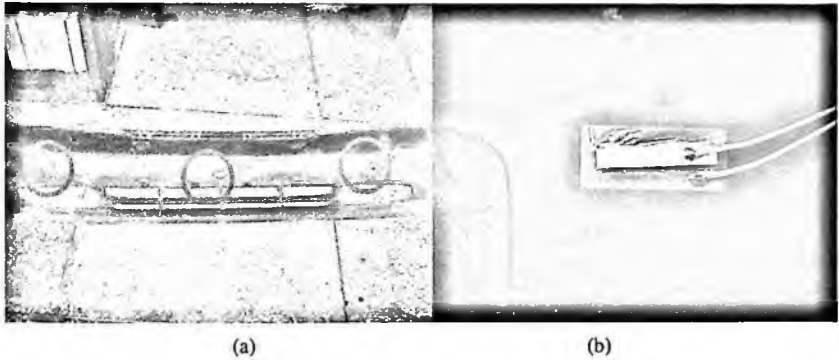
Fig. 1. (a) Integrate sensors into front bumper (b) The PZT sensor set on the film for conductivity

3.2. Impulsive Test Rig

(a)   (b)
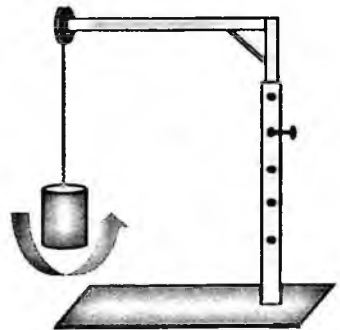
Fig. 2. (a) A test rig for impact test (b) A pendulum rig

As shown above the picture, pendulum impact tester was designed to discriminate the frequency pattern of the bumper impact, and to seek the velocity and impulsive force by hanging the objects. To discriminate the

velocity which is bumped against the bumper, this pendulum impact tester was designed to control the height by 5 steps.

4. Experiment Results

4.1. *Results of the Impulsive Forces*

The Velocity of each object was 4.427 m/s as $v=\sqrt{2gh}$ by form (1) and impulsive force was presented at below table by form (5).herein, the height of pendulum device is 1.5m. and we considered impact angles always be 90°.

Table 1. Impulsive forces of each material. It is calculated by form (5)

Impact materials	1.0m Impulsive forces (N)	1.7m Impulsive forces (N)
Soccer ball	0.336	0.442
Small bottle	0.323	0.387
Big bottle	0.635	0.796
Baseball	0.065	0.081

4.2. *Results of Time Analysis and Frequency analysis*

The obtained data, pendulum experiment values of each impact object, was processed by LABVIEW 8.2 program of *National instrument company* via signals from the PZT sensor of attached to front bumper. Figure 3 and 4 is result of Time and frequency analysis. From the results, we can know the fact that distribution patterns of frequency of each object are different. Because it is different that properties in mass, stiffness, size, damping efficient of each object.
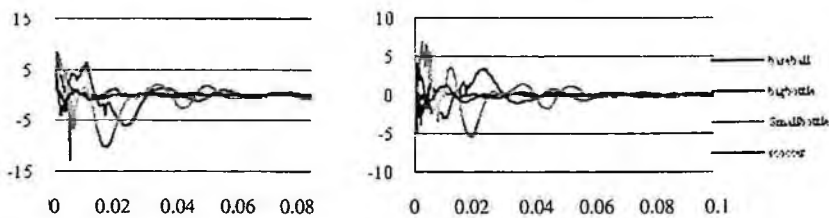
Fig. 3. Time Analysis result (1.0m height, 1.7m height)
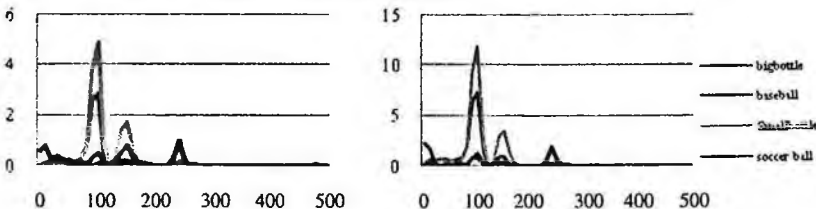
Fig. 4. Frequency Analysis result (1.0m height, 1.7m height)
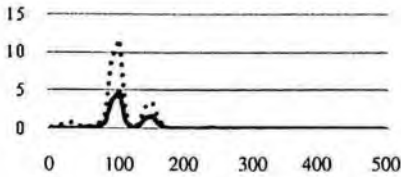
Fig. 5. The comparison graph of small bottle
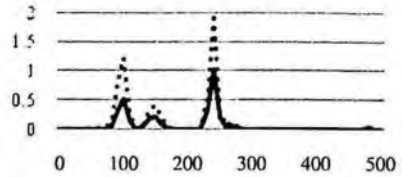
Fig. 6. The comparison graph of baseball
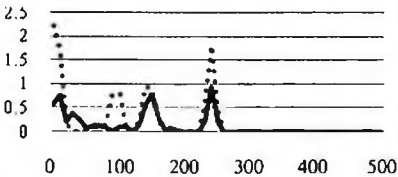
Fig. 7. The comparison graph of soccer ball
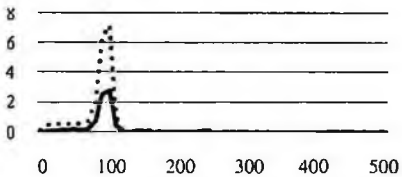
Fig. 8. The comparison graph of big bottle

5. Conclusion

According to the results of experiments, we verified the differences of frequency patterns of each impact object. In Figures 5~8, the frequency patterns are not altered by impulsive force(N) for the same object. It means that using frequency pattern analysis method we can know what object is crashed with the bumper and the amplitude of the impulsive force has no effect on the frequency pattern analysis results. Also we could apply to pattern recognition techniques on vehicles via frequency discrimination. Thus, at the next step, we will study about advanced recognition techniques discriminable whether impacted objects are human-like or not at the front bumper. And if impacted object is human, the signal is input to ECU for actuating the pedestrian safety devices. Herein the most important thing is sensitivity and durability from the harsh environments of sensors and fast signal transfer speed to ECU. Because the pedestrian-to-car accidents are take only 20 milli-seconds. The signal transferred to ECU actuate the pedestrian protection system.

Acknowledgments

References

1. A. Zanella, F. Butera and E. Gobetto, *European Workshop on Smart Structures in Engineering and Technology*, Proceedings of SPIE Vol.4763 (2003)
2. P. Cruz, C. Mitjans and J. Vinyals, *ABAQUS User's Conference* (2004)

WIDEBAND RADAR IMAGING OF
CONCRETE SPECIMENS FOR NDT

HONG C. RHIM

Department of Architectural Engineering, Yonsei University,
Seodaemum-gu Shinchon-dong, Seoul, 120-749, Korea

JINWON OH

Advanced Structures and Integrated Systems Laboratory, Yonsei University,
Seodaemum-gu Shinchon-dong, Seoul, 120-749, Korea

The research work presented in this paper focuses on the study of microwave techniques for nondestructive evaluation of concrete using a wideband imaging radar. Radar measurements of laboratory size concrete specimens were made with various inside configurations using wideband inverse synthetic aperture radar (ISAR). A parametric study has been performed to identify optimum combination of measurement parameters, which include center frequency, frequency bandwidth, incident angle, polarization of incident waves, and geometric and material (electromagnetic) properties of concrete targets. As results, for the concrete specimens and measurement setup used in this study, 2~3.4 GHz waveforms are found to be good for concrete thickness measurement, 3.4~5.8 GHz waveforms for monitoring of condition change inside concrete, and 8~12 GHz waveforms for detection of inclusions embedded inside concrete.

1. Background

The objective of nondestructive inspection for concrete systems is to detect incipient delamination, to determine the extent of damage, or to determine the exact location of steel reinforcing bars and other embedded objects, prior to carrying out appropriate maintenance and repair operations in a timely and effective way.

Radar is the electromagnetic analog of sonic and ultrasonic stress wave methods. It is governed by the processes involved in the propagation of electromagnetic energy through materials of different dielectric constants (Buyukozturk and Rhim, 1997). The principle of the radar method is to generate and transmit electromagnetic impulse signals into a concrete element. Reflection of the pulse from the material is monitored and interpreted to detect voids and delaminations. The radar has been applied for quality assessment, detection of substratum voids, delaminations, embedments, and the measurement of thickness

of concrete pavements. Advantages of the method include remote sensing capability without contacting the object under testing, measurement at high speed, sensitivity to metallic steel reinforcing bars, and flexibility in adjusting resolution and penetration depth. The limitations are due to expensive equipment and measurement procedure still under development.

Up to the present, the radar method has been applied generally to NDE of bridge decks and pavements in the infrastructure (Rhim, 2001). However, the technology is still premature for the radar method to be used for massive concrete structures such as large dams or for the structural elements of concrete systems such as beams, columns, slabs, and walls. The radar method is shown to have a potential of being an effective and practical tool for NDE of the structural elements of concrete structures (Chong et al, 1990). The success of the radar method as an NDE technique for concrete structures depends on the development of proper hardware and software systems which are suitable for concrete. It is also essential to understand concrete as a material with electromagnetic properties (Rhim and Buyukozturk, 1998).

2. Radar Measurement Parameters

Parameters which affect radar measurement results can be categorized into three groups: i) characteristics related to the incident waves of radar, such as center frequency, frequency bandwidth, and polarization, ii) characteristics related to the geometric and material properties of a target, such as size, shape, and electromagnetic properties, and iii) parameters related to measurement setup, such as measurement distance and angle (Rhim et al, 1995).

The parameters of the center frequency (f_c), frequency bandwidth (B) of the incident wave, and electromagnetic properties (real and imaginary parts of a complex permittivity) of concrete are important as they determine detection and penetration capabilities.

According to the principles of radar measurement, the resolution of closely-spaced objects can be obtained by narrowing the transmitted pulse width T in time and increasing the system bandwidth B in frequency so that $BT \approx 1$, thus yielding the range resolution $\rho_r \cong c / 2B$, where c is the speed of light in space ($3 \times 10^8 \ m/s$). A time-bandwidth product approximating unity is inherent in the class of pulse radars in which a carrier is amplitude modulated by a pulsed waveform. Resolution is the ability to distinguish between closely-spaced objects. An arbitrarily high degree of range accuracy can be obtained by using signals with a large bandwidth or high level of energy. The range resolution ρ_r, which can be

achieved by a wideband radar in concrete, is determined by the following relationship (Rhim and Buyukozturk, 2000):

$$\rho_r \ in \ concrete = (c / \sqrt{\varepsilon_r}) / 2B \qquad (1)$$

where ρ_r is the range resolution and ε_r the real part of the complex permittivity of concrete.

3. Concrete Specimens and Measurement Setup

Laboratory-size concrete specimens with different internal configurations are used as targets for the measurements. The concrete specimens were cast with a water/cement/sand/coarse aggregate mix ratio of 1:2.22:5.61:7.12 (by weight). Type I Portland cement was used. Coarse aggregates have maximum size of 38.1 mm. The aggregates are round-shape and from the river. They are properly stored and used prior to the mixing.

A plain concrete specimen is used for the thickness determination of different sets of center frequency and bandwidth. A specimen with delamination is used to examine the possibility of assessing condition change inside concrete by using radar. The present specimen has a relatively large size of delamination in the initial stage of the research work. The size of the delaminations is determined by the frequency range used by the radar, as described in this paper. Finally, a specimen with three 25.4 mm diameter steel bars is measured to investigate the detectability of the bars.

4. Measurement Result and Discussion

The measurement of concrete thickness is a basic but important application in the use of radar for the NDT of concrete systems. This thickness measurement can be used as a tool for quality control purposes after the construction of pavement, for example. Also, by measuring the remaining thickness of concrete components such as bridge decks, foundations, abutments, and retaining walls, the degree of deterioration occurring can be assessed.

Radar measurement results on a 304.8 mm (W) x 304.8 mm (H) x 101.6 mm (D) dry concrete specimen with 25.4 mm delamination at 50.8 mm depth are shown in Figures 1~4. The measurements are made at four different frequency ranges: 2~3.4, 3.4~5.8, 8~12, and 2~5.8 GHz. By examining the result in Figure 1, relatively narrow frequency bandwidth of 1.4 GHz from 2~3.4 GHz

wave gave no result in detecting the delamination. Meanwhile, the measurements at wider frequency bandwidth of 2.4 GHz in Fig. 2, and 4 GHz bandwidth in Fig. 3 gave good results in detecting the delamination. Also, the measurements at 2~5.8 GHz detected the delamination with success.
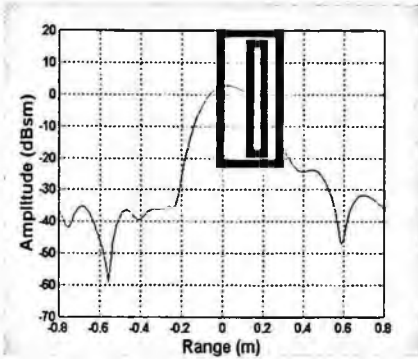
Fig. 1. Measurement result of a concrete specimen with delamination at 2~3.4 GHz.
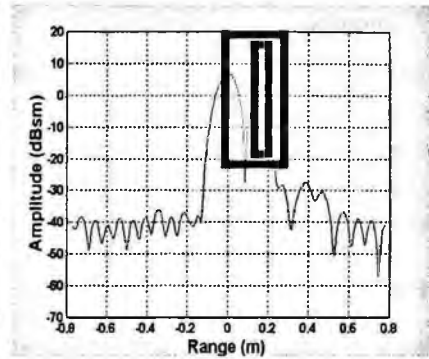
Fig. 2. Measurement result of a concrete specimen with delamination at 3.4~5.8 GHz.
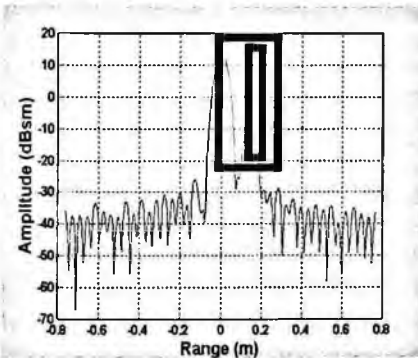
Fig. 3. Measurement result of a concrete specimen with delamination at 8~12 GHz.
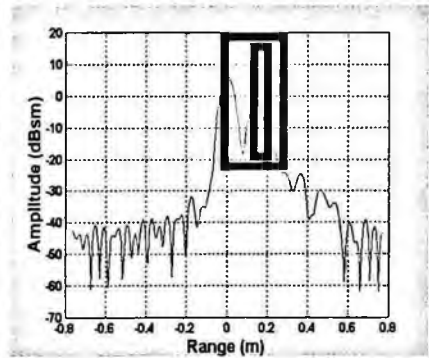
Fig. 4. Measurement result of a concrete specimen with delamination at 2~5.8 GHz.

5. Conclusion

A series of radar measurements are made on laboratory-size concrete specimens using Inverse Synthetic Aperture Radar (ISAR). The measurement setup was such that the antenna used was located at a distance from a concrete target for

remote measurement. Three different frequency ranges are used for the measurements at 2~3.4 GHz, 3.4~5.8 GHz, and 8~12 GHz. An application of the radar method is studied for the sensitivity of frequency bandwidth in detecting inclusions such as delamination inside concrete. Results showed that the wider frequency bandwidth is useful in improving resolution.

Acknowledgment

References

1. Rhim, H. C. and Buyukozturk, O. and Blejer, D. J., *Remote Radar Imaging of Concrete Slabs with and a without a Rebar, Materials Evaluation*, American Society for Nondestructive Testing, Vol. 52, No. 2, pp. 295-299, February (1995).
2. Buyukozturk, O. and Rhim, H. C., *Radar Imaging of Concrete Specimens for Non-destructive Testing, Construction and Building Materials*, Vol. 11, No. 3, pp. 195-198, (1997).
3. Rhim, H. C. and Buyukozturk, O., *Electromagnetic Properties of Concrete at Microwave Frequency Range, ACI Materials Journal*, Vol. 95, No. 3, pp. 262-271, (1998).
4. Chong K. P. and Scalzi J. B. and Dillon O. W., *Overview of Nondestructive Evaluation Projects and Initiative at NSF, Journal of Intelligent Materials, Systems, and Structures*, Vol. 1, No. 1, pp. 422-431, (1990).
5. Rhim, H. C. and Buyukozturk, O., *Wideband Microwave Imaging of Concrete for Nondestructive Testing, ASCE Journal of Structural Engineering*, Vol. 126, No. 12, pp. 1451-1457, (2000).
6. Rhim, H. C., *Condition Monitoring of Deteriorating Concrete Dams using Radar, Cement and Concrete Research*, Vol. 31, No. 3, pp. 363-373, (2001).

HEALTH MONITORING OF COMPOSITE STRUCTURES BASED ON ACOUSTIC WAVE SENSING USING FIBER OPTIC SENSORS

BASKAR RAO MATTAPALLY

Aerospace Engineering, Indian Institute of Science, Bangalore, India

M. R. BHAT

Aerospace Engineering, Indian Institute of Science, Bangalore, India

MURTHY C. R. L.

Aerospace Engineering, Indian Institute of Science, Bangalore, India

Structural Health Monitoring has gained wide acceptance in the recent past as a means to monitor a structure and provide an early warning of an unsafe condition using real-time data. Utilization of structurally integrated, distributed sensors to monitor the health of a structure through accurate interpretation of sensor signals and real-time data processing can greatly reduce the inspection burden. The rapid improvement of the Fiber Optic Sensor technology for strain, vibration, ultrasonic and acoustic emission measurements in recent times makes it feasible alternative to the traditional strain gauges, PVDF and conventional Piezoelectric sensors used for Non Destructive Evaluation (NDE) and Structural Health Monitoring (SHM). Optical fiber-based sensors offer advantages over conventional strain gauges, and PZT devices in terms of size, ease of embedment, immunity from electromagnetic interference (EMI) and potential for multiplexing a number of sensors. The objective of this paper is to demonstrate the acoustic wave sensing using Extrinsic Fabry-Perot Interferometric (EFPI) sensor on a GFRP composite laminates. For this purpose experiments have been carried out initially for strain measurement with Fiber Optic Sensors on GFRP laminates with intentionally introduced holes of different sizes as defects. The results obtained from these experiments are presented in this paper. Numerical modeling has been carried out to obtain the relationship between the defect size and strain.

1. Introduction

Advanced Fiber Reinforced Composites are finding numerous applications in load-bearing structures like aircraft fuselage, wing structures, and helicopter rotor blades etc., because of their specific advantages like high specific stiffness, high specific strength, corrosion resistance, design flexibility, and variable mechanical properties. However, they are susceptible to complex failure

467

mechanisms. It is very much necessary to have life time health monitoring of laminated composite structures, since damage is usually invisible from the surface, yet can be catastrophic. In addition, sections that must be monitored are often located in areas of the layered structures that are inaccessible to users, thus preventing the use of conventional Non-Destructive Evaluation (NDE) techniques. For continuous and in-situ monitoring of realistic structures, the use of surface bonded resistive foil strain gages, and PZT sensors offers a potential method. However, they are susceptible to Electro Magnetic Interference (EMI) in addition to signals obtained due to existing damage. Where as, Fiber Optic Sensors (FOS) have been proven for static strain, temperature, and acoustic wave (dynamic strain) sensing with such characteristics as light weight, small size, immune to EMI and capability for multiplexing sensors in a single optical fiber. They can be easily integrated into composite structures making them smart, so as to access inside material and structural locations where other sensing methods cannot easily probe.

This paper aims to numerically and experimentally study the effect of a induced damage (holes of different sizes) in GFRP and aluminum structures based on dynamic strain measurements using surface bonded EFPI sensor. The experimental results obtained are compared with the results obtained from ANSYS.

1.1. *Extrinsic Fabry-Perot Interferometric (EFPI) Sensor Theory*

EFPI sensors measure strain along the sensor axis. Axial strain produces change in output light intensity. The sensor consists of a single mode input/output fiber and another fiber whose inside end is used as a reflecting mirror. The two fibers are inside of an axially aligned capillary glass tube as shown in Figure 1. They are separated by an air gap of $30 - 50$ µm. the two partially reflecting fiber ends inside the tube are approximately parallel to each other and perpendicular to the fiber axis; together with the air gap they form a Fabry-Perot cavity produce optical power output variation as the sensor is strained. The number of sinusoidal cycles, usually referred to a fringes; is given by

$$\varepsilon = \frac{m\lambda}{2L_0} \tag{1}$$

Where, ε is strain along sensor axis, m is number of fringes, λ is wavelength of light, and L_0 is gage length of the sensor.

The change in the length of Fabry-Perot cavity causes changes in phase difference between the reference reflection and sensing reflection. This change in phase difference modulates the intensity of the light monitored at the output

arm of coupler. Since the reflectivity of glass/air interfaces in the EFPI is very low, the sensor is infact a low-finesse Fabry-Perot interferometer and can be treated as two-beam interferometer. The phase change Φ of the interference signal is given by.

$$\phi = \frac{4\pi d}{\lambda}$$ (2)

The number of interference fringes is determined by the EFPI cavity length (d). the cavity length can be determined from the separation of wave lengths across one or more complete fringes:

$$d = \frac{m\lambda_1\lambda_2}{2(\lambda_2 - \lambda_1)}$$ (3)

Where the difference between wavelengths λ_1 and λ_2 is $2m\pi$ and where m is an integer. The relation between the change of cavity length and starin can be described by:

$$\varepsilon = \frac{\Delta d}{L_0}$$ (4)
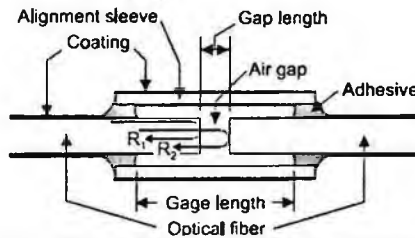
Fig. 1. Extrinsic Fabry-Perot Interferometric sensor

2. Experimental Setup Details

Dynamic response measurement of a cantilever beam made of glass fiber reinforced polymer composite with surface bonded EFPI sensor was conducted subjecting to impulse force. Figure 2 show the details of experimental set up.

A GFRP beam of 250mm long and 20mm wide with 2mm thick structure with surface bonded EFPI sensor was clamped to a table for the dynamic response measurements. And the sensor out is connected to Fiber Scan 2000 (EFPI interrogation system) for recording the sensor dynamic strain response and the analog output of Fiber Scan2000 was given to NI data acquisition system through a band pass filter to filter out the high frequency noise. The response was measured using a code developed in LabView. Here an impulse hammer with a charge amplifier was used to give an impulse force to the beam.

Fig. 2. Experimental setup details

3. Results and Discussion

As composites are anisotropic consequent to which the response would be complex, initially a bench work problem was attempted using an aluminium beam. The results obtained with experimental and analysis shown in figures (4-6). Experiments were carried out for seeing the effect of induced damage in GFRP composite structures based on dynamic strain measurements, in a frequency range of 0-50Hz recorded by surface bonded EFPI strain gages. To verify the proposed measurement system efficiency, the experimental results were compared with a commercial FEM software (ANSYS) using shell 63 elements as shown in figure 3, for this purpose experiments were carried on a Aluminum
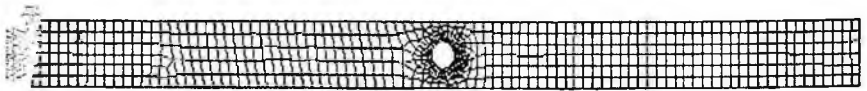
Fig. 3. ANSYS model of the specimen used for dynamic response measurement

cantilever beam of 300mm length, 20mm wide and 3mm thick with mechanical properties of young's modulus 70Gpa, Poisson's ration 0.3, and density 2700 kg/m^3. The frequency response of the ANSYS model shown in figure 4 for healthy specimen and figure 5 for induced damage and was compared with experimental results shown in figure 6.
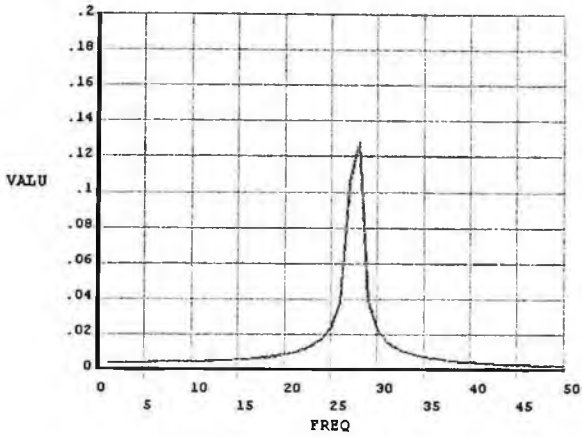
Fig. 4. Frequency response of a undamaged AL beam
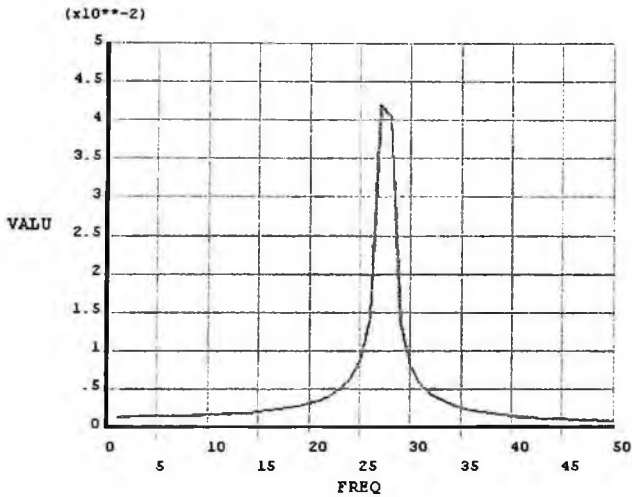
Fig. 5. Frequency response of a damaged AL beam

From the response it is clear that amplitude of the frequency response is decreased by a 60% due to an induced damage. From the experimental results the percentage of reduction in the amplitude is around 50%, the results obtained from the experiments and the numerical model results are well matched even

though there is marginal difference in the amplitude decrement, it is due to the variation in the applied impulse load as shown in figure 7.
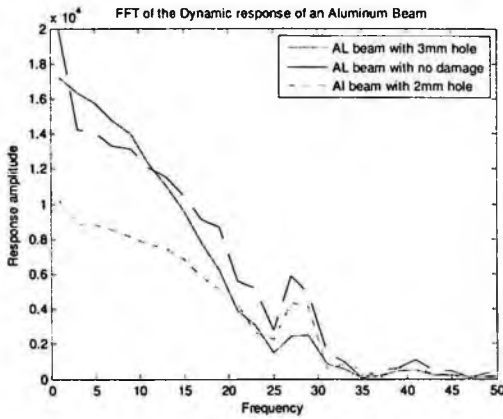
Fig. 6. FFT of dynamic response obtained experimentally using EFPI sensor
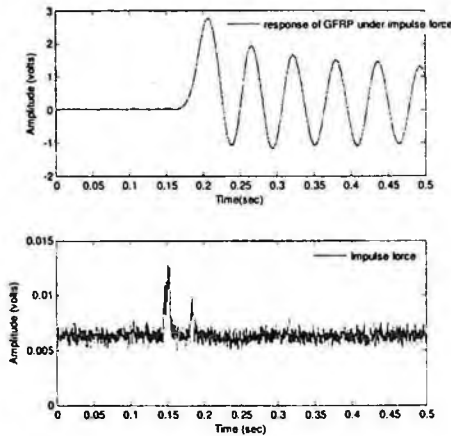
Fig. 7. EFPI sensor output (top figure) under the impulse load (bottom figure)

The second set of experiments was carried out to measure the dynamic response on GFRP composite specimens, made of 4-mil 20 layered E-glass woven fabric cured using micro-wave curing, with dimensions of 250mm length, 20mm wide and 2mm thick. Shown in figure 8, with induced damages of different size (holes).
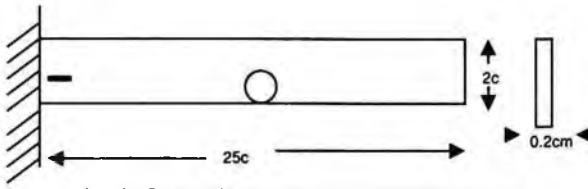
Fig. 8. Schematic representation of GFRP specimen

Figure 9, shows the dynamic response of the GFRP specimen with different sized induced damages middle of the cantilever beam, the amplitude of the response decreases as size of the damage increases. The FFT of the response was shown in figure 10. Percentage reduction in amplitude with damage size is tabulated and presented in table 1.
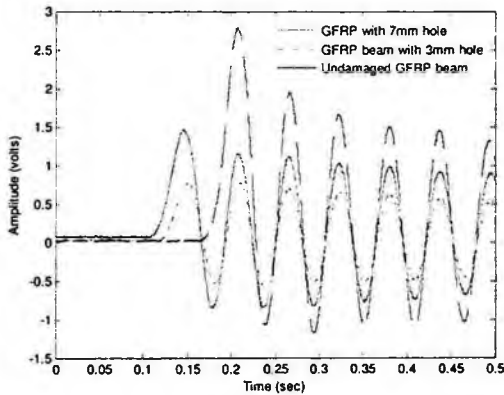
Fig. 9. Dynamic response of EFPI sensor with different sized damage
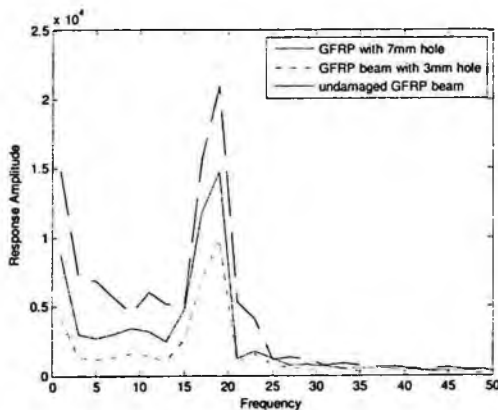
Fig. 10. FFT of figure 9

Table 1 Percentage of Amplitude variation in dynamic response with different induced damages

Damage (hole) size	Percentage of Amplitude variation
0	0
3mm	52.6
7mm	29

4. Conclusions

Dynamic strain measurements of a GFRP cantilevere beam with surface bonded EFPI sensors is presented. The results are encouraging in damage detection there is considerable change in response amplitude (about 30%), and EFPI sensors can become very much important in SHM due to their specific advantages over conventional sensors and they have high signal-to-noise ratio. Here only first fundamental frequency response was measured due to the system limitation. By measurement of higher fundamental frequency responses it is possible to detect, locate and quantifying damage is possible. For this, experiments were planed for acoustic emission sensing using FOSS system.

Acknowledgments

References

1. Steve E Watkins, Gilbert W Sanders, Farhad Akhavan and K Chandrashekhara, *Smart Mater. Struct.* **11**, 489–495(2002).
2. C. Boller, *Smart Materials and Structures*, Vol. 10, pp. 432-440(2001).
3. R. M. Jones, *Taylor and Francis*, (1999).
4. R. M. Measures, *Academic Press*, (2001).
5. E. Udd, *American Institute of Physics*, Vol. 66, pp. 4015-4030 (1995).
6. Daniel C Betz, Graham Thursby, Brian Culshaw and Wieslaw J Staszewski, *Smart Mater. Struct.* **12**, 122–128 (2003).
7. Robert F Anastasi and Craig Lopatin, NASA/TM-2001-211051 ARL-TR-2435 (2001).

APPLICATION OF GENETIC ALGORITHM AND GAUSS-NEWTON METHOD TO SYSTEM IDENTIFICATION

GRACE S. WANG

Construction Engineering, Chaoyang University of Technology, 168 Jifong E. Rd., Wufong Township, Taichung County, 41349 Taiwan

FU-KUO HUANG

Water Resources and Environmental Engineering, Tamkang University, 151 Ying-chuan Road, Tamsui, Taipei County, 25137 Taiwan

While the GA method has been developed as a powerful search tool in a global solution space, it is not necessarily efficient in fine-tuning for local convergence particularly when the search domain is large. In order to accelerate the convergence to the optimal solutions, a hybrid identification strategy, combining GA and local search technique such as Gauss-Newton method is proposed in this study. The hybrid computational strategy is applied to the Taiwan Electricity Main Building using records from the 331 earthquake (2002). The comparison is made between the predicted acceleration and the measured one for each case.

1. Introduction

Most of the identification methods mentioned are calculus-based search method. A good initial guess of the parameter and gradient or higher-order derivatives of the objective function are generally required. There is always a possibility to fall into a local minimum. On the other hand, genetic algorithms (GAs) are optimization procedures inspired by natural evolution. They model natural processes, such as selection, recombination, and mutation, and work on populations of individuals instead of a single solution. In this regard, the algorithms are parallel and global search techniques that search multiple points, and they are more likely to obtain a global solution. Many GA applications have been performed on a variety of optimization problems in engineering area. However, relatively few applications have been on structural identification. Koh et al.[1] proposed a hybrid strategy of exploiting the merits of GA and local search operator. Two local search methods were studied: an existing SW method and a proposed method called the MV method. The numerical study showed that the hybrid strategy performs better than the GA alone. The author[2] applied the real-coded GA to structural identification problems. The validity and the

efficiency of the proposed GA strategy were explored for the cases of systems with simulated input/output measurements. Moreover, the strategy was also applied to a real structure. In order to accelerate the convergence to the optimal solutions, a hybrid GA identification strategy that employs Gauss-Newton method as the local search technique is proposed and verified in this paper.

2. Hybrid GA Combining GA and Gauss-Newton Method

2.1. *Genetic Algorithm*

Genetic algorithms model natural processes. The algorithms work on populations of individuals instead of a single solution. In this way, the search is performed in a parallel manner. At the beginning of the computation, a number of individuals are randomly generated. The objective function is then evaluated for these individuals. If the termination criteria are not met, the creation of a new generation starts. Individuals are selected according to their fitness for the production of offspring. Parents are recombined to produce offspring. All offspring will be muted with a certain probability. The fitness of the offspring are then computed. The offspring are inserted into the population replacing the parents, producing a new generation. This cycle is proceeded until the optimization criteria are reached. Every subpopulation evolves over a few generation isolated before one or more individuals are exchanged between subpopulation using the mechanisms of migration and competition.

2.2. *Gauss-Newton Method*

Since Gauss-Newton method has been demonstrated to be an efficient method in the nonlinear least square problems, it is appropriate to use it for the optimization of the prediction error in system identification problems. For the problem of system identification, an objective function $E(\tilde{x})$ minimized is a sum of squares expressed as

$$E(\tilde{x}) = \frac{1}{2} \sum_{i=1}^{N} [f_i(\tilde{x})]^2 = \frac{1}{2} \sum_{i=1}^{N} [y_i - v_i(\tilde{x})]^2 \tag{1}$$

where $\tilde{x}$ is the vector of the parameters which will yield the minimized least square error between the measured response y_i and the predicted response $v_i(\tilde{x})$, and N is the number of measurement sequence. According to the quasi-Newton method, a new iterated parameter $\tilde{x}_{m+1}$ can be evaluated in terms of the current parameter vector $\tilde{x}_m$ as

$$\tilde{x}_{m+1} = \tilde{x}_m - H(\tilde{x}_m)G(\tilde{x}_m) \qquad (2)$$

where $G(\tilde{x})$ is the gradient vector of $E(\tilde{x})$, and $H(\tilde{x})$ is the Hessian matrix of $E(\tilde{x})$. Denoting the Jacobian matrix of $E(\tilde{x})$ as $J(\tilde{x})$ and using the definition in Equation (1), we have the iterative formula for the Gauss-Newton method

$$\tilde{x}_{m+1} = \tilde{x}_m - [J^T(\tilde{x}_m)J(\tilde{x}_m)]^{-1}J^T(\tilde{x}_m)[f_i(\tilde{x}_m)] \qquad (3)$$

2.3. *Hybrid GA Method*

The GA is a parallel and global search technique that searches multiple points and makes no assumption about the search space. However, GAs are inherently slow and are poor at hill-climbing. In order to compensate the computational inefficiency in hill-climbing when the solution yielded by GA approaches the optimal value, a local search operator compatible to GA is merged to the GA strategy. The Gauss-Newton method is the local search operator used in this paper and is performed after completing the evolution process of every 10 generations. Accordingly, a new hybridization of a GA with Gauss-Newton method is proposed. Figure 1 shows the structure for such a hybrid GA.
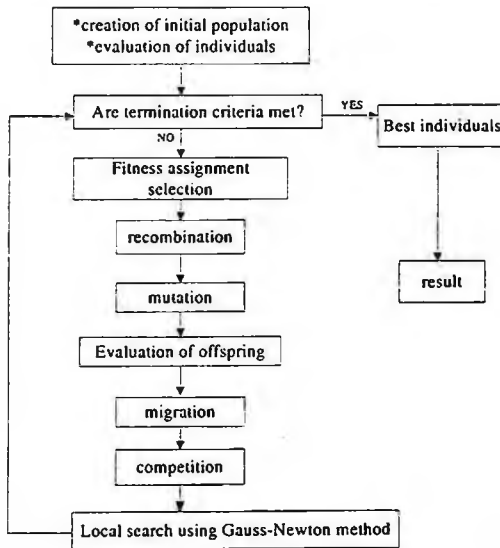
Fig. 1. Structure of hybrid GA.

3. Identification of a High-Rise Building

The real building identified here is the Taiwan Electricity Main Building located in Taipei. This building is a 28-story steel frame structure. Two seismographs are installed: one is on the third floor of the basement, and the other is on the top floor of the building. Three-component accelerograms are collected during earthquake on March 31, 2002. The magnitude of this earthquake is 6.8 with focal depth of 9.8 km. Through spectral analysis, estimation of frequencies is made and rational ranges of these parameters can be obtained when performing the GA identification procedure. Modal damping ratio, modal frequencies, and participations factors can be obtained on the basis of either longitudinal (L) or transverse (T) measurements.

3.1. *Modal Equation of MDOF System Under One-Component Eexcitation*

The motion equation of a MDOF system subjected to single excitation is transformed into modal equation through mode superposition as

$$\ddot{y}_m + 2\xi_m\omega_m\dot{y}_m + \omega_m^{\ 2}y_m = -P_m\ddot{u}_g \tag{4}$$

where y_m is the normal coordinate in mode m, ξ_m the damping ratio in mode m, ω_m the modal frequency in mode m, P_m the participation factor in mode m, and $\ddot{u}_g$ the ground acceleration in one direction. Premultiplying ϕ_{sm}, the mode shape in mode m at the sth DOF, equation (4) can be rewritten as follows:

$$\ddot{u}_{sm} + 2\xi_m\omega_m\dot{u}_{sm} + \omega_m^{\ 2}u_{sm} = -P_{sm}\ddot{u}_g \tag{5}$$

where u_{sm} is the modal displacement in mode m at the sth DOF, and P_{sm} the effective participation factor in mode m at the sth DOF associated with the ground motion $\ddot{u}_g$

$$P_{sm} = [\phi_{sm}\{\phi_m\}^T[M]\{l\}]/[\{\phi_m\}^T[M]\{\phi_m\}] \tag{6}$$

where $[M]$ is the mass matrix, $\{\phi_m\}$ the mode shape in mode m, and $\{l\}$ the ground influence coefficient matrix with elements 0 and 1. If only one accelerograph installed at the sth DOF, the measurement equation can be represented as

$$y = \ddot{u}_s = \sum_{m=1}^{N}\ddot{u}_{sm} = \sum_{m=1}^{N}P_{sm}\ddot{u}_g - 2\xi_m\omega_m\dot{u}_{sm} - \omega_m^{\ 2}u_{sm} \tag{7}$$

where $\ddot{u}_s$ is the relative acceleration at the sth DOF, and N the total number of modes. $2\xi_m\omega_m$, ω_m^2, and P_{sm} are the parameters to be identified in this case. In order to assess the accuracy of the proposed identification technique, the error index $E.I.$ is defined as the square root of the normalized square error:

$$E.I = [\sum_{i=1}^{Ns}(y_i - \hat{y}_i)^2 \Big/ \sum_{i=1}^{Ns} y_i^2]^{1/2} \tag{8}$$

where N_s is the number of measurement sequence, y_i is the measured relative acceleration response of the SDOF system at the ith sampling time, and $\hat{y}_i$ is the associated estimated or predicted relative acceleration response from the proposed GA. Equation (8) is also used to define the fitness function in GA.

3.2. *Identification of a High-Rise Building Under One-Component Excitation*

The data recorded from the basement and the top floor are analyzed. The first three modes are identified using the longitudinal excitation and response. Fig. 2(a) shows the comparison between the measured response and the identified one based on the three-mode analysis. The error index is 11.48%. In this case, we conclude that the first three modes can provide sufficient accurate results for the top floor response of the specific building, since the measured response is in good agreement with the predicted one. Furthermore, the longitudinal system parameters are summarized in Table 1. The results of the identified parameters using the transverse excitation and response are shown in Table 2. The predicted response in this direction is also shown in Fig.2(b). The predicted response is very close to the measured one for both cases.

Table 1. Identified parameters in the longitudinal direction.

	mode	2ξω	ω2	Psm	E.I.	Generation
Identified	1	0.091	4.943	1.438		
parameters	2	0.265	39.904	-0.543	11.048%	44
	3	0.765	129.600	0.289		

Table 2. Identified parameters in the transverse direction.

	mode	2ξω	ω2	Psm	E.I.	Generation
Identified	1	0.117	5.316	1.695		
parameters	2	0.271	46.264	-0.395	14.043%	34
	3	0.374	169.840	0.210		

480
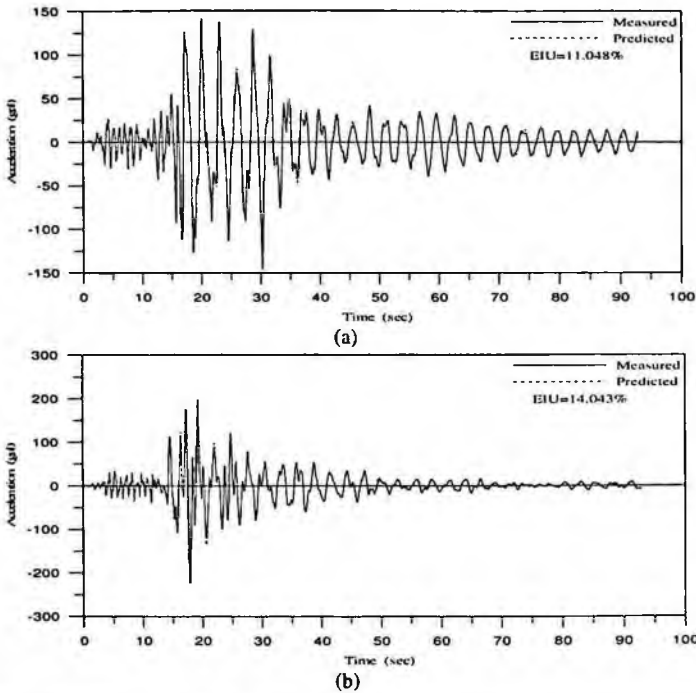
Fig. 2. Comparison of the measured response with the predicted one based on three-mode analysis: (a) in the longitudinal direction, (b) in the transverse direction.

4. Conclusion

An efficient hybrid GA identification strategy, which merges the local search method "Gauss-Newton Method" to GA, has been proposed. This new hybrid strategy is designed to preserve the merits of both GA and Gauss-Newton method. GA is employed to locate the neighborhood of global solution, while Gauss-Newton method is used as a local search operator to do the hill-climbing so as to accelerate the convergence to the global solution. The predicted responses and the measured responses of the real building coincide quite well. Moreover, the response of the first three modes is sufficient to represent the response of the specific high-rise building for both cases. In this regard, the efficacy of the propose identification technique is verified.

References

1. Koh, C. G. et al., Computers and structures **81**, 107(2003).
2. Wang, G. S. and Lin, H. H, J. of the Chinese institute of Civil Eng. and hydraulic Eng. **17(2)**, 281(2005).

A STUDY ON REMOTE MONITORING AND SECURITY OF CONTROL SYSTEM USING IPSEC[*]

HO JUN NA, WAN KYU LEE, SEUNG HOON NAHM[†]

*Division of Metrology for Quality Life, Korea Research Institute Standard Science,
Daejeon, Korea*

DAE-HYUN RYU

Div. of Information Technology, Hansei Univ., Korea

SANG-HOCUK LEE

CEO, K-Technocom, Co., LTD, Korea

SEOK-CHEOL LEE

Dept. of Information Security, Pukyong Nat'l Univ. Korea

This paper is focused on the development of remote-observation control system
supporting the excellent security functions. This control system uses VPN (Virtual
Private Network) supported by IPSec and public network like Internet. The developed
XBOX system is operated by embedded system which installed Linux operating system
and performs the functions of TCP/IP Protocol processing, security-communication, and
etc. Our developed XBOX system can be applied to various applications including an
attended device of remote crime prevention. This paper shows the example of
transmission the image of the cracking and transmitting the data using our developed
system.

1. Introduction

Recently, the research about development of remote-observation control system
has been carried out. This technology will be used to the computer system based
on internet and web architecture and will be operated in the difficult field which
is operated by people, for example, environmental monitoring, power plant
system and security system.

Remote monitoring and control system are introduced rapidly by the
appearance of wideband telecommunication like XDSL(ADSL/VDSL)

---

technology. Especially, Research about system environment construction using web based on internet or intranet has been carried out actively. If it is based on web, the system can be connected easily with DB and development of application system may be easy. Though most remote monitoring systems which have been studied so far are based on internet, security was not an important factor. But information security in remote monitoring system is very important because of weakness such as the user authentication and abusing by abnormal user.

In this study, the remote-observation system was developed to support IPSec (Internet Protocol Security) for the information security using the Virtual Private Network (VPN) based on the public network like internet. This system is embedded system which is operated by Linux OS and can perform the processing of the TCP/IP, encoded communication and so on.

Our developed system can provide not only an unattended remote prevention of crimes but also additional service like home security gateway. And it will be extended to the voice communication, multimedia and various network interfaces. Also, the developed system has advantages such as the possibility of home gateway, Integrated Access Device and remote-observation security system and so on.

2. System Configuration & Requirement

The developed system is consisted of two kinds of parts. One part is the terminal system which is called XBOX. It receives the data which is transmitted from the alarm sensor and converts to TCP/IP type protocols. The other part is to perform encrypting and transmits the data to public communication network. This system can utilize the commercial VPN device because the XBOX is used by IPSec. Figure 1 shows the schematic diagram of the developed system.
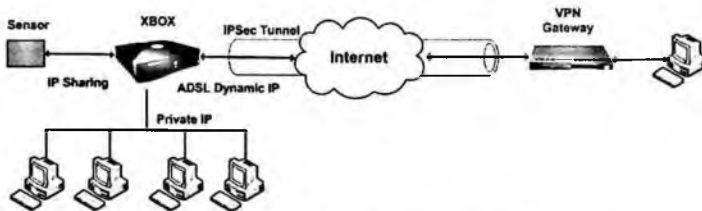
Fig. 1. Schematic diagram of the remote monitoring system.

So, this system requires the functions of RS-232C Serial interfaces, TCP/IP Stack, RS232C-to-IPSec, Internet Router, and etc. This system will be available to provide the multimedia service because this system can support the high level

internet connection. The data of security products like alarm devices are transmitted by encrypted message. The data of normal user are transmitted without any encrypt function through the internet. The XBOX system is installed to the terminal and has the following functions.

- Receiving the signal from the alarm devices through the RS-232C
- Available for TCP/IP Communication to user
- Internet Sharing
- Converting from RS-232C Signal to IPSec Protocol
- Encrypting/Decrypting

Various terminal systems transmit the data to VPN Gateway in control center through the public networks like internet or intranet. The hardware and software of this system is required the following specifications.

<Hardware Part>
- RS-232C interface: available for the communication to alarm devices
- TCP/IP Communication interface: sending the data by public network.

<Software Part>: Network Protocol Stack
- Functions of Network Protocol Stack (ARP, TCP/IP and etc.)
- Functions of converting from RS-232C to TCP/IP, Cryptography
- Internet Sharing Router: using NAT, DHCP
- Security: Firewall, Data Tracking, Web Filtering of the URL

3. Design and Implementation of the Remote Monitoring System

3.1. *Hardware Compositions*

Figure 2 shows the schematic diagram of remote monitoring system developed in this study. S3C4530 is the MCU (Micro Control Unit) and ARM7TDMI core is used in it. This MCU has hardware module which can improve the network functions. Internet MAC (Media Access Control) block is useful the controlling switch chip. We used the network interface circuit called by 'CS8900' for connecting the internet. It has the function of direct ISA interface and includes MAC and PHY (PHYsical layer protocol). So it was mapped to the external I/O area in S3C4530. UART (Universal Asynchronous Receiver / Transmitter) in S3C4530 has two drivers and the only external drivers are used. UART0 was used by console port while the program was developing and it was used by function of transmitting data of alarms to control center after Linux porting ends. The functions of IPSec encryption was implemented by porting appropriately freeswan 1.9 Open Sources to ARM7TDMI MCU.

484
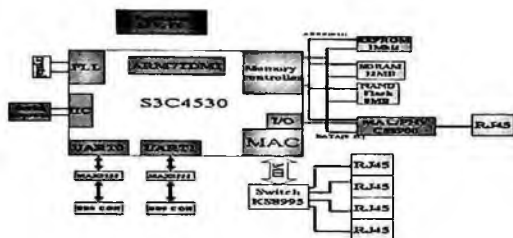
Fig. 2. Schematic diagram of system hardware.

3.2. *Conversion of Serial to Ethernet and Mechanisms of Cryptography*

The developed remote monitoring system has two functions of signal conversion and cryptography. One is the conversion of Serial to Ethernet called Seiper and the other is function of cryptography communications. The function of conversion of Serial to Ethernet is consisted of three sub-programs.

Seiper: (Serial to IP Changer) : This program is operated in XBOX.
 • Receiving the data from alarm sensors through RS-232C
 • Composing the message to UDP (User Datagram Protocol) packet
 • Transmitting the message packet to s1mon port(7101) in UDP Server
UDP Server: This program is installed to Control Server.
 • Analyzing UDP packet which is transmitted by Seiper program
 • Showing analysis results
UDP Sender: This program is installed to Control Server.
 • Transmitting control data to alarm sensors
 • If a signal is transmitted to s1control port (7102) in XBOX, the signal is grabbed by seiper program and then it is transmitted to serial line.
 • Non-blocking I/O, 7 bit, even parity, 1 stop bit, Baud rate : 300 bps

The Seiper program is operated in developed system and UDP Sender program is operated in control server. These programs should be inside encoded tunnel, so they are encrypted between XBOX system and VPN Gateway by ESP Protocol.

4. Experimental Test & Analysis

The parameters related with tunnel were set up through the Web Interface. The process foaming the tunnel is divided into two main procedures. At first process, imaginary interface such as IPSec on eth0 network interface is added. At second process, the information of tunnel configuration is transmitted to kernel using command of whack, and finally the tunnel is created. If the system has no request,

it is judged that VPN tunnel is corrupted. In that case, a new tunnel is created. If the system has the other problems such as removal of ADSL or Cable Model, interrupt of a signal and blocking of a message from VPN Gateway, the creation of a new tunnel is tried continuously.

5. Application to Remote Monitoring for Crack Propagation Using Mobile Communication Network

Various kinds of technologies should be combined each other organically to collect and handle image data using mobile communication network. Even if identical technology is used, level of embodied technology is depended on kinds of selected machines. The process of data acquisition through a mobile network is as following;

1) Image data acquired from CCD camera was changed in form that can be acquired, compressed and transmitted by gateway system.

2) The data is transmitted to mobile communication base station through mobile communication networks.
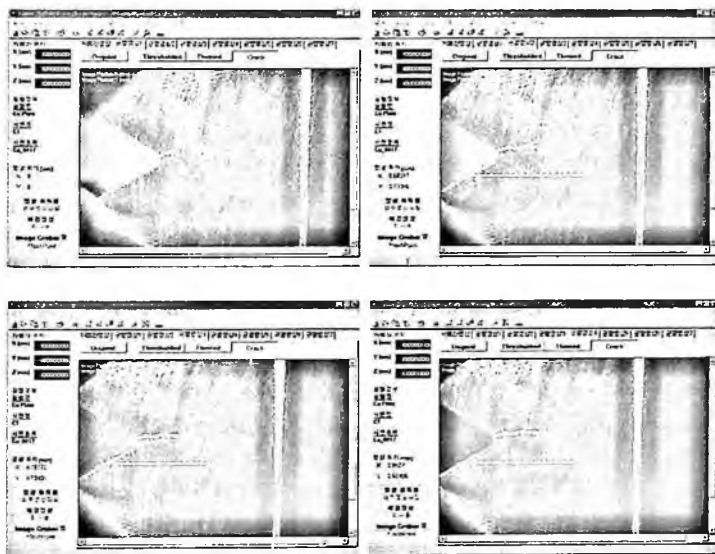
Fig. 3. The process of crack detection and its length measurement using mobile communication network.

3) The data is stored automatically as image data to internet server.

4) After the image is loaded to client system from the server, the image analysis is carried out using image processing program.

5) Finally, the results of image analysis are uploaded to internet server and the results are showed at any time and anywhere through web.

Figure 3 shows the process of crack detection for a compact tension specimen and its length measurement using the remote monitoring system developed in this study. Red line of Figure 3 is the size of crack propagation.

6. Conclusions

Superior remote monitoring system for security was developed by supporting IPSec, though public network was used in this study. The developed system has the function of encryption as well as decryption, firewall, internet sharing router and filtering the harmful web-site. So the system can be applied to the Ubiquitous Home Gateway module. Existing home gateway devices were not commercialized because the requirement of customers was not definite. But the developed XBOX system provides the additional service as well as multimedia functions, and it can be applied to the remote monitoring or control system, banking and etc. In addition, the technology can be extended to the various fields such as remote image control systems and integrated manufacturing process systems. Therefore, market value of remote monitoring and control system is great and the effect of the system on the safety or security industry is also great.

References

1. K.T. Erickson et al., "Reliability of SCADA Systems in Offshore Oil and Gas Platforms," Stability and Control of Dynamical Systems with Applications, Birkhauser Press, 2003, chapter 20.
2. A. Miller and K.T. Erickson, "Network Vulnerability Assessment: A Multi-Layer Approach to Adaptivity," Int'l Workshop Research and Education in Control and Signal Processing, NATO Symp. Adaptive, Defence in Unclassified Networks, 2004, pp. 13-1?13.8.
3. D. Craigen et al., "Multi-Layer Vulnerability Assessments of SCADA Networks," Proc. Ottawa, Cyber Security Workshop, 2005
4. US Computer Emergency Readiness Team, "Control Systems Cyber Security Awareness," US-CERT, 7 July 2005
5. A.B. Baker et al., A Scalable Systems Approach for Critical Infrastructure Security, tech. report SAND2002-0877, Sandia Nat'l Labs., Apr. 2002

HEALTH MONITORING OF STEEL CRANE GIRDER USING PZT SENSORS

Kyung Jae Shin

Professor, Sch. of Arch. & Civil Engrg., Kyungpook National University Daegu, Korea

Hongjin Kim

Professor, Sch. of Arch. & Civil Engrg., Kyungpook National University Daegu, Korea

Chan Woo Jung

Post-Doctor, Sch. of Arch. & Civil Engrg., Kyungpook National University Daegu, Korea

Whajung Kim

Professor, Sch. of Arch. & Civil Engrg., Kyungpook National University Daegu, Korea

Many studies of monitoring and detection of damages to structures have been conducted through piezoelectric sensors, and a number of damage detecting methods have been developed and renovated. This study aims to develop a monitoring system for a crane, focusing on that a crane moves in the direction of the work task. This means the actuating points of the crane are not fixed. Because actuating points are moving all over the girder supporting the crane, the points of damage to the structures can possibly be detected wherever they exist. The damage detection method is experimented, using a simply supported beam with a bolted splice at the center of beam. An impact load and a moving load test are performed for the crane girder. Both of loosening of the blots on the web and the flange connection plate of the crane girder are assumed as damaged incidents. The detection of potential damages is carried out in accordance with output measurement data of FFT (Fast Fourier Transformation) processing in the frequency domain. A coherence-based NDT method is used to identify the damage. The frequency of the first mode decreases as the damage increases. It is found that the ratio of the magnitude of the third mode to the first mode could be used to detect the loosening of the bolt.

Keywords: Damage detection; bolted connection; health monitoring.

1. Introduction

Health monitoring technologies for infrastructures have become widely used in Korea since the early 1990's. The intelligent health monitoring systems became ever more an important technology for civil infrastructures, such as long span bridge, offshore structures, nuclear power station, tall buildings and spatial structures. A method for the damage estimation of a bridge structures has been suggested by Yun et al. (2002), using ambient vibration due to traffic loading. This study showed that most of the inflicted damages can be detected successfully. As for a more efficient health monitoring of civil structures, its successful application to a vertical truss member has been reported by Park et al. (2003). The dynamic test using ambient vibration has been successfully applied to large scale cable-supported bridges such as the Golden Gate Bridge (Abel-Ghaffer and Scanlan 1985), the Quincy Bayview Bridge (Wilson and Gravelle 1991), and the Hitsuishijima Bridge (Okauchi et al 1997). A procedure for the system identification was used to base itself on output-only data. A study on output-only system identification for the structures using peak picking (PP) method and the time domain based stochastic subspace identification (SSI) method was tried by Ren (Ren 2002) based on the test result of the Beichuan Arch Bridge. The advantage and disadvantage of each method were also discussed.

The objective of this paper is to present a dynamic measurement method to identify potential damages to crane girders using piezoelectric sensors. Three types of forced vibration tests, such as free vibration testing, forced vibration testing, and ambient vibration testing, were tried on to identify the damage of the structures. Free vibration testing as a pre-test was performed for the cantilevers with or without a notch to check the sensitivity of the piezoelectric sensor. A constant displacement was applied at the tip of cantilever by dropping a weight. A vibration test was conducted on a simply supported beam subjected to an impact load of a Schmidt hammer. Next, a forced vibration test for the same beam was carried out for the moving load in order to investigate whether this method is applicable for the damage assessment or not. The beam is excited by moving the weight at a constant speed to simulate the crane girder. The potential damage identification is carried out according to the output measurement data of FFT (Fast Fourier Transformation) processing in the frequency domain. A coherence-based NDT method is applied to identify the damage to the test specimens subjected to both impact load and moving load.

2. Coherence-Based NDT Method

Damages to a structure such as cracks induce local flexibility and consequently loss of stiffness that affects the dynamic behavior of the structure to a considerable degree. Loss of stiffness results in reduction of natural frequencies and changes the mode shape. When the input to a structure is known and the response is measured, these changes in the dynamic behavior can be easily quantified by the frequency response function or the impedance function, which is the inverse of the frequency response function, of the intact and damaged systems.

When the input to a structure is not available, however, the frequency response function and the impedance can not be easily obtained. Then, the changes in the dynamic behavior need to be estimated based on the response output only. Since the local change in stiffness results in dynamic change, the change can be estimated by comparing individual outputs if more than one output are measured. If a defect exists between two adjacent measurement points, the linear relationship between two outputs is altered by the defect compared to the linear relationship between the two points where no defect exists. Therefore, by comparing the linear relationship between two adjacent outputs, the existence of a defect can be estimated.

In this paper, the linear relationship between two adjacent outputs is calculated using a coherence function. The coherence function provides nondimensional measurement of the linear dependence between two signals at each frequency. The coherence between $y_1(t)$ and $y_2(t)$ is defined as the ratio of the squared modulus of the cross-spectral density function to the auto-spectral density function as expressed in the following equation.

$$\gamma^2_{y_1 y_2}(\omega) = \frac{\left| S_{y_1 y_2}(\omega) \right|^2}{S_{y_1}(\omega) S_{y2}(\omega)} \tag{1}$$

where $S_{y_1 y_2}(\omega)$ is cross-spectral density function; and $S_{y_1}(\omega)$ and $S_{y2}(\omega)$ are auto-spectral density functions of $y_1(t)$ and $y_2(t)$, respectively. The value of the coherence function varies between 0 and 1:

$$0 \le \gamma_{y_1 y_2} \le 1 \tag{2}$$

Values near 1 indicate that the relationship between $y_1(t)$ and $y_2(t)$ at frequency ω is almost linear and very correlated, meaning that there is no defect between two points. If two signals are uncorrelated, their cross-correlation and

cross-spectral density have the value of zero, and consequently the coherence function is equal to zero, signifying the existence of local flexibility change.

Since the coherence-based non-destructive testing (NDT) method relies only on the measured output, this method is hardly affected by the input condition. Further, because the coherence function is based on the correlation between two signals, the coherence-based method is less dependent on noise.

3. Cantilever Beam Test

A series of free vibration tests were performed for the cantilever. The test structure is a cantilever beam of a steel plate with or without a notch as shown in Fig. 1. The purposes of this simple test are to examine how sensitive is the piezoelectric sensor to the normal strain due to bending and also to investigate the effect of the notch size. Piezoelectric sensors were used in this test because they are very cheap and sensitive and they do not require external electric power. Table 1 shows the electrical properties of the piezoelectric sensor used in this test.

Table 1. PZT properties

Item	Values
Resonant Frequency	6.5 ± 0.5kHz
Resonant Impedance	250Ω max
Operational Temp	$-20°C \sim +70°C$

The length from the free end to the fixed point is 270mm. Fig. 1 shows the location of PZT sensors and notch size. The notch at the beam was made by cutting out the plate to simulate a damage to the structure. In order to produce a consistent non-zero initial condition, a force of 3kN was applied at the tip and the thread was cut as shown in Fig. 2. After cutting the thread, the beam started to undergo free vibration, and the change in the voltage during the free vibration as measured by PZT sensors was obtained. The initial normal strain due to the bending moment at the location of PZT sensor can be calculated by a simple beam theory as expressed in the following equation.

$$\varepsilon = \frac{Ml}{EZ} = \frac{Pl \times 6}{E \times bt^2}$$ (3)

where, E is the modulus of elasticity of the steel; and P is the applied load; and l, b, and t are the distance from tip to PZT location, the width and the thickness of the plate, respectively. The calculated normal strain as measured at

the PZT location during the peak load was $32\mu\varepsilon$, which is a relatively small value compared to the yield stain ($1200 \sim 1600\mu\varepsilon$) of mild steel.

Fig. 3 shows the output voltage response from the PZT sensor for cantilever C0. Fourier transforms of the PZT data are shown in Fig. 4. The natural frequencies of undamaged beam (C0) and damaged beam (C30) were about 27.5 Hz and 25.4 Hz, respectively. As expected, natural frequencies are decreased as the size of the notch become bigger because the stiffness of the cantilever is decreased. It should be noted that the piezoelectric sensor responses very sensitively at very small normal strain and gives high voltage output at these test frequencies.
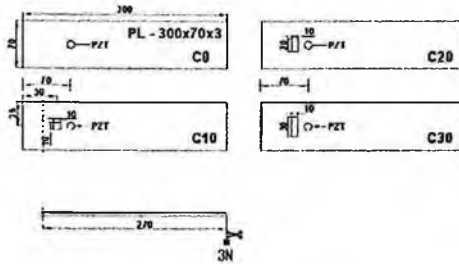
Fig. 1. Cantilever Beam   Fig. 2. Free vibration test of a cantilever beam
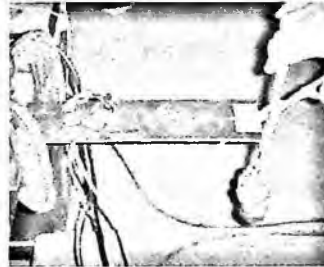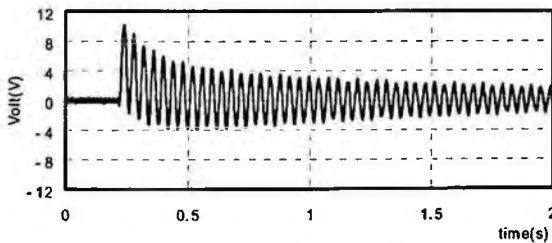
Fig. 3. Output voltage as measured by a PZT sensor for the cantilever specimen (C0)
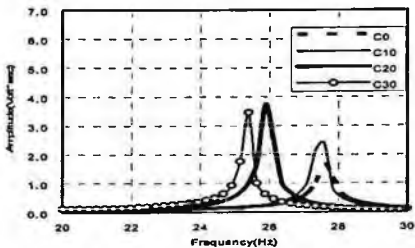
Fig. 4. Fourier transforms of the output data for the specimen with the weight of 3kN

4. Simply Supported Beam Subjected to Impact Load

4.1 Test setup and measurement

The damage detection methodology proposed in this study is illustrated experimentally using a simply supported 6000mm span beam with a bolted splice at the center (H-400 x200x8x13, SS400) as depicted in Fig. 5. An impact load using a Schumidt hammer was applied at the distance of 200mm from the center of the beam. The bolted splice was composed of 20 bolts - 8 bolts at the web and 12 bolts at the bottom flange only - as shown in Fig. 6. Four PZT sensors were attached as illustrated in Fig. 6.

The main causes of the damage to crane girders are the cracks around the welding or loosening of bolt connection due to the vibration. The variables of the test are whether the bolts are 'tightened (fixed)' or 'loosened (free)' on the web and flange. 'Fixed' represents the condition of the test that all group bolts are in slip-critical condition, which indicates a healthy connection. 'Free' represents the condition of the test that all group bolts are fully loosened and slightly tightened by a wrench, which indicates a damaged connection. The slip-critical connection was obtained by tightening all bolts (F10T M20) with torque of 14kN·m using a torque wrench as illustrated in Fig 7.

Table 2 summarizes the test variables depending on the tested connection damage(s). The data were sampled using PZT at a rate of 1000Hz for 20 seconds after applying the impact load. An oscilloscope (LeCory Scope Wavesurfer, WS454) was used for the data acquisition.

4.2 Test results

The time-history responses to the impact load were converted by FFT as shown in Fig. 9. A computer modeling using beam elements of the test specimen was also conducted to estimate the mode shapes and natural frequencies. It was found that the first mode, second mode and third mode occurred around 29Hz, 128Hz and 230Hz, respectively, as shown in Fig. 9. The second mode response is not clear because the tested simple beam is symmetrical, and PZT1~PZT3 are attached around the nodal point.

Fig. 10 shows the combined and enlarged FFT results for the four damage cases of the first mode as measured on PZT2. It can be seen that the frequency of 29.7Hz for [1]WX-FX specimen of healthy connection was decreased to about 28.7Hz for the cases of [2] and [3] with loosened bolts. The frequency and magnitude of each peak are selected and summarized in Table 3. It was found that

the frequency shifted to lower frequency direction once the bolts were loosened. However, it is not likely that the level of damage, from [2] to [4], does exactly portray the sensitive change in the frequency. Similarly, the frequencies and magnitudes of each peak around 230Hz for the third mode were selected and summarized in Table 3.

4.3 Review of test results

The magnitude of the third mode for each case was normalized to that of the first mode and shown in the last column of Table 3. The frequency changes are plotted in Fig. 11. As the level of damage increased, the natural period decreased. However, once the connection is damaged, it was not easy to identify the location of damage on the web or flange. Fig. 12 shows the change in the magnitude ratio of 3rd and 1st mode. It can be seen that the ratio tends to increase as the damage increases except for some cases.
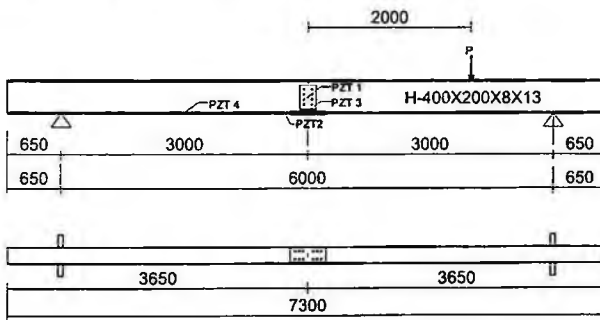
Fig. 5. Test setup
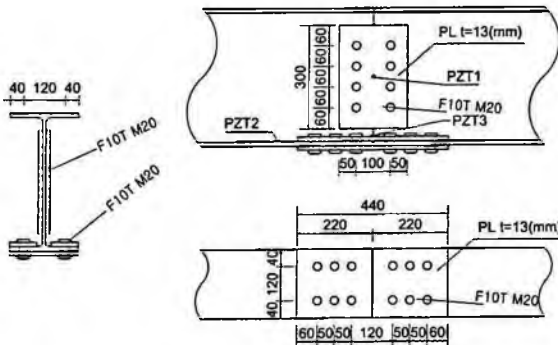
Fig. 6. Detail of the splice

Fig. 7. Bolt tightening by a torque wrench

Fig. 8. Applying the impact load

Table 2. Test variables

Test case	Web	Flange
[1]WX-FX	Web Fixed	Flange Fixed
[2]WF-FX	Web Free	Flange Fixed
[3]WX-FF	Web Fixed	Flange Free
[4]WF-FF	Web Free	Flange Free

Table 3. Test results

PZT	Test Case	1st Mode Freq. (Hz)	1st Mode Mag. (1)	3rd Mode Freq. (Hz)	3rd Mode Mag. (2)	Ratio (2)/(1)
PZT 1	[1]WX-FX	29.8	158.1	228.4	158.9	1.00
	[2]WF-FX	28.7	187.6	224.1	323.1	1.72
	[3]WX-FF	28.5	72.0	224.2	68.6	0.95
	[4]WF-FF	-*	-*	223.8	436.4	-*
PZT 2	[1]WX-FX	26.7	964.6	228.4	302.4	0.31
	[2]WF-FX	28.7	746.1	233.2	169.6	0.22
	[3]WX-FF	28.7	926.0	238.1	274.4	0.29
	[4]WF-FF	28.3	518.5	237.7	247.4	0.47
PZT 3	[1]WX-FX	29.7	367.7	235.1	157.8	0.43
	[2]WF-FX	28.7	260.9	230.4	160.0	0.61
	[3]WX-FF	28.7	507.6	229.4	208.1	0.41
	[4]WF-FF	28.3	345.1	228.6	163.8	0.47
PZT 4	[1]WX-FX	29.7	571.1	234.8	283.1	0.49
	[2]WF-FX	28.7	442.0	230.3	612.1	1.38
	[3]WX-FF	28.7	538.8	229.3	543.5	1.00
	[4]WF-FF	28.4	278.9	228.5	280.2	1.00

*: not clear
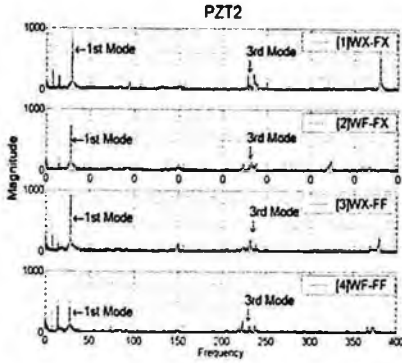
Fig. 9. FFT of the data measured on PZT2
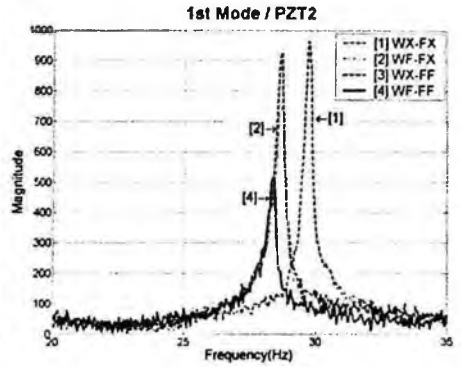
Fig. 10. FFT result of the 1st mode
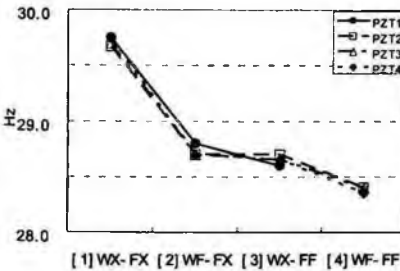
Fig. 11. Change of the first mode
Frequencies (Impact load)
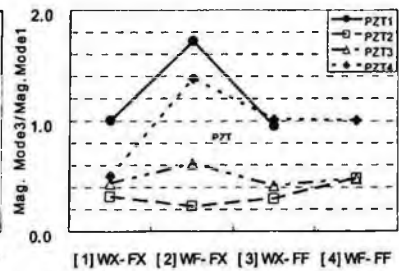
Fig. 12. Change in the magnitude ratio
of 3rd and 1st mode (3rd/1st, Impact load)

5. Simply Supported Beam Subjected to Moving Load

5.1 Test setup and measurement

The same beam described in the previous section was used for the simulation of the dynamic behavior of a crane girder under moving load condition. The force and constant speed of the moving load was 800N(80kgf) and 200mm/sec, respectively, as shown in Fig. 13. The same procedure of previous section was applied for the test case except for the moving load setup.

496

Fig. 13. Applying the moving load

5.2 Review of test results

The test results are summarized in Table 4. The frequency 23.2Hz of the first mode decreased in comparison with that of previous impact test because the mass of the moving system increased. Fig. 14 shows the change in the first mode frequencies. As the damage increased, the frequency also decreased except for the test case of [4]WF-FF with all loosened bolts. It is likely that the moment of

Table 4. Test results

PZT	Table Case	1st Mode		3rd Mode		Ratio (2)/(1)
		Freq. (Hz)	Mag. (1)	Freq. (Hz)	Mag. (2)	
PZT 1	[1]WX-FX	23.25	94.2	234.1	8.0	0.08
	[2]WF-FX	23.25	30.5	236.3	22.9	0.75
	[3]WX-FF	23.20	21.0	240.1	9.4	0.50
	[4]WF-FF	23.30	23.0	240.0	13.7	0.59
PZT 2	[1]WX-FX	23.25	337.0	232.5	13.1	0.03
	[2]WF-FX.	23.20	336.0	236.3	33.6	0.06
	[3]WX-FF	23.15	373.0	249.3	37.1	0.09
	[4]WF-FF	23.20	314.2	232.9	23.0	0.07
PZT 3	[1]WX-FX	23.25	154.2	239.9	12.9	0.08
	[2]WF-FX	23.20	103.0	236.3	29.0	0.28
	[3]WX-FF	23.15	196.5	240.1	12.2	0.06
	[4]WF-FF	23.25	208.5	236.3	17.6	0.08
PZT 4	[1]WX-FX	23.25	214.5	231.9	30.3	0.14
	[2]WF-FX	23.20	255.0	236.3	59.5	0.23
	[3]WX-FF	23.15	242.3	240.0	27.3	0.11
	[4]WF-FF	23.30	300.5	236.4	26.4	0.08
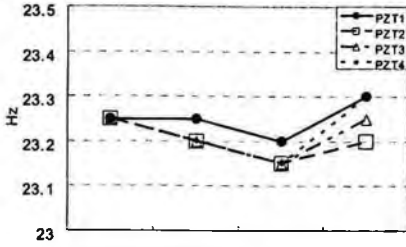
Fig. 14. Change of the first mode frequencies (Moving load)
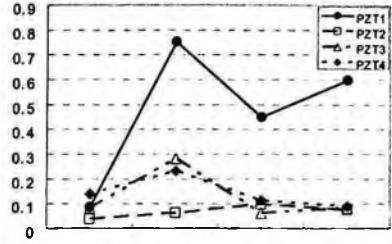
Fig. 15. Change in the magnitude ratio of 3rd and 1st mode ($3^{rd}/1^{st}$, Moving load)

inertia increased in this case by butting the top flanges when all bolts are loosened, which results in the increase of the stiffness of the system. Fig. 15 shows the magnitude ratio change after the inflicted damage to the specimen structure. When the web bolts are free while flange bolts are fixed, the magnitude ratio increases as measured by all PZTs. However, when the web bolts are fixed while the flange bolts are free, the magnitude ratio decreases again.

5.3 Analysis of coherence-based NDT method

The coherence-based NDT method is applied to identify the damage to the test specimens under both impact load and moving load conditions. Fig. 16 and Fig. 17 show the coherence between PZT2 and PZT3. The result indicates that the relationship between the flange connection plate and the flange becomes less linear as the stiffness of the entire system decreases.
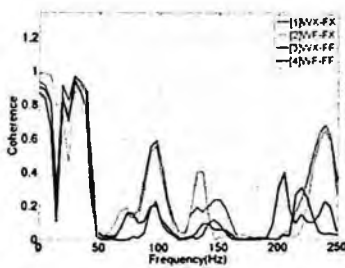
Fig. 16. Coherence between PZT2 and PZT3 (Impact load)
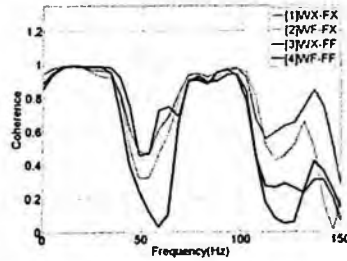
Fig. 17. Coherence between PZT2 and PZT3 (Moving load)

6. Conclusions

Both impact load and moving load tests were conducted for the identification of the inflicted damage to a crane girder. Only the bolt loosening technique was applied to simulate and test the damage to the steel girder. The responses of voltage history as measured by PZT sensors were converted through FFT as the output data to identify the damage of the girder. The frequency decreased as the damage increased. The amplitude of the first mode decreases as the bolts are loosened because the damping increases. The magnitude ratios of higher mode to lower mode tended to increase. The coherence between two adjacent PZT signals decreased as the stiffness decreased due to loosening of the bolt connection.

References

1. Abdel-Ghaffer, A.M. & Scanlan, R.H. 1985. Ambient vibration studies of Golden Gate Bridge. I: Suspended structure. *J. of Engrg. Mech.*, ASCE, 111(4): 463-482.
2. Bendat, J.S. & Piersol, A.G. 2000. *Random data analysis and measurement procedures*, New York, John Wiley & Sons.
3. Cunha, A., Caetano, E., & Delgado, R., 2001. Dynamic test on large cable-stayed bridge. *J. Bridge Engrg.*, ASCE, 6(1): 46-53.
4. Okauchi, I., Miyate, T., Tatsumi, M., & Sasaki, N. 1997. Field vibration test of a long span cable-stayed bridge using large exciters. *J. Struct. Engrg. / Earthquake Engrg.*, Tokyo, 14(1): 83-93.
5. Park, S.H., Yi, J.H., Yun, J.G., & Roh, Y.R. 2003. Impedance-based damage detection for civil infrastructures using smart PZT transducers. *Proceedings of the Sixteenth KKCNN Symposium in Civil Engineering.*: 255-260.
6. Ren, W.-X. 2002. Output-only system identification of civil engineering structures. *Proceeding of the US-Korea Workshop on Smart Infra-Structural System*, Busan, Korea: 333-343.
7. Wilson, J.C., & Gravelle, W. 1991. Modeling of a cable-stayed bridge for dynamic analysis. *Earthquake Engrg. and Struct. Dyn.*, 20: 723-747.
8. Yun, C.B., Lee, J.J., Kim, J.D., & Lee, J.W. 2002. Damage estimateion method for bridges using ambient vibration data. *Proceedings of the US-Korea Workshop on Smart Infra-Stuctural System*, Busan, Korea: 283-290.

CHARACTERIZATION OF CRACK DETECTION METHODS USING STRAIN MODE SHAPES ON PLATES WITH VARIOUS GEOMETRY

BEOM-SEOK KIM

*Test Center Team, Engineering and Technology Institute, KEFICO Corporation,
410, Dangjeong-dong, Gunpo-si, Gyeonggi-do, 435-716, Korea*

SEUNG-HYUN YOO

*Dept. of Mechanical Engineering, Ajou university,
Wonchon 5, Suwon-si, Gyeonggi-do, 442-749, Korea*

The existence of a crack in a structure produces changes in modal parameters of it such as natural frequencies, damping, displacement and strain mode shapes. This paper is focused on characterization of crack detection methods using strain mode shapes with hexagonal and circular hollow plates. We changed the location of crack and the geometry of plate. Rest of the condition was fixed. For crack detection criteria, COMAC, ECOMAC, ADSM and the new method have been used and the results are compared with each other. The COMAC, ECOMAC and ADSM showed limited capacity of crack detection on plates but the new method gave good results in 90% of all cases.

1. Introduction

Generally, all materials used in engineering system inherit initial flaws. That's why structure monitoring and structure health monitoring have been a popular research topic for the last several decades. The basic idea for this approach starts from the fact that changes of the physical properties such as boundary conditions, stiffness, mass and damping caused by damage in a system result in changes of the dynamic characteristics (i.e. natural frequencies, modal damping and mode shapes) of the system. In this approach, the initial data or the model of the undamaged system are required to perform damage detection. This is a drawback of damage detection using modal analysis.

Damage detection can be classified as following four levels. The four levels are [1]:

1. Identify that damage has occurred;
2. Identify that damage has occurred and determine the location of damage;

3. Identify that damage has occurred, locate the damage, and estimate its severity; and

4. Identify that damage has occurred, locate the damage, estimate its severity, and determine the remaining useful life of the structure.

Since it is found that using strain mode shapes for damage detection is more sensitive than displacement mode shapes, and our concern is on two dimensional structures, our research is focused on characterization of crack detection methods using strain mode shapes. In this paper, we want to find out which crack detection method is capable to identify a crack in the plate at least level 2 of damage detection shown above.

2. Implementation of Strain Mode Shapes

The DFRF (Displacement Frequency Response Function) $H_{jk}(\omega)$ between the excitation point k and response point j and SFRF (Strain Frequency Response Function) $S_{jk}(\omega)$ are [2]:

$$H_{jk}(\omega) = \sum_r \frac{_r\phi_j \cdot _r\phi_k}{\omega_r^2 - \omega^2 + i2\zeta_r \cdot \omega_r \cdot \omega}. \tag{1}$$

$$S_{jk}(\omega) = \sum_r \frac{_r\varepsilon_j \cdot _r\phi_k}{\omega_r^2 - \omega^2 + i2\zeta_r \cdot \omega_r \cdot \omega}. \tag{2}$$

where

ω_r , ζ_r : natural frequency and damping ratio of mode r, respectively;

$_r\phi_k$: displacement mode shape of mode r in point k;

$_r\varepsilon_j$: strain mode shape of mode r in point j

3. Specimens

(a) Hexagonal plate

(b) Circular hollow plate
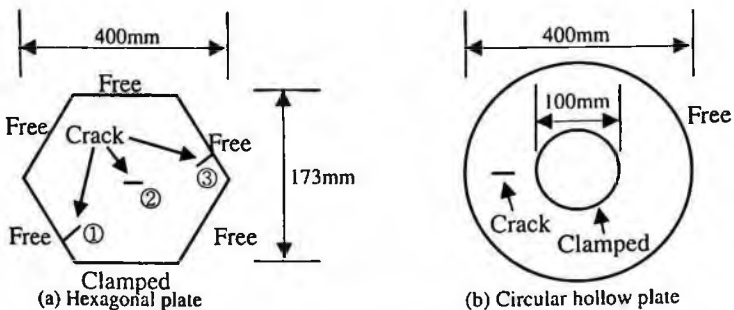
Fig. 1. Geometry of steel plates

A hexagonal and a circular hollow steel plates were chosen as specimens. Each plate has only one through-wall crack and the location of the crack is shown in Figure 1.

The material properties of these plates are; Young's modulus E=206.97GPa, Poisson's ratio v=0.296, Density ρ=7906.97kg/m^3 which are taken from real experiments. Table 1 shows the real and numerical experimental model of the plates. The finite element analysis was performed in ABAQUS 6.5.

Table 1. Experimental model of plates

Plate type	Dimension[mm]	Boundary condition	Finite element model	
			Element type	No. of elements
Hexagonal	400x173, t=1	Clamped in one edge	Shell S4R	266ea
Circular hollow	ID 100, OD 400, t=1	Clamped in inner rim	Shell S4R	288ea

4. Crack Detection Methods

There are lots of damage detection methods that can use strain mode shapes. As we are focused on damage detection methods that can at least detect the existence and the locations of the crack, COMAC(Coordinate Modal Assurance Criteria), ECOMAC(Enhanced COMAC), ADSM(Absolute Difference Strain Mode shape) and our proposed new method are examined.

COMAC(Eq. 3) is proposed to detect the differences occurred in the mode shape vectors and the location of the change [3]. ECOMAC(Eq. 4) is based on the average difference between the vector components [4]. ADSM(Eq. 5) is based on the absolute difference of strain mode shapes [5]. And the new method(Eq. 6) is based on the absolute difference of absolute value strain mode shapes [6].

$$\text{COMAC }(i) = \frac{\left(\sum_{j=1,2\ldots m} {}_i\phi_{Aj}\, {}_i\phi_{Bj} \right)^2}{\left(\sum_{j=1,2\ldots m} {}_i\phi_{Aj}^2 \right)\left(\sum_{k=1,2\ldots m} {}_i\phi_{Bk}^2 \right)} \, . \tag{3}$$

$$\text{ECOMAC }(i) = \frac{\sum_{j=1,2\ldots m} \left| {}_i\phi_{Aj} - {}_i\phi_{Bj} \right|}{2m} \, . \tag{4}$$

$$\text{ADSM} = \left| \Psi_A - \Psi_B \right| . \tag{5}$$

$$\text{New method} = \left\| \Psi_A \left| - \right| \Psi_B \right\| . \tag{6}$$

where,

m   : number of modes

$_i\phi_{Aj}$, $_i\phi_{Bj}$: i^{th} degree of freedom of jth strain mode shape without and with crack, respectively

Ψ_A , Ψ_B : strain mode shape matrix without and with crack, respectively

5. Crack Detection in Hexagonal Plate

5.1. *Crack Location* ①

(a) COMAC   (b) ECOMAC   (c) ADSM-2nd mode   (d) New method-2nd

mode
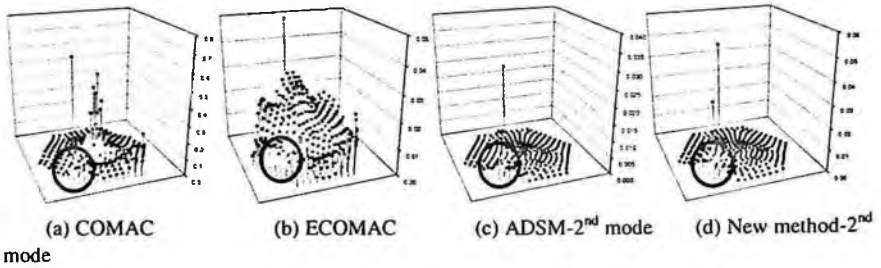
Fig. 2. Result of crack detection; Hexagonal plate

As shown in Figure 2, all crack detection criteria detected the crack ① in the hexagonal plate as damage detection level 2.

5.2. *Crack Location* ②

(a) COMAC   (b) ECOMAC   (c) ADSM-2nd mode   (d) New method-2nd

mode
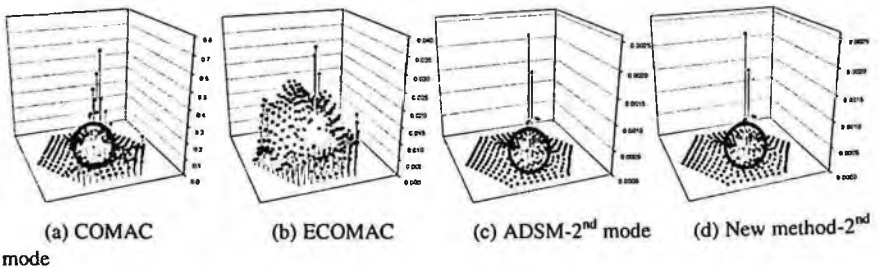
Fig. 3. Result of crack detection; Hexagonal plate

As shown in Figure 3, all crack detection criteria except ECOMAC detected the crack ② in the hexagonal plate as damage detection level 2.

5.3. Crack Location ③

(a) COMAC
mode

(b) ECOMAC

(c) ADSM-2nd mode
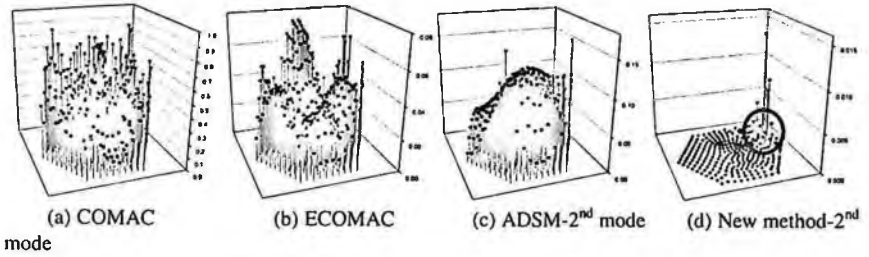
(d) New method-2nd

Fig. 4. Result of crack detection; Hexagonal plate

As shown in Figure 4, only the new method detected the crack ③ in the hexagonal plate as damage detection level 2.

6. Crack Detection in Circular Hollow Plate

(a) COMAC

(b) ECOMAC

(c) ADSM-4th mode

(d) ADSM-6th mode

(e) ADSM-10th mode
mode

(f) New method-4th mode

(g) New method-6th mode

(h) New method-10th
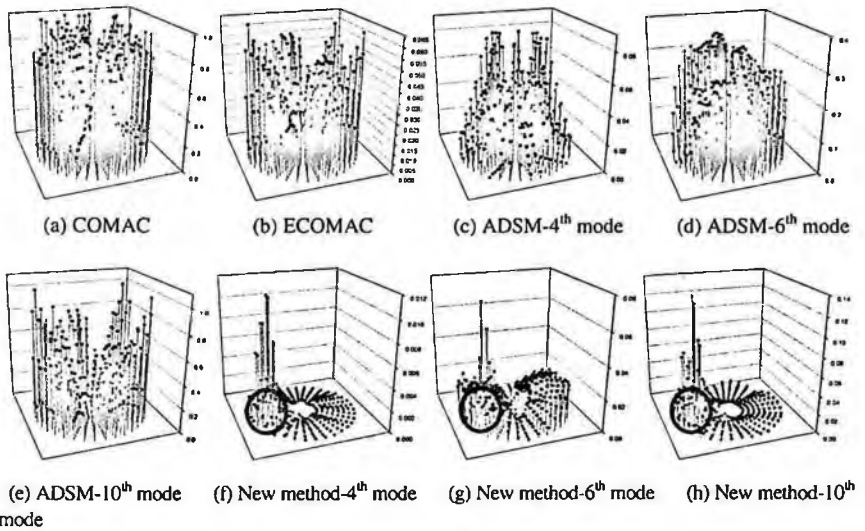
Fig. 5. Result of crack detection; Circular hollow plate

As shown in Figure 5, COMAC and ECOMAC failed to detect the crack in plate. ADSM found the crack only in few modes. But as for the new method, it detected the crack in plate in most cases. However, crack detection capability of both ADSM and the new method are affected by the applied mode number.

504
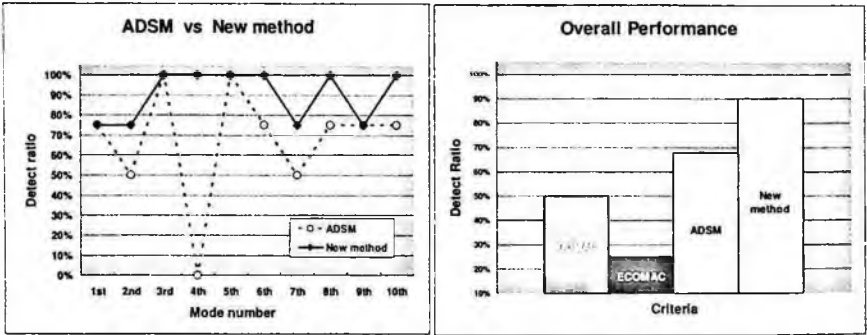
7. Overall Result

(a) ADSM vs new method   (b) Overall performance
Fig. 6. Overall performance of crack detection criteria

In Figure 6(a), the result comparison between ADSM and the new method is given. The new method shows better result than ADSM. ADSM detected crack 100% only in 3rd and 5th mode but the new method detected 100% in 3rd, 4th, 5th, 6th, 8th and 10th modes. The worst detection ratio of ADSM was 0% but that of the new method was 75%.

The overall performance of crack detection criteria mentioned in this paper is shown in Figure 6(b). COMAC and ECOMAC detected the crack in plate only by 50% and 25%, respectively while ADSM and the new method detected by 68% and 90%, respectively.

8. Conclusion

Characterization of crack detection methods is given by with hexagonal and circular hollow steel plates. COMAC, ECOMAC and ADSM showed limited capability in crack detection but the proposed new method seems to be robust enough and gives satisfactory results almost every case in crack detection using strain mode shapes.

References

1. A.Rytter, *Doctoral Dissertation, University of Aalborg* (1980).
2. J.H.Cha, T.H.Ha and G.M.Lee, *Transaction of the Korean Society for Noise and Vibration Engineering*, **V8**, 420 (1998).
3. S.Alampalli, G.Fu and E.W.Dillon, *J. of Structural Engineering*,237 (1997).
4. W.Heylen and P.Avitabile, *Proceedings of 16th IMAC*, 207 (1998)
5. Q.Quan and Z.Weoguo, *Proceedings of 16th IMAC*, 945 (1998).
6. S.H.Yoo, H.K.Kwak and B.S.Kim, *Proceedings of 17th IMAC*, 1902 (1999).

DETECTION OF VARIOUS DAMAGE PATTERNS USING IMPEDANCE MEASUREMENT AND STATISTICAL POST PROCESSING[*]

YONG HONG[+]

Department of Precision Mechanical Engineering, Chonbuk National University, Jeonju Si, Chonbuk 561-756, South Korea

SEUNG-HO HWANG

Department of Precision Mechanical Engineering, Chonbuk National University, Jeonju Si, Chonbuk 561-756, South Korea

DONG-PYO HONG

Department of Precision Mechanical Engineering, Chonbuk National University, Jeonju Si, Chonbuk 561-756, South Korea

YOUNG-MOON KIM

Department of Architectural Engineering, Chonbuk National University, Jeonju Si, Chonbuk 561-756, South Korea

Detection of various damage patterns that result in structural fatigue, fracture, etc. is presented in this paper. In addition to the one-fold damage pattern, diverse patterns of damage, such as cracks, bolt-loosening, holes, are more common forms in real structures. The smart sensors, i.e. piezoceramic (PZT) sensors, offer special opportunities for the detection of the different types of damages. When a structure suffers from damages, the mechanical impedance of the structure changes correspondingly. The change of the mechanical impedance of a structure by damage is sensitively indicated by the change of the electro-impedance of PZT sensors, which are bonded to the structure. However, because diverse damage patterns, i.e. cracks, holes, bolt-loosening, etc. have their own characteristic influences on the structure, it is considerably difficult to distinguish the damage patterns. Therefore, post processing based on a statistical method is performed to obtain information for the efficient estimation of diverse damage patterns. The results of the post processing can provide a unique estimation index for each damage pattern.

505

1. Introduction

Rapid economic development has given rise to much higher and stricter criteria and requirements for SHM. The NDE technique is especially a major concern. For the majority of large structures, beams are the most essential and primary components that connect and form the structures. The PZT sensors, which simultaneously act as an actuator and sensor, are widely used for SHM. The PZT technique based on E/M impedance is very sensitive in the evaluation of incipient and small damages[1, 2]. We present the performance of the electro-mechanical impedance based technique for detecting damage on a beam sample.

2. Impedance Measurement Method

2.1. *Basic Theory of Impedance Measurement Method*

The structures that are damaged by internal or external factors such as a crack or corrosion suffer from changes of stiffness and damping from their normal states as well as from the change of the mechanical impedance of the structure. Impedance measurement is used to assess the condition of a structure by utilizing the relation between the mechanical impedance of the structure and the electrical impedance of the PZT.

$$Y = i\omega \frac{w_a l_a}{h_a} \left[\varepsilon_{33}^T (1 - i\delta) - \frac{Z_s(\omega)}{Z_s(\omega) - Z_a(\omega)} d_{3x}^2 Y_{xx}^E \right] \tag{1}$$

The frequency-dependent electrical admittance can be obtained by using the PZT and the structure's mechanical impedance. If the impedance of the structure is constant under the undamaged condition, then we can assume that the resonance frequency band may be shifted by the variation of the impedance under the damaged condition.

2.2. *Synopsis of Impedance Measurement with Using a PZT*
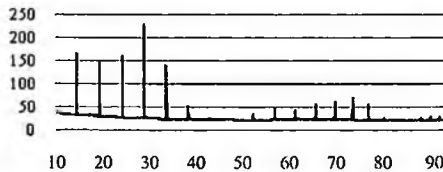
Fig. 1. Impedance response of health condition about beam structure.

By using an impedance analyzer, HP 4192A, we can detect minute damages in a structure [3]. To measure the mechanical impedance of the aluminum beam, a frequency region and resolution are input into the impedance analyzer by using a computer remote program. A certain alternating signal that corresponds to the input data is transmitted to the PZT. The electric potential within the PZT due to a harmonic longitudinal elastic wave generated in the beam changes, and the change of the electric impedance that is processed by the impedance analyzer is transmitted to the computer.

2.3. The Impedance Response of a Normal Structure

Table 1. Properties of aluminum beam and piezo-electric Sensor.

Aluminum Beam Element	Thickness	2
	Density	2.70
	Young's Modulus	7.06
Piezo-electric Element	Density	7.4
	Relative dielectric constant	2000 ±300
	Piezo-electricity constant	-195
	Young's Modulus	5.8
	Induced loss	2.1
	Frequency Constant	1400

When both ends of a beam are free or when they are fixed, the natural frequency of a beam by longitudinal elastic vibration is given by Eq. (2). By substituting the data from Table 1 into Eq. (2), the natural frequency of the specimens was found to be 2.062 kHz. Figure 1 presents the impedance response results from 10 kHz to 100 kHz in the health condition. We used the real part of the impedance for data analysis because it is easy to identify the resonant frequency of the beam with respect to the structural response.

$$f_n = \frac{c}{2l}n = \frac{n}{2l}\sqrt{\frac{E}{\rho}}, n = 1,2,3,\ldots$$

(2)

2.4. Experimental Method and Specifications

2.4.1. Test A: Damage by cyclic load

We attached sensors with the dimension of is 25×4×0.3 mm^3 to the end of specimen. Damage was applied to two regions which were apart from each other by as much as 100 mm and 200 mm, and we applied cyclic force until the specimen suffered from fatigue failure. We damaged the specimen gradually with the cyclic load, until we could see the surface of failure with the naked eye. Two points were examined, when the specimen began to show mechanical failure by the cyclic load. And the failure generated on both sides by the cyclic load.

Fig. 2. The impedance measurement instrument and test specimen.

508

(a)10cm health   (b)10cm damaged (c)10cm cracked   (d)20cm health   (e)20cm damaged
Fig. 3. Specimen of cyclic load test.

2.4.2. *Test B: Damage by tensile load*

Fig. 4. Load Input of tensile test.
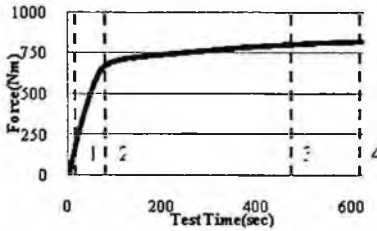
Test Spec	1	2	3	4
Force(Nm)	214.99	745.85	772.48	820.33
Time(sec)	20.2	84.4	464.4	605.4
Extended length(mm)	0.505	2.110	11.610	15.135

We extended the specimen by using a tensile machine and measured the impedance response in four regions as shown in Figure 4

3. Data Analysis

3.1. *Test A: Damage by Cyclic Load*
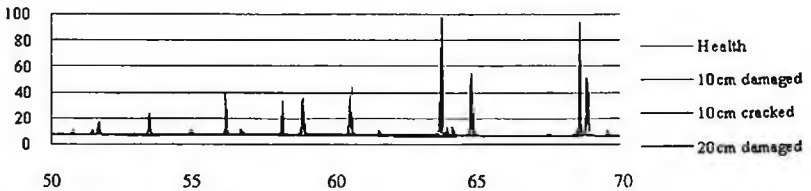
Fig. 5. Impedance response of cyclic load applied specimens.
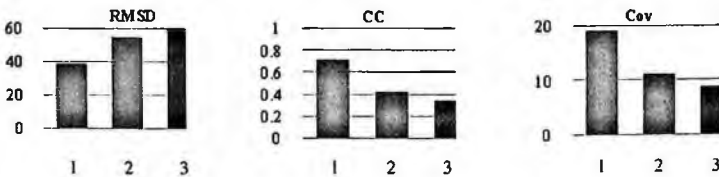
Fig. 6. Statistical analysis results of cyclic loaded impedance response data (1. 10cm damaged; 2. 10cm cracked; 3. 20cm damaged).

The tendency of impedance waveform of the specimen, which was damaged by cyclic load, was almost same with that of the specimen under the health condition. The peak frequency moved to a low frequency band over all. In one

region, 50~70 kHz, the amount of peak movement was prominent. The peak frequency shifts were not suitable for evaluating the damaged by cyclic load of the specimen. We applied statistical indices because the peak shift tended to be almost regular. The method that uses statistical evaluation indices is a simpler analysis algorithm and has a faster process rate than peak frequency shift quantity. Because the statistical evaluation index used all of the measured frequency domain,   error was reduced and the reliability was increased.

$$Cov = \frac{1}{N} \sum_{i=1}^{N} (x_i - \overline{x})(y_i - \overline{y}) \qquad CC = \frac{Cov(x, y)}{\sigma_x \sigma_y} \tag{3}$$

where, x_i is the impedance peak frequency of the damaged condition , y_i is the impedance peak frequency of the healthy condition , $\overline{x}$ is the mean value of x_i, $\overline{y}$ is the mean value of y_i.

As we can see in Figure 6, when the damage progresses, CC and Cov evaluation indices decrease, except the RMSD. The damage in this experiment was more local than that of the damage types, like slit type and hole type, in the previous experiment, but, generally, the damage spread.

3.2. *Test B: Damage by Tensile Load*

The impedance measurements of the extended specimens are shown in Figure 8. The impedance response is very different by cyclic load test. The cyclic load gives only local damage but stress and deformation by tensile load influence on whole specimen. The result, which was analyzed based on the statistical method data of the cyclic load test, was not quantitative data, so it was impossible to know the growth of the damage and the specimen condition through the result. Figure 7 shows the impedance peak frequency shift quantity.
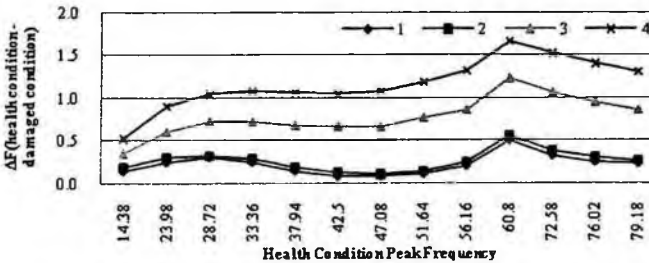
Fig. 7. Impedance peak frequency shifting value.

Peak frequency shift value of specimens 3 and 4, which showed great change of length by the tensile force, are more than specimens 1, 2 which showed a small change of length. Also, once the extension starts, the shift of the peak prominently grows, but the change of width is small, until the change of shape is large through the yield point. The tendency of change of impedance in the frequency domain is shown to be the same in all specimens, and we can realize the fact that the width of change is small in 35~50 kHz and the width of change is large in 55~75 kHz. Whether or not the magnitude of tension applied to the

510

specimen and the force of what?? Are over the yield point can be determined by observing the peak shift variation. Another impedance wave form variation is the variation of the value of the peak with the frequency band.
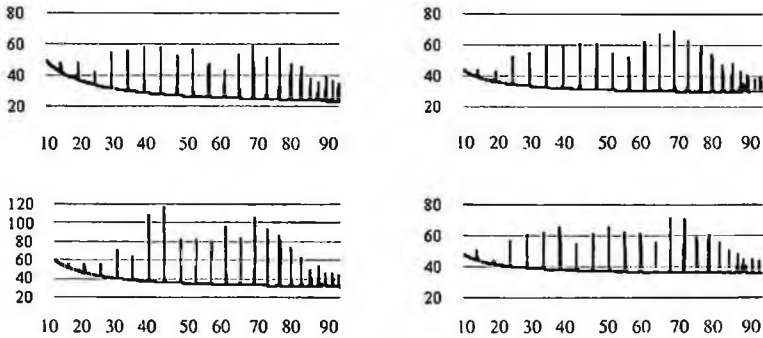
Fig. 8. Impedance response of tensile force loaded specimens (from left top specimen 1, 2, 3, 4).

4. Conclusions

The characteristic of whole test piece did not change in the first experiment , in which crack is produced in the test piece by cyclic load and impedance measurement is changed by the sectional damaged member. Therefore, the minute change of peak shifting must be analyzed. Statistical analysis index can be used to detect considerably small damages by comparison of what with what of the specimen under health condition and by quantitative estimation. Compare with health condition in the second experiment that whole characteristic alters in test piece and could know that tests piece whole characteristic altered by tensile force. Can know that as tensile force which is imposed in test piece increases, peak frequency shifting value increases and that frequency travel increases sharply if tensile force that pass over yield point of material is inflicted.

Acknowledgments

References

1. G. Park, H. Sohn, R. Farrar and D. J. Inman, *The Shock and Vibration Digest.* **Vol. 35 No.6,** 451 (2003).
2. G. Park, H. Cudney and D. J. Inman, *ASCE, Journal of Infrastructure System.* **6,** 153 (2000).
3. Victor G. and Andrei N. Z., *Journal of Vibration and Acoustics.* **Vol. 124,** (2002).

MEASUREMENT AND MONITORING OF MECHANICAL LOADS OF LARGE SLENDER STRUCTURES USING DISTRIBUTED FIBER OPTIC SENSOR

JONG WON LEE, YOUNG CHEOL HUH, JAE HEE PARK, YONG YUN NAM,
GEUN HO LEE, YOUNG JUN PARK

*System Engineering Research Division, Korea Institute of Machinery and Materials, 171
Jang-dong, Yuseong-gu, Daejeon, 305-343, Korea*

JUNG YUL KIM, YOO SUNG KIM, AND YONG BAE LEE

*Soam Consultant Co., Ltd., 92 Gwahagno, Yuseong-gu
Daejeon, 305-350, Korea*

A method for measurement and monitoring of mechanical loads in large slender structures is presented based on continuous strain data obtained from distributed fiber optic sensor. An experimental study was carried out on an aluminum cantilever beam. A static load test was performed and the calculated moment based on the measured strain from the distributed fiber optic sensor agrees well with the actual applied moment. A series of damages was inflicted on the beam, and free vibration tests were carried out for each damage case. The estimated natural frequencies using the dynamic strain measured by the distributed fiber optic sensor for each damage case are found to compare well with those from a conventional accelerometer and a numerical analysis based on an energy method.

1. Introduction

Measurement of mechanical loads of large slender structures such as blades and towers of large-scale wind turbines and long-span bridges is required before their operation. Furthermore, preventive maintenance and structural safety information for the large slender structures may be guaranteed by application of structural health monitoring (SHM) systems.

Recently, smart materials such as optical fiber and piezoelectric material have been well utilized in the field of SHM. Fiber optic sensors (FOSs) have a number of advantages over conventional sensors such as electro-magnetic interference (EMI) immunity and multiplexing capabilities. FOSs can be categorized according to whether sensing is distributed, localized (point), or multiplexed [1]. Brillouin optical time-domain reflectometer (BOTDR) are one of the typical distributed strain sensors. The measurement systems of the

BOTDR could measure static strain only [2]. However a measurement system (DTSS: distributed temperature and strain sensing) of the BOTDR which can measure not only static strain but also dynamic strain was recently developed by Sensornet. The advantage of the distributed FOS such as the BOTDR is to improve damage detection by having a large coverage of sensors on the structure with the long gage length and the long measurement range of one fiber optic cable. The local effects in the measurements can also be avoided by sensing with the long gage length.

In this study, a method for measurement and monitoring of mechanical loads in large slender structures is presented based on continuous strain data obtained from distributed FOS. Static and vibration tests were performed on an aluminum cantilever beam to verify the distributed FOS for measurement and monitoring. To our knowledge, this is the first time that the dynamic strain measured by the distributed FOS has been applied to SHM.

2. The Distributed Fiber Optic Sensor

The bulk of the scattering radiation in the fiber is Rayleigh scattering. A smaller portion of the scattered radiation is made up of Raman and Brillouin reflections. Both Raman and Brillouin reflections consist of two components, known as Stokes and anti-Stokes light. Because each has a different wavelength from the original light in the fiber, each appears as a different color. Figure 1 shows the 3 scatterings conceptually.
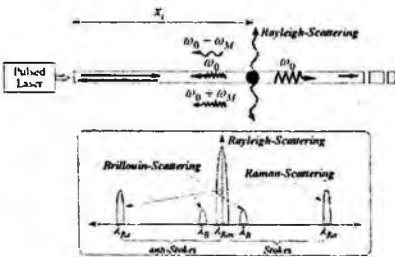
Fig. 1. Fundamentals of distributed FOS.
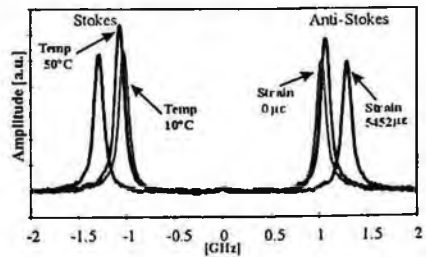
Fig. 2. Change of Brillouin frequency and power.

Figure 2 shows changes in both Brillouin frequency and power caused by changes in temperature and strain. The Sensornet DTSS measures the entire Brillouin spectrum (the Stokes light) at every 1 m along the fiber [3]. Analysis of this data allows to uniquely measure strain and temperature simultaneously and independently at every position along the fiber, resulting in no temperature and strain cross-sensitivity. The latest DTSS system provides a unique measurement

of dynamic distributed strain, allowing detection of real-time changes in structures by measuring strain at acquisition rates of up to 10 Hz.

3. Crack Modeling Using the Energy Method

An equivalent bending stiffness (EI_c) for the beam which has the open crack can be derived as Eq. (1) by using the change of strain energy due to the occurrence of the crack based on an energy balance approach, and by applying the stress intensity factor (K_I) of solid rectangular cross-section for opening mode (Mode I) [4].

$$EI_c = \frac{EI}{1 + EI \cdot R(a,c)/\{1 + [(x-c)/(k(a)a)]^2\}} \tag{1}$$

where $R(a,c) = \dfrac{2D(a)}{k(a)a\,[\arctan((1-c)/(k(a)a)) + \arctan(c/(k(a)a))]}$,

$D(a) = \dfrac{18\pi(F(a))^2 a^2}{Ebh^4}$, and $k(a) = \dfrac{3\pi(F(a))^2(h-a)^3 a}{[h^3 - (h-a)^3]h}$

where $F(a)$ is the boundary correction factor for K_I, a is the crack depth, c is the crack location, b is the width of beam, and h is the depth of beam.

For an Euler beam which has the crack, the characteristic equation can be obtained as

$$\frac{d^2}{dx^2}\left[EI_c \frac{d^2 W}{dx^2}\right] - m\omega_c^2 W = 0 \tag{2}$$

where m is the mass density along the beam length, $w(x,t) = W(x)Q(t)$ where $w(x,t)$ is the transverse displacement, and ω_c is the natural frequency of the cracked beam.

4. Experimental Study

4.1. *Experimental Setup and Test Procedure*

A cantilever beam was built to verify the applicability of the distributed FOS for measurement of mechanical load and SHM as shown in Figure 3. The length, width, and depth of the beam were 5.7 m, 0.05 m, and 0.05 m, respectively. The material of the beam was pure aluminum, of which modulus of elasticity and density were 70 GPa and 2710 kg/m^3, respectively.
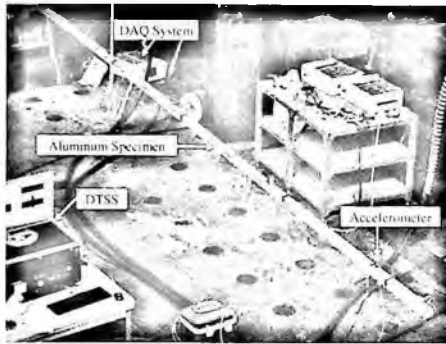
Fig. 3. Experimental setup for the cantilever beam.
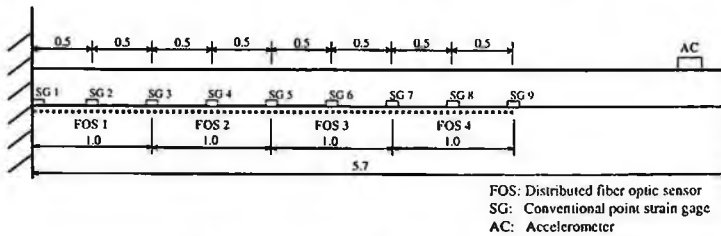
Fig. 4. Sensor locations (lengths in m).

The distributed FOSs (FOS 1 - FOS 4) that have the gage length of 1 m were attached along the beam to the bottom side as shown in Figure 4. For the purpose of comparison, the conventional point strain gages (SG 1 - SG 9) that have the gage length of 5 mm were also attached to the bottom side of the beam as shown in Figure 4. A conventional accelerometer was attached at the end of the beam to compare the vibration data measured by the distributed FOSs.

Static strains under a vertical point load (245 N) at the free end of the beam were measured using the distributed FOSs and conventional point strain gages. Static measurement using the DTSS was carried out for 20 minutes, and about 50 sweeps were performed during the 20 minutes.

The cracks were inflicted by making fine saw cuts in the top side of the beam at the location of 0.57 m ($c/L = 0.1$) from the fixed end. Five cases of damages ($a/h = 0.1, 0.2, 0.3, 0.4$, and 0.5) were introduced by changing the depth of the inflicted crack.

Three free vibration tests were performed for the intact case and each of the 5 damage cases. The dynamic strains were obtained by the distributed FOSs with the sampling rate of 8.7 Hz and sampling duration of 140 sec., while the vertical vibration of the beam was measured by the conventional accelerometer.

4.2. *Results of the Static Tests*

The 4 continuous static strains and the 9 point static strains are shown in Table 1 with the bending moments. It can be found that the distributed FOS can be applied for measuring the bending moment. The error for FOS 1 is bigger than those for the others because FOS 1 could not be fully attached to the fixed end of the beam considering the bending loss of the fiber optic cable. It is expected that the errors for the conventional gages become severe in real structures due to the EMI and local effects, while the distributed FOS can exclude those effects.

Table 1. Measured strains and bending moments.

Location (m)	Strain ($\mu\varepsilon$)		Bending Moment (Nm)		
	FOS	SG	From FOS	From SG	Applied
0.0	-	956	-	1394 (0.70)	1384
0.5	840	864	1225 (2.92)	1259 (0.19)	1262
1.0	-	781	-	1139 (0.03)	1139
1.5	695	699	1014 (0.29)	1019 (0.24)	1017
2.0	-	612	-	892 (0.20)	894
2.5	523	529	762 (1.26)	771 (0.04)	772
3.0	-	443	-	646 (0.51)	649
3.5	356	360	519 (1.47)	525 (0.34)	527
4.0	-	271	-	395 (2.17)	404

Note 1) Location is distance from the fixed end.
Note 2) Location of the FOS is distance between the center of the sensor and the fixed end.
Note 3) The values in parentheses are errors in % for the applied moment.

4.3. *Results of the Vibration and Damage Tests*

The first natural frequency of the intact beam estimated from the dynamic strain data measured by the distributed FOSs is 1.245 Hz, while those from the conventional accelerometer, the numerical analysis based on Eq. (2), and the exact solution are 1.250, 1.260, 1.260 Hz, respectively. Those are all agree well. The ratios of the first natural frequencies between before and after the damages (ω_c / ω) calculated using the numerical analysis based on Eq. (2) are compared with those obtained from the distributed FOSs and the conventional accelerometer for the 5 damage cases in Figure 5. The frequency decreases as the damage becomes severe, and the results from the distributed FOSs are found to be in good agreement with the results from the conventional accelerometer and numerical analysis. Hence, the distributed FOS can be utilized in the vibration-based SHM.

516
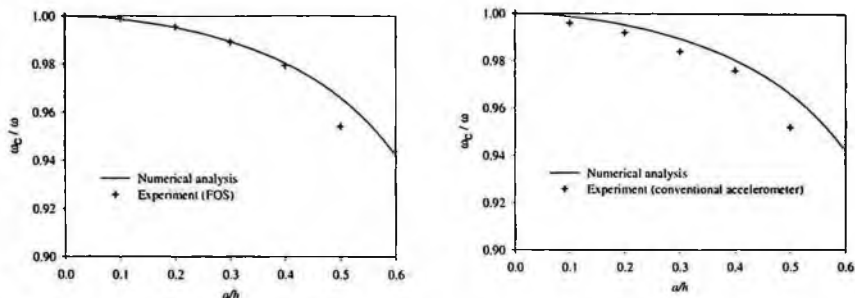
(a) Distributed FOS   (b) Conventional accelerometer

Fig. 5. Variation of the first natural frequencies according to crack depth.

5. Concluding Remarks

A method for measurement and monitoring of mechanical loads in large slender structures is presented based on continuous strain data obtained from distributed FOS. It has been found that the calculated moment based on the measured strain from the distributed FOS agrees well with the actual applied moment. It has been also found that the estimated natural frequencies using the dynamic strain measured by the distributed FOS for each damage case are found to compare well with those from a conventional accelerometer and a numerical analysis. Therefore, the distributed FOS can be well utilized for measurement and monitoring of mechanical loads in large slender structures.

References

1. C. I. Merzbacher, A. D. Kersey and E. J. Friebele, *Smart Mater. Struct.* **5**, 196 (1996).
2. H. Ohno, H. Naruse, M. Kihara and A. Shimada, *Optical Fiber Technology* **7**, 45 (2001).
3. T. R. Parker, M. Farhadiroushan, V. A. Hnderek and A. J. Rogers, *IEEE Photonics Technology Letters* **9**, 979 (1997).
4. X. F. Yang, S. J. Swamidas and R. Seshadri, *Journal of Sound and Vibration* **244**, 339 (2001).

MATERIAL CHARACTERIZATION OF LOCK PLATE FOR GAS TURBINE PLANT

YOUNHO CHO[†]

Associatet Professor, School of Mechanical Engineering, Pusan National University, San 30 Jangjeon-dong, Gumjeong-gu, Pusan, 609-735, Republic of Korea

KYONGSIK JEONG

Graduate Student, Schoool of Mechanical Engineering, Pusan National University, San 30 JangJeon-dong, Gumjeongn Pusan, 609-735, Republic of Korea

LIANJI JIN

Graduate Student, Schoool of Mechanical Engineering, Pusan National University, San 30 JangJeon-dong, Gumjeongn Pusan, 609-735, Republic of Korea

CHANGYEON LEE

GIM In Co., Republic of Korea

This study is aimed at measuring the material properties of lock plates for gas turbine plants by using ultrasonic guided waves. The material properties are nondestructively obtained and compared with mechanical testing results (from tensile and fatigue tests) for Inconel X-750. In addition, the optimum heat-treatment conditions to manufacture lock plates used in gas turbines are determined. The data from the nondestructive evaluation confirm that the material properties of Inconel X-750 are similar to those of the imported specimens used as benchmarks. It is expected that the present measuring method has potential as a nondestructive inspection method for the maintenance and repair of large-scale industrial structures such as gas turbine plants.

1. Introduction

The facility of gas turbine is developing very fast for increasing thermal efficiency and reliability, however only a few developed countries posses all of the necessary technology licences, while even importing skills is very difficult. In addition, the similar facility is being to change because gas turbine has been recently stopped often due to frequent accidents. The plate wave, a special

---

[†] *Corresponding Author*

ultrasonic wave, was first proved by Lamb and Worlton based on theoretical and experimental investigations, respectively [1-3]. In particular, Lamb identified there are two different modes propagating along a plate; symmetric and anti-symmetric. Worlton proved Lamb's theory with an experiment on a circular plate [1].

The more advanced theory of plate waves was developed by Rose and Cawley[3]. Cho et. al., in particular, used plate waves to characterize the material degradation in large-scale structures like power plants that have rigorous safety requirements and presented a promising result in enhancing material characterization sensitivity in comparison with a conventional bulk wave technique [4,6].

However, plate members such as the blade front-seal of a turbine rotor and lock plate have not been experimentally improved to a significant degree with use of Lamb waves for measuring the specifications and analyzing the wave mode. In addition, a study on the use of guided waves for material characterization is still relatively rare while a large number of bulk wave applications have been reported [5,6].

This paper aims to evaluate the material properties of the lock plate based on feasibility research using ultrasonic guided waves. This paper also attempts to experimentally determine the mechanical efficiency and reliability of a metal specimen without inducing any destructive material testing.

2. Physical Background on Guided Waves

The basic physics on guided waves are comprehensively reviewed in details via a number of references [ ] and are omitted in this paper. A large number of both transverse and longitudinal waves are produced when a guided ultrasonic wave is oblique incidence on a plate of thickness D due to mode transformation. This occurs by mutual interference and reiteration when the thickness of the specimen plate is greater than the wavelengths of the transformed longitudinal and transverse waves as illustrated in the following figure.
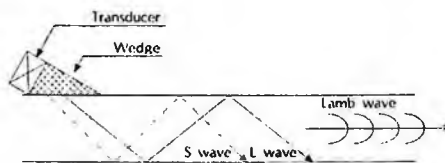
Fig. 1. Guided wave propagation in a plate

- Measurement of wave velocity

The longitudinal wave is toward a thickness of plate as shown in the flowing schematic. Only one sensor is used for measuring the longitudinal velocity. First, place the ultrasonic wave sensor on the plate. Here, a high-frequency (HF) wave sensor is used in order to obtain a clear signal. The fundamental symmetric Lamb mode converges into the plate wave mode at a low frequency time thickness limit, as illustrated in the following schematic and the equations.
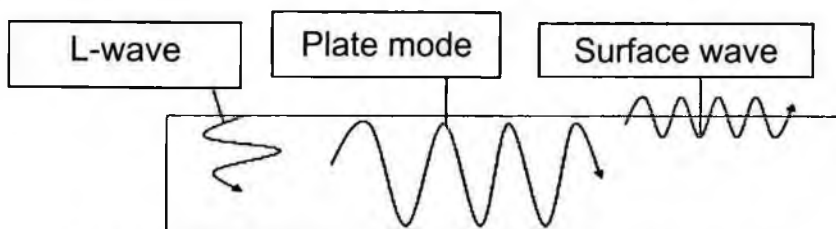
Fig. 2 A various wave modes used in the Lock plate material properties monitoring

$$C_L = \frac{1}{\sqrt{\rho}} \cdot \sqrt{\frac{E}{1+\nu}} \tag{1}$$

$$C_P = \frac{1}{\sqrt{\rho}} \cdot \sqrt{E(1-\nu^2)} \tag{2}$$

$$G = \frac{E}{2(1+\nu)} \tag{3}$$

Coupling the first two equations experimentally by measuring the longitudinal wave velocity and the one of the plate wave mode with a given density value, those material properties such as the Young's modulus, shear modulus and the Poisson's ratio can be non-destructively determined. It is simple to measure the velocity of a Lamb wave if the plate is thin; this is because it is simpler to obtain a signal when the internal section is thin as, in such a case, the Lamb wave propagates across the entire internal cross-section. Normally, when measuring along the plate direction, a HF sensor is not employed because of its short range; instead, a 1.0-MHz sensor is used as the transducer and a 1.5-MHz sensor as the receiver. After setting the unit distance (L_0), the transducer and receiver are placed on the plate and a peak point on the cursor of oscilloscope is selected.

After selecting one point, the two sensors are moved as long as ΔL then another peak point was selected. Here, points that are at the same position on the graph must be selected. Then, you can be determined Δt by measuring

the distance between the two points on the time axis. After several measurements, the average value is set as the plate-direction velocity.

3. The Experiment and Specimens

- Materials and specimen

We performed experiments to measure the Young's modulus and Poisson's ratio of Inconel X-750 and determined the reliability through the test of sine wave data with the Origin software. Subsequently, we analyzed imported specimens subjected to different heat-treatment conditions. We analyzed the differences between the original and heat-treated specimens through hardness tests, tensile tests, and microstructure analyses. Furthermore, we fabricated a prototype using Inconel X-750 with the optimum cutting speed, cutting tool, and cutting revolution.

Fig. 3 Choice of Inconel X-750 specimen

Table 1 shows the chemical compositions and Table 2 shows the estimated values for the specimens, both original and heat-treated. We fabricated a specimen using the heat-treating condition determined by reverse engineering for the design of imported specimen.

Table 1 Tension test result for Inconel X-750 following heat-treatment

	Alm	Raw material	A	B	C
Yield strength (N/mm^2)	630	429	778	747	808
Seal strength (N/mm^2)	970	836	1217	1173	1252
Elongation (%)	13	51	30	30	27
Hardness (HrB)	307 - 339	205	348	337	360

- Experimental results

Fig. 4 shows the relation between the longitudinal velocity with 10 MHz transducer and the hardness for different heat–treatment conditions (indicated by specimen serial numbers; 1- 4).

(a)   (b)
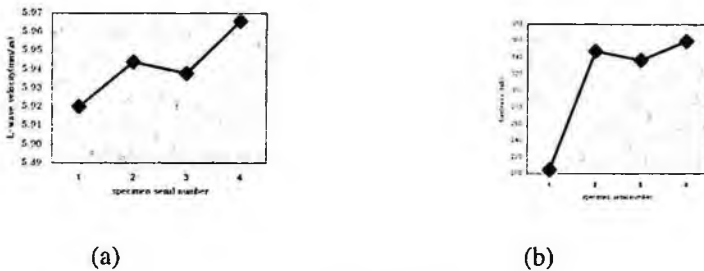
Fig. 4 Correlation between (a) L-wave velocity and (b) hardness

Although a slight variation is detected in L-wave velocity with respect to hardness change induced by specimen heat treatment, only a small difference in the longitudinal velocity can be observed for the original and heat-treated specimens in Fig. 4. Therefore, it is not fully reliable to evaluate the material properties of specimens only with the conventional bulk wave technique. To improve the sensitivity and reliability in measuring material properties, we also measured the velocity of the fundamental symmetric Lamb mode generated in three specimens from Siemens Co. and manufactured a lock plate with heat-treatment conditions C. To measure the velocity of a Lamb wave using a 1.5-MHz transmitter and a 1.0-MHz receiver: Fig. 5 shows the measurement of the plate wave velocity.

Fig. 5 Photograph of the setup of the plate wave velocity measurement

From this experiment, we obtained the Young's modulus and Poisson's ratio for Inconel X-750 by using those theoretical equations on the wave velocities given in the previous section. The results are pretty close to those determined from mechanical testing and can clearly show the enhancement in material properties due to appropriate heat treatment as given in the following table.

Table 3 Young's modulus & Poisson's ratio for experience

Material Properties	Original standard	Raw material	Domestic specimen	Imported specimen
Long.V. [mm/ μS]	5.70	5.92	5.91	5.94
Plate V. [mm/ μS]	3.023	2.856	3.073	3.092
Young's M (E)	92.97	84.14	97.37	97.54
Poisson's ratio(v)	0.431	0.444	0.434	0.434
Shear M. (G)	32.47	29.13	33.59	34.00

We were unable to find significant differences between the original and heat-treated specimens in the longitudinal wave experiments. However, considerable differences were evident between the original material and the specimen subjected to condition C with the additional data from the fundamental symmetric Lamb wave mode (the plate wave mode) experiment. From the experiment with condition C, we found a result for the influence of heat-treatment. We conclude that similar results of longitudinal wave velocity are obtained for imported and domestic specimens. Hence, we expect that, with further experimentation, cost reductions may be possible by replacing imported products with domestic ones instead.

4. Conclusions

The optimum conditions for heat-treatment that satisfy the yield and seal strength and elongation parameters are determined. The differences in material properties among specimens and analyzed ultrasonic waves with a variety of modes are successfully identified in a lock plate by combining the use of both

ultrasonic bulk wave and the fundamental symmetric guided wave mode, named "the plate wave".

Acknowledgment

References

1. D.C. Worlton, "Experimental Confirmation of Lamb Waves at Megacycle Frequencies, The AmericanInstitute of Physics. Vol. 32, No. 6, 1916, pp. 967-971.
2. I.A. Viktorov, *Rayleigh and Lamb Waves: Physical Theory and Applications*, Plenum Press, New York, 1967.
3. J.L. Rose, *Ultrasonic Waves in Soild Media*, Cambridge, 1999.
4. J.L. Rose and Y. Cho, Ultrasonic Guided Wave Inspection Potential in the Power Generation Field, Safety and NDT, 95(International Workshop on Application of NDT Technology for Failure Prevention and Safety Assurance of Structures), 1995, pp. 101-115.
5. Yamashita, M., Viswanathan, U. K. Yamamoto, I. and Kobayashi, T., "Service-induced Changes in the Microstructure and Mechanical Properties of a Cr-Mo-Ni-V Turbine Steel," ISU International, Vol. 37, No. 11, pp. 1133~1138 (1997)
6. Younho Cho, I. K. Park and J. L. Rose, "A Lamb Wave Study on Thermal Damage in a Degraded Plate," Review of Progress in QNDE, Vol. 22, 2002.

THE PRECISE MEASUREMENT OF STEEL CABLE TENSION IN CABLE STAYED BRIDGES BY NONDESTRUCTIVE MAGNETIC SENSOR[*]

HAEWON PARK[†], BONGYOUNG AHN, SEUNGSEOK LEE, AND WANGUI LEE

Safety Group, Division of Metrology for Quality Life, Korea Research Institute of Standards and Science, Daejeon, 305-340, Korea

There are a lots of measurement items to evaluate the health and safety for structures or cable stayed bridges. in this items it is very important to measure the tension of cable supporting bridge. Up to now, the tension measurement of cable is used generally resonance method of cable using accelerometer sensor. And according to research and develop this method. it becomes effective technologies for monitoring and measurement of parameters governing safety and health of structures in steady state of cable. But at this method, because it must to be applied to vibration by hitting the cable, it is difficult to applicate continuous measurement of cable tension. In this work, a magnetic sensor has been investigated and developed for measuring force in pre-stressed steel cables and tendons. The change in magnetic permeability of a material caused by mechanical stress is exploited to measure force in the material. To measure the cable tension by magnetic sensor, if it is applied magnetic field in ferromagnetic cable by a magnetizing coil of magnetic sensor, the induced voltage at pickup coil is dependent on a number of factors including the magnetic permeability of its cable which is a function of the core magnetizing current, temperature and tension. But ferromagnetic materials are varied the characteristics of magnetic domain according to amplitude of bias magnetic field. And investigates influence for frequency of exciting current. And then must find out the optimum setup condition of cable tension measurement.

Also the permeability is a function of temperature, it is necessary to investigate the influences for cable temperature and generation of heat by magnetizing current in sensor. By suitably compensations for the effects of temperature in the cable and suitably applying bias magnetic field in cable, the output voltage is a function of only the mechanical load in the cable, and can be calibrated for determination of force in pre-stressed cable.

Keyword: Sample cable; magnetic sensor; cable tension; bias magnetic fields.

1. Introduction

The need for measuring the tension of large-bridge cables is due to the
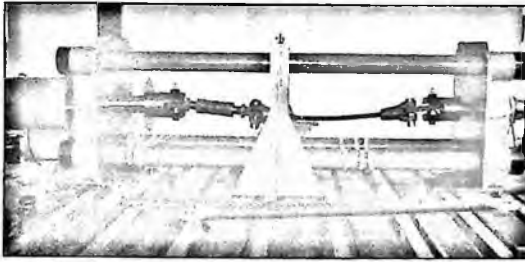
Fig. 1 Standards Tensile Testing Machine

requirement of monitoring the safety of major facilities. The collapse of the PC elevated bridge in North Carolina in 2000 (in service for only 7 years) is due to the corrosion of the high-tension steel bar (for supporting bridges) by sodium chloride which have flown into its grout,

and the collapse of the Seongsu Bridge and other recent bridge collapses demanded the acquirement of safety for large facilities and the necessity for safety checks resulted into the measurement of tensions in the cables supporting large-scale bridges.

Cables are used as a supporting structure of large-scale bridges such as cable-stayed bridges and suspension bridges, but it almost has no flexural rigidity leaving only tension and no compression.

A vibration method [1] of measuring the tension of such cable structures has started since the 1980s from a horizontal cable tension measuring research where M. S. Triantafyllou has developed an equation of motion that calculates the tension of incline cables that support marine structures. In the 2000s, Russel and Lardner's experiment completed an equation of motion that calculates the tension of cables and is currently in use today [2]. However, such equations are used inside labs for estimations of which their accuracies were very low due to the exclusion of various conditions of an actual bridge, but the measuring methods have been improved by many scientists and the accuracy has been enhanced. However it is still difficult to accurately deal with the numerous physical conditions of an actual bridge and measure its parameters and there is also the need for more researches to improve the extent of reliability.

The recently developed tension measuring technology [3] based on a magnetic method has been introduced by Professor Wang in the US. It uses the physical characteristics of the magnetic permeability of steel cables that changes in value to measure the tension of the cables.

This thesis paper develops an accurate tension measuring sensor using a magnetic method and constructs a calibration system to design and research a system that measures and calibrates the tension sensor in a laboratory for performing basic researches on designing a magnetic sensor for measuring the tension of cables that are supporting the bridges.

2. Manufacture of Testing Machine

In order to install a tension sensor in identical cables used in bridges and to test and develop a tension sensor characteristic, we needed to create a device that is capable of applying tension. This device is called a standards tensile testing machine and was structured to install tension-testing cables and accurately adjust tensions. The cable used to support the bridges that was created to test the tension in the tensile testing machine was called a sample cable. The cable needed to be easy-to-install as it was to be installed onto a tensile testing machine and required the identical characteristics of the cable used to support the bridges.

2.1. Manufacture of a Standards Tensile Testing Machine

The designing standards of the standards tensile testing machine is currently based on the tension of the cables used to support bridges and are created through the following conditions. Figure 1 shows the standards tensile testing machine.

Max. Tensile Force: 3 MN
Max. Cable Length: L=3000 mm ± 400 mm
  -Stroke Distance of Compression Cylinder = 3000 mm
  -Traveling Distance by Shuft Nut = 100 mm
Hydraulic System: Constant Pressure Method,
Control Device Error: Within 1%
Display Device: Load Cell,
Reading Error = Within 0.5%

2.2. Building a Sample Cable

The stressed materials used inside the concrete of bridges are called tendeons and the stressed materials used outside the concrete are called cables. Both are stressed monomers which are composed of multiple wires, steel bar, and strands, and as shown in Figure 2, the multiple wires in the center are called the core and is surrounded by several strands.

The cables used in this research are 50 mm in diameter and its specification is as follows.

Maker: Manho Rope & Wire Ltd in Korea
Commodity: Galvanized Steel Wire Rope
Construction: 6x37 IWRC
Specification: KSD3514
Rope Diameter = 50 mm (Actual = 51.300 mm)
Tensile Strength of Wires : Min = 182 kg/mm^2, Max = 188 kg/mm^2
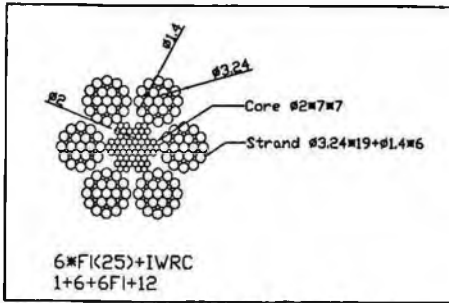
Fig. 2 Structure of a Cable with 50mm Diameter

A strand of the 50 mm cable used here is composed of 19 pieces of 3.24 mm (diameter) wires and 6 pieces of 1.4 mm (diameter) wires. The core is composed of 7 layers of 2.0 mm (diameter) wires and there are a total of 7 cores.

2.3. Designing a Tension Sensor for Cable Tension Measurement

Ferromagnetic materials change in length when placed inside a magnetic field and this effect is called magnetostriction. The strain ratio λ is as shown in Equation (1).

$$\lambda = \frac{\Delta l}{l} \tag{1}$$

Δl in this equation is magnetostriction. In a material that has the characteristics of positive magnetic distortion, its length increases when magnetized. When tension is applied to this magnetized material, it is elongated, and increased magnetization.

As shown in Figure 2, if there is no tensile force of ferromagnetic materials in the B-H curve, applying magnetic field of H1 allows magnetization by point A. Applying tensile force of σ_1 on this material under constant magnetic field will increase magnetization by point B. Increasing the magnetic field from H1 to H2 under no stress and decreasing it to zero will cause the residual flux density to become BR1, but it increases to BR2 when σ_1 stress exists. However, demagnetized materials with a magnetic field of H=0 will cause no change in magnetism because the dotted line and the solid line both intersect in the origin when stress is applied. [4]
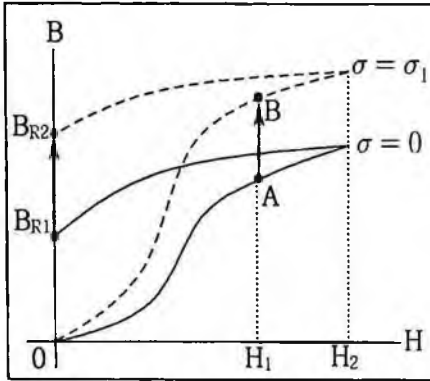
Fig. 3 Effect of tensile stress on magnetization

The reason why the magnetization curve changes according to stress is because the magnetic permeability changes according to tension.

The schematic diagram of the tension sensor is shown in Figure 4.

The voltage induced in the secondary coil when applying current $i_1(t)$ to the primary coil can be shown as Equation (2) by basing on Faraday's Law.

$$e_2(t) = -N_2 \frac{d\phi_{21}(t)}{dt} \tag{2}$$

$\Phi_{21}(t)$ is the magnetic flux induced in the secondary coil due to the primary coil. It is composed by the magnetic flux $\Phi_c(t)$ flowing inside the cable and the magnetic flux $\Phi_g(t)$ flowing within the air gap $S_g = S_2 - S_c$ inside the secondary coil. These results into the magnetic flux transferred to the secondary coil as shown in Equation (3).

$$\Phi_{21}(t) = \Phi_3(t) + \Phi_g(t)$$
$$= k \frac{N_1}{l} (\mu S_c + \mu_0 (S_2 - S_c)) i_1(t).$$
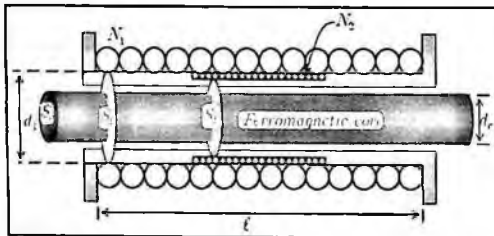
N_1: Number of turns in the primary coil .
N_2: Number of turns in the secondary coil
S_1: Cross-sectional area of primary coil (m^2)
S_2: Cross-sectional area of secondary coil (m^2)
S_C: Cross-sectional area of cable inside sensor (m^2
d_1: Diameter of primary coil (m),
d_2: Diameter of secondary coil (m)
d_C: Diameter of cable (m)
l : Length of solenoid (m)

Fig. 4 Schematic diagram of sensor for tension measurement

Here, $k = \dfrac{l}{\sqrt{d_1^2 + l^2}}$ and the voltage induced in the secondary coil is as

shown in Equation (4) which results by substituting Equation (3) into Equation (2).

$$e_2(t) = -k \frac{N_1 N_2}{l} (\mu S_c + \mu_0 (S_2 - S_C)) \frac{di_1(t)}{dt} \tag{4}$$

The vacuum permeability is $\mu_0 = 4\pi \cdot 10^{-7} H / m$ and knowing the magnetic permeability (μ) will allow the calculation of the voltage induced by the secondary coil. As described before however, magnetic permeability changes according to tension, temperature, and magnetic field and therefore the output voltage also changes accordingly. Equation (4) can therefore be expressed into Equation (5).

$$e_2(\sigma, T, H, t) = -k \frac{N_1 N_2}{l} (\mu(\sigma, T, H) S_c + \mu_0 (S_2 - S_C)) \frac{di_1(t)}{dt} \tag{5}$$

Meanwhile, the induced voltage $e_0(t)$ when no cables exist inside the secondary coil is as shown in Equation (6).

$$e_0(t) = -k\mu_0 S_2 \frac{N_1 N_2}{l} \frac{di_1(t)}{dt} \tag{6}$$

The ratio of Equation (5) and Equation (6) is expressed by Equation (7).

$$\frac{e_2(\sigma, T, H, t)}{e_0(t)} = \frac{\mu(\sigma, T, H) S_C}{\mu_0 S_2} + \frac{S_2 - S_C}{S_2} \tag{7}$$

Organizing this equation by $\mu_r(\sigma, T, H)$ will result into Equation (8). Here, $\mu_r = \mu/\mu_0$ is the relative permeability.

$$\mu_r(\sigma, T, H) = 1 + \frac{S_2}{S_C} (\frac{e_2(\sigma, T, H, t)}{e_0(t)} - 1) \tag{8}$$

By separately measuring the voltage induced with and without a cable inside the tension sensor results in the relative permeability $\mu_r(\sigma, T, H)$ through calculation from Equation (8).

2.4. Building a Tension Sensor
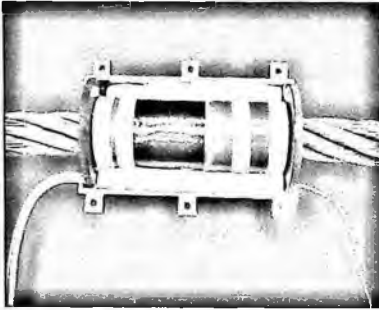
Fig. 5 Tension Measuring Sensor (TS-35)

We have decided to create a tension sensor through the theoretic background illustrated above and planned to find the operating conditions and the characteristic equation through several testings.

The output voltage of the tension sensor is different according to tension, temperature, and magnetic field as shown before in Equation (5). Therefore, in order to test the performance of the sensor, we decided to evaluate the output characteristics due to a magnetic field and the cable length, and also examine the magnetic characteristics of the cable.

This experiment uses a 50 mm (diameter) Galvanized Steel Wire Rope (6*37IWRC), which is generally used in bridges, to create a sample cable.

The tension measuring sensor in this experiment is as shown in Figure 5.

2.5. Cable Properties Test

2.5.1. Magnetic Resistance Test Due to Cable Length
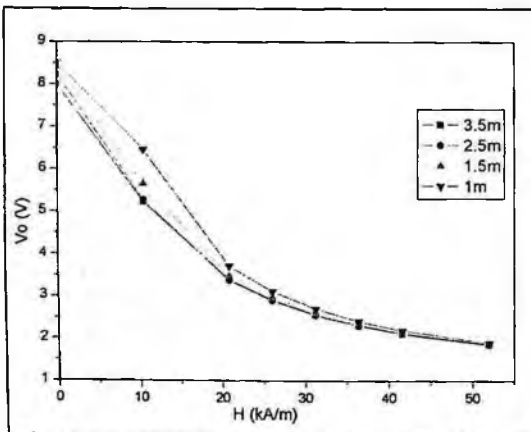
Fig. 6 Induced Voltage of Sensing Coil Versus Field Strength

The magnetic circuit resistance is different according to the length of a cable. Longer cable lengths will cause the magnetic resistance to become approximately equal, which is because the parallel magnetic resistance of the air-gap becomes equal.

As a result of preparing the cable in lengths of 1 m, 1.5 m, 2.5 m, and 3.5 m, and testing their output properties, the outcome is as shown in Figure 6. It shows that if a cable length exceeds 2.5 m, the magnetic resistance becomes identical.

In addition, the magnetic field used in an actual tension test is 20 ~ 35 kA/m, and from this we can see that the 1.5 m cable have a similar property with the 2.5 m cable. Therefore, we designed the length of the sample cable in lengths of 2.3 m.

The magnetic field applied to the cable during the test by the TS-35 tension sensor is as follows.

$$H(t) = 10.4 \cdot (I_{DC} + 0.05\sin(wt)) \tag{9}$$

$I_{DC} = DC$ DC Current applied to Primary Coil of Magnetic sensor (A)
$f = 50$ Hz

2.5.2. *Magnetic Property Testing of Cables*
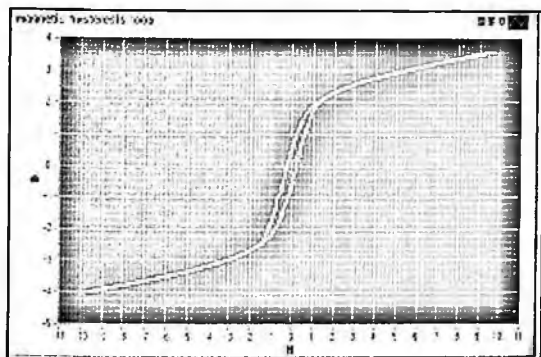
Fig. 7 Characteristic of hysteresis loop for steel cable

The measuring instrument used to test the magnetic properties of the cables is shown below. Through this test we were able to find the hysteresis loop, retentivity, and coercivity of the cables. Details on the testing instrument are as follows.

Data Acquisition Board: NI PCI-6251
-16 Analog input, 1.25 MS/s
-Resolution = 16 bit,
Operation Software: LabVIEW 8.21 Supplied by National Instruments LTD.
Power Amplification: 4520A Precision Power Amplifier from NF

The actual values of the X and Y axises of Figure 7 are as follows.
H = 10.4 x (X scale value) (kA/m)
B = 11.0 x (Y scale value) (mT)

2.5.3. Characteristic Test of Induced Voltage of Sensor vs Cable Temperature Change
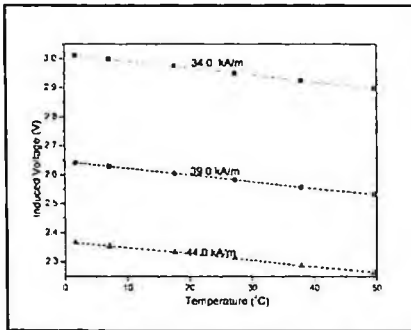
Fig. 8 Induced voltage of sensing coil according to temperature of cable

Inserting a test cable in the temperature chamber and applying the magnetic field of Equation (9) and measuring the induced voltage of the sensor according to temperature resulted in the temperature properties shown in Figure 8.

The test cables used here applies D=50 mm and L=500 mm and the direct current magnetic fields induced were measured in 34.0 kA/m, 39.0 kA/m, and 44.0 kA/m. The temperatures of the chamber were measured in 0, 10, 20, 30, 40, and 50 °C, and the surface temperature of the cable was measured in 3 points. The graph of the induced voltage (Vo) of the pickup coil when the 3 points approached the setup temperature is shown in Figure 8,

The induced voltage can be expressed as the following.

$$V_0(23°C) = V_0(T) + \alpha \cdot \Delta T \qquad (10)$$

Here, Vo (23 °C) is the output voltage converted in 23 °C.

Vo (T): measurement value (V)

$\Delta T = 23 - T(°C)$: Temperature Change

Tension Measurement Sensor: TS-35

Cable Type:

      6*37IWRC, Galvanized Steel Wire Rope

In Equation (10), α is the temperature correction factor and differs slightly according to H. The measurement of α is as follows.

α = 0.0024 for H = 34.0 kA/m

α = 0.0023 for H = 39.0 kA/m

α = 0.0021 for H = 44.0 kA/m

2.5.4. Magnetic Permeability Property Testing of Cables
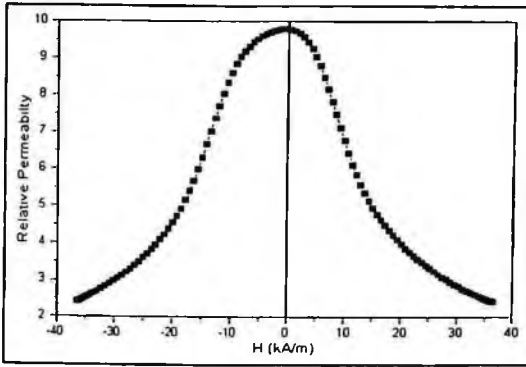
Fig. 9 Characteristic curve of relative permeability versus field strength

The relative permeability of the cable for the tension measuring sensor can be found through Equation (8). Changing the magnetic field to 36.4 ~ -36.4 kA/m and finding the relative permeability of the cable resulted into Figure 9. As shown in the figure, the cable had a maximum relative permeability of $\mu_r = 9.79$. The surrounding temperature during the measurement was 23 °C.

2.6. Tension Measurement
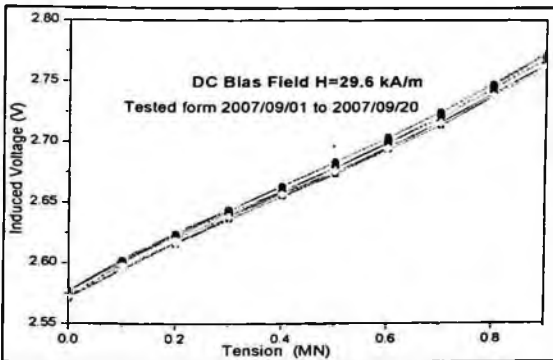
Fig. 10 Drift Test from Sept. 1 2007 to Sept. 20 2007

In order to measure the tension of a cable, there needs to be a large change in the output from the tension measurement sensor and there is the need for reproducibility. Such testing conditions have been introduced before. [8]

The values set according to the design data of the tension measurement sensor based on such information is set and tested as the following.

H_{dc} = 29.6 kA/m

H_{ac} = 0.419*sin(wt) kA/m, f=50 Hz

Temperature Conversion Formula: Equation (10)

Tension Measurement Range: 0 ~ 0.9 MN

Cable Type: 6*37IWRC, Galvanized Steel Wire Rope

With such conditions, the testing results from September 1, 2007 to September 20, 2007 are expressed by correcting the reference temperature as 23 °C. The measurement results are shown in Figure 10.

eohe testing conditions are as follows.
Hdc = 29.6 kA/m
Hac = 0.419sin(wt) kA/m, at f = 50Hz
Temperature Compensation = 23 °C (Converted)
Testing Period: Sept. 1, 2007 ~ Sept. 20, 2007
Result: Drift within 3%

3. Conclusion

We have found the characteristics of the cables used in bridges through the tests illustrated above and we were able to design a measurement sensor and test its characteristics to finalize experiment formulas on output characteristics and their methods of application allowing for the preparation of a design standard for the tension sensor.

However, the properties of the cable currently used in bridges are extremely diverse and so are its structures and sizes. Therefore, there is a need to perform tests on several types of cables and compare the results to find a characteristic formula based on the cable types.

In addition, we need to consider the temperature properties of cables to increase accuracy during tension measurement through an electromagnetic method. It must be designed to prevent the heat generated by the tension sensor during measurement from transferring to the cables and the temperatures must be measured accurately for testing. This is because the magnetic characteristics of the cables are very sensitive to temperature.

References

1. Zui, H. Shinke, T. Namita, Y. *"Practical Formulas for Estimation of Cable Tension by Vibration Method," Journal of Structural Engineering,* Vol. 122, Issue 6, pp. 651-656 (1996).
2. Russel, J. C., Lardner, T. J. *"Expremental Sertermination of frequence and Tension for Elastic Cable," ASCE Journal of Engineering Mechanics,* Vol. 124, No. 10, pp. 1067-1072 (1998).
3. Wang, M. L, *"Health Assessment and Monitoring of Long Span Concrete Segmental Bridge Bridge Research Center in University of Illinois at*

Chicago," presented in a seminar in the Safety Metrology Group of the Korea Research Institute of Standards and Science (2001).

4. B.D. Cullity, *"Introduction to Magnetic Materials," Addison-Wesley Publishing Company,* pp. 327-375 (1972).

5. Changseok Kim, *"Measuring and Standard of Electro/Magnetics," KSRI-ET-72, Korea Research Institute of Standards and Science* (1985).

6. Changseok Kim, *"Measuring of magnetic and test," KSRI-ET-33-1, Korea Research Institute of Standards and Science* (1987).

7. Byungwoo Park, *"Electomagnetics," Kyobomoongo* (2000).

8. Haewon Park, Bongyoung Ahn, Seungseok Lee and Jongwoo Kim *"Development of Magnetic Sensor for measurement of the Cable Tension of Large Scale Bridge," Journal of the Korean Society for Nondestructive Testing,* Vol. 27, No. 4, pp. 339-344 (2007. 8).

VISUALIZATION OF TOOTH FOR NON DESTRUCTIVE EVALUATION

HUI GAO, M. JULIUS HOSSAIN, AND OKSAM CHAE*

Department of Computer Engineering, Kyung Hee University
1 Seochun-ri, Kiheung-eup, Yongin-si, Kyunggi-do, 446-701, Korea

JIM X. CHEN

Department of Computer Science, MS 4A5, George Mason University
Fairfax, Virginia 22030-4444, USA

This paper reports an effort to develop 3D tooth visualization system from CT sequence images as a part of a non-destructive evaluation suitable for the simulation of endodontics, orthodontics, and other dental treatments. We focus on the segmentation and visualization for the individual tooth. The tooth CT images contain some teeth, touched with adjacent teeth or surrounded by the alveolar bones with similar intensity. We propose an improved level set method with shape prior to separate a tooth from other teeth as well as the alveolar bones. It uses the contour detected in the previous slice as shape prior based on the fact that the contour shape of the tooth from adjacent slices varies a little. We introduce a term representing sign adaptive force in the level set model so that a positive force is automatically imposed to make the evolving contour shrink when it moves outside the shape prior. On the other hand, a negative force is imposed to expand the curve when it is inside the shape prior. Thus the shape of the evolved curve is much closer to the shape prior. Reconstructed 3D model of individual tooth based on the segmentation results indicates that our technique is a very conducive tool for tooth visualization, evaluation and diagnosis. Some orthodontics simulation results validate the non-destructive function of our method.

1. Introduction

The nondestructive reconstruction of human body parts such as internal organs, bones, and teeth becomes an important tool for computer aided diagnosis (CAD) systems in both medical and dental field in recent years. They are essential to evaluate the structure and to plan the treatment of the parts without affecting human body. X-ray dental radiographs are intensively used for tooth restoration and human identification [1]. Range images are also used for the segmentation of dental study models [2]. However those images provide limited information for completely understanding the tooth structure. With the development of cone

---

* Corresponding author

beam CT (CBCT), dental CT images provide much more information for tooth visualization and dental treatment. As a consequence, segmentation and manipulation of individual tooth from CT images become a challenging issue recently.

In this paper, we propose a tooth reconstruction technique that can construct and visualize individual tooth in nondestructive manner for the pre-evaluation of individual tooth structure and the treatment planning. The proposed method works on the sequence images of teeth generated by CT which is regarded as a fundamentally nondestructive inspection tool. Our reconstruction procedure consists of two steps: the segmentation of tooth contours from the CT slices and the construction of the 3D model from the contours. We focus on the new algorithm for segmentation and the visual evaluation of the 3D tooth models.

The segmentation of a tooth from CT images has been a challenging problem due to the complex nature of the tooth in the CT image. In the image, a tooth is attached to other teeth with the same intensity or surrounded by alveolar bones. A tooth in a particular slice may split into several pieces of roots or crowns. The key point of this work is to separate the contour of individual tooth and create a virtual boundary in the case of unavailability of distinctive common boundary when one tooth touches other teeth or alveolar bones.

Note that tooth structures in adjacent images do not change much. We select the best slice of images where tooth structures are simple to segment out. Once the contours of tooth in the selected image are extracted, it can be an important reference for the next image. We utilize this reference as shape prior to constrain the area of the contour evolution as well as to create the virtual boundaries. We introduce a sign adaptive force term in the level set model so that a positive force is automatically imposed to make the evolving contour shrink when it moves outside the shape prior, otherwise a negative force is imposed. With minor user interaction our method can detect large shape variance and topological changes as well.

The next section will explore our method followed by the experimental results. In the final section we draw the conclusions.

2. Algorithm

2.1. *Level Set Method*

Level set method is also named as geometric snake. The curve C is represented implicitly via a signed distance function ϕ, by $C = \{(x,y)|\phi(x,y) = 0\}$, and the evolution of the curve is given by the zero-level curve at time t of the function

$\phi(t, x, y)$. Usually the curve is closed. In this paper, we define ϕ such that the value is negative for points inside the curve and positive for points outside the curve. The geodesic active contour (GAC) [3] is one of the important models for image segmentation using level set method. GAC aims to find the path of minimal curve length weighted by the image gradient. The energy functional to be minimized is as following:

$$E_{GAC}(C) = \int_0^1 |C'(s)| \cdot g\left(|\nabla u_0(C(s))|\right) ds \tag{1}$$

where $g(|\nabla u_0|)$ is an edge-detector which can be defined by a positive and decreasing function.

2.2. *Improved Level Set Method with Shape Prior*

Note that the energy minimization problem can be solved by level set method when curve C is embedded as the zero-level set of a signed distance function ϕ. The evolution equation is as following:

$$\begin{cases} \dfrac{\partial \phi}{\partial t} = |\nabla \phi| \left(\operatorname{div}\left(g\left(|\nabla u_0|\right) \dfrac{\nabla \phi}{|\nabla \phi|} \right) + \nu g\left(|\nabla u_0|\right) \right) & \text{in } [0, \infty) \times \mathbb{R}^2 \\ \phi(0, x, y) = \phi_0(x, y) \text{ in } \mathbb{R}^2 \end{cases} \tag{2}$$

The term $\nu g(|\nabla u_0|)$ is additional to the original GAC model for speeding up the evolution of the curve. ν is a coefficient. If $\nu < 0$, the curve will expand; if $\nu > 0$, the curve will shrink. ϕ_0 is the initial signed distance function generated by user given initial contour.

In our method we use the contour obtained from the previous slice as both shape prior and initial contour for the current slice. The key point while the contour evolving is that it goes far away from the shape prior by either shrinking or expanding. So we need a mechanism to pull it back to the prior once it is far away, which means we need to control the shrinking and expanding behaviors to constrain the contour in the vicinity of the shape prior. To control the contour evolution we utilize two different forces. A positive force drives the contour to shrink and the negative force drives it to expand. Thus, if the contour point moves to outside of the shape prior a positive force is automatically imposed to make it shrink, otherwise negative force is used. While the given initial contour deforming toward the shape prior, it also catches the object boundaries.

We use this coefficient ν for the shape prior. We replace ν with $\nu^1 \cdot d$ as following:

$$\frac{\partial \phi}{\partial t} = |\nabla \phi| \left(\operatorname{div} \left(g\left(|\nabla u_0|\right) \frac{\nabla \phi}{|\nabla \phi|} \right) + \nu' \cdot d \cdot g\left(|\nabla u_0|\right) \right) \tag{3}$$

Here d is the distance of a contour point to the shape prior and value of ν' controls the allowable variations of the final contour from the shape prior. ν' is empirically set to be 0.5.

Note that here d is a signed value. When the contour point is outside of the shape prior, d is positive and when it is inside of the shape prior, d is negative. This feature is consistent with the definition of signed distance function ϕ. So the signed distance function ϕ of the shape prior can be used directly as a substitute for d in Formula (3). We use the level set evolution without re-initialization [4] to implement our method for experimental results.

2.3. *Algorithm Summary for Tooth Segmentation*

Our method for individual tooth segmentation is described as following:

1. Preprocessing: Apply thresholding to eliminate the air pockets and soft tissues as well as to decrease the dynamic range of image. Use filtering to remove the noise. Normalization of the image from 16 bit to 8 bit can reduce the computational cost for level set method.
2. Initialization of the starting contour: Usually for slices in the middle position, most of the teeth have distinctive features. Thus the initial contour can be obtained there by using simple threshold method followed by a contour tracing algorithm. Use the contour for each tooth as the shape prior to segment the same tooth in the adjacent slice. Repeat the same procedure to segment this tooth in all the successive slices and then go for another tooth.
3. User interaction: In the case of large shape or topological variance between two adjacent slices, the shape prior may constrain the evolution of the curve. For instance, defect in tooth may result in the large shape variance and the branching of the roots may also lead to topological change. In this case we remove the constraint of the shape prior and restore to the original level set model without shape prior. By adjusting the coefficient ν to accommodate these changes, we do it in real time. After that we can use the new contour as the shape prior for the next slice.
4. 3D visualization: Based on the segmentation result we use common 3D reconstruction methods to visualize the tooth models [5]. Before the reconstruction we may need to smooth the contours in both horizontal and vertical orientations.

3. Experimental Results

We select one dataset and present both the segmentation and 3D reconstruction result by the proposed method. The image resolution is 16 bits and size is 512×512. The pixel spacing is 0.4×0.4mm. The slice thickness is 0.63mm. We use Universal Numbering System to number the teeth. We present the segmentation result in two slices: top jaw in Figure 1(a) and lower jaw in Figure 1 (b). The tooth contours are overlapped on the original images.
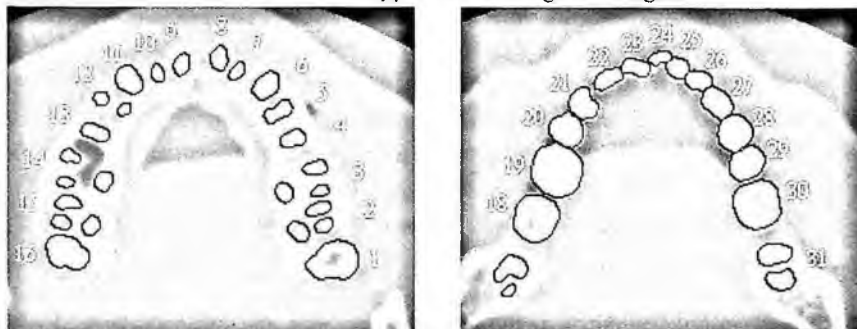
Fig. 1. Segmentation results in one slice, left and right show upper and lower teeth, respectively.

(a) Individual tooth

(b) Teeth and jaw bones together

(c) Separated individual teeth

(d) Teeth before orthodontics

(e) Teeth after orthodontics
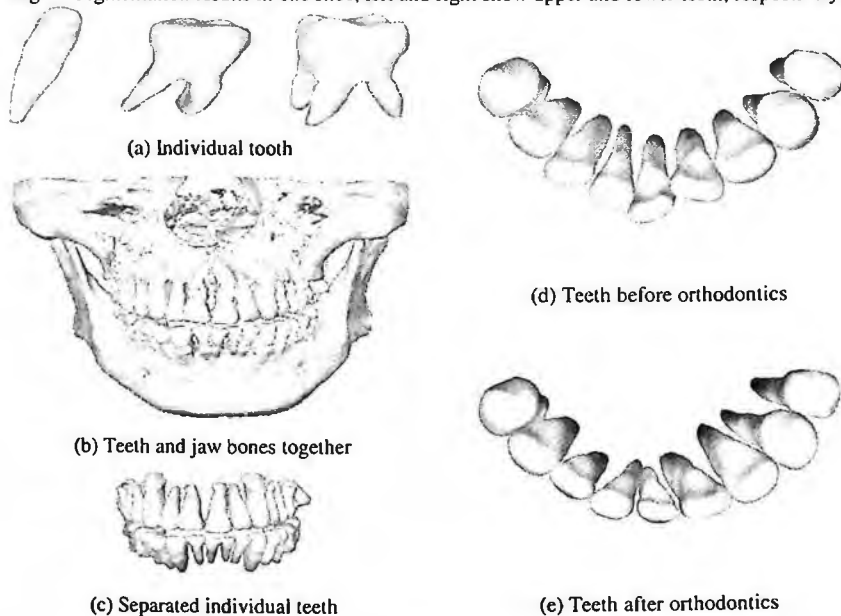
Fig. 2. 3D visualization results.

From Figure 1(a) note that for tooth #2 (the 2nd molar), tooth #3 (the 1st molar), tooth #12 (the 1st premolar), tooth #14 (the 1st molar), tooth #15 (the

2nd molar), all the roots have been correctly detected. In the case of the teeth which are touched with the alveolar bone including #14, #11, #6 and #3, the boundaries are also clearly segmented out. In Figure 1(b) most of the teeth are touched with each other. There is no boundary between the adjacent teeth. With the shape prior from the previous slice the common boundary has been generated.

Figure 2 presents the 3D visualization of teeth from different views. Figure 2(a) presents three individual tooth models: one cuspid (left), one first molar with two roots from lower jaw (middle), one first molar with three roots from upper jaw (right). In Figure 2(b) a full 3D visualization for both teeth and jaw bones is presented. The teeth and bones are attached together. However in Figure 2(c) all the teeth structures have been extracted out from the bones by proposed method. Figure 2(d) and (e) show the simulation results for orthodontics.

4. Conclusions

The proposed method presents a novel level set method with shape prior to segment tooth contours for 3D visualization from CT images. It segments the teeth from bones and separates the individual tooth from the adjacent teeth successfully. The proposed visualization technique is nondestructive which can be used in various dental treatments plan or simulation. Our future work is to provide further assistant diagnosis for dental diseases such as tooth lesion, cleft palate and interproximal caries based on our segmentation and visualization results.

References

1. O. Nomir and M. Abdel-Mottaleb, "A system for human identification from X-ray dental radiographs," *Pattern Recognition*, vol. 38, pp. 1295-1305 (2005).
2. T. Kondo, S.H. Ong, and K.W.C. Foong, "Tooth Segmentation of Dental Study Models Using Range Images," *IEEE Trans on Medical Imaging*, vol. 23, pp. 350-362 (2004).
3. V. Caselles, R. Kimmel, and G. Sapiro, "Geodesic active contours," *Int'l J. Comp. Vis.*, vol. 22, pp. 61-79 (1997).
4. C. Li, C. Xu, C. Gui, and M.D. Fox, "Level set evolution without re-initialization: a new variational formulation," *Proc. IEEE CVPR*, pp. 430-436 (2005).
5. W.E. Lorensen and H.E. Cline, "Marching cubes: A high resolution 3D surface reconstruction algorithm", *SIGGRAPH Computer Graphics*, 21(4) pp. 163-169 (1987).

IMAGE PROCESSING BASED DEFECT INSPECTION SYSTEM FOR PHARMACEUTICAL PRODUCTS[*]

HYUNGJUN KIM,   DAE-HYUN RYU

Division of Information Technology, Hansei University
604-5 Dangjung-dong Gunpo-si Kyunggi-do, Korea

TAE-WAN CHOI

Department of Mechatronics Engineering, Jinju National University
Jinju-si Kyungsangnam-do, Korea

We propose a fully automated defect inspection system using image processing techniques for use on assembly lines of pharmaceutical products. The inspection equipment consists of CCD cameras and an image processing system which utilizes a pattern matching algorithm. Methods for extracting pertinent product features are discussed with experimental results.

1. Introduction

As an example of nondestructive evaluation, many automatic visual inspection methods are used on assembly lines at companies for the purpose of improving product quality and reducing cost [1,2]. In order to resolve non-trivial inspection problems, new useful methods and devices have been developed [3,4].

We have developed a fully automated defect inspection system using image processing techniques for use on assembly lines of pharmaceutical products. The system automatically inspects items and determines whether the items will be qualified or disqualified based on predetermined criteria such as aluminum cap sealing status and scratch condition, the existence of a plastic cap cover, liquid quantity inspection, and label attachment status. The inspection equipment consists of CCD camera parts with LED lighting, a main image processing system and a control mechanism to remove defective items. For the image processing system, we have utilized a pattern matching algorithm and compared the input image data with characteristic information in order to decide whether the item is defective or not. However the factory environment often has poor optical conditions. Product illumination is affected by external light sources

causing light to be passed through the product. The floor vibrates continuously, which could affect the orientation of installed cameras and illumination devices. In this paper we have designed a system to overcome these problems and show that our inspection system is applicable to a pharmaceutical inspection line. Methods for extracting relevant product features are discussed in this paper.

2. Defect Inspection System Design

2.1. *The Structure of the Overall System*

The system for the inspection of pharmaceutical products incorporates three cameras. Approximately 150 frames per minute are captured by these cameras. Mirrors are installed in order to acquire the entire label of the pharmaceutical product. To precisely synchronize image capture timing, several optical sensors were utilized. Rejection of defective pharmaceutical products is performed using an air nozzle. Optical sensors are installed on each pharmaceutical product to detect interferences on the assembly line such as knocked-over products, etc. The structure of the overall system is shown in Figure 1.

2.2. *Hardware Design*

The hardware parts for inspection of pharmaceutical products are consisted as follows:
1. *Detection sensor for incoming products*: While a product goes along a conveyer belt, it will be identified by the optical sensors, which will trigger the three cameras to simultaneously capture an image of its label.
2. *Detection of knocked-over products*: Two optical sensors are installed on the conveyer at appropriate heights covering the top and bottom of each product to determine if the product is properly positioned during inspection. Well-positioned products will go through both sensors at the same time, whereas knocked-over products will only activate the bottom sensor.
3. *Detection sensor for outgoing products*: Two air nozzles are used to reject defective products with precise timing. Once again, an optical sensor is used to measure the accurate timing required to reject the products.
4. *Micro-controller*: A micro-controller manages and directs the entire process before the product enters the conveyer.
5. *Image processing computer system*: A high-speed computer system and three frame-grabbers are used to effectively process captured images.
6. *Cameras*: Three cameras capture the condition of the labels of the products. Two grayscale cameras and one color camera capable of 1024×768 pixel resolution are used. To be able to capture the entire surface of the products, mirrors are installed inside the capture area.
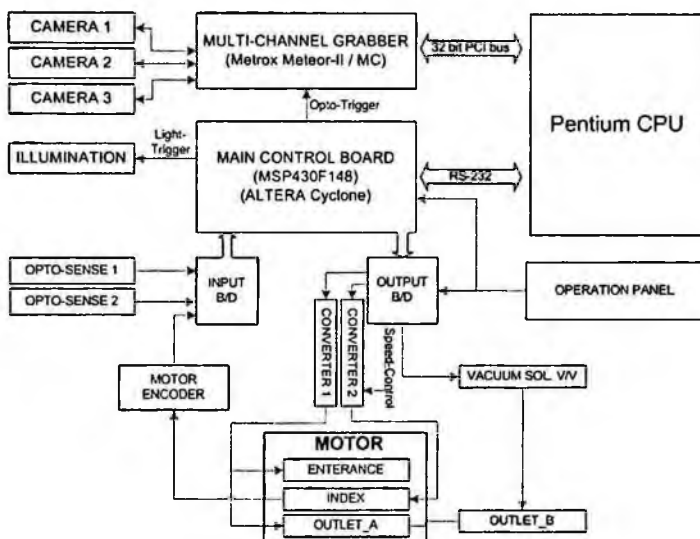
Fig. 1. The structure of the overall system

3. Image Matching

One of the most fundamental means of object detection within an image field is by template (i.e. the Region of Interest) matching, in which a replica of an object of interest is compared to all unknown objects in the image field. If the comparison between an unknown object and its template is sufficiently similar, the unknown object is labeled as being equivalent to the template object. An object is deemed to be matched wherever the difference is smaller than an established threshold value. Consequently, a common procedure is to produce a difference measure between the template and the image field. The processing speed required to perform the comparison as fast as possible without missing components is also important. We use an image of a perfect part as a template and compare the template with a test image sequence.

For templates with significant gray-level variations, also called features, normalized cross-correlation can be a very simple and effective template matching algorithm, even in cases of noisy data and changing lighting levels [5]. In the application of automatic optical inspection of pharmaceutical products, many components have labels on them and can be used as features for cross-correlation template matching. Therefore, we applied NCC (Normalized Cross-Correlation) for the matching process that compensates the gray level after subtracting the average gray value from the image itself as defined by Eq.(1):

$$C(u,v) = \frac{\sum_{i=0}^{M}\sum_{j=0}^{N}\left(I(u+i,v+j) - \bar{I}_{u,v}\right)\left(A(i,j) - \overline{A}\right)}{\sqrt{\sum_{i=0}^{M}\sum_{j=0}^{N}\left(I(u+i,v+j) - \bar{I}_{u,v}\right)^2 \sum_{i=0}^{M}\sum_{j=0}^{N}\left(A(i,j) - \overline{A}\right)^2}} \qquad (1)$$

where N, M are sizes of the templates, and I, A are the part of the image and the template, respectively [6]. Also, $\bar{A}$ is the mean of the template and $\bar{I}_{u,v}$ is the mean of $I(u,v)$ in the local region under the template. After registering the template image, the input image is scanned from left to right to find out the best matching position between the template image and the input image. As there is no significant divergence along the vertical axis due to the conveyer belt, the search region is restricted to the horizontal axis. Also, to minimize searching process time, the search region is restricted within an area twice as wide as the template image. Because the input image is sampled under the same conditions as the perfect image, it can be guaranteed that the best matching position can be found within the search region. Once those images are associated we calculate the difference between them and if it is greater than a certain threshold value, we consider the input image as containing defects.

4. Experiments

Figure 2 shows the diagram and overview of the proposed defect inspection system with the positioning of the three cameras. The color camera which is located at the center checks the color of the cap and label from the front view and the other two grayscale cameras verify other features. Note that the three input images are captured at the same time: the color camera captures one image directly from the front while the other cameras capture the front of the product directly and the rear of the product from the reflection. Therefore a total of five bottle images are captured simultaneously, which is enough to cover a 360 degree of view around the tested bottle. The speed of the conveyer belt is about 0.5 m/sec and the processing time to inspect is 161.5 (msec) as shown in the first 100 samples in Figure 3, and therefore the processing speed is sufficient to ensure smooth processing. Figure 4 shows an example of three input images. An example of the user defined ROI and an example of the final result are also shown in Figure 5.

This system can be used almost without any further research or development due to its precise automatic detection process and its efficient algorithm. Not only can this system be used for the pharmaceutical products, but also as a non-destructive vision inspection system for a variety of products.
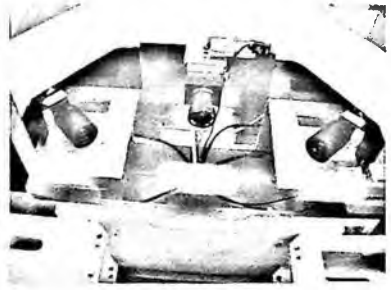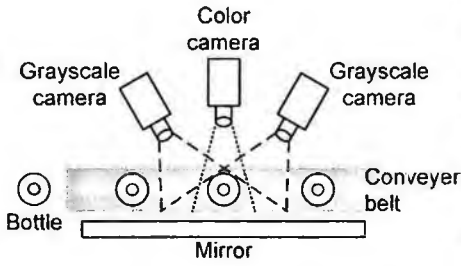
Fig. 2. The diagram and overview of the defect inspection system with the positioning of the three cameras
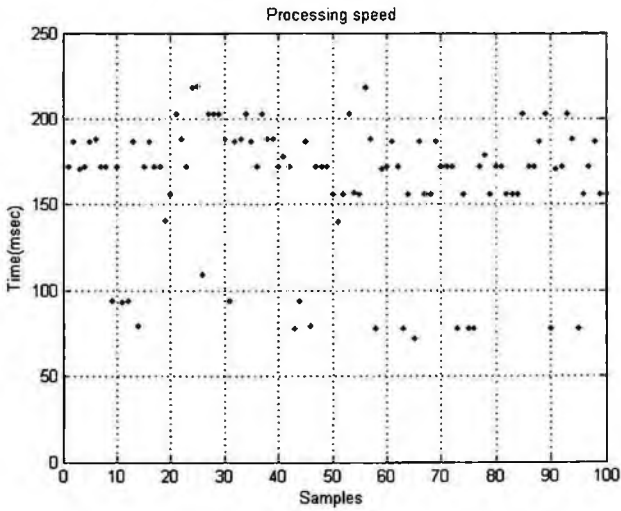
Fig. 3. Processing speed of the first 100 samples
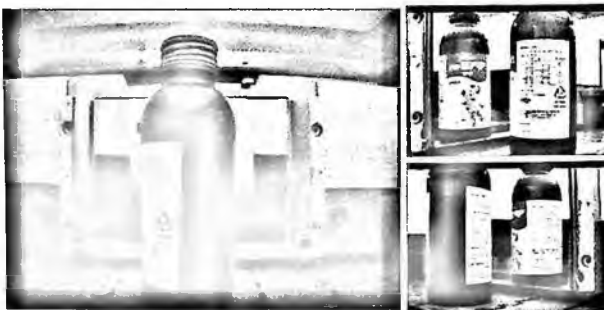
Fig. 4. Three input images
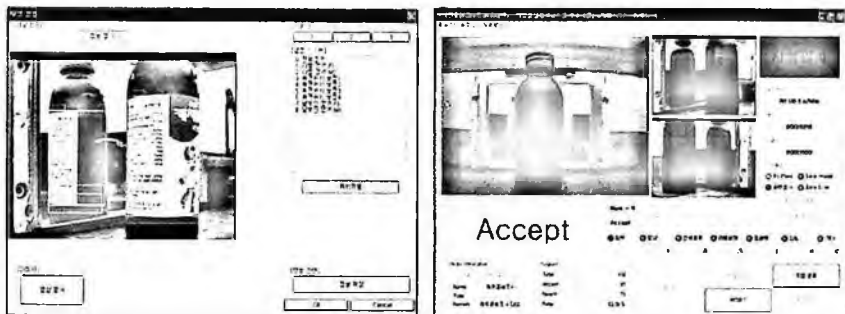
Fig. 5. The Region of Interest (ROI) and an example of the final result

5. Conclusions

We have developed a fully automated defect inspection system using image processing techniques for use on assembly lines of pharmaceutical products. The system automatically inspects items and determines whether the items will be qualified or disqualified based on predetermined criteria such as aluminum cap sealing status and scratch condition, the existence of a rubber stopper, the existence of a plastic cap cover, and label attachment status. The detection rate of the system depends on the light levels in the environment; where light levels are poor further enhancement of the stability of the product is required. To speed up the processing rate, additional improvements to the algorithm are being researched.

References

1. M. Bukovec, Ž. Špiclin, F. Pernuš, and B. Likar, Automated visual inspection of imprinted pharmaceutical tablets, *Meas. Sci. Technol.* **18**, 2921-2930 (2007).
2. A. Berman, Reducing medication errors through naming, labeling, and packaging, *J. Med. Syst.* **28**, 9-29 (2004).
3. T. S. Newman and A. K. Jain, A survey of automated visual inspection, *Comput. Vis. Image Underst.* **61**, 232-262 (1995).
4. E. N. Malamas, E. G. M. Petrakis, M. Zervakis, L. Petit, and J. D. Legat, A survey of industrial vision systems, applications and tools, *Image Vis. Comput.* **21**, 171-188 (2003).
5. J. P. Lewis, Fast template matching, *Vision Interface,* 120-123 (1995).
6. B. Kai and U. D. Hanebeck, Template matching using fast normalized cross correlation, *Proceedings of SPIE* **4387**, 95-102 (2001).

CHARACTERIZATION OF SELF-ASSEMBLED MONOLAYERS BY USING A NEAR-FIELD MICROWAVE MICROPROBE[*]

HARUTYUN MELIKYAN, TIGRAN SARGSYAN, ARTUR HOVSEPYAN
ARSEN BABAJANYAN, SEUNGWAN KIM, JONGCHUL KIM
KIEJIN LEE

*Department of Physics and Interdisciplinary Program of Integrated Biotechnology,
Sogang University, Seoul 121-742, Korea*

BARRY FRIEDMAN

*Department of Physics, Sam Houston State University
Huntsville, TX 77340, USA*

RASTISLAV LEVICKY

*Department of Chemical and Biological Engineering, Polytechnic University,
New York, NY 11201, USA*

A near-field microwave scanning microprobe technique has been used to investigate the material properties of self-assembled monolayers (SAMs) on gold. We demonstrate that near-field microwaves can achieve noncontact detection of the thickness of SAMs. By measuring the reflection coefficient S_{11} at an operating frequency near 5.3 GHz, we could observe that the thickness of SAMs. This nano-scale measurement of SAMs has a great potential for investigating the surface profile with high sensitivity.

1. Introduction

The near-field microwave microprobe (NFMM) detection technique has attracted considerable attention recently as a promising alternative sensor platform for use in chemical solution and biological detection methods [1-3]. Moreover, the near-field technique offers a label-free detection method that overcomes the need for targeting the molecules with fluorescent or radioactive labels. In addition to these important applications in molecular recognition, the NFMM technique is a unique experimental tool for investigating the physical properties at the nano-scale. The nano scale probing technique using a NFMM

means that it interacts in response to extremely small material properties changes created by molecular structure changes. The reflection coefficient changes can be easily measured using a commercial network analyzer. Self-assembled monolayers (SAMs) on gold are of significant interest and have been widely investigated since the adsorption of di-n-alkyl disulfides on gold has been reported [4-6] SAMs of alkanethiols have been investigated and characterized by various methods, which have revealed a densely packed, highly ordered and oriented monolayer structure on gold. Here we demonstrate that NFMM can achieve noncontact detection of differences in SAMs thickness. A near-field microwave microprobe functions by sensing changes in electrostatic coupling between a probe tips and the SAMs on gold due to an interaction which occurs under near-field conditions.

In this paper, we monitored the SAMs on gold using a NFMM technique. The NFMM detector consisted of a dielectric resonator coupled to the probe tip at an operating frequency of about 5.3 GHz. The changes of the alkyl chain length due to a change of permittivity of the SAMs were investigated by measuring the reflection coefficient S_{11} of the resonator. The change of the SAMs is directly related to the change of the reflection coefficient due to a near-field electromagnetic interaction between the probe tip and the SAMs. In order to demonstrate the probe selectivity, we scanned over the patterned SAMs on gold.

2. Experiment

For the preparation of alkanethiol SAMs; hexanethiol (C6), octanethiol (C8), decanethiol (C10) and dodecanethiol (C12), were purchased from Aldrich. Glass slides were cleaned with a 70/30 mixture of concentrated sulfuric acid and hydrogen peroxide solution with 30 % at 100 °C for 20 minutes, washed well with deionized water and dried. The slides were coated with a 10 nm adhesion layer of chromium followed by 1 μm layer of gold. The experimental setup of our NFMM is presented in Fig. 1 (A) and was described in detail in ref. 7. We designed a NSMM system with a tuning fork distance control system to keep a constant distance between the sample and the tip. The probe tip was made of gold wire with diameter of 50 μm. The probe tip was oriented perpendicular to the sample surface and the other end of the tip was directly connected to a coupling loop in the dielectric resonator. To drive the tuning fork, an AC voltage was applied to one contact on the tuning fork at its resonance frequency using the oscillator of a lock-in amplifier. All NFMM measurements were made at the same sample-tip distance. The sample was mounted onto an x-y-z-translation stage for coarse adjustment which was driven by a computer-controlled microstepping motor with a resolution of 0.02 μm, whereas fine movement of the sample was controlled by a PZT tube.
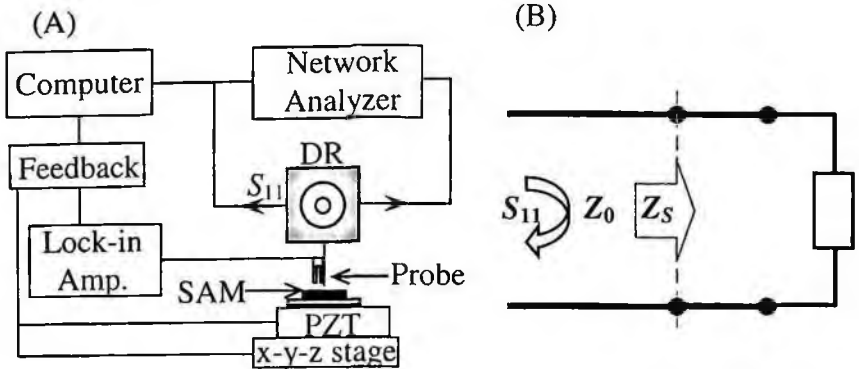
Fig 1. (A) Experimental setup of NFMM system. The microwave reflection coefficient S_{11} was measured by using a network analyzer. A quartz tuning-fork is used for distance control. The distance is about 10 nm between the tip and the sample. (B) Transmission line theory model for the probe tip and sample. Z_0 is the impedance of input loop (50 Ω), Z_g is the impedance of gold and Z_s is the impedance of the n-alkylthiol.

3. Theory

We develop expressions for the microwave reflection coefficient S_{11} of SAMs. A formula showing how the reflection coefficient S_{11} depends on the thickness increase due to the dielectric constant increased of the SAMs can be derived by using standard transmission line theory [8]. We assume by impedance matching between the probe tip and the microwave source as shown on Fig. 1 (B). An interpretation of the S_{11} magnitude in terms of medium parameters could go as follows:

$$S_{11} = 20 \log \left| \frac{Z_s - Z_0}{Z_s + Z_0} \right| \tag{1}$$

where Z_0 is the impedance of the input loop (50 Ω), Z_s is the impedance of the n-alkylthiol on the gold film and it can written as

$$Z_s = Z_0 + \Delta Z \tag{2}$$

where ΔZ is the change in Z_s due to the deviation from matching conditions which is caused by the increased thickness of the SAMs. Therefore

$$\Delta S_{11} = 20 \log \left| \frac{\Delta Z}{\Delta Z + 2Z_0} \right| \tag{3}$$

Assuming that gold is a perfect metal with thickness of about 1 μm, one gets $Z = iZ_n \tan(k_n t); \ (k_n \Delta t << 1) \Rightarrow \Delta Z = iZ_n k_n \Delta t$, where Δt is the thickness change of the n-alkylthiol, k_n is the wave vector of n-alkylthiol and equals 149 m^{-1} at 5.3 GHz and Z_n is the impedance of n-alkylthiol and equals 281 Ω. Thus, the reflection coefficient variation ΔS_{11} dependence on the changes of thinkness Δt of SAMs can be estimated as

$$\Delta S_{11} = 20 \log \frac{Z_n k_n \Delta t}{2Z_0} \tag{4}$$

4. Results and Discussion

A NFMM functions by sensing changes in electrostatic impedance coupling between SAMs and the probe-tip. The electrostatic impedance increased due to the dielectric constant increase as the SAMs thickness increased. In our design the probe tip is a sharpened metal wire coupled with dielectric resonator at microwave frequencies. For tip-sample distance maintained at about 10 nm, tip-sample interactions occur under near-field conditions. Since Z_0 includes contributions from probe-sample interactions, tuning by necessity requires selection of a reference level for the sample. A change in probe-sample interactions, for example due to binding of analyte molecules to the surface, perturbs the system from the reference state and results in a change in reflection coefficient S_{11}.

Figure 2 shows frequency-sweep data for the reflection coefficient S_{11} measured from a series of n-alkanethiol SAMs at a tip-sample separation of about 10 nm. Alkanethiol SAMs thicknesses were increased systematically from about 0.5 nm to over 2 nm by adjustment of the alkyl chain length. The SAMs were prepared on gold-coated glass slides with the thickness of the gold equal to the skin depth 1.1 μm of the microwave radiation so as to approximate a semi-infinite medium.

As the frequency of the microwave source is swept, each trace in Fig. 2 exhibits a minimum corresponding to the standing wave mode for that particular resonator-sample combination. The minimum is most pronounced for the butanethiol (C6) specimen since this sample was also used as the reference level. Clear changes are evident in response to differences in SAM thickness.
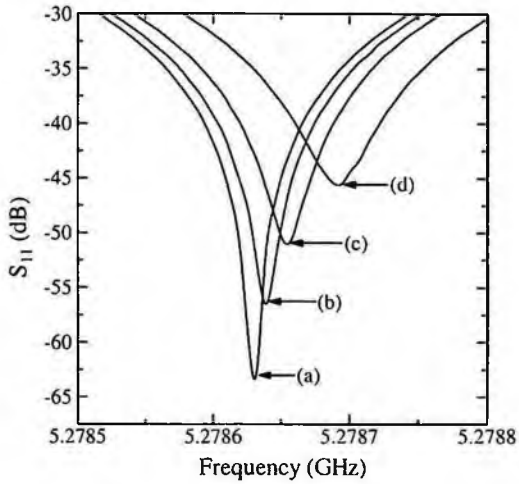
Fig. 2. Microwave reflection coefficients S_{11} for a series of n-alkanethiol SAMs: (a) hexanethiol (C6), (b) octanethiol (C8), (c) decanethiol (C10) and (d) dodecanethiol (C12).

The increase in reflection coefficient S_{11} with SAMs thickness, measured at the resonance frequency of the C6 minimum is plotted as the open circles in Fig. 3. Film thickness was assumed to increase by $\Delta t = 0.22$ nm per two methylene units [9].
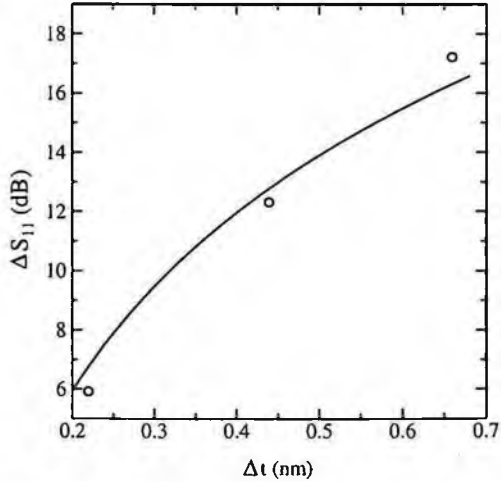
Fig. 3. The reflection coefficient S_{11} of the series of n-alkanethiol SAMs, at the reflection minimum, plotted against the changes of thickness of samples. A solid line shows a fit to Eq. (5) with $Z_0 = 50 \ \Omega$.

Over the investigated thickness the empirical dependence of S_{11} on thickness can be estimated using Eq. 4. Figure 3 plots the measured increase in reflection coefficient variation, ΔS_{11} of SAMs of C8, C8 and C12, at the reflection minimum, versus thickness changes, Δt of SAMs. As the thickness change of SAMs increased from the C8 to C12, the intensity of the reflection coefficient variation increased as expected from Eq. 4. The reflection coefficient S_{11} of C6, which has the smallest dielectric constant, shows a minimum value of -62.939 dB. Clearly the change of the thickness of SAMs affected the change of the microwave reflection coefficient S_{11}. We found a good agreement with theory between the variation of reflection coefficient S_{11} and the thickness of SAMs with a fit to Eq. (4).

5. Summary

We observed the thickness of SAMs using a NFMM. The thickness changes for SAMs were observed by measuring the reflection coefficient S_{11}. We developed a calculation model how the reflection coefficient S_{11} depended on thickness of the SAMs which can be derived by using standard transmission line theory. These results clearly show the sensitivity and usefulness of this microwave microprobe for these type investigations.

References

1. M. Tabib-Azar, P. Pathak, G. Ponchak and S. Le Clair, *Rev. Sci. Instrum.* **70**, 2783 (1999).
2 M. Abu-Teir, M. Golosovsky, D. Davidov, A. Frenkel and H. Goldberger, *Rev. Sci. Instrum.* **72**, 2073 (2001).
3. S J. Kim, S. Kim, K. Lee, J. Lee, D. Cha and B. Friedman, *Meas. Sci. Technol.* **14**, 7 (2003).
4. Y.C. Hou, Y.S. Chen, N.A. Amro, K. Wadu-Mesthrige, P.R. Andreana, G.Y. Liu and P.G. Wang, *Chem. Commun.* **19**, 1831 (2000).
5. P.E. Laibinis, C.D. Bain, R.G. Nuzzoand and G.M. Whitesides, *J. Phys. Chem.* **99**, 7663 (1995).
6. K. Sinniah, J. Cheng, S. Terrettaz, J.E. Reutt-Robey and C.J. Miller, *J. Phys. Chem.* **99**, 14500 (1995).
7. B. Friedman, M. Gaspar, S. Kalachikoc, K. Lee, R. Levisky, G. Shen and H. Yoo, *J. Am. Chem. Soc.* **127**, 9666 (2005).
8. D. M. Pozar, *Microwave Engineering*, John Wiley & Sons Inc. (1998).
9. M. D. Porter, T. B. Bright, D. L. Allara and C. E. D. Chiddey, *J. Am. Chem. Soc.* **109**, 3559 (1987).

IMAGE SEGMENTATION BASED ON FUZZY MFA[*]

KYU-DAE BAN

Computer Software, University of Science and Technology
Daejeon, KOREA

YUN-KOO CHUNG

Intelligent Robot Research Division, ETRI
Daejeon, KOREA

In this paper, Fuzzy - Mean Field Annealing (MFA) based image segmentation is introduced. MFA is based on the Mean Field Theory which assumes that the spin values of all particles, except a special particle, are fixed and those spin values affect that of the special particle on the average. A method especially for the segmentation of longitudinal cracks image will be developed. Experiments show that the fuzzy MFA algorithm with adequate preprocessing techniques is applicable to image segmentation.

1. Introduction

Image segmentation plays an important role in many applications such as machine vision, object recognition, face recognition and medical imaging. Segmentation refers to the process of partitioning a digital image into multiple sets of pixels. The goal of segmentation is to simplify and change the representation of an image into something that is more meaningful and easier to analyze. [1] Image segmentation is typically used to locate objects and boundaries in images. Several algorithms and techniques have been developed for image segmentation. Generally, most of these approaches are based on two strategies, e.g. generating regions or recognizing contours considering homogeneity [2] or discrepancy of image features. More specifically, traditional techniques such as thresholding, template matching [3] and characteristic feature clustering [4] are based on obtaining regions adopting homogeneity of image features. While various edge detection operators, utilizing the discrepancy of image features, segment the image by searching the contours of different objects. This paper investigates a clustering method of fuzzy mean field annealing [5] and its application in image segmentation. Fuzzy clustering is useful for partitioning a set of objects into a certain number of groups by assigning the membership probabilities to each object. In the fuzzy MFA, the values of

membership matrix are updated in parallel until they reach the global optimal solution. The fuzzy MFA perturbs the membership probability, and determines whether the perturbed state should be accepted or not according to the changes of the energy. The MFA combines characteristics of the simulated annealing and the neural network and exhibits the rapid convergence of the neural network while preserving the solution quality afforded by Stochastic Simulated Annealing (SSA). Experiments show that fuzzy mean field annealing method is applicable to image segmentation.

2. Fuzzy mean filed annealing

A clustering approach involves minimization of the objective function. The Fuzzy C-Means algorithm minimizes the least squares functional that is given by a generalized within-groups sum of square errors function:

$$S(g,r,Y_{new})^{t+1} = \sum_{i=1}^{n}\sum_{m=1}^{c}(\mathbf{Y}_{i,m})^{r}\sum_{k=1}^{p}(\mathbf{X}_{i,k} - \mathbf{Z}_{m,k})^{2} \quad 1 < r < \infty \qquad (1)$$

Where $\mathbf{X}_i = (x_{i1}, \cdots, x_{ip})$ $(i = 1, \cdots, n)$ is the vector of ith data object, $\mathbf{Y}_i = (y_{i1}, \ldots, y_{ig})$ is the probability of the ith data belonging to the ith category, and $\mathbf{Z}_m = (z_{m1}, \cdots, z_{mp})$ $(m = 1, \cdots, g)$ is the center of the mth cluster:

$$\mathbf{Z}_{m,k} = \frac{\sum_{i=1}^{n}(\mathbf{Y}_{i,m}^{r} * \mathbf{X}_{i,k})}{\sum_{i=1}^{n}\mathbf{Y}_{i,m}^{r}} \qquad (m = 1, \cdots, g; \ k = 1, \cdots, p) \qquad (2)$$

Fuzzy MFA algorithms can be summarized as follows. [5]

Initialize:
    Pick T, Y^0, r, ε then at step t, t = 0, 1, 2, ...
While $(T < T_f)$ {
Step 1. //do each of $y_{i,k}$ in parallel

$$y_{i,k} \in \mathbf{Y}^{t+1} \quad | \quad \mathbf{Y} \in \mathbf{R}^{c \times n}; \mathbf{Y} \in \{\mathbf{Y}_{i,k} \in [0,1] \ \forall \ i,k\}$$

$$\sum_{i=1}^{c}\mathbf{Y}_{ik} = 1 \ \forall i; \quad \sum_{k=1}^{n}\mathbf{Y}_{ik})0 \ \forall k$$

Step 2. //perturb for get a new Y
    $< y_{i,k} >$new $= < y_{i,k} > + \varepsilon;$

Step 3. //calculate;

      Calculate squared error function Eq. (1)

      Calculate Cluster center matrix in Eq. (2)

$$\Delta S = S(g, r, \mathbf{Y}_{new})^{t+1} - S(g, r, \mathbf{Y}_{old})^{t+1}$$

Step 4. //check acceptance

      if ($\Delta S < 0$) //accept

            $< y_{i,k} > = < y_{i,k} >$new

      else if ($\exp(-\Delta S/T) > \text{random}(0..1)$) //accept

            $< y_{i,k} > = < y_{i,k} >$new

      else // reject;

            $< y_{i,k} > = < y_{i,k} >$

      Set t=t+1

Step 5.

      repeat step2 ~ step4 sufficiently.

Step 6.

      Calculated the average of accepted state from step2~step5

      and then set the average as $< y_{i,k} >$ in T

    $T = \alpha * T;$

}//end while

3. Experiment and results

In order to verify the receptiveness of the fuzzy mean field annealing, we adopt test image which shows longitudinal cracks along welding process [6]. The resolution of the original sample image is 1280*1312. Many image processing techniques is global rather than local and hence the image processing with large size images have a difficulty due to the required computing time. So we resize and crop the sample image by resolution of 50*50. Fig. 1 shows sample image. This section shows the experimental result of longitudinal cracks segmentation using a series of preprocessing and fuzzy MFA.
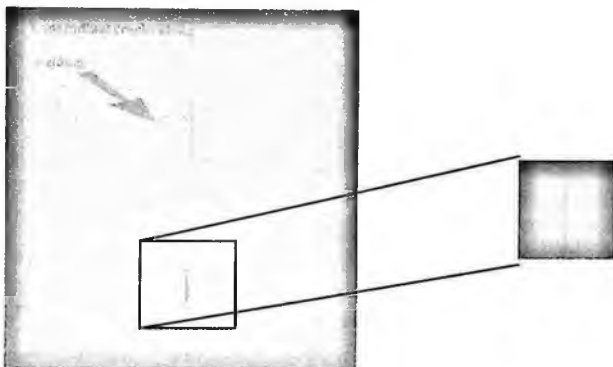
Fig. 1. Longitudinal cracks along welding image and test image

The preprocessing procedure of our experiment is following:

1. Adaptive histogram equalization.
2. Morphological opening to estimate the background of enhanced image.
3. Subtract the background image from the enhanced image.

Unlike general histogram equalization, adaptive histogram equalization operates on small data regions rather than the entire image. Each small region's contrast is enhanced so that the histogram of each output region approximately matches the uniform distribution. The definition of a morphological opening of an image is erosion followed by dilation, using the same structuring element for both operations. Morphological opening is applicable to remove small objects from an image while preserving the shape and size of larger objects in the image. By using this morphological opening, we make the background model of histogram equalized image heuristically. Fig. 2 shows the illumination distribution of background image.
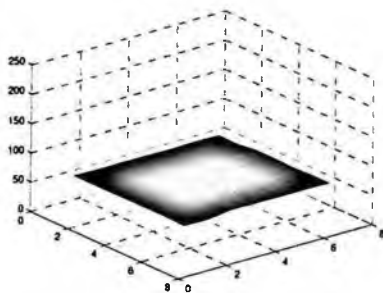
Fig. 2. Background illumination distribution of enhanced image
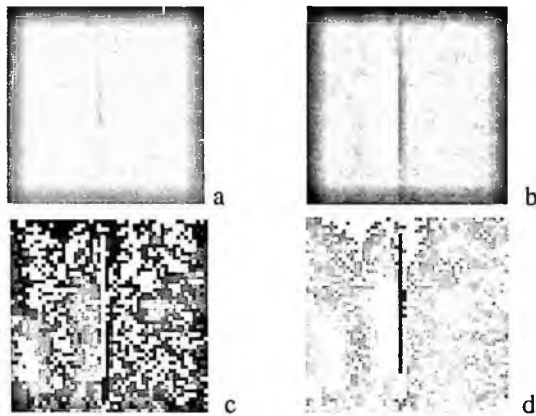
Fig. 3. Original test image and enhanced image

Fig. 3 shows the segmentation result of longitudinal cracks along welding image using fuzzy MFA method. Fig. 3(a) is resized and cropped image of original longitudinal crack image, Fig. 3(b) is adaptive histogram equalization result of Fig. 3(a). Fig. 3(c) and Fig. 3(d) is segmentation result of Fig. 3(b). Longitudinal cracks is shows a white line and blue line at the middle of image, respectively. We select the number of cluster to 6. The initial temperature for fuzzy MFA algorithm is 0.1 and last temperature is 0.01. The temperature decreased by 90% at the one iteration process. This result image shows the fuzzy MFA clustering method is applicable to image segmentation.

4. Conclusion

In this paper, we can see a possibility of fuzzy FMA clustering method is applicable to image segmentation. In the fuzzy MFA, Perturbing only one variable with carefully designing the annealing schedule can realize to attain global optimal state. But if the image resolution is large, the longer computation time is needed to find the cluster membership function and cluster center. By using the parallel processing to perturb the one variable, we can adopt the fuzzy MFA algorithm to image segmentation more efficiently.

References

1. Linda G. Shapiro and George C. Stockman : "Computer Vision", pp 279-325, New Jersey, Prentice-Hall, (2001).
2. E. Navon, *et al*, "Color image segmentation based on adaptive local thresholds", *Image Vision Computer*. Vol. 23, pp 69-85 (2005).
3. X.Y. Zeng, *et al*, "Texture representation based on pattern map", *Signal Process*. Vol. 84, pp. 589–599. (2004).
4. S. Eschrich, *et al*, "Fast accurate fuzzy clustering through data reduction", *IEEE Trans. Fuzzy Syst*. Vol. 11, pp. 262–270, (2003).
5. C. H. Song, *et al*, "A Mean Field Annealing Algorithm for Fuzzy Clustering," *FSKD*, Vol. 2, pp. 193-197, (2007).
6. VIDISCO LTD. http://www.vidisco.com/Inspection.asp

LOW ERROR AND REAL-TIME STEREO VISON ALGORITHM FOR 3D VISUAL INSPECTION

SUNG-CHAN PARK, HONG JEONG[†]

Pohang University of Science and Technology
790-784, Korea

To visually assess a structure such as corrosion, cracks as well as other irregularities, visual inspection is typically used. From the 3D information of the stereo camera, we can detect their exact shape and location. To inspect this defect by the robot which surveys around the structure, we need a small-size, low error, and real-time stereo vision module which produces 3-D spatial information from a pair of 2-D images. In this paper, we will present a fast and small stereo vision chip which has a low error rate. By adding the smoothness cost model between image scan lines, we can obtain a high quality disparity image with a small computational complexity. The architecture has the form of linear systolic array using a simple processing element (PE)s that are connected with neighboring PEs. The chip is embedded in the robot's vision board, which can output 3D depth image of 320 by 240 size and 128 levels at 30 frames/s.

1. Introduction

The stereo matching algorithms find the corresponding points in a pair of images to locate the 3D positions. They can be classified into either local or global matching approaches [1]. The local approaches, like correlation and dynamic programming methods, deal with only subimages. These approaches have the advantage of the real-time speed [2], but tend to produce high errors. The global methods can solve these local problems but suffer from the huge processing time. Recently, a few real-time global methods have been implemented through GPU in the graphics card or MMX of CPU [3], [4]. GPU and MMX are not the special processors of the full parallel architecture, so that there is a restriction of parallel processor number. Furthermore, these systems are largely impractical for compact applications like the inspection robot, due to their size. We propose a systolic array VLSI chip based on a dynamic programming (DP)-based stereo matching method that is highly suited to parallel solution. This single chip system can input two digital images directly and output the disparity in real time.

By considering the interline smoothness, we can suppress the noises and produce a high quality disparity image.

2. Trellis Based Stereo Matching System
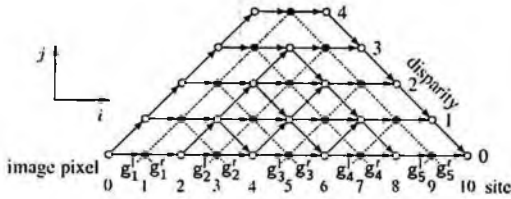
Fig. 1. Disparity trellis for M = 5.

We will explain the energy model of the trellis based stereo matching system [5]. Given the observations g^l and g^r of the M by N image and D disparity levels, we wish to obtain a maximum a priori (MAP) estimate of the disparity $\hat{d} = arg \max_d P(d \mid g^l, g^r)$. The energy function of this solution space based on the graph in Fig. 1, is as follows.

$$U(d) = \sum_{i=1}^{2N}[\text{m}(d_i)o(i+d_i) + \gamma \mid d_i - d_{i-1} \mid], \; \text{m}(d_i) = \left| g^l_{\frac{1}{2}(i-d_i+1)} - g^r_{\frac{1}{2}(i+d_i+1)} \right| . \quad (1)$$

which can be minimized by the forward and backward sequence of DP for each single scan line. Here the first term is the matching cost, the second term is the occlusion cost decided by the parameter γ and o() is a function that is 1 when the argument is odd and 0 otherwise.

3. New Trellis Based Stereo Matching Algorithm

We use the simple truncated linear model $V(a,b)$ as the vertical line dependence function for interline dependence and add it to the energy function in Eq. (2). Given the weight and the smoothness parameter, we can represent the surface smoothness cost $\mid a - b \mid$ as the inlier case $\mid a - b \mid < \lambda$ and the discontinuity cost λ as the outlier case.

$$V(a,b) = \eta \min(\lambda, \mid a - b \mid). \quad (2)$$

Given the disparity data $d(i, n-1)$ of the previous scan line and the matching cost $\text{m}(d_i)$ in Eq. (1), our energy model can be expressed as follows:

$$U(d) = \sum_{i=1}^{2N} [m(d_i)o(i+d_i) + \gamma \mid d_i - d_{i-1} \mid + V(j, d(i, n-1))].$$ (3)

3.1. New Trellis VLSI Sequence and Architecture

In this algorithm, we use the subscript to represent the index of the memory resources. Given the pixel data g^l and g^r, the accumulated register $U_j(i)$, stack $V_{i,j}(n)$, the activation flag bit $a_j(i,n)$, and D processors which are located at each j as shown in Fig. 1, we can find the disparity $\hat{d}$ which corresponds to the minimum energy in Eq. (3), in parallel at each step i on scan line n by the forward and backward processors based on the DP technique [5], as follows.

1. Forward recursion: Find the local best path for each node $j = 0,...,2M$.

$$CostV(i, j, n-1) = \begin{cases} \eta|p| & if \sum_{p \in [-\lambda, \lambda]} a_{j+p}(i, n-1) \neq 0, \\ \eta\lambda & otherwise. \end{cases}$$

(a) If $i + j$ is odd

$$U_j(i) = U_j(i-1) + m(i, j, n) + CostV(i, j, n-1), \quad V_{i,j}(n) = 0.$$

(b) If $i + j$ is even

$$U_j(i) = \min_{p \in [-1,1], j+p \in [0, N-1]} U_j(i-1) + \gamma p^2 + CostV(i, j, n-1),$$

$$V_{i,j}(n) = \arg \min_{p \in [-1,1], j+p \in [0, N-1]} U_j(i-1) + \gamma p^2.$$

2. Backtracking: Find the optimal disparity by tracing back the path $j = 0,...,2M$.

$$a_j(i+1, n) = \sum_{p \in [-1,1]} a_{j+p}(i, n) * \delta(p + V_{i,j+p}(n)),$$

$$\hat{d}_j(i+1, n) = \hat{d}_j(i, n) + \sum_{j \in [0, D-1]} a_j(i+1, n) * V_{i+1, j, n},$$

The main engine is the two kinds of processors: one for the forward process and the other for backward process. The matching cost $m(i, j, n)$ of the forward processor can be calculated through the pipeline architecture in real time. Each forward processor accepts the pixel data and calculates the matching cost. After receiving the signals $a_{j+p}(i, n-1)$ of $p \in [-\lambda, \lambda]$ which were calculated in the backward processors of the previous line, if there exists the activated signal among them, the smooth cost module outputs $\eta|p|$ and otherwise outputs $\eta\lambda$. That is, the interline smoothness cost $V(j, d(i, n-1))$ is calculated by considering the distance between the activated signal index $j + p$ and the current forward

processor index j. If $i+j$ is odd, then the pixel matching cost (i,j,n) and $V(j,d(i,n-1))$ are added to the accumulated cost $U_j(i-1)$, otherwise a comparison is made between that its cost and the costs coming from the neighboring processors above and below. The chosen local path is pushed into a stack.

During the backward phase, the decisions $V_{i,j}(n)$ stored in the stacked are output to the backward processors. Only one processor is active at one time as indicated by the register containing the activation flag $a_j(i,n)$, which indicates the optimal disparity path of the trellis graph in Fig. 1. The activation flag is passed between the backward processors according to the input local path decision $V_{i+1,j}(n-1)$. If a backward processor is active, it outputs the path decision to a bus to communicate with the external host and accumulated to obtain the disparity $\hat{d}_j(i+1,n)$ output. $a_j(i,n)$ can be used by the forward processor of the line n+1.
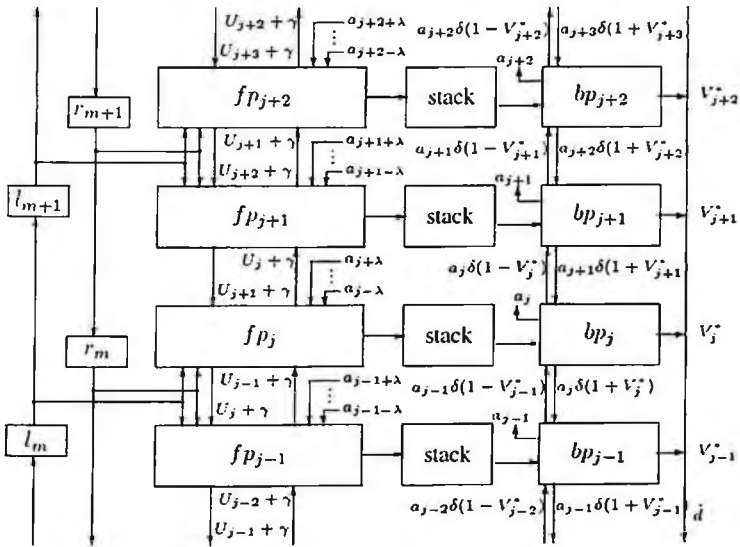
Fig. 2. PE array structure.

The overall architecture is a linear systolic array of PEs as shown in Fig. 2. Communication extends only to neighboring PEs and the array is completely regular in structure, making the actual hardware design relatively simple.

3.2. Computational Complexity

This algorithm has the total time complexity O(NM2D) if the forward and backward part are processed sequentially for the total 2M step and D disparity levels. Its complexity reduces to O(2MN) by the parallel D forward and backward processors, so that it can process in the real-time.

4. Experimental Results

First, we will verify the algorithm quantitatively and qualitatively using the Middlebury data set by the software simulations. Fig. 3 shows the comparison results between the single-line DP method [5] which has the stripe noises and our method where they are effectively suppressed.

(a) Venus left image   (b) Ground truth   (c) Single-line DP Chip   (d) Our Chip
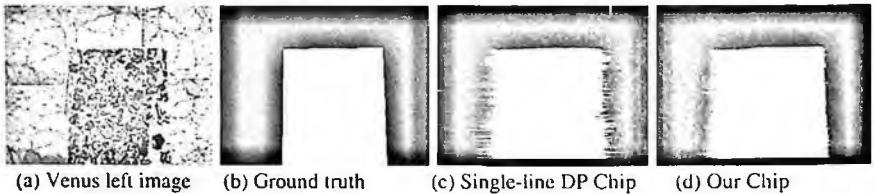
Fig. 3. Resulting depth maps from the Middlebury stereo data set.

(a) Plate left image   (b) Plate right image   (c) Output result   (d) Our system board
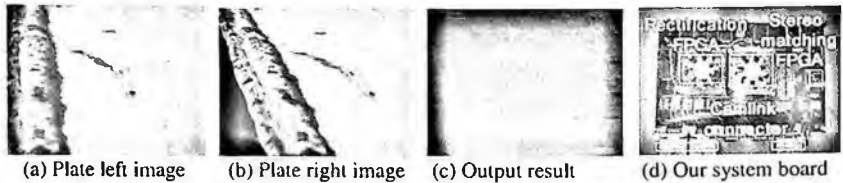
Fig. 4. Disparity image outputs and system board.

Table 1. Disparity error(%) and speed performance in several methods.

Image	Tsu-kuba	Map	Ve-nus	Sawt ooth	Image size	Lev els	Fps	Sys-tem
Single-line DP[5]	5.57	4.12	8.72	5.22	190x1000	400	15	FPGA
Real-time DP[4]	2.85	6.45	6.42	6.25	320x240	100	26.7	MMX
Our Chip	2.63	0.91	3.44	1.88	320x240	128	30	FPGA
Real-time GPU[3]	2.05	NA	1.92	NA	320x240	48	18.5	GPU
Real-time BP[6]	1.49	NA	0.77	NA	320x240	16	16	GPU

We will quantify our algorithm through the output error performance in Table 1. The error calculating method represents the error rate for disparity error more than 1 at the unoccluded area. Our method is better than single-line DP and real-time DP, but worse than real-time GPU and real-time BP. The real-time GPU

and BP require the full image range of smoothness dependence. They need more computational complexity. Single-line DP exhibits the highest speed because it has a full parallel VLSI structure like ours. Our method also displays the second ranking performance due to the full parallel processor on VLSI chip. Real-time BP and GPU have the computational limitation because they're based on the sequential computations although they produce lower error. They're dependent on the high clock speed and small number of processors. That is, it is hard to increase disparity resolution and processing speed with the general PC's MMX or the GPU graphics card. In Fig. 4(d), our VLSI system is described. The disparity data is calculated by the stereo matching chip from the camera images. The result data is transferred from the FPGA to the grabber through the Camlink cable. PC then reads the computed disparity, converts it to a gray scale image and displays it on the screen. Our architecture was implemented on Xilinx Virtex II pro-100 FPGA which incorporates 128 PEs. We can easily extend the image size and the disparity level by increasing processors and the clock hertz on the FPGA if necessary. Fig. 4(a)-(c) shows the observed 3D shape of metal plate for inspection with our real-time system.

5. Conclusions

We have presented a real time stereo matching chip and board to inspect the structure by 3D shape information on the robot. For a pair of images with M by N pixels, only O ($2M$) time is required for each scan line. We implemented a chip on Xilinx FPGA with 128 linear array processors.

References

1. 1. Scharstein D. et al: 'A Taxonomy and Evaluation of Dense Two-Frame Stereo Correspondence Algorithms'. IJCV 47(1/2/3):7-42, Apr. (2002).
2. M. Hariyama et al. Architecture of a stereo matching VLSI processor based on hierarchically parallel memory access. In The 2004 47th Midwest Symposium on Circuits and Systems, number 2, pages II245~II247, (2004).
3. L.Wang and et al. High-quality real-time stereo using adaptive cost aggregation and dynamic programming. In 3DPVT, (2006).
4. S. Forstmann et al. Real-time stereo by using dynamic programming. In CVPR, Workshop on real time 3D sensors and their use, (2004).
5. H. Jeong and S. C. Park. Generalized trellis stereo matching with systolic array. In LN CS, volume 3358, pages 263~267, (2004).
6. Q. Yang and et al. Real-time global stereo matching using hierarchical belief propagation. In The British Machine Vision Conference, (2006).

ANALYSIS OF THE DETECTION OF VOIDS OF CONSTRUCTION JOINTS AND SHAPES OF INNER CAVITIES IN CONCRETE USING AN ULTRASONIC PULSE VELOCITY METHOD

PARK, SEOK KYUN

Dept. of Civil Engineering, Daejeon University, 96-3 Yongun-dong, Dong-gu Daejeon, 300-716, Korea

CHOI, DONG HO

Dept. of Civil Engineering, Hanyang University, 17 Haengdang-dong, Seongdong-gu Seoul, 133-791, Korea

The voids of construction joints and the inner cavity treatment of concrete are important technical problems in construction. In particular, voids in construction joints and inner cavities created during concrete construction result in serious weakness in terms of both structural and water-barrier functions. In the present study, an ultrasonic pulse velocity method was used for detecting the voids of construction joints of steel frame-reinforced concrete (SRC) columns and the inner cavities of concrete blocks. The advantages and limitations of direct and semi-direct methods of measuring ultrasonic pulse velocity were investigated through the non-destructive inspection of three types of voids of construction joints and four types of inner cavity shapes in concrete specimens. From the results, it has been verified that the semi-direct measurement method is more effective than the direct measurement method for detecting the voids of construction joints and the shapes of inner cavities through the use of an ultrasonic pulse velocity method with an image processing technique.

1.   Theoretical Background of Ultrasonic Technique

Ultrasonic pulse velocity methods for concrete can be classified into direct, semi-direct, and indirect measurement methods according to the arrangement of the probes, as in Figure 1. From among the ultrasonic pulse velocity measurement methods noted above, the present study uses direct and semi-direct measurement methods to detect defects as these approaches are appropriate to the goals of the study. These approaches require relatively less time and effort for measurement than topographic methods.

(a) Direct measurement method   (b) Semi-direct measurement method

(c) Indirect measurement method
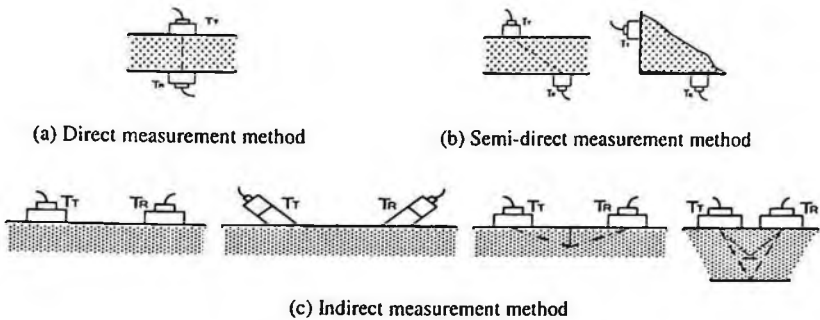
Fig. 1. Arrangement of ultrasonic probes

2. Experiment Plans and Conditions

2.1. *Specimen production and experiment overview*

In structures constructed using the top-down construction method, columns are structural elements that show the most severe problems according to concrete filling conditions. With columns as objects of study, the following seven types of specimens were produced: a steel frame-reinforced concrete (SRC) specimen (Figure 2) and a zero-defect non-reinforced concrete specimen with plane-shaped joint voids; a non-reinforced concrete specimen (Figure 3) with plane-shaped and V-shaped joint voids; and a non-reinforced concrete specimen (Figure 4) with cubical, rectangular parallelepipedal, and spherical inner cavities. SRC specimens were reduced, simulated, and produced to measure $50 \times 50 \times 100$ (cm), and non-reinforced concrete specimens measured $50 \times 50 \times 50$ (cm).

As for SRC specimens, D19 steel reinforcements were arranged at intervals of 20 cm. The cover depth was 4 cm and the H-beam measured $30 \times 30 \times 150$ (cm). When steel frames (H-beams) exist in traditional concrete specimens that only have steel reinforcements, interference can be compared and reviewed during ultrasonic measurement. Furthermore, this configuration takes into account in the simulation that a top-down construction method is mainly used in the construction of SRC structures. SRC specimens solely with plane-shaped voids were produced and non-reinforced concrete specimens in defective areas with plane-shaped and V-shaped voids were produced. As for non-reinforced concrete specimens with inner cavities, three types of voids with different shapes were artificially produced and inserted: a cube measuring $20 \times 20 \times 20$ (cm); a rectangular parallelepiped measuring $30 \times 10 \times 20$ (cm); and a sphere with a

568

diameter of 20 cm. All of these voids and cavities were produced using cellular styrofoam.
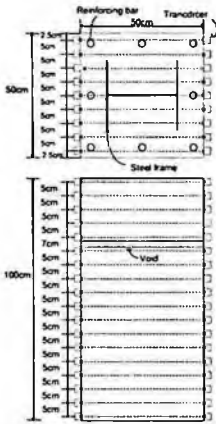
Fig. 2. SRC structure column specimen
(plane-shaped joint voids)
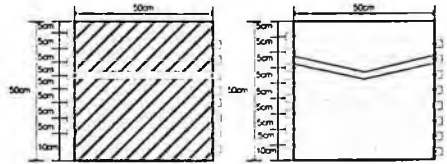
Fig. 3. Non-reinforced concrete structure blocks
(plane-shaped and V-shaped joint voids)
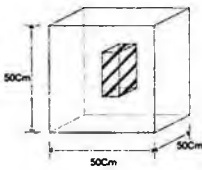
(a) Specimen with rectangular parallelepipedal simulated cavities
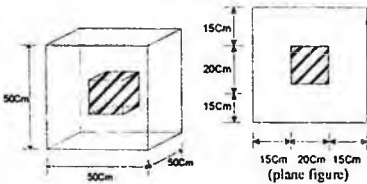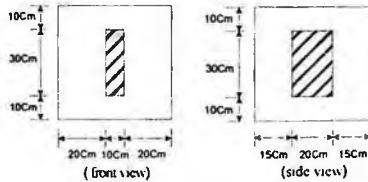
(b) Specimen with cubical simulated cavities   (c) Specimen with spherical simulated cavities
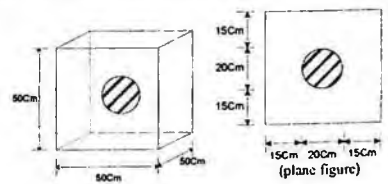
Fig. 4. Types of inner cavity specimens

The principal mixing conditions of the concrete specimen are W/C: 64%, s/a: 48%, Slump: 7.5cm, G_{max}: 25mm and f_{ck}: 21MPa.

2.2. *Experiment methods*

As for measurement methods, (a) direct measurement method and (b) semi-direct measurement method in Figure 1 were used. For example, in case of direct measurement, the locations of the transmitter and the receiver were made symmetrical (- - -line) as shown in Figure 2 for SRC structure. On the other hand in case of semi-direct measurement, the locations were made asymmetrically as shown in Figure 3 for non-reinforced concrete structure.

3. Experiment Results

Figure 5-8 show images of the ultrasonic pulse velocity values measured according to the direct and semi-direct measurement methods. Measurement result per measurement method and specimen type will be analyzed. Here, images were processed so that darker colors would reflect shorter ultrasonic arrival time and lighter colors would reflect longer arrival time.

3.1. *Direct measurement method*

Figure 5-6 show images of the ultrasonic pulse velocity values measured according to the direct measurement methods.

(a)SRC column   (b)Zero defects   (c)Plane-shaped joint   (d)V-shaped joint
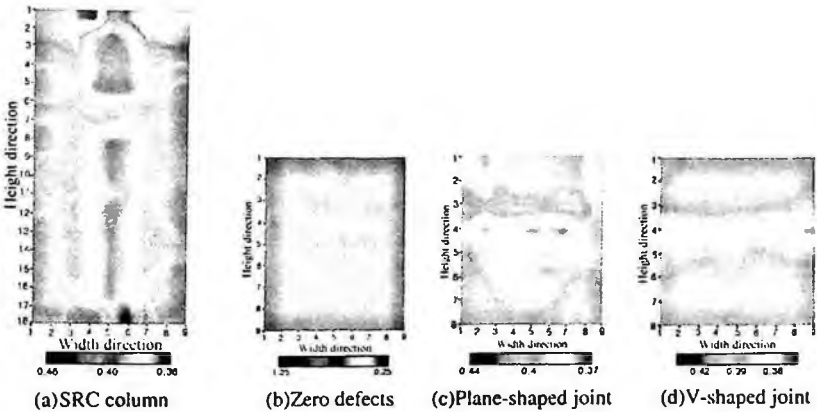
Fig. 5. Inner concrete joint void measurement image processing results using direct measurement method ($\times$ 1000 (m/s) = ultrasonic pulse velocity)
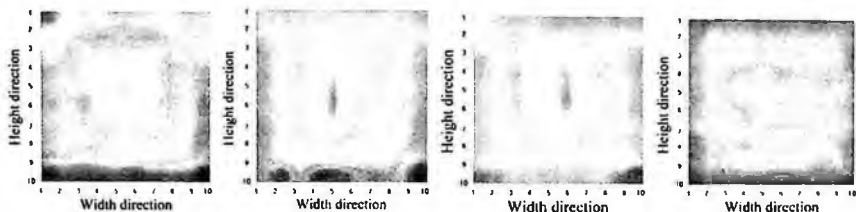
(a) Cubical (b) Rectangular parallelepipedal(small area) (c) R. parallelepipedal(large) (d) Spherical

Fig. 6. Inner concrete cavity measurement image processing results using direct measurement method ($\times$ 1000 (m/s)=ultrasonic pulse velocity)

3.2. *Semi-direct measurement method*

Figure 7-8 show images of the ultrasonic pulse velocity values measured according to the semi-direct measurement methods.
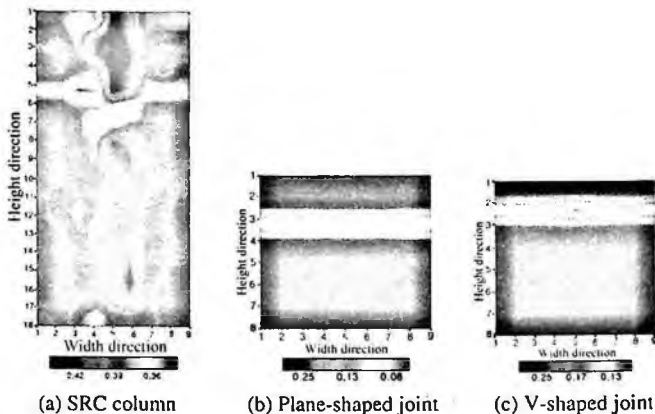
(a) SRC column　　　(b) Plane-shaped joint　　　(c) V-shaped joint

Fig. 7. Inner concrete joint void measurement image processing results using semi-direct measurement method ($\times$ 1000 (m/s) = ultrasonic pulse velocity)
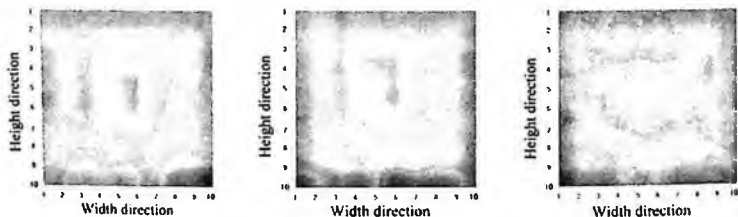
(a) Cubical　　(b) Rectangular parallelepipedal(large area)　　(d) Spherical

Fig. 8. Inner concrete cavity measurement image processing results using semi-direct measurement method ($\times$ 1000 (m/s) = ultrasonic pulse velocity)

4. Result Analysis and Conclusions

The result analysis and conclusions of the present study, which aimed at investigating the conditions of joint voids and inner cavities in concrete specimens by using the ultrasonic pulse velocity method, are as follows:

(1) Regarding the identification of joint voids, the semi-direct measurement method was more effective than the direct measurement method in determining the existence of voids regardless of the forms of structural elements (SRC structures, non-reinforced concrete structures). However, both measurement methods were limited in identifying the shapes of voids (plane-shaped, V-shaped). In particular, differences in the distribution of ultrasonic pulse velocity in areas where steel frames (H-beams) were embedded were relatively clear regardless of whether the direct measurement method or semi-direct measurement method was used, thus making it possible to indirectly verify the existence of steel frames (H-beams).

(2) According to the results of measurements depending on changes in the shapes of inner cavities (cubical, rectangular parallelepipedal, spherical), both measurement methods likewise were able to verify the existence of cavities. As for the identification of the shapes of cavities, the semi-direct measurement method was more effective than the direct measurement method.

(3) Consequently, based on the research results above, the ultrasonic pulse velocity method was determined to be valid for the detection of joint voids and inner cavities, which can readily occur in concrete structures. In addition, when measurement data were analyzed using image processing technique, such defective areas could be determined more easily and effectively.

Acknowledgments

References

1. S.K. Park et al., *"Non-destructive Inspection of Top-Down Construction Joints of Column in SRC Structure using Ultrasonic Method"*, *Journal of the Korean Society for Nondestructive Testing, Vol. 20, No. 4, pp.290-295,* (2000).

RADIAL IMAGE PROCESSING IN THE DISCRETE POLAR COORDINATE[*]

WONHA KIM

College of Electronic and Information Engr., Kyunghee University
Yongin-si, Gyeonggi-do, Republic of Korea

HYUNGJUN KIM

Division of Information Technology, Hansei University
Goonnpo-si, Gyeonggi-do, Republic of Korea

SUNGMIN KIM

Department of Biomedical Engr., KonKuk University
Choongju-si, Chungchung-namdo, Republic of Korea

We propose a radial image processing method in a discrete polar coordinate system based on L^1-norm. For this purpose, we first verified that the polar coordinate based on L^2-norm can not exist in discrete system and then develop a method converting the Cartesian coordinate to the discrete polar coordinate. We apply the proposed method to smooth mass images of breast tissue. Compared to the Gaussian smoothing method performed in the Cartesian coordinate system, the proposed method stabilized the image signal while maintaining the overall radial shape of mass images.

1. Introduction

Many image signals tend to propagate radially from their centers. For example, cancerous mass images of breast tissue diffuse radially. Other examples of such images include iris, smoke, biomedical cells and hippocampus. Rather than processing such images in the Cartesian coordinate system, it is more appropriate to process such images in a polar coordinate system [1].

Because pixels in a digital domain are regularly arranged squares, the set of pixels forms a Z^2 lattice structure [2]. The coordinates of pixels are the centers of squares, i.e., lattice points. To perform radial image processing in this lattice structure, the pixel locations should be represented in a discrete polar coordinate.
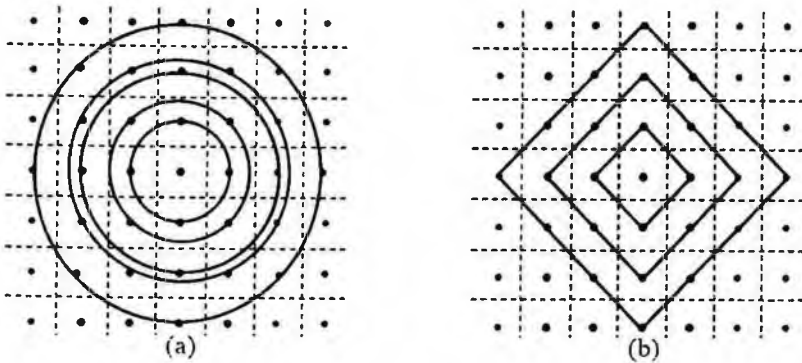
Fig. 1. Z^2-lattice structures of pixel areas. Distribution of pixels belonging to (a) Circles using L^2-norm distance and (b) Pyramids using L^1-norm distance

Using L^2-norm distance, the set of all pixels equidistant from the origin forms a circle. Fig. 1.(a) illustrates the distribution of pixels on the circles. The radii of the circles where the pixels are located increase irregularly (for example $r = 1$, $\sqrt{2}$, 2, $\sqrt{5}$, $2\sqrt{2}$, etc). The number of pixels located on each circle also increases irregularly corresponding to the increase in radius (for example $N= 4$, 4, 4, 8, 4, etc.). Therefore, if L^2-norm is used, it is impossible to construct a discrete polar coordinate system mathematically.

Alternatively, using L1-norm distance, the set of all pixels equidistant from the origin forms a pyramid. As shown in Fig. 1.(b), the radii of the pyramids where the pixels are located increase regularly ($r = 1, 2, 3, 4$, etc.). The number of pixels located on each pyramid also increases regularly ($N = 4, 8, 12, 16,.... = 4r$) [2,3]. Therefore, if L1-norm is used, it is possible to construct a discrete polar coordinate system. The pixel locations can also be completely converted between the discrete Cartesian and the discrete polar coordinate systems.

In this paper, we have developed a method for radial image processing in a discrete polar coordinate system based on L1-norm. In order to verify advantages of the proposed method, we applied the method for smoothing a mass-type cancer image.

2. Radial Image Processing

We derive equations that convert pixel positions from (r, Θ) in a discrete polar coordinate system to (m, n) in a discrete Cartesian coordinate system. Using $r = |m| + |n|$ and the symmetrical property of the coordinate systems, the
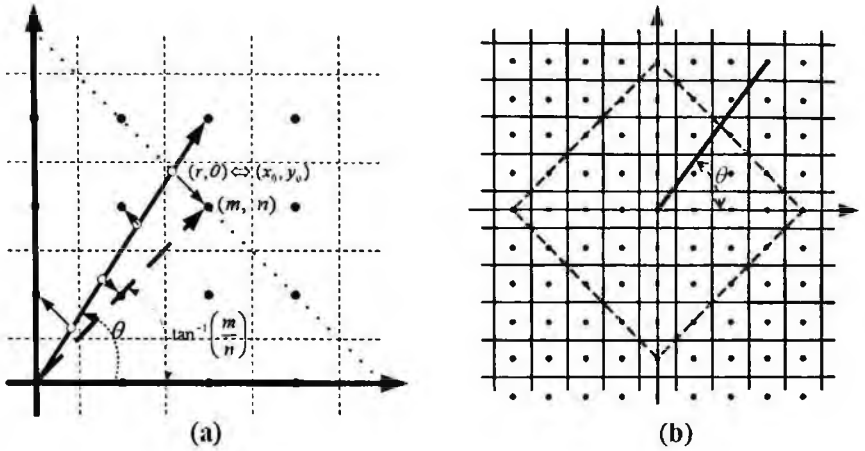
Fig. 2. (a) The continuous Cartesian coordinate to a discrete polar coordinate based on L^1-norm. (b) Pixels at $\theta = \tan^{-1}(5/4)$

coordinate position (m,n) at any quadrant can be determined from the symmetrical position $(|m|,|n|)$ at the first quadrant as follows:

$$(m,n) = \begin{cases} (r-|n|,|n|) & if \ \ 0^\circ \le \theta < 90^\circ \\ (-r+|n|,|n|) & if \ \ 90^\circ \le \theta < 180^\circ \\ (-r+|n|,-|n|) & if \ \ 180^\circ \le \theta < 270^\circ \\ (r-|n|,-|n|) & if \ \ 270^\circ \le \theta < 360^\circ \end{cases} \tag{1}$$

From Eq. (1), we can find the discrete Cartesian coordinate position (m,n) corresponding to (r,θ) by determining $|n|$.

As shown in Fig. 2.(a), the angle θ of the polar lattice point (r,θ) is closer to the angle $\tan^{-1}(|n|/|m|)$ of the Cartesian lattice point $(|m|,|n|)$ than the angles of any other lattice points on the pyramid of the radius r. Thus, we can use Eq. (2) to find $(|m|,|n|)$:

$$(|m|,|n|) = \underset{(|p|,|q|)}{\arg\min} \left\{ \left| \theta - \tan^{-1}\left(\frac{|q|}{|p|} \right) \right| \right\} \ \ where \ \ p,q \in Z, \ \ |p|+|q| = r \tag{2}$$

Since $r = |p|+|q|$ and the tangent function increases monotonously at the first quadrant, Eq. (2) is equivalent to the following Eq. (3).

$$|n| = \underset{0 \le |q| \le r}{\arg\min} \left\{ \left| \frac{|q|}{r - |q|} - \tan\theta \right| \right\} \tag{3}$$

In order to find $|n|$ in Eq. (3), we define a function $D(y)$ of a real variable y such as:

$$D(y) = \frac{y}{r - y} - \tan\theta \quad where \quad 0 \le y \le r$$

Since $D(y)$ is a monotonously increasing function and $D(0) < 0$, $D(r) > 0$, there exists only one solution of $D(y) = 0$. The solution is as follows:

$$y_0 = \frac{r \cdot \tan\theta}{1 + \tan\theta}$$

The continuous Cartesian coordinate corresponding to (r, θ) is (x_0, y_0) where $r = |x_0| + |y_0|$. As shown in Fig. 2, (r, θ) belongs to the pixel area located at the discrete Cartesian coordinate $(|m|, |n|)$. Therefore, the discrete Cartesian coordinate $(|m|, |n|)$ corresponding to the polar coordinate (r, θ) is the integer coordinate closest to (x_0, y_0) on the radius r. Thus,

$$|n| = \partial(y_0) = \partial\left(\frac{r \cdot \tan\theta}{1 + \tan\theta} \right) \tag{4}$$

where $\partial(\alpha)$ is the rounding operation that finds the closest integer to α.

As in the above, the discrete Cartesian coordinate (m, n) corresponding to (r, θ) can be determined from Eq. (1) and (4). There is a complete 1:1 mapping between the discrete Cartesian coordinate (m,n) and the polar coordinate (r, θ). Figure 5.(b) shows the pixels on the line drawn at $\theta = \tan^{-1}(5/4)(\cong 51.34^o)$. In this case, we can find the following relation

$$\left\{ (r, \theta = 51.34^\circ) \middle| (0, \theta), (1, \theta), (2, \theta), (3, \theta), (4, \theta), (5, \theta), (6, \theta), (7, \theta) \right\}$$

$$= \left\{ (m, n) \middle| (0,0), (0,1), (1,1), (1,2), (2,2), (2,3), (3,3), (3,4) \right\}$$

Note that if L2-norm is used, the radii of the circles where the pixels are located are irregular. In addition, the continuous Cartesian coordinate closest to the discrete coordinate is not guaranteed to be on the same radius. Thus, using L2-norm, it is impossible to determine the discrete Cartesian coordinate (m, n) corresponding to a polar coordinate (r, θ). For example, the discrete Cartesian coordinate closest to a point $1.\exp(j\frac{24}{100}\pi)$, whose actual radius is 1, is $(1,1)$ of which radius is not $r = 1$ but $r = \sqrt{2}$.

3. Application to Image Processing

The image of cancerous masses of breast tissue is an example of bio-medical images. The masses diffuse outward from their centre radically. In order to reduce the local irregularities of the image signals, it is necessary to smooth the images. To smooth the image in a discrete polar coordinate system, we apply the LMS filtering to the pixels on the line stretching from the origin outward. The line is rotated 360 degrees about the origin. At any given angle, the positions of the pixels on the line can be found using Eq. (1) and (4). Figure 3 depicts the proposed radial smoothing method.

Figure 4 shows comparisons among the original image, an image smoothed using Gaussian filtering [4], and an image smoothed using the proposed radial filter, respectively. The filter order was set to 7 for both smoothing filters for comparative purposes. As shown in the figure, the Gaussian filter blurs the overall shape of the mass. However, the proposed method reduces instability of the image signal while maintaining the overall radial shape of the mass.
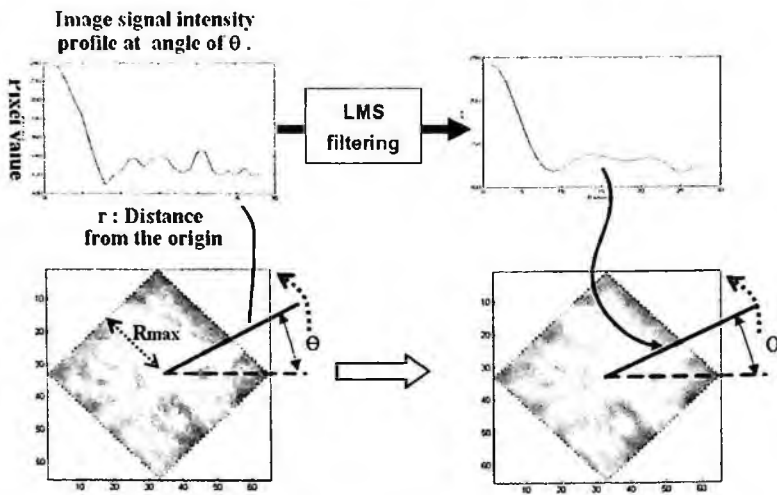
Fig. 3. A diagram of the proposed radial filtering method
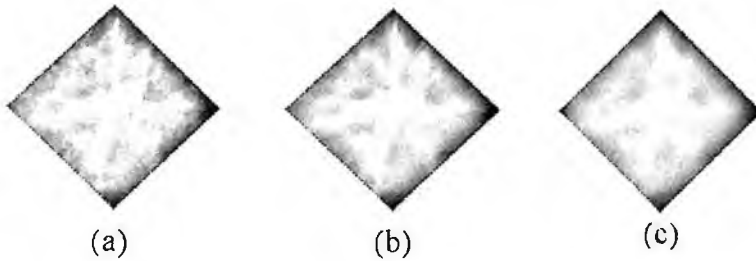
Fig. 4. Smoothing mass-cancer image: (a) Original mass image, (b) The proposed radial filtering method using LMS filter, and (c) Gaussian filtering

4. Conclusions

In this paper, since it is impossible to construct a discrete polar coordinate system using L2-norm, we have developed a method for constructing a discrete polar coordinate system based on L1-norm. Processing images with radial properties, such as bio-medical images, in a discrete polar system efficiently preserves the radial characteristics of such images. Processing similar images in a conventional Cartesian system deteriorates the radial characteristics of the image being processed.

References

1. Rangayyan R.M., Mudigonda N.R. and Desautels J.E.L., *Medical and Biological Engineering and Computing*, **Vol. 38**, 487 (2000).
2. Barlaud M., 'Wavelets in Image Communication', ELSEVIER, 131 (1994).
3. Barlaud M., Sole P., Antonini M. and Mathieu P., *IEEE trans. on Image Processing*, **Vol. 3**, 367 (1994).
4. Gonzalez R.C. and Woods R.E., *Digital Image Processing*, Prentice Hall, (2002).
5. Gibson J. and Syood K., *Advanced Electronic Physics*, **Vol. 72**, 259 (1988).

NONLINEAR DIFFUSION EQUATION FOR IMAGE DENOISING IN MIXED-GAUSSIAN NOISE ENVIRONMENT

HEE IL HAHN

Dept. of Information and Communications Eng., Hankuk University of Foreign Studies, Yongin-Si, Kyunggi-Do, Korea

DAE HYUN RYU

Dept. of IT, Hansei University, 604-5 Gunpo-Si, Kyunggi-Do, Korea

We propose a nonlinear image denoising algorithm obtained by applying nonlinear function to the partial differential equation. The statistics for the neighbor differences between the particular pixels and their neighbors are introduced. They are incorporated into the filter to remove additive mixed-Gaussian noise contaminating images. The derived denoising method corresponds to the maximum likelihood estimator for the heavy-tailed Gaussian distribution. The error norm corresponding to our estimator from the robust statistics is equivalent to Huber's minimax norm. Our estimator is also optimal in the respect of maximizing the efficacy under the above noise environment.

1. Introduction

For the past 20 years or so, a diverse set of researches took place in the computer vision in order to analyze signals or image in multiscale. It is possible to express signals in multiscale via iterative filtering. However, linear scale spaces manifest many limitations in the areas of segmentation, denoising, deblurring and so forth. In other words, blurring and distortion of the location and form of the edge are inevitable as results of repeated filtering. These are pointed out as limitation of linear time invariant filtering. High frequency component should be eliminated to remove noise while it is needed to retrieve high frequency component to find clear edges. There is a dilemma in which two objectives cannot be achieved simultaneously with linear time-invariant filters[1, 2, 5].

To overcome the limitations of the linear scale space, Perona and Malik proposed the concept of non linear scale space to remove noise while preserving the contrast at the boundaries. They emphasized the boundaries between regions while blurring is allowed within the regions. As such, they sought to enhance the visual quality or accurately segment regions by decreasing the possibility of changing the location of the edge in accordance with the scale. However, it is not

easy to suppress blurring at the boundaries as the scale increases. Pollak modified the algorithm suggested by Perona and Malik, and proposed that adjacent samples merged and grouped together as soon as they have the same pixel values [3].

In this paper, we propose a robust image denoising algorithm which can be implemented in nonlinear scale space. The error norm corresponding to our algorithm is equivalent to Huber's minimax norm. Our algorithm proves to be optimal in the respect of maximizing the efficacy under the mixed-Gaussian noise environment whose density function is Gaussian on $(-\delta, \delta)$, but Laplacian outside the region as given by

$$
f(x) = \begin{cases} Ce^{-a\delta^2/2}e^{-a\delta(x-\delta)}, & x > \delta \\ Ce^{-ax^2/2}, & -\delta \le x \le \delta \\ Ce^{-a\delta^2/2}e^{a\delta(x+\delta)}, & x < -\delta \end{cases} \tag{1}
$$

where, of course, C should be chosen so that the density $f(x)$ has unit area by proper adjustment of a and δ.

2. Proposed Algorithm

In deriving our robust denoising filter, we employ an observed image model corrupted with additive Gaussian and impulsive noise

$$
y_i = x_i + n_i, \quad i \in \mathbb{Z}^2 \tag{2}
$$

where n_i is a zero-mean additive white Gaussian noise plus impulsive noise. n_i is uncorrelated to the image sequence x_i and y_i is the observed noise-contaminated image sequence. In this case, n_i can be assumed to have a density function whose tails are heavier than Gaussian. To ensure the unbiasedness of the maximum likelihood estimator, its density function is assumed to be symmetric.

The MLE of μ that maximizes the above density function is given by

$$
\hat{\mu} = \frac{1}{M}\sum_{i=1}^{M} x_i = \arg\min_{\mu} \sum_{i=1}^{M}(x_i - \mu)^2 \tag{3}
$$

The MLE is just the sample mean and $\hat{\mu}$ is known to be a minimum variance unbiased and consistent estimate. This means that the MLE for estimating the signal under the additive Gaussian model is a mean filter. It can be interpreted as optimum filter in the sense of mean-square errors.

Likewise, when the observations have a density of Laplacian instead of Gaussian, the density function for M independent observations is

$$p_L(x/\eta) = \frac{1}{(2)^{M/2}\sigma^M} e^{-\frac{\sqrt{2}}{\sigma}\sum_{i=1}^{M}|x_i-\eta|} \tag{4}$$

and the MLE of η that maximizes the above equation is given by

$$\hat{\eta} = \arg\min_{\eta} \sum_{i=1}^{M}|x_i - \eta| \tag{5}$$

Its MLE corresponds to the median filter which selects the sample located at the center after arranging the observations in the ascending order. Thus, combining the results given in Eq. (7) and (9) we obtain the MLE of θ for the density function given in Eq. (5).

$$\hat{\theta} = \arg\min_{\theta} \left\{ \sum_{|x_i|\le\delta}(x_i - \theta)^2 + \sum_{|x_i|>\delta}|x_i - \theta| \right\} \tag{6}$$

The corresponding filter can be easily implemented by

$$\hat{\theta}_\delta = \sum_{i=1}^{M} g(x_i) \tag{7}$$

where

$$g(x) = \begin{cases} a\delta, \ldots\ldots\ldots x > \delta \\ ax, . -\delta \le x \le \delta \\ -a\delta, \ldots\ldots x < -\delta \end{cases} \tag{8}$$

We call this filter as an amplitude-limited sample average filter (ALSAF). The efficacy of the estimate can be found out as follows,

$$\xi = \frac{\left[\int_{-\infty}^{\infty} g'(y)f(y)dy \right]^2}{\int_{-\infty}^{\infty} g^2(y)f(y)dy} \tag{9}$$

In the above equation, $f(x)$, given in Eq.(5), represents the density function for each observation.

Since $g(x) = -f'(x)/f(x)$. Efficacy ξ has the maximum value. Thus, the ALSAF given above is the optimal estimate in terms of maximizing the efficacy under the above noise environment. The error norm corresponding to our estimator from the robust statistics is given by

$$\rho(x) = \begin{cases} ax^2/2 \ldots\ldots\ldots\ldots\ldots |x| \le \delta \\ a\delta|x| - a\delta^2/2 \ldots\ldots\ldots |x| > \delta \end{cases} \tag{10}$$

This is equivalent to Huber's minimax norm [6]. To apply our denoising filter, we need to choose the variables a and δ as given in Eq. (5) and Eq. (10), which depends on the statistics of the noisy images. The value of δ is inversely proportional to the amount of outliers such as impulsive noise. If the value of δ is equal to the standard deviation σ of the density function given in Eq. (5), the distribution will be similar to Gaussian, which means that the outliers rarely exist. Thus, δ should be less than σ (typically $\delta = 0.8\sigma$). The probability p_G that the noise is greater than δ is computed as

$$p_G = 2Ce^{-a\delta^2/2} \int_\delta^\infty e^{-a\delta(x-\delta)}dx = \frac{2C}{a\delta}e^{-a\delta^2/2} \tag{11}$$

And the probability p_L that the noise is less than δ is

$$p_L = C\frac{\sqrt{2\pi}}{\sqrt{a}}\left(\Phi\left(\sqrt{a}\delta\right) - \Phi\left(-\sqrt{a}\delta\right)\right) \tag{12}$$

where $\Phi(x) = \frac{1}{\sqrt{2\pi}} \int_{-\infty}^x e^{-\frac{y^2}{2}}dy$.

a is chosen empirically for each specific image such that $p_G = p_L$ to optimize the estimate. The ALSAF is iteratively applied to reduce any residual noise by estimating the variables a and δ from the statistics of the neighbor differences at each iteration. The algorithm stops when the residual error between the current and the next estimate falls below some threshold at each pixel, which is usually less than δ. Recall the Perona-Malik (PM) anisotropic diffusion [4]

$$I_t = \bar{\nabla} \cdot \left\{ h\left(\left|\nabla I\right|\right) \nabla I \right\} \tag{13}$$

where $\bar{\nabla}, \nabla$ denotes divergency and gradient, respectively. Since the robust estimation can be posed as:

$$\min_I \int_\Omega \rho\left(\left|\nabla I\right|\right)d\Omega \tag{14}$$

where Ω is the domain of the image. Eq. (18) can be solved using the gradient descent as follows:

$$I_t = \bar{\nabla} \cdot \left\{ \rho'\left(\left|\nabla I\right|\right)\frac{\nabla I}{\left|\nabla I\right|} \right\} \tag{15}$$

Comparing Eq. (14) with Eq. (19), we can obtain the relation

$$h(x) = \frac{\rho'(x)}{x} = \begin{cases} a.................\left|x\right| \le \delta \\ ak\dfrac{\text{sgn}(x)}{x}....\left|x\right| > \delta \end{cases} \tag{16}$$

Thus, our denoising algorithm can be implemented using PM anisotropic diffusion by selecting the edge stopping function $h(x)$ given in Eq. (20).

3. Experimental Results

The widely used gray-scale "Lena" and "House" images are selected to test our proposed method. Two kinds of noise statistics are exploited in this paper. One is the Gaussian noise injected to the test image. The other is symmetric α − stable random noise, which is best defined by its characteristic function

$$\varphi(w) = E\left[e^{jwx}\right] = \exp\left(j\delta w - \gamma |w|^{\alpha}\right) \tag{17}$$

where α is the characteristic exponent restricted to the values $0 < \alpha \le 2$, $\delta(-\infty < \delta < \infty)$ is the location parameter, and $\gamma(\gamma > 0)$ is the dispersion of the distribution. For example, Gaussian and Cauchy distributions are special cases of symmetric α − stable distribution of $(\alpha = 2)$ and $(\alpha = 1)$, respectively. Simulations are carried out for a wide range of noise density levels and varying α values.

The performance of our denoising method is evaluated by way of mean-square-error (MSE) metric and peak signal-to-noise ratio (PSNR). Fig. 1 shows the simulation results when the gray scale Lena image of size 256×256 is corrupted with Gaussian noise of variance $\sigma_n^2 = 924$. Our denoising filter tends to suppress noise without severely destroying the fine details, compared with that of PM anisotropic diffusion although their objective quality of measure is similar. Fig. 2 shows the experimental results when the "House" image is corrupted with α -stable(α =1.8) random noise. Our proposed algorithm shows an excellent performance in reducing heavy-tailed Gaussian noise as well as Gaussian noise.

| (a) | (b) | (c) |

Fig. 1. (a) Lena image corrupted with Gaussian noise of variance $\sigma_n^2 = 924 (PSNR = 20dB)$. (b) PM anisotropic diffused image after 10 iterations with $\sigma_n^2 = 153.3$ and $PSNR = 26.3dB$ (c) Output of the ALSAF after 10 iterations with $\sigma_n^2 = 137.6$ and $PSNR = 26.8dB$.

(a)   (b)   (c)
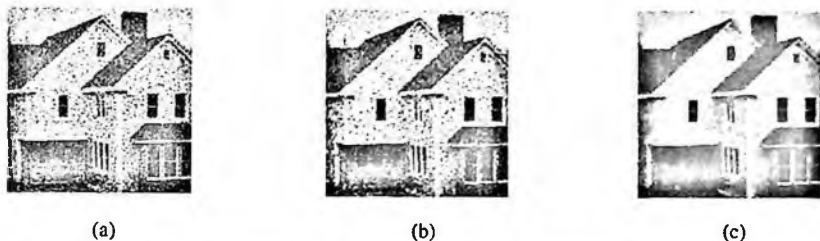
Fig. 2. (a) House image of size 256x256 corrupted with α-stable(α =1.8) random noise whose power and PSNR are 2040.3 and 15.03. (b) Output of myriad filter with $\sigma^2 = 982.9$ and $PSNR = 18.2dB$ (c) Output of the ALSAF after 10 iterations with $\sigma^2_* = 733.3$ and $PSNR = 19.5dB$.

4. Conclusions

Optimal nonlinear filter which maximizes the efficacy under mixed Gaussian noise environment is derived. This filter effectively can be implemented using PM anisotropic diffusion by selecting the appropriate edge stopping function. By combining amplifier-limiter which is a MLE in mixed Gausian noise with a PM anisotropic diffusion, the resulting filter is shown to effectively remove heavy-tailed Gaussian noise.

References

1. R. Yang, L. Yin, M. Gabbouj, J. Astola, and Y. Neuvo, "Optimal weighted median filters under structural constraints", *IEEE Trans. Signal Processing*, Vol. 43, No. 3, pp. 591-604, Mar, 1994.
2. A. Ben Hamza, P. Luque, J. Martinez, and R. Roman, "Removing noise and preserving details with relaxed median filters", *J. Math. Imag. Vision*, Vol. 11, No. 2, pp. 161-177, Oct., 1999.
3. Ilya Pollak, Alan S. Willsky, Hamid Krim, "Image segmentation and edge enhancement with stabilized inverse diffusion equations," pp. 256-266, *IEEE Trans. Image Processing*, Vol. 9, No. 2, Feb., 2000.
4. Pietro Perona and Jitendra Malik, "Scale-space and edge detection using anisotropic diffusion," pp. 629-639, *IEEE Trans. Pattern Analysis and Machine Intelligence*, Vol. 12, No. 7, July, 1990.
5. A. B. Hamza and H. Krim, "Image Denoising: A Nonlinear Robust Statistical Approach," pp. 3045-3054, *IEEE Trans. Signal Process.*, Vol. 49, No. 12, Dec., 2001.
6. P. Huber, *Robust Statistics*. New York: Wily, 1981.

STUDY ON THE FIBER ORIENTATION OF WELD LINE PARTS DURING THE INJECTION MOLDING OF FIBER REINFORCED PLASTIC BY IMAGE PROCESSING

JIN-WOO KIM[†]

Department of Precision Mechanical Engineering, Chosun University Graduate School
375, Seosuk-Dong, Dong-Gu, Gwangju 501-759, South Korea

DONG-GI LEE

Department of Mechatronics Engineering, Chosun University, University
375, Seosuk-Dong, Dong-Gu, Gwangju 501-759, South Korea

In injection molded products using fiber reinforced plastic, weld line is unavoidable due to mold shaping factors such as the position and size and number of mold gate. The weld line leads to fiber orientation perpendicular to resin flow direction, suddenly lowering reinforcement effect and resultantly degrading mechanical properties of molded products. So far, there is no research on the measurement of fiber orientation in weld line using image processing. Using the image processing method, the fiber orientation distribution of weld-line in injection-molded products is assessed. And the effects of fiber content and injection mold-gate conditions on the fiber orientation are also discussed.

1. Introduction

Fiber reinforced plastic (hereinafter referred to as FRP) is superior to monomer resin in mechanical properties such as specific strength, specific stiffness, and heat resistance, and widely used for industrial products that require precision and light weight, such as in autos, plane and military suppliers and sports industries, and highly recognized as replacements due to its excellence that exceed properties of metals and ceramics.

There are various FRP molding methods: injection molding, compression molding, pressure molding and thermal molding. In using plastic materials for industrial products, the injection molding does rarely require finishing process and has quite higher productivity than others and is increasingly widely used.

In injection molded products using FRP, weld line is unavoidable due to mold shaping factors such as the position and size and number of mold gate. The weld line leads to fiber orientation perpendicular to resin flow direction,

---

[†] Corresponding Author: dglee@chosun.ac.kr

suddenly lowering reinforcement effect and resultantly degrading mechanical properties of molded products.

It is possible to prevent weld line by adjusting molding factors such as mold temperature, flow speed and pressure but it is basically difficult to free from other problems in production speed and improved contraction rate. Especially, the weld line can not be avoided in the injection mold that is equipped with multi gates even though it varies depending on the number of gates. To reinforce strength of weld line area by controlling fiber orientation, fiber orientation related studies may be necessary.

Most of studies on the movement of fiber in flow molding were conducted in Newton fluids but no studies were made on fiber orientation/content ratio of reinforcements in injection molding. This study examined how one gate and double gate molding factors affect fiber orientation/content ratio in injection molding that use FRP compound.

2. Theoretical background

Since most of FRP are very thin compared to their widths and lengths, the fiber is treated as two dimensional aggregations and fiber orientation angle distribution is measured. In case fiber is distributed in the planes of x-y, fiber orientation angle θ that forms with the x-axis is within the scope of $0 \leq \theta \leq \pi$. Therefore, between a variable that indicates a yardstick of fiber orientation distribution state (Hereinafter, called as the fiber orientation function J) and fiber orientation angle distribution $H_D(k)$, the relationship is defined as Eq. (1) [1].

$$H_D(k) = \frac{1}{\pi}\left[\left(\frac{1-J}{1+J}\right)\cos^2\theta + \left(\frac{1+J}{1-J}\right)\sin^2\theta\right]^{-1} \tag{1}$$

where J is a fiber orientation function that expresses the state of fiber orientation distribution in 2D; in case the fiber orientation is isotropy, fiber orientation function value is $J=0$, and in case of being in only one-direction (anisotropy), the value is $J=1$, and when it is arranged in rotation direction of 90° for the direction of $J=1$, then it is $J=-1$.

When calculating the fiber orientation angle by the intensity difference of pixel using the image processing from injection moldings' soft X-ray photo, the fiber orientation angle θ is calculated by Eq. (2) after calculating ΔH, ΔV in both horizontal and vertical directions of the central image element (Hereinafter, called as the pixel) using the Sobel operator.

$$\theta = \tan^{-1}\left(\frac{\Delta V}{\Delta H}\right) + \frac{\pi}{2} \tag{2} \qquad C = \frac{(|\Delta H| + |\Delta V|)}{2} \tag{3}$$

When calculating the fiber quantity C with the θ direction of fiber orientation angle, the intensity value of pixel is calculated by using Eq. (3).

When fiber orientation angle θ and fiber quantity C were obtained for all pixels by reading the numerical data of the intensity obtained from soft x-ray photo. Fiber orientation angle distribution $H_D(k)$ would be calculated by Eq. (4) [2].

$$H_D(k)\frac{N_\theta(k)}{\sum_{i=0}^{n-1}N_\theta(i)}, \text{k=0, 1, ..., n-1} \tag{4}$$

where n is the division number at $0\leq\theta\leq\pi$, and $N_\theta(k)$ is the number of pixels in the contour line direction of the fiber at $(2k-1)\,\pi/2n\leq\theta\leq(2k+1)\,\pi/2n$.
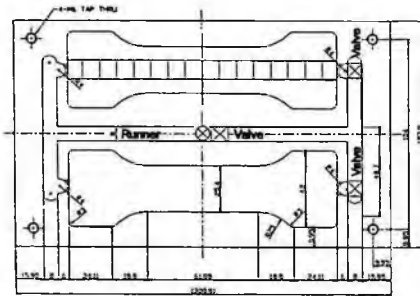
Fig. 1 Dimensions of injection mold and parts for measuring using image processing
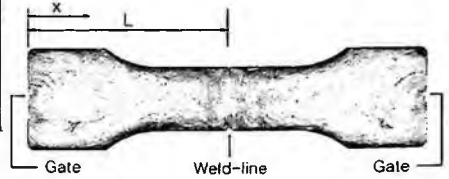
Fig. 2 Soft X-ray photography of products after injection molding

Combustion specimens for measuring the fiber content ratio are extracted in the neutral of the specimen in Fig. 1. And it was heat and burn specimens at 600℃ for 30 minutes using an electrical furnace and measured fiber contents ratio in the weight before and after burning using precision electronic scale. (1/10,000g) fiber content ratio Q_{fr} would be calculated by Eq. (5).

$$Q_{fr} = \frac{Q_f}{Q_{f0}} \tag{5}$$

where Q_f is weight fiber content ratio after injection molding, and Q_{f0} is weight fiber content ratio before injection molding.

3. Test

FRP compound includes polypropylene (hereinafter referred to as PP) as matrix and glass fiber as reinforcement (reinforcement: glass fiber 10mm in length, 17μm in diameter). Fiber content ratio was 50wt% and injection molded product was in the form of pellet that was added by glass fiber and PP. The fiber length is 10mm. LG's IDE75ENII was used as injection molding machine, which has screw diameter of Φ36mm, and shaping strength of 75ton, and maximum

injection weight of 103g and maximum injection pressure of 1400kg /cm², and shaping travel of 270mm. A mold with double gates and two cavities, with gate and runner of 8mm, respectively in diameter, was made for use in this study as shown in Fig. 1. The final shape taken from FRP injection molded product had thickness of 4mm, width of 25.4mm and length of 150mm.

Fig. 2 shows soft X-ray photo of FRP injection molded product, wherein dark part represents glass fiber, and bright part PP, respectively. Due to collision of resin sprayed from double gate, fiber is oriented almost perpendicular to resin's flow direction in the weld line part and fiber is oriented in a fountain wave form while flow occurs from small nozzle to large nozzle in the gate part. It can be seen that fiber is oriented toward the flow direction in the central part between gate and weld line. Fiber orientation distribution has close relation with dynamical property.

Area for measurement of fiber orientation and fiber content ratio distribution from mold gate to weld line was taken by 10mm×10mm as shown in Fig. 1 The measurement area was taken by 80×80 pixels and density info of each pixel was examined by image scanner and the data processed binary and pixels with higher density than threshold value were taken as fiber.

In this experiment, threshold value is 0 and fiber orientation x-axis of flow direction was set at 0° and fiber was entirely measured clockwise and counterclockwise, and n was divided into 18 fractions at $0 \leq \theta < \pi$ and measured fiber orientation angle θ was 10°.

Fiber orientation angle θ is calculated by using density info obtained from soft X-ray in Eq. (2). All pixels in entire images, fiber orientation angle distribution is calculated in Eq. (4) and fiber orientation function J value is obtained by the least square method in Eq. (1) and it could act as quantitative measure for inferring fiber orientation state.

A specimen was made according to ASTM D638M and the experiment was conducted by using UTM (HOUNDS FIELD Universal Testing Machine 5ton). At this time, cross head velocity was set at 1.24mm/min.

4. Test results and considerations

Fig. 3 shows relationships between relative length (x/L) from gate and fiber orientation function. FRP materials, which consist of solid glass fiber and fluid PP, undergo separation and orientation resulting from difference in flow velocity during injection molding at high temperature. It can be seen as shown in Fig. 2 that fluid resin returns along the wall of mold in the weld line part for double

gate, the end part of wall across the mold gate for one gate, respectively, and that solid fiber is oriented in the form of fountain waves by mutual interference.

In case of weld line, fiber orientation function (J) value largely varied at about 0.8 of relative length (x/L) from mold gate when flow path narrowed. It can be seen that this phenomena is affected by the collision of glass fiber with PP in weld line, not by mold pellet part, and PP flows back and glass fibers are tangled with each other and fiber is oriented vertically at about 0.8 of relative length.
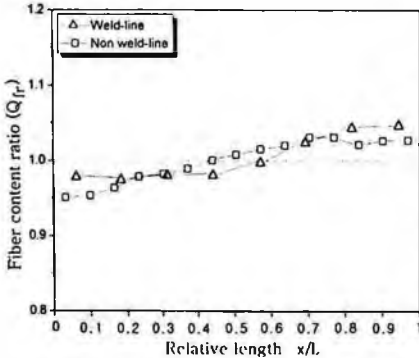
Fig. 3 Relationship between relative length (x/L) from gate and fiber orientation function J
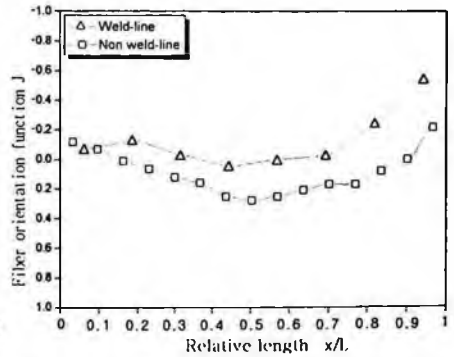
Fig. 4 Relationship between relative length (x/L) from gate and fiber content ratio Q_{fr}

In case of non weld line, fiber orientation is greatly affected by mold pellet part when resin and fiber flow at high temperature from large nozzle to small nozzle, and back to large nozzle. The fiber orientation occurs when resin and fiber flows at high temperature from large nozzle to small nozzle and fibers are collided with the end part of wall across mold gate when flowing from small nozzle to large nozzle and oriented perpendicular to the flow direction. In case of non weld line, fiber orientation underwent sudden change vertically to the flow direction at about 0.8 of relative length from mold gate.

Fig. 4 shows relationship between relative length from gate and fiber content ratio Q_{fr}. The more distant from mold gate, the more increasing fiber content ratio. For double gate in flow line, fiber content ratio was about 5% more, compared with one gate. As shown in Fig. 4, in case of weld line in the central part of molded product, fibers are tangled in the form of crater by mutual interference with collided fibers and flow velocity difference between fiber and resin drive melted resin to return.

Fig. 5(a) shows broken part of specimen with weld line that underwent tensile stress and Fig. 5(b) shows broken part of specimen with non weld line. For double gate, breakage occurred in weld line, and for one gate, breakage

occurred at about 0.8 point of x/L from mold gate. Tensile strength of weld line is 26MPa. Tensile strength of non weld line is 26MPa.

When tensile stress is applied to FRP injection molded specimen, fiber is oriented vertically to load direction and is not almost under load and instead, resin is under most of load. As a result, tensile stress is lowered and reinforcement effect is also reduced. It can be inferred that the specimen, which is cleared of weld line, has three times higher tensile stress than that with weld line.
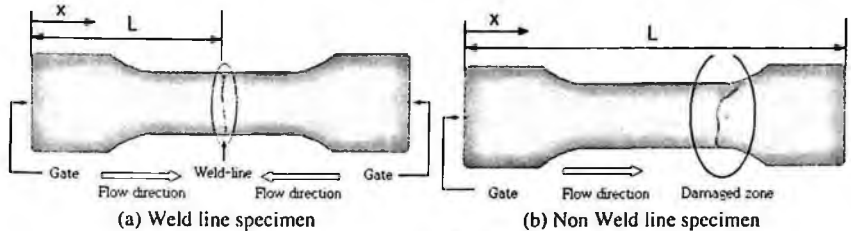
(a) Weld line specimen   (b) Non Weld line specimen
Fig. 5 Schematic view of failure due to tensile strength

5. Conclusion

In case of weld line, fiber orientation takes place when fibers are tangled in weld line, and in case of no weld line, fiber orientation are largely affected by mold pellet part. Irrespective of weld line, fiber orientation suddenly varies at about 0.8 point of relative length from mold gate. For melted materials flowing from mold gate, the more distance from gate due to flow velocity difference, the more increasing fiber content ratio. In case of weld line, fiber content ratio was about 5% more than non weld line due to mutual interference between fibers that collided in flow line. It can be seen that during tensile stress test of FRP injection molded product, damage occurs when fiber orientation function value suddenly changes, resultantly reducing reinforcement effect as well as lowering tensile stress.

References

1. K. Yamada and A. Horikaw, *Textile Machinary Soc. of Japan*, **37**, 51-64 (1984).
2. H. Tamura, S. Mori, and T. Yamawaki, *IEEE Transactions on Systems, Man, and Cybernetics*, **8**, 460-472 (1978).
3. J. W. Kim and D. G. Lee, *Key Engineering Materials*, **321-323**, 938-942 (2006).

REAL-TIME FACE AND HAND DISCRIMINATION AND 3D POSITION EXTRACTION USING A STEREO VISION EMBEDDED SYSTEM

YOUNG-KEUN KIM

Department of Computer Software & Engineering Korea University of Science and Technology, Daejeon, Korea
placeo@etri.re.kr

HO CHUL SHIN

Intelligent Robot Division, Electronics and Telecommunication Research Institute Daejeon, Korea
creatrix@etri.re.kr

JAE IL CHO

Intelligent Robot Division, Electronics and Telecommunication Research Institute Daejeon, Korea
jicho@etri.re.kr

DAE-HWAN HWANG

Intelligent Robot Division, Electronics and Telecommunication Research Institute Daejeon, Korea
hdh@etri.re.kr

In this paper, we propose real-time face and hand discrimination and 3D position extraction using a stereo vision embedded system. We used the stereo vision process on FPGA to get the disparity image and also developed the embedded system to obtain the image sequence and to perform image processing. Then we applied the simple and reliable algorithm we developed to detect and discriminate head and hand in real-time. The algorithm is based on various spatial image processing and trigonometry. We also show the experimental result to support validity of the system and the algorithm.

Keywords: 3D position; stereo vision; head and hand detection; head and hand discrimination; embedded system.

Topic area - Interfaces to multimedia and multimodal interaction

1. Introduction

The detection and discrimination of the hand and face is very important in many image related application like gesture recognition and to execute natural human-computer interaction, real-time implementation is demanded. So, simple and fast algorithm is necessary [1]. And for the purpose of practical and economic use, It is necessary the system to be composed of embedded system. To implement these requirements, we propose new real-time face and hand discrimination and 3D position extraction using a stereo vision embedded system.

In this research, we used the stereo vision system on FPGA which aims to ASIC that produces disparity image and also developed embedded system for obtaining the image sequence and image processing. And we applied the 3D head and hand detecting algorithm to this system. This algorithm is based on various spatial domain image processing like edge detection, skin color and trigonometry that is used to obtain distance, width and height information. We also made the decision rule to discriminate head and hand which uses height and edge information.

Using proposed system, we could execute head and hand detection by 30 fps and 80x60 resolution with high accuracy, and also discriminated head and hand. Finally we show inspection result of the system performance by diverse experiments.
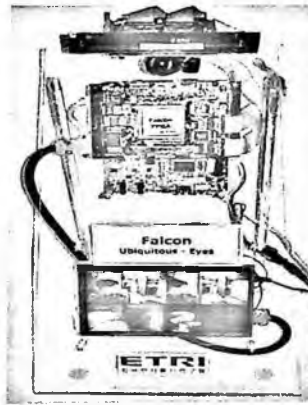
Fig. 1. Developed embedded system and FPGA

2. Proposed Method

2.1. Hardware Configuration

Developed hardware system is mainly divided into two parts. The FPGA board processes images from two cameras and produces disparity image. The embedded system obtains image from FPGA board and executes various image processing.

1) Stereo vision FPGA : The stereo vision has wide range of usage and many applications have been developed. Due to recursive simple computation, it is desirable to be implemented by ASIC. In ETRI, ASIC is being developed which is based on Trellis DP algorithm [2]. Now, it is verified the algorithm implemented on FPGA. The used number of gate is about 2,000,000 gates. Developed FPGA outputs disparity image that has 320x240 pixels and frame rate of 30fps shown as Figure 2.

Fig. 2. Stereo vision result

2) Embedded system for image acquisition and processing : The embedded system controls CMOS camera and receives the image sequence from two cameras, then sends to FPGA.

After stereo vision processing in FPGA, the embedded system receives computed data from FPGA.

We adopted i.MX21(350MHz) embedded processor from Motorola's 6th generation Dragon Ball and it was optimized. With i.MX21 main processor, we developed main control board, MIM (Multi-modal Interface Module) which operates at Linux 2.4.20 shown as Figure 3.

2.2. The Detection of Head and Hand

Skin color detection is widely used to face detection, recognition, gesture recognition and etc. But skin color has defects that can be easily affected by illumination, background, camera characteristic and ethnicity. Illumination and camera characteristic is affected by the performance of camera, this background color problem can be solved by using stereo vision [3].

In this research, we eliminated background by using stereo vision then detected face and hand region by using skin color. In case abnormal detection, we performed adaptive color compensation.
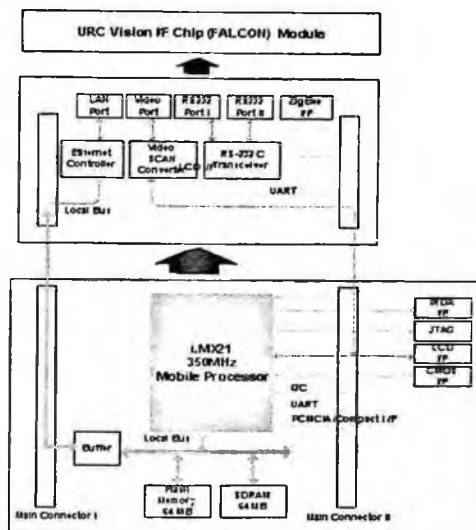
Fig. 3. Embedded system structure

1) Background elimination, skin color extraction and segmentation : Shown in Figure 4, initially the foreground skin color region detection is executed by using actual color image and disparity image. The image binarizing was frequently used in order to detect the detected region. And to reduce computational power, resolution is reduced to 80x60. First, the skin color region is extracted by using the chrominance components of actual image. YUV color space is mainly used because chrominance components of this space don't be affected by illumination much [5]. And using disparity map, background subtraction is performed. Then, foreground skin region is extracted by comparing with formerly extracted skin region. To reduce noise, Gaussian filtering is performed to foreground skin region. 5x5 Gaussian mask is used to our implementation. Next, remaining regions are segmented. To segment extracted region, we used seed method. Seeds are sprayed to the Gaussian filtered image with regular interval, then volumes are enlarged in case of extracted region, if not, volume growing is stopped. After that, each volume is labeled. Finally, the depth, size and position are calculated to the foreground skin region divided after labeling process in the pixel domain. This calculation is performed by using the trigonometry. By calculating the average disparity value of extracted region, the disparity value of object is obtained. And this disparity

value is converted to the distance value. By using the triangulation, the height and width of an object is calculated as shown in Figure 5. Finally these values are transmitted to next stage. Foreground skin region detection procedure is depicted in Figure 6.

2) *Skin color compensation* : In the Foreground skin detection, dominant problem is the case of a man wearing the cloth which is similar to the skin color. In this case, since it becomes the segmentation and labeling about the whole body
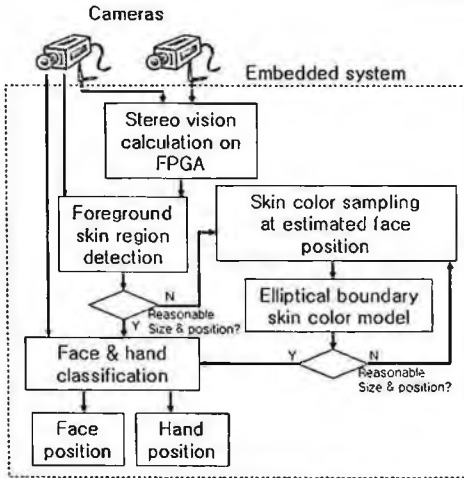
Fig. 4. Face and hand detection procedure

Fig. 5. Segmented and labeled skin region
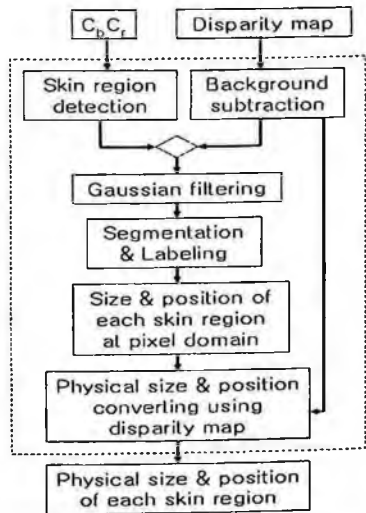
Fig. 6. Foreground skin region detection

of a man, the physical size of extracted region is appeared largely like an a and b compared with normal case c and d as shown in Figure 7. To extract the skin color region only, the candidate area is set by referencing the height of all labeled objects. We assumed that the head height is 22cm. because the head is usually positioned in the top, we can only get the head candidate region using trigonometry. After sampling skin color from the candidate region, elliptical boundary model is applied using the chrominance components.

Elliptical boundary model is defined as [7]

$$\Phi(c) = [c - \Psi]^T \Lambda^{-1}[c - \Psi] \tag{1}$$

$$\Psi = \frac{1}{n}\sum_{i=1}^{n} c_i, \Lambda = \frac{1}{N}\sum_{i=1}^{n} (c_i - \mu)(c_i - \mu)^T \tag{2}$$

Where c is the is the chrominance component matrix, N is the total number of samples, μ is the mean of the chrominance matrix in the sampled data set. c_i is the sampled chrominance matrix. Λ is the covariance matrix. $\Phi(c)$ is called the mahalanobis distance. The pixel chrominance c is classified as a skin color pixel, if $\Phi(c) < \phi$, where ϕ is a threshold value chosen empirically as a trade-off between the true and false positives.
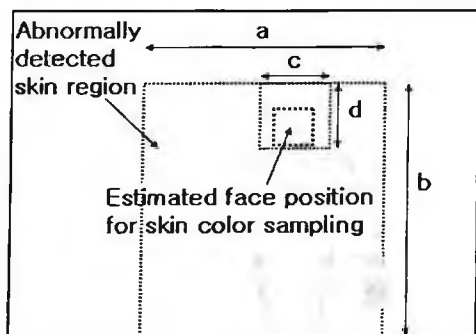
Fig. 7. Estimated face position for skin color sampling

2.3. Face and Hand Discrimination

After foreground skin region detection, each region is classified as face or hand. Generally, the face height is larger than hand and face has more horizontal patterns such as eyebrow, eye, nose and mouth. For the horizontal pattern detection, we used the horizontal sobel mask for the detected skin region and calculated the amount of horizontal patterns. We defined the face score by multiplying detected skin region height and amount of horizontal pattern as

shown in Figure 8. If face score is larger than the threshold value, the detected skin region considered as face.

3. Experimental Results

3.1. Face Detection Performance

The performance of the face detection can be different to people, because every one has a difference of the face size, color, brightness, the hair style, and etc of the face. Moreover, as the distance of a man and camera becomes further, the probability of an error being generated is increased. Figure 9. shows the face detection success ratio according to the distance of a man and camera from 100cm to 300cm. The face detection performance is measured in the proportion of the whole disposed frames to the frames determined by face.
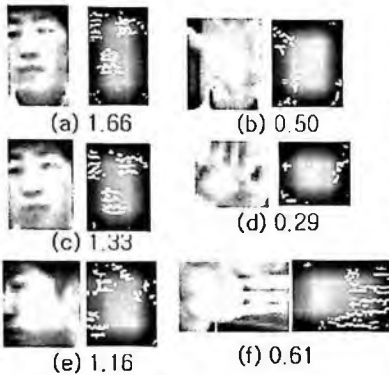
Fig. 8. Face scores for face-hand classification
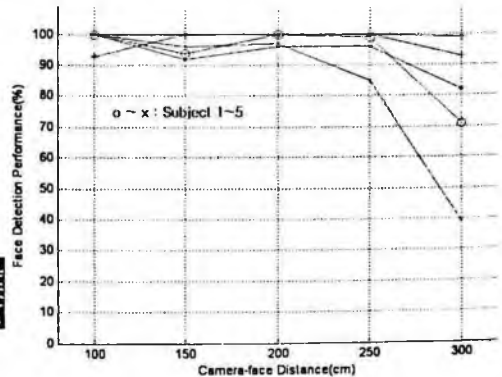
Fig. 9. Face detection performance

In the Table 1, the face-hand discrimination accuracy can be looked at. We determined whether the head and hand are correctly discriminated or not apart 1m and 2m from the camera.

3.2. 3D Position Accuracy of the Head and Hand

The distance of a camera and the area which is detected by using the average disparity value at the detected area can be calculated. The accuracy of the measured distance according to a distance between the face and a camera is shown at Figure 10. Usually if the distance between the camera and head is further, error is also increased. In Figure 11., the hand position accuracy on perpendicular direction to camera axis can be looked at.

Table 1. Face-hand discrimination accuracy

Distance	1m	2m
Performance	90%	87%
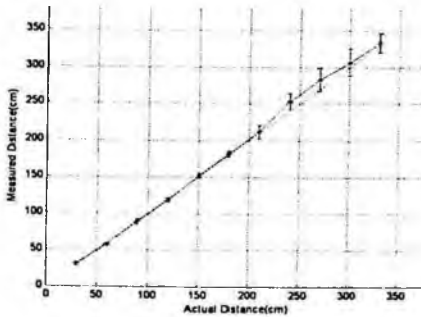
Fig. 10. Detected face distance accuracy
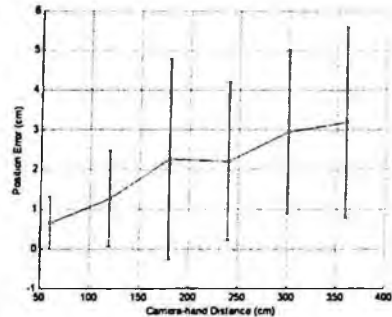
Fig. 11. Hand position accuracy on perpendicular direction to camera axis

4. Conclusion and Future Work

In this study, we developed a stereo vision embedded system and simple and fast real time face and hand discrimination and 3D position extraction algorithm. The developed system can detect foreground skin region using stereo vision background subtraction and skin region extraction. This system can recognize abnormal skin region detection such as skin color similar outfits, and extract minute skin color for elliptical skin color model from estimated face position using head shape from stereo vision. To classify face and hand, we defined a head score multiplied horizontal sobel edge density by physical height of detected region.

The developed system shows 98% face detection accuracy and 89% face-hand discrimination accuracy within 2 meters. It also shows the ±5cm 3D position error of face and hand within 2 meters. This system can be easily applied to various applications and we are developing a gesture recognition system.

References

1. Mau-Tsuen Yang, Shih-Chun Wang, Yong-Yuan Lin, "A multimodal fusion system for people detection and tracking," *International journal of imaging systems and technology*, v.15 no.2, 2005, pp.131-142.
2. Hong Jeong, Yuns Oh, *"Parallel Trellis Based Stereo Matching Using Constraints,"* *Lecture notes in computer science*, pp. 227-237, 2000.
3. N. Jojic, B. Brumitt, B. Meyers, S. Harris, T. Huang, "Detection and estimation of pointing gestures in dense disparity maps," *Automatic Face and Gesture Recognition,* 2000, pp. 468-475.

4. D. Chai, K.N. Ngan, *"Face segmentation using skin-color map in videophone applications,"* *IEEE Trans. Circuits Syst.* Video Technol. 9 (4), 1999.

5. P. Kakumanu, S. Makrogiannis, N. Bourbakis, *"A survey of skin-color modeling and detection methods,"* *Pattern Recognition,* Volume 40, Issue 3, pp. 1106-1122, March 2007.

6. Quan Huynh-Thu, M. Meguro, M. *Kaneko, "Skin-color extraction in images with complex background and varying illumination," Applicatinos of Computer Vision, 2002 (WACV 2002),* pp. 280-285.

7. J.Y. Lee, S.I. Yoo, *"An elliptical boundary model for skin color detection," Proceedings of the International Conference on ImagingScience, Systems and Technology,* 2002.

NON-DESTRUCTIVE EVALUAION OF CEMENT-GROUT BY SURFACE ELECTRICAL RESISTIVTY METHOD*

MUHAMMAD FAROOQ

Department of Mineral Resources and Energy Engineering, Chonbuk National University, Jeonju, 561-756, South Korea

JUNG HO KIM

Geotechnical Engineering Division, Korea Institute of Geoscience and Mineral Resources, Deajeon, 350-305, South Korea

SAMGYU PARK

Geotechnical Engineering Division, Korea Institute of Geoscience and Mineral Resources, Deajeon, 350-305, South Korea

YOUNG SOO SONG

Department of Mineral Resources and Energy Engineering, Chonbuk National University, Jeonju, 561-756, South Korea

Artificial lowering of the groundwater level in karst region has led to the formation of sinkholes and subsidence. Where ground movements develop, it has become standard practice to drill boreholes to inject cement mortar (slimes), cement mortar is injected into limestone cavities beneath the road in the project area, in order to improve strength and reduce permeability; the extent to which grout has penetrated in cavities need to be monitored in order to determined effectiveness of cement-grout. Geophysical approaches, offer great potential for monitoring and evaluating the grout injection process in cost-effective and nondestructive way. This paper presents the applicability of surface electrical resistivity method to examine the evaluation of the cement-grout. In order to image the cement-grout, time-lapse surface electrical resistivity surveys were conducted to compare electrical resistivity images before, during and after injection. Cement-grout was imaged as anomalies exhibiting low resistivity than the surrounding rocks. In accordance with field monitoring, laboratory study was also designed to monitor the resistivity changes of cement mortar specimens. Time-lapse laboratory measurements indicated that electrical methods are good tool to identify the grouted zone. Pre-grouting, during grouting and post grouting electrical images showed significant changes in subsurface resistivity at grouted zone. The study showed that electrical resistivity

---

imaging technology can be a useful tool for detecting and evaluating changes in subsurface resistivity due to the injection of the cement-grout.

1. Introduction

Grouts are injected into fractured rock, subsurface cavities and foundation wall in order to increase mechanical resistance and reduce permeability. The extent to which grout has penetrated needs to be monitored in order to determine effectiveness of grouting work. Furthermore, the monitoring of the grouting effect during grouting reinforcement would be meaningful to control the actual grouting operation for better performance. Monitoring of the success of grout injection currently relies on hydraulic test and boreholes drill. These are time consuming, expensive and drilling boreholes can provide only point information at drilling location [2]. On the other hand geophysical approaches present a quick and relatively inexpensive approach, can provide the continuous two-and-three dimensional images of grouted zone.

Geophysical methods such as ground penetrating radar, electrical resistivity and seismic are perhaps the most know nondestructive technique among geophysicist and geotechnical engineer [1]. In the study area, ground penetrating radar could not be applied, due to salinity and seismic method could not be applied, due to heavy traffic. Under these conditions electrical resistivity is the most suitable method for the investigation of grout material. Since the electrical conductivity of cement mortar is fairly high [4]. This paper described that electrical resistivity investigations were carried out to assess the success of grout modification work. Electrical resistivity surveys were carried out in three phases, pre, during and post grouting injection. In accordance with the field monitoring, laboratory study was also designed to monitor the resistivity change of cement-monitor specimens. We tried to examine the applicability of electrical method to the evaluation of the cement-grout during ground stabilization.

2. Data Acquisition and Processing

To monitor the changes in ground resistivity pre, during and post grouting, surface resistivity survey has been conducted. Nine resistivity traverse namely, line 1, line 2 ... line 9 were conducted along the survey area. The orientation and extent of those lines are shown in figure 1. Each survey line was double scanned using dipole-dipole and modified pole-pole [5] array. Electrodes were installed with 5 m spacing and length of each profile was about 95 m. Lines 4, 5 and 6 has been permanently installed in the monitoring area, to which a data acquisition system has been hooked up each time. At the first stage of monitoring, electrodes were buried at 10 cm depth to improve the electrode contact. Resistivity survey data were measured using SuperSting R8/IP™ systems made by Advanced Geosciences Inc. The data acquisition process was completely controlled by software, which checked that all electrodes were connected and properly ground

before actual measurement started. DIPROfWin, two dimensional resistivity interpretation software developed by KIGAM, coded based on the 2.5 dimensional finite element modeling and the smoothness constrained least-squares inversion adopting Active Constraint Balancing (ACB) method [3] has been used for data processing.

Monitoring Phase	Acquired data	Grouting injection condition
Phase 1	04 Feb. 2006	Pre-grouting
Phase 2	17 Feb. 2006	Start of grouting
Phase 3	07 Mar. 2006	During injection
Phase 4	04 Apr. 2006	During injection
Phase 5	05 May 2006	Post-grouting
Phase 6	07 Jul 2006	Post-grouting

Table: History of resistivity monitoring profiles

Figure 1. Field layout of electrical survey

3. Laboratory Experiment

Laboratory measurements were conducted to investigate the time-lapse electrical changes that occur as the grout specimens undergo two different conditions (in air and in water). Four identical specimens were made, having 20 cm in length and 10 cm in diameter. Four electrodes were embedded within specimen to measure the electrical resistivity of the specimen. The outer two electrodes (C1 and C2) were used to apply current to the specimen. Two inner electrodes (P1 and P2) were used to measure the potential difference. Resistivity of specimens was measured by Mini OHM™ (OYO, Co, Japan). Four specimens were exposed two different environmental conditions. Specimen (1) and Specimen (2) were exposed to air, while Specimen (3) and Specimen (4) were placed inside water container. Grout specimens resistivity was measured at different ages, for about 8 weeks. In general, electrical resistivity of grout specimen will increase with time. Increase will be greater for air curing than for moist curing. In our study, it is observed that electrical resistivity vary over a wide range, mainly influenced by the moisture content. It was observed that electrical resistivity of exposed specimens was mainly depending on the moisture content and temperature. The resistivity of specimens was increased with time when the specimen was drying out. It is shown in Figure 2. On the other hand, the specimens within water environment absorbed water and gradually started cementation, showing the steady increase in resistivity. The resistivity of the specimens within water condition, increased so slowly that we could hardly

identify the amount of resistivity increases with time-lapse. After two month monitoring, the resistivity of saturated specimen remained less than 20 ohm-m (Figure 2). The graph shows that grout will be imaged as low resistivity because it is injected below the water table. The laboratory result indicated that electrical method is good tool to identify the grouted zone.
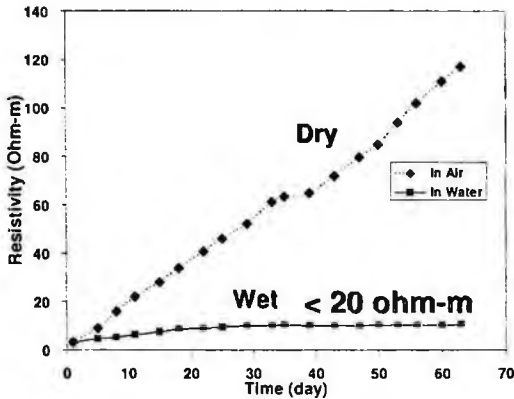
Fig. 2. Change of the resistivity of cement mortar specimen with curing time

4. Results and Interpretation

Pre-grouting survey data was collected. This data set was necessary for the comparison with subsequent data acquired during and after the grout injection. Resistivity ratios were calculated relative to pre-grouting survey. The resistivity of subsurface material before grouting is higher than 30 ohm. Figure 3 a and b present two-dimensional images collected during and after the grout injection. The laboratory experiment showed that the resistivity of the cement mortar in fully saturated condition did not exceed 15 ohm-m after two month curing. The ground water level of the monitored area is just 2 meter. Thus the grout is injected in groundwater must be saturated. In difference images, grouted region must be imaged as an anomalous zone. As discussed earlier, greater difference between the grout electrical properties and the surrounding rock, thus grout would be imaged as anomalous body. Figure 3a and b illustrated examples of differences images of line 6 and line 4. The time-lapse images of resistivity difference clearly show the grouted region by the decrease of resistivity. The phase 6 of line 6 shows the most obvious change of ground condition to the location of 60 m. Figure 3b illustrated the difference images of line 4, which show little changes of subsurface condition compared to line 6. The amount of cement injected through the boreholes adjacent to line 4 was much less than that of line 6.

5. Direct Investigation

Video camera shots have taken in the grouted zone provided physical sport and confirmation of the data provided by the electrical method. Two boreholes were drilled at the location where large amount of grouting material was injected, to check the directly consolidation state of grouted zone by using borehole televiewer (BHTV). The pictures reported in figure 4b shows the presence of a 1~2 meter of cement-grout at different depth. The BHTV and core cutting results, shows that the cavities are not filled completely. This may be due to leakage of grout material which might be due to interconnectivity of subsurface cavities.

6. Conclusions

In this study we examined the applicability of 2D electrical surveys to detect and map the cement gout in the subsurface cavities area. The major findings of the study are summarized as. Using time-lapse monitoring approach, we could easily and clearly identify the decrease of resistivity region, where the grout material was injected and infiltrated.

In this study surface electrical method was used because it is a non-destructive technology and the technology also provide good level of resolution to detect grouted zone due to big contrast between grout material and surrounding rock. A comparison of the pre and post grouting results showed a significant change in subsurface resistivity at the grouted zone.
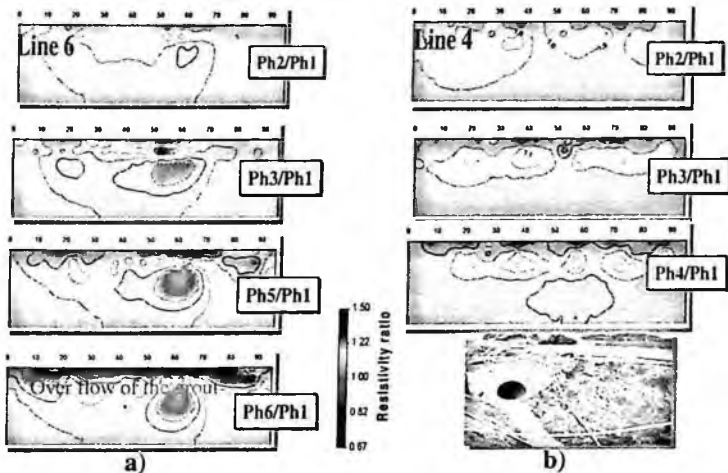
Fig. 3. a) Shows a series of two dimensional resistivity changes of line 6. which show how the electrical resistivity of the subsurface cavities during the grout injection. These resistivity ratios were calculated relative to the pre-grouting survey. b) Grout material was injected in few boreholes along line 4, shows shallow subsurface change in resistivity due to grout injection.

604
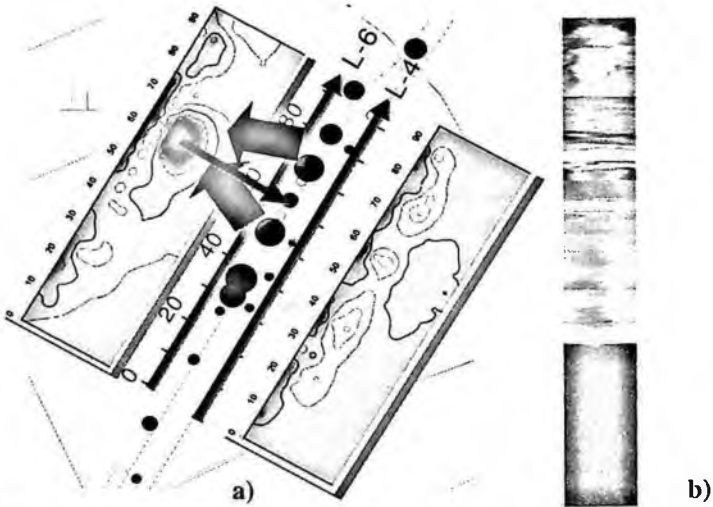
Fig. 4. a) The size blue dot represents the amount of grout injected at that location. Image shows that grout material migration has been taken place due to the interconnectivity of subsurface cavities. b) Determination of directly consolidation using BHTV carried out at the location where maximum amount of grout material was injected, the result shows that cavities are not filled completely and might be migrated from injection location.

The result of this study can be summarized that electrical method is an effective method to monitor grout injection.

Reference

1. Jung Ho Kim, -Jong Yi, Yoonho Song and Seung-Hwan Chung, *Mullt-Tamsa*, **Vol. 5, No. 4,** pp. 206~216 (2001)
2. Samgyu Park, Jung-Ho Kim, Changryol Kim, Seong-Jun Cho and Jeong-Sul Son, *Symposium on subsidence investigation, design and construction, KIGAM,* **pp. 71~85** (2005)
3. Yi, M.J, Kim, J.H, and Chung, S.H., *Geophysics,* **Vol. 68,** 931-941 (2003)
4. Wei, X, Li, Z *Materials and structures* **Vol. 38,** pp 411~417 (2005)
5. Jung Ho Kim, Yi, M.J, Song Yoon Ho, *Mulli-Tamsa* **Vol. 5, No. 4,** pp. 206~216 (2001)

EFFICIENT CLUSTERING BASED ON THE IMAGE CONTEXT FOR THE OBJECT RECOGNITION

EUNJIN KOH

Computer Software & Engineering, UST-ETRI,
Deajeon, South Korea

PHILL KYU RHEE

Computer & Software, Inha University
Incheon, South Korea

JONGHO WON

Digital Home, ETRI
Deajeon, South Korea

CHANGSEOK BAE

Digital Home, ETRI
Deajeon, South Korea

The image recognition using the pattern recognition and computer vision can be applied to various industry areas that need convenience, diversity, comfortable and nondestructive evaluation. Traditional object recognition techniques consider only the features of the object itself. But Givens' research [1] shows that we need to consider together the environments of the object. In order to consider the environments, we need to cluster the object images along the environmental features in training time. The adaptive selection of the cluster numbers that guesses the proper number of employs the Genetic Algorithm (GA). For using the GA that needs the clustering validity evaluation as a fitness function, we adopt the enhanced Dunn's measure [3] to assess the clustering validity.

1. Introduction

While there has been much research regarding to the object recognition in the image processing area, many of them that consider only the feature of objects suffer from the accuracy problems. The accuracy of the object recognition can be increased by considering the feature of interesting objects with the additional information, which we call the image context. Examples of the image context

can be the illumination information, the direction of the light sources, and the shadows or the skin tones of faces for the case of face recognition, especially. Furthermore, the performance of the object recognition can be improved by minimizing the number of training images to be evaluated. In this paper, we propose a clustering of images based on the image context.

The clustering is an unsupervised learning algorithm since there are no prior information that would represent the certain clusters, and depends on the features of images and the initial assumptions for determining each cluster. Hence, it is critical to classify the set of images into the correct cluster, and we propose a novel method that consists of the image context representation phase and the adaptive selection phase of the cluster numbers.

For the image context representation, we adopt modified 2D Haar wavelet transformation to establish the images into bands that are districted based on their orientation and frequency. The distribution of the bands represents well the salient traits of the illumination gradient. The adaptive selection of the cluster numbers that guesses the proper number of clusters in the absence of the prior information employs the Genetic Algorithm (GA). For using the GA that needs the clustering validity evaluation, we adopt the enhanced Dunn's measure [3] to assess the clustering validity.

2. Object Recognition

The image recognition using the pattern recognition and computer vision can be applied to various industry areas that need convenience, diversity, comfortable and noncontact. The noncontact feature of image recognition offers remote and nondestructive evaluation advantages. Especially, the object recognition is most powerful example that can show the advantages.

Vision based object recognition is one of the most successful applications in image processing, pattern recognition, computer vision and nondestructive evaluation fields. Many algorithms have been proposed for the object recognition area. Research for what kind of attribute of the objects and the environments that make harder or easier recognizing the target is going on recently. For example, some persons are more difficult to recognize than the others in face recognition field. G. Givens et. al. [1] research that which features make recognizing persons easier or not. That features are age, race, gender, skin tones, glasses, beards, makeup, frontal hairs, illuminations and expressions. Traditional object recognition techniques consider only the features of the object itself. But Givens' research shows that we need to consider together the environments of the object such as illuminations, glasses and skin tones at the

face recognition case. In order to consider the environments, we need to cluster the object images along the environmental features in training time.

3. Clustering

The block diagram of the proposed object recognition training method using the image context is presented in Figure 1. Many images are clustered by the image context cluster and trained for each recognizer. Each recognizer has different model and parameters each others because the model and the parameters are produced with different images. If the images are properly clustered, the *n-th* object recognizer composes more robust model and parameters for the recognition.
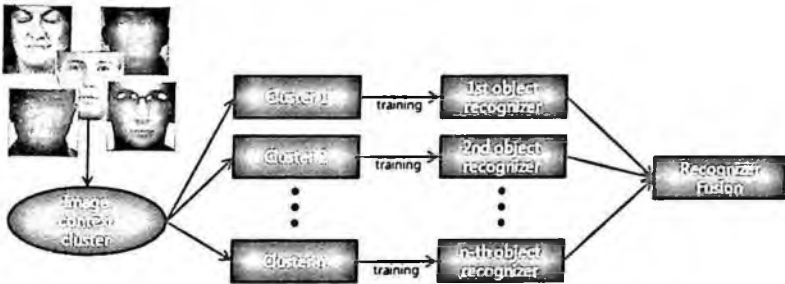
Fig. 1. The block diagram of the proposed object recognition method

3.1. K-means

We employ the k-means algorithm for clustering images. The k-means algorithm is the simplest unsupervised algorithm which solves the well known clustering problem. The algorithm is a simple and easy way to cluster a given data set through a *k* cluster number fixed in advance. The algorithm is following [2]:

1. Set *k* points into the space represented by the data that are being clustered. These points represented initial group means.
2. Assign each data to the group that has the closest mean.
3. When all data have been assigned, recalculated the positions of the *k* mean.
4. Repeat step 2 and step 3 until the means no longer move.

Because the clustering algorithm depends on the number *k*, the accuracy of the recognition system is affected by the *k* and how to decide the *k* is a serious problem. Whether you select *k*-means clustering algorithm or others, you will face to the deciding *k* problem. Because how to decide the *k* is a difficult problem, we propose the deciding *k* method as mentioned in section 3.2 and 3.3.

3.2. Cluster Validity

Clustering is mostly unsupervised process thus the evaluation of the clustering algorithm is very important. In the clustering process there are no predefined classes therefore it is difficult to find an appropriate measuring that determines whether the cluster composition is acceptable or not. To solve the problem, Dunn [3] proposed cluster validity method in 1974. The definition is given as follows:

$$, \text{where}$$

$$d(c_i, c_j) = \min_{x \in c_i, y \in c_j} \{d(x, y)\} \quad and \quad diam(c_i) = \max_{x, y \, | c_i} \{d(x, y)\} \tag{1}$$

where k is the number of clusters and c_i is l-th cluster. If a data set contains well-divided clusters, the distances among the clusters are large and the radiuses of the clusters are small. Therefore the clustering that has large D is better cluster configuration.

3.3. Deciding k problem

Like as we choice the Dunn's method as measurement means, we also select Genetic Algorithm (GA) to determine the best number k. The detail step of the object recognition method using image context with the clustering validity and the GA is given in the following:

1. Initialize the chromosomes of the GA
2. Set k as the initial number affected by chromosomes.
3. Set the cluster validity method as the fitness function.
4. Start to search for an optimized the number of cluster k.
    i.   Cluster training images into k clusters.
    ii. Evaluate the fitness function of the clustering.
    iii. Search the k that maximize the fitness function and keep those as the best chromosomes.
5. Train the i-th object recognizer with the images the members of the each i-th cluster.

4. Experiments

The block diagram of the proposed recognition method is shown in Figure 2. The clusters are made in the training time and the image context cluster is also use the k mentioned in training step as the number of clusters. The image context cluster in Figure 2 analyzes to cluster an input image and pass the image

to the proper recognizer along the cluster number. The object recognizers recognize the image using its model and parameters.
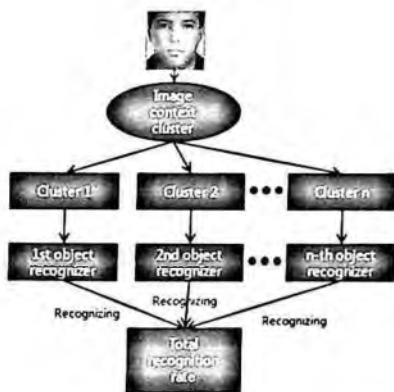
Fig. 2. Face images clustered according the image context.

We use FERET and Yale face data sets for training and recognizing. We use 1038 images as testing (recognizing) images. The GA algorithm of section 3.3 determines the best number k is 9 by experiment. In The number of images of each cluster is shown in Table1. The comparison of the proposed method with the traditional recognition method that uses whole images for training and testing is shown Table 2. Table 2 shows the proposed method is superior to the traditional method and the proposed method has effect to the object recognition. As the k-means and the Dunn's cluster validity method are the simplest and weak method, the experiment result is valuable.

Table 1. The number of images of each cluster.

Cluster number	The number of images
1	144
2	128
3	75
4	141
5	112
6	99
7	113
8	118
9	108

Table 2. The comparison of the recognition rate.

Cluster number	Recognition rate of the traditional recognition method	Recognition rate of the proposed method
1	91.91%	93.05%
2		92.96%
3		92.00%
4		92.90%
5		91.96%
6		91.92%
7		92.03%
8		92.37%
9		92.59%
Total		92.48%

5. Conclusions

The image context is used to improve the object recognition accuracy in this paper. We use k-means to cluster the images, and in order to estimate the fitness of the clustering we use Dunn's clustering validity method. As the k-means and the Dunn's cluster validity method are the simplest and weak method, the experiment result is valuable. While the deciding k problem is also solved by GA, we lose the speed of the system. In the future work we will develop the method to improve the speed of the system. The system will be more accuracy and speed up object recognition system.

Acknowledgments

References

1. G. Givens et al., *How Features of the Human Face Affect Recognition: a Statistical Comparison of three Face Recognition Algorithms*, IEEE Computer Society Conference on Computer Vision and Pattern Recognition, 2004.
2. E.-S. Jung, *Adaptive Face Recognition using Cluster Validity*, Inha Univ. M.S. course thesis.
3. J. C. Dunn, *Well Separated Clusters and Optimal Fuzzy Partitions*, Journal of Cybernetica, Vol. 4, pp. 95-104, 1974.

THE DEVELOPMENT OF DISPLACEMENT MEASUREMENT SYSTEM BY USING CCD CAMERA

HYEONG-SEOP JEON[†]

Advanced Condition Monitoring &Diagnostics Lab, Korea Atomic Energy Research Institute(KAERI) 150 Duckjin-dong Yuseong-gu, Daejeon-shi, Korea

YOUNG-CHUL CHOI

Advanced Condition Monitoring &Diagnostics Lab, Korea Atomic Energy Research Institute(KAERI) 150 Duckjin-dong Yuseong-gu, Daejeon-shi, Korea

JAE-CHEOL LEE

Advanced Condition Monitoring &Diagnostics Lab, Korea Atomic Energy Research Institute(KAERI) 150 Duckjin-dong Yuseong-gu, Daejeon-shi, Korea

JONG WON PARK

Information Communication Engineering, Chungnam National University, 220 Gung-dong, Yuseong-gu, Daejeon-shi, Korea

This paper proposes a way to measure the displacement of a moving object by using a CCD camera. Generally in measuring displacement, gab sensor, which is a displacement sensor, is used. However, it is difficult to measure displacement by using a common sensor in places where it is unsuitable to attach a sensor, such as high-temperature areas or radioactive places. In this kind of places, non-contact methods should be used to measure displacement and in this study, images of CCD camera were used. When displacement is measure by using camera images, it is possible to measure displacement with a non-contact method. It is simple to install and move a displacement measuring device so that it is advantageous to solve problems of spatial constraints.

1. Introduction

Accelerometer, laser vibrometer, and gab sensor are used to measure vibration of large structures such as buildings, bridges, and pipes. However, it is difficult to measure vibration with an existing sensor due to possible mounting and explosion in high-temperature and radioactive areas such thermal power plants and atomic power plants. Therefore, it is necessary to measure vibration at a long

---

distance without attaching a sensor. This study proposes a way to measure vibration and displacement of structures by using CCD camera from a long distance. In the case of CCD camera, the number of frames becomes sampling frequency and resolution is directly related to dynamic range. It might be difficult to measure high-frequency vibration such as ultrasound. However, large structures such as bridges or large pipes vibrate at low frequencies, so it should be sufficient to measure vibration with CCD camera [1][2]. Also, because of use of images, it is possible to simultaneously measure at several points on screen, which could readily generate not only vibration frequencies but also mode shapes.

In the following sections, methods to use CCD camera to measure vibrations of structures are reviewed, followed by methods to identify vibration displacement, frequencies, and mode shapes through steel beam and spring experiments.

2. Vibration Measurements by Using CCD Camera

Images obtained from CCD camera were processed to obtain conversion coordinates of select areas, which could allow measuring vibration displacement. This section discusses a way to measure vibration displacement through image processing [3][4].

2.1. *Obtainment of Images of Piping Structure by Using CCD Camera*

In order to take vibration images of pipelines by using CCD camera, an area to be measure for vibration displacement is marked as shown in Figure 1. It is possible to mark several locations for measurement.

(a) Gray image   (b) Filtered image
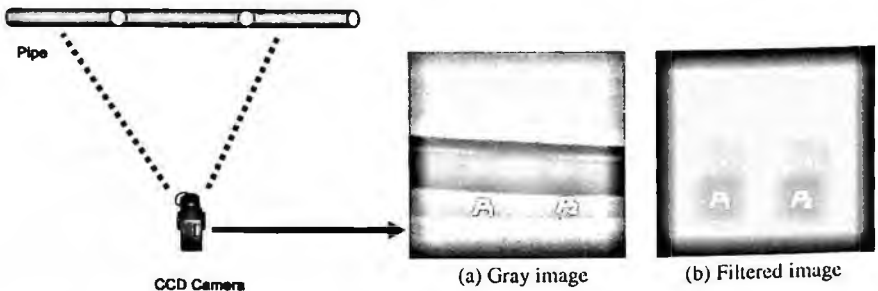
Fig. 1. Outline for measuring vibration of structure by using CCD camera, (a) Gray image, (b) Filtered image.

2.2. *Conversion Coordinates of the Select Area through Image Processing*

As shown in Figure 1, images of piping structures are used to measure displacement in a selected area. Figure 1 (a) shows a gray image of the first frame of CCD camera, and Figure 1 (b) shows an image that separated the marked area from Figure 1 (a).

A process to have conversion coordinates of piping structure by separating Figure 1(b), P_1, P_2 area, from Figure 1 (a) is as follows:

1. The gray image of Figure 1 (a) is binary image through histogram analysis.
2. By using Formula (1) Dilation and Formula (2) Erosion of Morphological Filtering, an image of the separated area (P_1, P_2), as shown in Figure 1 (b), is obtained.

$$A \oplus B = \{ z \mid (\hat{B})_z \cap A \neq \phi \} \tag{1}$$

$$A \ominus B = \{ z \mid (B)_z \subseteq A \} \tag{2}$$

3. The location of the P_1, P_2 area is found in the image of Figure 1 (b) by using Glassfire Algorithm of Labeling Technique.
4. Central coordinates $P_1 M(x, y)$, $P_2 M(x, y)$ of the P_1, P_2 area is found by using Formula (3).

$$x = \frac{1}{n} \sum_{i=1}^{N-1} x_i \quad , \quad y = \frac{1}{n} \sum_{i=1}^{N-1} y_i \tag{3}$$

5. By continuously repeating Steps 1~4 in the next frame image, central coordinates of the P_1, P_2 area in each frame image are obtained.

According to this method, displacements between central coordinates indicate vibration displacement of structures, and therefore, by using vibration displacement, vibration frequencies and mode shapes could be identified.

3. Verification through Experiments

In order to test the theoretical hypothesis explained above, steel beam and spring experiments were conducted.

614

3.1. *Beam Experiment*

Figure 2 illustrates an experiment device that measures vibration displacement by using steel beams as shaker. Here, a function generator was used to set the first mode frequency of the beam as 2.3Hz. CCD Camera took 60 fps and its resolution was 640 x 480. Therefore, sampling frequency of signals measured by using CCD camera was 60Hz.

(a)   (b)
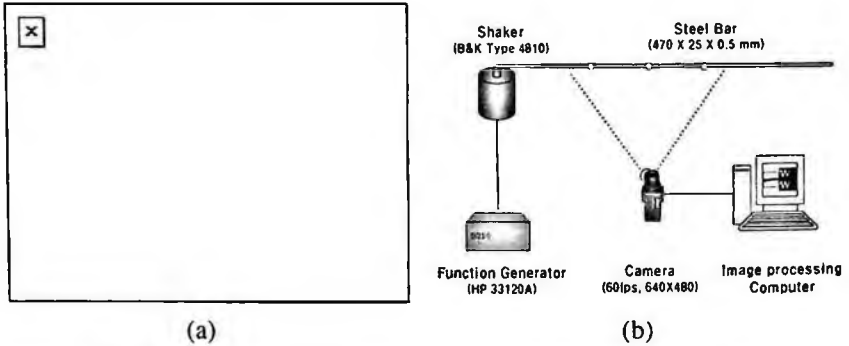
Fig. 2. (a) Picture (b) Outline of experimental setup for steel beam vibration.

Figure 3 (a) shows actual images taken by the camera and the graphs measured of actual displacement from theses images are shown in Figure 3(b). It shows that actual vibration shapes are well followed. Also, as shown in Figure 3(c), when the spectrum of displacement signals is observed, the actual frequency was found to be identical with 2.3Hz.

(a)   (c)
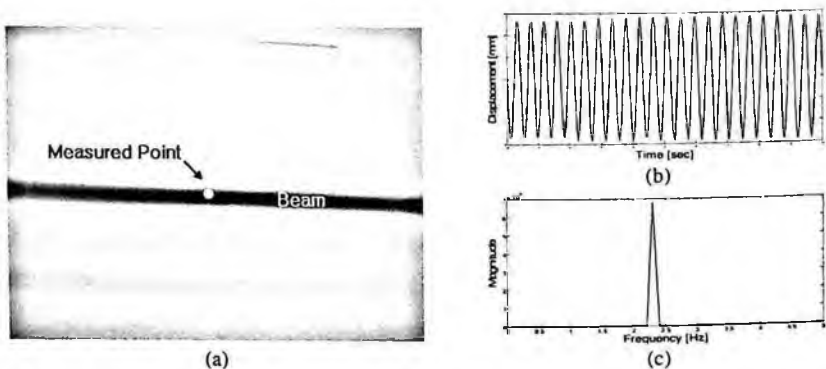
Fig. 3. Experimental results, (a) Camera image, (b) Displacement of beam, (c) Power spectrum which is coincide with exciting frequency.

3.2. *Spring Experiment*

One of the most important advantages in measure displacement with a CCD Camera is that it can measure several points simultaneously, which means that it is possible to measure mode shapes as well.

Figure 4 describes a 1m-long spring experimental device to measure mode shapes.
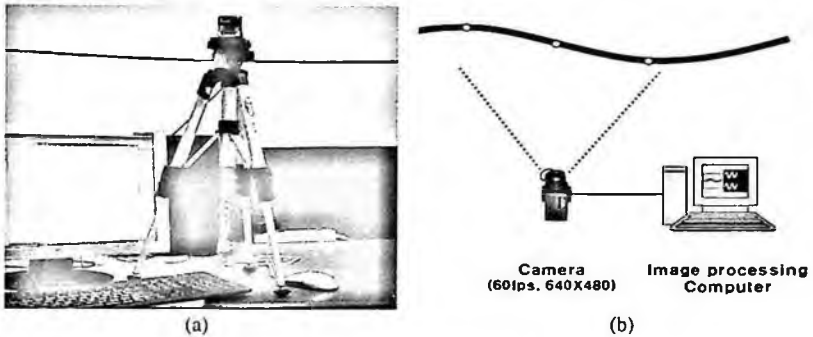
Fig. 4. (a) Picture (b) Outline of experimental setup for spring.

The result of measuring three points at the same time with a CCD camera is shown in Figure 5. As shown in the figure, frequencies at Point 1 and Point 3 are similar at 2.3 Hz, but there is 180-degree difference in phase.
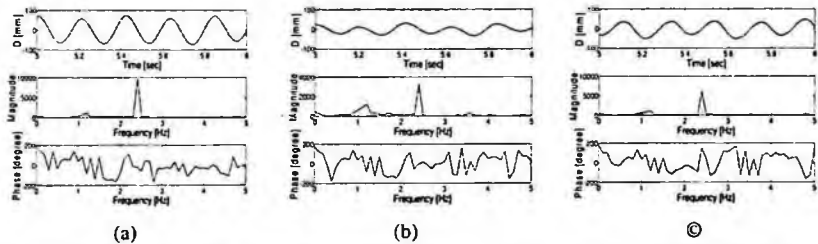
Fig. 5. Experimental result. Upper figure is displacement, middle figure is spectrum and bottom figure shows phase at (a) point 1, (b) point 2, (c) point 3.

Therefore, it is possible to obtain vibration mode shape at 2.3Hz like in Figure 6 (b), and this is identical with the actual vibration shape in Figure 6(a).
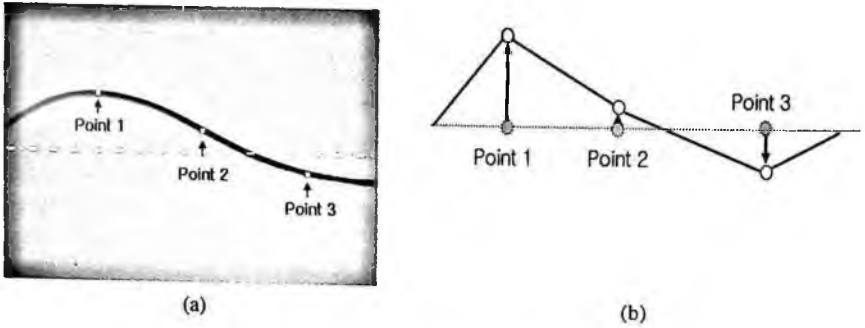
Fig. 6. Mode analysis, (a) True vibration shape, (b) Calculated mode shape.

4. Conclusion

This study verifies that it is possible to use CCD camera to measure vibration frequencies and displacement at places where it is difficult to use sensors such as high-temperature or radioactive areas. Also, it allows measuring several points in a desired area and the experiments of this study confirmed that vibration mode shapes of structures could be readily found. Compared to other previous methods, it is simple to install equipments and it has little spatial constraint, so it could be used for safety monitoring and maintenance of large structures.

Acknowledgments

References

1. James R. Parker, Algorithms for Image Processing and Computer Vision, John Wiley & Sons, New York, 1997.
2. R. C. Gonzalez and R. E. Woods, Digital Image Processing, Addison Wesley, 1992.
3. Chowdhury, M. H. and W. D. Little, "Image Thresholding Techniques", 1995, IEEE Pacific Rim Conference on Communications, Computers, and Signal Processing, pp. 585-589.
4. Otsu, N., 1979, "A Threshold Selection Method from Gray-level Histograms", IEEE Trans. Syst. Man Cybern. 9, pp. 62-66.

IMAGE RESTORATION BY USING A WIENER FILTER DESIGNED FOR DIGITAL X-RAY IMAGING SYSTEMS*

S. Y. LEE

Department of Radiological Science, Yonsei University, Wonju, 220-710, Korea

S. I. CHOI[1], H. S. CHO[1,†], J. E. OH[1], K. Y. KIM[1], B. S. LEE[2], S. KIM[3]

[1]*Department of Radiological Science, Yonsei University, Wonju, 220-710, Korea*
[2]*School of Biomedical Engineering, Konkuk University, Chungju, 380-701, Korea*
[3]*Department of Nuclear Engineering, Cheju National University, Cheju,690-756, Korea*

In this paper, in order to restore the blurred images taken from a digital X-ray imaging system we applied the direct-inverse filtering and the Wiener filtering techniques by using the measured noise power spectrum (NPS) or different Wiener constants and compared their image quality quantitatively. According to our test results, the image sharpness for the Wiener filtering was considerably improved with better noise characteristics, compared with the blur images, whereas for the direct-inverse filtering the image sharpness was also enhanced but with worse noise characteristics. Thus, the application of the Wiener filtering with an optimal Wiener constant or with the measured NPS to the digital X-ray images could be effective in the reduction of the system blurring effect.

1. Introduction

Images acquired by digital X-ray imaging systems are inherently degraded due to system degradation process and additive noise sources. The system degradation in image quality is typically described as the system response function characterized by the modulation transfer function (MTF) and the noise term described as the noise power spectrum (NPS). If an imaging system can be assumed linear and shift-invariant, the degraded image, $g(x,y)$, is mathematically represented as a convolution of the original image, $f(x,y)$, and the system response function, $h(x,y)$, plus some additive noise, $\eta(x,y)$ [1]:

$$g(x, y) = f(x, y) * h(x, y) + \eta(x, y) \qquad (1)$$

---

†Corresponding author: hscho1@yonsei.ac.kr, +82-33-760-2428 (phone), +82-33-760-2815 (fax)

In this case, we can restore the blur image as close as possible to the original image by using Wiener filtering, as we know more precisely about the MTF and the NPS. In this study, we restored the X-ray images acquired at a given test condition to the original images by applying both direct-inverse filtering and Wiener filtering techniques with the measured MTF and the NPS experimentally.

2. Materials and Methods

2.1. *Direct-inverse Filtering & Wiener Filtering*

The simplest image restoration, so-called the direct-inverse filtering, can be performed as the following equations:

$$\hat{F}(u,v) = \frac{G(u,v)}{H(u,v)} \tag{2}$$

$$\hat{f}(x,y) = \Im^{-1}\left\{\hat{F}(u,v)\right\} = \Im^{-1}\left\{\frac{G(u,v)}{H(u,v)}\right\} \tag{3}$$

where $G(u,v)$ and $H(u,v)$ are the Fourier transforms of the degraded image and the system response function, respectively, and $\hat{f}(x,y)$ and $\hat{F}(u,v)$ are the estimated original image restored with the direct-inverse filtering and its Fourier transform [2]. From the model described in Eq. (1), the Fourier transform of the original image can be expressed as the following equation:

$$F(u,v) = \hat{F}(u,v) - \frac{N(u,v)}{H(u,v)} \tag{4}$$

where $N(u,v)$ is the Fourier transform of the additive noise. Thus, in the direct-inverse filtering the noise is overemphasized in the restored image at high frequency region, resulting in incomplete restoration.

Wiener filtering is one of the earliest and best known approaches to linear image restoration technique to minimize the statistical error, as describe in the following equation [3]:

$$\hat{F}(u,v) = \left[\frac{H*(u,v)}{|H(u,v)|^2 + k\Phi_N / \Phi_O(u,v)} \right] G(u,v) \tag{5}$$

where $H^*(u,v)$ is the complex conjugate of $H(u,v)$, k is a positive constant arbitrarily, and $\Phi_N / \Phi_O(u,v)$ is the ratio of the power spectrum of the noise to the power spectrum of the undegraded.

2.2. *Experimentals*

Figure 1 shows (a) a commercially-available CMOS imaging sensor we used in this study and (b) the experimental setup which consists of a CMOS imaging sensor of a 48 x 48 μm^2 pixel size and a 10.0 x 5.0 cm^2 active area (RadEye^{TM}2 from Rad-icon Imaging Corp.) and a general X-ray generator with a focal spot size of about 1.0 mm (350-600 mA; < 150 kV_p). Test images for image restoration were taken from the imaging system at an operation condition of 70 kV_p and 12.5 mA, 100 cm apart from the X-ray tube.

(a)   (b)
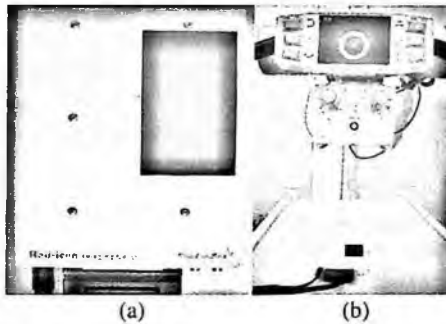
Fig. 1. (a) A commercially-available CMOS imaging sensor we used and (b) the experimental setup.

2.3. *Measurements of MTF and NPS*

Figure 2 shows (a) a slit camera with a 10 μm width (Nuclear Associate Corp., 07-624-1) and its X-ray image acquired with the operation condition, (b) the resultant LSF curve, and (c) the resultant MTF curve. Here the LSF curve was determined from the acquired X-ray image of the slit and the MTF curve was then calculated as the normalized Fourier transform (FT) of the LSF.

(a)   (b)   (c)
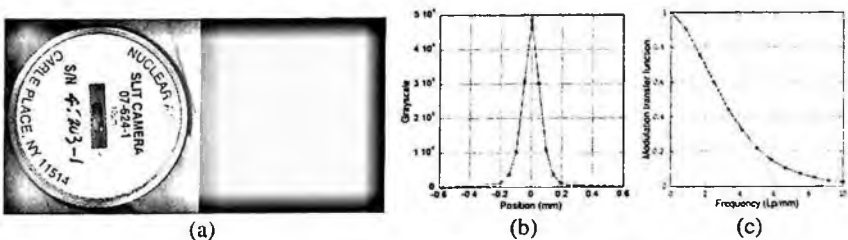
Fig. 2. (a) Slit camera with a 10 μm width and its X-ray image acquired, (b) the resultant LSF curve, and (c) the resultant MTF curve.

The NPS describes the distribution of the noise frequency component in the image area. Figure 3 shows (a) the white image acquired with the same operation condition and (b) the resultant 2D NPS. Here the 2D NPS was computed from the acquired white image.

(a) (b)
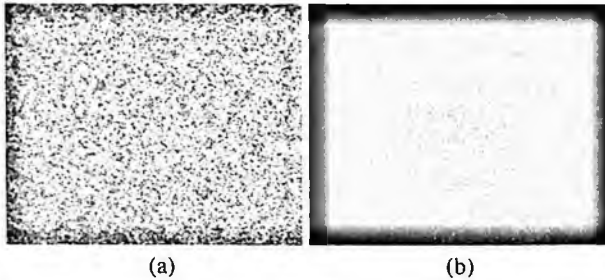
Fig. 3. (a) White image taken with an operation condition of 70 kV$_p$ and 12.5 mA and (b) the resultant 2D NPS.

3. Results and Discussion

For the image restoration, we applied both direct-inverse filtering and Wiener filtering techniques to the X-ray images acquired from the digital X-ray imaging system, measuring the MTF and the NPS. Figure 4 shows (a) blurred images of an electric device and a resolution pattern taken from the imaging system before image restoration, (b) the restored images after direct-inverse filtering, and (c) the restored images after Wiener filtering by using the measured NPS. Figure 5 shows the edge profiles of the resultant images (a) before image restoration,

(a) (b) (c)
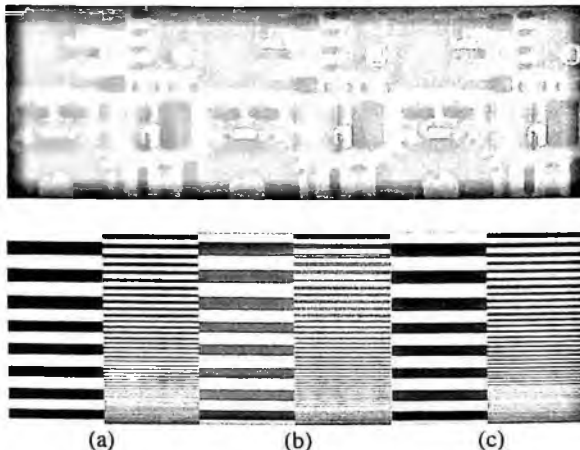
Fig. 4. Resultant images of an electric device and a resolution pattern (a) before image restoration, (b) after direct-inverse filtering, and (c) after Wiener filtering by using the measured NPS.
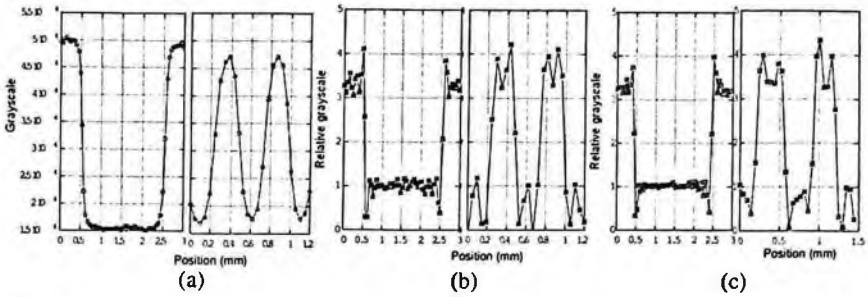
Fig. 5. Edge profiles of the resultant images (a) before image restoration, (b) after direct-inverse filtering, and (c) after Wiener filtering, measured at frequencies of 0.5 LP/mm (left) and 4.2 LP/mm (right).

(b) after direct-inverse filtering, and (c) after Wiener filtering, measured at frequencies of 0.5 LP/mm (left) and 4.2 LP/mm (right). As shown in Figure 5, the sharpness of the image enhanced for both direct-inverse filtering and Wiener filtering, compared with that of the blurred image before image restoration, while the image components of higher frequency was more emphasized for direct-inverse filtering than Wiener filtering.

Figure 6 shows the blurred image before image restoration and the restored images after Wiener filtering for the Wiener constants (i.e., $k\Phi_N/\Phi_O(u,v)$) of (b) 1.0×10^6, (c) 4.0×10^6, and (d) 1.0×10^7. Figure 7 shows (a) the modulated system response function for the given Wiener constants, and the grayscale distributions of (b) the blurred image and of (c) the restored images by Wiener filtering measured in high frequency region. The modulation values calculated at a frequency of 7 LP/mm were about 1.29, 0.94, and 0.86 for the Wiener constants of 1.0×10^6, 4.0×10^6 and 1.0×10^7, respectively. As shown in Figure 6 and 7, the restored image with smaller Wiener constant near to zero approaches to that with direct-inverse filtering, while with larger constant to the blurred image.
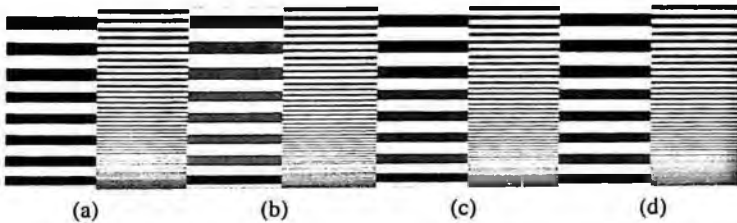
Fig. 6. (a) Blurred image before image restoration and restored images after Wiener filtering for the Wiener constants of (b) 1.0×10^6, (c) 4.0×10^6, and (d) 1.0×10^7.
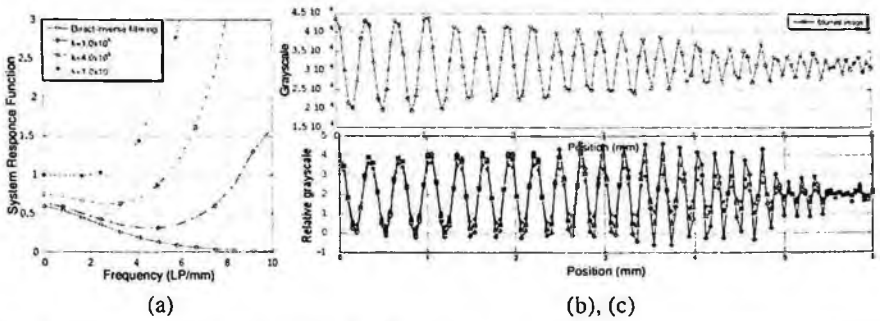
Fig. 7. (a) Modulated system response function for the given Wiener constants, and the grayscale distributions of (b) the blurred image and of (c) the restored images by Wiener filtering measured in high frequency region.

4. Conclusions

In this paper, we applied the direct-inverse filtering and the Wiener filtering techniques and compared the image quality quantitatively. The image sharpness enhanced for both direct-inverse filtering and Wiener filtering, compared with that of the blurred image before image restoration, while the image components of higher frequency was more emphasized for direct-inverse filtering than Wiener filtering. The modulation values calculated at a frequency of 7 LP/mm were about 1.29, 0.94, and 0.86 for the Wiener constants of 1.0×10^6, 4.0×10^6 and 1.0×10^7, respectively, and the restored image with smaller Wiener constant near to zero approaches to that with direct-inverse filtering, while with larger constant to the blurred image. Thus, the application of Wiener filtering with an optimal Wiener constant or with the measured NPS to the digital X-ray images could be effective in the reduction of the system blurring effect, provided that the imaging system preserves the shift-invariant and linear properties reasonably.

Acknowledgments

References

1. Andrew E. Yagle and Siddharth Shah, *EECS. ICIP* **vol. 2,** 2037 (1995).
2. C. Vural, W.A. Sethares, *ECE. DSP* **16**, 137-148 (2006).
3. J.R. Fienup, D. Griffith, and L. Harrington, optics, *Optics. SPIE* **4792-01** (2002).

CURRENT AND FUTURE ROLE OF MEDICAL THERMOGRAPHY

JUNG YUL PARK, MD.,PH.D.

Department of Neurosurgery, Korea University Medical Center, Ansan Hospital, #516 Gojan-Dong, Danwon-Gu, Ansansi, Gyeonggi-Do, 425-707, Korea

The object of this study is to review up-to-dated developments, scientific proofs, limitations and disadvantages, and to address the role of current and future of the medical thermography. Electronically searchable articles in literature were first acquired through Medline/Embase under headings of "medical thermography" or "medical thermogram" All articles were categorized and indexed into various clinical fields. A total of 5426 references were retrieved. There were two peaks with regards to number of published articles; one in eighties and second one late nineties through recent years. Most common category studied was breast disorder followed by injuries, neurological disorders, pain, endocrine, metabolic, and vascular disorder. The main reasons for sharp decline of its use in the past were indiscreet use without standardized protocol, too much expectation but no regulation, poor sensor quality and poor imaging processing, poor understanding of physiological mechanism of thermal sensing technique and various clinical disorders, and lobbying effects of major insurance industry. However, with current modernized both hardware and software for the image acquisition, standardized protocol, and better understanding of physiologic mechanisms various disorders including pain it seems reasonable to reconsider its use in many clinical settings. Some of in progress projects are automated 3-D thermal image reconstruction, image fusion, automated add-on diagnostic software using pattern recognition, network transfer protocol, and functional imaging technique. Despite many inherent limitations and disadvantages related to infrared thermography in medical field, authors believe that it can be a great tool in medical field when strict protocol of its usage is applied in selected patients not only because it has several invaluable potential advantage but also its technology has been improving and many ancillary appealing features, along with its core development, are under intense investigations. However, many good designed, controlled, with large population-based, studies with currently available techniques will be needed in the future to be considered a scientifically valid, compatible diagnostic tool that can provide unique and valuable information compared to other diagnostic modalities.

1. Introduction

The first use of thermography in medicine came in 1957 when R. Lawson discovered that the skin temperature over a cancer of the breast was higher than that of normal tissue. (1) In 1982 the American FDA approved the procedure. It was soon realized that thermography could clearly, objectively and easily

demonstrate the physiological component of pain and injury (trauma, see picture on the left), especially to the spinal column due to car accidents, job injuries and a host of other laws suits. Everyone involved benefited these positive findings - with the exception of the insurance industry. (2,3)

In the 1980's and 90's the US insurance industry placed an all-out effort to diminish the value of thermography in courts of law due to high litigation costs. Lobbying at the House of Delegate's and at Medicare brought about the removal of thermographic coverage by most insurance companies and greatly reduced utilization of thermography in the US. (4,5) However, there were other reasons for the decline in the use of medical IR include poor sensor quality, poor image processing techniques, inadequate physiological knowledge, indiscreet use and improper interpretation with no standardized protocol, and too much expectations and no regulation. (6,7)

The purpose of this study was to review up-to-dated developments, scientific proofs, causes of decline of its use, current limitations and disadvantages, and reasons for the reconsidering the use of thermography in medical fields. Also, current developments and future direction of medical thermography are reviewed and discussed.

2. Materials and Methods

Electronically searchable articles in literature were first acquired through medline and EMBASE under headings of "medical thermography" or "medical thermogram" from 1963 to 2005. All articles were categorized and indexed into various clinical fields. Citations that contained controversial points on its usefulness versus drawbacks were collected in separate fields. Sensitivity, specificity, predictive values, and usefulness in various clinical disorders were also evaluated.

3. Results

A total of 4965 references were retrieved. There were two peaks with regards to number of published articles; one in eighties and second one late nineties through recent years. (Fig.1). These number represent, in percentage, 8.5% in 2004, 20.9% in 2005, and 10.0% in 2006 of total number of articles published in the field of thermogrphy. Of these, 97% of works were related to the diagnostic aid and only in 3% thermography was used for the monitoring for the therapeutic effect and disease progression. And, it was used in investigation of litigation, compensation program, and disability determination in 0.6% of cases. The number of published articles in last 5 years according to study on different

regions is described in Fig. 2. Most common category studied was breast disorder followed by injuries, neurological disorders, pain, endocrine, metabolic, and vascular disorder (Fig. 3).

The main reasons for sharp decline of its use in the past were indiscreet use without standardized protocol, too much expectation but no regulation, poor sensor quality and poor imaging processing, poor understanding of physiological mechanism of thermal sensing technique and various clinical disorders, and lobbying effects of major insurance industry. However, with current modernized both hardware and software for the image acquisition, standardized protocol, and better understanding of physiologic mechanisms various disorders including pain it seems reasonable to reconsider its use in many clinical settings. Currently, some of ongoing progress projects are automated 3-D thermal image reconstruction, image fusion, automated add-on diagnostic software using pattern recognition, network transfer protocol, and functional imaging technique.
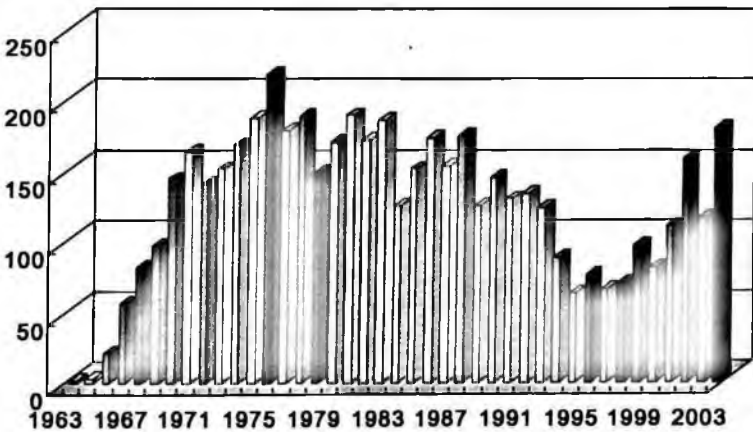
Fig. 1. Number of articles listed in Medline/EMBASE from 1963 to 2005.

At present, there are standardized protocols for image acquisition in various clinical settings. Also, refined digital still imaging and real-time continuous acquisition of images using mobile sensor and cameras are available. The powerful image processing provide image of 8-11 bit quality with more than 640×480 pixel resolution. The spatial resolution is at least 1 mrad (detection of 1 × 1 mm at 1 meter range). The thermal resolution offer that temperature of objects can be differentiated with the range of temperature greater than 0.08 °C.

Variety of newer techniques to augment diagnostic accuracy and image intensification, such as dynamic, functional thermography and image fusion technique, have been introduced and some of these are already in use in various clinical settings. Standardized transfer and retrieval protocol using DICOM are installed in most of thermographic device for universal exchange of thermographic images. All of these modern thermographic imaging techniques used in clinical or research studies are being witnessed with better scientific proofs in major publications. Also, thermographic devices are now much less expensive with smaller sizes.
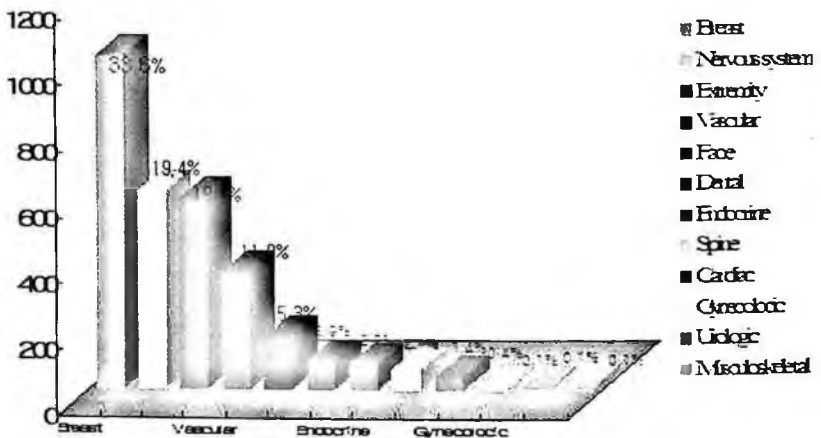
Fig. 2. Number of published articles in last five years categorized according to the organ system.

Other major areas that thermography has been a very useful tool include peripheral and cerebral vascular surgery, monitoring of completeness of surgery or pain procedure, and monitoring of large population for screening of disorders with fever or increased metabolism (e.g., SARS, food poisoning, toxic reaction, etc).

These new technologies provide much more sensitive and better thermographic images that could add invaluable information to the physicians for the optimal management for the patients. Unfortunately, new technology today is not widely understood and being appreciated in the traditional medical community.
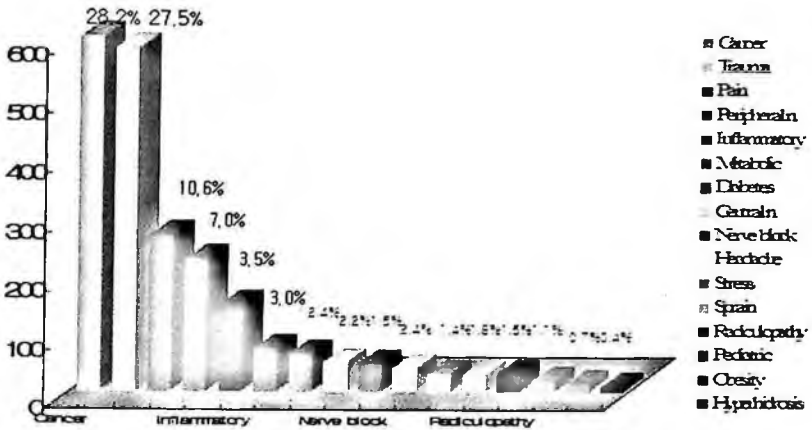
Fig. 3. Number of published articles categorized according to the clinical settings.

Limitations and disadvantages of thermographic use in medical field include superficial depth of penetration (i.e., 2.5 mm in infrared, 30 mm in near-infrared), need for examination environment, various factors affecting precise measurement, imaging acquisition and interpretation, and no international standardized protocol and equipment. There needs to be international consortium on setting the guidelines and standardizations for these in near future before making a justification for use and exchange thermographic images worldwide.

In summary, recognizing the true value in thermography and understand these inherent medical diagnostic limitations are paramount importance. In overall, the thermography, with new ultra-sensitive high resolution digital infrared devices, shows neurophysiological evidence of the presence of sensory/autonomic nerve, metabolic, and circulatory impairments. Moreover, response to various treatments can be objectively measured and recorded.

4. Conclusion

Despite many inherent limitations and disadvantages related to infrared thermography in medical field, authors believe that it can be a great tool in medical field when strict protocol of its usage is applied in selected patients not only because it has several invaluable potential advantage but also its technology has been improving and many ancillary appealing features, along with its core development, are under intense investigations. However, many good designed,

controlled, with large population-based, studies with currently available techniques will be needed in the future to be considered a scientifically valid, compatible diagnostic tool that can provide unique and valuable information compared to other diagnostic modalities.

References

1. RN Lawson, *Can. Med. Assoc. J.* **13**, 517(1957).
2. American Chiropractic College of Thermology and ACA Council on Diagnostic Imaging, ratified by ACA House of Delegates. Policy statement on thermography, 1988.
3. CE Wexler, *Acta. Thermographica.* **5**, 3 (1980).
4. AMA Council on Scientific Affairs, *Thermology.* 2, 600 (1987).
5. SA Weinstein, G Weinstein, *Post. Grad. Med.* Special ed., 44 (1988).
6. M Anbar, *IEEE Engineering in Medicine and Biology,* 25 (1988).
7. H Hooshmand, M. Hashmi and EM. Phillips, *Thermology international.* **11 (2)**, 53(2001).

EXPERIMENTAL DESGN AND EVALUATION OF THERMOGRAPHIC REFERENCE BLOCK*

WONTEA KIM

*Department of Bio-Mechanical Engineering, Kongju National University
Yesan, Chungnam, 340-702 South Korea*

JEONGHAK PARK

*Safety Metrology Group, Korea Research Institute of Standard and Science
P.O.Box 102, Yuseong Daejeon 305-600 South Korea*

KISOO KANG[†]

*Safety Metrology Group, Korea Research Institute of Standard and Science
P.O.Box 102, Yuseong Daejeon 305-600 South Korea*

This paper proposes a reference block for the reliability evaluation of optical lock-in thermography. Basically, thermography depends on environmental disturbances, which is related to the defect detection ability of thermography system in non-destructive testing. Reference block can be useful in evaluating the detection capability and the detection range of a defect under a given environmental condition. The proposed reference block can be supply the defect size, location and depth by quantitative evaluation technique. We hope that a reference block will improve the reliability of thermography in nondestructive testing.

1. Introduction

Infrared thermography in nondestructive testing is well known as the technique used for detecting the abnormal heating of component, resulted from the deterioration of electronic power system or from the increased friction of mechanical part. Recently, a modulated external heat source, induced to the object, is used to improve the defect detecting capability of infrared thermography and this technology is focused on the development of the signal processing technologies such as lock-in and pulse. In addition, the improved technology is widely applied to various areas such as metal material corrosion testing, fine surface crack test, composite delamination test and so on [1, 2].

---

* This paper was originally presented at 4th Pan American Conference for NDT, Argentina, 2007.
† Corresponding author

Basically, the environmental variables existing between object and detection device such as humidity, surrounding temperature, wind and so on have influence on the inspection results [3]. Most of nondestructive test technologies are exposed to these problems and the reference block in each method has been used for the evaluation or calibration of detecting capability depending on the surrounding environments or material properties of object. We may not disregard the effect of surrounding environments in the nondestructive test using the infrared thermography. The development of reference block required for evaluating the detecting capability of inspection system helps improving the reliability of thermography. This paper proposes reference block of optical lock-in thermography, which can supply defect size, location and depth by quantitative evaluation technique.

2. Optical Lock-in Thermography

The lock-in infrared thermography technique is the method used for acquiring the change of phase and amplitude by processing the response signal detected when inducing the infrared heat source to the object modulated as the periodic function. The optical, ultrasound, vibration and eddy current, controlled by the periodic function according to type of detect, are commonly used as the stimulus source. In this paper, optical lock-in thermography uses the light sources such as halogen lamp as a stimulus source. Figure 1 shows the system configuration and the principle of optical lock-in thermography. Optical wave of modulated halogen lamp is converted into thermal wave. It propagates into the inside where it is reflected at the boundaries of defect so that the wave moves back to the surface where it is superposed to the initial wave. A defect is distinguished by the local change of phase angle [4].
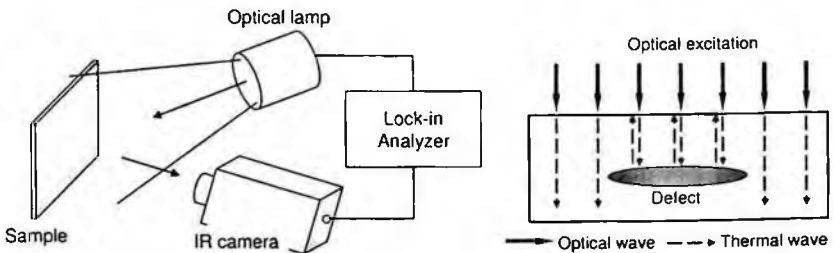
Fig. 1. System configuration and detection principle of optical lock-in thermography.

3. Design of Reference Block & Test Results

3.1. *Design of Reference Block*

Reference block for optical lock-in thermography can be used in the test site for forecasting the size, location and depth of detectable defect. Therefore, the reproducibility of detecting the same size, location, and depth of defect must be guaranteed under the same test conditions. We manufacture the block as shown in Figure 2 in consideration of influence factors when deciding the size and depth of defect. The block size is decided with 180×180 mm^2, since it is required that the field of view ($10° \times 8°$) of thermography camera at 1 m distance covers 180 mm length sufficiently and whole surface of block has to be uniformly heated by a lamp. Defect shape is back-drilled–bottom-plate circular hole, which can supply clear boundary condition and easy manufacturing. Spatial resolution of thermography camera is considered for determining the defect size of reference block. In case of camera with 320×260 pixel, spatial resolution is calculated with 0.7 mm/pixel at 1 m distance, which means that a defect with less than ϕ 4 mm diameter exists under the range of error (±0.7 mm). Also, maximum defect size is experimentally determined with ϕ 16 mm in consideration that the defect at maximum defect depth (5 mm) has to be detected sufficiently.
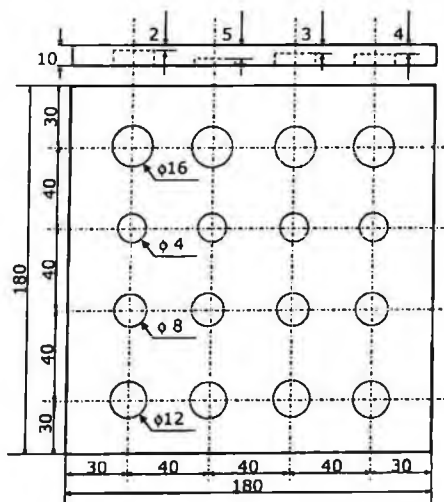
Fig. 2. Reference block for optical lock-in thermography.

In order to eliminate the interference between defects in evaluating the defect size, the distance between defects is experimentally designed as 40 *mm*. Defect depth is experimentally decided with 2, 3, 4, 5 *mm* respectively, which depends on heat capacity of reference block material. In our experiment, quantitatively detectable maximum depth in case of φ 16 *mm* defect is 6 *mm*. In this paper, reference block is made with stainless steel (STS304).

3.2. *Evaluation of Defect Depth*

The defect depth is estimated by using the thermal diffusion depth [5]. In this technique, the detectable depth is limited according to frequency of induced heat source. The limiting frequency is known as blind frequency, where the defect of specific depth is not detected [6]. In experiment, the blind frequency, acquired by decreasing the frequency, is the frequency at which a certain deep defect is started to appear. The defect depth, *d* is evaluated with Eq. (8). using the acquired blind frequency, and

$$d = C \cdot \sqrt{\frac{\alpha}{\pi \cdot f_b}} \tag{8}$$

where, f_b is blind frequency and α is thermal diffusivity. In this paper, the correlation coefficient, C of reference block is investigated by diffusion length from the blind frequency and the known defect depth. Figure 3 shows the thermal phase image measured at induced frequencies.

| (a) 0.007 Hz | (b) 0.01 Hz | (c) 0.075 Hz | (d) 0.11 Hz |

| (e) 0.19 Hz | (f) 0.31 Hz | (g) 0.41 Hz | (h) 0.46 Hz |
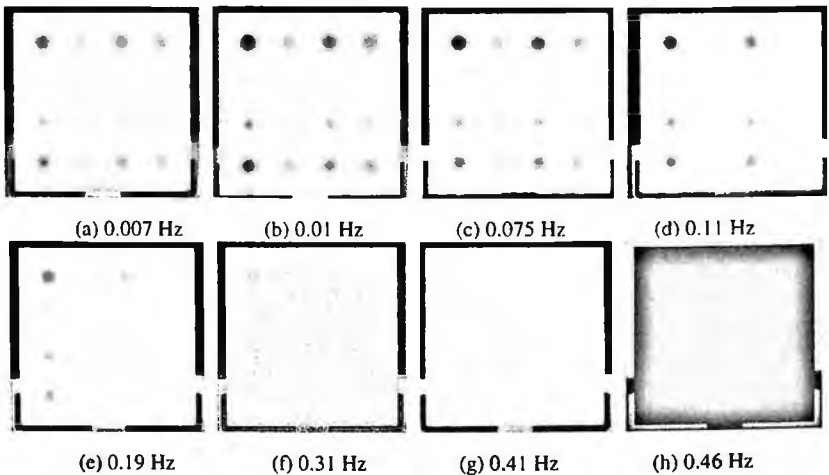
Fig. 3. Thermal phase images of reference block at each induced heat source.

In Figure 3, all defects is not detected at frequency of 0.46 Hz but according to decreasing frequency, 2 mm deep defects except ϕ 4 *mm* are stared to appear at 0.41 Hz, 3 *mm* deep defects are also stared to appear at the frequency of 0.19 Hz, 4 *mm* deep defects is at 0.11 Hz, and 5 *mm* deep defects is at 0.075 Hz. And also, Table 2 shows the blind frequency at each defect depth, diffusion length, and the estimated correlation coefficient is estimated by dividing actual defect depth by diffusion length. From these values, the correlation coefficient of reference block is as decided as 1.15.

Table 2. Correlation coefficient of reference block

Actual defect depth (*mm*)	2	3	4	5
Blind frequency (Hz)	0.41	0.19	0.11	0.075
Diffusion Length (*mm*)	1.8	2.6	3.4	4.1
Correlation coefficient	1.13	1.15	1.17	1.21

3.3. *Evaluation of Defect Size*

The size of defect is evaluated by applying the shearing phase technique for the thermal phase image [7]. In this technique, the defect size is decided between maximum and minimum points and the location can be determined as the zero point. Figure 4 shows the thermal phase distribution and the shearing phase distribution on ϕ 12 *mm* defects at the frequency of 0.01 Hz. The size of defects is easily recognized from the shearing phase distribution of Figure 4.
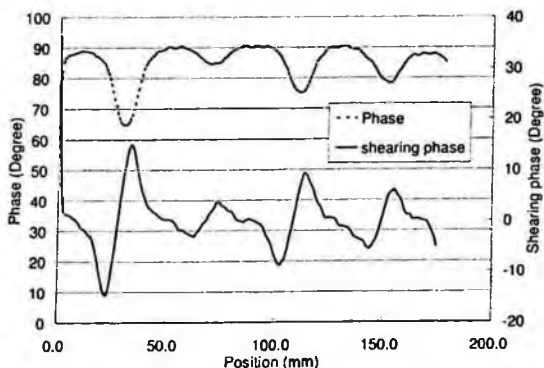
Fig. 4. Thermal Phase and shearing phase distribution at 0.01 Hz of ϕ 12 mm.

The results acquired by measuring three defects of φ 8, 12 and 16 *mm* are shown in the Table 3. Although the defects with 5 *mm*-deep φ 8 *mm* have large error, the other test results show the high accuracy within the range of 10 %.

Table 2. Inspected defect size (mm) of reference block

Size(*mm*) / Depth (*mm*)	φ 8	φ 12	φ 16
2	8.32	11.34	15.13
3	9.08	12.10	15.88
4	9.08	11.34	15.13
5	11.34	10.59	17.39

4. Conclusions

This paper proposes a reference block for nondestructive optical lock-in thermography. Reference block can be used for evaluating the reliability of an inspection system and the detection range of a defect from given environmental condition. The geometric conditions of block are experimentally optimized and inspection results are depicted. The proposed reference block can be supply the defect size, location and depth by quantitative evaluation techniques. We hope that a reference block will improve the reliability of thermography in nondestructive testing.

References

1. C. Meola, G. M. Carlomagno, A. Squillace, A. Vitiello, *Eng. Failure Analysis* **13**, pp. 380 (2006).
2. H. Berglind, A. Dillenzb, *NDT&E International* 36, 395 (2003).
3. G. Gaussorgues, 'Infrared thermography (translated by S. Chomet)', Champman & Hall, 1994.
4. G. Busse, D. Wu and W. Karpen, *J. Appl. Phys.* **71**, 3962 (1992).
5. L. D. Favro and X. Han, *Sensing for Materials Characterization, Processing and Manufacturing, ASNT TONES* **1**, 399 (1998).
6. W. Bai, B. S. Wong, *Meas. Sci. Technol.* **12**, 142–150 (2001).
7. K. Kang, M. Choi, J. Park, W. Kim, K. Kim, S. Yang, *APCNDT*, 49 (2006).

DETECTION OF DEFECTS IN LUMBER USING IR THERMOGRAPHY

CHANG-DEUK EOM

Department of Forest Sciences, Seoul National University,
San 56-1, Shillim 9-dong, Gwanak-gu, Seoul, 151-921, Korea

YEON-JUNG HAN

Department of Forest Sciences, Seoul National University,
San 56-1, Shillim 9-dong, Gwanak-gu, Seoul, 151-921, Korea

KWANG-MO KIM

Department of Forest Products, Korea Forest Research Institute,
207, Cheongyangni 2-dong, Dongdaemun-gu, Seoul, 130-712, Korea

KI-BOK KIM

Center for Environment & Safety Measurement, Korea Research Institute of Standards
and Science, Daejeon, 305-764, Korea,

JUN JAE LEE

Department of Forest Sciences, Seoul National University,
San 56-1, Shillim 9-dong, Gwanak-gu, Seoul, 151-921, Korea

HWANMYEONG YEO

Department of Forest Sciences, Seoul National University,
San 56-1, Shillim 9-dong, Gwanak-gu, Seoul, 151-921, Korea

In this study, we examined the heating and cooling rates due to the differences of thermal characteristics of timber parts. The result of the analysis for detecting knot parts showed that the heating and cooling rates of sound area were faster than those of knot area, and the surface temperature differences were mainly due to the different physical characteristics between the two textures, including the arrangement of cells, microfibril angles, heat conductivity, specific heat, and specific volume. It is expected that the development of an optimal infrared thermography system that includes a more appropriate heat source and with improvements in the accuracy and speed of a calculation algorithm will realize a quicker defect evaluation in the field.

1. Introduction

The nondestructive testing method is an examination to estimate the physical properties of a material or construction using nondestructive equipment. A nondestructive testing method that uses an infrared camera is called thermography analysis and is used frequently in many industries because it can quickly get-real time data in non-contact way. Thermography analysis is particularly used widely in the examination of buildings and construction[1]. The principle of thermography is the following. The material emits radiant energy when heat is supplied in materials, and the temperature distribution can be measured using the infrared camera. Temperature distribution is varied according to the thermal properties of the materials.

When timber is graded by visual inspection to use wooden resources as construction elements and interior materials, it's hard to quantify the knots area, and a trainee must invest much time to measure the knot area. Therefore, there have been studies of detection and quantification of knot by visual inspection, CCD camera, X-ray, ultrasonic waves, infrared, etc. [2,3]. Construction of wooden houses has increased gradually. Because the decay causes a loss of strength damage and influences a bad effect in stability of construction. The degree of decay must be investigated in member of construction to prevent collapse. Tanaka and Divos[3] examined the factors that influence the surface temperature of wood, such as, density, knot, decay, void, in thermography.

In the study, we detected knots in wood with thermography and checked the possibility of detecting decay through infrared analysis to confirm.

2. Materials and Methods

2.1. *Materials*

To carry out this study, Japanese larch(*Larix leptolepis*) with diameter breast height of 30cm was obtained from Hongcheon province in Korea. Sawn lumbers were kiln-dried to about 12% moisture contents(oven dry basis) and were planed with a cross section of 20mm(thickness) and 140mm(width). Then the specimen (length 75mm) including knots was prepared. Four types of artificial decays were made in specimens, Hole with diameter 12, 10, 5.5, 3mm, length 10mm. and crack with width 6mm and depth 10mm on the middle of specimens. We manufactured different depth of decay from the surface as verifying number of veneers (thickness 0.5mm) from 1 to 3.

2.2. *Methods*

The experiment was conducted by infrared camera(IR FLEXCAM PRO, Infrared Solutions). The sensitivity of the infrared camera was 0.08°C, and the resolution was 120 x 160pixels. We observed surface temperature with the infrared camera after supplying heat to the surface of the specimens as a way to do convection heating.
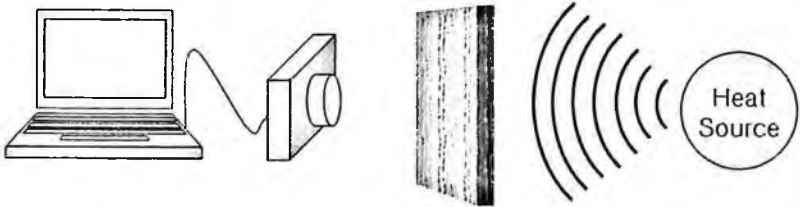
Fig. 1. Schematic diagram of the infrared thermography.

To detect knots, the heat source used was an oven with 100°C, output was 2,000W, and the heat source used for detecting decay was used the air heater, the central temperature was higher than 100°C and output was 2,800W, and cooling was conducted at room temperature(25°C). The surface temperature was measured every 1 minute between the heating and the cooling times until no differences in surface temperature were observed. To analyze the surface temperature of the specimens, FLEX View 1.30 was used to analysis the temperature changes for each part. The quantification of the knot area was gained by calculating the number of pixels in infrared thermography.

3. Results and Discussion

3.1. *Detection of knot*

We discovered that the sound area and the knots part in one wood responded differently to heat. The surface temperature on knots increased more slowly than the temperature of the sound area during the heating period and was lower during cooling period. Thus, the temperature fluxion of the knots surface was smaller than that of the sound area. For the heating time 5minutes, the maximum temperature of the specimens was approximately 30°C in the knots area, which meant that it was lower than approximately 32°C at the sound area. During the early cooling period, it was hard to distinguish the knots area from the sound area due to a little difference in temperature, but 5 minutes later, the distinction was definite. The temperature of the knots area was higher than that of the sound

area, which decreased quickly. Detection of knots was reliable as keeping 2 ℃ of temperature difference until about 20 minutes, and then temperature difference was reducing rapidly, just there became under 1 ℃ and finally it's not possible to distinguish.
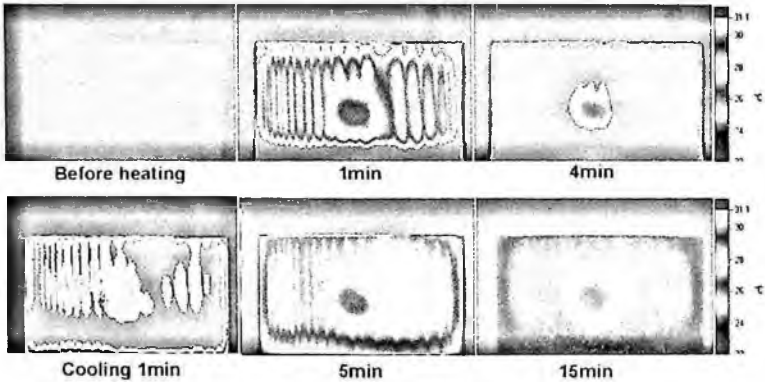
Fig. 2. Thermal images of specimens during heating period and cooling period.

The difference in temperature between the sound area and the knots area in the experiment was maximum 3.06 ℃ and average 1.16 ℃ for the heating period. In the case of larch, detection of knots during the heating period is more profitable because a temperature difference is bigger during the heating than during the cooling period. The graph on the right in figure 3 shows the temperature difference between the knots area and the sound area according to time period.
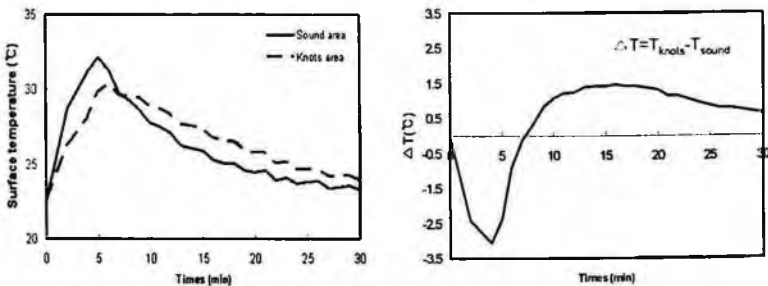
Fig. 3. Temperature changes(left) and temperature differences of the sound area and the knots area during heating and cooling.

3.2. *Detection of decay*

In the thermography, the temperature change of in the decay parts was larger. Because the temperature fluxion in the sound area was higher than in the decay

area, the temperature of the decay area rose faster than that of the sound area, and decreased quickly during the cooling period. The temperature change reacts are different according to the shape (size) in artificial decay area. Because the temperature of Artificial decay of diameter 12mm and central crack rose to about 53 ℃ and that of the sound area rose to 51 ℃, it was distinguished easily each other.
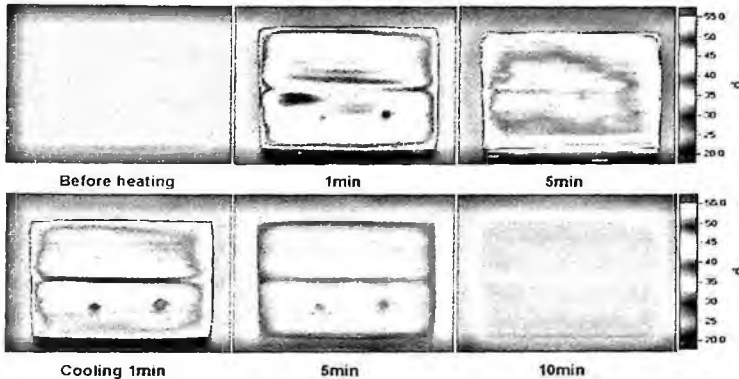
Fig. 4. Surface temperature of artificial decay and sound area during heating and cooling period.

Unlike large artificial decay, which has a high temperature difference, it is not easy to distinguish sharply between a small artificial decay area (5mm) and the sound area, because of the small temperature difference. The thermography analysis in this experiment failed to detect artificial decay of diameter 3mm that have a small temperature difference. During the cooling period, the temperature of the artificial decay decreased faster than that of the sound area. Figure 5 shows that the temperature of the artificial decay area is lower than that of the sound area. At about 15 minutes after cooling, the temperature difference became slight, and detection was impossible.

In artificial decay within a depth of 1.5mm from the surface, the temperature difference between the artificial decay area and the sound area was a maximum of 2 ℃, an average of 1 ℃, and detection of decay was the most suitable during the early cooling period because of the big temperature difference.
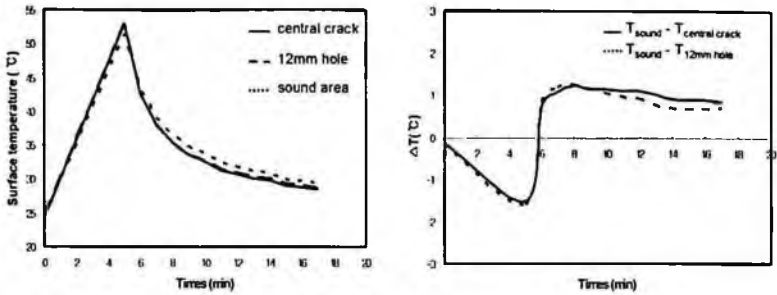
Fig. 5. Surface temperature changes(left) and temperature differences (right) of decay and sound area.

4. Conclusions

In this study, the results showed that in knots detection of larch the temperature of the sound area was higher during the heating period but lower during the cooling period. The surface temperature differences were mainly due to the different physical characteristics between the two textures, including the arrangement of cells, microfibril angles, heat conductivity, specific heat, and specific volume. Using the different reactions of the decay and sound areas for the heat, a distinction can be made using infrared thermography. However, there is difficulty in detection because decay exists in the inside of the wood. It is expected that the development of an optimal infrared thermography system that includes a more appropriate heat source and with improvements in the accuracy and speed of a calculation algorithm will realize a quicker defect evaluation in the field.

Acknowledgments

References

1. Wiggenhauser H, Infrared Physics & Technology. 43:233-238 (2001).
2. Sadoh, T. and K. Murata, Mokuzai Gakkaishi. 39(1):13-18 (1993).
3. Tanaka, T. and F. Divos, Proceedings of the 12th International Symposium on Nondestructive Testing of Wood. (2001).

A STUDY ON NONDESTRUCTIVE EVALUATION OF PAINTED METAL BY USING IR THERMOGRAPHY

SEUNG HYUN CHOL

Department of Precision Mechanical Engineering, Chosun University Graduate School 375, Seosuk-Dong, Dong-Gu, Gwangju 501-759, South Korea

KYUNG SEOK SONG

BK21 Education Center of Mould Technology for Advanced Materials & Part, Chosun University, 375, Seosuk-Dong, Dong-Gu, Gwangju 501-759, South Korea

JAE YEOL KIM

Department of Mechatronics Engineering, Chosun University, University, 375, Seosuk-Dong, Dong-Gu, Gwangju 501-759, South Korea

Importance on the detection of corrosion-related defect is undeniable from the fact that it can prevent significant economic loss and enhanced safety in mechanical equipments, pipes, ships, bridges, and other applications. Conventionally researched measurement methods for defect and thinning from corrosion are acoustic emission, EMAT using ultrasound, laser induced ultrasound, etc. However, these non-destructive testing methods have the shortcoming of accessibility to on-site. For instance, EMAT should be close to several millimeters to generate magnetic field in structure. For laser application, it can be applied to remote non-destructive testing, but some defect might not be possible to be detected by the surface condition of structure. In this study, infrared thermography camera is utilized to determine the degree of corrosion on paint-coated metal. In addition, fundamental researches to develop corrosion detection system for on-site metallic structure are conducted to provide the applicability of IR camera and possibility of thermal analysis method.

1. Introduction

Corrosion are acoustic emission, EMAT using ultrasound, laser induced ultrasound, etc. However, these non-destructive testing methods have the shortcoming of accessibility to on-site. For instance, EMAT should be close to several millimeters to generate magnetic field in structure. For laser application, it can be applied to remote non-destructive testing, but some defect might not be possible to be detected by the surface condition of structure.

One of the prospecting testing methods for NDT is infrared thermography, which can solve the shortcomings of conventional ones. Infrared thermography

detects infrared from the surface of material, and temperature distribution is displayed as thermal image. Infrared thermography can be efficiently utilized in two dimensional non-contacting non-destructive testing technique for material with thermal characteristics [1].

Infrared camera features active photography, and requires thermal energy transmission to material while analyzing the inside of it. Infrared thermography gives much information about thermal resistance, size, depth from surface of defects, which are invaluable NDT criteria [2-4].

In this study, infrared thermography camera is utilized to determine the degree of corrosion on paint-coated metal. In addition, fundamental researches to develop corrosion detection system for on-site metallic structure are conducted to provide the applicability of IR camera and possibility of thermal analysis method.

2. Principles and Experimental Equipment for Thermography

Infrared thermography camera is a measurement tool to detect reflected infrared wavelength from measuring material using external light source. By Stefan-Boltzmann Law for equation of temperature and wavelength, detected infrared wavelength can be converted to temperature, and high and low of temperature is seen as image.

$$I_m = I(T_{obj}) \cdot \tau \cdot \varepsilon + \tau(1-\varepsilon) \cdot I(T_{amb}) + (1-\tau) \cdot I(T_{atm}) \tag{1}$$

Fig. 1. Measurement Situation of Infrared Thermography

Fig. 2. Infrared Thermography Camera

As shown in Fig 1, total standard radiation energy can be express as Eq. (1). First term is radiation emitted by the surroundings and reflected in the object, and second term is radiation emitted by the object. Third term is radiation emitted by the atmosphere. Infrared thermography camera that is used in experiment is AGEMA Thermovision 900 SW/TE. Cooling method for infrared thermography camera is TE (thermal electric), and detector has the features like 2 split, serial scanning, 2~5.4 micron spectrum response, -10 ℃ ~ 500 ℃ of

temperature range (detectable up to 2000℃ with high temperature filter), 0.1℃ of sensitivity at 30℃, 104 element/line (50% modulation) of spatial resolution, and 3.5kHz of IR line frequency. In Fig. 2, Research Package 900 that can connect Thermovision 900 system, which is based on X-Windows OS (operating system), to Microsoft Windows OS based laptop computer.

Pulsed thermography is one of the most popular thermal stimulation methods in thermography. One reason for this popularity is the quickness of the test relying on a short thermal stimulation pulse, with duration going from about 3 ms for high conductivity material testing(such as metal parts) to about 4s for high conductivity specimens(such as plastics and graphite epoxy laminates). Such quick thermal stimulation allows direct deployment on the plant floor with convenient heating sources, Moreover, the brief heating (generally a few degrees above initial component temperature) prevents damage to the component and pulse duration varies from about 3 ms to 2s.

Basically, pulse thermography consists of briefly heating the specimens and then recording the temperature decay curve. Qualitatively, the phenomenon is as follows. The temperature of the material changes rapidly after the initial thermal pulse because the thermal front propagates, by diffusion, under the surface. The presence of a discontinuity reduces the diffusion rate so that when observing the surface temperature, discontinuities appear as area of different temperatures with respect to surrounding sound area once the thermal front has reached them. Consequently, deeper discontinuities will be observed later and with a reduced contrast. In fact, the observation time t is a function (in a first approximation) of the square of the depth z and the loss contrast C is proportional to the cube of the depth.

$$t \cong \frac{z^2}{\alpha} \qquad (2) \quad \text{and} \qquad C \cong \frac{1}{z^3} \qquad (3)$$

Where α is the thermal diffusivity of the material.
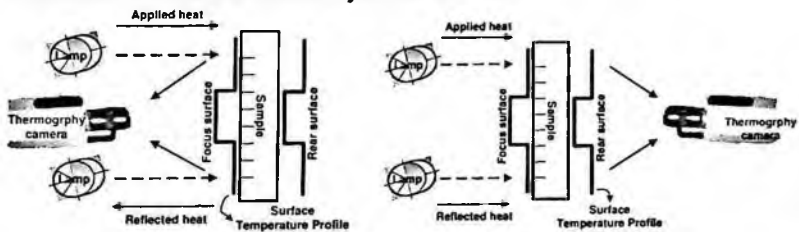
(a) in Reflection   (b) in Transmission
Fig. 3. Observation Techniques for Infrared Thermography

Test specimen with artificial defect detected by infrared thermography camera is manufactured as size of 150mm×50mm×3mm (L×W×T) from high carbon steel. As for defects, Circle and rectangular corrosion shapes with various sizes are created to verify the defect detection performance of thermography. In addition, crack in 0.2 mm depth is fabricated to compare the detectability of area defect and line detect. Shapes and sizes of defects are shown in Fig. 4.
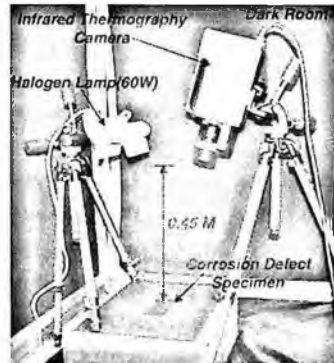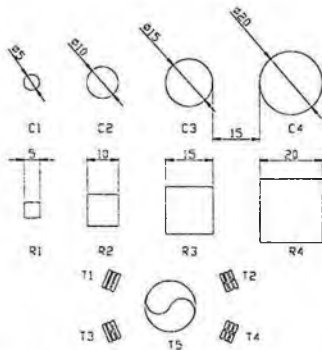
Fig. 4. Sizes, Shapes, Locations of Corrosion Defect in Test Specimen

Fig. 5. Experiment Diagram for Defect Detection

Difficulty in IR thermography testing is uniform supply of vast thermal energy through testing surface [5,6]. For infrared thermography of test specimen, heater that can maintain constant temperature is needed. In this study, surface of test specimen is homogeneously heated using light. At the distance of 0.45 m from specimen, halogen lamp is used for heating. To match the actual welding condition, surrounding of test specimen is not insulated. In addition, dark room is produced to maintain optimal experiment condition by blocking external heat source.

3. Experimental Method and Results

Specimen with different shapes and depths is prepared, and the other side is heated with halogen lamp. The difference in heat conductivity is measured at the opposite side using infrared thermography camera. In addition, the distance between infrared thermography camera and specimen is set as 1 meter, optimal focus distance, for clear thermal imagery to minimize loss of infrared ray from air.

Heating method for specimen is 60W halogen lamp, and its temperature is about 200℃. Distance between lamp and specimen is also 1 meter to remove any

effect on thermography camera. Surface of specimen is painted with black paint to exclude diffused reflection from external light source.

Thermography image is taken one frame for 10 seconds, and sample is heated for 30 minutes and cooled for 10 minutes. Total 240 frames are taken.

From Fig. 7 to 9, thermography images and temperature distributions by crossing the center of defect by the shapes of defect and material are shown.
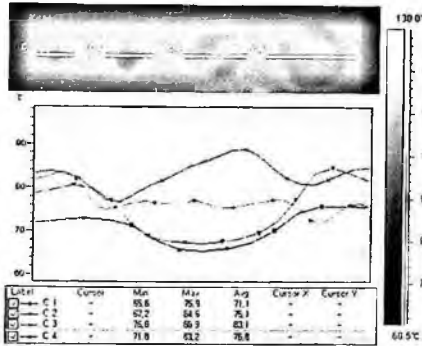
Fig. 7. Thermography Image and Temperature Distribution for Circle
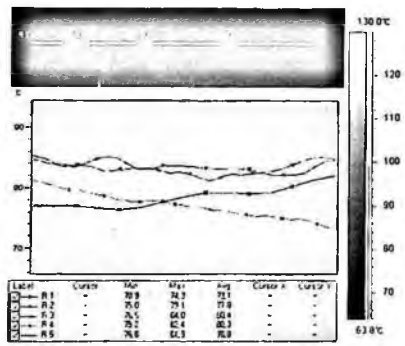
Fig. 8. Thermography Image and Temperature Distribution for Rectangular
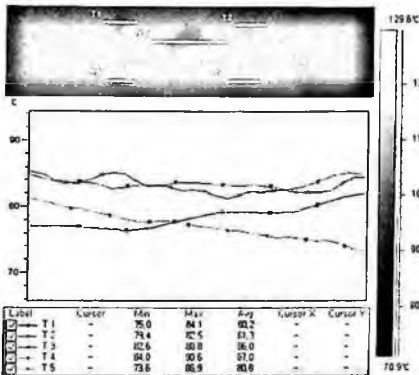
Fig. 9. Thermography Image and Temperature Distribution for Artificial defect
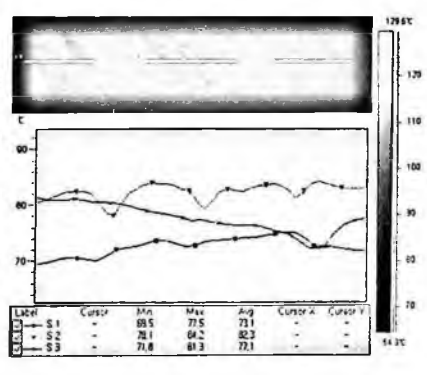
Fig. 10. Thermography Image and Temperature Distribution for Crack Defect in Soft Steel

As shown in thermography image, defect is well detected regardless of shape and size in defect. There is $2 \sim 10\,°C$ of difference in average between defect and no-defect area. Temperature of corrosion defect area is lower than the surrounding, and it can be explained from different size of thermal energy that is transmitted to specimen by thermal conduction element from corrosion crack.

For the crack defect, it can cleary be seen in thermography image as corrosion crack, and temperature at crack defect area is lower than the surrounding.

Temperature difference between high carbon steel and soft steel is negligible, and it can be surely said that thermographical defect detection method is possible to be applied in material with similar thermal conductivity.

4. Conclusion

In this paper, pulse infrared thermography is utilized to defect corrosion and crack defect under paint with halogen lamp heating. Results of the research can be summarized as the following.
1. Defects with different shapes and sizes of corrosion defect at metal surface are detectable through infrared thermography image.
2. Quantified infrared thermography can predict shape and location of defect.
3. Not only area defect but also line defect like crack can be detectable through infrared thermography.
4. Comparing to other NDT, not only higher testing efficiency but also applicability of infrared thermography to various conditions in the field is confirmed.

Acknowledgments

References

1. Cielo P, Maldauue X, Eeom Aa, Lewak R. *Thermograhpic Nondestructive Evaluation of Industrial Materials and Structures*, The American Society for Nondestructive Testing, Vol 45, 452-465(1987)
2. Vavilov V, *Thermal Nondestructive Testing : Hort History and State-of-art.* In : Balageas D, Busse G, Carlomagno GM, Editors Proceedings of the Qirt 92, Eurotherm Series 27. EETI ed, 179-193(1992)
3. Giorleo G, Meola C. *Location and Geometry of Defects in Composite Laminates from Infrared Images.* ASM int J Master Eng Perform (1998)
4. Maldague X. *Application of Infrared Thermography in Nondestructive Evaluation.* In: Rastogi P, Editor. Trends in Optical Nondestructive Testing(Invited Chapter), 591-609(2000)
5. Cawley P. *The Rapid Nondestructive Inspection of Large Composite Structrues.* Composites. 351-357(1994)
6. Hobbs CP, Temple A. *The Inspection of Aerospace Structure using Transient Thermography.* British Journal of Nondestructive Testing. 183-189(1993)

FAST AND RELIABLE DETECTION OF SUPERFICIAL INTRACRANIAL HEMORRHAGE BY HAND-HELD DEVICE USING NEAR-INFRARED

JUNG-YUL PARK, SANG-DAE KIM, DONG-JUN LIM

*Department of Neurosurgery, Korea University Medical Center, Ansan Hospital, #516
Gojan-Dong, Danwon-Gu, Ansansi, Gyeonggi-Do, 425-707, Korea*

Whereas infrared rays do not penetrate thick skull, near-infrared can penetrate the skull and to the depth of maximum 3cm tissue thickness. Thus, it can be used to detect most of traumatic intracranial hemorrhage. Object of this study was to validate usefulness of portable optical measuring device using near-infrared in detection of intracranial hemorrhage of superficial location. In this study, authors have tested in 110 normal subjects for the control and 20 patients who later confirmed to have intracranial hemorrhages. In control group, there were 68 males and 42 females. Average age was 46 with range between 8 and 74. In patient group, there were 12 males and 8 females and average age was 49 years. All, except 4 patients (2 with bilateral lesions and 2 with deep parenchymal hemorrhage), showed OD greater than 0.45 in corresponding regions. There were considered as false negative cases. However, there were no missed cases where there were hemorrhages located within 3 cm from scalp. Also, there were no side effects or complications form using this device. These results indicate that it would be particularly suitable in screening of intracranial hemorrhage, acute or delayed, located within 3 cm from skin where the most of traumatic intracranial heamorrhages take place.

1. Introduction

Majority of intracranial hemorrhages following head trauma belong to superficial hemorrhages. Although CT scans are usually performed in cases of suspected intracranial hemorrhage when it is available, some patients may develop even with good clinical conditions or later develop delayed hemorrhage in whom initial CT scans are not performed or repeated examination is not followed. However, sequential CT scans are not routinely recommendable because it requires transfer of patient to CT room each time when patient's condition is not suitable for such examination and it is still high cost. Radiation exposure adds another disadvantage to patients. In such cases, normal neurological profile may be abruptly switched to mental deterioration [1] or notable changes may not be evident in some patients [2-5]. In patients with delayed intracranial hemorrhage, although they are in need of surgery,

approximately 20% of them were noted to have normal intracranial pressure. This remains problematic [4,6,7].

Thus, appropriate measures are required to make a prompt screening and to monitor sequentially the clinical course in suspected or possible intracranial hemorrhage following head trauma. Authors have evaluated the clinical usefulness of portable optical measuring device using near-infrared in screening and monitoring the clinical course of patients with possible intracranial hemorrhage following head trauma.

2. Clinical Materials and Methods

One-hundred-and-ten healthy individuals were served as controls for the measurement of normal OD values in each region. In the patient group, the mean age was 48.82±27.43 years (range 3-86 years) and a male-to-female ratio was 12:8. In the control group, the mean age was 46.19±16.9 years (range 8-74 years) and a male-to-female ratio was 68:42. The patient group included subdural hematoma (7 cases), epidural hemtoma (6 cases), hemorrhagic contusion (3 cases), intraparenchymal hemorrhage (2 cases) and subarachnoid hemorrhage (2 cases).

In each patient, using Crainscan®, six landmarks were chosen bilaterally on the frontal, parietal and occipital region. (Fig. 1) The optical density (OD) was obtained at each landmark. Then, the differences in the ODs measured bilaterally (ΔOD) were calculated. *Chi*-square and bivariate correlation test were performed to analyze the mean differences at six landmark and to identify the correlations between them. Statistical analysis was done using statistical software(SPSS® Ver. 10.0 for Windows). P value less than 0.05 was considered as statistically significant.

3. Results

In the control group (n=110), the ODs measured on the left and right side were as follows: 7.49±0.64 and 7.60±0.62 in the frontal region; 8.48±0.75 and 8.66±0.79 in the parietal region; and 8.54±0.94 and 8.62±0.88 in the occipital region.

The ODs were significantly higher in the parietal and occipital regions than the frontal region ($p=0.000$). There were no statistical differences between the ODs measured in the parietal region and those measured in the occipital region ($p=0.625$).

The values of ΔOD were 0.36±0.25 in the frontal region; 0.38±0.30 in the parieto-temporal region; and 0.41±0.31 in the occipital region.
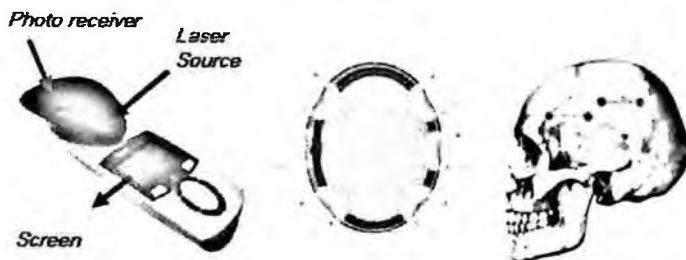
Fig. 1. The crainscan® contains a laser source and a neighboring photo-receiver which are both pressed to the patient's head (left). Frontal, parietal, and occipital regions are evaluated consecutively for the detection of intracranial hemorrhages in various areas (center and right).

In the patient group (n=20), bivariate correlation test was performed to analyze the location of hematoma and the value of ΔOD at each location. Pearson's correlation coefficiency was 0.544 in the frontal region, 0.287 in the occipital region and 0.177 in the parietal region. Statistical significance was seen in this series ($p<0.05$).

Regarding the type of hematoma, Pearson's correlation coefficiency was 0.456 in the frontal region and 0.301 in the occipital lesion. This was regarded as statistically significant ($p<0.05$). On the other hand, Pearson's correlation coefficiency in temporal region was 0.144, which was not regarded as statistically significant. In case 5, subdural hemorrhage was predominantly seen on brain CT scan. However, there was no statistical significance in the values of ΔOD because subdural hemorrhage was bilaterally manifested. In case 4 and 11, the temporal lesions were not consistent with CT findings. Presumably, this inconsistency may be due to difficulty in measuring the ODs. On the other hand, in cases of tentorial subdural hematoma, the values of ΔOD were increased in the occipital region.

In cases of epidural hematoma, Pearson's correlation coefficiency was 0.551 in the frontal region, 0.265 in the parietal region and 0.369 in the occipital region. As with other types of hematoma, epidural hematoma showed the normal values of ΔOD in the temporal region. In cases of hemorrhagic contusion, Pearson's correlation coefficiency was 0.189 in the frontal region (p<0.05). In cases of subcortical hemorrhage in the parieto-occipital region, the values of ΔOD were statistically significant. In cases of subcortical hemorrhage in the

basal ganglia, however, the values of ΔOD were less than 0.45. This was regarded as false negative. Pearson's correlation coefficiency was 0.151 in the parietal region and 0.032 in the occipital region. In two cases of subarachnoid hemorrhage, the values of ΔOD were not significantly increased. Finally, there were 3 patients who were later confirmed to have delayed epidural hemorrhage after screening with this device, 2 within 48 hours and 1 within 24 hours following trauma, in whom initial examination even with CT scans were normal.

4. Discussion

The infrared ray is referred to as the light generated laterally to the end of the red spectrum that emitted from the sun or other thermogenic bodies. The near-infrared ray is referred to as the infrared ray whose wavelength is the shortest. Jobsis first used the near-infrared ray in quantifying the metabolic profile of brain [8]. Unlike to infrared, it penetrates scalp, skull, dura mater and cerebral cortex to the depth of 3 cm from the skin. Based on this property, it is possible to obtain the intracranial data by quantifying the attenuation of light within the skull [9]. To date, it has been used to quantify the cerebral ischemia or the abnormal intracranial blood flow [10] and to diagnose the metabolic brain injury in pediatric patients [11]. Recently in the field of neurosurgery, this technique has been used to evaluate the vascular function following arterial bypass surgery [12] and to locate the actual site of lesion by intra-operatively distinguishing between white and gray matter [13]. Besides, in cases of glioma, it has been used to assess the metastatic potential of tumor cells and to predict the prognosis based on the degree of oxygen saturation [10].

In 1993, Gopinath *et al.* first reported the method of locating the actual site of intracranial hemorrhage using near-infrared spectroscopy [14]. Three types of light-absorbing molecules exist within the skull, which include oxyhemoglobin, deoxyhemoglobin and cytochrome aa3 [15]. Oxyhemoglobin and deoxyhemoglobin absorb the light at a wavelength of approximately 760nm [16]. Accordingly, the increased light absorbance at a wavelength of 760nm can be interpreted as the increased amount of deoxyhemoglobin. In the presence of intracranial hematoma in which the amount of deoxyhemoglobin increases, the near-infrared ray is increasingly absorbed at 760nm [14,17].

Mechanism of this device is based on the near-infrared ray that measures OD in the local tissue. Emitted from the light source, the near-infrared ray transmits scalp, skull and dura mater. Then, the near-infrared ray migrates along the cerebral cortex. Absorbed by the photo-receiver, the near-infrared ray is used

to calculate the OD extending scalp $\rightarrow$ skull $\rightarrow$ cerebral cortex $\rightarrow$ skull $\rightarrow$ scalp. OD is calculated based on the following formula:

$$OD = \log_{10} I_o/I_a$$

where, I_o: the intensity of light emitted from the light source

I_a: the intensity of light absorbed by the photo-receiver [14].

In cases of hematoma which impedes the light path, the absorbance of the near-infrared ray is increased. This results in high OD. OD is much affected by the thickness of skull, scalp and CSF [18,19]. Accordingly, the absolute magnitude of OD is not clinically significant. Rather, it is important to measure OD at symmetrical sites of both sides to evaluate the differences of Ods (ΔOD) for clinically significance. Preliminary study results using control patients indicated that the ΔOD value greater than 0.45 was considered to be certain that there is intracranial hemorrhage within 3 cm from the scalp.

In our series, ΔOD was significantly increased in cases of epidural or subdural hematoma compared to control. However, ΔOD was not significantly increased in cases of intracranial hemorrhage such as subarachnoid or intraparenchymal hemorrhage. These results were expected because these were bilateral lesions and ΔOD would not be high after subtraction of values from two sides. Also, deep seated lesions, such as 2 cases in our series, would not be detected due to deeper than 3cm from the scalp. Theoretically, both OD and ΔOD on the affected sites should be increased in cases of subcortical or intraparenchymal hemorrhage. This is based on the phenomena that the near-infrared ray transmits the cerebral cortex in a depth of 3 cm and then affects the absorbance of light [9]. In the present study, the absolute magnitude of ΔOD was also increased. However, statistical significance was not seen in our series. According to Okada et al., the thicker the skull or scalp were, the shallower the degree of phototransmission became [19]. Therefore, it can be inferred that the intracranial hemorrhage was not correlated with the degree of phototransmission since it is more affected by the independent factors such as the thickness of skull, head position and age than subdural or epidural hematoma. Gopinath et al. have reported that the consecutive monitoring was useful in diagnosing delayed the intracranial hemorrhage following head trauma or the recurrent intracranial hematoma following the surgery [20]. Also, on noticing the change of ΔOD, they were able to diagnose and treatment patients with early-stage delayed intracranial hematoma.

Despite the limitations described above, the clinical usefulness of near-infrared device deserves special attention. It is a versatile diagnostic device enabling physicians from various backgrounds to screen the patients who are suspected of head trauma or who may develop delayed intracranial hemorrhage

in a prompt, simplified manner. Also, the consecutive use enables to monitor the delayed or recurrent hemorrhage in different clinical settings.

References

1. HA Young, JR Gleave, HH Schmidek, and S Gregory, *Neurosurgery.* **14**, 22 (1984).
2. BT Andrews, *Contemp. Neurosurg.* **10**, 1 (1988).
3. FG Diaz, DH Yock Jr, D Larson, and GL Rockswold, *J. Neurosurg.* **50**, 217 (1979).
4. SK Gudeman, PR Kishore, JD Miller, AK Girevendulis, MH Lipper, and DP Becker, *Neurosurgery.* **5**, 309 (1979).
5. H Sakai, H Takagi, H Ohtaka, T Tanabe, T Ohwada, and K Yada K, *J. Neurosurg.* **68**, 566 (1988).
6. BT Andrews, LH Pitts, MP Lovely, and H Bartkowski, *Neurosurgery.* **19**, 408 (1986).
7. R Bullock, J Golek, and G Blake. *Surg. Neurol.* **3**, 181 (1989).
8. FF Jobsis, *Science.* **198**, 1264 (1977).
9. B Chance, JS Leigh, H Miyake, DS Smith, S Nioka, and R Greenfeld, *Proc. Natl. Acad. Sci.* **85**, 4971 (1988).
10. S Asgari, HJ Rohrborn, T Engelhorn, and D Stolke D, *Acta. Neurochir. (Wien)* **145**, 453 (2003).
11. B Chance, DS Smith, M Delivoria-Papadopoulos, and DP Younkin, *Crit. Care. Med.* **17**, 65 (1989).
12. Y Murata, Y Katayama, K Sakatani, C Fukaya, and T Kano, *J. Neurosurg.* **99**, 304 (2003).
13. CA Giller, H Liu, P Gurnani, S Victor, U Yazdani, and DC German, *J. Neurosurg.* **98**, 1299 (2003).
14. SP Gopinath, CS Robertson, RG Grossman, and B Chance B, *J. Neurosurg.* **79**, 43 (1993).
15. S Wray, M Cope, DT Delpy, JS Wyatt, and EO Reynolds, *Biochim, Biophys. Acta.* **933**, 184 (1988).
16. DS Smith, W Levy, M Maris, and B Chance, Anesthesiology. **73**, 12 (1990).
17. O Hazeki, and M Tamura, *J. Appl. Physiol.* **64**, 796 (1988).
18. E Okada, and DT Delpy, *Appl. Opt.* **42**, 2906 (2003).
19. E Okada, and DT Delpy, *Appl. Opt.* **42**, 2915 (2003).
20. SP Gopinath, CS Robertson, CF Contant, PK Narayan, RG Grossman, and B Chance, *J. Neurosurg.* **83**, 438 (1995).

AE CHARACTERISTICS OF PRE-CRACKED CHARPY SPECIMENS FOR THE MULTI-PASSED WELDMENT FOR THE PRESSURE VESSEL STEEL

NA EUI GYUN*

Department of Mechanical Engineering, Kunsan National University, 68 Miryong Dong, Kunsan City, Korea

KIM HOON

Department of Mechanical and Automotive Engineering, Chonam National University, 96-1 Doonduk Dong, Yosu City Korea

LEE SANG KEUN

1103 Hangang Apt 459-1 Dongsan-dong Deokjin-gu, Jeonju City, Jeollabuk-do, Korea

The purpose of this study is to examine the relations between AE characteristics and material properties such as plastic zone size at notch tip and strength, to investigate the AE signals in the deformation process of the pre-cracked Charpy size specimens of the multi-passed weld region for the pressure vessel steel. Four point bend and AE tests were conducted. In all cases, the weldment was very active over the whole plastic deformation region with 6 events, whereas the basemetal showed only 2 events. In case of basemetal, plastic deformation process is simple. However, deformation processes for the weldment consist of various steps because weld region includes the discontinuous mechanical properties and complex micro-structures. Amplitude for the weldment was the largest among specimens. Oxides which were formed in the course of welding in air are the AE sources and AE signals for the basemetal are emitted from the second phase particles which are formed in the process of steel manufacturing.

1. Introduction

AE techniques have been used in evaluating the dynamic and micro-mechanistic aspects of deformation and detecting the location of crack initiation during operation of the structures in fields[1,2,3]. Besides, fracture mechanisms for the various steels and composites were verified through the analysis of the AE signals which were obtained under the applied load. Recently, Na et al [4] found out that four point bend test was the appropriate test to obtain the AE data at notch tip efficiently compared with the three point test and there are some correlations between AE signals and mechanical properties for the pressure vessel steel such as SA 516 steel.

The purpose of this study is to examine the relations between AE characteristics and material properties of the weld specimens such as plastic zone size and strength, to investigate the AE signals at notch tip in the deformation process of the weld region.

2. Experimental procedures

The material used in this study is the pressure vessel steel plate of 38-mm thickness. Table 1 shows the chemical compositions and mechanical properties in air. Submerged-arc welding with 26 passes was conducted along the rolling direction. Weld block was given to post weld heat treatment(PWHT) like following conditions: heating rate of 145°C/hr, heating temperature of 650°C and holding time of 60 min. Charpy size specimens were extracted from the weld zone as shown in Figure 1 and V-notch (45°) was machined with the depth of 2mm and pre-crack of 0.5mm length was made using the universal fatigue test machine under the three point bend and load of ±1.5kN with 3 Hz was applied under stress control. Notch was centered on the fusion line.

Table 1. Chemical compositions and mechanical properties of SA-516(grade11)

(a) Chemical compositions

C	Si	Mn	P	S	Cr	Ni	Cu	V	Sol Al
0.21	0.237	1.06	0.016	0.004	0.02	0.02	0.02	0.012	0.26

(b) Mechanical properties

Yield strength (MPa)		Tensile strength (MPa)		Elongation (%)
358.7		519.5		29.0
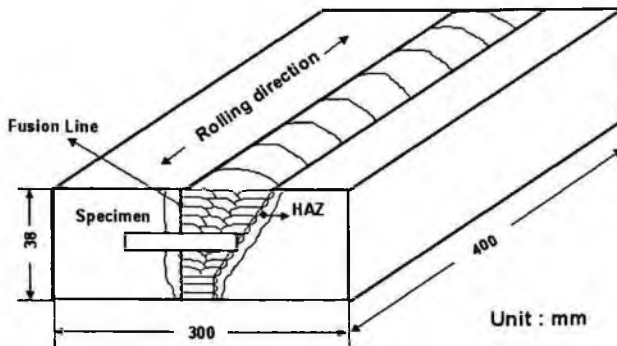
Fig. 1. Extraction of Charpy specimen from the multi-passed weld block.

Four point bend test was conducted, including AE test[4]. Test was conducted at a constant speed of 0.002mm/s at room temperature. Span length was 40 mm and the top-loading span was 10 mm. AE measurements were obtained using two AE sensors (PAC-R15) and preamplifiers (PAC-1220A, 40 dB gain). Two transducers were attached to both end of the specimens. AE win software was used. Threshold value of 40 dB was fixed for the all specimens.

Generally, lots of noises are introduced during AE test. It is necessary to eliminate the noises after test for obtaining the real AE signals at notch tip. In order to eliminate the noises from loading pins, only AE waves which arrived within 10 μs to both channels were chosen for analysis. Further discrimination was conducted based on the event location. Among AE waves thus discriminated, AE waves, which differ in rise-time of >3 μs, were ignored.

3. Results and discussion

Figure 2 represents the load and AE signal strength plotted against deflection for the samples with pre-crack. Tests were terminated at the near maximum load.

(a) Basemetal   (b) Weldment
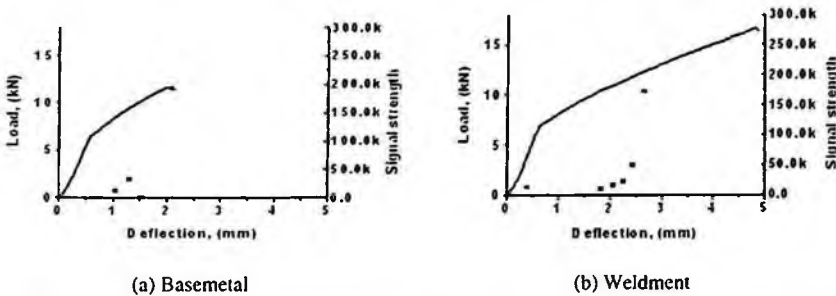
Fig. 2. Load and AE signal strength plotted against deflection for the samples with pre-crack.

In all cases, AE signals were almost absent within the elastic region and a small number of signals were produced in the process of plastic deformation. The weldment was very active over the whole plastic deformation region with 6 events, whereas the basemetal showed only 2 events. The maximum signal strength of the basemetal and weldment increased in order and the maximum signal strength for the basemetal and weldment varied from 198,000 to 50,000. The pre-cracked specimens generated lower numbers of AE signals and lower signal strength over the whole deflection range. The reason for showing the low level signal strength for the pre-cracked specimens is that stress concentration factor is so high that plastic deformation zone size becomes smaller than that of blunt notch specimens.

Figure 3 shows the relations between cumulative AE count and plastic zone size at notch tip for the basematal and weldment. Plastic zone size was calculated using the following equations[5].

$$K = \frac{3PL}{TW^2} \sqrt{\pi a} \cdot F(\alpha), \quad \alpha = \frac{a}{W}$$

$$F(\alpha) = 1.122 - 1.121\alpha + 3.740\alpha^2 + 3.873\alpha^3 - 19.05\alpha^4 + 22.55\alpha^\varepsilon$$

$$R_y = \frac{1}{2\pi} \left(\frac{K}{\sigma_y} \right)^2$$

Where K is stress intensity factor in MPa m, P is the applied load, T is the specimen thickness, W is the specimen width, a is the crack length, L is the specimen length and Ry is the plastic zone size.
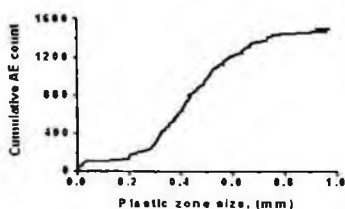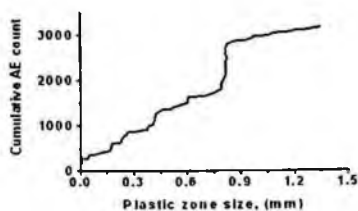
(a) Basemetal   (b) Weldment

Fig. 3. Relations between cumulative AE count and plastic zone size at notch tip for the basemetal and weldment.

As shown in these figures, deformation processes are different each other. In case of the basemetal, plastic deformation process is simple. However, deformation processes for the weldment consist of various steps because weld region includes the discontinuous mechanical properties and complex micro-structures. AE count increasing rate for the all specimens is almost constant over severe plastic deformation. It is necessary to investigate the these processes from the point of deform mode at notch tip. According to the past study [6], the shape of plastic deformation at notch tip of weldment spreads out with some angle to the notch direction, whereas that of the basemetal proceeds to the notch direction, even though plastic deformation size at notch direction of the weldment becomes smaller. This was evident in the sample loaded to the maximum load. Macro-cracks in weldmetal samples started to spread along the expected shear bands. More AE signals are emitted due to the increased area of cracking.

Figure 4 shows the relationship between amplitude and AE count for the basemetal, PWHT specimen and weldment.

(a) Basemetal   (b) PWHT specimen   (c) Weldment
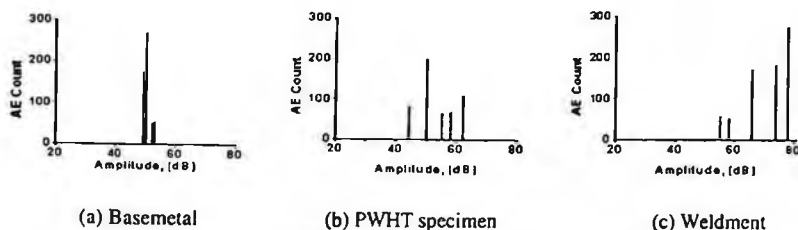
Fig. 4. Relationship between amplitude and AE count for the basemetal and weldment.

Amplitude ranges from 50 to 53 for the basemetal, 43 to 62 for the PWHT specimen, 57 to 78.9 for the weldment. Besides, number of total AE count for the weldment was the most, followed by PWHT specimen and basemetal. The reason for showing these results is that matrix of the weldment is the strongest compared with the two specimens. These results are similar with the previous study[4].

Figure 5 shows the photos(x100) which are taken against the notch tip after unloading at 2mm of deflection. As shown in these figures, crack tip for the basemetal was damaged compared with those of the PWHT specimen and weldment.

(a) Basemetal   (b) PWHT specimen   (c) Weldment
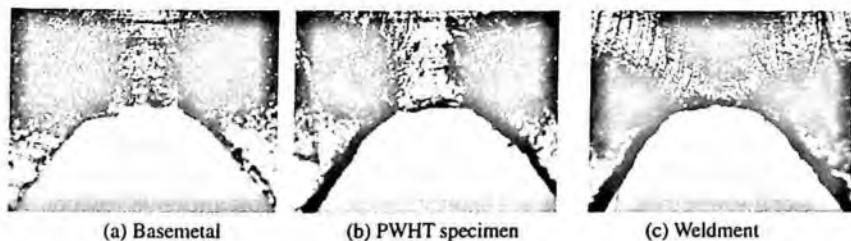
Fig. 5. Optical photos for the basemetal, PWHT specimen and weldment at notch tip.

Considering these photos and test results mentioned above, it can be concluded that ductility at notch tip for the basemetal does not attribute to emit AE signals. Accordingly, it is necessary to find out the other mechanisms which cause to emit more AE signals for the weldment in detail. For this, SEM observations were made against the center region of the fractured surfaces along the notch where tri-axial stress state exists under the bend load.

Figure 6 represents the SEM photos of the basemetal, PWHT specimen and weldment with high magnification of 3500.

(a) Basemetal   (b) PWHT specimen   (c) Weldment
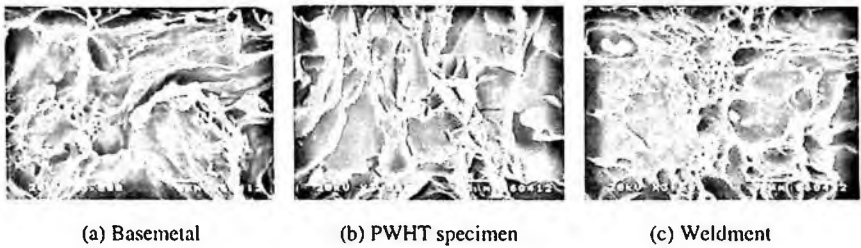
Fig. 6. SEM photos for the basemetal, PWHT specimen and weldment on the fractured surfaces.

In case of the weldment, lots of particles were distributed on the fractured surface unlike the basemetal. These particles were known to be oxides such as MgO, FeO etc. which were formed in the course of welding in air[4]. As the load is applied, debonding phonemena between matrix and particles occur so that more AE signals are produced. However, AE sources for the basemetal is presumed to be the second phase particles which are formed in the process of steel manufacturing.

It is recommended that welding method to decrease the oxides in the course of welding in air has to be improved because cracks are initiated at boundaries between oxides and matrix for the weld structures during in-services.

4. Conclusions

AE signals were almost absent within the elastic region and a small number of signals were produced in the process of plastic deformation. The weldment was very active over the whole plastic deformation region with 6 events, whereas the basemetal showed only 2 events. Deformation processes are different each other. In case of the basemetal, plastic deformation process is simple, whereas deformation process for the weldment consist of various steps because mechanical properties at weld region are discontinuous and complex. AE signals for the basemetal are emitted from the second phase particles which are formed in the process of steel manufacturing, whereas oxides which were formed in the course of welding in air causet to emit more AE signals.

It is recommended that welding method to decrease the oxides in the course of welding in air has to be improved because cracks are initiated at boundaries between oxides and matrix for the weld structures during in-services.

References

1. K. Ono, H.B. Teoh and I. Roman: *Fracture Induced Acoustic emission of A533B Steel – Effects of Test Temperature and Fracture Mechanisms*, Progress in Acoustic Emission II, pp. 105-113, (1984).

2. N. Nakamura, N. Ringshall, Y. Fukuzawa and A. Adachi: *Acoustic Emission during the Deformation of Iron Crystals*, Proc. of the 5th International Acoustic Emission Symposium, pp. 318-325, (1980).

3. C.K. Mukhopadhyay, T. Jaykumar, B. Raj and K.K. Ray: *The Influence of Notch on the Acoustic Emission generated during Tensile Testing of Nuclear Grade AISI Type 304 Stainless Steel*, Materials Science and Engineering A276, 83-90, (2000).

4. Na. E. G, K. Ono and Lee. D. W: *Evaluation of Fracture Behavior of SA-516 Steel Welds Using Acoustic Emission Analysis*, Journal of Mechanical Science and Technology (KSME Int. J.), Vol. 20, No. 2, pp. 197-204, (2006).

5. D.P. Rooke and D.J. Cartwright: Compendium of Stress Intensity Factors, (1976).

6. Park. C. H: *Plastic zone size and shape at notch tip for the weldment fo the steel*, Jeonbuk National University, Ph. D Thesis, (1987).

DEFORMATION OF PURE MAGNESIUM IN TENSILE TEST INVESTIGATED BY STFT OF AE SIGNALS

YUNPING LI, MANABU ENOKI[†]

Department of Materials Engineering, School of Engineering, The University of Tokyo,
7-3-1 Hongo, Bunkyo-ku, Tokyo 113-8656, Japan

In the present research, the deformation mechanism of rolled pure magnesium in tensile test was investigated by short time Fourier transform (STFT) of acoustic emission (AE) signals at room temperature. Two kinds of samples were designed: one with the tensile direction parallel to the rolling direction and the other vertical to the roll direction. The results showed that the AE signal from twinning has a relatively higher frequency than that from the dislocation slipping because of the higher twinning formation velocities. By analyzing the STFT of AE signals at different strain levels, the evolution behaviors of dislocation slipping and twinning activity were analyzed systematically.

1. Introduction

Deformation of magnesium typically occurs through crystallographic slipping and twinning, since the uniform deformation of materials needs at least five independent slipping systems while only basal slipping system is active at room temperature [1-2], and the other system especially twinning has to be activated. Twinning of magnesium plays an important role in the deformation process. The twinning behavior of magnesium and its alloys are strongly influenced by the external factors such as the grain size, strain rate, and temperature etc. In a specific deformation process, the twinning activity varies accordingly with increasing strain levels [3]. It has been proved in our previous research that by analyzing the twinning size - twinning density - applied strain distribution, the twinning activities especially twinning nucleation process are very high at the initial stage of deformation process, and in the later stage (higher strain level) the twinning activity gradually evolves to a twinning size growth dominated process [4]. Besides, in the commercial draught magnesium and its alloys, strong basal texture was formed in which the c- axes of the crystalline cell are mostly aligned normal to the extrusion or rolling direction. The draught block shows different mechanical behaviors in different loading directions because of the anisotropy of the manufactured block.

[†]Corresponding author: enoki@rme.mm.t.u-tokyo.ac.jp

Acoustic emission (AE) is a unique technique in observing the internal dynamic behavior of microstructure evolution in deformation process [5]. Twinning is one of the most important sources of AE and the formation of twinning can produce much stronger elastic waves than that from the dislocation slipping [6]. Due to the different formation velocities between the twinning formation and dislocation slipping process, different frequency peaks of AE signals from twinning formation and dislocation slipping should be observed. So, if an AE measurement is applied in the deformation process of magnesium, an in-situ observation of the evolution mechanism is possible.

2. Experimental

Rolled pure magnesium with a purity of about 99.95wt% produced from Osaka Fuji Corp. was selected as present research materials. Samples were with average grain size of about 25-30µm.

Two kinds of tensile specimens were prepared in which one was with the rolling direction parallel to the tensile direction and the other with the rolling direction vertical to the tensile direction. At the end of the tensile sample a hole was drilled so that in the following procedure the sample was tensioned through a pin inside of the hole. Holes were drilled with a suitable diameter and the maximum stress along the edge of hole was designed to be lower than the average stress applied to the sample, because the AE signals from the ends of sample will interfere with the signals from the center area of sample in deformation if the pin hole is too small (Figure 1).
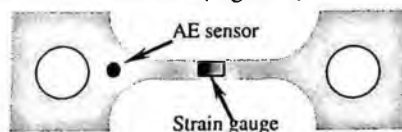
Fig. 1. Schematic figure of the tensile sample.

Samples in tensile test were conducted at a strain rate of about 1.67×10-4/s. A low noise type AE sensor (M304A, Fuji Ceramics, Japan) was used in experiments. The frequency distributions of AE signals as a function of time (Short time Fourier transition, STFT) as well as other parameters in deformation process were observed by Continuous Wave Memory (CWM) AE system [7].

3. Results and Discussion

Typical deformation curves of pure magnesium tensioned parallel and vertical to the rolling direction are shown in Figure 2. Yielding stress of the vertical sample

shows a high value than that of the parallel sample. Obvious anisotropic properties of the samples along two directions were observed. In the rolling process, the stress applied around the sample was not uniform, which resulted in the anisotropic characteristics of the materials.
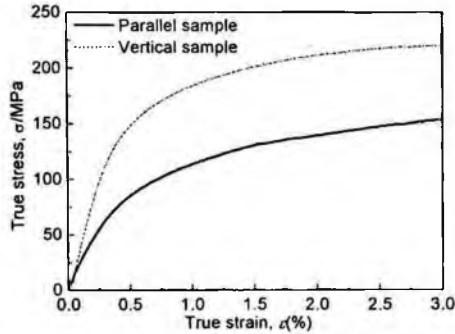
Fig. 2. Tensile behavior of pure magnesium parallel and vertical to rolling direction.

The different tensile behaviors of the two samples could be clearly expressed by strain hardening rate as shown in Figure 3. For the vertical sample, the strain hardening rate decreases gradually with the increase of strain level all the time. In contrast, an increase of strain hardening rate could be observed at higher strain level in parallel sample. Above tensile behaviors of the two kinds of samples are thought to be resulted from the different twinning behavior in different loading directions. For the parallel sample, the Schmidt factor for twinning formation is lowest and the twinning formation is extremely difficult [8], and the other slipping system such as non-basal slipping system has to be more active than that in the vertical sample. At higher strain level, when the internal stress or applied stress exceeds the critical resolved shear stress (CRSS) above certain strain level, the twinning can be activated. Due to the higher CRSS of twinning formation than both non-basal slipping and basal slipping systems, an increase of strain hardening rate at higher strain level could be observed. In contrast, for the vertical sample twinning can be formed relatively easily compared to the parallel sample in the initial stage of tensile process. In this stage, a higher strain hardening rate than that of the parallel sample could be observed because of the higher CRSS of twinning formation as mentioned above. At higher strain level, the deformation evolved to a twinning size growth process as well as the non-basal slipping due to the change of grain orientation. In both twinning growth and the non-basal slipping process, a relatively lower CRSS is required than the twinning formation (or twinning nucleation) [8] leading to continuing the decrease of strain hardening rate with increase of strain level.
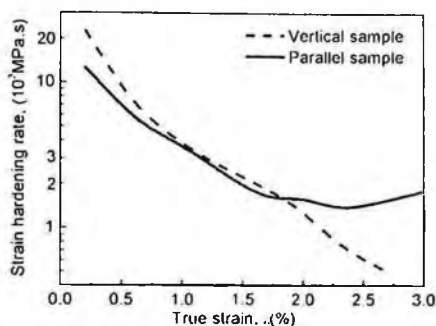
Fig. 3. Strain hardening rate in tensile process.

In the deformation process of pure magnesium, twinning and dislocation slipping (both basal and non-basal slipping) are dominant deformation mechanisms. In fact, in the present tensile process, only two frequency peaks at about 200 and 500 kHz could also be observed as shown in Figure 4 for a typical short time Fourier transform (STFT) of pure magnesium at strain of about 0.5%. The X-axis, Y-axis and Z-axis of the STFT distribution are time, frequency and the magnitude of AE signals, respectively. The signals with lower frequency are thought to be related to the dislocation motions and the signals with higher frequency are related to the twinning formation (twinning nucleation and growth) process. It is well known that the frequency of the AE signal is determined by the rise time of AE sources [9]. The twinning nucleation with relatively higher CRSS is accompanied with a large decrease of stress and this formation velocity of twinning can exceed the transverse velocity of sound [10], while the slipping velocity of dislocation is only about 0.3-0.4 times of the transversal sound velocity [11]. It is thought that dislocation slipping distance is in the order of the grain size (about 20-30μm), while the twinning nucleation distance (or the critical twinning length for twining nucleation) is smaller than that of the grain size. The above characteristics results in AE signals with longer rise time or lower frequency for dislocation slipping and shorter rise time or higher frequency for the twinning nucleation. The frequency for twinning nucleation is expected to be 2.5-3 times of that for slipping from above analysis. It has to be mentioned that the twinning growth and twinning nucleation are all jump-wise formation processes and are supposed to have the same frequency although the magnitude of twinning nucleation is much larger than that from the twinning growth for the higher CRSS in the twinning nucleation process [8].
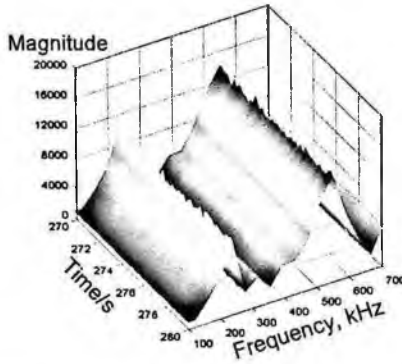
Fig. 4. Typical STFT of AE signals in tensile process of pure magnesium at strain of about 0.5%.
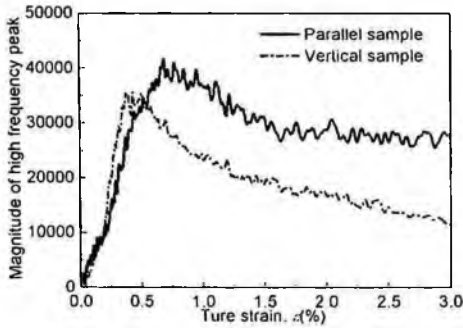
Fig. 5. Strain dependence of high frequency peak (about 500kHz) in tensile process.

The higher frequency peak of STFT of AE signals is related to the twinning behavior closely as mentioned above. Then, dynamic twinning behavior in tensile process could be expressed by the true strain dependences of the magnitude of the high frequency peak of about 500kHz as shown in Figure 5. The difference of twinning behavior in the two samples could be clearly observed. Before the yielding point, the twinning activity in parallel sample is relatively lower compared to the vertical sample. However, after the yielding point the twinning activity in parallel sample becomes higher than that of the vertical sample. Present results by STFT analysis are in good agreement with the previous discussion by analyzing the deformation behavior (Figure 2) and strain hardening rate (Figure 3). Besides, relative twinning behaviors compared to the dislocation slipping could also be obtained from the ratio between the high frequency peak and the low frequency peak (200kHz) as shown in Figure 6.
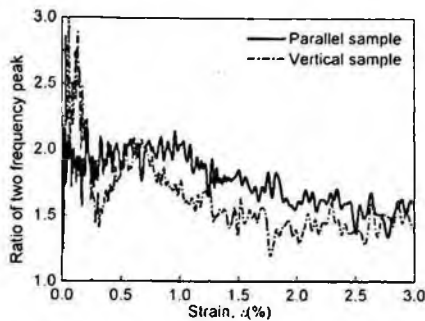
Fig. 6. Ratio between the high frequency peak (about 500kHz) and low frequency peak (about 200kHz).

Conclusion

1. The strain hardening rate for the parallel sample showed different behavior to vertical sample at high strain level due to different activity of twinning.
2. At lower strain level, the twinning activity for vertical sample is higher than the parallel sample, and in the later stage the twinning activity for parallel is higher by observing the high frequency peak of AE signals.

References

1. B.L. Mordike and T. Ebert, *Mater. Sci. Eng.* **A302**, 37(2001).
2. J. Koike and T. Kobayashi, *Acta Mater.* **51**, 2055(2003).
3. Y. Li and M. Enoki, *Mater. Trans.* **48**, 1220(2007).
4. Y. Wang, G. Liu and Z. Fan, *Acta Mater.* **54**, 689(2006).
5. R. K. Miller, *Nondestructive testing handbook*, second edition, volume **5**, AE testing, (American society for nondestructive testing, 1987) pp.1-50.
6. M. R. Barnett, Z. keshavarz, A.G. Beer, and D. Atwell, *Acta Mater.* **52**, 5093 (2004).
7. K. Ito and M. Enoki, *Mater. Trans.* **48**, 1221(2007).
8. X. Y. Lou, M. Li, R.K. Boger, and S.R. Agnew, *Int. J. Plast.* **23**, 44(2007).
9. W. Schaarwachter and H. Ebener, *Acta Metall. Mater.* **38**, 195(1990).
10. P. Gumbsch, and H. J. Gao, *Science* **283**, 965(1999).
11. J. Friedel, *Dislocation* (Pergamon press, New York, 1964) pp 55-96.

DYNAMIC CHARACTERIZATION ON AL-ALLOY FOAM DAMAGED BY CYCLIC LOAD

ILHYUN KIM, SUNG-GAUN KIM, AMKEE KIM[†]

Division of Mechanical and Automotive Engineering, Kongju National University, Kongju, Chungnam 314-701, Korea

SEUNG-JOON KIM, JUNHONG PARK

Department of Mechanical Engineering, Hanyang University, Seongdong-Gu, Seoul 133-791, Korea

The permanent residual strain of aluminum alloy foams gradually increases with the number of cycles by the cyclic fatigue stress. The progressive shortening of specimen in compressive-compressive fatigue is associated with cyclic fatigue failure and ratcheting in the damaged foam which degrades the dynamic material performance which is closely related with sound and energy absorption. In this paper, the specimens were made in the shape of beams to generate vibration of the controlled boundary conditions and the dynamic modulus and loss factor were measured using a beam transfer function method. As result, the dynamic moduli decrease significantly from increasing fatigue damage for entire frequency ranges of measurements. On the contrary, the loss factors increase by more than twice with increasing level of damage.

1. Introduction

Metallic foams, especially aluminum (Al) alloy foams have received a considerable amount of attention in recent years because of their extremely low density and unique functional properties such as impacting energy absorption, sound absorption and flame resistance. They are growing in use in sandwich structure for panels, tubes, shells, packaging, crash protection devices, and the weight sensitive construction parts in transportation and aerospace industries [1]. In particular, the applicability of Al foams can be found for sound and energy absorption of light weight structure [2, 3].

The permanent residual strain gradually increases with the number of cycles by the cyclic fatigue stress. The progressive shortening of specimen in compressive-compressive fatigue is associated with cyclic fatigue failure and

---

[†] Corresponding author: E-mail: amkee@kongju.ac.kr Phone: +82-41-550-0258 Fax: +82-41-555-9123

ratcheting in the damaged foam which degrade the dynamic material performance which is closely related with sound and energy absorption.

In this paper, we investigated the dynamic behavior of Al-alloy foams damaged by the quasi-static compressive strain and the cyclic compressive strain. For investigation of structural dynamic characteristics, the specimens were made in a shape of beam to generate vibration of the controlled boundary conditions. Using the measured vibration data, the dynamic modulus and loss factor were measured using a beam transfer function method. The dependence of dynamic characteristics on damage was investigated in the frequency ranges near the fundamental frequency of the specimens. The data of specimens compressed by fatigue were compared to those of the specimen compressed by quasi-static load.

2. Experimental

2.1. *Material and specimen*

The material used in this study was closed cell Al-Si-Ca foam obtained from commercial manufacturer (FOAMTECH Korea). The material was produced using the melt-based process and was obtained in a form of panel

The foam has a relatively uniform microstructure. The foam used in this study had the cell diameter of about 3-4 mm and the relative density of about 0.11. Specimens of size $40 \times 150 \times 40$ mm^3 were machined from the foam panel for static, fatigue and dynamic tests.

All the cyclic and static compression tests on specimens along the thickness direction were performed using an MTS 858 servo-hydraulic test machine at a load ratio of R = 0.1 and three different endurance ratios ($|\sigma_{max}|/\sigma_{pl}$) in the range of 0.6, 0.7 and 0.8. Here, σ_{max} is the maximum stress in the fatigue cycle and σ_{pl} is plateau stress taken as average value within plateau region. The frequency of cyclic load was 50 Hz. The detailed condition of fatigue test is shown in Table 1.

Table 1. Specification of the fatigue test

Thickness	Endurance ratio ($|\sigma_{max}|/\sigma_{pl}$)	Relative density (ρ^*/ρ_s)	σ_{pl} (MPa)
40	0.6	0.11	2.1
	0.7	0.10	
	0.8	0.10	

Fig. 1. Al-alloy specimen.
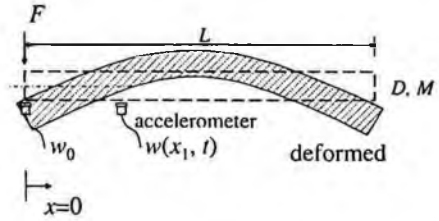
Fig. 2. Beam for dynamic characterization by transfer function method.

2.2. Test method for dynamic characterization

The beam transfer function method is the experimental method of measuring the flexural stiffness and vibration dissipation characteristics of arbitrary beam structure [4-6]. When the effects of shear deformation and rotary inertia are negligible compared to those of bending deformation, the equation of motion for vibrating beam in Figure 2 is

$$D\frac{\partial^4 w}{\partial x^4} + M\frac{\partial^2 w}{\partial t^2} = 0 \tag{1}$$

where $D = EI$, E is the dynamic modulus, I is the cross-sectional area moment of inertia, and M is the mass per unit length of the beam. Assuming harmonic motion, i.e., $w(x,t) = \mathrm{Re}\{\hat{w}(x)e^{i\omega t}\}$, the complex stiffness is widely used to model the dissipation of vibration energy within a structure. The complex bending stiffness, $\hat{D}(\omega) = D(\omega)[1 + i\eta_D(\omega)]$, is related to the complex modulus of the beam materials, $\hat{E} = E(\omega)[1 + i\eta_E(\omega)]$ as $\hat{E} = \hat{D}/I$. The satisfying beam function for the boundary value problem is:

$$\hat{w}(x) = \hat{A}_1 \sin \hat{k}_b x + \hat{A}_2 \cos \hat{k}_b x + \hat{A}_3 e^{\hat{k}_b(x-L)} + \hat{A}_4 e^{-\hat{k}_b x} \tag{2}$$

where $\hat{k}_b$ is the wavenumber. When the free-free beam was excited at a free end as shown in Figure 2, the response of transfer function is compared to the measured values:

$$\Lambda e^{i\phi} = \frac{\hat{w}(x_1)}{\hat{w}_0} = \frac{\hat{A}_1 \sin \hat{k}_b x_1 + \hat{A}_2 \cos \hat{k}_b x_1 + \hat{A}_3 e^{\hat{k}_b(x_1-L)} + \hat{A}_4 e^{-\hat{k}_b x_1}}{1 + \hat{A}_3 e^{-\hat{k}_b L} + \hat{A}_4} \tag{3}$$

where Λ is the amplitude and ϕ is the phase of the measured transfer function between displacements. Then, the Newton-Rapson method is applied to solve Eq. (3) with respect to the complex wavenumber, $\hat{k}_b = k_{br} - ik_{bi}$. Consequently, the complex bending stiffness of the beam structure is obtained, $\hat{D} = \omega^2 M / \hat{k}_b^4$.

3. Results and Discussion

3.1. *Quasi-static compression*

Figure 3 shows the compressive static stress-strain curve of Al-Si-Ca foam having thickness of 40 mm. From the stress-strain curve, it is found that the linear elasticity only appears at a very low compressive strain (about -0.03 <) where partially reversible cell wall bending occurs, followed by a plastic plateau stress at which successive bands of cells collapse, buckle and yield, and finally densification region takes place at a strain level of approximately -0.45 where the stress rises sharply as compaction commences. The plateau stress, which is defined as the mean value of flow stress during strain $\varepsilon = -0.05 \sim -0.20$ in the curve was about 2.1 MPa.
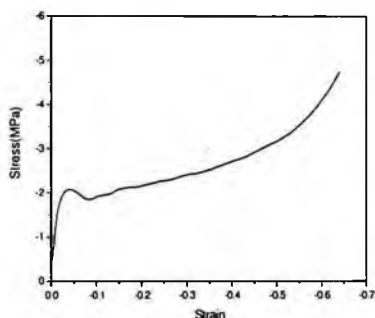
Fig. 3. The quasi-static compression stress-strain curves.
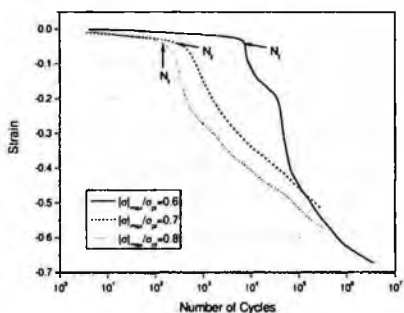
Fig. 4. The strain versus number of cycles curve.

3.2. *Fatigue compression*

The strain versus number of cycle curves of Al-Si-Ca foams in case of load ratio, R= 0.1 are shown in Figure 4. Three different endurance ratios ($|\sigma_{max}| / \sigma_{pl} \approx 0.6$, 0.7 and 0.8) were utilized.

All the curves show that the compressive strain increases with the number of cycle which means that progressive shortening of the specimen takes place with increasing number of cycle. However, an incubation period is evident for all values of endurance ratio, at the end of which the rate of shortening is accelerated abruptly. The progressive shortening of specimen in compressive-compressive fatigue is associated with cyclic fatigue failure and ratcheting in the damaged foam which degrades the dynamic material performance. This sudden rise of progressive shortening takes place at a strain level of approximately -0.05 which is equal to the static yield strain of the foam.

3.3. *Dynamic properties of foam damaged by fatigue*

Impact hammer tests (see Figure 2) were performed to measure dynamic characteristics of damaged Al-alloy foams. Figure 5 shows the measured transfer functions for different levels of induced quasi-static and fatigue compression strains (0, 0.05, 0.10 and 0.15). The resonance frequencies are larger than 2 kHz. The resonance frequencies decrease with increasing level of fatigue damage. Using the measured transfer function, the complex bending stiffness is obtained as Figure 6. As result, the dynamic moduli decrease significantly from increasing fatigue damage for entire frequency ranges of measurements. The measured dynamic stiffness decreases with increasing frequency more rapidly for damaged specimens. This decrease of moduli is more pronounce in fatigue compression than in quasi-static compression. For linear vibration of the material without shear deformation, the dynamic stiffness should monotonically increase with increasing frequency. This suggests that the non-linear vibration behavior become more significant with the increasing fatigue strain.
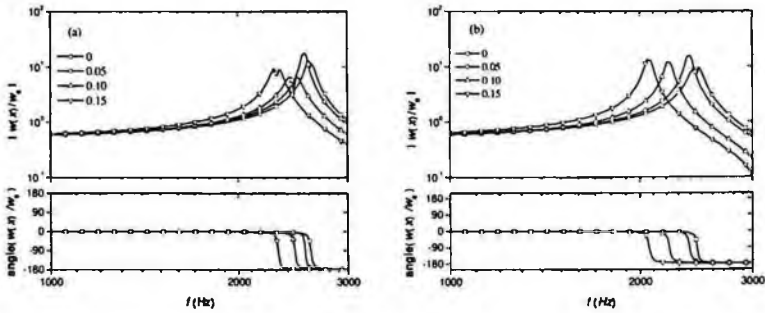
Fig. 5. Measured transfer functions from impact hammer tests. (a) Quasi-static compression and (b) Fatigue compression.
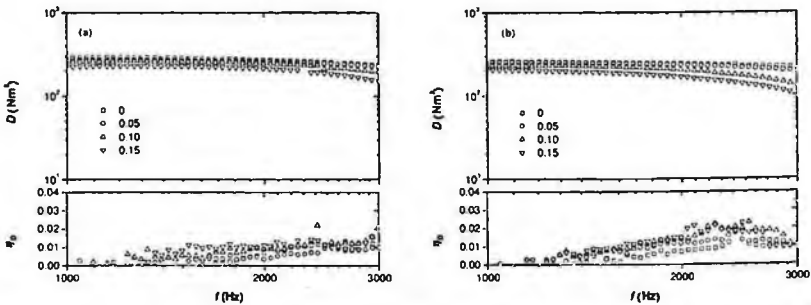
Fig. 6. The bending stiffness of the foam measured from the transfer function methods. (a) Quasi-static compression and (b) Fatigue compression.

The frequency dependent variation of the loss factor is also shown in Figure 6. The loss factor is close to 0.01 when undamaged. The loss factor is increased by more than twice with increasing level of fatigue damage. It depends on the method of compression. The measured loss factors are larger for the dynamically compressed specimen compared to those of the quasi-statically compressed one in the frequency ranges of data acquisition. This suggests better vibration absorption capability for dynamically fatigued foams.

4. Conclusions

1. This sudden rise (transition) of the rate of progressive shortening took place at a strain level of approximately -0.05 which was equal to the static yield strain of the foam.
2. The dynamic moduli were decreased significantly by increasing fatigue damage for entire frequency ranges of measurements. The measured dynamic stiffness decreased with increasing frequency more rapidly for damaged specimens. This decrease of moduli was more pronounce in fatigue compression than in quasi-static compression.
3. The loss factor was close to 0.01 when undamaged. The loss factor increased by more than twice with increasing level of fatigue damage. And it depended on the method of compression.

Acknowledgments

References

1. M.F. Ashby, A.G. Evans, L.J. Gibson, J.W. Hutchinson, N.A. Fleck, H.G.N. Wadley, *Cellular Metals: A Design Guide, Butterworth Heinemann.* 92 (1998)
2. M.C. Gui, D.B. Wang, J.J. Wu, Yuan and C.G. Li, *Mat. Sci. and Engg.* **286**, 282 (2000).
3. I.S. Golovin and H.R. Sinning, *J. of All. and Comp.* **355**, 2 (2003).
4. W. Lins, G. Kainl, H. Peterlik, K. Kromp, *Rev. of Sci. Instr.* **70**, 3052 (1999).
5. R.B. Thompson, G.A. Alers, D.O. Thompson, M.A. Tennison, *J. of Acoust. Soci. of Amer.* **57**, 1119 (1975).
6. J. Park, *J. of Sou. and Vibr.* **288**, 57 (2005).

GLUCOSE CONCENTRATION MONITORING USING A SURFACE PLASMON POLARITON[*]

ARSEN BABAJANYAN, JONGCHUL KIM, KIEJIN LEE

Department of Physics and Interdisciplinary Program of Integrated Biotechnology, Sogang University, Seoul 121-742, Korea

ROBERT KHACHATRYAN, KHACHATUR NERKARARYAN

Department of Radiophysics, Yerevan State University, Yerevan 375049, Armenia

We measured the glucose concentration using an excitation of surface plasmon polariton (SPP) with a gold coated end of optical fiber. The glucose concentration was proportional to the signal intensity of SPP. We could observe the concentration of glucose up to 500 mg/ml with a interval 50 mg/ml. Depending on the glucose concentration in aqueous solution, the activated resonance due to the SPP could be observed and it intensity was changed by the changes of permittivity of the glucose solution. The measured signal-to-noise was about 48 dB and the minimum detectible signal was about 0.002 $(mg/ml)^{-1}$.

1. Introduction

The detection and quantification of glucose with high sensitivity, selectivity and accuracy is required in many different areas. Accurate and rapid measurement of glucose concentration is very important in biological analysis, clinical monitoring and in the food processing industry [1,2]. Accurate measurements of dielectric properties of glucose in aqueous solutions are essential for both fundamental studies and biomedical application. Glucose biosensors have taken several forms, based on electrochemical, optical, piezoelectrical, thermal and mechanical principles [3-5]. Surface plasmon polariton (SPP) glucose biosensors are optical sensors exploiting electromagnetic waves of a SPP by probing the interactions with the glucose solution on the sensor surface [6,7]. We take advantage of real-time analytical evaluation capabilities using SPP biosensors. Experimental excitation of the plasmon polariton has allowed construction of glucose biosensors.

In this paper, we monitor the glucose concentration using a SPP excitation technique [8-11]. The changes of glucose concentration due to a change of permittivity of the glucose solution are investigated by measuring the SPP intensity at the end of a gold coated fiber tip. The change of the glucose concentration is directly related to the change of the intensity of SPP due to a near-field electromagnetic interaction between the fiber tip and the glucose solution.

2. Theory

In this section the energy transfer from an optical fiber mode (OFM) to the SPP mode is discussed. We consider the case when the radius of the fiber exceeds the light wavelength and the process of the wave propagation can be described by geometric optics. Figure 1 (A) shows the track of an optical ray in a longitudinal section covered by the metal layer of the conical tip apex. The incident wave propagates across the waveguide axis. If the opening angle of the cone is 2α then each of the incident angles ϑ_m are

$$\vartheta_m = \frac{\pi}{2} - (2m-1)\alpha; \quad m = 1,2,3,..., \tag{1}$$

where $m = 1$ corresponds to the first reflection, $m = 2$ corresponds to the second reflection, etc. The planar SPP excitation by means of the Krichman configuration [13-15] is similar to the above situation. When the bending radius is much greater then the wavelength, the wave vector of the SPP can be determined by the formula for the planar SPP [14,15]:

$$k_{SPP} = \frac{2\pi}{\lambda} \sqrt{\frac{\varepsilon_g \varepsilon_s}{\varepsilon_g + \varepsilon_s}}, \tag{2}$$

where k_{SPP} ($k_{SPP} = 14\ \mu\mathrm{m}^{-1}$) is the wave number of the SPP, λ ($\lambda = 0.633\ \mu\mathrm{m}$) is the wavelength, ε_g ($\varepsilon_g = -12$ [7,16]) and ε_s ($1.77 < \varepsilon_s < 2$ [17]) are the permittivity of the gold layer and the surrounding dielectric media (glucose aqueous solution), respectively. Then the incident angle for the excitation of the SPP is given by

$$\sin \vartheta_{SPP} = \frac{\lambda}{2\pi} \frac{k_{SPP}}{\sqrt{\varepsilon_q}} = \sqrt{\frac{1/\varepsilon_q}{1/\varepsilon_s + 1/\varepsilon_g}}, \tag{3}$$

where ε_q is the dielectric permittivity of the fiber core (fused quartz: $\varepsilon_q = 2.25$). SPP will be excited when $\vartheta_{SPP} = \vartheta_m$ for some m is satisfied and can be realized only under certain values of opening angle of the cone 2α and dielectric permittivity of the surrounding media ε_s. To obtain resonant excitation of SPP on

a metal surface, a thin layer of transparent dielectric is typically added [9]. In our case, excitation is realized through variation in the glucose concentration. For glucose solution, dependence of permittivity on glucose concentration is approximately linear and is often expressed as the molar increment γ [18]. The permittivity of glucose solution is complex with $\varepsilon_s = (\varepsilon_w' + c\gamma') - j(\varepsilon_w'' + c\gamma'')$, where ε_w is the permittivity of water ($\varepsilon_w' = 1.773$ and $\varepsilon_w'' = 0.00136$ for $\lambda = 0.633$ μm at 25 °C [17]), c is the concentration of the glucose solution and γ is the increase in permittivity when the glucose concentration is raised by 1 unit ($\gamma' = 0.0004$ (mg/ml)$^{-1}$ and $\gamma'' = 0.00001$ (mg/ml)$^{-1}$). Combining Eq. (1) and (3) one obtains the following condition for SPP excitation

$$\cos\{(2m-1)\alpha\} = \sqrt{\frac{1/\varepsilon_q}{1/(\varepsilon_w' + c\gamma') + 1/\varepsilon_g}}; \quad m = 1,2,3,\ldots \qquad (4)$$

For any m SPP can be excited for only one value of the glucose concentration c.

3. Experiment

Figure 1 (B) shows the experimental setup. Radiation from a HeNe laser, with 0.633 μm wavelength and 25 mW power, enters into the optical fiber with inner diameter of 150 μm. The other end of the fiber is a cone with an opening angle $2\alpha = 20°$ and is coated by a gold thin film layer with thickness of 80 nm. Preparation of tip is done by a chemical etching method. During the experiments the temperature is kept at 25 °C ± 0.2 °C.

We could observe two different resonant excitation of SPP on the gold-coated conical apex of the optical fiber. For this purpose we used two processes of transfer wave energy from the OFM mode to the SPP mode [9-11]. Meniscus angle and concentration of the glucose dielectric layer played the important role of the varying parameters. These situations could be realized when the probe tip was located in glucose solution and when the probe tip surface was covered with the meniscus of the glucose solution due to liquid surface tension. For the position of the tip induced changes of the meniscus angle of the glucose solution varies the resonant intensity of the SPP. For the optical fiber placed totally in the glucose solution, resonant excitation of SPP can be obtained by the continuously changing of the glucose concentration.
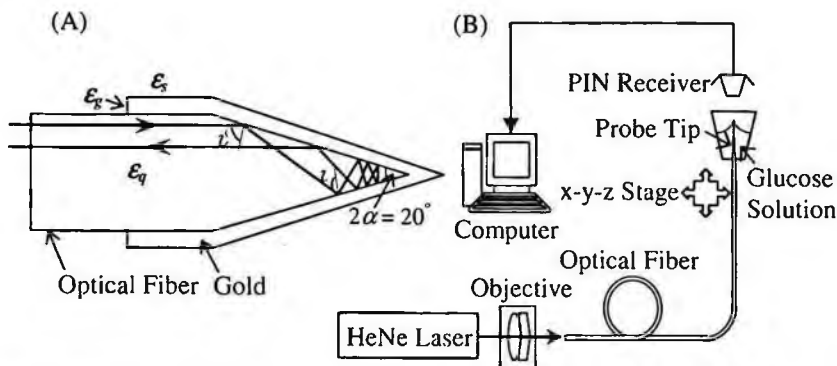
Fig. 1. (A) Trajectory of laser beam transmitting through optical fiber with the gold coated conical end apex. (B) Experimental setup for excitation of SPP in fluid.

4. Results and Discussion

Figure 2 shows the glucose concentration dependence on the SPP intensity for high concentration regime from DI water to 500 mg/ml with concentration increase of 50 mg/ml. As the glucose concentration increased, SPP intensity increased due to the increase the permittivity of glucose solution.

The inset of Fig. 2 shows a time diagram of output intensity for the 100 mg/ml glucose concentration measured by the method of meniscus angle variation. Output intensity level (b) in glucose solution and (c) in air is 0.228 and 0.209, respectively. When the probe tip surface was covered with a glucose thin layer due to surface tension, (a) resonant SPP was enhanced as with level of about 0.246. Resonant SPP was excited only when the meniscus angle of glucose solution satisfied the condition of Eq. (4).

Figure 3 shows the SPP intensity dependence on glucose concentration for high concentration from DI to 500 mg/ml with 50 mg/ml steps. The inset of Fig. 3 shows a time diagram of SPP intensity for the glucose concentration of (a) DI, (b) 100, (c) 200, (d) 300, (e) 400 and (f) 500 mg/ml measured by a using the concentration changing method. The time scale has a conditional sequence and it just demonstrates the real-time measurements for ordered concentration from DI water to 500 mg/ml. The SPP intensity changes as the glucose concentration changed due to the changed of glucose dielectric permittivity. The background level was measured in air. The SPP intensities increase monotony as the glucose concentration increased except for 500 mg/ml glucose concentration. The intensity of plasmon resonance for DI water is up to 12 times smaller than that of 500 mg/ml. This is due to the maximum resonant SSP induced when the maximum matched to condition for Eq. (4) at high glucose concentration.
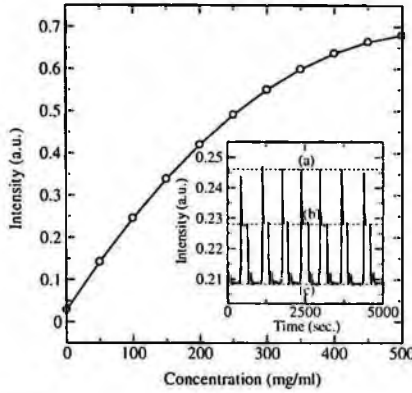
Fig. 2. The dependence of SPP intensity on glucose concentration for excitation of SPP in the high concentration regime; up to 500 mg/ml with interval 50 mg/ml. The inset shows the time diagram of output intensity for (a) SPP excitation, on the (b) glucose and (c) air interface measured by a using meniscus angle changing method. Glucose concentration is 100 mg/ml and volume was 50 µl.
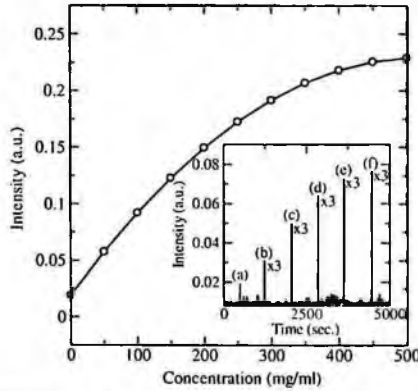
Fig. 3. The dependence of SPP intensity on glucose concentration for the high concentration regime; up to 500 mg/ml with interval 50 mg/ml. The inset shows the time diagram for intensity of resonant SPP for the different concentrations of glucose: (a) DI water, (b) 100, (c) 200, (d) 300, (e) 400 and (f) 500 mg/ml glucose concentration measured by a using glucose concentration continuously changing method. Glucose solution volume was 50 µl.

From the linear relationship as a function of glucose concentration, we observed that the SPP intensity variation dependence on concentrations change of glucose for lower concentration regime was $\Delta I/\Delta c = 0.013$ (mg/ml)$^{-1}$. The root-mean-square (rms) statistical noise for experimental system in the linear scale was about $5 \cdot 10^{-5}$ [19,20]. The measured signal-to-noise (SNR) was about 48 dB in glucose solution. The smallest detectable change in concentration based on a criterion of SNR of 48 dB was about 0.1 mg/ml and the minimum detectible signal was about 0.002 (mg/ml)$^{-1}$.

5. Summary

We demonstrated the measurement of glucose concentration in aqueous solutions using a SPP excitation technique. The SPP intensity was sensitive to the concentration of glucose in solution and it has a linear relation in the low concentration regime. The measured SNR was about 48 dB and the minimum detectible signal was about 0.002 $(mg/ml)^{-1}$. This SPP biosensor has been particularly successful for detection the concentration of glucose in aqueous solutions. Practical development of this system will require significant advances in miniaturization and development of SPP biosensing platforms, with high specificity and long storage life, integration of SPP sensor platforms with microfluidic devices and application- specific sampling systems.

References

1. A. Heller, *Annu. Rev. Biomed. Eng.* **1**, 153 (1999).
2 J. Wang, *Electroanalysis* **13**, 983 (2001).
3. J. McKee and B. Johnson, *IEEE Trans. on Inst. Measur.* **49**, 114 (2000).
4. A. Subramanian, P. Oden, S. Kennel, K. Jacobson, R. Warmack, T. Thundat and M. Doktycz, *Appl. Phys. Lett.* **81**, 385 (2002).
5. S. Zhang, G. Wright and Y. Yang, *Biosens. Bioelectron.* **15**, 273 (2000).
6. J. Homola, *Anal. Bioanal. Chem.* **377**, 528 (2003).
7. J. Holoma, *Surface Plasmon Resonance Based Sensors*, Springer (2006).
8. N. Janunts and Kh. Nerkararyan, *Appl. Phys. Lett.* **79**, 299 (2001).
9. A. Babajanyan, N. Margaryan and Kh. Nerkararyan, *J. Appl. Phys.* **87**, 3785 (2000).
10. N. Janunts, K. Bagdasaryan and Kh. Nerkararyan, *Phys. Lett.* **A 269**, 257 (2000).
11. T. Abrahamyan and Kh. Nerkararyan, *Phys. Lett.* **A 364**, 494 (2007).
12. A. Lalayan, K. Bagdasaryan, P. Petrosyan and Kh. Nerkararyan, *J. Appl. Phys.* **91**, 2965 (2002).
13. S. Kawata, M. Ohtsu and M. Irie, *Nano-Optics, Springer*, Berlin (2002).
14. V. Agranovich and D. Mills, *Surface Polaritons*, North-Holland (1982).
15. H. Raeter, *Surface Plasmons on Smooth and Rough Surfaces and on Grating*, Springer (1988).
16. S. Kawata, *Near-Field Optics and Surface Plasmon Polaritons*, Springer (2001).
17. D. Lide, *Handbook of Chemistry and Physics*, CRC Press (2004).
18. W. Arnold, *IEEE Trans. on Iind. Appl.* **37**, 1468 (2001).
19. A. Babajanyan, J. Kim, S. Kim, K. Lee and B. Friedman, *Appl. Phys. Lett.* **89**, 183504 (2006).
20. B. Friedman, M. Gaspar, S. Kalachikov, K. Lee, R. Levisky, G. Shen and H. Yoo, *J. Am. Chem. Soc.* **127**, 9666 (2005).

STIFFNESS AND ENERGY LOSS CHARACTERISTICS DURING SATURATING-DRYING PROCESS IN LOW POROSITY ROCK

TAE-MIN OH

Dept. of Civil and Environ. Eng., Korea Advanced Institute of Science and Technology (KAIST) 373-1 Guseong-dong, Yuseong-gu, Daejeon 305-701, Republic of Korea

MINSU CHA

Dept. of Civil and Environ. Eng., Korea Advanced Institute of Science and Technology (KAIST) 373-1 Guseong-dong, Yuseong-gu, Daejeon 305-701, Republic of Korea

GYE-CHUN CHO

Dept. of Civil and Environ. Eng., Korea Advanced Institute of Science and Technology (KAIST) 373-1 Guseong-dong, Yuseong-gu, Daejeon 305-701, Republic of Korea

EUN-SOO HONG

Geotechnical Engineering Div., Korea institute of Geoscience & Mineral Resources (KIGAM), Gajeong-dong, Yuseong-gu, Daejeon 305-350, Republic of Korea

The degree of saturation affects the wave velocity and attenuation characteristics, which are important factors in the evaluation of the seismic properties of rocks. This study explores the effect of the degree of saturation on the dynamic properties (stiffness and energy loss) of low porosity rocks. The dynamic properties of granite and mudstone specimens are measured during the saturating–drying process using the free-free resonant column test and the point-source travel time method. Experimental test results show that acoustic wave velocities are nearly constant, while attenuation increases with the degree of saturation. Although, in high porosity rocks, the attenuation is pore water distribution dependant, the results of the saturating and drying processes show that low porosity rocks (less then 3%) are not influenced by the distribution of pore water. P-wave velocity and damping ratio are theoretically predicted using Biot theory and are compared to experimental data. The measured velocities are in good agreement with predicted velocities while the values of attenuation between the measured and predicted data have a large discrepancy; however, the damping ratio tendencies of both are similar.

1. Introduction

Stiffness resulting from the acoustic wave velocity and attenuation have found increased interest as parameters that can help with the seismic design. However, engineers have not considered to a great extent the effect of water in low porosity rocks in the evaluation of the proper attenuation and stiffness in laboratory tests, as it is generally believed that fluid little affects to the properties

in low porosity, despite the fact that the presence of water can influence attenuation and stiffness. Several previous researchers have investigated the fluid effect on attenuation and stiffness, mainly focusing on high porosity rocks (mostly greater than 20% of porosity) such as limestone [1] and sandstone [2-5]. In particular, it has been noticed that attenuation is severely influenced by the degree of saturation, as fluid saturation increases attenuation [2, 6], and by the spatial distribution of water with a constant water content in high porosity rocks [1]. However, reliable data regarding the seismic properties of rocks, which can be only obtained from well-controlled laboratory conditions, remain limited to validate published theoretical models or derive a new model. This study places emphasis on the seismic behavior of low porosity rocks, focusing on the wave velocity and attenuation, during the saturating and drying processes.

2. Experimental Method

2.1. Specimen Preparation

Four granite and mudstone specimens (5 cm in diameter and 10 cm in length) with different weathered conditions and properties (e.g., appearance, density, and Young's modulus) are prepared for the experimental study. The properties of each specimen are summarized in Table 1.

Table 1. Properties of specimens used.

	Porosity (%)	Damping ratio		Density (kg/m³)		Young's modulus (GPa)
		Dry	Saturation	Dry	Saturation	
Granite 1 (GN1)	1.16	0.024	0.105	2591	2603	9.4
Granite 2 (GN2)	1.26	0.028	0.158	2596	2609	3.3
Mudstone 1 (MS1)	0.96	0.003	0.00726	2628	2637	62.9
Mudstone 2 (MS2)	2.61	0.005	0.023	2626	2652	45

2.2. Acoustic Measurements

Free-free resonant column (FFRC) tests are performed to obtain the Young's modulus from the longitudinal wave and damping ratio of the rock specimens. The rock specimen is suspended using two thin strings such that the boundary conditions are free at both ends. The FFRC test setup consists of a point source, an accelerometer, a signal conditioner, and an oscilloscope. The basic process involves applying an impact at one end of the specimen and monitoring the response at the other end. The time series signals stored in the oscilloscope are transformed into the frequency domain in order to obtain the resonant frequency

of the specimen in the first mode. The damping ratio can be obtained by fitting the response curve of the Single Degree of Freedom system to measured data (Fig. 1). Additionally, the P-wave velocities are obtained via the point-source travel time method in which an impact source is employed and the transit time of the propagated wave is obtained. Here, the P-wave velocity is calculated from the propagated length divided by the transit time.
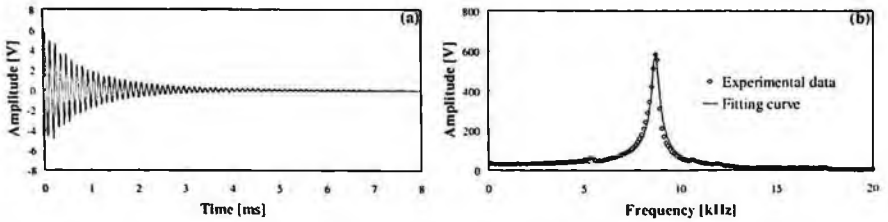
Fig. 1. A typical signal example in FFRC test (a) Time domain (b) Frequency domain.

2.3. Saturating – Drying Procedure

The rock specimens are perfectly dried at a constant temperature of 50 °C for 72 hours in order to prevent any damage induced by thermal shock, although the standard drying temperature is 110 °C (recommended by ASTM D-2216-05). The effective porosity of each rock specimen is calculated by the ratio of pore volume to the bulk sample volume. After drying the rock specimens, a saturating process is performed by immersing the specimens in water with periodic agitation so as to remove trapped air. The saturation levels are then evaluated by measuring the mass via a scale with 0.1 g accuracy. The signals are captured regularly until the measured masses and damping ratio values converge to a certain value. A drying process is also performed in the same manner.

3. Experimental Results

3.1. Stiffness Change during the Saturating and Drying Processes

The wave velocity is governed considerably by the conditions of the particles and pores. However, it has been shown that water in the effective pores does not play a significant role in the determination of the acoustic wave velocities in rocks, as compressional waves mostly propagate through a solid structure. Therefore, it is concluded that the stiffness levels of low porosity rocks are scarcely affected by the degree of saturation and distribution of water (Fig. 2).
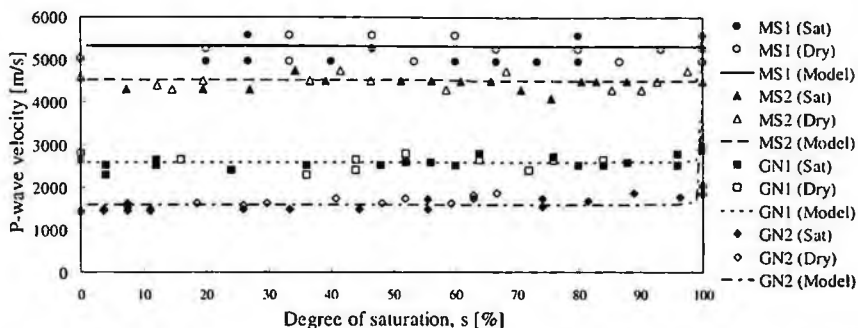
Fig. 2. Comparison of P-wave velocity between experimental and theoretical results. Denotations: Sat: saturating process, Dry: drying process, Model: predicted by the Biot model [7].

3.2. Attenuation Change during the Saturating and Drying Processes

In general, the energy loss increases during the saturating process and decreases during the drying process. This study shows that the damping ratios in the fully saturated condition are much larger than in a dry condition (e.g., nearly 4~5 times higher for granite and 2~4 times greater for mudstone). In addition, a hysterical loop of the saturating/drying processes can be expected in high porosity rocks [1] due to their different pore water distributions. Figure 3 shows that no hysteresis exists during the saturating and drying processes. It is noted that low porosity rocks are only slightly influenced by the distribution effect.
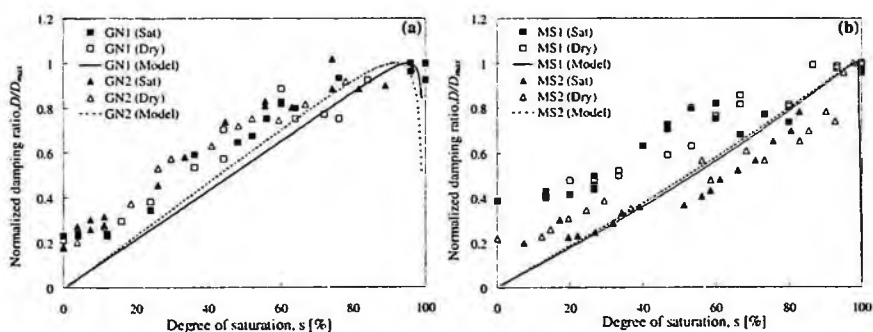
Fig. 3. Comparison of the attenuation between the experimental and theoretical results in (a) Granite and (b) Mudstone (Note: the damping ratios (D) are normalized by the maximum damping ratio (D_{max}).).

4. Discussion - Implications

4.1. Effect of Pore Water - Comparison with the Biot Model

The Biot's theory [7] is known to be applicable for porous media with low attenuation characteristics and without internal microcracks [4]. In this study, Biot's theory is selected to interpret the experimental data because the specimens here have very low porosities, and because this theory provides reliable information concerning the overall seismic behavior. Additionally, it is easier to control the parameters with experimentally verified properties.

In the comparison of the P-wave velocity between the experimental and theoretical results, the wave velocity obtained for each specimen in the laboratory test has a similar value to the fast P-wave velocity using Biot model (Fig. 2).

The normalized damping ratio (D/D_{max}) measured in the experiments and predicted by the Biot model show similar tendencies (Fig. 3). However, it is found that the model regularly underestimates the level of attenuation, as Biot's model idealizes the porous media with no microcracks despite the fact that natural rocks typically contain internal microcracks, which has a significant effect on the attenuation characteristics. In addition, the model shows a sudden drop in attenuation in the fully saturated condition due to the absence of friction by the fluid flow [7] while the experimental results do not. Thus, it is found that the atmospheric environment is unable to provide perfectly saturated conditions due to the surface tension force in the pores.

4.2. Comparison with prior-published data

Figure 4 shows prior-published experimental data (longitudinal excitation) gathered from a literature review along with the data from this study [1, 2, 4, 5]. The trend of the attenuation versus the volumetric water content varies clearly with the rock type. In low porosity rocks, the variation of the attenuation with saturation has more sensitive and linear characteristics compared to the finding for high porosity rocks. In addition, although Massilon sandstone has similar porosity (22%) to Berea sandstone, the energy loss tendencies of these rocks are wholly different. It reflects that there are more critical factors than porosity (e.g. microcracks).

5. Conclusions

In this study, the attenuation and stiffness characteristics with the degree of saturation are explored through non-destructive tests involving low porosity rocks (less than 3%). Although, large changes of stiffness according to the

degree of saturation are not found and the pore water-distribution effect is nil, it is verified that the level of the energy loss increase with the degree of saturation (nearly 4~5 times higher for granite and 2~4 times greater for mudstone). Increasing damping ratios with degree of saturation are also shown in the Biot model. In addition, the damping ratios of low porosity rocks are more sensitive than high porosity rocks (more than 20%) with the volumetric water contents. For these reasons, in low porosity rocks, the degree of saturation should not be ignored to obtain the precise level of energy loss.
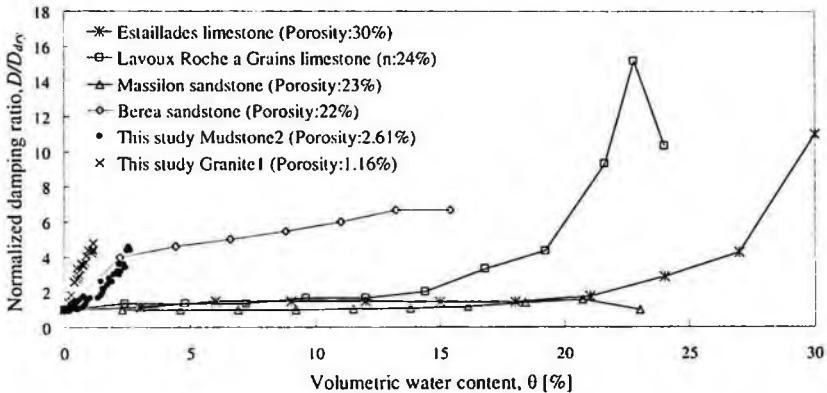
Fig. 4. Normalized damping ratio (D/D_{dry}) in various rocks with the volumetric water content.

Acknowledgments

References

1. T. Cadoret, G. Mavko, and B. Zinszner, *Geophysics*, **63**, No. 1 (1998).
2. G. H. F. Gardner, M. R. J. Wyllie, and D. M. Dorschak, *J. Petr. Tech.*, **16**, 189 (1964).
3. M. N. Toksöz, D. H. Johnston, and A. Timur, *Geophysics*, **44**, No. 4 (1979).
4. K. W. Winkler and A. Nur, *Geophysics*, **46**, Number 1 (1982).
5. W. F. Murphy, III, *J. Acoust. Soc. Am.*, **71**, No. 6 (1982).
6. G. M. Mavko and A. Nur, *Geophysics*, **44**, NO. 2 (1976).
7. M. A. Biot, *J. Acoust. Soc. Am.*, **28**, No.2, 168 (1956).

NUMERICAL AND EXPERIMENTAL STUDIES ON COOLING PATTERNS OF AL-MG SYSTEM ALLOY MATERIAL DURING THE CASTING PRODUCT PROCESS

YOOL-KWON OH

Department of Mechatronics Engineering, Chosun University, 375 Seosuk-dong, Dong-gu, Gwangju, 501-759, South Korea

HEE-SUNG YOON

Department of Advanced Parts and Materials Engineering, Chosun University, 375 Seosuk-dong, Dong-gu, Gwangju, 501-759, South Korea

HO-DONG YANG

Department of Precision Mechanical Engineering, Chosun University, 375 Seosuk-dong, Dong-gu, Gwangju, 501-759, South Korea (corresponding author)

This paper investigates on cooling pattern inside the casting product by numerical and experimental method during solidification process, and verifies the propriety of numerical results. In this study, the metal casting device used to manufacture tire mold product at manufacturing field analyzed by analysis model. Numerical analysis applying a finite element method (FEM) is performed using the COMSOL Multiphysics 3.3™ and analysis model is designed to 3D model. In experimental study, temperature variations inside the casting mold are measured using thermocouples and are obtained by data acquisition unit from the initial injection time to solidification completely. From the results of this study, temperature variations are rapidly dropped from the initial state to 15 minutes and its results are similar tendency when the experimental result is compared with the numerical result.

1. Introduction

It is a modern trend that casting products are made highly functional and precise, and the competitiveness of the final products depends on the design technology for the casting process and the temperature profile of the casting [1]. In the casting process, it is very important for evaluating the metal structure and quality of the end products to know the change of temperature by time [2]. So, many researches for this have been reported in the literature. Analysis on the high temperature fatigue and brittle damage of the casting mould due to thermal stress were investigated by Yoh *et al.* (2003) [1]. Vijayaram *et al.* (2006) investigated

the numerical simulation of casting solidification in permanent metallic molds [3]. Numerical simulation of filling and solidification of permanent mold casting was investigated by Shepel *et al.* (2002) [4]. So, this paper investigates on the cooling pattern inside the casting product by numerical and experimental method during solidification process, and verifies the propriety of numerical results.

2. Numerical and Experimental Methods

In this study, the cooling pattern inside the casting products was investigated using the numerical analysis method and experimental method. The metal casting device used for manufacturing the tire mold products for automobiles in the actual industrial field was analyzed with the analysis model, and Al-Mg system alloy widely used for metal casting was selected as the mold material. Physical property and chemical composition of the Al-Mg system alloy are shown in Table 1 and Table 2, respectively.

Table 1. Physical properties of Al-Mg system alloy.

Properties	Value
Solidification temperature	590 °C
Melting temperature	640 °C
Thermal conductivity	140 W/m·K
Young's modulus	70 Gpa
Poisson's ratio	0.33
Density	2670 Kg/m³
Specific heat	0.88 kJ/kg·K
Thermal expansion coefficient	23.6 × 10-6

Table 2. Chemical composition.

Ingredient	Content[%]
Ni, Pb, Sn	0.05
Zn, Cr	0.15
Si, Ti	0.2
Cu	0.25
Fe	0.3
Mn	0.6
Mg	3.5~5.5
Al	92.5~94.5

2.1. *Numerical Analysis Method*

While the mold product for the automobile tire was manufactured, the numerical analysis was performed based on the finite element method (FEM) in order to predict the cooling pattern of the mold. For the numerical analysis, "COMSOL Multiphysics 3.3™," a commercial program for heat transfer analysis and thermal-structural analysis, was used. Figure 1 (a) shows the 3-dimensional analysis model. The analysis model consisted of the metal casting device, the core and the mold. Figure 1 (b) shows the measurement points of mold.

Numerical analysis condition set the following conditions:

1. The initial temperature condition of each parts was pre-determined as 300 ℃ for the metal casting device, 80 ℃ for the core and 680 ℃ for the mold.

2. The boundary condition was set with the metal casting device; the contact surface between the core and the mold was assumed to be in conduction state; and the inside of the parts other than the contact surface was assumed to be in convection state.

3. It was carried out by calculating the temperature profile, displacement and stress of the mold for 15 minutes from the initial state.

4. It was carried out by calculating the temperature profile, displacement and stress of the mold from 15 minutes after the casting mold separated from the metal casting device to 420 minutes on 9 measurement points.
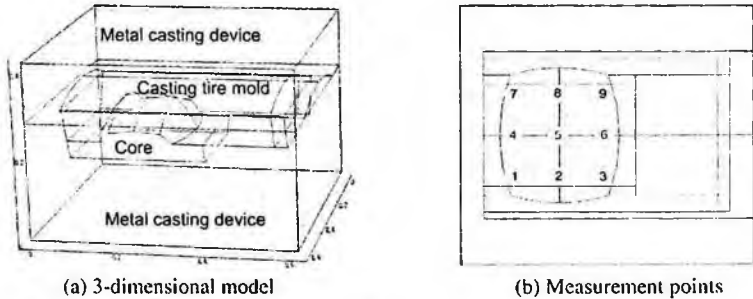
(a) 3-dimensional model (b) Measurement points
Fig. 1. Schematic diagram of analysis model.

2.2. *Experimental Method*

In order to verify the results calculates by the numerical analysis, the experiment was carried out using the metal casting device actually used for manufacturing the mold. As shown in Figure 2, the experimental apparatus consisted of metal casting device, data acquisition unit, K-type thermocouple and PC. In order to measure the temperature profile of the mold during the cooling process, 9 thermocouples were installed on the pre-determined points on the core surface. When the mold material was completely injected into the metal casting device, the temperature of the mold inside the metal casting device was measured.
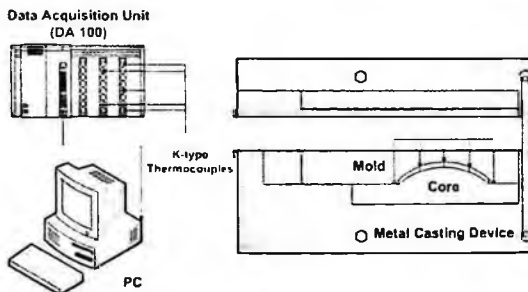
Fig. 2. Schematic diagram of experimental apparatus.

In order to minimize the mold deformation caused by rapid temperature difference at the time when the casting mold material was injected, the metal casting device and the core were pre-heated. The temperature of the mold was measured at an interval of 1 minute from the moment the injection was completed to 15 minutes, and also measured from 15 minutes after the mold separated from the metal casting device to 420 minutes.

3. Results and Discussion

3.1. *Numerical and Experimental Results of Temperature Profile*

Figures 3 (a) and (b) show the temperature profile calculated by the numerical analysis of the mold and the one measured by experiment from the initial state to 15 minutes, respectively. As shown in Figure 3 (a), because the metal casting device was in contact with the mold surface, rapid heat transfer occurred on both side parts of the mold and thus the temperature profile at the middle part (i.e., points 4, 5 and 6) appeared to be higher than that for both side parts.

(a) Numerical analysis method   (b) Experimental method
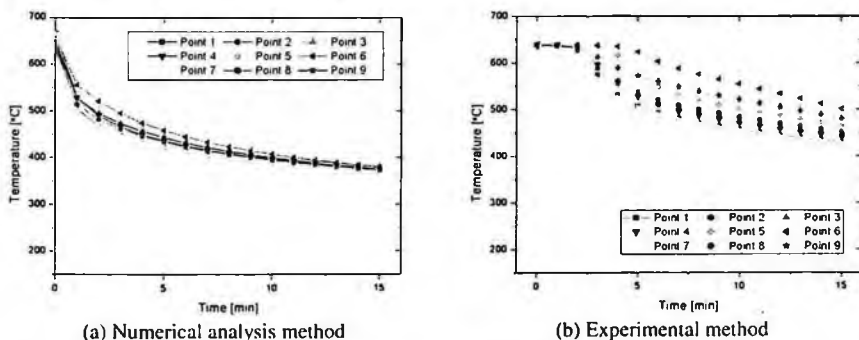
Fig. 3. The temperature profile inside the casting mold for 15 minutes.

(a) Numerical analysis method   (b) Experimental method
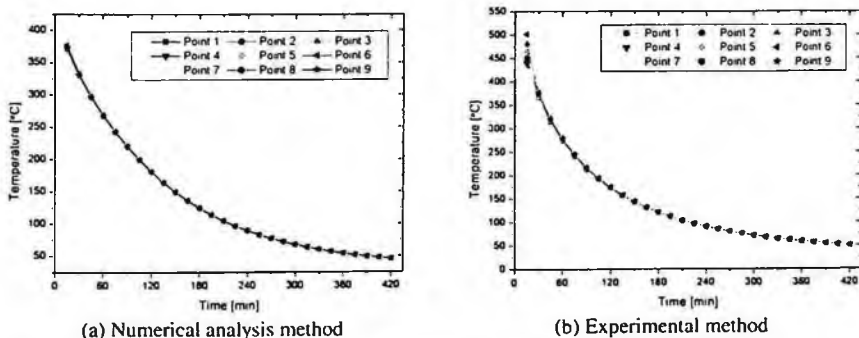
Fig. 4. The temperature profile inside the casting mold from 15 minutes to 420 minutes.

Figures 4 (a) and (b) show the temperature profile calculated by the numerical analysis of the mold and the one measured by experiment from 15 minutes when the mold was taken out from the metal casting device to 420 minutes. The cooling patterns on all measurement points appeared to be similar. When the temperature profile calculated by the numerical analysis and the one actually measured by the experiment were compared with each other, it appeared that there was a slight temperature difference between them because of the latent heat of the Al-Mg system alloy but their cooling patterns were almost similar.

3.2. *Numerical Result of Displacement*

Displacement and stress are generated by the temperature difference to the surface of the mold material. This temperature difference is closely related to the precision and the cooling pattern of the mold. Figures 5 (a) and (b) show the displacement inside the mold for 15 minutes from the initial state and the one until it was completely cooled after 15 minutes when it was separated from the metal casting device. For 15 minutes, the displacement profile of the middle part (i.e., points 4, 5 and 6) appeared to be higher than that for both side parts. From 15 minutes after the casting mold was separated from the metal casting device to it was completely cooled at natural cooling, the displacement profile of points 1, 4 and 7 appeared to be larger than that for other points because points 1, 4 and 7 is the nearest location to contact surface between mold and atmosphere.

(a) For 15 minutes   (b) From 15 minutes to 420 minutes
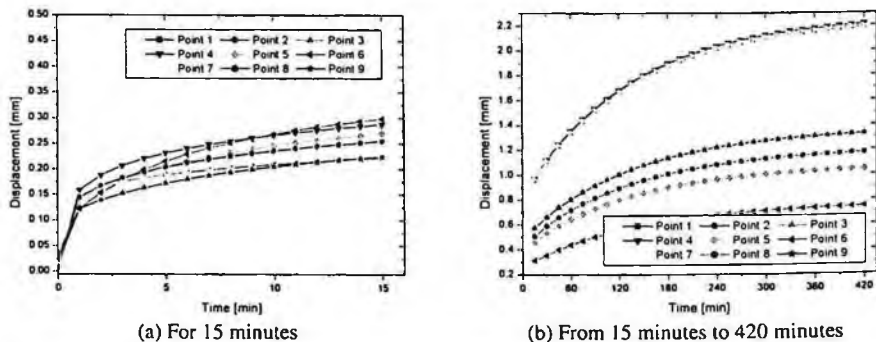
Fig. 5. The displacement profile inside the casting mold by the numerical analysis.

3.3. *Numerical Result of Stress*

Figure 6 (a) shows the stress profile inside the mold for 15 minutes and it appeared to be larger at the center part (points 2, 5 and 8) of mold than on its other parts. The cooling speed at the center part was slower than the one on its other parts because of the flow characteristic of the mold material, and the stress

was larger at the center part because of the shrinkage caused by the cooling speed difference. Figure 6 (b) shows the stress profile calculated until the mold was completely cooled after it was separated from the metal casting device in 15 minutes, which appeared to be larger on points of 2, 5 and 8 than that for other points because of slow cooling speed.

(a) For 15 minutes   (b) From 15 minutes to 420 minutes
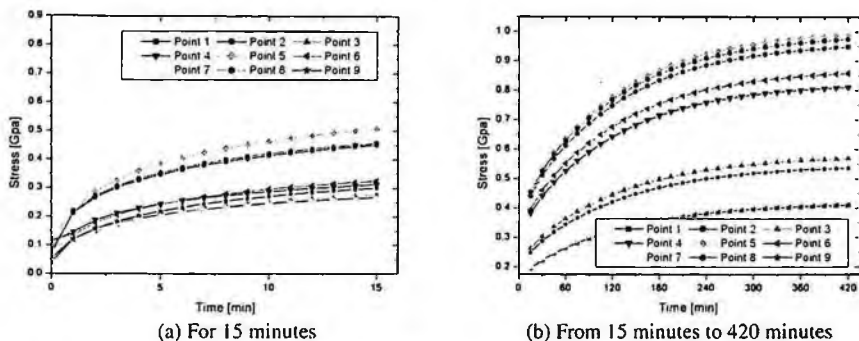
Fig. 6. The stress profile inside the casting mold by the numerical analysis

4. Conclusion

1. When the temperature profile calculated by the numerical analysis and the one actually measured by the experiment were compared with each other, it appeared that there was a slight temperature difference between them because of the latent heat of the Al-Mg system alloy but their cooling patterns were almost similar.

2. The displacement for 15 minutes appeared to be larger at the middle part of the mold than on its both side parts, and the one calculated for the time until it was completely cooled at natural cooling after it was separated from the metal casting device appeared to be larger on points 1, 4 and 7 near to contact surface between mold and air than that for other points.

3. The stress inside the mold appeared to be larger at the center part because of the shrinkage caused by the cooling speed difference for 15 minutes, and larger on the points 2, 5 and 8 when the mold was separated from the metal casting device because of slow cooling speed.

References

1. E.G. Yoh and Y.S. Lee, *Trans. KSAE.* 1563-1568 (2003).
2. Y.T. Lim and Y.H. Chen, *Trans. KSME.* 134-137 (1990).
3. T.R. Vijayaram, S. Sulaiman, A.M.S. Hamouda and M.H.M. Ahmad, *Journal of Materials Processing Technology.* **178**, 29-33 (2006).
4. S.V. Shepel and S. Paolucci, *Applied Thermal Engineering.* **22**, 229-248 (2002).

HOMOGENIZED MATERIAL PROPERTIES AND MECHANICAL BEHAVIOR OF HYBRID FUNCTIONALLY GRADED COMPOSITES[*]

JOO-HYOUNG CHOI, JIN-RAE CHO[†]

School of Mechanical Engineering, Pusan National University
Kumjung-Ku, Busan 609-735, Korea

A unit-cell-based numerical technique for estimating the homogenized material properties of dual-phase functionally graded materials (FGMs) is presented, targeting for the material hybridization for which the detailed inclusion information is prerequisite. A local-wise RVE in FGMs which contains an inclusion with arbitrary shape and angle is modeled as 2-D orthotropic and its homogenized material properties are estimated by making use of the superposition method and the unit cell finite element analysis.

1. Introduction

The extension of material property space which can be spanned by existing materials such as metals, ceramics, glasses, elastomers and polymers has been a great challenging subject in the community of materials science and engineering. One may consider the creation of new materials in order to extend the current material property space, but this approach is extremely impractical in aspects of feasibility, cost and time. A practical approach is the hybridization of existing materials, which can be made by combining two/more existing materials, changing the structural configuration (in macro) and the particle shape (in micro), or by altering the molecular structure [1]. The *hybrid materials* which are in the worldwide spotlight were introduced according to this new material concept.

Functionally graded material (FGM) [2] in which two or more base material particles are mixed up becomes an excellent candidate for the material hybridization, because the target material properties show the significant dependence on the shape, the inclination angle, the dispersion structure and the volume fraction of base particles. According to our brief literature survey [3], material properties of FGMs have been predicted by the volume-fraction-averaged homogenization technique. However, this approach encounters

[†] Corresponding author, *E-mail:* jrcho@pusan.ac.kr.

difficulties in designing hybrid materials because the detailed information about interior constituent particles is not taken into consideration.

In this context, this study intends to introduce a unit-cell-based homogenization technique to predict the material properties of FGMs, by considering the shape and inclination angle of inclusions. The unit cell is assumed to be orthotropic and the corresponding material constants are estimated by making use of the superposition method and the unit cell finite element analysis. The predicted material constants are examined through the thermoelastic analysis of metal-ceramic functionally graded composite beams.

2. Functionally Graded Composite and 2-D Orthotropic Cell

The volume fraction and the dispersion structure as well as the size and shape of inclusion in real FGMs are random, so that a representative volume element (RVE) can not be defined for the entire FGM domain. However, we assume that those are distributed locally in the uniform or periodic pattern such that RVEs can be defined at least in the local sense, as illustrated in Figure 1.
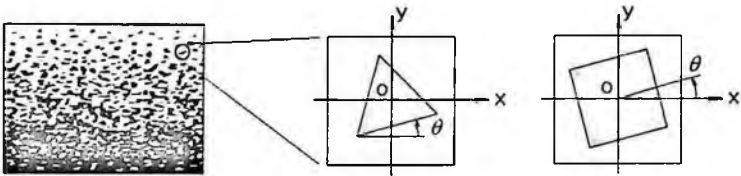
Fig. 1. Modeling of local-wise RVE of dual-phase hybrid FGMs into a unit cell.

When the unit cell is assumed to be 2-D orthotropic, its thermoelastic constitutive relations are expressed in terms of the (3×3) compliance matrix [4], where the subscripts 1 and 2 stand for x and y, respectively. The symmetry of the compliance matrix implies $E_1 v_{21} = E_2 v_{12}$, so that the total number of independent material constants to be determined is five.

$$
\begin{Bmatrix} \varepsilon_1 \\ \varepsilon_2 \\ \gamma_{12} \end{Bmatrix} = \begin{bmatrix} 1/E_1 & -v_{21}/E_2 & 0 \\ -v_{12}/E_1 & 1/E_2 & 0 \\ 0 & 0 & 1/G_{12} \end{bmatrix} \begin{Bmatrix} \sigma_1 \\ \sigma_2 \\ \tau_{12} \end{Bmatrix} + \begin{Bmatrix} \alpha_1 \\ \alpha_2 \\ 0 \end{Bmatrix} \Delta T \tag{1}
$$

3. Unit Superposition Method and Unit Cell Analysis

Referring to Figure 2, an original problem under the unidirectional uniform tension of the unit cell can be decomposed into a linear combination of two sub-problems. In sub-problem 1, two surfaces facing to the x – direction are subject

to uniform displacement $u_x = 1$ but the other two surfaces are clamped. Then, the force resultants F_x^1 and F_y^1 exerted on the surfaces of the unit cell can be computed by the unit cell analysis. In this manner, sub-problem 2 is defined and the corresponding force resultants F_x^2 and F_y^2 are to be computed.
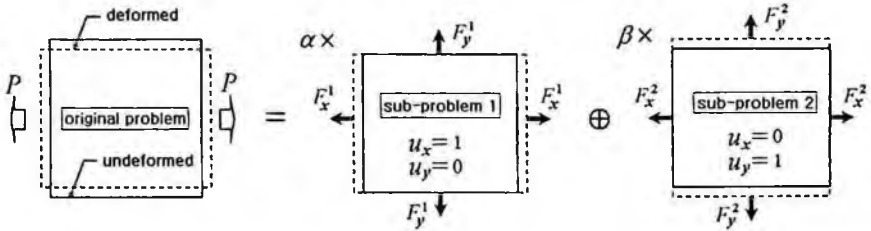
Fig. 2. Schematic representation of the superposition method (original and decomposed systems).

Then, three coefficients α and β which are included in the linear combination of sub-problems can be determined from the static equivalence between the original and the decomposed systems:

$$\begin{bmatrix} F_x^1 & F_x^2 \\ F_y^1 & F_y^2 \end{bmatrix} \begin{Bmatrix} \alpha \\ \beta \end{Bmatrix} = \begin{Bmatrix} P \\ 0 \end{Bmatrix} \tag{2}$$

Two uniform normal strains ε_1 and ε_2 of the original system are calculated by $\varepsilon_1 = \alpha \varepsilon_{xx}^1$, $\varepsilon_2 = \beta \varepsilon_{yy}^2$. And, the effective Poisson's ratio v_{12} of the unit cell can be determined by $v_{12} = -\varepsilon_2 / \varepsilon_1 = -\beta \varepsilon_{yy}^2 / \alpha \varepsilon_{xx}^1$. On the other hand, the work W done by the uniform external load P and the internal strain energy U stored in the original system are as follows: $2W = Pu_x = P(\varepsilon_1 \Delta x)$ and $2U = \int_A \sigma_1 \varepsilon_1 dV = E_1 (\varepsilon_1)^2 \Delta x \Delta y$. Equating U with W leads to the effective Young's modulus E_1 of the unit cell given by $E_1 = P / (\Delta x \Delta y)\varepsilon_1 = P / \alpha (\Delta x \Delta y)\varepsilon_{xx}^1$. In this manner, the other effective Young's modulus E_2 is determined by applying the external load P in the y – direction.

Fig. 3. Unit cell: (a) under the pure shear; (b) under the uniform thermal expansion.

In order to determine the effective shear modulus G_{12}, we apply the pure

shearing force P_s on the top surface of the unit cell, while keeping the bottom surface fixed, as shown in Figure 3(a). Then, the external work done and the internal strain energy are as follows: $2W = P_s \delta_s = P_s \gamma_{xy} \Delta y$ and $2U = \int_A \tau_{12} \gamma_{12} \, dV = G_{12} (\gamma_{12})^2 \Delta x \Delta y$. Equating the work done and the internal strain energy leads to the effective shear modulus G_{12}: $G_{12} = P_s / \gamma_{12} \Delta x$.

While, the calculation of the effective thermal expansion coefficients α_1 and α_2 is straightforward from the elementary heat transfer theory. Referring to Figure 3(b), two effective thermal expansion coefficients are determined with the free expansions δ_x and δ_y such that $\alpha_1 = \delta_x / \Delta x \Delta T$ and $\alpha_2 = \delta_y / \Delta y \Delta T$.

4. Numerical Experiments

Metal-ceramic FGM composites manufactured with Ni and Al_2O_3 are taken for the numerical experiments. Material properties of two base constituents are given in Table 1, and inclusions are Ni with uniform volume fraction V_m of 20%. Inclusion shapes are set by triangle and quadrilateral, then the material periodicity is $\theta = 60^o$ in the former and $\theta = 45^o$ in the latter. The side length of unit cells is set by $1cm$ and each unit cell is uniformly discretized with 100,000 4-node finite elements. Uniform extension of $0.5mm$ is applied to two vertical sides of the unit cell for sub-problem 1 (two horizontal sides for sub-problem 2). On the other hand, δ_x and ΔT are set by $1mm$ and 300°, respectively.

Table 1. Material properties of Ni and Al_2O_3.

Constituents	$E\,(GPa)$	v	$G\,(GPa)$	$\alpha \times 10^{-6}/K$	$\kappa\,(W/m \cdot K)$
Ni	199.5	0.30	76.7	15.4	90.7
Al_2O_3	393.0	0.25	157.2	7.4	30.1

Referring to Figure 4, in the quadrilateral case, the effective Young's modulii decrease with the inclination angle while the effective Poisson's ratios decrease. And this trend is shown to be reverse in the triangle case. The noticeable fact is that the material anisotropy in the quadrilateral case is too small when compared with the triangle case. This feature is also observed in the effective thermal expansion coefficients shown in Figure 5, implying that the material anisotropy becomes smaller as the inclusion becomes polygon. The effective shear modulus increases in proportional to the inclination angle for quadrilateral inclusion, but its variation is negligible for triangle inclusion. On the other hand, in case of the thermal expansion coefficient the dependence on the inclination angle is negligible for quadrilateral inclusion, differing from triangle inclusion which shows the sine wave-like increase with the angle.
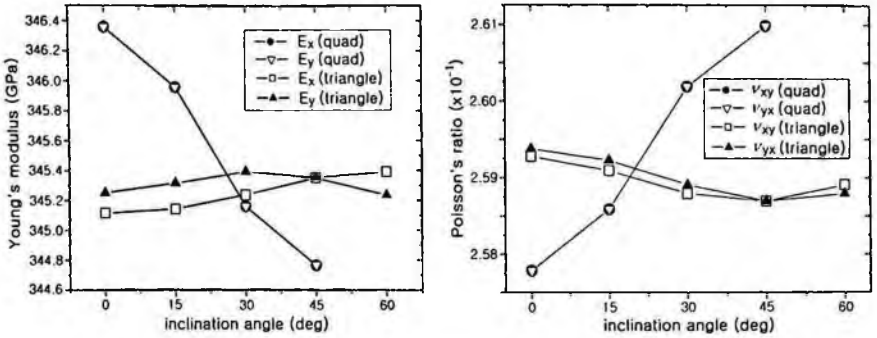
Fig. 4. Variations to the inclusion angle: (a) Young's modulus; (b) Poisson's ratio.
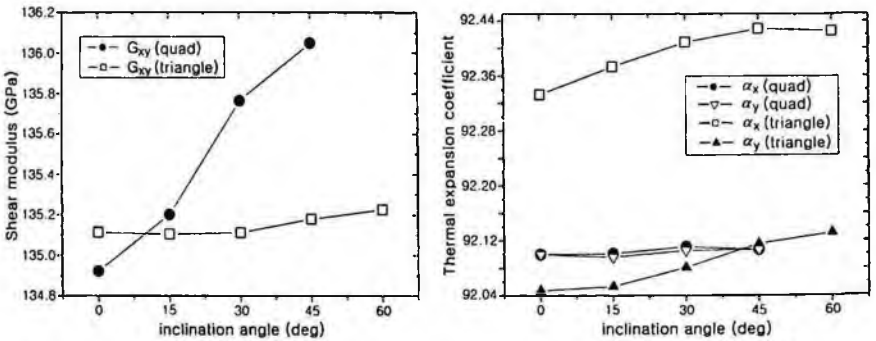
Fig. 5. Variations to the angle: (a) shear modulus; (b) thermal expansion coefficient ($\times 10^{-7} / K$).

Figure 6 shows a Ni-Al_2O_3 composite beam with uniform triangle inclusions ($50 \times 10EA$) subject to a tip load and uniform heating at the top surface, where the metal volume fraction of Ni (inclusions) is set by 20%. The thermoelastic analysis is performed by two different approaches, one by considering the detailed inclusions and the other by assuming the beam as an orthotropic body. For the latter case, the homogenized orthotropic materials which were estimated just above are used, except for the isotropic volume-averaged thermal expansion coefficient κ which is estimated by the Wakashima-Tsukamoto estimate [5]. Regardless of the numerical analysis approach, the entire beam domain is uniformly discretized with 500×100 4-node finite elements.
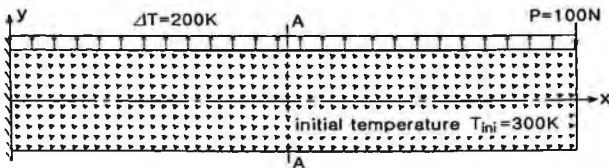
Fig. 6. A FGM composite cantilever beam (length=$50cm$, thickness=$10cm$).

Figure 7 represents the axial and shear stress distributions along the vertical line A-A when the inclination angle is $45°$. Owing to the inherent sharp material discontinuity along the vertical line A-A, the axial and shear stresses obtained by the detailed cell models exhibit the significant fluctuation in their distributions. But, the orthotropic model using the homogenized material properties estimated by the present method leads to the axial and shear stress distributions which are consistent well with those obtained by the detailed models, in the average sense.
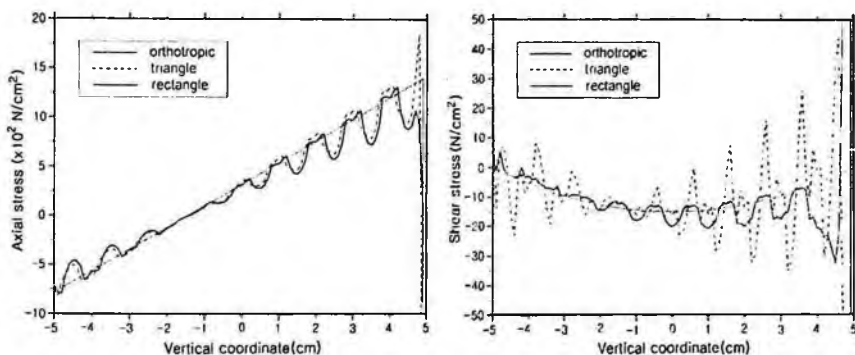
Fig. 7. Verification for the angle $\theta = 45°$: (a) axial stress; (b) transverse shear stress.

5. Summary

A unit-cell-based numerical technique for estimating the homogenized orthotropic material properties of dual-phase functionally graded composites has been introduced. From the unit cell analyses for two different inclusion shapes, the material anisotropy decreases in the mechanical properties but increases in the thermal expansion coefficient, as the inclusion becomes polygon. But, the variation magnitude to the inclination angle of inclusion was shown to be directly opposite to the material anisotropy. The comparison of thermoelastic responses between the orthotropic model and the detailed cell model confirmed that the estimation accuracy of the present method is quite acceptable.

References

[1] M.F. Ashby and Y.J.M. Brechet, *Acta Mater.* **51**, 5801 (2003).

[2] J.R. Cho and J.T. Oden, *Comput. Meth. Appl. Mech. Engrg.* **188**, 17 (2000).

[3] J.R. Cho and D.Y. Ha, *Mater. Sci. Eng.* **A302**, 187 (2001).

[4] I.M. Daniel and O. Ishai, *Engineering Mechanics and Composite Materials*, Oxford University Press, New York, 1994.

[5] K. Wakashima and H. Tsukamoto, *Mater. Sci. Eng.* **146**, 291 (1991).

GLUCOSE BIOSENSING BY USING A MICROWAVE
DIELECTRIC RESONATOR*

JONGCHEL KIM, ARSEN BABAJANYAN , SEUNGWAN KIM
HEEKYUN LEE, JOOYOUNG KIM, KIEJIN LEE

Department of Physics and Interdisciplinary Program of Integrated Biotechnology,

Sogang University, Seoul 121-742, Korea

We report a near-field microwave biosensor based on a dielectric resonator to detect the glucose concentration in biological systems. Near-field microwave biosensors with a high Q dielectric resonator allow observation of the small variation of the permittivity due to the glucose by measuring the shift of the resonance frequency and the microwave reflection coefficient, S_{11}. We observed the concentration of glucose with a detectable resolution up to 1 % at an operating frequency of $f = 1.7$ GHz. The change of the glucose concentration is directly related to the change of the reflection coefficient due to the electromagnetic interaction between the dielectric resonator and the glucose solution. The operation principal is explained by the plane-wave solution model. A glucose biosensor using near-field microwave provides a unique approach for glucose monitoring.

1. Introduction

There is a wide spread need for highly sensitive and stable glucose biosensors in clinical monitoring, biological research and in the food processing industry [1-2]. Aqueous glucose solutions play a fundamental role in many chemical processes in a variety of chemical and biological systems. Sensitive detection of glucose concentration in water may become a useful tool for studying the biological properties of samples. Glucose biosensors have taken several forms, based on electrochemical, optical, piezoelectrical, thermal or mechanical principles [3-6]. Amperometric enzyme electrodes hold a leading position among present glucose biosensor systems and have already found a large commercial market. Recently, a number of mechanically based glucose biosensors based on the cantilever platform have been demonstrated. Commercial development of these devices has allowed measurement of glucose concentration with sufficient accuracy for some applications. However, in order to better characterize the concentration of glucose, we take advantage of the evaluation capabilities using

a microwave dielectric resonator (DR). Near-field microwave sensing techniques with high sensitivity have been developed [7-10]. An important ability of the microwave dielectric resonator biosensor is a new approach to characterize the glucose solutions.

In this paper, we monitored the glucose concentration using a microwave dielectric resonator technique. The glucose biosensor consisted of a $\lambda/4$ dielectric resonator coupled to a microstrip line at an operating frequency of about $f = 1.7$ GHz. The changes of glucose concentration due to a change of permittivity of the glucose solution were investigated by measuring the reflection coefficient S_{11} of the resonator. The change of the glucose concentration is directly related to the change of the reflection coefficient due to an electromagnetic interaction between dielectric resonator and the glucose solution. A glucose biosensor using a dielectric resonator provides a unique approach to monitoring the glucose concentration.

2. Experiment

The glucose biosensor consisted of a dielectric resonator with cylindrical air gap coupled to a microstrip line at an operating frequency $f = 1.684$ GHz as shown on Fig. 1 (A). The dielectric resonator consists of a high temperature ceramic sample with a dielectric permittivity of 88 and dimensions 14 mm $\times$ 5.1 mm $\times$ 6.7 mm. At resonance, the mode we used was TE_{01} and the unloaded Q factor was 4030. A network analyzer (Agilent 8753ES) was used in measuring the reflection coefficient S_{11}. All measurements were done at temperature 25 °C.
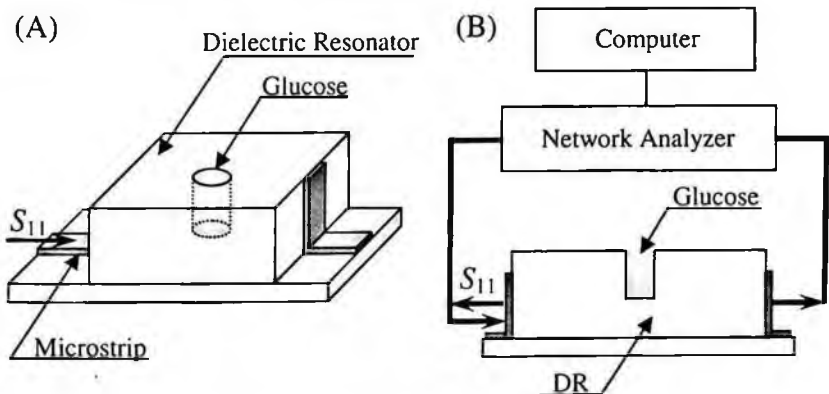
Fig. 1. (A) Dielectric resonator coupled with a microstrip line and (B) experimental setup.

The temperature dependence on reflection coefficient change of our dielectric resonator was $\Delta S_{11}/\Delta t = 0.07$ dB/°C. Glucose solution was dropped directly into the dielectric resonator. The basic experimental setup is shown in Fig. 1 (B). The glucose biosensor consisted of a high Q $\lambda/4$ dielectric resonator coupled to a

microstrip transmission line. A metal strip on the dielectric resonator is used as an electrode that excites TE_{01} mode in the dielectric waveguide. To determine the glucose concentration changes, we measured the reflection coefficient S_{11} of the dielectric resonator at an operating frequency at $f = 1.684$ GHz.

3. Theory

The operation principal could be explained be the plane-wave solution model. An interpretation of the S_{11} magnitude in terms of medium parameters could go as follows [11]:

$$S_{11} = 20\log\left|\frac{Z_{in}^R - Z_0}{Z_{in}^R + Z_0}\right| \tag{1}$$

where Z_0 is the effective impendence of the microstrip line and equal to 50 Ω, Z_{in}^R is the real part of complex input impedance of the dielectric resonator with glucose solution. The dependence of permittivity on solute glucose concentration is approximately linear and is often expressed as the molar increment δ [12]. The permittivity of glucose solution is complex with $\varepsilon_g = \varepsilon' - j\varepsilon''$ and it can be written as

$$\varepsilon_g = \left(\varepsilon_0' + c\delta'\right) - j\left(\varepsilon_0'' + c\delta''\right) \tag{2}$$

where ε_0 is the permittivity of water ($\varepsilon_0' = 77.75$ and $\varepsilon_0'' = 6.4$ for 1.7 GHz at 25 °C [13]), c is the concentration of the glucose solution, $\delta = \delta' - j\delta''$ is the increase in permittivity when the glucose concentration is raised by 1 unit ($\delta' = 0.0577$ (mg/ml)$^{-1}$ and $\delta'' = 0.0015$ (mg/ml)$^{-1}$ at 25 °C [9]). Thus, the real part of complex input impedance is estimated as

$$Z_{in}^R = Z_a\sqrt{\varepsilon_d}\frac{\left(1 + \varepsilon_d k_a^2 t_d^2\right)\left(1 + \left(\varepsilon_0' + c\delta'\right)k_a^2 t_g^2\right)\left(\varepsilon_d + \left(\varepsilon_0' + c\delta'\right)^2 k_a^2 t_g^2\right)}{\varepsilon_d^3 k_a^2 t_d^2\left(1 + \left(\varepsilon_0' + c\delta'\right)k_a^2 t_g^2\right)^2 + \left(\varepsilon_d + \left(\varepsilon_0' + c\delta'\right)^2 k_a^2 t_g^2\right)^2} \tag{3}$$

where Z_a is the impedance of air (377 Ω), k_a is the wave vector of air (36 m^{-1} at 1.7 GHz), t_d is the half width of the DR (1.7 mm), ε_d is the dielectric permittivity

of dielectric resonator (88) and t_g is the diameter of cylindrical gap in dielectric resonator (1.7 mm).

4. Results and Discussion

Figure 2 shows the microwave reflection coefficient S_{11} profile of glucose concentrations ranging from de-ionized (DI) water (i.e. no glucose) to 300 mg/ml glucose concentration with an interval of 50 mg/ml.
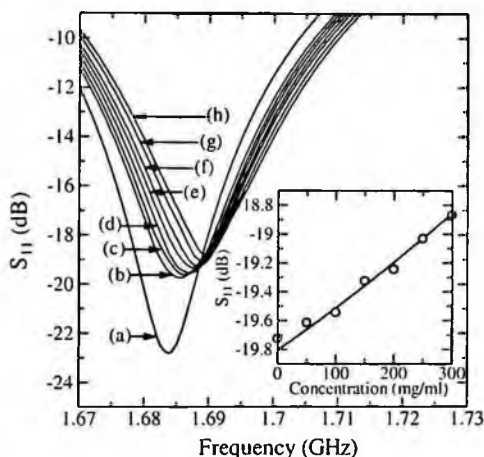
Fig. 2. Measured microwave reflection coefficient S_{11} for (a) air, (b) for DI water and for different glucose concentrations: (c) 50, (d) 100, (e) 150, (f) 200, (g) 250 and (h) 300 mg/ml. The inset shows microwave reflection coefficient S_{11} plotted as a function of the glucose concentration from DI water to 300 mg/ml with the interval of 50 mg/ml at 1.684 GHz. A solid line shows a fit to Eq. (1) with $Z_0=50$ Ω.

As the glucose concentration increased, the dielectric permittivity of the glucose solution increased and the intensity of the reflection coefficient S_{11} increased as shown in the inset of Fig. 2. The permittivity of the glucose solution may be estimated by the intensity of the reflection coefficient at the resonance frequency. We found a good agreement with theory between the variation of reflection coefficient S_{11} and the glucose concentrations. The glucose concentration of the sample may thus be estimated by the intensity of the reflection coefficient S_{11}. From the linear relationship as a function of glucose concentration, as observed at lower glucose concentrations, $\Delta S_{11}/\Delta c=0.0036$ dB/(mg/ml). The root-mean-square (rms) statistical noise in S_{11} is about 10^{-5} dB [8-9]. The measured signal-to-noise (SNR) was about 50 dB. The smallest detectable change in concentration based on a criterion of SNR of 50 dB was about 0.0032 mg/ml.
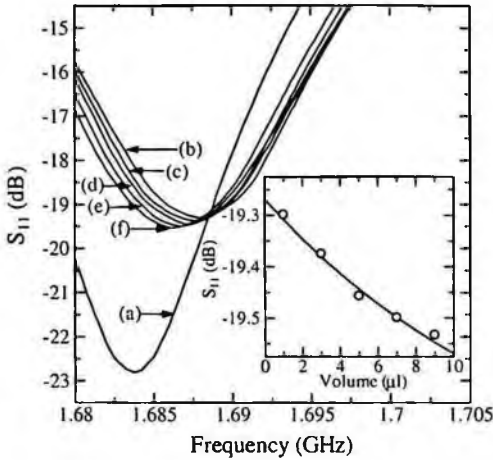
Fig. 3. Measured microwave reflection coefficient S_{11} for (a) air and for different volume of glucose solutions with concentration of 100 mg/ml: (b) 1 μl, (c) 3 μl, (d) 5 μl, (e) 7 μl and (f) 9 μl. The inset shows microwave reflection coefficients S_{11} plotted as a function of volume of the glucose solution at 1.684 GHz. A solid line shows a fit to Eq. (1) with $Z_0 = 50\ \Omega$.

By increasing the Q factor of the resonator, the slope becomes steeper and the sensitivity can be further enhanced.

The reflection coefficient S_{11} of glucose solution depends on the volume of solution. The reflection coefficient decreased as the volume of glucose solution increased as shown on Fig. 3. DR gap volume changed from 1 μl to 9 μl, by interval 2 μl with the constant gap high of 3.3 mm and glucose concentration fixed at 100 mg/ml. Initially as the volume increased, the reflection coefficient decreased. As the volume further increased, the reflection coefficient S_{11} becomes saturated. Note that, according to the approximate theoretical calculation, the reflection coefficient S_{11} also shows a saturation behavior. We found a good agreement with theory between the variation of reflection coefficient and the volume of glucose solutions.

5. Summary

We demonstrated the measurement of glucose concentration using a microwave DR technique. The reflection coefficient change is very sensitive to the concentration of glucose. These results clearly show the sensitivity and usefulness of this DR for glucose biosensing using a noncontact and label-free technique without the added complications of sample treatment. Optimizing system design will allow for effective implementation of this platform for sensitive noncontact and label-free biosensing.

References

1. J. Wang, *Sensors Update* **10**, 107 (2002).
2 A. Heller, *Annu. Rev. Biomed. Eng.* **1**, 153 (1999).
3. S. Zhang, G. Wright and Y. Yang, *Biosens. Bioelectron.* **15**, 273 (2000).
4. J. McKee and B. Johnson, *IEEE Trans. Inst. Measur.* **49**, 114 (2000).
5. A. Subramanian, P. Oden, S. Kennel, K. Jacobson, R. Warmack, T. Thundat and M. Doktycz, *Appl. Phys. Lett.* **81**, 385 (2002).
6. B. Choudhry, R. Shinar and J. Shinar, *J. Appl. Phys.* **96**, 2949 (2004).
7. M. Abu-Teir, M. Golosovsky, D. Davidov, A. Frenkel and H. Goldberg, *Rev. Sci. Instrum.* **72**, 2073 (2001).
8. B. Friedman, M. Gaspar, S. Kalachikov, K. Lee, R. Levicky, G. Shen and H. Yoo, *J. Am. Chem. Soc.* **127**, 9666 (2005).
9. A. Babajanyan, J. Kim, S. Kim, K. Lee and B. Friedman, *Appl. Phys. Lett.* **89**, 183504 (2006).
10. M. Tabib-Azar, J. Katz and S. Le Clair, *IEEE Trans. Inst. Measur.* **48**, 1111 (1999).
11. D. Pozar, *Microwave Engineering*, John Wiley & Sons Inc. (1998).
12. W. Arnold, *IEEE Trans. Ind. Appl.* **37**, 1468 (2001).
13. D. Lide, *Handbook of Chemistry and Physics*, CRC Press (2004).

INFLUENCE OF FINENESS OF LIMESTONE POWDER ON EXTERNAL SULFATE ATTACK

HO-SEOP JUNG

Underground Structure Research Division, KICT, 2311 Daehwa-dong Ilsanseo-gu, Goyang, Kyeonggi-do, 411-712, KOREA

SEUNG-TAE LEE

Department of Civil Engineering, Kunsan National University, San 65 Miryong-dong Kunsan, Jeollabuk-do, 573-701, KOREA

KWANG-PIL PARK

Department of Civil Engineering, Daejin University, San 11-1 Seondan-dong Pocheon, Kyeonggi-do, 487-711, KOREA

SEONG-SOO KIM

Department of Civil Engineering, Daejin University, San 11-1 Seondan-dong Pocheon, Kyeonggi-do, 487-711, KOREA

This study describes the sulfate resistance of mortar and paste specimens incorporating limestone powder(LSP) at ambient temperature. The mail variable is the fineness level of the LSP, which are divided into 1,010, and 2,650m²/kg blaine sulfate area. Expansion and compressive strength were regularly investigated to evaluate the sulfate resistance of mortar specimens with or without LSP for 270 days. XRD analysis on paste sample was carried out to examine the products formed by sulfate attack. Experimental results indicated that mortar specimens with a high fineness LSP showed a poor resistance to sulfate attack compared with those of lower fineness. It may be attributable to the preferable possibility of thaumasite formation in a high fineness LSP-cement system due to sulfate attack. The XRD data also confirmed that the thaumasite formation with a strong intensity was primarily responsible for the severe damage in the high fineness LSP-cement system.

1. Introduction

Deterioration of concrete by sulfate attack is commonly observed in structures exposed to soil or groundwater containing a high concentration of sulfate ions. During the previous few decades, it has been reported that the proper initial

curing of blended cement concrete, mixtures with low water-cement ratio, and using Type V cement with low C3A content were recommended as the methods to resist sulfate attack [1].

In order to improve the properties of cement concrete of aggressive environment, many researchers studied blended cement. In order to improve the performance of concrete, generally, modern cements often incorporate several mineral admixtures [2]. On the other hand, limestone is important material for cement manufacture. It has been increasingly used in concrete as a filler or main cement constituent for many years. The addition of limestone to Portland cement may significantly improve several cement properties such as compressive strength, water demand, workability, durability and several effects on the mechanism and kinetics of cement hydration [3]. There have been numerous studies on durability of limestone concrete when exposed to aggressive conditions. Most of these studies were focused on the effects of limestone on concrete durability.

The objectives of this study were to monitor the physical deterioration of mortar specimen with different fineness levels and replacement ratio of limestone powder, and to analyze the possible products formed by sodium sulfate attack.

2. Experimental Details

2.1. *Materials and specimen preparation*

(1) ASTM C 150 Type I cement was used for all mixtures. The specific gravity and specific surface area are 3.15 and $328m^2/kg$, respectively.

(2) Aggregates: The fine aggregate, river sand, which is a fine aggregate immune to most chemical agent and has little organic compounds, is employed for manufacturing cement matrix specimens. The fine aggregate was entirely passed from the sieve of 5 mm. Its specific gravity and fineness modulus is 2.60 and 2.80, respectively.

(3) Limestone powder: There are two kinds of limestone powders which is used it this study; their mean diameters are 3.11 μm (hereinafter referred to as LSA) and 18.62 μm (hereinafter referred to as LSB), respectively. Four replacement levels (0, 10, 20, and 30% by mass) of limestone powder as a partial replacement of the cement were chosen as the main variable.

(4) Test solution: The exposure solution used to provide sulfate attack to the specimens was by dissolving reagent grade chemical in water. The chemical used was the 5% sodium sulfate solution. Water and solutions temperature were kept 20±1 ℃ during the test period. Before immersion, mortar specimens were tested to determine the initial compressive strength and length change. These solutions were renewed every 4 weeks.

2.2. *Methodologies*

(1) Expansion: The expansion test was conducted on accordance with ASTM C 1012 at each immersion period. All expansion profiles were compared with the initial length of prism mortar after 7 days of curing in tap water.

(2) Compressive strength: The compressive strength measurements were conducted on 50 mm cube mortar specimens. All specimens, those mortar specimens were de-molded after 1 day of mixing and cured in tap water at room temperature for an additional 6 days. And then, some of them were moved to test solutions and were continuously immersed during predetermined periods. The compressive strength tests were performed on each mixture at each immersion periods.

(3) XRD analysis: XRD analysis was performed on paste samples exposed to sodium sulfate solutions. It was conducted using the RINT D/max 2500 (Rigaku, Japan) X-ray diffractometer. For the XRD tests, CuKα radiation with a wave length of 1.54 Å at a voltage of 30kV, scanning speed of 2°/min. and current of 30 mA were used.

(4) Specimen prepare and mixture proportions: Mortar and paste specimens were demoulded 24 hr after casting, and cured in tap water at room temperature for an additional 6 days. Thereafter some of the specimens were transferred to the sulfate solutions. The temperature of tap water and sulfate solutions was maintained at 20 ± 1 ℃ during the test period. Table 3 shows the details of the mortar and paste mixtures used in the tests.

3. Results and Discussion

3.1. *Expansion profile of mortar specimen*

Expansion of mortar specimens was measured on the basis of ASTM C 1012. The expansion profile of LSA and LSB mortar specimens with different replacement ratio levels immersed in sodium sulfate solution are presented in Figure 1. It was clearly evident that mortar specimens replaced with 20 and 30% of LSA showed a significant expansion in the solution. On the other hand, the mortar specimen with 10% of LSA showed a better sulfate resistance against expansion. The expansion value of LSA10 mortar specimen was 0.118% after 270 days of sulfate exposure, whereas LSA20 and LSA30 mortar specimens were 0.595% and 0.692% at the same exposure period, respectively.

The tendency of length change of LSB mortar specimens was the relatively excessive expansion of LSB30 mortar specimen. Furthermore, comparing to that of control mortar specimen, a better sulfate resistance of LSB mortar specimen

with 20% replacement was also investigated. Therefore, it is concluded that approximately 10% replacement for LSA mortar specimen was more effective on sulfate resistance, whereas up to 20% replacement for LSB mortar specimen. This conclusion suggests that the thaumasite formation formed in mortar specimens incorporating limestone powder affects more reduction in compressive strength, compared to expansion. This is why the lack of cohesiveness and the mushy effect of thaumasite formed in mortar specimen system. In other words, as more cement is replace by limestone powder, the increased amount of thaumasite led to the more pronounced degradation of mortar specimens.
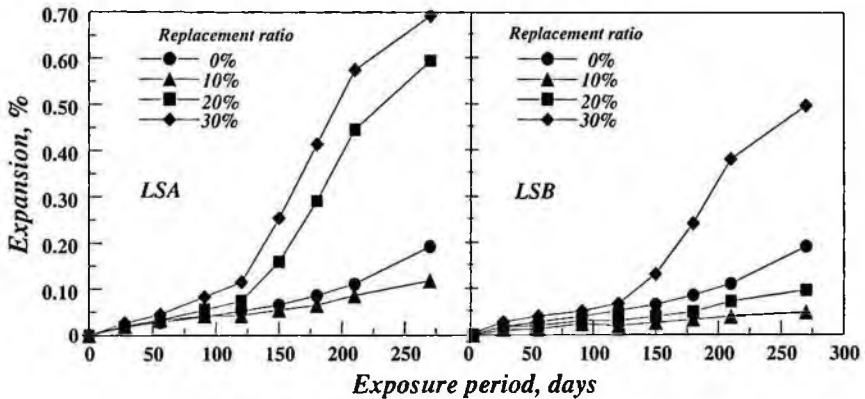
Fig. 1. Expansion profile of mortars

3.2. *Compressive strength*

The strength deterioration ratio of mortar specimens with different fineness levels of limestone powders exposed to sodium sulfate solution were presented in Figure 2. The ratios were calculated at the 28, 56, 91, 180 and 270 days of exposure. All mortar specimens showed negative values of strength deterioration at 28 days of exposure. These negative values signify an increase in compressive strength, which is attributable to the filling up of the pores by reaction products, densifying the mortar matrix in early period of exposure [3, 4]. After 56 days of exposure, the ratio of strength deterioration of control, LSA20 and LSA30 mortar specimens increased with immersion period. However, for LSA10 mortar specimen, the deterioration ratio was somewhat stable with increase of immersion period. After 270 days of exposure, the ratios, indicating about 26% to 29%, of control, LSA20 and LSA30 mortar specimens were similar, whereas

LSA10 mortar specimen showed about 12.6% in strength deterioration ratio at the same immersion period.

The LSB10, LSB20 and LSB30 mortar specimens placed in sodium sulfate solution for 270 days recorded about 13.9%, 22.8% and 23.0% in strength deterioration ratios, respectively. From the results of this test, it was revealed that mortar specimen with replacement ratio of 10% by cement mass, irrespective of fineness levels of limestone powder, showed a good sulfate resistance with respect to strength reduction.
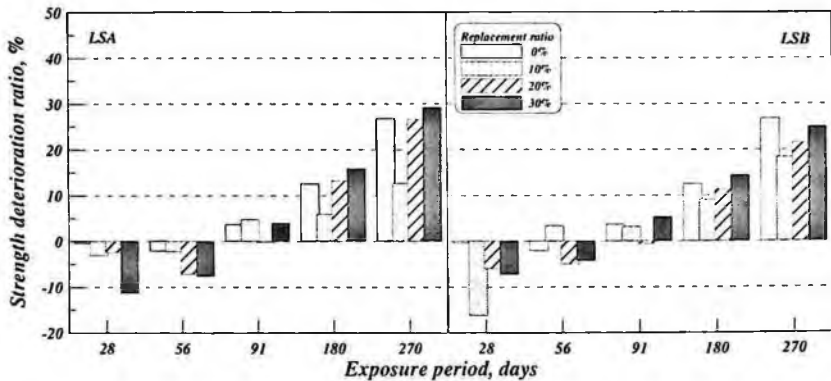
Fig. 2. Compressive strength of mortar specimens

3.3. *XRD analysis*

Deteriorated parts of paste specimens containing limestone powders were examined by XRD after 270 days of exposure. The curves of the LSA and LSB paste specimens exposed to sodium sulfate solution are presented in Figure 3. The XRD of control paste specimen is also compared to investigate the influence of limestone powder on the products formed by sulfate attack. For XRD trace of control paste specimen, the presence of thaumasite and ettringite was obvious at around $9.1°2\theta$. Furthermore, the two major peaks are also present in both minerals at $16.0°$ and $32.3°2\theta$. Actually, it is difficult to distinguish thaumasite formation from ettringite formation, when only small amount are present in cement matrix system, because of their structural similarities.

In Figure 3, it was clear that the intensity peaks for calcite were increased with increase of limestone powder replacement. On the contrary, intensity peaks for Portlandite showed a reverse tendency with increase of limestone powder replacement. From the result, it was found that the main factor causing deterioration of cement matrix with limestone powder was the thaumasite formation. Another important observation in these XRD traces was the absence

of gypsum formation. The XRD trace corresponding to control paste specimen did not show a symptom of the product even at $11.7°2\theta$, which is the main peak intensity.
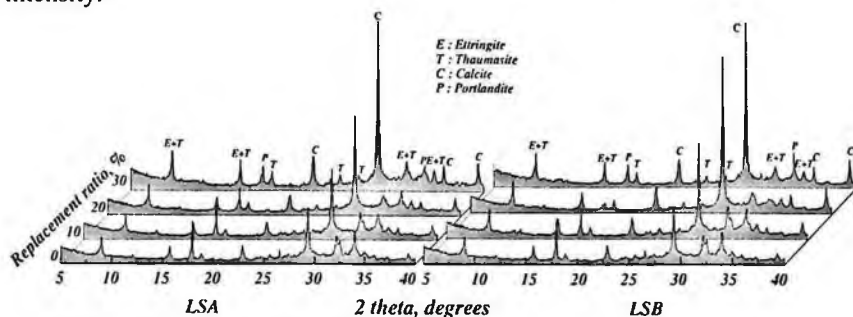
Fig. 3. XRD analysis of paste samples

4. Conclusion

The main conclusions of the paper can summarized as follow:

(1) Regardless of fineness levels of limestone powder, expansion of mortar specimens with only 10% replacement was much lower than that of 20% or more replacement.

(2) Mortar specimens with 30% replacement of limestone powder were significantly deteriorated. However, LSB mortar specimen was less deteriorated with respect to strength reduction.

(3) From the XRD result of paste samples exposed to sodium sulfate solution, it was found that the main factor causing deterioration of cement matrix with limestone powder was the thaumasite formation.

References

1. Al-Amoudi, O. S. B., Maslehuddin, M., and Abdul-Al, Y. A. B, *Role of chloride ions on expansion and strength reduction in plain and blended cements in sulfate environments*, **Const. and Bld. Mater.**, Vol. 9, No. 1, pp. 25~33.(1995).

2. S. Tsivilis, G. Kakali, A. Skaropoulou, J.H. Sharp, R. N. Swamy, *Use of mineral admixtures to prevent thaumasite formation in limestone cement mortar*, **Cem. Conc. Compo.**, 25(8) 969-976(2003).

3. Brown, P. W., *An evaluation of sulfate resistance of cements in a controlled environment*, **Cem. and Conc. Res.**, Vol. 11, pp. 719~727(1981).

4. Cohen, M. D., and Bentur, A., *Durability of portland cement-silica fume pastes in magnesium sulfate and sodium sulfate solutions*, **ACI Materials Journal**, Vol. 85, No. 3, pp. 148~157(1988).

ENHANCEMENT OF DETECTION EFFICIENCY FOR G-TYPE NERVE AGENT SIMULANTS BASED ON DBR POROUS SILICON

SEUNGHYUN JANG

Department of Chemistry, Chosun University, 375 Seosuk-Dong, Dong-gu, Gwangju, Korea

JIHOON KIM

Department of Chemistry, Chosun University, 375 Seosuk-Dong, Dong-gu, Gwangju, Korea

YOUNGDAE KOH

Department of Chemistry, Chosun University, 375 Seosuk-Dong, Dong-gu, Gwangju, Korea

HONGLAE SOHN*

Corresponding author, Department of Chemistry, Chosun University, 375 Seosuk-Dong, Dong-gu, Gwangju, Korea, hsohn@chosun.ac.kr

The various detection methods using distributed Bragg reflector porous silicon (DBR PSi) for sensing G-type nerve agent mimics have been developed. The versatile PSi has been prepared by an electrochemical etching through applied square current waveform for DBR. The manufactured DBR PSi exhibits unique optical properties providing the reflection of a specific wavelength in the optical reflectivity spectrum. The detection methods involve the shift of DBR peaks in reflectivity spectra under the exposure of vapors of nerve agent mimics. Rapid detections have been achieved in few seconds, *in situ*, when a laser is used as a light source. The red-shift of reflection peak resulted from the increase of refractive indices in PSi. Real-time detection for the nerve gases indicates that the measurement is reversible. The detection efficiency for nerve agent mimics is also increased, when LED (λ=520 nm) or laser (λ=530 nm) is used as an incident light source instead of tungsten-halogen lamp.

Keywords: Detection; nerve agent mimic; reflectivity; red-shift; LED; laser.

1. Introduction

The nerve agent mimics such as diethyl-chlorophosphate (DCP), triethylphosphate (TEP), dimethyl-methylphosphonate (DMMP), and diethyl-

ethylphosphonate (DEEP) are among the most toxic substances and are thus commonly used as chemical warfare agents (CWA) and pesticides. There are urgent needs for innovative analytical tools for the detection of CWA due to the toxicity of these compounds. Therefore the rapid detection of sarin, soman, and nerve agent mimics is currently of great interest. There are growing concerns about their use as chemical weapons for terrorist or war action. A G-type nerve agent has lethality depending on both concentration and exposure time. The LCt_{50} for sarin by inhalation of the vapor form is 100 milligrams of sarin per cubic meter of air for one minute.[1] The main method currently used to detect nerve agents is based on a surface acoustic wave (SAW) device.[2-3] Other methods using enzymes,[4] single-walled carbon nanotubes,[5] metal oxides,[6] and organic polymers[7] have been recently reported. PSi is also an alternative method to detect chemical nerve agents.[8-9] Photonic crystals of PSi have been a topic of interest because of their unique properties, including surface area and convenient surface chemistry, as well as their optical signal transduction capability. These properties have led to its use in chemical and biological sensors,[10-13] biomaterials,[14] and optical devices.[15] Multistructured rugate PSi have been recently investigated in terms of their possible applications.[16-23] In the present work, we report on various detection methods based on changes in the spectral interference of PSi to specify nerve agent mimics.

2. Experimental

2.1. *Generals*

All nerve agent mimics such as DCP, DMMP, DEEP, and TEP are commercially purchased from Sigma-Aldrich, Inc. and used without further purification. Optical reflectivity spectra of multistructured PSi interferometer have been measured by using a tungsten-halogen lamp, LED (λ=520), laser (λ=530 nm), and Ocean Optics S2000 CCD spectrometer fitted with a fiber optic input. The reflected light was collected at the end of the fiber optic positioned at the focal plane of the optical microscope. SEM images have been obtained by a cold field emission scanning electron microscope (FE-SEM, S-4800, Hitachi).

2.2. *Fabrication of multistructured porous silicon interferometers*

DBR PSi samples were prepared by electrochemical etch of heavily doped p^{++}-type silicon wafers (boron doped, polished on the <100> face, resistivity; 0.8-1.2 mΩ -cm, Siltronix, Inc.). The etching solution consists of a 3:1 volume mixture of aqueous 48% hydrofluoric acid (Aldrich Chemicals) and absolute

ethanol (Aldrich Chemicals). Galvanostatic etching was carried out in a teflone cell applying 20 cycles of a two-electrode configuration. DBR PSi has been prepared by using a square wave current between 5 mA/cm^2 for 90 s and 50 mA/cm^2 for 3 s for single reflectivity.

The anodization current was supplied by Keithley 2420 high-precision constant current source meter controlled by a computer. To prevent the photogeneration of carriers, the anodization was performed in the dark. After formation, the samples were rinsed with absolute ethanol and dried with nitrogen gas.

3. Results and Discussion

3.1. *FE-SEM images of DBR PSi*

The surface and cross-sectional SEM images of PSi samples were obtained by a cold field emission scanning electron microscope. Fig. 1 shows the surface and cross-sectional SEM images of DBR PSi. The cross-sectional images of DBR PSi illustrates that the multilayer DBR PSi has a depth of a few microns. A repeating etching process results in two distinct refractive indices.
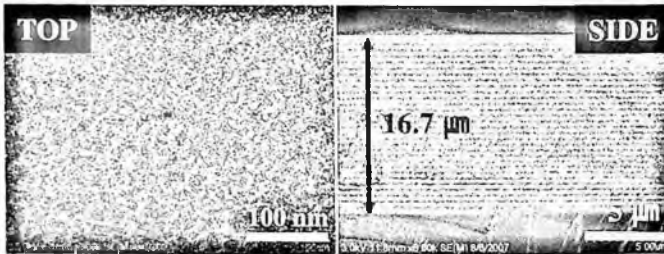
Fig. 1. Surface (A) and cross-sectional (B) SEM images of DBR PSi.

3.2. *Detection of nerve agent mimics based on DBR PSi interferometer*

DBR PSi exhibits a high reflectivity band with the Bragg wavelength, λ_{Bragg}, depending on the thickness of the layers (d_1, d_2) and the corresponding refractive indices (n_1, n_2). The mth order of the Bragg peak is given by:

$$m\lambda_{Bragg} = 2(d_1n_1 + d_2n_2) \tag{1}$$

Typical etch parameters for DBR PSi structure involves using a periodic square wave current between low and high current densities. The dissolution times for a $\lambda/4$ layer of Bragg structures were 90 s for 5 mA/cm^2 and 3 s for 50 mA/cm^2. Prepared DBR PSi samples displayed excellent reflection peak at 570 nm in the

reflection spectrum. These chips are exposed to a flux of DMMP (partial pressure of 0.22 torr) in air with a flow rate of 5 L/min. Fig. 2 illustrates the detection mechanism based on DBR PSi interferometer, while exposing the detector to the vapor of DMMP. Capillary condensation causes the reflection peak to shift to longer wavelengths under the exposure DMMP vapors. Reflection spectra from DBR PSi by using tungsten-halogen lamp for the detection of nerve agent were recorded under the exposure of vapor of analyte and shown in Fig. 3A. 25 nm of red-shift were observed for 1 min.
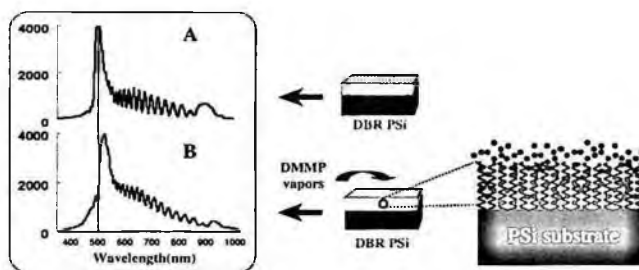
Fig. 2. Schematic diagram for the detection mechanism based on DBR PSi interferometer.

Another DBR PSi sample with its reflection band at 520 nm was prepared by using a periodic square wave current between 5 mA/cm^2 for 100 s and 50 mA/cm^2 for 3 s to match the emission wavelength of LED. When LED was used as the incident light source instead of the tungsten-halogen lamp, 20% decrease of the reflectivity resulting from the red-shift of reflection peak were observed in the reflectivity spectra for 1 min.(Fig. 3B)
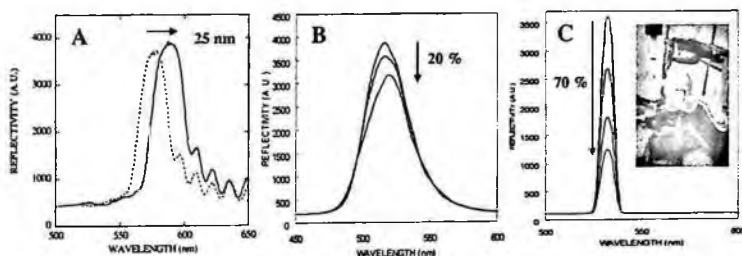
Fig. 3. Reflectivity spectra of DBR PSi samples under a flux of DMMP by using tungsten-halogen lamp (A), LED (B), and laser (C), as incident light source.

Fig. 3C showed the change of reflectivity spectrum recorded every 15 sec, *in situ*, when a laser is used as the incident light source instead of LED to enhance the sensitivity. 70% decrease of the reflectivity were observed in the reflectivity spectra for 1 min. The detection of DMMP vapor by using laser based on DBR PSi interferometer was achieved within few seconds. Response time for the DMMP vapor was faster by 2.5 times compared to LED due to the narrower bandwidth of laser.

3.3. Detection limits

Vapor of sarin has a lethality that is indicated by both concentration and exposure time. If a group of people breathed a concentration of 100 mg of sarin per cubic meter of air for 1 min., this would be a lethal dose for 50% of a group. At 1 mg/m^3 = 0.17 ppm for sarin, 100 mg/m^3 is equal to 17 ppm.[9] The detection limit was measured at the fixed reflective wavelength maxima and showed in Fig. 4. While the detection limit of DMMP with tungsten-halogen lamp was 1.5 ppm, the detection limit with LED was 150 ppb. It is interesting to note that 150 ppb of detection limit with laser was observed, but the response time for DMMP vapor was faster than those with LED. This result suggests that 150 ppb of DMMP vapor might be the minimum concentration for the capillary condensation for this DBR PSi chips.
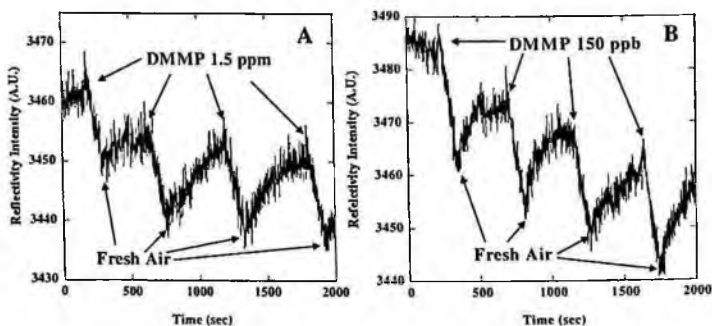
Fig. 4. Plots for showing the detection limits of DMMP at fixed reflection wavelength maxima with tungsten-halogen lamp (A) and LED (B) as incident light source.

4. Conclusions

Various detection methods based on DBR PSi interferometer for sensing of G-type nerve agent mimics have been developed. Rapid detections have been achieved in few seconds, *in situ*, and observed by the changes of reflection peak

resulted from the increase of refractive indices in DBR PSi. Real-time detection for the nerve gases indicates that the measurement is reversible. The detection efficiency is increased when a laser are used as an incident light source. Our detection limit for DMMP vapors based on laser/DBR PSi interferometer was lower than 150 ppb.

References

1. Office of the special assistant for Gulf War Illness, Department of Defense, Fact Sheet on Exposure Limits for Sarin (GB), 1997.
2. M. S. Nieuwenhuizen and J. L. N. Harteveld, *Sens. Actuators B.* **40** 167 (1997).
3. D. Williams and G. Pappas, *Field Anal. Chem. Technol.* **3**, 45 (1999).
4. K. E. LeJeune, J. R. Wild, and A. J. Russell, *Nature*, **395**, 27 (1998).
5. E. S. Snow, F. K. Perkins, E. J. Houser, S. C. Badescu, and T. L. Reinecke, *Science*, **307**, 1942 (2005).
6. N. Taranenko, J.-P. Alarie, D. L. Stokes, and T. Vo-Dinh, *J. Raman Spectrosc.* **27**, 379 (1996).
7. A. R. Hopkins and N. S. Lewis, *Anal. Chem.* **73**, 884 (2001).
8. S. E. Letant, S. R. Kane, B. R. Hart, M. Z. Hadi, T.-C. Cheng, V. K. Rastogi, and J. G. Reynolds, *Chem. Commun.* 851 (2005).
9. J. Dorvee and M. J. Sailor, *Phys. Stat. Sol.* **202**, 1619 (2005).
10. H. Sohn, S. Letant , M. J. Sailor, and W. C. Trogler, *J. Am. Chem. Soc.* **122**, 5399 (2000).
11. S. Chan, S. R. Horner, B. L. Miller, and P. M. Fauchet, *J. Am. Chem. Soc.* **123**, 11797 (2001).
12. P. A. Snow, E. K. Squire, P. S. J. Russell, and L. T. Canham, *J. Appl. Phys.* **86**, 1781 (1999).
13. C. Pacholski, M. Sartor, M. J. Sailor, F. Cunnin, and G. M. Miskelly, *J. Am. Chem. Soc.* **127**, 11636 (2005).
14. L. T. Canham, M. P.Stewart, J. M. Buriak, C. L. Reeves, M. Anderson, E. K. Squire, P. Allcock, and P. A. Snow, *Phys. Status Solidi A*, **182**, 521 (2000).
15. V. Lehmann, R. Stengl, H. Reisinger, R. Detemple, and W. Theiss, *Appl. Phys. Lett.* **78**, 589 (2001).
16. T. A. Schmedake, F. Cunin, J. R. Link, and M. J. Sailor, *Adv. Mater.* **14**, 1270 (2002).
17. F. Cunin, T. A, Schmedake, J. R. Link, Y. Y. Li, J. Koh, S. Bhatia, and M. J. Sailor, *Nat. Mater.* **1**, 39 (2002).
18. M. S. Yoon, K. H. Ahn, R. W. Cheung, H. Sohn, J. R. Link, F. Cunin, and M. J. Sailor, *Chem. Commun.* 680 (2003).
19. J. R. Dorvee, A. M. Derfus, S. N. Bhatia and M. J. Sailor, *Nat. Mater.* **3**, 896 (2004).
20. M. J. Sailor, and J. R. Link, *Chem. Commun.* 1375 (2005).
21. Y. Y. Li, F. Cunin, J. R. Link, T. Gao, R. E. Betts, S. H. Reiver, V. Chin, S. N. Bhatia, and M. J. Sailor, *Science*, **299**, 2045 (2003).
22. B. -J. Lee, S. Jang, and H. Sohn, *Solid State Phenom*, **124-126**, 491 (2007).
23. A. Janshoff, K. -P. S. Dancil, C. Steinem, D. P. Greiner, V. S.-Y. Lin, C. Gurtner, K. Motesharei, M. J. Sailor, and M. R. Ghadiri, *J. Am. Chem. Soc*, **120**, 12108 (1998).

AN ANALYSIS FOR MECHANICAL PROPERTIES OF RUBBER GRANULE LAYER OF SYNTHETIC SURFACED TRACK

KI-WEON KANG[†]

Ph.D., Dept. of Sports Eng. Korea Institute of Sport Science, Seoul, Korea

HEE-JIN SHIM

Graduate Student, Dept. of Mech. Eng., Hanyang University, Seoul, Korea

JUNG-KYU KIM

Professor, School of Mech. Eng., Hanyang University, Seoul, Korea

JONG-BU PARK

Korea Elastic Compound Pavement Industry Association, Seoul, Korea

The paper aims to identify an optimal mixing condition of the rubber granule layer which are sub-part of the elastic compound pavement system for the athletics and public use tracks. For this goal, the rubber granule layers are fabricated according to the manufacturer' recommended process and the design of experiments. And then, the unidirectional tensile testes are performed on the rubber granule specimens to identify the mechanical properties. Also, to evaluate the dynamic performance, impact tests are performed by using a pendulum type impact tester. Finally, based on the experimental results, the response surface methodology has been used to decide the optimal mixing condition to achieve the high level of mechanical properties.

1. Introduction

Modern synthetic surfaces have been widely used in the world due to their dynamic performance, durability and all-weather capability for the athletics tracks [1, 2]. There are several sub-division of surface type: some are prefabricated in the factory and delivered to site as rolls of material which are adhesive bonded to the base. Some (elastic compound pavement system) are fabricated on site by machine mixing and laying the raw material ingredients. Others are composites of these two systems [1]. Among them, since the elastic compound pavement system has several versatile characteristics such as variable dynamic performance, all-terrain capability and ease of maintenance, the system

---

[†] To whom correspondence should be addressed. Fax: 82-2-970-9593; E-mail:kwkang68@daum.net

has been mostly used for the athletics tracks as well as the out-doors tracks for public use in Korea [3].

Unfortunately, there are considerable numbers of manufactures and installers which have offered the elastic compound pavement system [3]. Moreover, the compatibility of the raw material ingredients is of vital importance and the end properties of such system are very dependent on the nature of the raw materials delivers to site: there is a possibility that the each component has an adverse effect on another forming part of the same surfacing product [1]. It is, therefore, of necessity, to decide the optimal mixing condition for the mechanical properties in the elastic compound pavement system.

The present paper aims to identify the optimal mixing condition of rubber granule layer which are sub-part of the elastic compound pavement system. The rubber granule layers are fabricated according to the manufacturers' and installers' recommended process. To minimize a required number of tests, the test matrix is established by using the design of experiments (DOE). And then, the tensile and impact testes are performed on the rubber granule specimens to evaluate the static behavior and the dynamic performance. Based on the experimental results, the response surface methodology has been used to decide the optimal mixing condition to achieve the high level of mechanical properties.

2. Experimental and Analysis Procedure

2.1. *Material and specimens*

The rubber granule layer is the sub-part of the elastic compound pavement system as shown in Fig. 1. And this layer is composed of rubber granule and bonding material [3] as illustrated in Fig. 2 (black: granule, grey: bonding material). The granule used here was made from the EPDM (Ethylene Propylene Dien PolyMethylene) rubber. The bonding materials are provided by the five major manufactures in Korea. The layers are fabricated according to the manufacturer' recommended process with the dimension of 400×200×15mm (L×W×T). The layers were then cut into specimens with the dimensions of 180×30×15mm and 40× 40×15mm for tensile and impact tests, respectively.

2.2. *Tensile and impact tests*

The tensile tests were conducted at the ambient temperature by using a servo-hydraulic testing machine (Instron 8801). The static tests were performed under displacement control mode with a crosshead speed of 50±0.5mm/min and the elongation was monitored by using an extensometer with a gage length of 50mm,

according to KS M 6518 [4]. And the impact tests were conducted by using the pendulum type impact tester that is specified at KS M 6518. Here each test was performed 7 times to improve the reliability of test results.
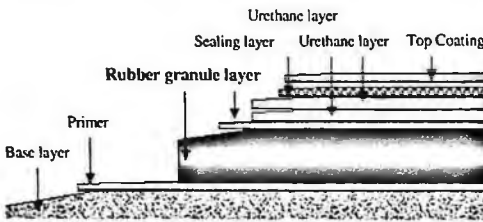
Fig. 1 Elastic compound pavement system
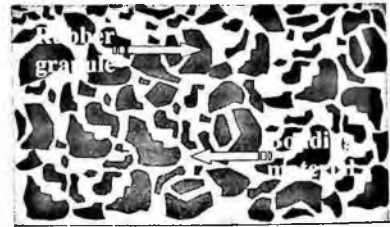
Fig. 2 Rubber granule layer

Table 1 Design of experiments for tensile and impact tests

Series No.	x_1	x_2	x_3	Series No.	x_1	x_2	x_3
1	-1	-1	-1	9	-1.287	0	0
2	-1	-1	1	10	1.287	0	0
3	-1	1	-1	11	0	-1.287	0
4	-1	1	1	12	0	1.287	0
5	1	-1	-1	13	0	0	-1.287
6	1	-1	1	14	0	0	1.287
7	1	1	-1	15	0	0	0
8	1	1	1	16	0	0	0

2.3. *Design of experiment*

The mechanical properties of the rubber granule layer may be affected by several factors, according to the manufacturers and installers of synthetic surfaces. Among them, the authors are concerned with three factors of the mixing condition: bonding material, content of bonding material and mesh distribution of rubber granule. Table 1 shows the range of the design variables and the test matrix according to DOE (central composite design) [5, 6]. Here x_1, x_2 and x_3 indicate the type of bonding material, content of bonding material and mesh distribution of rubber granule, respectively. The levels of design variable x_1 mean the bonding material manufactures (manufacturer: A~E).

3. Results and Discussion

3.1. *Results from design of experiments*

Basically, in the response surface methodology, the experimental model of the response should firstly be established, and then fitted response surface models

are optimized simultaneously in a region of interest. Typical second order models for the response are given by

$$\mu = \beta_0 + \sum_{i=1}^{k} \beta_i x_i + \sum_{i<j}^{k} \beta_{ij} x_i x_j \tag{1}$$

in which μ and k are the estimated value of the responses (performance factors) and number of design variable, respectively. Also, β is the coefficients of the fitted response surface.

According to the manufacturers' recommendation, the tensile strength, failure strain and elastic rebound are selected as the performance factors. And then, the authors performed the tensile and impact tests according to the central composite design. The response surfaces are fitted by using Eq. (1) and the non-linear regression method [6]. The results are summarized in Table 2.

Table 2 Estimated coefficients in Eq. (1)

Performance	b_0	b_1	b_2	b_3	b_4	b_5	b_6	b_7	b_8	b_9
Tensile Strength	46.07	-0.69	7.66	0.71	-6.36	0.64	0.22	0.10	0.57	-0.42
Failure Strain	30.42	-6.39	-0.34	-0.29	-3.28	3.17	1.23	0.30	0.85	0.32
Elastic Rebound	37.61	1.17	0.04	-0.06	-2.08	-1.47	-0.74	-0.48	-0.13	-0.23
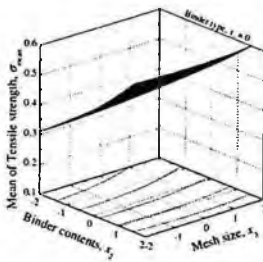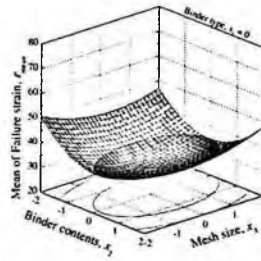
(a) Tensile strength   (b) Failure strain   (c) Elastic rebound
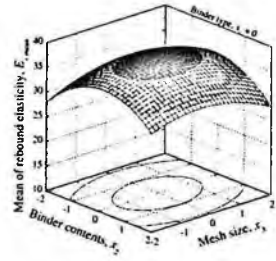
Fig. 3 Response surface for performance factors

Table 3 ANOVA table of response function for each performance factor

Performance		SOS	DOF	RMS	F_o	$F_{(a=0.05)}$	R^2
	SSR	902.86	9	100.32	15.336	4.099	0.958
Tensile Strength	SSE	39.25	6	6.54			
	SST	942.11	15				
	SSR	949.86	9	105.54	3.012	2.958	0.905
Failure Strain	SSE	210.21	6	35.04			
	SST	1049.70	15				
	SSR	56.63	9	6.29	2.688	2.395	0.860
Elastic Rebound	SSE	14.04	6	2.34			
	SST	65.87	15				

Table 2 and Eq. (1) indicate the approximate function of the performance factors. Fig. 3 shows the typical approximated response surface with each performance factor. From the figure, the mechanical properties of rubber granule layer are affected by all the design variables and their behavior differs from each other. Also, the variance analysis (ANOVA) table for Eq. (1) and Table (2) is shown in Table 3. From the table, Eq. (1) and Table 2 are statistically significant to 85% confidence level at least.

3.2. *Optimization of performance factors*

The goal of this design study was to determine the optimum values of the design parameters (bonding material, content of bonding material and mesh distribution of rubber granule) for the aforementioned performance factors. To obtain the optimum mixing condition for rubber granule layers, it is of necessity to formulate the optimization problem. According to the relevant standards to the rubber granule layer [1, 4], the mechanical properties of the layer should be maximize to improve the durability and dynamic performance of the synthetic surface tracks. Therefore, the objective function and constraint was set up as follows:

$$\text{Maximize: } \mu \tag{2}$$

$$\text{Subjected to: } -1.287 \leq x_i \leq +1.287, \quad i = 1, 2, 3 \tag{3}$$

in which the constraint Eq. (3) means the range of design variables.

The optimization problem was solved by MS-EXCEL solver (Generalized Reduced Gradient approach). Here, it should be noted that the installers have generally chosen and layered various bonding materials considering the economic and environmental situation: hence, it is more realistic to optimize the mixing conditions for each bonding material.

Table 4 shows the optimized design variables and corresponding expected mechanical properties for each bonding material. As the bonding material increases, the tensile strength intends to maximize but the bonding material shows the adverse effect on the failure strain. The mesh distribution has the identical effect on both the tensile strength and failure strain. And these tensile properties have somewhat different optimum design variables for each bonding material. These behaviors may results from the different bonding characteristics of each bonding material, together with the rubber granules. However, the elastic rebound exhibits a quite different behavior from the tensile properties: it has the almost same optimum design variables for all bonding materials. This may results from the fact that for the elastic rebound, the most important factor is

mainly properties of rubber while the bonding material plays only a role of holding the rubber granule.

Table 4 Optimized design variables and expected mechanical properties

Design Variables	Tensile strength [MPa]		Failure strain [%]		Elastic rebound [%]	
	Optimal value	Expected value	Optimal value	Expected value	Optimal value	Expected value
x_1	B/M A		B/M A		B/M A	
x_2	29.435	0.483	16.565	43.754	24.105	32.736
x_3	53.913		53.913		70.407	
x_1	B/M B		B/M B		B/M B	
x_2	29.435	0.521	16.565	43.646	23.875	34.407
x_3	53.913		53.913		70.188	
x_1	B/M C		B/M C		B/M C	
x_2	29.435	0.576	16.565	39.052	23.080	37.612
x_3	86.088		53.913		69.450	
x_1	B/M D		B/M D		B/M D	
x_2	29.435	0.514	16.565	28.296	22.285	36.751
x_3	86.088		86.088		68.700	
x_1	B/M E		B/M E		B/M E	
x_2	29.435	0.473	29.435	25.691	22.060	35.753
x_3	86.088		86.088		68.488	

4. Conclusions

1. Design variables were defined for the mechanical properties of rubber granule layer, which are the type of bonding material, the content of bonding materials and mesh distribution of rubber granule.

2. Based on the design of experiments, a response surface was constructed to optimize the mixing condition for the tensile strength, failure strain and elastic rebound in the rubber granule layer.

3. The optimization problem was formulated and solved to maximize the tensile properties and elastic rebound. The tensile properties are governed by the contents of bonding material and mesh distribution of rubber granule. The elastic rebound is mainly affected by the properties of rubber granule.

References

1. IAAF, *Track and Field Facilities Manual*, **Ed**. 2003
2. S.J. Dixon, A.C. Collop and M.E. Batt, *Med. Sci. Sports. Exe.*, 1919(2000)
3. KECPIA, *Elastic Compound Pavement System*, **1** (2005)
4. KSA, *KS M6518* (2006)
5. S.H. Park, *Modern Design of Experiment*, MinYoung (2003)
6. H.J Shim and J.K. Kim, *KSME Trans,* **A30**, 1041 (2006) (in Korean)

THE MEASUREMENT OF THERMAL DIFFUSIVITY FOR SEMI-INFINITE SOLID USING THE PHOTOTHERMAL DISPLACEMENT METHOD

P. S. Jeon, J. H. Kim

Department of Mechanical Engineering, Ajou University,
San-5, Wonchun-dong, Youngtong-gu, Suwon, 443-749, Korea

H. J. Kim[†], J. Yoo

Department of Mechanical Engineering, Ajou University,
San-5, Wonchun-dong, Youngtong-gu, Suwon, 443-749, Korea
e-mail : hyunkim@ajou.ac.kr

The more accurate measurement method for the thermal diffusivity using photothermal displacement spectroscopy was developed. In previous works, thermal diffusivities for materials with a finite thickness were determined by the deformation angle and phase angle as the relative position between the pump and probe beams. In this study, however, a complete theoretical treatment and experimental measurement by the photothermal displacement technique has been performed for semi-infinite solid materials. To verify the developed method, the measurement has been carried out about the pure copper and nickel alloy with a finite and a semi-infinite thickness. In results, the measured values for a semi-infinite materials have the accordance with the literature values within 1% standard deviation, while those for a finite materials show about 3% one. Consequently, the semi-infinite solid model was proposed as a high accurate measurement method for thermal conductivities.

Keywords: Thermal diffusivity; semi-infinite solid; photothermal displacement method.

1. Introduction

The photothermal technique is a very useful tool for the measurement of thermo-physical properties for solid/liquid etc. As the measurement method of thermo-physical properties using the photothermal effect, a photothermal radiometry, photothermal refraction, photothermal deflection, and photothermal

---

[†]Corresponding Author. Tel.: +82 31 219 2340; Fax.: +82 31 219 7108
E-mail address : hyunkim@ajou.ac.kr (H. J. Kim)

displacement method have been reported and developed by many researchers. Among them, the photothermal displacement method used in this study is a useful method to measure the gradient and phase of the thermoelastic deformation, which is produced by the absorbed light energy during a heating period on the surface of materials. Because previous studies were conducted for the samples with the finite thickness, the error from the thickness measurement causes relatively large uncertainty [1-4]. Also, the adiabatic condition between the back of sample surface and ambient results in a theoretical error in the case of long thermal diffusion length materials. Therefore, the independent model from the effect of sample thickness is proposed in this study by using semi-infinite model. And experimental measurements are carried out for pure metal and nickel alloy to verify the accuracy of the developed model.

2. Principle and Theory

The Figure 1 schematically shows the principle of the photothermal displacement method. The photothermal displacement method is based on detection of the deformation of the sample surface produced by the absorption of energy from a modulated light beam incident on the sample. The heating of the sample by the pump beam produces a temperature rising and thermoelastic deformation of the sample, which can be measured by detecting deflection of the probe beam reflected from the sample surface. And the thermophysical properties of the sample can be obtained from measurements of deflection. Because thermoelastic deformation is changed by the thermal and optical properties, the difference between the deflected and undeflected angle is proportional to the deformation gradient. The thermal diffusivity can be determined by the comparison of the experimental and theoretical results of phase lag of deformation gradient.

In order to obtain the gradient of deformation, temperature distribution of specimen must be determined. For this, a two-dimensional solid model which has an infinite length in the direction of r and z is adopted as shown in Figure 1 [5,6]. The governing equation is the 2-D heat conduction equation having heat source in cylindrical coordinate:

$$\nabla^2 T_i - \frac{1}{\alpha_i}\frac{\partial T_i}{\partial t} = -\frac{1}{k_i}Q_i \qquad (i = f, s) \tag{1}$$

where T is temperature, k is thermal conductivity, α is thermal diffusivity and Q is heat source produced by a pump beam. The subscript f indicates the front gas of specimen and the subscript s represents the domain of specimen.

722

Heat flux and temperature of front air and specimen are constant at $z=0$ and it is assumed that temperature is nearly zero because the thermal effect by pump beam can not have an influence on the specimen where z approaches an infinite.
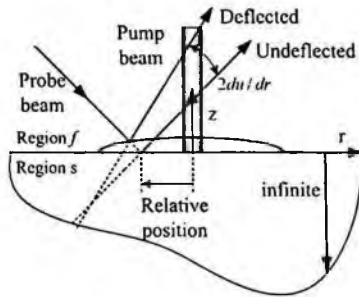
Fig. 1. Measurement principle of the photothermal displacement method.

The pump beam as a heat source has a Gaussian intensity distribution and is controlled by the modulation frequency(f). The radius of the pump beam is decided at the $1/e$ value of maximum intensity and the absorption coefficient(λ) is defined using the exponential law of light absorption. At the front gas region, light energy is not absorbed. Therefore the heat source is given by

$$Q_s = \left(\frac{P\lambda}{4\pi a^2}\right) e^{-r^2/a^2 + \lambda_s z} e^{i\omega t} \tag{2}$$

where the P represents an absorbed energy into specimen.

The temperature distribution can be solved by Hankel transform and complex method as follows

$$T_s(r,z,t) = \frac{P\lambda e^{i\omega t}}{8\pi k_s} \int_0^\infty \beta d\beta J_0(\beta r) \left(e^{\lambda z} - \frac{k_s\lambda + k_f\delta_f}{k_f\delta_f + k_s\delta_s} e^{\delta_s z} \right) \left(\frac{e^{-\beta^2 a^2/4}}{\delta_s^2 - \lambda^2} \right) \tag{3}$$

where $J_0(\beta r)$ is the Bessel function of 0th order and $\delta_i = (\beta^2 + i\omega/\alpha_i)^{1/2}$ $(i = f,s)$.

The thermoelastic equation and boundary conditions with temperature T is given by

$$\nabla^2 \vec{u} + \frac{\nabla(\nabla \cdot \vec{u})}{1-2\nu} = \frac{2(1+\nu)}{1-2\nu} \alpha_{th} \nabla T$$

$$\sigma_{rz}\big|_{z=0} = 0, \ \sigma_{zz}\big|_{z=0} = 0, \ \lim_{z \to -\infty} \vec{u} = 0 \tag{4}$$

where ν is the Poisson's ratio, $\vec{u}$ is the displacement vector and α_{th} is the thermal expansion coefficient [6,7].

The solution $u(r,z)$ can be expressed in cylindrical coordinates by introducing the displacement potential and the Love function. The deformation gradient at sample surface can be solved by Hankel transform as the following

$$\left.\frac{du_z}{dr}\right|_{z=0} = -\frac{(1+v)\alpha_{th}P\lambda}{4\pi k_s} \int_0^\infty \beta^2 d\beta J_1(\beta r) \frac{e^{-\beta^2 a^2/4}}{\delta_s^2 - \lambda^2}\left(\frac{1}{\lambda+\beta} - \frac{k_s\lambda_s + k_f\delta_f}{(\delta_s+\beta)(k_f\delta_f + k_s\delta_s)}\right) \quad (5)$$

where $J_1(\beta r)$ is the Bessel function of first order.

For the known radius of the pump beam, the phase lag is determined by integrating Eq. (5), which consists of a complex number and a rather intricate integral term including thermal diffusivity, etc.

3. Experiment

The experimental arrangement is shown in Figure 2. The pump beam is obtained by the acousto-optic modulation of a continuous-wave laser beam delivered by an Ar+ laser (488nm), and it is critically important that the pump beam spatial profile be Gaussian. The pump beam spot size on the sample is 55 μm radius, based on the $1/e$ point of pump beam intensity profile. The probe beam is provided by a He-Ne laser (633nm), with power of 5mW and a beam diameter 30μm. Both the pump and probe beams are expanded through collimators.
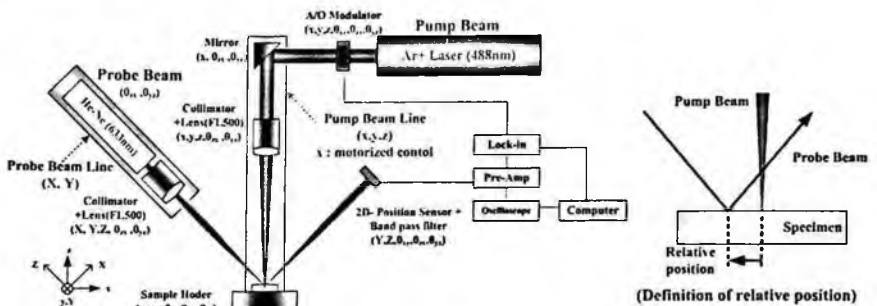
Fig. 2. Illustration of experimental apparatus and optical alignment.

The deflection of the probe beam is measured by using 2-dimensional position sensor. The amplitude and the phase lag of the deflected probe beam are measured by a lock-in amplifier, which is synchronized with the modulation frequency.

The position of the probe beam is aligned with the centerline of the pump beam spot. After aligning the probe beam and the pump beam positions, the measurement is carried out by traveling the probe beam along the centerline of

the deformation. The probe beam is moved along the centerline from the center of pump beam spot to set the relative position of a probe beam to a pump beam by using an arrangement of mirrors and micropositioners. The micropositioners are controlled with an accuracy of ±0.5 μm. Experiments were carried out on samples of pure copper and nickel alloy which are polished using alumina paste.

4. Results and Discussion

The semi-infinite solid model can be formulated by setting that thickness of z direction is infinite in theoretically analysis. But, for experiment, we need to come up with a finite sample thickness that can be considered having physical similarity with the semi-infinite solid. Therefore, the reasonable sample thickness is decided through comparison of the semi-infinite solid model and the slab model [8]. This thickness is defined as critical thickness.
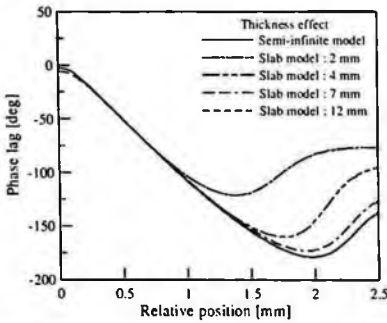
Fig. 3. Critical thickness for the semi-infinite solid model.
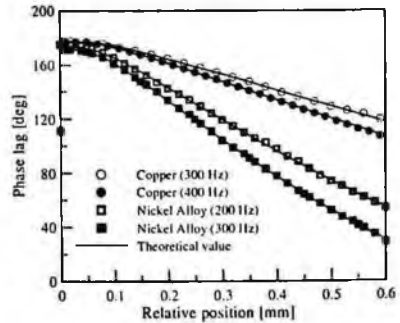
Fig. 4. Experimental results for the semi-infinite solid model.

Because the thermal diffusion area varies as the thermal diffusion length ($L_{th} = (\alpha/\pi f)^{1/2}$) changes, critical thickness is found out in changing the thermal diffusion length. The range of thermal diffusion length in this study is 100~400μm. The thermal diffusion length of 350μm is used to investigate the effect of thickness. In case of the sample thickness of longer than 12mm, the result agrees with the curve of semi-infinite solid model with the relative error less than 1% as shown in Figure 3. According to this, samples are prepared with the thickness over 12mm in this experiment.

When the thermoelastic deformation in the sample surface is generated by pump beam, we determine the thermal diffusivity from the offset value between phase curves of the probe and the pump beam. The slope of the phase signal of the probe beam with respect to the relative position between the pump and the probe beam is quite sensitive to the thermal diffusivity of a sample. The measured and calculated phase lag curves are matched each other in the region

of a quarter to three quarters below the relative position of minimum phase lag. A thermal diffusivity is determined when the standard deviation between the measured and calculated phase lag curve in Eq. (5) is minimized by using bisection method.

In the case of slab model, thermal diffusivities are measured by applying the pure metal samples of 1mm thickness. In the case of semi-infinite solid model, the sample thickness over 12mm is called the semi-infinite solid experimentally. The results of phase lag for semi-infinite solid in Figure 4 shows that experimental results agree with the theoretical analysis very well. The analysis are carried out in that conditions of the modulated pump beam frequencies are 300Hz and 400Hz for pure copper, 200Hz and 300Hz for nickel alloy(UNS N02201), respectively.

Measurement results of thermal diffusivity by comparing the phase curve measured from experiment data with the curve obtained from theoretical analysis are shown in Table 1. The measured thermal diffusivity for a semi-infinite materials have the accordance with the literature values within 1% standard deviation, while those for a finite materials show about 3% one. This result shows that finite-thickness slab model includes relatively higher error than semi-infinite solid model. Therefore, it could be said that the measurement of thermal property using semi-infinite solid model which is unnecessary to consider the thickness of samples is more accurate method.

Table 1. Comparison of the literature thermal diffusivity and measured value (f : modulation frequency, L_{th} : thermal diffusion length, L : literature value, M : measured value) [9].

Model	Material	f [Hz]	L_{th} [μm]	Thermal diffusivity (m²/s)×10⁵		Relative Error [%]
				L	M	
Slab	Silver	728	275	17.3	16.94	2.08
	Copper	763	220	11.6	11.13	4.05
	Zinc	185	275	4.4	4.26	3.18
	Iron	269	165	2.3	2.22	3.61
Semi -infinite	Nickel Alloy [UNS N02201]	200	176	1.947	1.96	0.69
		300	144	1.947	1.956	0.48
	Copper	300	351	11.6	11.656	0.48
		400	304	11.6	11.495	0.91

Uncertainty analysis results of semi-infinite solid model and slab model with finite constant one are compared. Through the parametric study in slab model[8], it is verified that sample thickness and radius of pump beam affected the thermal diffusivity dominantly. In case of semi-infinite solid model, on the other hand, only radius of pump beam becomes the cause of error because there is no effect

of sample thickness. Uncertainty is 1.7% in slab model and 0.2% in semi-infinite solid model.

5. Conclusion

Most of studies for measurement of thermal diffusivity using the photothermal displacement method have been in the condition of finite thickness of samples. Because the thickness of samples causes many kinds of error in measuring thermal properties, new theoretical analysis and experimental measurement which could exclude these are accomplished in this study. From the results, following conclusions were drawn.

(1) Thermoelastic analysis from the result of thermal analysis to obtain the deformation gradient caused by photothermal effect on the sample surface is performed.

(2) The experiment for the sample of semi-infinite solid type shows that thermal diffusivities are measured within 1% standard deviation.

(3) As a result of analyzing the uncertainty for semi-infinite solid model and slab model, it shows that semi-infinite solid model has relatively higher accuracy. The reason is consider that the effect of sample thickness and the assumption of ideal adiabatic boundary condition can be excluded among the factors that affect the phase lag. Therefore it is concluded that semi-infinite solid model suggested in this study will improve the reliability of thermal property measurement by photothermal displacement method.

Acknowledgments

References

1. M. A. Olmstead, N. M. Amer, and S. Kohn, *Appl. Phys. A*, **Vol. 32**, 141, (1983).
2. B. Li, Z. Zhen, and S. He, *Appl. Phys. D*, **Vol. 24**, 2196, (1991).
3. E. T. Ogawa., C. Hu, and R. S. Ho, *J. Appl. Phys.*, **Vol. 86(11)**, 6018, (1999).
4. E. H. Lee, K. J. Lee, P. S. Jeon, J. Yoo, and K. H. Kim, *JSME International Journal B*, **Vol. 43(4)**, 694, (2000).
5. H. S. Carslaw and J. C. Jaeger, *Conduction of Heat in Solids* (Oxford University Press, 1959).
6. P. S. Jeon, K. J. Lee, J. Yoo, Y. M. Park and J. H. Lee, *KSME International Journal*, **Vol. 18(10)**, 1712, (2004).
7. W. Nowacki, *Thermoelasticity*, 2nd ed (Pergamon Press, 1986).

8. P. S. Jeon, K. J. Lee, J. Yoo, Y. M. Park and J. H. Lee, *KSME International Journal*, Vol. **17(12)**, 2078, (2003).
9. J. F. Shackelford, *CRC Material Science and Engineering Handbook*, (CRC Press, 2001).

A STUDY ON THE BAUSCHINGER EFFECT OF GUN BARREL HIGH STRENGTH STEEL[*]

WOO-SUNG SHIM[1], JAE-HOON KIM[1†], YOUNG-SHINE LEE[1]

[1]*BK21 Mechatronics Groups, Dept. of Mechanical Design Engineering, Chungnam National University, 220 Kung-dong Yuseong-gu, Daejeon, 305-764, Korea*

SUK-KYUN HONG[2], GI-UP CHA[2]

[2]*Propulsive Group, Agency of Defense Development, Yuseong P.O. Box 35 Daejeon, 305-301, Korea*

The uniaxial tension-compression tests were conducted to evaluate Bauschinger effect in gun barrel high strength steel. The Bauschinger effect is originally defined as the phenomenon which plastic deformation causes a loss of yield strength restraining in the opposite direction. The Bauschinger effect factor (BEF), defined as the ratio of the yield stress on reverse loading to the initial yield stress, is a measure of the magnitude of the Bauschinger effect. As this factor is utilized to calculate the accurate residual stress in thick-walled cylinder after autofrettage process, evaluation of this factor is very important. The aim of the present paper is to evaluate the influence of plastic deformation and the behavior of the Bauschinger effect. From the experimental results, BEF is found to be a strong function of prior plastic strain.

1. Introduction

The thick walled cylinder subjected to cyclic internal pressure loading is the structure which is used for various industries, such as cannon or high-pressure reactor. These structures should be designed and machined to assure the safety at the operating conditions [1]. In the inner part of these structures, tensile tangential stress which is largest at the bore can occur, then crack initiation and crack propagation begin. The autofrettage process is usually utilized to overcome these problems. The autofrettage process is the favorable method that introducing and utilizing the compressive residual stress [2].Compressive residual stress can prevent crack initiation and crack propagation effectively [3].

This is a study on the Bauschinger effect of gun barrel high strength steel. If Basuchinger effect occurs in the autofrettaged material, reverse yielding

---

[†]Corresponding author : TEL +82 42 821 6645: FAX 82 42 821 8894
E-mail : kimjhoon@cnu.ac.kr (Jae Hoon Kim)

phenomenon may take place adjacent to the inner surface when the internal pressure is removed. This may result in the loss of the beneficial effect of autofrettage.

The aim of the this work is to quantitatively evaluate the influence of Bauschinger effect in gun barrel material by experimental data. The obtained experimental information enables residual stress calculations of autofrettage. Therefore this study is to know the Bauschinger effect, Bauschinger behavior prior to autofrettage process, and evaluate elastic modulus and yield stress as a function of plastic strain. The obtained experimental information could be readily useful for calculating residual stress field of autofrettage

2. Materials and Experimental Procedures

2.1. *Material and Specimen*

This study is carried out with SNCM8 high strength steel for gun barrel material. The chemical compositions of this material represented in Table 1. Table 2 summarizes the results of mechanical properties of SNCM8. Figure 1 shows the shape and dimensions of the tested specimen.

Table 1. Chemical compositions of SNCM8

C	Si	Mn	P	S	Cr	Mo	Ni
0.36~0.43	0.15~0.35	0.6	≤0.30	≤0.30	0.6~1.00	0.15~0.30	1.60~2.00

Table 2. Mechanical properties of SNCM8

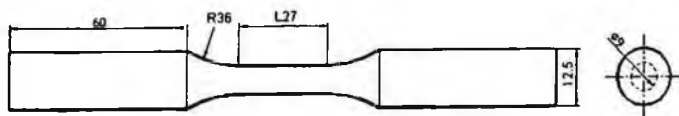| Elastic modulus, E(GPa)	Tensile strength, σ_u (MPa)	Yield strength, σ_{ys} (MPa)	Elongation, EL(%)	Reduction of area, RA(%)
202.2	1272	1129	19	59.2

Fig. 1. Shape and dimensions of specimen

2.2. *Experimental Condition*

To evaluate the influence of plastic strain for SNCM8 high strength steel, two kinds of different tests were performed using a hydraulic servo-controlled test machine (Model: MTS 810). The strain mode controlled by the 25mm extensometer in the gauge length. First test was run in a load control mode at 75kN ~ -55kN, 10Hz, and conducted for 10 cycles. In the test, single specimen was subjected to a series of consecutive loading and unloading. Next test was run in a strain control mode at a strain rate of 0.0001mm/mm/sec. Each of the specimens was conducted at total strain range of 0.5%, 1%, 2%, 3%, 4%.

3. Results and Discussion

3.1. *The Influence of Plastic Strain in a Load Control*

Figure 2 shows stress-strain curves obtained from the successive loading-unloading of specimen for 10 cycles under load control. After repeated plastic straining, elastic modulus and yield stress were reduced respectively.

The plots of 2nd and 10th stress-strain curves were extracted to compare the effect of plastic straining after cyclic loading (Figure 3). After a series of consecutive loading and unloading, the reduction of yield stress and elastic modulus were found. These reductions were a strong function of plastic strain.
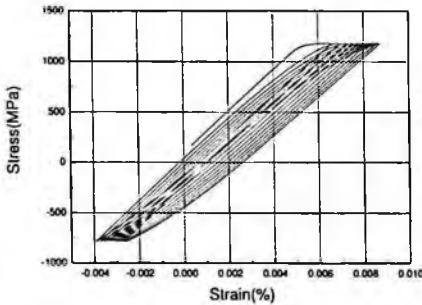

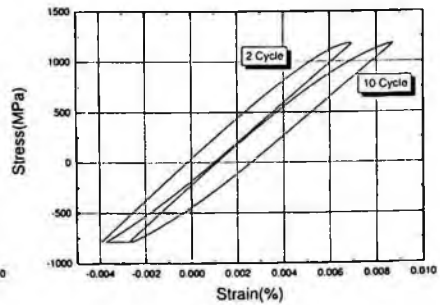Fig. 2. Uniaxial tension-compression test under load control

Fig. 3. Uniaxial tension-compression test under load control

3.2. *The Bauschinger Effect on Yield Strength*

As the influence of Bauschinger effect on yield strength may enable the material to occur reverse yielding during autofrettage process, we should consider

Bauschinger effect very carefully. This is why these phenomena could have a counter result or reduce the autofrettage process advantage.

The Bauschinger effect factor (BEF) serves as a measure of these effects and defined by Milligan et al [4]. By prior load control test, we simply noticed that a trend of decreasing in yield strength and elastic modulus. By latter experiment, we are to know the exact relationship between plastic strain and yield strength, elastic modulus.

Figure 4 shows fully reversed engineering stress-strain plots of SNCM8 at total strains of 1% to 4%. Stress-strain plots were divided into elastic and plastic range by a predetermined 0.1% offset in an attempt to evaluate the influence of plastic strain on reduction of yield strength and elastic modulus. Table 3 shows the tension and compression yield strength and the Bauschinger effect factor determined using 1% offset method. The utilization of these data has lead to the following Figure 5. Figure 5 shows the relationship between plastic strain and the Bauschinger effect factor of SNCM8 and reference data [4]. The results of two gun barrel high strength steels have a similar trend. At the range of plastic strain from 0% to 1.5%, Bauschinger effect factor decreases as the plastic strain increases. Over the range of plastic strain 1.5%, Bauschinger effect factor is a weak function of plastic strain.

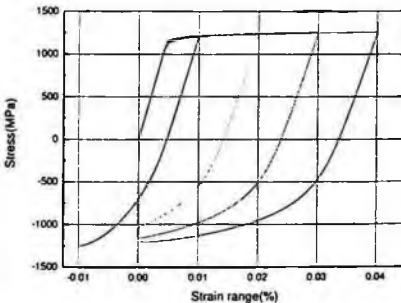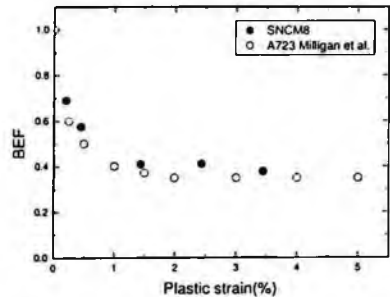Fig. 4. Stress-strain curve of SNCM8

Fig. 5. Bauschinger effect factor as a function of plastic strain

Table 3. Results of experimental data by 0.1% offset method

$\varepsilon_{plastic}$	Yield strength(MPa)		BEF
	Tension	Compression	
0.448	1164	-670	0.575
1.433	1178	-483	0.410
2.433	1180	-486	0.411
3.444	1143	-433	0.378

3.3. *The Bauschinger Effect on Elastic Modulus*

The relationship between plastic strain and elastic modulus was found by the experimental test. As the total strain changes, plastic strain also changes. Total strain was divided into plastic and elastic range by offset method, elastic modulus was determined at each plastic strain range.

At initial tensile loading range, elastic modulus was similar to elastic modulus of tensile test. At reversal loading after tensile loading, elastic modulus reduction was found. There were lots of differences between loading and unloading modulus. Table 4 shows the experimental results of elastic modulus ratio. Compressive modulus and modulus ratio decrease sharply as tensile plastic strain increases. The elastic modulus upon unloading decreases about 27% at the tensile plastic strain of 3.4%. Elastic modulus is a strong function of plastic strain. The difference in reduction of elastic modulus and yield strength is that yield strength reduction saturates at the range of 1.5%, but elastic modulus decreases as the plastic strain range increases.

Figure 6 shows the relationship between plastic strain and ratio of elastic modulus. There are another two materials which is used for gun barrel steel, A723 and PH13-8-1380 [5]. The elastic reduction ratios were compared with SNCM8. There were some differences between the materials, but the trend of elastic modulus for gun barrel steels has a similarity.

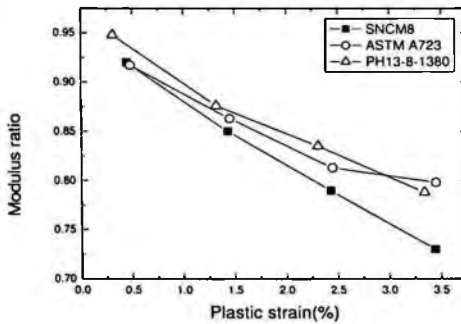Fig. 6. Elastic modulus versus plastic strain curve

Table 4 Experimental results

$\varepsilon_{plastic}$	Modulus(GPa)		Modulus ratio
	Tension	Compression	
0.448	209	192	0.92
1.433	201	170	0.85
2.433	207	164	0.79
3.444	213	157	0.73

4. Conclusion

Uniaxial tension-compression tests were carried out to evaluate the Bauschinger effect factor and elastic modulus reduction for gun barrel high strength steels. By utilizing these data, accurate compressive residual stress could be obtained when the material is autofrettaged. The conclusions obtained from experimental results are as follows.

1. The amount of reduced compressive yield strength is a strong function of the initial plastic strain. At the range of plastic strain from 0% to 1.5%, the Bauschinger effect factor decreases sharply as the plastic strain increases. Above these plastic ranges, the Bauschinger effect factor is constant regardless of plastic strain.

2. Compressive modulus and modulus ratio decrease sharply with the increase of tensile plastic strain. The elastic modulus upon unloading decreases about 27% at the tensile plastic strain of 3.4%.

3. Using these datum, the accurate compressive residual stress could be obtained when the material was autofettaged.

Acknowledgments

References

1. Jae.-Hyun Park, Young-Shin Lee, *Tras. Of the KSME.* Vol. 7, No. 7, pp. 800~807(2007)
2. X. P. Huang, W. C. Cui. *Journal of Pressure Vessel Technology*, Vo. 128 Issue 2, pp. 212~216(2006)
3. Stacey, A. and Webster, G. A., *High Pressure in Science and Technology*, pp.203~220(1984)
4. Milligan, R. V., Koo, W. H. And Davidson, T. E., *ASME J. Basic Eng.*, 88, pp. 480~488
5. Parker, A. P, Troiano, E., Underwood, J. H, *Journal of Pressure Vessel Technology* Vol. 125, Issue 3, pp. 330~334(2003)

THE EFFECT OF SHOT PEENING ON THE IMPROVEMENT OF FATIGUE STRENGTH AND FATIGUE CRACK CHARACTERISTICS OF THE ALUMINUM ALLOYS

TAE-HOON SONG

Department of Mechanical and Precision Engineering, Graduate School, Gyeongsang Nat'l., Univ., Tongyoung, Gyeongnam, 650-160, Korea
hanawon96@gnu.ac.kr

MAN-BAE LIM[1], SUN-CHUL HUH[2], WON-JO PARK[†]

[1]*Department of Mechanical and Precision Engineering. Gyeongsang Nat'l., Univ., Tongyoung, Gyeongnam, 650-160, Korea*
mblim@gnu.ac.kr
[2]*Research Center for Aircraft parts Technology, Gyeongsang Nat'l., Univ., Jinju, Gyeongnam, 660-701, Korea*
schuh@gnu.ac.kr
[†] *Department of Mechanical and Aerospace Engineering, Gyeongsang Nat'l., Univ. Institute of Marine Industry, Tongyoung, Gyeongnam, 650-160, Korea*
wjpark@gnu.ac.kr

Anti-fatigue failure technology takes an important the part of current industries. Currently, the shot peening is used for removing the defect from the surface of steel and improving the fatigue strength on surface. Therefore, in this paper, the effect of compressive residual stress of aluminum alloys (Al7075-T6 and Al6061-T6) by shot peening on fatigue characteristics in stress ratio was investigated with considering fracture mechanics. There is difference between shot peening specimen and un-peening specimen. Fatigue crack growth rate of shot peening specimen was lower than that of un-peening specimen. Fatigue life shows more improvement in the shot peening material than in the un-peening material. In this study, shot peening and un-peening materials were used to investigate the fatigue characteristics using fatigue tester (MTS 810, 10 tonf). Also, after examining the fatigue crack growth and fatigue life, in order to investigate the quality of fatigue fracture surface, observation of the aspect of fracture surface was conducted by using SEM.

1. Introduction

Nowadays, many components used in aerospace and automobile industry require light-weight and high-strength. The high strength materials have problem

---

[†] Corresponding author

which the propagation rate is fast when the crack exists. Shot peening is an effective method to improve the fatigue characteristics of metal. The compressive residual stress is generated by shot peening. Hammand and Meguid report that compressive residual stress delays the fatigue crack growth at initial crack growth so shot peening effectively prevent the fatigue crack growth. In this study, peening and un-peening materials were used to investigate the fatigue characteristics using fatigue tester (MTS 810, 10 tonf). Also, after examining the fatigue crack growth and fatigue life, in order to investigate the quality of fatigue fracture surface, observation of the aspect of fracture surface was conducted by using scanning electron microscope (SEM).

2. Experiment method

2.1. *Material and specimen*

The material used in this study is aluminum alloy (Al7075-T6 and Al6061-T651) whose chemical compositions refer to Table 1. The tensile test was achieved according to ASTM E8 regulation and results mechanical properties like in Table 2. The fatigue crack growth specimen was picked from the steel plate. It has a thickness of 12.5 mm and ASTM E647 CT standard specimen. The picking was done with L-T directions.[1-2]

Table 1 Chemical compositions of specimen (Al – Remainder), (wt %)

Al7075-T6	Si	Fe	Cu	Mn	Mg	Cr	Zn	Ti+Zr
	0.15	0.29	1.6	0.14	2.4	0.19	5.7	0.25
Al6061-T651	Si	Fe	Cu	Mn	Mg	Zn	Ni	Pb
	11.38	0.37	1.85	0.15	0.87	0.27	0.69	0.06

Table 2 Mechanical properties of specimen

Material	Tensile Strength [MPa]	Yield Strength [MPa]	Elongation [%]	Vikers Hardness [HV]
Al7075-T6	661	610	11	175
Al6061-T651	404	372	17	107

Table 3 Condition of shot peening

Specimen	Shot Velocity [m/sec]	Time [min]	Shot ball diameter [mm]	Arc height [mmA]
Al7075-T6 and Al6061-T651	40			0.292
	50	2	0.8	0.342
	70			0.368

2.2. *Shot peening process*

Shot peening was processed on condition such as Table 3 in high speed turbine shot peening machine to give compression residual stress in test specimen before fatigue crack growth test was done. Shot ball used is made from hard steel wire (HSW) cut at a fixed size. Diameter of shot ball is 0.8 mm and the shot ball projecting peening velocity are 40, 50 and 70 m/sec. Shot peening coverage was kept 100% in quality terms and Arc Height level was formed Arc Height condition of 0.292 mmA, 0.342 mmA and 0.368 mmA according to the shot ball projecting velocity.

2.3. *Compressive residual stress*

Compressive residual stress measurement achieved according to ASTM E830-99 regulation and the program used is American Measurements Group Company's Re-stress and H-Drill software. The compressive residual stress measurement is measured with interval 0.1 mm from surface up to 1.6 mm depth.

2.4. *Fatigue crack growth test and fatigue life test*

The equipment which is used in fatigue crack growth experiment was Servo hydraulic fatigue testing machine (MTS 810, 10 tonf), it executed repetitive tensile load in regular amplitude load method. The condition of the precrack frequency is 10 Hz, at the sinusoid and regular load amplitude inserted from a notch tip with 2 mm. Initial notch ratio of crack length a and the width W of the specimen is 0.26. The experimental condition frequency is 13 Hz, with the sinusoid and stress ratio R=0.5 executed from room temperature. The fatigue crack length measurement about under using measured COD gauges with Compliance Raw. And the fatigue test was conducted in room temperature. The test of fatigue using rounding specimen, I was testing performed according to ASTM E466-96, under constant amplitude loading. A stress ratio R=0.1 and 10 Hz frequency.

3. Results and Discussion

3.1. *Compressive residual stress*

In this experiment, selected Blind Hole method and hole depth penetrated 0.1 – 1.6 mm. Fig. 1 is showing compression residual stress value that is formed in test specimen by projecting velocity of shot ball, did by compression residual stress value formed for 0.2 mm from specimen surface according to ASTM E837-99. Al6061-T651, soft property, was evaluated compression residual stress

low than hard Al7075-T6. The effect of residual stress appeared low as day residual stress appears high in the velocity and the speed is high. Surface parts receives compressive stress and compressive stress decreases in inside. Also, receive tensile stress if depth exceeds 0.4 ~ 0.6 mm and tensile stress increased in inside. But, Al6061-T651 and Al7075-T6 were some change of value according to depth. And change of compression residual stress appeared remarkably as Al6061-T651, ductile of the material, goes to inside. These causes can know that compression remaining stress distribution by condition is increased in Al7975-T6 alloy in mechanical properties of materials and shot peening. Fig. 2 shows residual stress distribution by shot velocities. Maximum compressive residual stress was -261 MPa then optimum shot velocities were 50 m/sec (Al7075-T6). And Maximum compressive residual stress was -188 MPa then optimum shot velocities were 40 m/sec (Al6061-T651). But the compressive residual stress decreases from 50 m/sec of Al7075-T6 with 40 m/sec of Al6061-T651. I think that value of compressive residual stress decrease a case by over peening.[3, 4]
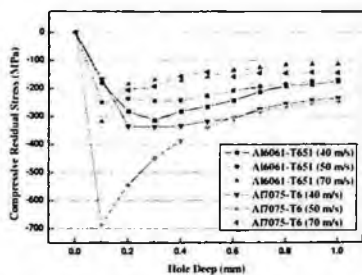

Fig. 1 Relation between hole depth and
compressive residual stress
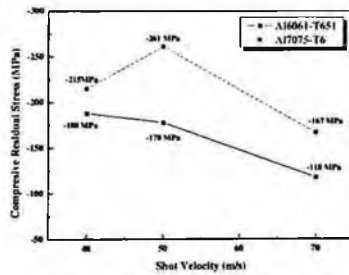
Fig. 2 Relation between shot velocity and
compressive residual stress

3.2. *Fatigue crack growth behavior*

Fig. 3 shown fatigue crack growth rate da/dN and stress intensity factor range of two materials. Al7075-T6 and Al6061-T651 two materials could represent fatigue crack growth rate that do not depend on the shot peening velocity. Thus, compressive residual stress has elastic-plastic deformation behavior at plastic region neighborhood of fatigue crack tip. Therefore, fatigue crack growth was controlled by repeat tension load and compressive load. In fatigue crack growth test, fretting is caused because random of microstructure and compressive loading, and happen crack open and close phenomenon. When is accelerated by 70 m/sec of Al7075-T6, 50 m/sec, 70 m/sec of Al6061-T651, fatigue crack growth rate was accelerated more than 50 m/sec, 40 m/sec that is optimum. But,

excessive shot peening is happened impact energy in test specimen surface by over peening, and surface compression residual stress is decreased. Therefore, fatigue crack growth rate was decreased. [5-6]

Fig. 3 Relation between stress intensity factor range and fatigue crack growth rate of Al7075 and Al6061 alloys

3.3. Fatigue life test
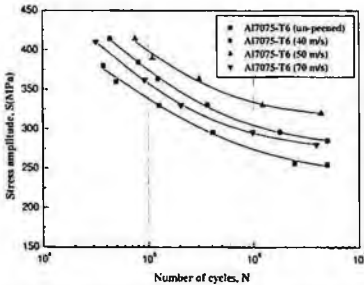
Fig. 4 S-N curves of shot peened Al7075-T6   Fig. 5 S-N curves of shot peened Al6061-T651
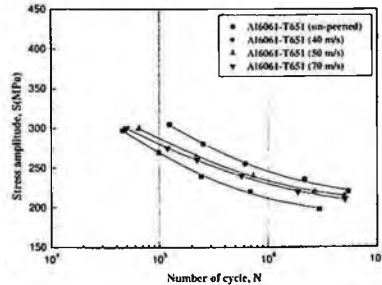
Fig. 4 and Fig. 5 are showing Al7075-T6, Al6065-T651 relationship fatigue life curved line and Al7075-T6 showing the highest fatigue strength when it is 50 m/sec, Al6061-T651 40 m/sec. But, all materials were shown phenomenon that fatigue strength drops preferably as the shot peening velocity increases. Because when has the excessive shot peening velocity, be responsible for stress concentration with serious damage on the test specimen surface and contributed in initiation and growth of crack, is thought that it is. Also, when Al7075-T6 is 40 m/sec, because thing which when it is 50 m/sec more, fatigue strength is low

is lacking compression residual stress to under peening, energy that can constrain crack growth is considered by small thing relatively. In this case of soft material such as Al6061-T651, plastic deformation acts as notch happening greatly and became origination and cause of stress concentration that accelerate growth of crack on the test specimen surface because delivered kinetic energy increases by projecting velocity of shot ball increases. As aforesaid, shot peening material contributed fatigue strength elevation effect by surface micro structure change and compression residual stress.

3.4. *Fracture surface analysis*

Fatigue fracture is generated by slip band or slip line that be occurred a part plastic deformation by repetition fatigue load. Fig. 6 shows fracture surface by the Al7075-T6 and Al6061-T651 alloy. The striation spacing is correspond repetition stress of 1 cycle. The striation spacing increases the first area as go to the end area. Also Fig. 6 shows the striation of middle area each shot velocity. Shot peening material narrower spacing than un-peening. The narrowest striation was shown 50 m/sec (Al7075-T6), 40 m/sec (6061-T651).

| Un-peening | 40 m/sec | 50 m/sec | 70 m/sec |
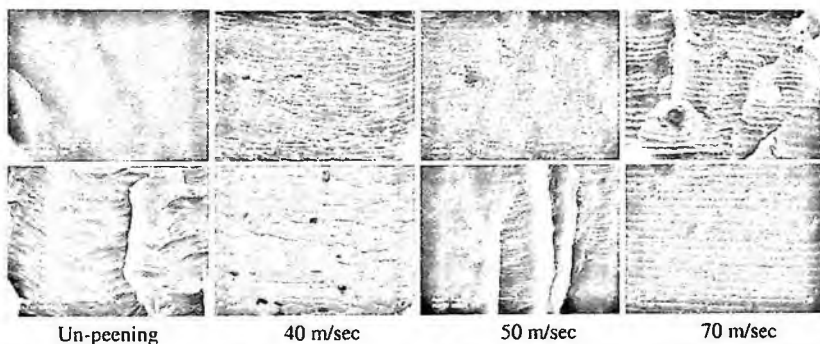
Fig. 6 SEM fractography showing fracture surface by the Al7075 (up) and Al6061 (down) alloy

Forms of fatigue fracture repeat fatigue very of according to stress concentration degree as well as size greatly change. Fracture pattern and shape relation between fracture surfaces forms exist. Fracture analysis becomes information that is influential on cause searching examination of destruction accident and when destruction progresses, accident courtesy call and analysis are available. Test specimen that do excessive shot peening with this study need cause searching examination is caused in surface parts and fatigue life is reduce. When stress concentration is big, progress crack because many crack is begun at the same time in surface parts. When is less enough to do not consider stress

concentration, initiation number of crack is few. Virgin material of low notch sensitivity cause plastic deformation in high stress of surface and crack growth progresses into inside in surface and destruction was gone in specimen surface.

Fig. 7 Relation between stress distributed and initiation fracture point by the surface hardening layer (un-peening)

Fig. 8 Relation between stress distributed and initiation fracture point by the surface hardening layer (shot peening)

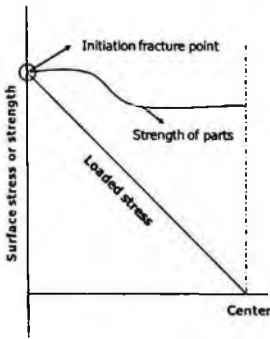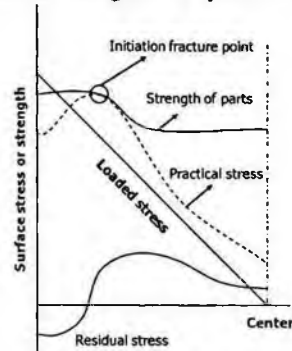Fig. 7 is schematic diagram that express fatigue crack growth initiation point of virgin material. Destruction was begun in typical surface layer that virgin material appears to general steel materials and fatigue fracture area was increased more than peening material. Fig. 8 showing that crack happens in inside because internal stress is greatened because outside stress is reduced in surface by compressing residual stress in peening materials mimetic diagram that notch sensitivity is high. Fig. 9 is fracture surface of Al6061-T651 by the virgin and peening material. When hardening layer by compression residual stress exists, because hardening strength is showing that crack initiation point appears fish-eye phenomenon that appear on inside. Also, area decrease as virgin materials widens area of last fracture surface that fatigue failure is gone, and notch is sharp in equal condition of stress and growth manner of fatigue failure was spread by fatigue fracture that have both virgin and peening materials radiation shape. And soft materials such as over shot peening condition and Al6061-T651 materials that the two sites total peening velocity is 70 m/sec provided cause that fatigue life is underrated becoming crack starting point in surface part by damage that is excessive on the surface effect notch. Virgin material of striation phenomenon is appearing clearly more than 40 m/sec compare with peening velocity 40 m/sec occasion with Al6061-T651 materials virgin and can know that size of interval great. Material increase fatigue life weakening drive force that need in fatigue failure development while take the

shot peening speed decreased sectional area of test specimen remarkably in 40 m/sec and there is section that is controlled repeated stress and it was seen that brittle striation interval increases. If striation interval is big, because crack growth rate quickened, fatigue life was under estimated. Therefore, compression residual stress effect is judged for important factor that peening measure of virgin material. Fig. 10 is showing Al7075-T6's SEM fractography. The left fractography is shown fracture pattern that Al7075-T6 is the more brittle fracture than Al6061-T651, and can know that fracture surface is flat. The middle fractography is appearing dimple on fatigue fracture surface and fast fracture parts border. Can know that these phenomenon' s grow gradually as test specimen sectional area decreases. The last fractography can see typical striation that appear from fatigue part and interval was about 0.3 μm. Crack initiation point happens in test specimen surface layer in virgin material but is, and 40 m/sec that have best fatigue strength happened crack initiation point in inside by surface residual stress effect.[7]
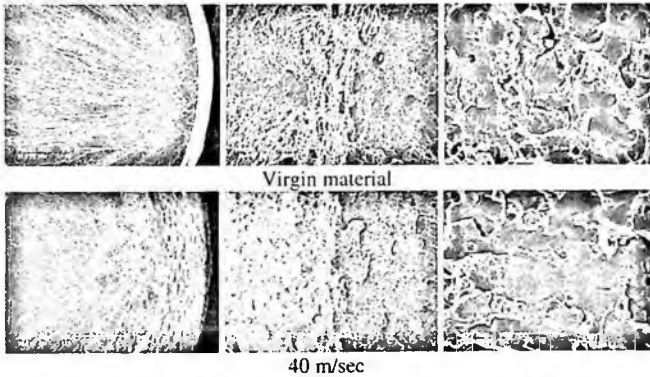

Virgin material

40 m/sec

Fig. 9 SEM fractography showing fracture surface by the Al6061-T651
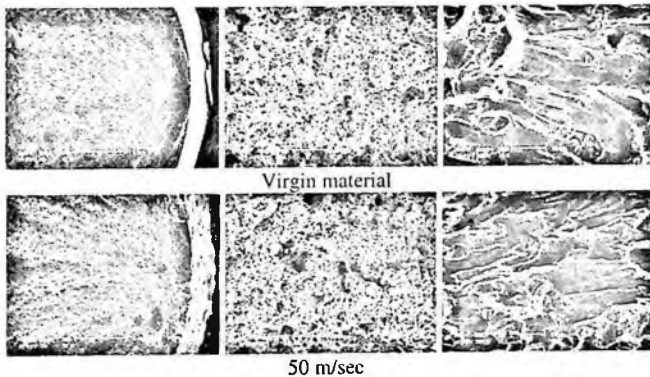

Virgin material

50 m/sec

Fig. 10 SEM fractography showing fracture surface by the Al7075-T6

Conclusion

1.In case of the Al7075-T6, Maximum compressive residual stress was -261 MPa then optimum shot velocities were 50 m/sec. In case of the Al6061-T651, Maximum compressive residual stress was -188 MPa then optimum shot velocities were 40 m/sec. But the compressive residual stress decreases on 70 m/sec (Al7075-T6) and 50, 70 m/sec (Al6061-T651) by over peening.

2.The shot peening generate compressive residual stress that delay the crack growth rate and improve fatigue life.

3.The optimum shot peening velocity condition for a fatigue life improvement was 50 m/sec (Al7075-T6) and 40 m/sec (Al6061-T651).

4.According to increase of shot velocity, the spacing of striation differs. Also shot peening material narrower spacings than un-peening. The narrowest striation was shown 40 m/sec (6061-T651), 50 m/sec (Al7075-T6).

5.When residual stress by shot peening exists in surface hardening layer, because strength of surface hardening layer is higher than outside stress, fish-eye phenomenon that crack initiation point appears on inside appears.)

Acknowledgments

References

1. ASTM E8, 1997, "Standard test method of Tension Testing of Metallic Materials," pp. 56~76.
2. ASTM Standard E647-97, 1997, "Standard Test Method for Measurement of Fatigue Crack Growth Rates," pp. 1~6.
3. J.O.Almen, J.H. Black, 1963, "Residual Stresses and Fatigue in Metals", Mc Graw, pp. 42~80.
4. W.-B. Koster, 1991, "Effect of Residual Stress on Fatigue of Structural Alloys", Practical Applications of Residual Stress Technol., Proc. of the Third Int. Conf., Indianapolis, IN, USA. 1.
5. G. S. Was, R. M. Pelloux, 1979, "The Effect of Shot Peening on the Fatigue Behavior of Alloy 7075-T6," Met. Trans 10A, 665~672.
6. O. Vohringer, 1987, "Changes in the State of the Material by Shot Peening," Shot Peening, DGM, 185.
7. L. Wanger, 1999, "Mechanical Surface Treatments on Titanium, Aluminium and Magnesium Alloys," Materials Science & Engineering A 263, 210.

A STUDY ON THE X-RAY DIFFRACTION ANALYSIS AND THE FATIGUE CRACK GROWTH BEHAVIOR FOR THE ALUMINUM ALLOYS

MANBAE LIM

*Department of Mechanical and Precision Engineering, Gyeongsang Nat'l., Univ.
Tongyoung, Gyeongnam, 650-160, Korea
mblim@gnu.ac.kr*

JIANG JUN[1], SUNCHUL HUH[2], WONJO PARK[†]

*[1]Department of Mechanical and Precision Engineering,Graduate School, Gyeongsang
Nat'l., Univ. Tongyoung, Gyeongnam, 650-160, Korea
[2]Research Center for Aircraft parts Technology,Gyeongsang Nat'l., Univ. Jinju,
Gyeongnam, 660-701, Korea
[†]Department of Mechanical and Aerospace Engineering, Gyeongsang Nat'l., Univ.
Institute of Marine Industry, Tongyoung, Gyeongnam, 650-160, Korea
[1]jiangjun442@sina.com, [2]schuh@gnu.ac.kr, [†]wjpark@gnu.ac.kr*

This study evaluated fatigue crack growth characteristics, Besides consider compressive residual stress effect and verified the most suitable shot peening velocity. Fatigue crack growth delay effect was compressive residual stress, but over peening did action projecting velocity that accelerate fatigue crack growth rate. X-ray diffraction technique according to crack length direction was applied to fatigue fractured surface. Fracture mechanics parameters could be estimated by the measurement of X-ray parameters, and the fractography observation was performed using a scanning electron microscope (SEM) for fatigue fracture surface. As the shot peening velocity increases, striation width increased. The changes in X-ray material parameters described above are directly related to the process of fatigue until the initiation of fatigue crack and X-ray diffraction pattern is thought that failure prediction with stress distribution is possible.

1. Introduction

Recently, car, shipbuilding and aircraft parts etc. are accuracy for design and manufacture, hardness and high strength are very important that it is. Fatigue life estimate is factor and that decide quality of product with nano-technology. High strength aluminum alloy characteristic are high tension strength and yield strength and corrosion resistance, toughness etc. is excellent. Therefore, high strength aluminum alloy is used widely in aircraft industry. But, can have more

---

[†] Corresponding author.

economical efficiency if solve problem that keep the most efficient material characteristic and performance, life-time using parts used present. Is achieving shot peening processing on weak part of aircraft parts back in advanced nation, and to increase fatigue life, is handling shot peening processing to parts that get fatigue damage. This study predicted the optimum projecting velocity and fatigue strength processing shot peening, and makes stress ratio fixed by projecting velocity 40 m/sec of shot ball, 50 m/sec, 70 m/sec using Al7075-T6 and Al6061-T651 material and filmed diffraction pattern to use X- ray diffraction equipment on fatigue fracture surface of Al7075-T6 and Al6061-T651. Analyze stress distribution in diffraction pattern observed fracture surface with scanning electron microscope.

2. Experimental and method

2.1. *Material and test specimen*

The material used in this study is Al7075-T6 and Al6061-T651, and Table 1 is showing chemical compositions of material. The tension test achieved according to ASTM E8 regulation, and Table 2 is showing mechanical properties of material. Fatigue crack growth test specimen is ASTM E647 CT type specimen and manufactured to L-T direction.[1, 2]

Table 1 Chemical compositions of specimen (Al – Remainder), (wt %)

Al7075-T6	Si	Fe	Cu	Mn	Mg	Cr	Zn	Ti+Zr
	0.15	0.29	1.6	0.14	2.4	0.19	5.7	0.25
Al6061-T651	Si	Fe	Cu	Mn	Mg	Zn	Ni	Pb
	11.38	0.37	1.85	0.15	0.87	0.27	0.69	0.06

Table 2 Mechanical properties of specimen (Table 3 – Condition of shot peening

Material	Tensile Strength [MPa]	Yield Strength [MPa]	Elongation [%]	Vikers Hardness [HV]
Al7075-T6	661	610	11	175
Al6061-T651	404	372	17	107

2.2. *Shot peening process*

Before fatigue crack growth rate test, project shot ball on the CT test specimen surface and processed shot peening. The shot ball used cut wire shot ball that make cutting hard steel wire (HSW) to fixed size, and diameter of shot ball did by 0.8 mm. Coverage kept 100% in experimental condition, and Table 3 is showing shot peening condition by the shot ball projecting velocity.

Table 3 Condition of shot peening

Specimen	Shot Velocity [m/sec]	Time [min]	Shot ball diameter [mm]	Arc height [mmA]
Al7075-T6	40			0.292
and	50	2	0.8	0.342
Al6061-T651	70			0.368

2.3. Compressive residual stress

Compression residual stress measurement achieved according to regulation of ASTM E830-99. Analysis used American Measurements Group Company's Re-stress and H-Drill software. Residual stress measurement depth measured to 1.6mm from surface to 0.1 mm interval.

2.4. Fatigue crack growth rate experimental

The fatigues testing machine is MTS 810, and fatigue crack condition is 10Hz, sine wave and given load amplitude, and crack length is 2 mm and a/W=0.26. and experimental condition achieved at room temperature by frequency 13Hz, sine wave, stress ratio R = 0.3, and crack length measurement uses that is COD gage and measured by compliance method.

2.5. X-ray diffraction pattern and fracture surface analysis

The striation measurement analyzed striation direction and interval moving test specimen central part. Figure 1 shown fatigue fracture surface schematic diagram to film diffraction pattern, and that is X-ray parameter. Irradiation area did in ⌀2 mm's circle, and, investigated stress distribution by crack progress direction. Figure 2 is X-ray diffraction equipment GADDS XRD System to analyze diffraction pattern, and Table 4 shown X- ray diffraction condition.

Table 4 X-ray diffraction condition for Al7075-T6 and Al6061-T651 alloy

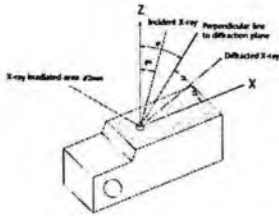| Test condition	Characteristic X-ray	Diffraction plane	Diffraction angle(2θ)	Tube voltage	Tube current
Parallel beam method	$Cu\text{-}K_\alpha$	(311)	45°	40KV	40mA
Test condition	Divergence angle	Scanning speed	Time constant	Distance from specimen to film	Plane distance
Parallel beam method	0.5°	0.5°/min	20sec	15mm	1.3497Å

Fig. 1 Schematic illustration of X-ray irradiated area on fatigue fracture surface

Fig. 2 Overview of X-ray diffraction Experimental result and discussion

3. Experimental result and discussion

3.1. *Compressive residual stress*

The residual stress measurement of Hole Drilling method is through hole method and Blind hole method. This examination selected Blind Hole method, and depth measured to 1.0mm to 0.1 mm interval. Figure 3 shown compression residual stress value and that is formed in test specimen by projecting velocity of shot ball. The compression residual stress value was based to ASTM E837-99 regulation. Effect of residual stress by two materials Al6061-T651 than Al7075-T6 compression residual stress low evaluate, and Compression residual stress distribution was increased in mechanical properties of material and shot peening condition by Al7075 -T6.
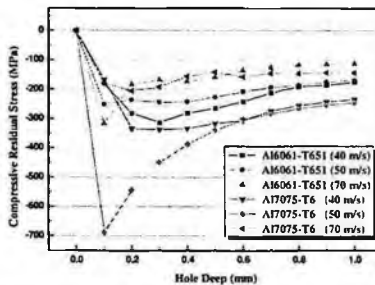
Fig. 3 Relation between hole depth and compressive residual stress

3.2. *Fatigue crack growth behavior*

Figure 4 shown fatigue crack growth rate da/dN and stress intensity factor range of two materials. Al7075-T6 and Al6061-T651 two materials could represent fatigue crack growth rate that do not depend on the shot peening velocity. Thus, compressive residual stress has elastic-plastic deformation behavior at plastic region neighborhood of fatigue crack tip. Therefore, fatigue

crack growth was controlled by repeat tension load and compressive load. In fatigue crack growth test, fretting is caused because random of microstructure and compressive loading, and happen crack open and close phenomenon. When is accelerated by 70 m/sec of Al7075-T6, 50 m/sec, 70 m/sec of Al6061-T651, fatigue crack growth rate was accelerated more than 50 m/sec, 40 m/sec that is optimum. But, excessive shot peening is happened impact energy in test specimen surface by over peening, and surface compression residual stress is decreased. Therefore, fatigue crack growth rate was decreased.
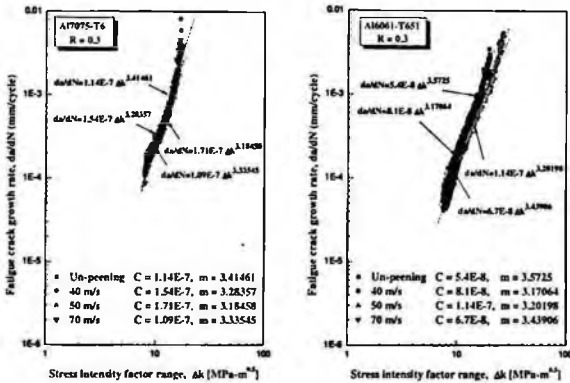

Fig. 4 Relation between stress intensity factor range and fatigue crack growth rate of Al7075-T6 and Al6061-T651 alloy

3.3. *X-ray diffraction pattern and fracture surface analysis*

If repeat fatigue load interacts, the fracture surface occurs plastic deformation, and in surface, unevenness by slip band and slip line occurs, and this apply to crack source. The fatigue crack is formed according to crystal lattice plane, and microscopic striation spacing is corresponded with repeated stress of 1 cycle. And spacing is microscopic crack growth rate, and striation spacing mean value agrees well with crack growth rate da/dN that measure as macroscopic. As a consequence, the striation spacing and the macroscopic crack growth rate agree well in the 10-4-10-3 um/cycle.[3] Figure 5 is showing the SEM that observes fracture surface behavior of plane strain part in the test specimen. In over-peening velocity 70 m/sec, striation phenomenon observed more definitely than other experimental condition. This is phenomenon that can see from ductile material or high strength. Also, if striation spacing is longer, it means that predicted shot fatigue life and the striation spacing depended on repeated stress level, frequency, stress concentration factors and shot peening velocity. Therefore, because of effect of compressive residual stress, shot peening

748

material was decreased drive force more than un-peening material, it is necessary in fatigue crack propagation. Finally, we think that fatigue life increase is the factors and among various factors, can know merit of shot peening effect on the surface.
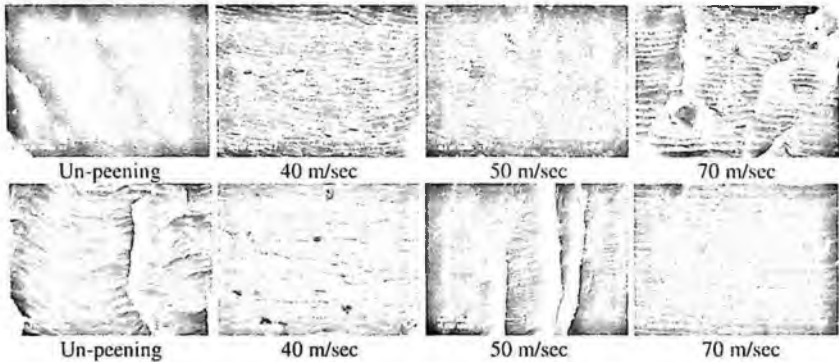

Fig. 5 SEM fractography showing fracture surface by the Al7075(up) and Al6061(down) alloy

Figure 6 is diffraction pattern that is showing diffraction pattern and distribution of stress about crystal lattice plane (311) of Al6061-T651 fatigue crack growth test specimen. Polycrystal diffraction pattern that crystal orientation becomes anarchically as can see from picture becomes in equal circle. In this study, used material leans to direction that crystal face is particular. Therefore, diffraction pattern was not equal circle, and was seen by arc shape.[4] Outside circle is diffraction pattern by characteristic X- ray Cr- Kα1 and inside circle is showing separation each other by diffraction pattern by Cr-Kα2. According as crack propagation rate increases, the circular diffraction pattern was scattered to radius and tangential. Figure 7 is showing diffraction pattern of Al7075-T6 alloy and diffraction pattern phenomenon distributed to radius and tangential more than Al6061-T651 alloy was not seen. This cause is superior to do site mechanical properties of matter and is because crack propagation rate was gone fast. Therefore, is thought that affect in crystal lattice transformation that repeated stress that contribute in diffraction pattern if crack propagation rate is slow has enough time. Therefore, in fracture analysis is thought that damage analysis about fatigue crack is available if use striation's width and diffraction pattern's stress distribution. But, consider well and should applies X-ray parameter in case it is texture. Figure 8 is showing pole figures to analyze texture of Al6061-T651 alloy and Texture used diffraction intensity that use Cu Kα radiation. Basal pole does not form texture of tangential and texture was seen to

radius. This texture structure is uncertain reproduction in residual stress measurement.
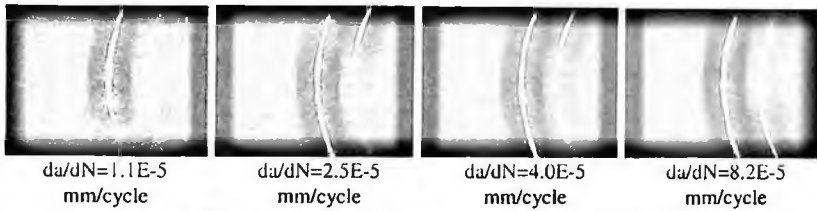

| da/dN=1.1E-5 mm/cycle | da/dN=2.5E-5 mm/cycle | da/dN=4.0E-5 mm/cycle | da/dN=8.2E-5 mm/cycle |

Fig. 6 X-ray diffraction patterns for fracture surface by the Al6061-T651 alloy

| da/dN=1.7E-4 mm/cycle | da/dN=2.1E-4 mm/cycle | da/dN=2.9E-4 mm/cycle | da/dN=2.1E-4 mm/cycle |
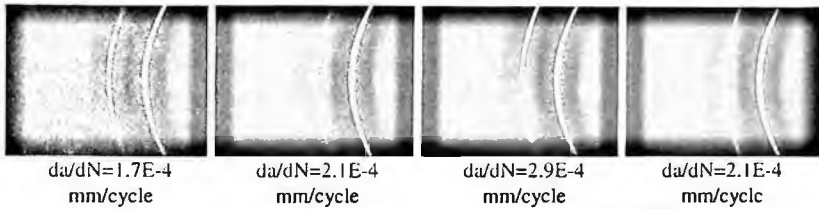
Fig. 7 X-ray diffraction patterns for fracture surface by the Al7075-T6 alloy

Two-Dimension	Third-Dimension	Two-Dimension	Third_Dimension
Al7075-T6		Al6061-T651	
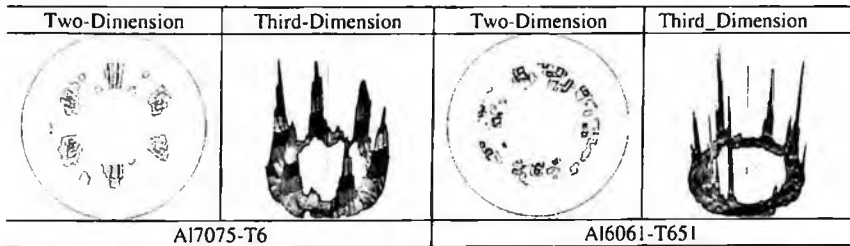
Fig. 8 Direct pole figure for diffraction plane (311) of specimen surface by the Al7075-T6 and Al6061-T651 alloy

In the case of aluminum alloy, when process board, can know that direction of crystal structure is strong texture by cold rolling, and is appearing as peak intensity of diffraction profile analysis is small. Specially, an aluminum alloy is large crystallization grain size than general steel materials, and it is that contribute in diffraction per unit area less very. Therefore, using residual stress, it can be trouble in accuracy and integrity that texture structure uses in fracture mechanics analysis. Finally, the damage analysis of fatigue fracture surface is available if use parameter such as X- ray diffraction pattern and pole figure.

4. Conclusion

In this study, Al7075-T6 and Al6061-T651 material used to aircraft parts estimates optimum shot peening velocity through a fatigue crack growth experimental and analyzes X-ray diffraction pattern and fracture surface analysis and gets following conclusion.

1. Effect of residual stress by the shot peening velocity appeared, in low velocity compressive residual stress appears high in the velocity.
2. The shot peening material was decreased drive force more than un-peening material, it is necessary in fatigue crack propagation.
3. Most optimum shot peening velocity condition for fatigue life elevation was in the Al7075-T6 of 50 m/sec and the Al6061-T651 of 40 m/sec
4. Using residual stress, it can be problem in accuracy and integrity that texture structure uses in fracture mechanics analysis. But, we are thinking that useful damage analysis is available if use parameter such as X- ray diffraction pattern and pole figure.

Acknowledgments

References

1. ASTM E8, 1997, "Standard test method of Tension Testing of Metallic Materials," pp. 56~76.
2. ASTM Standard E647-97, 1997, "Standard Test Method for Measurement of Fatigue Crack Growth Rates," pp. 1~6.
3. Zenjiro Yajima, Yukio Hirose and Keisuke Tanaka, 1983, "X-ray Diffraction Observation of Fracture Surface of Ductile Cast Iron," Adv. X-ray Anal. 26, pp. 291~298.
4. Yuji Sekita, Shotaro Kodama, Hiroshi Misawa, 1983, "X-ray Fractography on Fatigue Fracture Surface," JSMS, Vol. 32, No. 354, pp. 258~263.

A STUDY ON LASER SURFACE HARDENING OF TOOL STEEL USING OPTICAL PYROMETRY

YOUNG-TAE YOO

Department of Mechatronics Engineering, Chosun University,
375 Seosuk-dong Dong-gu Gwang-ju, 501-759, Korea

HO-JUN SHIN

Department of Precision Mechanical Engineering, Chosun University,
375 Seosuk-dong Dong-gu Gwang-ju, 501-759, Korea (Corresponding Author)

The objective of this research work is to investigate the influence of the process parameters, such as surface tempature, beam travel speed and defocused spot position, on the characteristics of laser surface hardening for the case of tool steel. Laser surface hardening technology is a method in which the high power laser beam quickly irradiates the specimens surface to increase rapidly the specimen surface temperature that is higher than the phase-transformation point and lower than the melting point. In addition, the heat input capacity at the surface determines the temperature profile and the depth of hardening. By applying optimum process parameters, a surface hardening layer can be modified to give a wide variety of properties. Their value depends on temperature field distribution in the specimen resulting from the specimen surface absorbing laser energy. We measure the surface temperature change by the infrared pyrometer when the laser beam irradiates on the specimen surface. The Nd:YAG laser with a continuous wave(CW) is selected as the heat source.

1. Introduction

Surface hardening using laser beam use the characteristics of self-quenching that cool rapidly into inside of materials without using cooling water unlike general surface hardening[1-2]. When the energy density of the laser beam is high enough, heat is transferred to the inner part of the material and accumulated on its surface at the rate faster than the rate of heat loss, causing the temperature to rise instantaneously. While the thin layer of the surface reaches the Austenitizing temperature within a very short period of time, the temperature of the part core does not rise but stays cool. As a result, fine and uniform structure is formed on the material surface, to improve mechanical characteristics of the material. However, as the laser surface hardening uses high-density energy heat source, it is difficult to control process parameters. For this reason, it has been brought to the fore that it is impossible to estimate and measure in real time the

quality of thermally processed parts in controlling the laser heat source. Most of the preceding researchers have controlled the optimum laser surface hardening process through the empirical and the numerical analyses [3-5]. The purpose of this study is to present a method to estimate and measure in real time the optimum surface hardening process by empirically analyzing the surface temperature profile during the laser surface hardening [6]. In general, through real-time monitoring for estimation and process monitoring, it is possible to detect signals generated during the interaction between the laser beam and the material, such as hardening shape, temperature, plasma, and reflected light. As the surface heat source of the material formed by the laser beam dominates temperature change, it is possible to derive the optimum process from temperature measurement. In particular, the laser surface hardening heats the metal surface to the temperature between transformation point and melting point by the heat source from the laser beam irradiated onto the surface. When the laser beam is removed afterwards, the heat on the surface layer is transferred into fine continuous structure, rapidly cooling down the heated area. In this study, the temperature profile characteristic during the laser surface hardening of SKD61 and SCM4 steel used as the injection mold materials is examined.

2. Experimental Setup and Method

CW Nd:YAG laser used for this study had the wavelength of $1.06 \mu m$ and the maximum power of 2.8kW. Figure 1 is diagram of experimental set up. When the laser beam was irradiated onto the specimen surface, the surface temperature was measured in real time using the infrared pyrometer (Impac Inc., Germany). As the laser surface hardening might generate spatter resulting in the damage of the pyrometer, a filter was fixed to the optical head during the experiment. The infrared pyrometer specification is shown in Figure 2 Chemical compositions of the specimen used for this study are shown in Table 1.

As the specimen should be self-quenched, it should have a certain amount of critical mass and thickness. For this reason, the specimen size was fixed as $100 \times 50 \times 10$mm. In order to investigate the surface temperature characteristic, the surface hardness property of each temperature profile was analyzed.

Table 1. Chemical composition of specimen (wt.%).

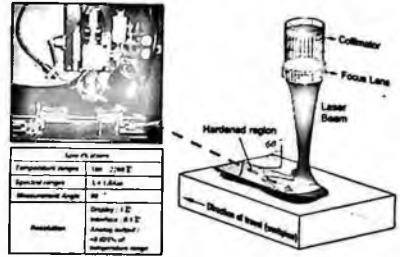|	C	Si	Mn	P	S	Cr	Mo	V	Ni
SKD61	0.41	1.12	0.41	0.02	0.01	5.2	1.23	1.10	1.1
SCM4	0.83	0.25	0.75	0.03	0.03	0.09~1.2	0.25	-	-

Fig. 1. Experimental Set-up.

Fig. 2. Measurement of surface temperature.

3. Monitoring of Surface Temperature change by Laser Surface Hardening

In this research works, the correlation between the surface bead shape and the surface temperature was examined using the infrared pyrometer when the laser beam was irradiated onto the specimen. Figure 3 shows the surface temperature profile of SKD61 steel during laser surface hardening. Measurement angle, sense response time, temperature range, and analog output of the infrared pyrometer were maintained constantly as 60, 0.01sec, 500 ~ 2200, and 0-20mA respectively. The infrared temperature sensor should be maintained a certain focal position of the infrared range beam on the measurement location, and the one used for this research work had the focal position of 200mm. The temperature around the specimen surface rose considerably high above 1100℃ in general while the laser surface hardening was made progress. Such high temperature was reached when the structure temperature rose to Austenitizing temperature as the laser beam was irradiated locally on the material surface. However, as the material surface was rapidly cooled immediately after the laser beam was removed, the grain growth was minimized even though the Austenitizing temperature by the laser beam was high. This phenomenon varies considerably with the heat input, one of the laser process parameters. As a general result of the experiment, it was shown that when the laser beam travel speed was fast, there was no sufficient time to transmit heat to the inner part of the material and thus the surface temperature profile was low. The hardened surface bead also revealed that there was a distinct correlation between the surface bead and the surface temperature profile. When the laser beam travel speed was 0.8m/min, the transaction time between the laser beam and the material was 0.12sec and the average surface temperature was measured as about 650℃. It was because the input heat was not enough when the laser beam was irradiated onto the specimen and thus the temperature at the material surface did not rise above A_3 transformation temperature.
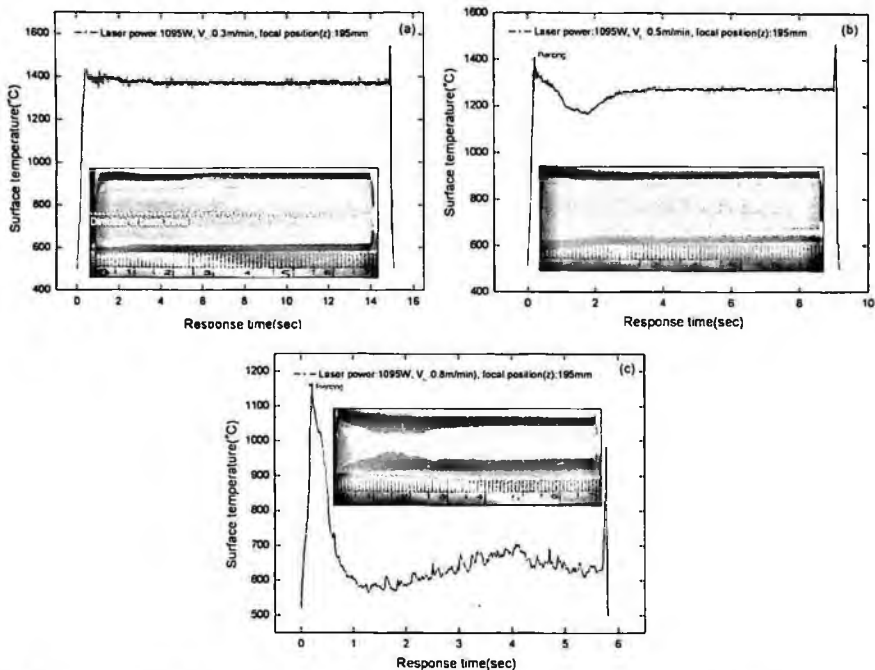
Fig. 3. As the result of surface temperature monitoring by laser surface hardening (SKD61).

When the heating rate of the laser beam is too fast, the surface temperature cannot rise to the Austenitizing temperature and as a result it is difficult for carbon redistribution by diffusion to occur. Therefore, if carbide is not fully dissolved, the Austenitizing structure of which grain is inhomogeneous and whose grain growth is controlled is made, so that the hardness of the structure cannot be high. On the contrary, when the laser beam travel speed was 0.3m/min, the average temperature was about 1400℃. It means that when the laser beam travel speed was reduced by 2.6 times, the surface temperature increased by 2.15 times. As the time of correlation between the laser beam and the specimen was 0.32sec which was good enough for the surface temperature to rise to Austenitizing temperature above A_3 transformation temperature, the surface temperature profile and the bead shape became homogeneous. Therefore, it is an important variation for the laser surface hardening to raise the surface temperature steadily up to Austenitizing temperature and then let the laser beam travel homogeneously at a steady speed. In Figure 3(c), it is shown that when the laser beam travel speed was 0.8m/min the initial temperature was high. It occurred because of the piercing time to let the laser beam move slowly to be effectively absorbed onto the specimen surface. It is a physical property between
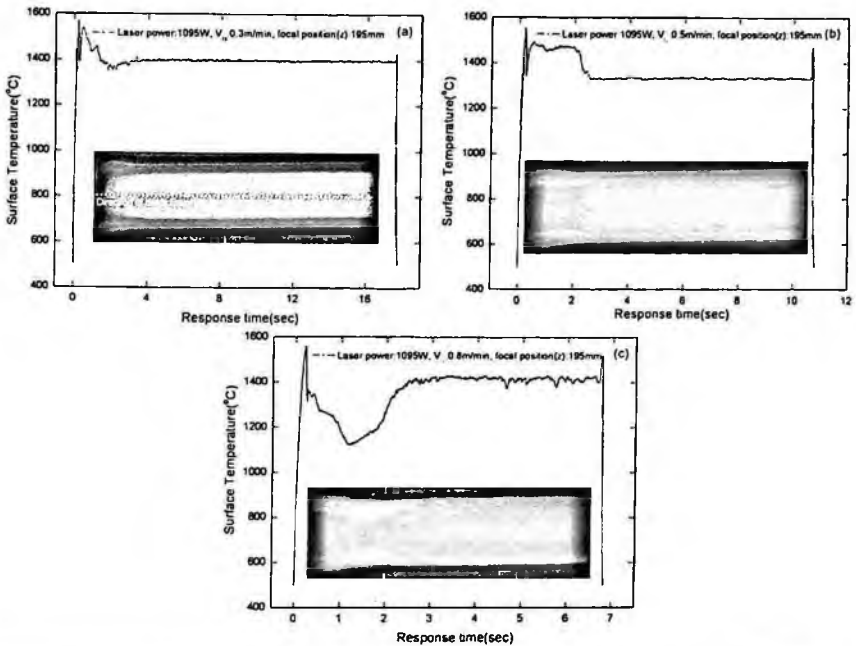
Fig. 4. As the result of surface temperature profile monitoring by laser surface hardening(SCM4).

the laser beam and the metal, by which the laser beam in the infrared area is reflected mostly on the metal surface. Concentrating the laser beam in order to reduce the reflectivity in the early state is called "piercing." In this study, the piercing time was set as 1 second. After the piercing time was over, the laser beam was transferred. When the laser beam travel speed was 0.5m/min and 0.8m/min, the heat input was rapidly transferred to the inner part of the metal, resulting in temporary temperature drop as a momentary excessive phenomenon.

On the contrary, when the laser beam travel speed was 0.3m/min, the heat input was increased and the excessive phenomenon by piercing did not happen, forming homogeneous hardened surface. Based on this result, it was found that when the heat input was constant during the piercing time, the momentary excessive phenomenon did not occur but homogeneous hardening bead and hardness distribution could be obtained. As shown in Figure 4, when SCM4 steel was subject to laser surface hardening, the surface temperature profile was 1400 ℃. The SCM4 steel had similar composition to that of SKD61 steel. For the experiment, the process parameters of the SCM4 were set the same as those of SKD61 for the purpose of comparison. When the laser beam was irradiated on to the specimen surface with the heat input changed by changing the laser beam

travel speed, the temperature profile of the specimen shows the initial excessive phenomenon, similar to that of SKD61. When the laser beam was irradiated at the travel speed of 0.8m/min, its travel speed got faster after piercing and thus the temperature of the specimen dropped temporarily down to 1100℃ due to the heat transfer to the inner part of the specimen and then rose up to the laser surface hardening temperature of 1400℃. When the laser beam travel speed was set as 0.5m/min, there was a section in the early stage where 1500℃ was kept for 2 seconds, which appeared the same during several repeated experiments. Figure 4(a) shows that when the laser beam travel speed was 0.3m/min, the temperature of the specimen rose rapidly during the piercing period to increase the initial laser beam absorption rate, transferring the heat to the inner part of the specimen and maintaining constant temperature. Unlike SKD61 steel, this result can explain the cooling phenomenon shown in Figure 4(c) by heat transfer to the inner part of the specimen when the laser beam was irradiated at a fast speed and the initial high temperature caused by large amount of heat input at a slow laser beam travel speed. However, the surface temperature profile made when the laser beam travel speed was 0.5m/min still needs to be studied more.

4. Conclusion

For the mold steel used in the mold industry as the specimen, the relationship among surface temperature, surface bead shape, and hardness profile of the surface hardened by the laser beam was examined using the infrared pyrometer. As a result of the experiment, it was shown that the surface temperature, surface bead shape, and hardness profile of the hardened surface were very closely related. So, it is thought that the laser surface hardening is useful for monitoring and controlling the hardening quality in real time and thus can be used as a control factor to maintain uniform hardened width.

References

1. T. M. Yue, L. J. Yan and C. P. Chan, *Applied Surface Science*. **252**, 5026 (2006).
2. Q. B. Wang, M. J. Chao, K. Yang, B. Yuan and E. J. Liang, *Heat Treatment of Metals(China)*. **30**, 81(2005).
3. Y. S. Tian, C. Z. Chen, D. Y. Wang and T. Q. Lei, *Heat Treatment of Metals(China)* **30**, 29(2005).
4. R. Vilar, R. Colaco and A. Almeida, *Optical and Quantum Electronics* **27**, 1273(1995).
5. E. H. John, G. K. Michelle and L. M. Angela, *Engineering Failure Analysis,* **13**, 1397(2006).
6. M. Kulla, *Applied Surface Science,* **236**, 98(2004).

THE EFFECT OF NIOBIUM ACCORDING TO SOLUTION ANNEALING AND AGE HARDENING OF HIGH STRENGTH STEEL

BYUNG HUI CHOI

Department of Mechanical Engineering, Graduate School, Chosun University, Gwangju, 501-750, Korea

KYUNG CHEUN JANG

Gwangju Research Center, Korea Institute of Industrial Technology, Gwangju, 506-824, Korea

BYUNG KI CHOI[†]

Department of Mechanical Engineering, Chosun University, Gwangju, 501-750, Korea, bkchoi@chosun.ac.kr

It is very important to study and develop ultra strong maraging steel which is metal having high tensile strength and good impact toughness and which is excellent in formability, workability, corrosion resistance, high temperature strength, weldability and the like. In this study, to the basic chemical composition, Nb(Niobium) is added which is high corrosion-resistance and heat-resistant as a heat resisting alloy with sufficient malleability and ductility to produce the maraging steel. The maraging steel is taken heat treatment under the general condition of the solution annealing and age hardening. The mechanical properties according to the content of Nb are observed. The results, Equally in all conditions, strength was increased significantly for 1 hour age hardening after solution annealing and it showed the trend of the increase of strength as the aging time was increased. The fatigue life of solution-annealed specimen is decreased by the content of Nb.

Keywords: Nb(Niobium); Solution annealing; age hardening; Maraging steel.

1. Introduction

With industrial development, highly reliable materials of high strength and high toughness are increasingly demanded. In particular, steel material has been used as the most important material that is considered significantly important for the safety of automobiles. Therefore, functionality and reliability considering

---

mechanical properties and fatigue fractures, etc. of each component of a automobile is a very important part for improving safety.

High strength steel is applicable to frames, crossmembers, impact bars, front hoods, trunk lids, etc. that require strength. Application of ultra high strength steel of more strength is continuously increasing. It is very important to study and develop ultra strong maraging steel which is metal having high tensile strength and good impact toughness and which is excellent in formability, workability, corrosion resistance, high temperature strength, weldability and the like. The name of maraging steel is originated in that high strength is obtained by age hardening martensite. Since precipitation-hardened alloying elements of Co, Mo, Ti, Al and the like are used at the Fe-Ni martensite of extra low carbon ($C \leq 0.03\%$), it is enhanced by precipitation of inter-metal compounds through age hardening [1-6].

In this study, to the basic chemical composition, Nb(Niobium)[7-8] is added which is high corrosion-resistance and heat-resistant as a heat resisting alloy with sufficient malleability and ductility to produce the maraging steel. The maraging steel is taken heat treatment under the general condition of the solution annealing and age hardening. The mechanical properties according to the content of Nb are observed.

2. Experimental Method

In this paper, ingots were manufactured using VIM after adding 0.00%, 0.03% and 0.06% of Nb respectively, which is known to be effective in refining grains, into 18% maraging steel. The Capacity of VIM was 30kg, heat temperature 1,650°C, degree of vacuum 10^{-3}Torr and melting time 45min/charge.

And after hot rolling the manufactured ingots, the most common solution annealing was carried out for 1 hour at 815°C and age hardening was carried out in three ways at 455°C, 482°C and 510°C based on ±30°C of general condition of 480°C. In addition, at each age hardening temperature, maintenance time was increased to 1 hour, 2 hours, 4 hours, and 8 hours respectively. And age hardening is performed the salt bath with 48%KNO$_3$ and 52%NaNO$_3$. Through this process, the test of tensile and fatigue performed to investigate the effect of the maraging steel when Nb content, solution annealing and age hardening condition is applied.

Table 1 shows the chemical compositions of manufactured ingot.

Table 1. Chemical composition of steels.(wt.%)

Steels	Ni	Co	Mo	Ti
Standard	18.00	8.50	5.00	0.40
0.00%Nb	18.03	8.42	4.99	0.41
0.03%Nb	17.96	8.39	4.94	0.41
0.06%Nb	17.98	8.43	4.96	0.40

3. Results and Discussion

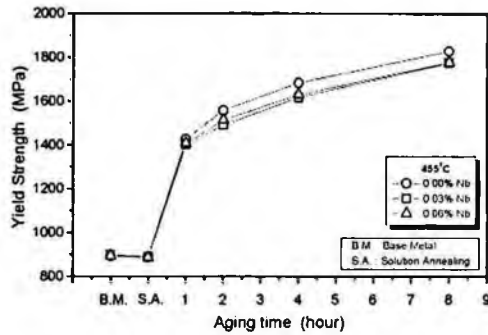### 3.1. *Effects on the strength*

Fig. 1 is graphs indicating per aging temperature for examining the effects of addition of Nb and heat treatment condition on strength.

The effect of addition of Nb on strength as a whole, yield strength showed a little lower for specimens with solution annealing than the base metals but there was no significant difference. In addition, equally in all conditions, strength was increased significantly for 1 hour ageing after solution annealing and it showed the trend of the increase of strength as the ageing time was increased but that increase rate was significantly reduced as the ageing temperature was higher but it showed almost same strength after 2 hours in case of ageing at 510℃ and at 8 hours, the strength was rather decreased. In addition, up to 1 ~ 4 hours of ageing, strength was increased in order of precedence of 455℃, 482℃, and 510℃ as the ageing temperature became higher but the difference was significantly reduced and showed almost same strength during ageing for 8 hours.

These causes are in compliance with the results that, in general, as ageing temperature was higher, ageing time is reduced and when aging for a long time at high temperature, strength is rather reduced. In addition, reviewing the effects of addition of Nb, in case of aging at 455℃, strength of the base metals without content of Nb was all superior than specimens containing addition of Nb in all aging times but almost similar strength was shown at 482℃ and 510℃. And after 1 hour aging, changes of strength was rapidly deteriorated and showed almost nor difference between 4 hours aging and 8 hours aging. While at 510℃, in case of aging for 8 hours, it showed lower strength than other specimens with the same conditions and such cause is analyzed that it is due to over aging during aging for a long time at high temperature.

Summarizing the effects of Nb content and aging condition on strength to find out specimen with the most excellent strength, the highest strength was in
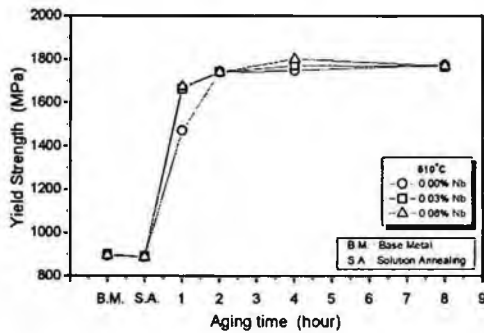
case of aging specimen with 0.06%Nb for 8 hours at 482 ℃ and it showed that strength was increased by more than approximately two times of the base metals.

(a) 455 ℃
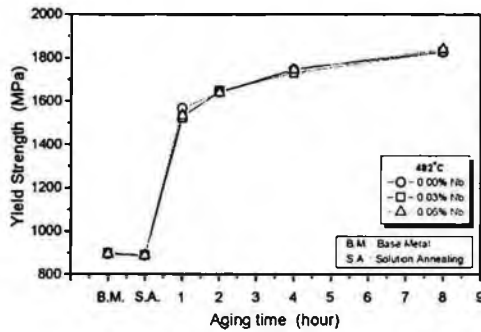
(b) 482 ℃

(c) 510 ℃

Fig. 1. Effect of Nb content and age hardening on strength.

3.2. *Effects on the fatigue life*

Fig. 2 is a line plot for a base metal and a specimen solution-annealed at 815℃ for 1 hour and represents the relation between the content of Nb and the number of cycles.

With respect to fatigue life of base metal, the specimen of 0.03%Nb and 0.06%Nb showed similar results and had about 4% longer life than the fatigue life of the specimen of 0.00%Nb without Nb. Therefore, in case of base metal, adding Nb improves the fatigue life, but did not significantly change the fatigue life depending on the changes in the content of Nb. And with respect to solution annealing, the specimen of 0.00%Nb without Nb showed the longest fatigue life, and fatigue life decreased in order of the specimen of 0.03%Nb and then 0.06%Nb. Therefore, it is considered that adding Nb decreases the fatigue life in solution annealing.

As a result, comparing the fatigue life between the specimen solution-annealed at 815℃ for 1 hour and the base metal of non-heat treatment, the fatigue life of the specimen containing Nb was longer than the specimen of 0.00%Nb in the base metal. However, in the solution-annealed specimen, fatigue life decreased depending on the amount of added Nb. Therefore, with respect to solution annealing, fatigue life decreased as the amount of Nb increased to 0.03% and 0.06%.
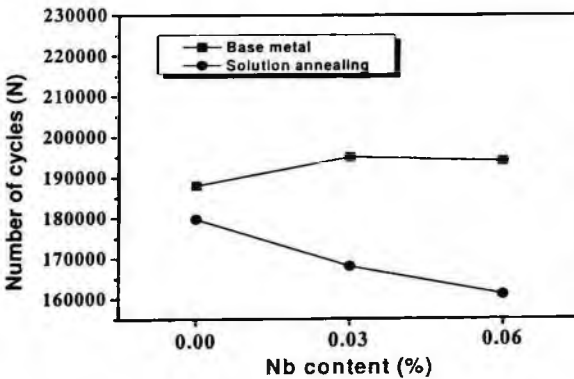

Fig. 2. Effect of Nb content on fatigue life for base metal and solution annealing.

762

4. Conclusion

In this paper, the effect of niobium according to solution annealing and age hardening of high strength steel is studied.

Strength showed a little lower for specimens with solution annealing than the base materials but there was no significant difference. In addition, equally in all conditions, strength was increased significantly for 1 hour age hardening after solution annealing and it showed the trend of the increase of strength as the aging time was increased. Condition of the most excellent yield strength was the case of aging of 0.06% Nb specimen for 8 hours at 482 ℃ and the strength was increased by more than approximately two times of the base metal.

With respect to fatigue life, the specimen of 0.03%Nb and 0.06%Nb showed similar results and had about 4% longer life than the fatigue life of the specimen of 0.00%Nb without Nb. Therefore, in case of base metal, adding Nb improves the fatigue life, but did not significantly change the fatigue life depending on the changes in the content of Nb. With respect to solution annealing, the specimen of 0.00%Nb without Nb showed the longest fatigue life, and fatigue life decreased in order of the specimen of 0.03%Nb and then 0.06%Nb. Therefore, it is considered that adding Nb decreases the fatigue life in solution annealing.

References

[1] W. Y. Kim, T. Hisao, M. S. Kim and H. Shuji: *Mater. Sci. Engin.*, A346, 65(2003).
[2] L. T. Shiang and C. M. Wayman: Published in *Metallography 21*, 399(423), 529(1998).
[3] K. Stiller, M. Hattestrand and F. Danoix: *Acta Materialia*, 46(17), 6063(1998).
[4] Y. H. Keyang, Q. Wenshen and S. Guoyue: *Materials Letters 56*, 763(2002).
[5] K. Nagayama, T. Terasaki, K. Tanaka, F. D. Fischer, T. Antretter, G. Cailletaud and F. Azzouz: : *Mater. Sci. Engin.* A, 308(1-2), 25(2001).
[6] K. Hussain, A. Tauqir and A. Q. Khan: *Inter. journal of Fatigue*, 21(2), 163(1999).
[7] J. H. Lee, S. H. Hong and K. S. Lee: *Mater. Research Society*, 9(7), 740(1999)
[8] S. W. Lee and E.Y. Joo: *Journal of the KSHT*, 13(5), 346(2000)

A STUDY ON THE SUPERCOOLING CHARACTERISTICS OF TMA-WATER CLATHRATE COMPOUND AS LOW TEMPERATURE LATENT HEAT STORAGE MATERIAL

CHANG OH KIM[1]

Department of Mechanical Design Engineering, Graduate School, Chosun University, #375 Seosuk-dong, Gwangju, 501-759, Republic of Korea

NAK KYU CHUNG[2†], JIN HEUNG KIM[3]
[2]Department of Mechanical Design Engineering, Chosun University, #375 Seosuk-dong, Gwangju, 501-759, Republic of Korea
[3]Department of Mechanical Engineering, Chosun University, #375 Seosuk-dong, Gwangju, 501-759, Republic of Korea

Materials that can store low temperature latent heat are organic/inorganic chemicals, eutectic salt system and clathrate compounds. A clathrate compound is the material that host (water; H_2O) molecule in hydrogen bond forms cage and guest (Gas) molecule is included into it and combined. Crystallization of hydrate is generated at higher temperature than that of ice from pure water. And physical properties according to temperature are stable and congruent melting phenomenon is occurred without phase separation and it has relatively high latent heat. But clathrate compound still has supercooling problem occurred in the course of phase change and supercooling should be minimized because it affects efficiency of equipment very much. Therefore, various studies on additives to restrain this or heat storage methods are needed. This study was investigated the cooling characteristics of the TMA-water clathrate compound as a low temperature latent heat storage material. And additive was added to TMA-water clathrate compound and its supercooling restrain effect was studied experimentally.

1. Instruction

Low temperature latent heat storage systems are supplied more and more so that power load in the daytime due to refrigeration demand in the summer is moved into the nighttime and the equalization of the whole power load. However, in the case of ice storage systems that water is used as low temperature latent heat storage material, refrigerator capacity is increased and COP (performance factor) is decreased because the refrigerator is operated at low temperature due to supercooling of water in the course of the phase change from solid to liquid.

† Corresponding Author: nkchung@chosun.ac.kr; Phone.+82-62-230-7175; FAX.+82-62-230-7175

Materials that can store low temperature solidification latent heat are organic/inorganic chemicals, eutectic salt systems and clathrate compounds. A clathrate compound is a material that host (water; H_2O) molecule of hydrogen bond forms cage and guest (Gas) molecule is included into it and combined. Crystallization of hydrate is generated at higher temperature than that of ice from pure water. And physical properties according to temperature are stable and congruent melting phenomenon occurs without phase separation and it has a relatively high latent heat. But clathrate compound still has supercooling problems. TMA (Tri-methyl-amine, $(CH_3)_3N$), the third amine series, is a colorless gas and soluble in water, ether and alcohol. A TMA gaseous molecule that is mixed with water is included by water molecule in the hydrogen bond at a temperature of phase change and forms a clathrate compound of cluster type [1, 2].

This study was conducted to investigate the cooling characteristics of the TMA-water clathrate compound including of 20~25 wt% as a low temperature latent heat storage material. Ethanol (CH_3CH_2OH) was added and its cooling characteristics were studied experimentally to restrain the supercooling of TMA-water clathrate.

2. Experiment devices and method

In this study, the experimental device was prepared as in the following Figure 1 to measure cooling characteristics of TMA-water clathrate compound. A Pyrex bottle was sealed with epoxy and silicon because K-type thermocouple was installed. 20~25wt% of TMA was added to water in each Pyrex bottle and Pyrex bottle that was filled up to 60g was maintained at 20℃ in high temperature experiment reservoir. After that, this was refrigerated at low temperature experiment reservoir that cooling source temperature was controlled at -5℃ constantly. The next 0.1wt%, 0.3wt% and 0.5wt% of ethanol was added to TMA 25wt%-water in each Pyrex bottle and Pyrex bottle that was filled up to 60g was maintained at 20℃ in high temperature experiment reservoir. After that, this was refrigerated at low temperature experiment reservoir in which the cooling source temperature was maintained at -6℃, -7℃ and -8℃ constantly. Because supercooling depends on the volume and purity of the solution, cooling rate, container surface condition, and agitation state of the solution, the same container was used and its weight was maintained for accurate results of experiment and the cooling source temperature was fixed for constant cooling rate in this study.
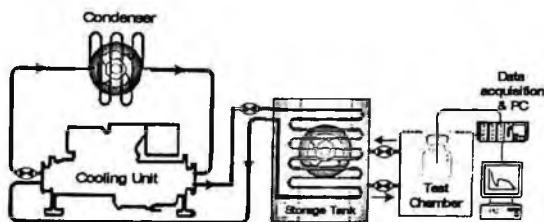
Fig. 1. Schematic diagram of experimental apparatus

The Test Chamber that was prepared and used in this study was made sufficiently bigger than Pyrex bottle for reliability. The Test Chamber and the Storage Tank were connected by circulating pump to maintain a constant cooling source temperature during experiment. The Test Chamber was insulated by using a thickness of 100mm insulating material to minimize influence from outside. A thermocouple was installed to measure temperature. Phase change temperature and supercooling degree were analyzed and averaged obtain cooling characteristics data of prepared TMA 25wt%-water clathrate compound by adding ethanol as per weight concentration.

3. Experimental result and discussion

3.1.1. *Phase change temperature*

In this study, phase change temperature that was solidified as cluster type while it was cooled at each cooling source temperature and maintained at constant temperature was defined as a phase change temperature. Figure 2 and 3 show average phase change temperature graph of 20~25wt% of TMA-water clathrate compound and 0.1wt%, 0.3wt% and 0.5wt% of ethanol is added to TMA 25wt%-water clathrate compound.

The phase change temperature at this point was 5.4~5.8 °C on average according to the weight concentration of TMA at cooling source temperature of -5 °C which was higher than that of pure water, and as the weight concentration of TMA became larger, the phase change temperature was found to be higher. Especially, a clathrate compound with 25wt% of TMA showed an average of 5.8 °C of phase transition temperature which was the highest of all.

The phase change temperatures of the TMA 25wt%-water clathrate compound in the case in which ethanol was not added were 5.5, 5.3 and 5.1 °C respectively according to cooling source temperatures of -6 °C, -7 °C and -8 °C. When 0.1 and 0.3wt% of ethanol were added to this, the average phase change temperatures were 5.4 °C and 5.1 °C, 5.3 °C and 5.2, 5.0 °C respectively. And in

the case in which 0.5wt% of ethanol was added, average temperature was 3.8 ℃ and it was the minimum phase change temperature.

TMA 25wt%-water clathrate compound was the material that showed congruent melting phenomenon without phase separation mechanism and phase change temperature was changed because gas molecules were included to hydrogen bonds in the water molecules and crystallization of hydrate was generated at a higher temperature than pure water. And phase change temperature was varied by adding ethanol because of colligative properties of the solution. Phase change is occurred from limitation of cluster segmentation movement and it is because induced time and cluster size are different until complete crystal is formed. TMA 25%wt-water clathrate compound by hydrogen bond has the characteristic of a high phase change temperature but it is considered that phase change temperature is lowered because the freezing point depression phenomenon occurs by adding an additive.
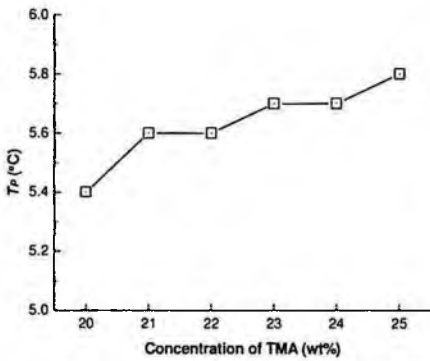

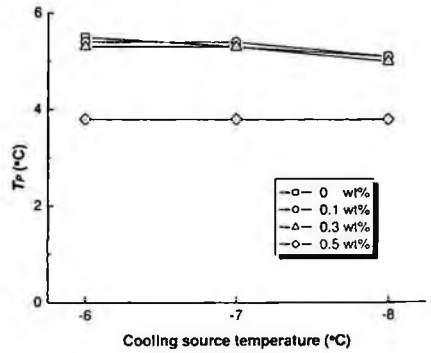Fig. 2. The phase change temperature as weight concentration of TMA at cooling source temperature of -5 ℃

Fig.e 3. The phase change temperature of TMA 25wt%-water clathrate compound with ethanol at various cooling source temperature

3.1.2. *Supercooling*

In this study, suppercooling degree (ΔT) was the difference between phase change temperature (T_P) and minimum supercooling temperature (T_S) and calculated by Equation (1). Figure 4 and 5 shows average supercooling degree graph.

$$\Delta T = T_P - T_S [°C] \tag{1}$$

If a clathrate compound which contains TMA per weight concentration was cooled to its cooling source temperature of -5 ℃, pure water was cooled to its

cooling source temperature without withdrawing from a supercooled state, but, in the presence of TMA, the water showed a phase change by withdrawing from a supercooled state after maintaining its liquefied state to a certain extent. The average supercooling degree decreased as the weight concentration of TMA was higher and especially in case of a clathrate compound with 25wt% of TMA, the mean temperature was shown to be the lowest at 8.0℃.
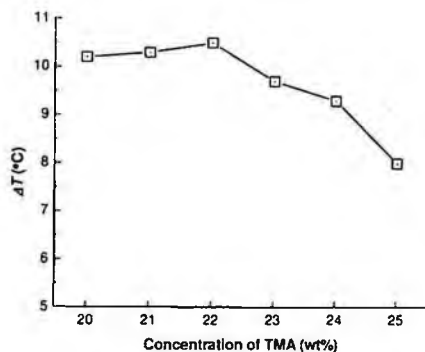

Fig. 4. The supercooling degree as weight concentration of TMA at cooling source temperature of -5℃
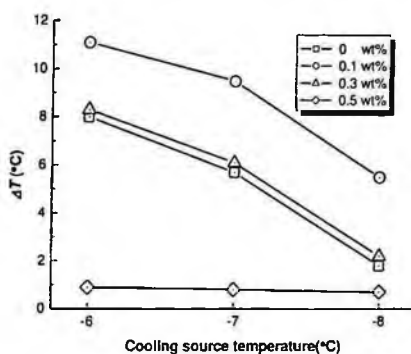
Fig. 5. The supercooling degree of TMA 25wt%-water clathrate compound with ethanol at various cooling source temperature

In this manner, it could be confirmed that the supercooling degree was decreased and the retention time of liquid phase was shortened as the weight concentration of TMA became higher. And the cooling process as liquid could be considered to affect the supercooling. It can be concluded that the formation of the clathrate compound of the water molecules and TMA gas molecules is affected by the weight concentration of TMA. Especially, in the case of a clathrate compound with a TMA concentration of over 23wt%, a suppressing effect on supercooling is significant and the activation level for forming a clathrate compound is considered to increase. And this is considered as the speed of TMA molecules becoming a clathrate compound and forming a cluster is increased by activating the hydrogen bonding of the water molecules since the enthalpy is increased as the weight concentration of TMA becomes higher.

The average supercooling degrees of TMA 25wt%-water clathrate compound in which ethanol was not added were 8.0℃ and 5.7, 1.8℃ at cooling source temperatures of -6℃, -7℃ and -8℃. The average supercooling degrees in the case that 0.1wt% and 0.3wt% of ethanol was added to this respectively are 11.1, 9.5, 5.5℃ and 8.3, 6.1, 2.2℃. In the case in which 0.5wt% of ethanol was added, the average supercooling degrees were 0.9℃ and 0.8, 0.7℃ (minimum)

respectively according to cooling source temperature and it had the effect of restraining supercooling.

We can confirm that supercooling was improved by adding 0.5wt% of ethanol to TMA 25wt%-water clathrate compound. In the case of pure water, phase is changed from liquid to solid by generation of homogeneous or non-homogeneous nuclear, but in the case of TMA 25wt%-water clathrate compound, TMA gas molecules are included in the hydrogen bonds in water molecules and cluster is formed. Hydrogen bond of the host molecule is activated by additive, a ethanol, and inclusion phenomenon of the guest molecule, and the cluster forming rate is increased. Therefore, residence time in liquid phase from initial cooling temperature to minimum supercooling temperature is shortened and supercooling degree is reduced and supercooling is restrained.

4. Conclusion

(1) The phase change temperature was 5.4~5.8℃ on average according to the weight concentration of TMA at a cooling source temperature of -5℃. Especially, a clathrate compound with 25wt% of TMA showed an average of 5.8℃ of phase change temperature which was the highest of all. And Phase change temperature was decreased by freezing point depression phenomenon in the case in which ethanol was added. Especially, when 0.5wt% of ethanol was added, it was minimized to 5.1℃ and 5.0, 3.8℃ according to cooling source temperature of -6℃ and -7℃, -8℃.

(2) The supercooling degree was decreased as the weight concentration of TMA was higher and especially in the case of a clathrate compound with 25 wt% of TMA, the supercooling degree was shown to be the lowest at 8.0℃. And when 0.5wt% of ethanol was added, minimum average supercooling degrees were 0.9℃ and 0.8, 0.7℃ according to cooling source temperature and it showed restraint effect of supercooling.

References

1. J. H. Kim, N. K. Chung and S. H. Kim, C. O. Kim, The Effects of Additives on the Cooling Characteristic of a Clathrate Compound., *Korean Journal of Air-Conditioning and Refrigeration Engineering*, Vol. 17, No. 2, pp. 125-130 (2005).
2. C. O. Kim, J. H. Kim and N. K. Chung, A Study on the Cooling Characteristics of TMA Clathrate Compound with Additives., *Key Engineering Materials*, Vols. 326-328, pp. 1275-1278 (2006).

OPTICAL CHARACTERIZATION OF SENSORY RHODOPSIN II THIN FILMS USING A NEAR-FIELD MICROWAVE MICROSCOPE[*]

SONGHUI KIM, YOUNGWOON YOON, AHREUM CHOI
KWANGHWAN JUNG, KIEJIN LEE

*Department of Physics and Interdisciplinary Program of Integrated Biotechnology
Sogang University, Seoul 121-742, Korea*

BARRY FRIEDMAN

Department of Physics, Sam Houston State University, Huntsville, Texas 77341, USA

TAKAYUKI ISHIBASHI

*Department of Materials Science and Technology, Nagaoka, Niigata University of
Technology,1603-1 Kamitomiokamachi, Nagaoka, Niigata 940-2188, Japan*

We studied the electro-optical properties of the Sensory Rhodopsin II using a near-field
microwave microscope (NFMM). In order to characterize the optical properties of
Natronomonas pharaonis Sensory Rhodopsin II (NpSRII), we measured the absorption
spectra and the transient differences of sensory rhodopsin II (SRII) from Natronomonas
pharaonis using a UV/VIS spectrophotometer with a Nd-Yag Laser at the wavelength
532 nm. The observed photo-cycle reaction was discussed and confirmed by measuring
the microwave reflection coefficient S_{11} and compared with the results of a photo-cycle
of NpSRII.

1. Introduction

Rhodopsin is known as a photoreceptor pigment with a retinal as a
chromatophore via a protonated Schiff base and consists of seven α-helical
transmembrane segments. In our experiment the sensory rhodopsin II (SRII)
from Natronomonas pharaonis was expressed in the E. coli UT5600 with a
retinal biosynthesis system and was purified with Ni+2-NTA affinity
chromatography in the presence of 0.02 % DM (Dodecyl Maltoside). Previous
studies have shown that the physical properties of NpSRII do not change

significantly with variation in ion concentration, pH, heat and detergent. NpSRII in the presence of UV light in blue-green range circulates in photo-cycle with five major spectroscopic defined intermediates, known as K, L, M, N, and O [1-3]. NpSRII has a characteristic absorption spectrum with a maximum peak at 500 nm that was shifted to the NpSRII-M state which exhibited a blue-shifted spectrum (400 nm) as a ground state for 100 ms, and then undergo thermal decay via O photo-intermediate.

In this study, in order to investigate the electro-optical properties of NpSRII, we took advantage of the non-contact and noninvasive evaluation capabilities of the near-field microwave microscope (NFMM). This method complements existing physical methods in the Rhodopsin field such as UV/VIS spectroscopy, FTIR spectroscopy or Raman spectroscopy. The NFMM technique has been developed for the microwave- and millimeter wave ranges [4-8] and can directly evaluate important physical properties of samples, such as dielectric constant, conductivity and permeability with high sensitivity. In this paper, we investigated the electro-optical properties of NpSRII using a NFMM and compared with the absorption spectrum of the photo-cycle of NpSRII in the process of electro-optic variations.

2. Experiment

The basic experimental setup of our NSMM is presented in Fig. 1. The stainless-steel probe tip with a diameter of 50 μm was attached to one prong of a quartz tuning fork and directly coupled to a high-quality dielectric resonator. The probe tip was oriented perpendicular to the sample surface. The distance between tip and sample was maintained about 10 nm by a tuning fork distance control system [9-12].
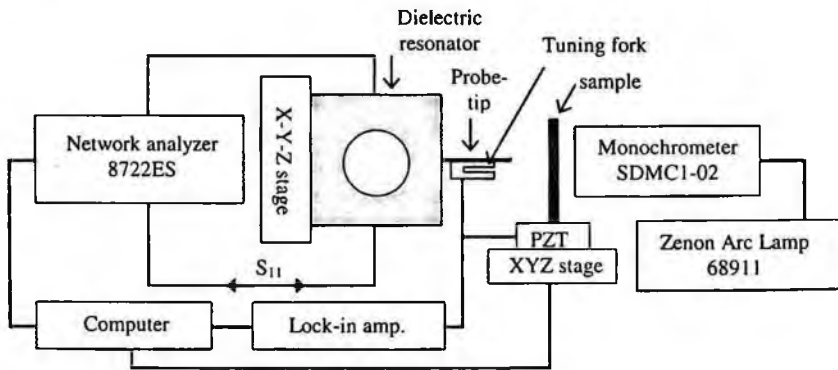

Fig. 1. Schematic of the basic experimental setup of the NSMM with a tuning fork distance control system. The sample used after dropped NpSRII solution on the glass substrate and dried three times, respectively.

A network analyzer (Agilent 8722ES) was used to measure the microwave reflection coefficient S_{11}. A Xenon ArcLamp (68911) was used as a light source. We applied a monochromatic light souce obtained by a monochrometer (SDMC1-02) to the sample surface.

We measured the absorption spectra and the transient difference of NpSRII using a UV/VIS spectrophotometer (Shimadzu UV-2450) with Nd-Yag Laser at about 532 nm. The observed photo-cycle reaction was confirmed by measuring the microwave reflection coefficient S_{11} at an operating frequency of $f = 3.5$-5.0 GHz and compared with the results of a photo-cycle of NpSRII. We also measured the microwave reflection coefficient S_{11} in accordance with a measurement environment of the fluorescent lamp; the dark and the monochromatic light at 548 nm.

3. Results and Discussion

Figure 2 shows the frequency-sweep data for the reflection coefficient S_{11} measured under the UV/VIS light source and dark conditions. The microwave reflection coefficient S_{11} of NpSRII shows higher value under the light source than that for the dark because NpSRII-O was generated. This process of creation of NpSRII-O seems to bring an increase in the value of dielectric constants of NpSRII.

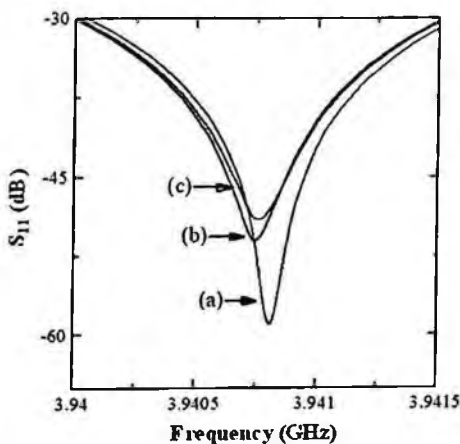
Fig. 2. The measured microwave reflection coefficient S_{11} of (a) NaCl solution with the concentration 25 %, NpSRII (b) under the dark and (c) the light source conditions, respectively.

Figure 3 shows the measured absorption spectrum of NpSRII at a wavelength from 350 nm to 600 nm using a UV/VIS spectrophotometer and Nd-Yag Laser. The ground state of photo intermediates spectra of NpSRII, NpSRII-M state, and NpSRII-O state were observed at 498 nm, 400 nm, and 550 nm during the photo-

cycle. For the absorbance was excited at a wavelength from 450 nm to 550 nm, the characteristic curve of molecules of NpSRII was observable at about 460 nm and the ground state of NpSRII was observed at 498 nm. The observed characteristic curve in range of around 420 nm was caused by the cytochrome C protein of a membrane.
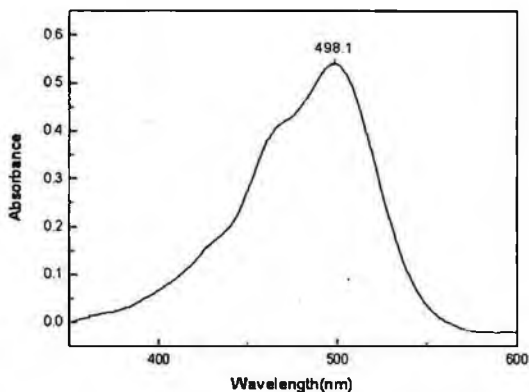

Fig. 3. Absorption spectrum of NpSRII measured in the range of 350-600 nm wavelengths. The ground state of photo intermediates spectra of NpSRII, NpSRII-M state, and NpSRII-O state were observed at 498 nm, 400 nm, and 550 nm during the photo-cycle.
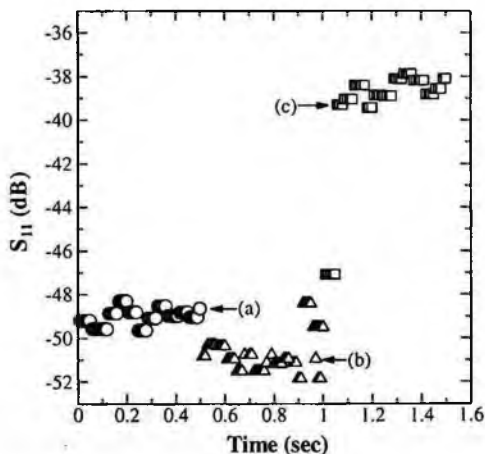

Fig. 4. Microwave reflection coefficient S_{11} of NpSRII under (a) the fluorescent lamp, (b) the dark condition, and (c) the monochromatic light at a wavelength of 548 nm.

Figure 4 shows the time dependence of microwave reflection coefficient S_{11} measured 50 times with 0.01 sec time delay under (a) the fluorescent lamp, (b) the dark condition, and (c) the monochromatic light at a wavelength of 548 nm. Due to the largest conformational change of NpSRII molecules the monochromatic light, the microwave reflection coefficient S_{11} was highest in this case.

We compare the measured absorbance time dependence for a photocycle of NpSRII with the measured microwave reflection coefficient S_{11}.
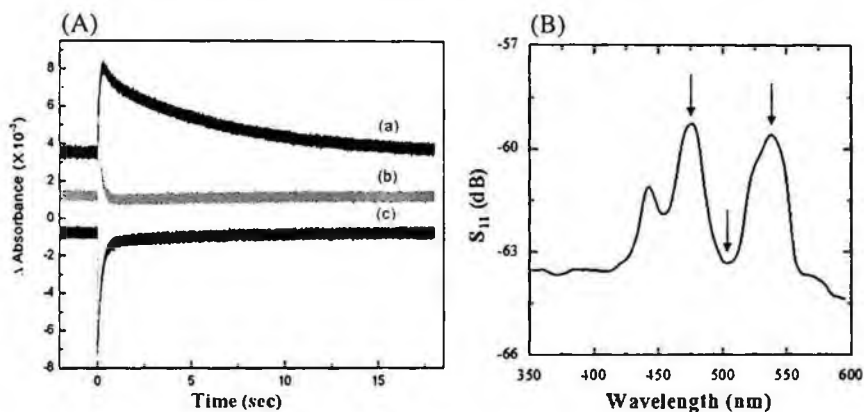

Fig. 5. (A) Time dependence absorbance characteristic of NpSRII for (a) the ground state at 500 nm, (b) NpSRII-M state at 400 nm and (c) NpSRII-O state at 550 nm. (B) Wavelength dependence microwave reflection coefficient S_{11} of NpSRII.

Figure 5(A) shows the photo-cycle reaction of NpSRII absorbance characteristic dependence on time for (a) the ground state at 500 nm, (b) NpSRII-M state at 400 nm and (c) NpSRII-O state at 550 nm, respectively. The observed peaks corresponded to when NpSRII received energy and showed an excited state in the photo-cycle. Figure 5 (B) shows the microwave reflection coefficient S_{11} dependence on wavelength for NpSRII. Here, for the range around 475 nm we found that the characteristic curve indicate the NpSRII-N state.

4. Summary

The electro-optical properties of NpSRII were observed using a NFMM technique and these results were compared with absorption spectra obtained from a UV/VIS spectrophotometer. We demonstrated a noninvasive measurement possibility using NFMM for studies on the optical properties of bio-material specimens of NpSRII.

References

1. J. L. Spudich, C. S. Yang, K. H. Jung and E. N. Spudich, *Annu. Rev. Cell Dev. Biol.* **16**, 365 (2002).
2. J. Sasaki and J. L. Spudich, *Biochim. Biophys. Acta.* **1460**, 230 (2000).
3. Chizhov, G. Schmies, R. Seidel, J.R. Sydor, B. Luttenberg and M. Engelhard, *Biophys. J.* **75**, 999 (1998).
4. M. Tabib-Azar, P. Pathak, G. Ponchak and S. Le Clair, *Rev. Sci. Instrum.* **70**, 2783 (1999).
5. A. Subramanian, P. Oden, S. Kennel, K. Jacobson, R. Warmack, T. Thundat and M. Doktycz, *Appl. Phys. Lett.* **81**, 385 (2002).
6. M. Abu-Teir, M. Golosovsky, D. Davidov, A. Frenkel and H. Goldberger, *Rev. Sci. Instrum.* **72**, 2073 (2001).
7. S J. Kim, S. Kim, K. Lee, J. Lee, D. Cha and B. Friedman, *Meas. Sci. Technol.* **14**, 7 (2003).
8. A. Lann, M. Golosovsky, D. Davidov and A. Frenkel, *Appl. Phys. Lett.* **73**, 2823 (1998).
9. K. Sinniah, J. Cheng, S. Terrettaz, J.E. Reutt-Robey and C.J. Miller, *J. Phys. Chem.* **99**, 14500 (1995).
10. B. Friedman, M. Gaspar, S. Kalachikoc, K. Lee, R. Levisky, G. Shen and H. Yoo, *J. Am. Chem. Soc.* **127**, 9666 (2005).
11. A. Babajanyan, J. Kim, S. Kim, K. Lee and B. Friedman, *Appl. Phys. Lett.* **89**, 183504 (2006).
12. S. Kim, H. You, K. Lee, B. Friedman, M. Gaspar and R. Levicky, *Appl. Phys. Lett.* **86**, 153506 (2005).

Advanced
Nondestructive Evaluation II

Proceedings of the International Conference on ANDE 2007

This volume comprises papers presented at the 2nd International Conference on Advanced Nondestructive Evaluation (ANDE 2007) held in Busan, Korea, on October 17–19, 2007. Many of the excellent papers included in this book show the current state of nondestructive technologies, which are experiencing rapid progress with the integration of emerging technologies in various fields. As such, this volume provides an avenue for both specialists and scholars to share their ideas and the results of their findings in the field of nondestructive evaluation.

World Scientific